Imperial College London

Doctoral Thesis

Identifying the modes and mechanisms of action of transmission-blocking antimalarials against *Plasmodium falciparum*

Author:

Sabrina Yahiya

Supervisors:

Prof. Jake Baum

Prof. Matthew Fuchter

A thesis submitted in fulfillment of the requirements

for the degree of Doctor of Philosophy

in the

Baum Laboratory

Department of Life Sciences and Chemistry

December 15, 2021

Statement of Originality

I, Sabrina Yahiya, declare that this thesis titled, "Identifying the modes and mechanisms of action of transmission-blocking antimalarials against *Plasmodium falciparum*" and the work presented in it are my own. I confirm that:

- This work was performed while in candidature for a research degree at Imperial College London.
- Any work presented in thesis that has previously been submitted for another degree at Imperial College London or any other institution has been clearly stated.
- Any consultation of the published work of others is always clearly attributed.
- Where any published work of others has been used in this thesis, the source has been appropriately cited.
- Where work presented here has been performed by myself jointly with others, contributions made by myself and others have been stated. With the exception of this, all work presented in this thesis is entirely my own.

Signed:

Date: December 15, 2021

Copyright Declaration

The copyright of this thesis rests with the author. Unless otherwise indicated, its contents are licensed under a Creative Commons Attribution-Non Commercial 4.0 International Licence (CC BY-NC).

Under this licence, you may copy and redistribute the material in any medium or format. You may also create and distribute modified versions of the work. This is on the condition that: you credit the author and do not use it, or any derivative works, for a commercial purpose.

When reusing or sharing this work, ensure you make the licence terms clear to others by naming the licence and linking to the licence text. Where a work has been adapted, you should indicate that the work has been changed and describe those changes.

Please seek permission from the copyright holder for uses of this work that are not included in this licence or permitted under UK Copyright Law.

IMPERIAL COLLEGE LONDON

Abstract

Faculty of Natural Sciences
Department of Life Sciences and Chemistry

Doctor of Philosophy

Identifying the modes and mechanisms of action of transmission-blocking antimalarials against *Plasmodium falciparum*

by Sabrina Yahiya

Phenotypic drug screening has transformed the antimalarial development pipeline, facilitating the discovery of compounds targeting unexplored parasite proteins at a drastically accelerated rate. Breaking the cycle of malaria transmission is crucial to eradication and centres around inhibition of the sexual stage gametocytes and gametes. Transmissible sexual stages represent a population bottleneck of the *Plasmodium* life-cycle which face little selective pressure and are hence a desirable target of drug intervention. Recently discovered in a phenotypic screen, the *N*-((4-hydroxychroman-4-yl)methyl)-sulphonamide (N-4HCS) compounds potently inhibit *P. falciparum* male gamete formation (microgametogenesis) in the mosquito. By combining study of the remarkable *Plasmodium* gametocyte cellular biology with medicinal chemistry and chemical proteomics, here we performed a detailed analysis of N-4HCS compound activity.

Adhering to a traditional drug developmental pipeline, we first performed N-4HCS hit-to-lead development and yielded compounds with activity in the nanomolar concentration range and favourable safety profiles. Furthermore, an N-4HCS photoaffinity probe was utilised in a proteome-wide photoaffinity labelling study, identifying the *P. falciparum* sexual stage-specific protein, Pfs16, as the compound target. Notably, the Cellular Thermal Shift Assay confirmed label-free specificity of N-4HCS compounds to Pfs16. Flow cytometry and phase-contrast, widefield-fluorescence and electron microscopy revealed compounds exclusively inhibited microgametogenesis, with a cellular phenotype consistent with published reports on the targeted gene disruption of *Pfs16*. We therefore present the 16kDa parasitophorous vacuole membrane protein, Pfs16, as a desirable antimalarial target and the N-4HCS compounds as potent candidates for future development. Additionally, a live-cell fluorescence microscopy workflow was devised to enable visualisation of microgametogenesis from the onset of activation through to exflagellation. Crucially, our imaging approach was applicable to drug discovery and is accessible to the malaria research community, thereby facilitating future study of transmission-blocking drug candidates. This thesis hence addressed the urgent requirement for novel antimalarial interventions, developing and aiding future discovery of transmission-blocking drugs.

Acknowledgements

First and foremost, I would like to extend my sincerest gratitude to my supervisor, Jake Baum. The guidance and support you have provided me over the years made this project possible and for that, I am truly grateful. Your continued enthusiasm in the '007' project, invaluable knowledge of *Plasmodium* and passion for science has inspired me throughout my time in the lab. I am hugely thankful for all the patience and compassion you have shown me. Thank you for being a wonderful mentor.

I would also like to thank Matt Fuchter for being a great co-supervisor throughout my time at Imperial College. The project was made possible with your expertise in chemistry and drug discovery, from which I have learned so much.

I would like to thank Michael Delves for his great mentorship and guidance on all things transmission and antimalarial discovery. A huge thank you to gametocyte-whisperer Ursula Straschil for so generously sharing her wisdom on *Plasmodium* culture, equipping me with all the tricks to keep 'gams' happy and healthy throughout my project.

Thank you to Ed Tate and Anna Barnard for your guidance on the chemistry and chemical biology aspects of this project. Without members of the Fuchter, Tate and Barnard groups, this project would not have been possible. With special thanks to Charlie Saunders, Ainoa Rueda-Zubiaurre, Oliver J. Fischer, Xiaojun Hu, Sachi Sharma and Junting Shen for generously synthesising and sharing the compounds that the project centred around. An additional thanks to Charlie Saunders, Sarah Hassan, Henry Benns and Ryan Howard for their huge generosity, with both hands-on support and guidance with the photoaffinity labelling experiments.

This project was made possible by the combined efforts of many collaborators who I would like to acknowledge, including Gema Vizcay-Barrena (King's College London) for assisting with electron microscopy; Jane Srivastava and Jessica E Rowley for their training and assistance in all flow cytometry experiments; David Gaboriau for assistance with image analysis, including the continual trouble-shooting and creation of the automated batch-deconvolution algorithm; Beatriz Urones Ruano, Ollala Sanz and Sonja Ghidelli-Disse (GSK and Cellzome) for valuable discussions on target identification; Mathieu Brochet and colleagues for assisting the design of assays to measure microgametocyte ploidy; members of the Baker, Ishino, Lasonder, Marti, Sauerwein and Van Voorhis labs for their generosity with parasite lines, drugs and antibodies required to carry out this project and Robert Sinden for sharing his unrivalled knowledge of microgametogenesis in discussions around live-imaging. With added thanks to members of the Baum lab for their guidance, such as Silvia Haase for help with electron microscopy and protein assay design; Kathrin Witmer for the continued guidance on gametocyte biology, especially for studies of sexual conversion; Adrian Najer for advice and discussions around the project; George Ashdown for the direction in designing the live-imaging platform, and to Holly Smith and Sarah Jordan for all the hard work in producing imaging data. For all the support I've received from fellow Imperial staff and students, including Gaya, thank you.

I would also like to acknowledge EPSRC for generously funding this project and the Dundee Drug Discovery unit for compiling the Global Health Chemical Diversity Library.

To all the members of the Baum Lab, past and present, thank you for your friendship, moral support and guidance. With special thanks to all members of the gametocyte team, including Ursula, Michael, Kathrin, Farah, Eliana, Irene, Oriol, Sarah, Alisje, Karolina, Toyin and Dave for the 'gam lunches', best company during long days in the CL3 and all the sacrificed weekends. Thanks to George and Sarah for being the dream team in developing our live-imaging study. I am grateful to have made some good friends along this journey.

To my ever-growing and hugely supportive family, thank you. I would like to make special thanks to my big brother, Bhaiya, for 'celebration-dancing' your way through each of my big moments. To Sue and Af, thank you for your sisterly support. With a very special thanks to the little ones, Idrees, Lana, Inayah and Eva, for always being rays of sunshine. Finally, I would like to thank Amma for the support and endless sacrifices that led me here.

Shehab, I will always be grateful to you for encouraging me throughout this journey. Thank you for your boundless support, patience and belief in me. I dedicate this to you.

Publications

Works published during PhD candidature, relating to this thesis:

- Delves, M. J. et al. (2018). "A high throughput screen for next-generation leads targeting malaria parasite transmission". In: *Nat Commun* 9.1, p. 3805. DOI:10.1038/s41467-018-05777-2.

- Rueda-Zubiaurre, A. et al. (2019). "Structure-activity relationship studies of a novel class of transmission blocking antimalarials targeting male gametes". In: *J Med Chem*. DOI:10.1021/acs.jmedchem.9b00898.

- Yahiya, S. et al. (2019). "The antimalarial screening landscape-looking beyond the asexual blood stage". In: *Curr Opin Chem Biol*, 50, pp. 1–9. DOI:10.1016/j.cbpa.2019.01.029.

Works currently in review and accessible in pre-print form, relating to this thesis:

- Yahiya, S. et al. (2021). "*Plasmodium falciparum* protein Pfs16 is a target for transmission-blocking antimalarial drug development". In: *bioRxiv*, p. 2021.06.14.448287. DOI:10.1101/2021.06.14.448287.

- Yahiya, S. et al. (2021). "4D live-cell imaging of microgametogenesis in the human malaria parasite *Plasmodium falciparum*". In: *bioRxiv*, p. 2021.07.28.454129. DOI:10.1101/2021.07.28.454129.

Works published during PhD candidature, unrelated to this thesis:

- Witmer, Kathrin et al. (2020). "Transmission of artemisinin-resistant malaria parasites to mosquitoes under antimalarial drug pressure". In: *Antimicrobial Agents and Chemotherapy*, 65.1, e00898–20. DOI:10.1128/AAC.00898-20.

- Davidson, Mira S. et al. (2021). "Automated detection and staging of malaria parasites from cytological smears using convolutional neural networks". In: *Biological Imaging*, pp. 1–22. DOI:10.1017/S2633903X21000015.

Contents

Statement of Originality **3**

Copyright Declaration **5**

Abstract **7**

Acknowledgements **8**

List of Figures **18**

List of Tables **19**

1 Introduction **21**
1.1 Malaria . . . 21
1.2 The biology of *Plasmodium* . . . 24
1.2.1 The Apicomplexan phylum . . . 24
1.2.2 The *Plasmodium* genus . . . 25
1.2.3 The *Plasmodium* lifecycle . . . 27
1.2.3.1 Liver Stages . . . 27
1.2.3.2 Asexual blood stage replication . . . 30
1.2.3.3 Sexual development . . . 33
1.2.3.4 Gametocytogenesis . . . 37
1.2.3.5 The gametocyte proteome . . . 44
1.2.3.6 Sexual differences . . . 45
1.2.3.7 Translational Repression . . . 45
1.2.3.8 Gametogenesis . . . 46
1.2.3.9 Microgametogenesis . . . 46
1.2.3.10 Macrogametogenesis . . . 49
1.2.3.11 Signalling cascade . . . 49
1.2.3.12 Mosquito stages . . . 50
1.2.3.13 'Omics' and AI for *Plasmodium* life cycle study . . . 53
1.3 Malaria treatment strategies . . . 54
1.3.1 Antimalarial drugs . . . 55
1.3.1.1 Artemisinin combination therapies . . . 55
1.3.1.2 Artemisinin and derivatives . . . 55
1.3.1.3 4-aminoquinolines and aminoalcohols . . . 58
1.3.1.4 Alternative drugs . . . 58

1.3.2 Drug discovery pipeline . . . 59
1.3.3 Vector control . . . 60
1.3.4 Vaccines . . . 62
1.4 The antimalarial screening landscape . . . 63
1.4.1 Asexual blood stage screens (TCP-1) . . . 64
1.4.2 Pre-erythrocytic screens (TCPs 3-4) . . . 66
1.4.3 Transmission blocking (TCP-5) screens and assays . . . 67
1.4.3.1 Standard Membrane Feeding Assay . . . 68
1.4.3.2 Sex and stage specificity . . . 68
1.5 The Global Health Chemical Diversity Library screen . . . 71
1.5.1 GHCDL screening framework . . . 71
1.5.2 Chemical profiling . . . 73
1.5.3 *In vivo* transmission-blocking activity . . . 74
1.5.4 The N-4HCS compounds . . . 76
1.6 Aims and hypotheses . . . 77

2 Materials and methods **79**
2.1 Materials and reagents . . . 79
2.2 *In vitro* culture of *Plasmodium falciparum* . . . 80
2.3 *P. falciparum* Male Gamete Formation Assay . . . 81
2.4 HepG2 Viability . . . 82
2.4.1 HepG2 cell culture . . . 82
2.5 Alamar Blue viability assay . . . 82
2.6 Target identification and validation . . . 83
2.6.1 Photoaffinity labelling of live gametocytes . . . 83
2.6.2 Gametocyte purification by density barrier isolation . . . 84
2.6.3 Cell lysis by sonication . . . 84
2.6.4 CuAAC and protein precipitation . . . 84
2.6.5 nLC-MS/MS sample pulldown . . . 85
2.6.6 Digestion and TMT labelling . . . 86
2.6.7 nLC-MS/MS preparation and acquisition . . . 86
2.6.8 Proteome Database Search and Analysis . . . 87
2.7 Target validation by photoaffinity labelling . . . 87
2.7.1 Streptavidin-based enrichment . . . 87
2.7.2 Separation by gel glectrophoresis and fluorescence detection . 88
2.7.3 Immunoblot . . . 88
2.8 Target validation by CETSA . . . 88
2.8.1 Production of parasite cell lysate . . . 88
2.8.2 Cellular Thermal Shift Assay . . . 89
2.8.2.1 Melting curve . . . 89
2.8.2.2 Isothermal Dose Response . . . 90
2.8.2.3 T_{Agg} extrapolation and dose response . . . 90
2.9 *Pf*2004/164-tdTomato sexual conversion assay . . . 91
2.9.1 *Pf*2004/164-tdTomato parasite preparation . . . 91
2.9.2 N-4HCS treatment . . . 91
2.9.3 Conversion rate by flow cytometry . . . 92

2.10 DDD01035881 activity window . . . 93
2.10.1 Activated microgametocyte treatment . . . 93
2.10.2 Exflagellation rate quantification . . . 93
2.11 Phenotypic characterisation by microscopy . . . 94
2.11.1 Parasite treatment and fixation for immunofluorescence assays 94
2.11.2 Immunofluorescence labelling . . . 94
2.11.3 Electron microscopy . . . 95
2.12 Ploidy determination by flow cytometry . . . 96
2.12.1 Sample preparation . . . 96
2.12.2 Flow cytometry . . . 97
2.13 Live-cell fluorescence imaging of microgametogenesis . . . 97
2.13.1 Live gametocyte staining . . . 97
2.13.2 Live widefield microscopy of microgametogenesis . . . 98
2.13.2.1 Timelapse deconvolution . . . 98
2.13.2.2 Timelapse analysis . . . 99

3 Lead development of the N-4HCS series 101
3.1 Introduction . . . 101
3.2 Results . . . 103
3.2.1 Microgamete Formation Assay . . . 103
3.2.2 Insights into N-4HCS SAR . . . 104
3.2.3 Safety profiling . . . 108
3.3 Discussion . . . 110

4 N-4HCS target identification 113
4.1 Introduction . . . 113
4.2 Results . . . 115
4.2.1 Proteome-wide photoaffinity labelling . . . 115
4.2.1.1 N-4HCS photoaffinity probe . . . 115
4.2.1.2 Photoaffinity labelling workflow . . . 115
4.2.2 N-4HCS target identification by PAL . . . 118
4.2.3 PAL protein hits . . . 118
4.2.4 Sexual stage-specific hits . . . 120
4.2.5 Pfs16 and Pfg377 target validation by PAL . . . 122
4.2.6 Label-free target validation of Pfs16 and Pfg377 . . . 125
4.2.6.1 Cellular thermal shift assay . . . 126
4.2.6.2 Pfs16 and Pfg377 thermal stabilisation . . . 128
4.2.6.3 Isothermal dose response . . . 131
4.3 Discussion . . . 134

5 Phenotypic characterisation of the N-4HCS series 137
5.1 Introduction . . . 137
5.2 Results . . . 139
5.2.1 N-4HCS impact to gametocytogenesis . . . 139
5.2.1.1 *Pf*2004/164-tdTom sexual conversion assay . . . 139
5.2.1.2 Pfs16 and Pfg377 thermal stabilisation in stage I-III gametocytes . . . 143

5.2.2 N-4HCS phenotype during microgametogenesis . . . 148
5.2.2.1 The DDD01035881 activity window is consistent with Pfs16 function . . . 148
5.2.2.2 Microgametocyte DNA replication is not inhibited by N-4HCS treatment . . . 150
5.2.2.3 DDD01035881 cellular phenotype . . . 154
5.2.2.4 Microgametogenesis . . . 154
5.2.2.5 DDD01035881 cellular phenotype during microgametogenesis . . . 160
5.2.3 Inhibition of microgametogenesis regulators . . . 168
5.2.4 GHCDL hit phenotypes . . . 174
5.3 Discussion . . . 177

6 Live-cell imaging of *P. falciparum* microgametogenesis 181
6.1 Introduction . . . 181
6.2 Results . . . 184
6.2.1 Development of a live-cell fluorescence imaging protocol . . . 184
6.2.1.1 Stain optimisation . . . 184
6.2.1.2 Live-cell widefield microscopy . . . 186
6.2.2 Insights into microgametogenesis . . . 189
6.2.3 Cytoskeletal rearrangements . . . 189
6.2.3.1 Microtubule polymerisation . . . 189
6.2.3.2 Microgametocyte rounding . . . 191
6.2.4 Changes to DNA during microgametogenesis . . . 192
6.2.4.1 DNA segregation . . . 192
6.2.4.2 DNA replication . . . 192
6.2.5 Drug discovery application . . . 197
6.2.6 Live-cell phenotypes of known inhibitors . . . 198
6.2.6.1 Live-cell phenotype of PKG-inhibition . . . 198
6.2.6.2 Live-cell phenotype of CDPK4-inhibition . . . 202
6.2.7 Proteasome inhibition during microgametogenesis . . . 204
6.2.8 Novel insights by live-cell fluorescence microscopy . . . 205
6.3 Discussion . . . 208

7 Discussion 211
7.1 The developmental pipeline of *N*-4HCS compounds . . . 212
7.2 Facilitation of transmission-blocking identification studies . . . 215
7.3 Conclusions and future directions . . . 216

Bibliography 220

List of Figures

1.1 Global distribution of malaria in 2019 22
1.2 The *Plasmodium* lifecycle 28
1.3 Regulation of commitment to gametocytogenesis 36
1.4 Stage I-V *P. falciparum* gametocyte morphologies 38
1.5 Development of the gametocyte IMC 41
1.6 Electron micrographs from landmark studies of microgametogenesis . 47
1.7 Signalling pathways involved in regulation of gametogenesis 51
1.8 Profiles for antimalarial drug candidates 56
1.9 The antimalarial drug pipeline 61
1.10 The antimalarial phenotypic screening landscape and corresponding TCPs of the *Plasmodium* life cycle 65
1.11 Scope, phenotype and activity profiles derived from the DGFA 70
1.12 GHCDL screen workflow 72

3.1 **DDD01035881** structure 102
3.2 Microgamete formation assay (MGFA) 104
3.3 Summary of N-4HCS structure activity relationship (SAR) 105
3.4 Impacts of stereochemistry on N-4HCS activity 106
3.5 HepG2 Viability under N-4HCS treatment 109

4.1 Photoaffinity labelling for N-4HCS target identification 117
4.2 N-4HCS target identification by proteome-wide photoaffinity labelling 119
4.3 Pfs16 and Pfg377 target validation by photoaffinity labelling 123

4.4 Photoaffinity labelling validation by probe **8** and **DDD01035881** competition . . . 124
4.5 The cellular thermal shift assay workflow . . . 127
4.6 Optimisation of conditions for CETSA . . . 129
4.7 Full CETSA western blots utilised to derive protein melting curves . 130
4.8 Label-free CETSA validation of Pfs16 and Pfg377 binding . . . 131
4.9 Pfs16 CETSA melting curves under N-4HCS treatment . . . 132
4.10 Isothermal dose response (ITDR) CETSA of Pfs16 and **DDD01035881** 133

5.1 *Pf*2004/164-tdTom sexual conversion assay workflow . . . 141
5.2 *Pf*2004/164-tdTom flow cytometry gating strategy to measure sexual conversion . . . 142
5.3 Relative sexual conversion and gametocyte production rates of N-4HCS-treated *Pf*2004/164-tdTom parasites . . . 143
5.4 *P. falciparum* stage I-III gametocyte cellular thermal shift assay-derived western blots . . . 144
5.5 CETSA melting curves of Pfs16 and Pfg377 using *P. falciparum* stage I-III gametocyte lysate . . . 145
5.6 CETSA melting curves of N-4HCS-treated Pfs16 . . . 147
5.7 **DDD01035881** activity window and reversibility during microgametogenesis . . . 149
5.8 Gating strategy to measure ploidy of *Pf*DynGFP/*P47*mCherry microgametocytes . . . 151
5.9 *Pf*DynGFP/*P47*mCherry microgametocyte ploidy under drug treatment . . . 153
5.10 *P. falciparum* microgametogenesis . . . 155
5.11 Immunofluorescence time-course of *P. falciparum* microgametogenesis 157
5.12 *P. falciparum* microgametogenesis imaged by electron microscopy . . 159
5.13 Ultrastructure of *P. falciparum* gametocyte cellular traits . . . 160
5.14 **DDD01035881** phenotype during microgametogenesis by immunofluorescence . . . 162

5.15 **DDD01035881** disruption to Pfs16 and the PVM during microgametogenesis . . . 164
5.16 Ultrastructural **DDD01035881** phenotype during microgametogenesis 167
5.17 PKG inhibition phenotype during *P. falciparum* microgametogenesis . 169
5.18 CDPK4 inhibition phenotype during *P. falciparum* microgametogenesis 171
5.19 Cellular phenotypes of GHCDL compounds during microgametogenesis by immunofluorescence . . . 175
5.20 Predicted Pfs16 domain structure alignment . . . 178

6.1 Cellular events encompassed by microgametogenesis . . . 185
6.2 Live-cell fluorescence imaging of *P. falciparum* microgametogenesis workflow . . . 187
6.3 Cytoskeletal transformations of developing *P. falciparum* microgametes 190
6.4 DNA segregation and replication during *P. falciparum* microgametogenesis . . . 194
6.5 *P. falciparum* microgametogenesis erythrocyte egress mechanisms . . 195
6.6 Emergence of *P. falciparum* microgametes by exflagellation . . . 197
6.7 Microgametocyte cellular phenotypes upon PKG, CDPK4 and proteasome inhibition . . . 199
6.8 Microgametocyte microtubule polymerisation and morphological transformation under drug treatment . . . 201
6.9 Microgametocyte egress and DNA replication under drug treatment . 203
6.10 Novel observations on untreated and drug-treated microgametogenesis 207

List of Tables

1.1 **DDD01035881** activity profile 75

3.1 Structures and MGFA IC_{50}s of notable N-4HCS analogues 107

4.1 Structures and MGFA-derived IC_{50}s of GHCDL N-4HCS hits and derivatives for target identification and validation 116

4.2 Probe-protein interaction profile determined by nLC-MS/MS analysed photoaffinity labelling 121

A1 Full background-independent enrichment profile from nLC-MS/MS analysed photoaffinity labelling 242

A2 Full competed protein profile from nLC-MS/MS analysed photoaffinity labelling 243

Chapter 1

Introduction

1.1 Malaria

Malaria threatens half of the world's population, disproportionately impacting the World Health Organisation (WHO) African Region in which 94% of malaria cases and deaths were reported in 2019. The Americas, Eastern Mediterranean, South-East Asia and Western Pacific regions are among the other regions that are impacted by malaria (Figure 1.1). A huge 229 million cases and 409,000 deaths were reported in 2019, with children under the age of 5 accounting for 67% of total deaths and infants, pregnant women and HIV/AIDS patients being particularly vulnerable to malaria (World Health, 2020). Unicellular protozoan parasites of the genus *Plasmodium* are the causative agents of malaria. *Plasmodium* demonstrates remarkable cellular plasticity as it adapts over a complex lifecycle, transitioning between a vertebrate host and *Anopheles* mosquito vector. *P. falciparum*, the most virulent of *Plasmodium* species, accounts for the majority of malaria burden, causing 99.7% of WHO African Region cases in 2018 (World Health, 2019). Of the many *Plasmodium* species, *P. vivax*, *P. malariae*, *P. ovale* and *P. knowlesi* cause malaria in humans, additionally to *P. falciparum*.

Propelled by the Roll Back Malaria Initiative and United Nations Millennium Development Goals (MDGs), the turn of the millennium was a landmark moment in the global commitment to eliminate malaria (Bhatt et al., 2015). Concerted efforts resulted in a twenty-fold increase in funding, transforming the landscape of malaria

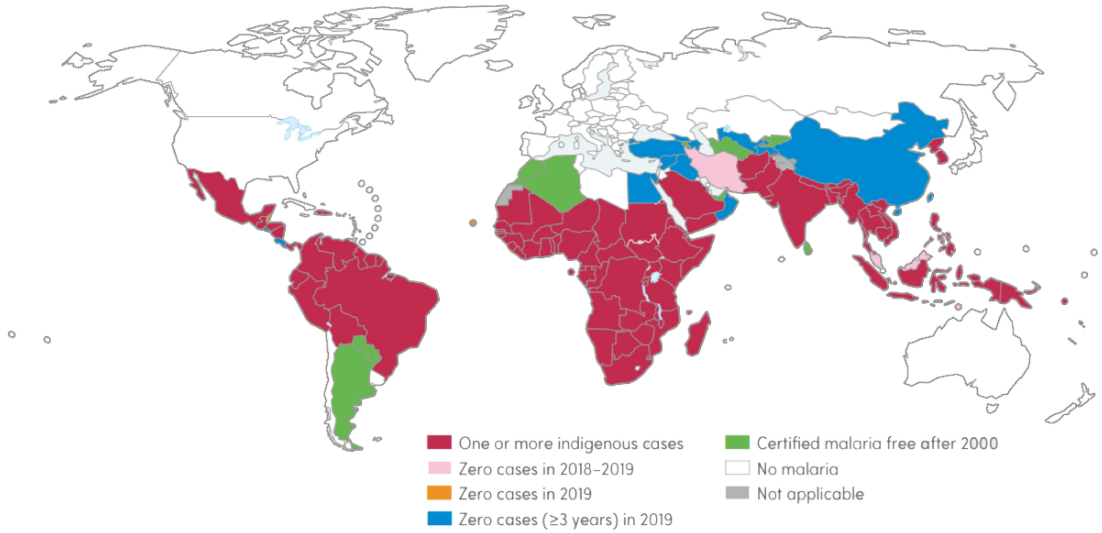


Figure 1.1: Global distribution of malaria in 2019. The status of countries with indigenous malaria cases in 2000 (figure from World Health, 2020).

control as intervention strategies were implemented at an unprecedented level (Bhatt et al., 2015). Vector control by indoor-residual spraying (IRS) and administration of long-lasting insecticide-treated nets (LLINs) were pivotal to gains made, with LLINs averting 68% of malaria cases alone (Bhatt et al., 2015). Prior to intervention by the WHO, clinical treatment followed a syndromic approach, on the assumption that all fevers were a result of malaria and thus warranted antimalarial treatment. Further guidance was provided by the WHO to direct administration of the front-line antimalarial artemisinin-combination therapies (ACTs) when warranted (World Health, 2015). ACTs have been highly effective in averting malaria-associated deaths, working by clearing the parasite reservoir in affected patients (Tilley et al., 2016; Ashley, Pyae Phyo, and Woodrow, 2018; World Health, 2010). To aid accurate diagnosis at a parasitological level, the use of rapid diagnosis tests (RDTs) in health clinics was recommended, providing further rationale for ACT treatment (World Health Organization. Roll Back and International, 2000; World Health, 2020). These combined efforts resulted in the aversion of an estimated 663 million clinical cases between 2000 and 2015, drastically reducing the burden of malaria (Bhatt et al., 2015).

Despite campaigns to move towards eradication, a plateau in the reduction of malaria burden and mortality has since challenged the gains made in disease control (World Health, 2020). Although the total death rate was reported to decrease, there

is an evident deceleration in progress and of the countries with the greatest malaria burden, Nigeria and Ghana even reported an increase in cases (World Health, 2020). Among the biological threats to malaria control are the emergence of parasite resistance to artemisinin (Tilley et al., 2016) and vector resistance to insecticides (Toé et al., 2014; Van Bortel et al., 2008; Dykes et al., 2015; Ondeto et al., 2017). Gains made in the diagnosis of malaria are also threatened by emergence of field isolates with mutations that deem parasites undetectable by RDTs (Gamboa et al., 2010). To reinvigorate progress made against malaria, the high burden to high impact (HBHI) approach was launched in 2018, coordinated by the WHO and Roll Back Malaria (RBM) Partnership to End Malaria (World Health, 2020). The HBHI approach consists of four key response elements, including targeted subnational tailored interventions to countries of high burden, based on various contextual information such as epidemiological, climatic and entomological factors (World Health, 2020).

Any strides made in malaria control and intervention are now at risk of further jeopardy, given the ongoing COVID-19 pandemic. As severe acute respiratory syndrome coronavirus 2 (SARS-Cov2) reached all malaria endemic countries by April 2020, it was predicted that insecticide-treated bed net (ITN) mass distribution plans and patient access to antimalarial drug treatment would face disruption (Teboh-Ewungkem and Ngwa, 2021). Guidance to isolate upon the development of a fever was likely to cause febrile diseases, such as malaria, to be left untreated. A geospatial modelling study predicted that in the worst-case scenario of a 75% reduction in ITN and antimalarial distribution, malaria incidence could rise by 21.5% and associated deaths could double (Weiss et al., 2021). Early in the pandemic, chloroquine and hydroxychloroquine gained significant traction for their potential therapeutic benefit to COVID-19 patients. The initiation of global stockpiling and sales of these drugs and associated starting materials, used for the respective treatment of *P. vivax* malaria and ACT drug synthesis, created a great strain on malaria treatment. Data later deemed chloroquine and hydroxychloroquine as unbeneficial for COVID-19 treatment, resulting in donation of the drugs for *P. vivax* treatment (World Health, 2020). Management of the COVID-19 pandemic and malaria as two global health priorities is crucial in preventing any further reversal to gains made.

Pervasive implementation of existing malaria interventions has given rise to resistance and a subsequent deceleration in gains made against malaria. Navigation of the research agenda towards discovery and development of novel tools and treatments is therefore key to reach goals of elimination. Drug discovery is one of many approaches at the forefront of research priorities, considering widespread artemisinin resistance.

1.2 The biology of *Plasmodium*

1.2.1 The Apicomplexan phylum

Among the eukaryotic Alveolata infrakingdom is the Apicomplexa phylum which is comprised of a plethora of diverse intracellular obligate parasites. Apicomplexan parasites are infectious to a variety of hosts, both vertebrate and invertebrate, with species such as *Plasmodium* spp. causing severe disease in human hosts (Dos Santos Pacheco et al., 2020; Frénal et al., 2017). Of this phylum, additional pathogens of veterinary and human threat are *Toxoplasma gondii*, *Cryptosporidium parvum*, *Theileria annulate* and *Babesia bovis*, the causative agents of toxoplasmosis, cryptosporidiosis, theileriosis and babesiosis, respectively.

Apicomplexans exist over a complex life cycle, alternating between sexual and asexual stages. The unicellular parasites of this phylum undergo repeated developmental cycles which start upon invasion of host cells, where parasites grow and proliferate before egressing, subsequently invading new cells (Frénal et al., 2017; Morrissette Naomi and Sibley, 2002). Apicomplexan parasites are unified in certain cellular features which facilitate motility and host cell invasion at the zoite stage. Highly polarised zoites contain a series of specialised organelles at the apical pole, including the rhoptries and micronemes which are secretory organelles with roles in host cell adhesion and invasion, motility and parasitophorous vacuole formation (Dos Santos Pacheco et al., 2020; Morrissette Naomi and Sibley, 2002). Zoite substrate-dependent locomotion, or gliding motility, is a further distinct characteristic of these organisms which classifies them into the Apicomplexa phylum. Gliding motility is driven by an actomyosin system, the glideosome machinery, which powers migration,

invasion and egress (Frénal et al., 2017). An additional trademark of these parasites is the apicoplast, a chloroplast-resembling organelle and the inner membrane complex (IMC), which lies beneath the parasite plasma membrane (PPM) and has roles in motility and invasion (Frénal et al., 2017; Morrissette Naomi and Sibley, 2002).

Plasmodium spp. display a combination of unique and characteristic Apicomplexan traits across their complex two-host lifecycle (Votýpka et al., 2017), illustrated in Figure 1.2.

1.2.2 The *Plasmodium* genus

First identified by Charles Laveran in the late 19th century, the *Plasmodium* genus is comprised of a wealth of species. A broad range of vertebrate hosts are vulnerable to infection by *Plasmodium* and of the total number of species, which exceeds 250, only five infect humans (Faust and Dobson, 2015). A cross-species transmission event from a non-human primate (NHP) malaria to human gave rise to the two most threatening *Plasmodium* spp., *P. falciparum* and *P. vivax* (Faust and Dobson, 2015; Liu et al., 2010; Prugnolle et al., 2013; Prugnolle et al., 2010). *P. falciparum* accounts for the bulk of human malaria-associated deaths in sub-Saharan Africa (Gething et al., 2016). Cases of *P. falciparum* malaria, which also occur in malarious tropical areas, are associated with complications in pregnancy and severe malaria (SM) (Phillips et al., 2017), with clinical manifestations of SM varying according to the age of infected patients (Dondorp et al., 2008). Whilst children are vulnerable to severe anaemia and hypoglycaemia, cases of jaundice, acute pulmonary oedema and acute kidney injury are more common in adults. Cerebral malaria and acidosis occurs in all age groups suffering from SM (Dondorp et al., 2008).

Attachment of infected erythrocytes to endothelial surface receptors of capillaries and veins, termed cytoadherence, gives rise to sequestration of parasitised erythrocytes in vital organs, such as the brain. Cytoadherence therefore disrupts microcirculatory flow and vascular endothelium function and, given sequestration of mature parasites, accounts for an underestimation of parasitemia (Pongponratn et al., 2003). Although sequestration of *P. falciparum*-infected erythrocytes in deep vasculature has long been associated with cerebral malaria and fatality, the initi-

ation and molecular basis of coma is yet to be fully resolved (Clark and Alleva, 2009). *P. vivax* and *P. knowlesi* can also cause SM, although this is considerably less common than it is with *P. falciparum*. All *Plasmodium* spp. can give rise to asymptomatic and uncomplicated malaria (Phillips et al., 2017).

Survival of *P. vivax* in unfavourable climates accounts for its abundance in malarious tropical and temperate regions. As well as causing most of the malaria cases in Central and South America, *P. vivax* malaria is also found in Southeast Asia and Ethiopia (Phillips et al., 2017). The characteristic trait of *P. vivax* infection is its association with relapsing malaria, which arises when parasites form intrahepatic hypnozoites able to maintain dormancy (White, 2011). In malaria endemic regions, there is evidence of systemic febrile illness, caused by *P. vivax* or *P. falciparum* malaria, leading to hypnozoite activation and relapse. Varying dependent on antimalarial treatment, relapses can occur at three-week intervals and in temperate regions, long-latency periods can give rise to an eight- to ten-month delay between initial infection and relapse (White, 2011). Relapse is not limited to *P. vivax*, but also occurs in *P. ovale* and *P. cynomolgi*, with the latter being one of many simian malarias associated with recurring infection (White, 2011; White et al., 2014a). The detriment to wellbeing caused by recurring malaria make *P. vivax* a priority for treatment.

Originally thought to impact only macaque monkeys, natural infections of *P. knowlesi* in humans were reported to be rare (Chin et al., 1965; Fong, Cadigan, and Coatney, 1971) until 2004, when 120 cases were found in Malaysian Borneo (Singh et al., 2004). Upon reinspection of historical blood smears, it was later found that many cases of *P. knowlesi* had been misidentified as *P. malariae* over the previous decade (Singh et al., 2004; Lee et al., 2009). Although the precise mechanistic links giving rise to *P. knowlesi* infection are not understood, there is a probable link in the emergence of infections to land use change (Brock et al., 2016). Given the fatality and link to SM, *P. knowlesi* transmission threatens aims to eliminate malaria.

Plasmodium ovale curtisi and *Plasmodium ovale wallikeri*, two sympatric species, are found in Oceania and Asia, but most common in sub-Saharan Africa (Sutherland, 2016). *P. malariae* is most common in the tropics and subtropics. Infections

of *P.o. curtisi*, *P.o. wallikeri* and *P. malariae* are all of chronic, low-density multispecies asymptomatic nature (Sutherland, 2016): low density *P. ovale* spp. and *P. malariae* have been frequently found in mixed infections alongside *P. falciparum* and *P. vivax* (Sutherland, 2016). Extensive *in vivo* research using rodent malaria models *P. berghei*, *P. yoelii*, *P. chabaudi* and *P. vinckei* have shaped our knowledge of *Plasmodium* (Sutherland, 2016).

1.2.3 The *Plasmodium* lifecycle

Transmitted by female mosquitos of various *Anopheles* spp., *Plasmodium* parasites adopt a range of diverse morphologies, encompassed over a complex lifecycle (Figure 1.2). These parasites demonstrate extreme plasticity as they encounter multiple cell environments in both a vertebrate host and mosquito vector. Stages of *Plasmodium* development vary between sexual, invasive and replicative forms, with differentiation relying on the tight regulation of a compact genome. *Plasmodium* species-specific expression patterns and morphologies permit survival over the plethora of host and vector species.

1.2.3.1 Liver Stages

Vector-to-host transmission of *Plasmodium* commences when motile sporozoites are deposited in the skin of a vertebrate host (Vanderberg and Frevert, 2004), following an infected female *Anopheles* mosquito bite. Carried in the saliva, eight- to fourteen-μm-long (Frischknecht and Matuschewski, 2017) crescent shaped sporozoites are injected into the dermis from the salivary glands, traversing the dermis before contacting a blood vessel. Upon entering circulation, parasites are then transported to the liver. Whilst some sporozoites have been shown travel to the liver through the lymphatic system (Krettli and Dantas, 2000), an intravital microscopy study also revealed that sporozoites failing to traverse the dermis were drained by lymphatics (Amino et al., 2006). Intravital microscopy has also been of great value in elucidating the locomotion of sporozoites, using *P. berghei* to observe sporozoite migration by gliding motility (Vanderberg and Frevert, 2004). It is well established that the motility and host tissue migration of sporozoites relies on gliding motil-

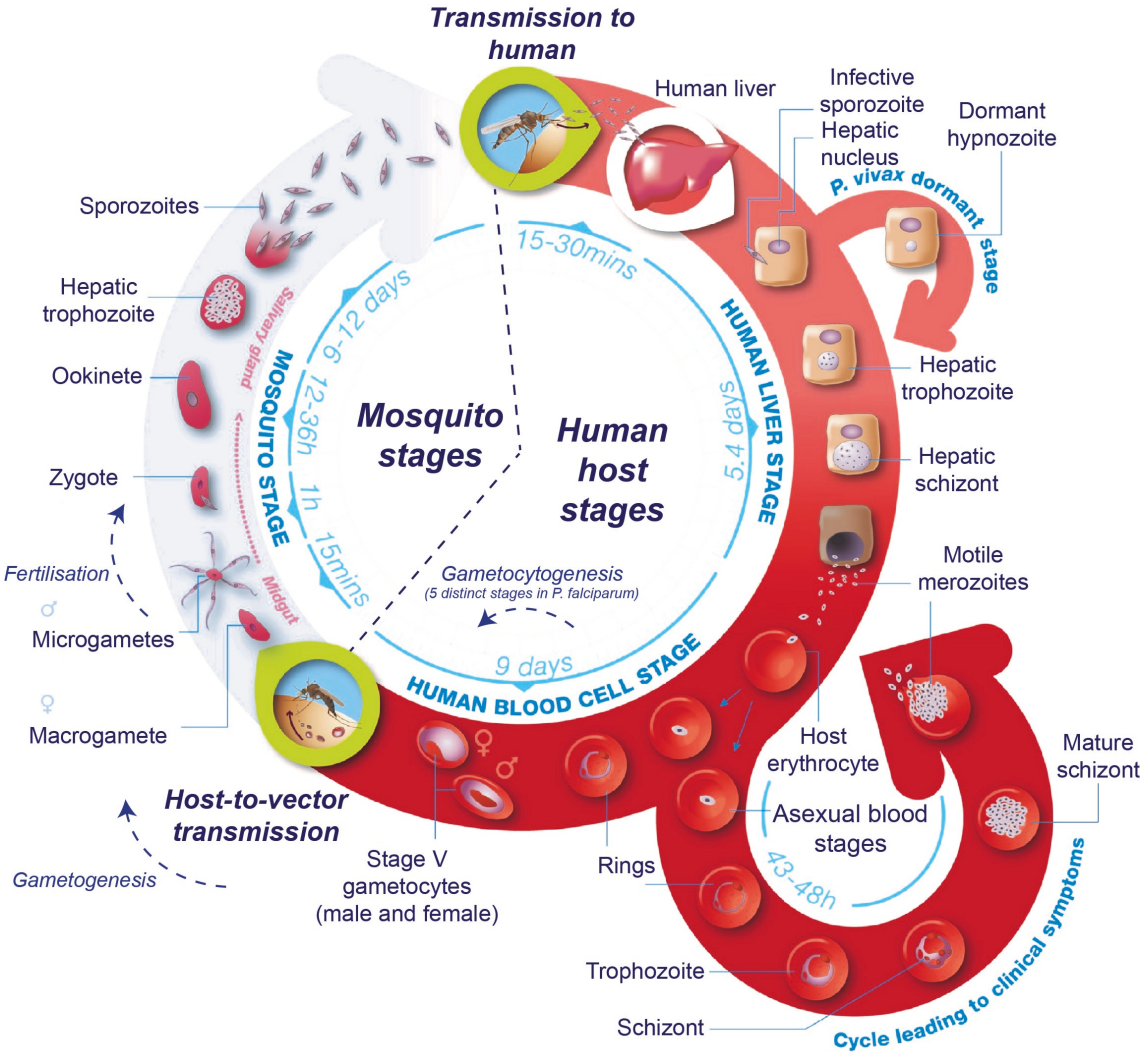


Figure 1.2: The *Plasmodium* lifecycle. Upon an *Anopheles* mosquito bloodmeal, *Plasmodium* sporozoites are injected into the human host dermis before reaching the liver. Once a sporozoite invades a hepatocyte, hepatic schizogony commences and resulting merozoites enter the blood stream to initiate the symptomatic asexual blood stages. A subset of asexual parasites commit to gametocytogenesis, forming the male and female gametocytes which, when mature, are transmissible to feeding *Anopheles* mosquitos. Gametogenesis is activated in the mosquito midgut, followed by fertilisation and onwards development in the mosquito. Sporozoites are formed and migrate to the salivary glands to infect another host, restarting the cycle. Adapted from Duffey et al., 2021.

ity (Frischknecht and Matuschewski, 2017; Mota et al., 2001). Studies have shown the importance of the circumsporozoite protein (CSP) and thrombospondin-related anonymous protein (TRAP) to gliding motility (Stewart and Vanderberg, 1988; Sultan et al., 1997).

Upon entering circulation, sporozoites reach the liver sinusoids and they glide over the endothelium, where CSP plays a role in hepatocyte and stellate cell heparan sulphate proteoglycan (HSPG) interaction (Prudêncio, Rodriguez, and Mota, 2006; Sinnis et al., 1996; Ying et al., 1997). Prior to hepatocyte invasion, sporozoites have been shown to traverse Kupffer cells (Frevert et al., 2006) preferentially over endothelial cells (Pradel and Frevert, 2001). After migrating across many hepatocytes, parasites invade a host cell and form a parasitophorous vacuole. To facilitate hepatocyte invasion, CSP has a role in attachment (Pinzon-Ortiz et al., 2001), TRAP is involved in internalisation (Pinzon-Ortiz et al., 2001) and apical membrane antigen 1 (AMA-1) has a role in invasion (Silvie et al., 2004). HSPGs on the hepatocyte surface are again involved in CSP and TRAP interaction, enabling binding and internalisation. Additionally, the host membrane protein CD81 has been implicated in the invasion of *P. falciparum* and *P. yoelii*, although the parasite ligand associated with this interaction is yet to be resolved (Silvie et al., 2003). Further elucidation of the host receptors involved in invasion is required (Prudêncio, Rodriguez, and Mota, 2006).

Once internalised and fully ensconced in a parasitophorous vacuole membrane (PVM), the parasite must disassemble and clear its inner membrane complex (IMC) and invasive organelles as exocytotic vesicles. A concurrent morphological transformation occurs, in which the plasma membrane expands and an invasive sporozoite differentiates into an intracellular trophozoite (Vaughan and Kappe, 2017). Dormancy associated with *P. vivax* infection is initiated in this transition, with hypnozoites forming as dormant trophozoites and resulting in relapsing malaria. Liver stage schizogony ensues as trophozoites transform to replicative schizonts, during which rapid replication produces up to 29,000 exoerythrocytic merozoites in under two days with rodent malaria (Baer et al., 2007) and up to 90,000 merozoites in six-seven days for *P. falciparum* (Vaughan et al., 2012). The final release of mero-

zoites occurs by the budding of merosomes, merozoite-filled vesicles, which enter the lumen of liver sinusoids (Sturm et al., 2006). Being of host-cell origin, the merosome plasma membrane is protected from dendritic or Kupffer cell recognition and thus able to enter circulation to commence the intraerythrocytic stage of the *Plasmodium* life cycle (Sturm et al., 2006).

1.2.3.2 Asexual blood stage replication

The intraerythrocytic asexual blood stages (ABS) are the cause of symptomatic malaria and represent the peak in parasite population number during the *Plasmodium* life cycle (Venugopal et al., 2020). During the ABS, parasites cycle through repeated stages of invasion, replication and host cell egress within erythrocytes of the vertebrate host.

Invasion

The ABS commence when a free invasive merozoite, only one- to two-μm in size, invades a circulating erythrocyte. Being vulnerable to host immune attack (Cowman, Berry, and Baum, 2012; Harvey, Gilson, and Crabb, 2012), merozoite invasion has evolved to be immensely rapid to avoid immune detection. Multiple pioneering studies (Dvorak et al., 1975; Glushakova et al., 2005; Gilson and Crabb, 2009) have defined invasion as a stepwise mechanical process, occurring over distinct phases: merozoite interaction and host erythrocyte deformation; apical interaction and invasion; echinocytosis and recovery of the newly invaded host erythrocyte (Cowman et al., 2017). Studies have demonstrated the conservation of the kinetics and sequential steps of invasion across *Plasmodium* spp. (Dvorak et al., 1975; Glushakova et al., 2005; Gilson and Crabb, 2009). In species such as *P. vivax*, merozoites predominantly invade reticulocytes, a form of immature erythrocyte which comprises only a small fraction of total circulating erythrocytes (Venugopal et al., 2020; Lim et al., 2016). *P. falciparum*, being able to additionally invade erythrocytes, is associated with high parasite burden and subsequent SM (Phillips et al., 2017).

The compartmentalisation of specialised organelles at the apical end of merozoites, such as micronemes, rhoptries, and dense granules, facilitates invasion by

enabling the temporal release of ligands required for each of the mechanical steps (Cowman et al., 2017). Initial attachment of merozoites to host erythrocytes likely involves the merozoite surface proteins (MSPs) and adhesins released by micronemes (Duffy-binding-like (DBL), erythrocyte-binding-like (EBL) and reticulocyte-binding-like (Rh or RBL) proteins). Upon apical reorientation, erythrocyte membrane wrapping and cytoskeletal reorganisation permits merozoite tight attachment (Dasgupta et al., 2014). Pore formation, mediated by the *Pf*Rh5/*Pf*Ripr/CyRPA complex (Volz et al., 2016; Reddy et al., 2015), precedes the development of a tight junction at which AMA1 of the merozoite and RON2 of the erythrocyte form a high-affinity interaction (Riglar et al., 2011). Reverse mobilisation of the merozoite actomyosin complex powers parasite entry into the host erythrocyte, moving the tight junction from the apical to posterior pole. Simultaneously, rhoptry contents are released to facilitate parasitophorous vacuole membrane (PVM) formation, enclosing the merozoite. Echinocytosis, a process by which the erythrocyte shrinks and produces projections due to water loss from the erythrocyte cytosol, occurs as the PVM and host plasma membrane seals and host homeostasis is subsequently recovered (Cowman et al., 2016). Knowledge of actin-based motility and proteins associated with the glideosome have been developed with extensive study (Tardieux and Baum, 2016; Baum et al., 2006b; Baum et al., 2006a; Baum et al., 2008b).

Schizogony

Once intraerythrocytic, ABS undergo further development which can be categorised as three distinct stages; the ring, trophozoite and schizont stages. Following invasion, parasites divide by schizogony in which rapid asynchronous rounds of genome replication produce 16-32 merozoites (Francia and Striepen, 2014), reaching 10^{12} parasites in symptomatic patients (Cowman et al., 2016; Phillips et al., 2017). The subsequent rupture of mature schizonts releases replicated merozoites into circulation to invade new erythrocytes. The asexual cycle varies in length between *Plasmodium* spp., lasting roughly 24 hours for *P. knowlesi*, 48 hours for *P. falciparum*, *P. ovale* and *P. vivax* and 72 hours for *P. malariae* (White et al., 2014a).

Plasmodium parasites are auxotrophic, acquiring all amino acids required for

survival by degradation of host erythrocyte haemoglobin, with the exception of isoleucine which is obtained exogenously. Digestion of haemoglobin produces the toxic waste product haem, which is converted to inert haemozoin by lipid-mediated crystallisation. Haemozoin crystals accumulate in the digestive vacuole, visible as blue pigment by light microscopy which makes trophozoites morphologically distinguishable from immature ring forms (Wunderlich, Rohrbach, and Dalton, 2012).

Egress

Biogenesis of intracellular merozoites, occurring by segmentation of schizonts, is rapidly followed by activation of cyclic GMP (cGMP)-dependent protein kinase G (*Pf*PKG) (Collins et al., 2013). PKG activation triggers mobilisation of Ca^{2+} and subsequently activates plant-like calcium-dependent protein kinases (CDPKs), with *Pf*CDPK5 being crucial for efficient egress, through a mechanism which remains elusive (Dvorin et al., 2010). PKG activation additionally triggers the discharge of a parasite subtilisin-like serine protease, *Pf*SUB1 (Collins et al., 2013), which proteolytically modifies merozoite surface proteins and parasitophorous vacuole proteins (PV) in the PV lumen (Yeoh et al., 2007; Monerri et al., 2011). *Pf*SUB1-modified proteins include serine-repeat antigens 6 (SERA6) (Ruecker et al., 2012) and the abundant merozoite surface protein, MSP1, which facilitates host cell rupture by interaction with the spectrin network of the erythrocyte cytoskeleton (Das et al., 2015).

Merozoite egress is now widely accepted to occur by an 'inside-out' model, in which the PVM ruptures prior to rupture and vesiculation of the host erythrocyte membrane (Tan and Blackman, 2021). Shortly prior to merozoite egress, rounding and increased permeability of the PVM being observed (Hale et al., 2017). Segmented merozoites have been observed to orient from an irregular structure to a symmetrical 'flower-like' alignment (Tan and Blackman, 2021), prior to PVM vesiculation into multilamellar vesicles within the erythrocyte membrane (Tan and Blackman, 2021). Erythrocyte membrane rupture then follows, involving pore formation and vesiculation at the site from which parasites are released (Glushakova et al., 2005; Abkarian et al., 2011).

1.2.3.3 Sexual development

A developmental switch occurs in a subpopulation of ABS parasites, in which the commitment to sexual development, or gametocytogenesis, is initiated in the vertebrate host (Sinden, 1983a; Dixon and Tilley, 2021; Ngotho et al., 2019). Differentiation into sexual stage parasites, the male (micro) and female (macro) gametocytes, represents the conclusive step in *Plasmodium* development within the vertebrate host. *P. falciparum* gametocyte maturation occurs over five discernible morphological stages, taking 10-12 days to reach full maturity. Gametocytogenesis is markedly different in alternative *Plasmodium* spp.; occurring over a shorter developmental period of up to three days, involving a simpler morphological transformation and varying in the number of discernible stages compared to *P. falciparum* (Gautret and Motard, 1999). Unlike asexual development, DNA replication and nuclear division is halted in gametocytogenesis as parasites exhibit a reduction in metabolism. Once mature, male and female gametocytes are transmissible to feeding female *Anopheles* mosquitos upon a bloodmeal. *P. falciparum* derives its name from the characteristic falciform morphology of its mature gametocytes (Dixon et al., 2012), a morphology also adopted by *P. reichenowi* (Bray, 1956). Being one of the key parasite population bottlenecks and stages responsible for host-to-vector transmission, gametocytes are a desirable target of malaria intervention.

Commitment to gametocytogenesis

The developmental switch to gametocytogenesis is thought to occur by two separate routes, next-cycle conversion or same-cycle conversion. Next cycle-conversion is the canonical route in which commitment precedes schizogony, whereby each merozoite of a schizont forms only a sexual or asexual parasite (Bruce et al., 1990). Of the parasites committed to sexual development, the sex of each merozoite is also predetermined, such that each merozoite of a schizont forms either a male or female (Silvestrini, Alano, and Williams, 2000; Smith et al., 2000). Same-cycle conversion describes commitment that occurs without parasites undergoing a round of schizogony, with early ring stages directly converting to sexual development (Bancells et al., 2019). Although the mechanisms of commitment have been somewhat elusive,

recent evidence of genetic, epigenetic, transcriptional, environmental and metabolic regulation, both prior to and following commitment, have emerged as depicted in Figure 1.3 (Josling, Williamson, and Llinás, 2018).

Genetic and epigenetic regulation

Continuous *in vitro* culture of *Plasmodium* can impair the ability of a laboratory strain to produce gametocytes. Instances of failed gametocytogenesis have been reported from repeated blood passage in *P. berghei* and *P. falciparum* lines (Sinha et al., 2014; Alano et al., 1995; Eksi et al., 2012), and forward genetics of deficient lines identified mutations in the *ap2-g* locus in independent studies (Sinha et al., 2014; Kafsack et al., 2014). This finding was further corroborated by reverse genetics (Kafsack et al., 2014) and genetic complementation of a targeted deletion mutant of *pbap2-g* (Sinha et al., 2014). Expression of *ap2-g* allows commitment which is otherwise prevented in parasites not expressing *ap2-g*, which continue to develop asexually. Part of the ApiAP2 family of DNA-binding proteins (Josling, Williamson, and Llinás, 2018; Bechtsi and Waters, 2017), PfAP2-G is considered to be the master regulator of commitment to gametocytogenesis.

In *P. falciparum*, *pfap2-g* is marked by histone 3 lysine 9 trimethylation (H3K9me3), a histone modification which is characteristic of epigenetic silencing (Lopez-Rubio, Mancio-Silva, and Scherf, 2009). H3K9me3 is a docking site for the conserved transcriptional repressor, heterochromatin protein 1 (HP1) (Bechtsi and Waters, 2017; Brancucci et al., 2014). The association of *pfap2-g* with both H3K9me3 and HP1 points to the epigenetic silencing of this gene in most parasites. Histone deacetylase 2 (Hda2) is also implicated in the epigenetic silencing of *ap2-g* (Coleman et al., 2014).

Furthermore, forward genetics also identified the deletion of *gdv1* (gametocyte development 1) in *P. falciparum* and with overexpression of GDV1 being associated with increased gametocyte production, it is strongly implicated in the regulation of sexual development (Eksi et al., 2012). It is now known that GDV1 plays a role in the removal of HP1 from *ap2-g*, permitting commitment to gametocytogenesis (Filarsky et al., 2018). The *gdv1* locus is absent in rodent malaria species, pointing

to an alternate pathway of AP2-G activation in these species (Ngotho et al., 2019).

Transcriptional regulation

Prior to commitment, various transcription factors, such as AP2-G3, are thought to be involved in directing *ap2-g* transcription (Josling, Williamson, and Llinás, 2018). Upon expression, PfAP2-G can bind a DNA motif enriched in promoters of gametocyte genes, pointing to a role as a transcriptional activator (Kafsack et al., 2014). PfAP2-G exhibits a positive-feedback loop in which it actives transcription by binding its own promotor, self-sustaining expression to maintain high PfAP2-G levels. Recent studies reported a role of PfAP2-G in the direct orchestration of transcription into the initial stage of gametocytogenesis, additionally to commitment (Bancells et al., 2019; Josling et al., 2020). In a study utilising chromatin immunoprecipitation followed by next generation sequencing (ChIP-seq), the occupancy of PfAP2-G was shown to vary depending on whether commitment occurred by next or same cycle conversion (Josling et al., 2020). The study also identified unknown targets of PfAP2-G, such as genes implicated in erythrocyte invasion (Josling et al., 2020). Puf1 and Puf2 of the Puf family of RNA-binding proteins are also implicated in transcriptional regulation of committed parasites (Josling, Williamson, and Llinás, 2018).

Environmental cues

Various environmental factors have been identified to trigger commitment to gametocytogenesis. Host cell age has been shown to influence commitment, with a seven-fold increase in gametocytaemia in blood enriched with reticulocytes (Trager and Gill, 1992). Parasite-conditioned media, or spent media, has long been reported to increase the proportion of stage two and three gametocytes relative to cultures fed with standard culture media (Williams, 1999). Spent media is now widely utilised in the *in vitro* culture of *P. falciparum* gametocytes. A recent study found that addition of human serum reversed the gametocytogenesis induction effects of spent media, thus hypothesising that the depletion of certain contents of human serum

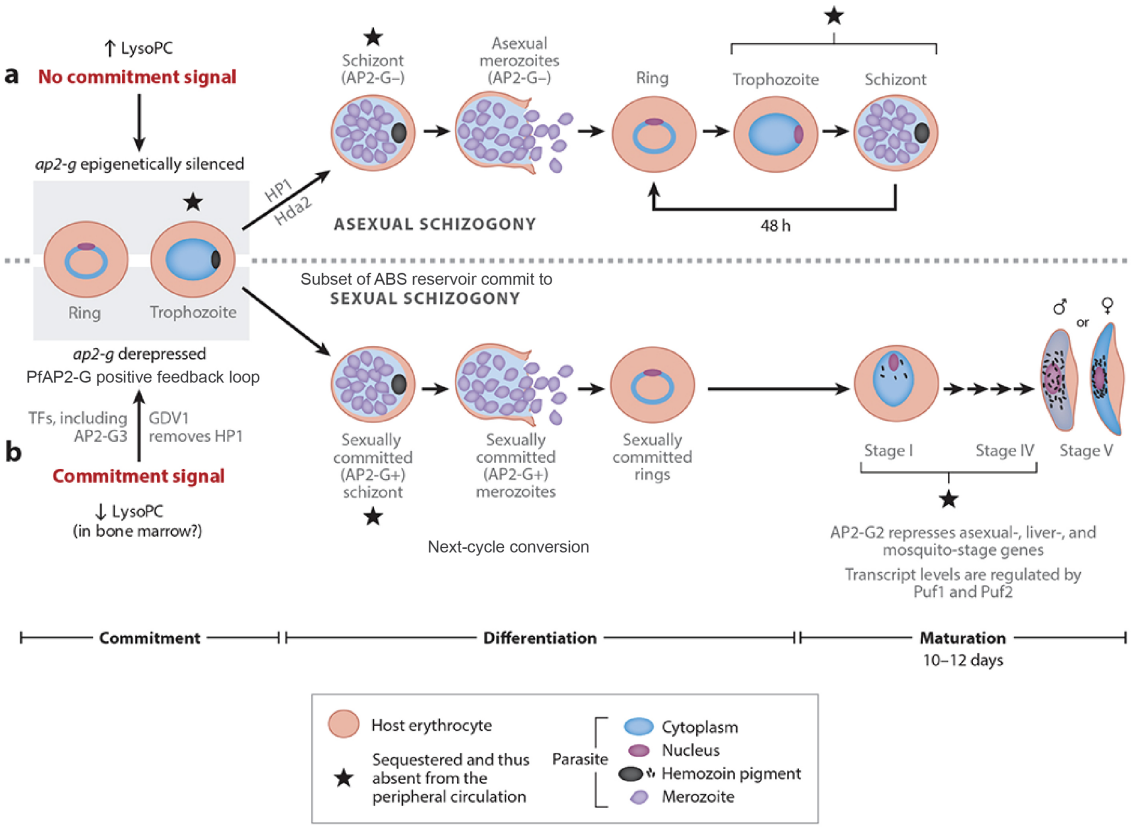


Figure 1.3: Regulation of commitment to gametocytogenesis. (A) HP1 and Hda2-meditated epigenetic silencing of the *ap2-g* locus occurs in the presence of lysophosphatidylcholine (LysoPC) and permits asexual schizogony to continue. (B) Commitment to gametocytogenesis occurs with reduced LysoPC levels. Transcription factor (TF) and GDV-1-mediated removal of HP1 allows *ap2-g* transcription, which is regulated by a positive feedback loop. Further epigenetic and transcriptional regulation occurs downstream of AP2-G to aid gametocytogenesis, with Puf1 and Puf2 regulating transcript levels. AP2-G continues to repress genes of other lifecycle stages. Figure adapted from Josling, Williamson, and Llinás, 2018.

in spent media mediated its effects. Authors of the study found the host-derived lipid lysophosphatidylcholine (LysoPC), a component of human serum, acted as an environmental inhibitor to commitment. The block to commitment was found to indirectly stimulate epigenetic regulation by introducing metabolic changes (Brancucci et al., 2017).

1.2.3.4 Gametocytogenesis

Morphology

The architectural changes to gametocyte morphology as they mature from stages I-V have been defined by multiple pioneering electron microscopy (EM) studies (Sinden, 1982; Sinden, Canning, and Spain, 1976; Billker et al., 2004). Upon reaching maturity, *P. malariae*, *P. ovale* and *P. vivax* gametocyte morphology is not too dissimilar to that of late trophozoites, demonstrating only an increase in size and food vacuole abundance and distribution (Sinden, 1998). The five stages of *P. falciparum* gametocytogenesis (Figure 1.4) are categorised according to multiple distinct features:

Stage I

Stage I gametocytes are morphologically indistinguishable from trophozoites (Dixon et al., 2012), but are instead categorised based on transcriptomic differences to ABS parasites (Ngotho et al., 2019).

Stage II

Gametocytes become discernible from ABS parasites at stage II of development. A dense network of microtubules which is scaffolded by the inner membrane complex (IMC), a cisternal membrane structure, is placed beneath the parasite plasma membrane (PPM) in stage II gametocytes. This appears as a narrow strip of dense membrane and slightly elongates the parasite morphology (Dixon and Tilley, 2021).

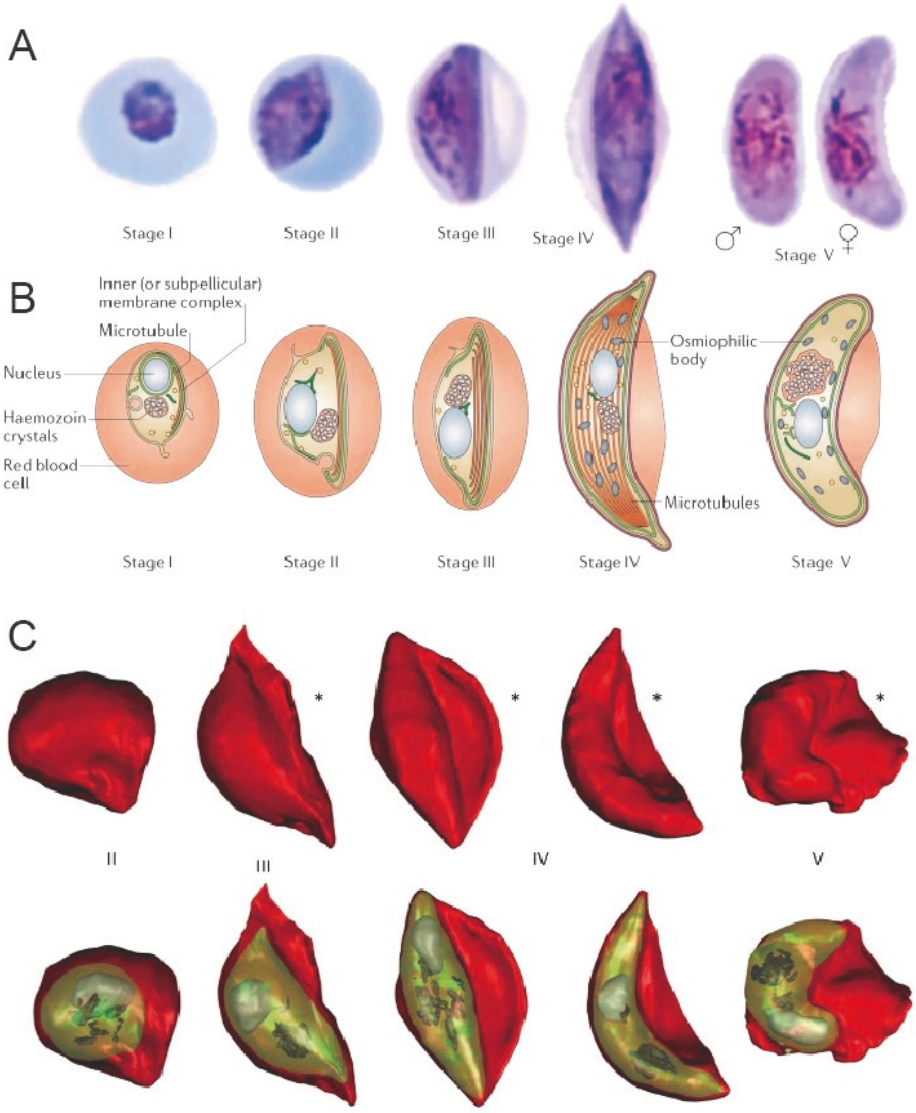


Figure 1.4: Stage I-V *P. falciparum* gametocyte morphologies. Morphologies are depicted as (A) Giemsa-stained blood smears imaged by light microscopy, (B) schematic diagrams and (C) rendered X-ray tomograms. Stage I gametocytes are morphologically indistinguishable from trophozoites, but the D-shape adopted at stage II makes gametocytes discernible from ABS parasites. Further parasite elongation occurs at stage III and peaks at stage IV, during which female osmiophilic bodies form. Stage V gametocytes adopt the characteristic falciform morphology and the sexes are discernible by light microscopy. The host erythrocyte is substantially morphed during gametocyte development, forming a flattened extension called the Laveran's bib (*). Images adapted from Josling and Llinás, 2015 and Dixon et al., 2012.

Stage III

By stage III, the parasite lengthens to double its width as the dense strip of membrane elongates. Stage III gametocyte morphology resembles the letter 'D' and slight distortion of the host erythrocyte can be observed (Talman et al., 2004). Nuclear elongation is another hallmark of gametocyte maturation, as the maximum length of the nucleus is reached at stage III (Parkyn Schneider et al., 2017). Sexual dimorphism becomes apparent by light microscopy of Giemsa-stained thin blood smears, with males and females exhibiting a difference in colour. By electron microscopy, nuclei appear larger in the microgametocyte compared to the macrogametocyte. Macrogametocytes have a greater content of mitochondria, ribosomes, Golgi vesicles and endoplasmic reticulum (ER) than microgametocytes at stage III (Sinden, 1982; Talman et al., 2004).

Stage IV

Stage IV gametocytes adopt a characteristic thin, elongated morphology with pointed tips, reaching the maximum gametocyte length of $\sim$12 μm. Host erythrocytes are greatly distorted at this stage as they are reduced to a thin layer around the parasite, with a flattened extension forming on a single side of the parasitised erythrocyte, termed the Laveran's bib (Sinden, 1982). Garnham bodies, membrane whorls found within vesicles in the host erythrocyte, become visible by EM (Sinden, 1982). Gametocytes are entirely enveloped by the IMC, restoring symmetry of the parasite. Microtubules remain associated with the IMC, forming doublets or triplets (Sinden, 1982).

Haemoglobin digestion is complete by stage IV (Hanssen et al., 2012) and the appearance of haemozoin crystals by light microscopy differs between males and females; whilst pigment is scattered in microgametocytes, it is denser in macrogametocytes. Sexual dimorphism is additionally apparent in the cytoplasmic content of stage IV gametocytes, with increased rough ER, mitochondria and membrane-bound osmiophilic bodies in the macrogametocyte. In contrast, microgametocytes contain mostly smooth ER and have a larger nucleus. Within the microgametocyte nucleus, a large electron-dense intranuclear body is connected to the microtubule

organising centre (MTOC) by a nuclear pore, when visualised by EM (Sinden, 1982; Talman et al., 2004). Though the identity of the intranuclear body is not known, it is closely located to the centriolar plaque of the first division spindle which aligns at the MTOC for synchronised segregation during microgametogenesis (Sinden et al., 1978).

Stage V

Immature stage I-IV gametocyte metabolism slows as they sequester in the bone marrow and spleen. When reaching maturity at stage V, gametocyte-infected erythrocytes display increased deformability which depends on a reduction to cyclic adenosine monophosphate (cAMP) signalling and raised phosphodiesterase expression at this stage of gametocyte development (Ramdani et al., 2015). Further to this, deformability is regulated by protein kinase A (PKA)–mediated phosphorylation of the parasite "subtelomeric variable open reading frame" (STEVOR) proteins (Naissant et al., 2016). Depolymerisation of microtubules results in a reduction in length and the rounding of gametocyte tips, transforming parasites into the characteristic falciform morphology (Parkyn Schneider et al., 2017).

Stage V microgametocytes and macrogametocytes, which exist in a 1: 3-5 population ratio, remain discernible by light microscopy as male pigment is noticeably more scattered than the dense pigment observed in females (Talman et al., 2004). To a trained eye, a subtle difference in morphology of the sexes is also visible. The kinetochore complex of the microgametocyte remains adhered to the nuclear envelope in preparation for transformation during gamete formation (gametogenesis). The density of ribosomes and mitochondria is markedly reduced in microgametocytes relative to macrogametocytes, with the latter also containing many osmiophilic bodies and a smaller nucleus (Dixon and Tilley, 2021; Dixon et al., 2012; Talman et al., 2004).

Gametocyte inner membrane complex

The gametocyte IMC, previously referred to as the subpellicular membrane (Dixon et al., 2012; Sinden, 1982) plays a structural role in the sexual stages, in con-

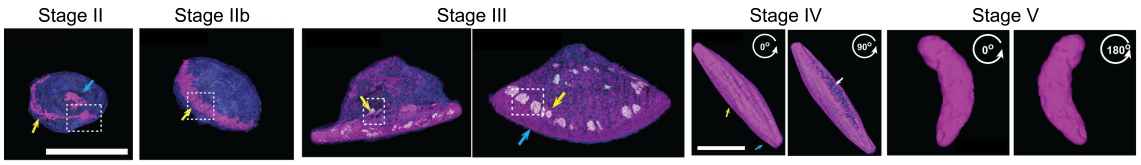


Figure 1.5: Development of the gametocyte IMC. Rendered models from Serial Block Face Scanning Electron Microscopy (SBF-SEM) of stage II-V gametocytes. IMC plate organisation and expansion differs across stages: at stage II, the IMC is a narrow strip of thickened membrane at the gametocyte periphery (yellow arrow); at stage IIb, a ribbon of disc-like plates form (yellow arrow); at stage III, the IMC expands and thickens at the leading edges (yellow arrows); at stage IV, plates become visible (yellow arrows) and at stage V, the IMC is relaxed. The PPM and IMC are depicted in blue and magenta, respectively. Scale bars = 1 μm. Images from Parkyn Schneider et al., 2017.

trast to the IMC role in invasion and gliding motility of the zoite stages (Baum et al., 2008a). The gametocyte IMC falls between the microtubules and multiple membranes; the host erythrocyte membrane, PVM and PPM. The molecular composition of the gametocyte IMC was found to be analogous to the invasive stages, containing glideosome-associated proteins (GAPs) GAP45 and GAP50, myosin tail domain interacting protein (MTIP) and MyoA. Although these are key proteins of the glideosome, gliding motility is not displayed by gametocytes (Dearnley et al., 2012). The IMC defines nascent gametocyte polarity, forming a longitudinally orientated spine during early gametocytogenesis (Kono et al., 2012). An IMC-resident protein was found to localise to transverse sutures, forming a filamentous meshwork. A symmetric lattice has been observed and is comprised of multiple ring-like plates which provides gametocytes with a segmented appearance (Kono et al., 2012). A recent study found IMC proteins PIP1 and PhIL1 may play roles in membrane trafficking and gametocyte morphological transformation (Parkyn Schneider et al., 2017). The same study utilised 3D electron microscopy techniques to dissect the genesis, development and expansion of the gametocyte IMC, as depicted in Figure 1.5 (Parkyn Schneider et al., 2017).

Gametocyte cytoskeleton

Recruited to the nascent IMC plates of immature gametocytes, an array of microtubules play a role in parasite elongation during gametocytogenesis (Parkyn Schneider et al., 2017). Located beneath the gametocyte IMC, microtubules are linearly arranged and separated by 10-25 nm, eventually forming a cage around gametocytes at stage IV of development as shown in Figure 1.5 (Dixon and Tilley, 2021; Parkyn Schneider et al., 2017; Dearnley et al., 2012).

Actin is crucial to the motility of Apicomplexan parasites and *Plasmodium* expresses two isoforms which are divergent from mammalian and yeast actins, actin I and actin II (Hliscs et al., 2015; Wesseling et al., 1989). Whilst actin I is present across all *Plasmodium* life cycle stages and other apicomplexan parasites, actin II is specific to the stages of *Plasmodium* involved in transmission, such as the gametocytes, gametes and sporozoites (Hliscs et al., 2015). F-actin and Formin-1, an actin-binding protein, have been shown to concentrate at the tips of gametocytes (Hliscs et al., 2015). Assembled in the early stages of gametocyte development, F-actin is localised at the apex of microtubules and in regions of the IMC where microtubules are yet to establish. Upon early microtubule organisation, F-actin concentrates at the tips of gametocytes (Hliscs et al., 2015).

Sequestration

Modifications to the host erythrocyte upon parasite infection permits cytoadherence, avoiding circulation and splenic clearance (Venugopal et al., 2020). Sequestration of erythrocytes infected with mature *P. falciparum* asexual parasites in the host microvasculature is mediated by erythrocyte membrane protein-1 (PfEMP1) (Baruch et al., 1995). Raised platforms of trophozoite or schizont-infected erythrocytes, referred to as knobs, present PfEMP1 to enable interaction with host ligands and subsequent sequestration. The bone marrow and spleen are major sites of gametocyte sequestration (Thomson and Robertson, 1935) and it has been hypothesised that the haematopoietic niche may provide an environment that is conducive for commitment, with depleted levels of commitment-repressor LysoPC (Brancucci et al., 2017; Venugopal et al., 2020). However, the latter hypothesis is yet to be demonstrated

in humans, instead tested in mice despite LysoPC not being crucial for *P. berghei* gametocyte production (Brancucci et al., 2017). Although gametocytes in the early stages (I-IV) of development sequester in the spleen and bone marrow (Smalley, Abdalla, and Brown, 1981), knobs are absent in gametocyte-infected erythrocytes (Tibúrcio et al., 2013), suggesting an alternative mechanism of sequestration (Day et al., 1998; Silvestrini et al., 2012).

PfEMP1 expression plummets as gametocytes mature (Day et al., 1998) and adhesion to endothelial receptors is not detectable with stage III-IV gametocyte infected erythrocytes, including endothelial cells derived from bone marrow (Silvestrini et al., 2012). Variants of the STEVOR proteins and "repetitive interspersed families" (RIFIN) polypeptides have been associated with gametocyte sequestration. STEVOR proteins are trafficked to the host membrane and regulate gametocyte deformability (Tibúrcio et al., 2012; McRobert et al., 2004).

Deformability

Erythrocyte deformability is greatly compromised by *Plasmodium* infection, with occupancy of a large volume of the cell and export of parasite proteins contributing to the reduction in membrane viscoelasticity (Dixon et al., 2012). The changing biophysical characteristics of *P. falciparum* gametocytes contribute to the avoidance of splenic clearance. Several studies on the deformability of *P. falciparum* gametocytes have been performed, measuring increased deformability of stage V gametocytes relative to ABS and immature gametocytes (Aingaran et al., 2012). Additionally, host erythrocyte deformability was found to be compromised when infected with immature gametocytes and restored at stage V (Tibúrcio et al., 2012; Dearnley et al., 2012). These traits are considered to contribute to sequestration in the low-flow areas of the bone marrow and spleen (Dixon and Tilley, 2021; Dixon et al., 2012). Disassembly of the stage V gametocyte microtubule network contributes to the reduction in rigidity of these stages. Additionally, reorganisation of STEVOR proteins in mature gametocytes is linked to the increased deformability (Naissant et al., 2016). Upon reaching maturity, stage V gametocytes can thus passage interendothelial slits for entrance into the circulation for transmission (Dixon

and Tilley, 2021).

1.2.3.5 The gametocyte proteome

Differing patterns in the proteomes of the asexual and sexual stages, and the male and female proteomes of the latter, reflect the divergent roles between these parasites. A large-scale mass spectrometric study of the *P. falciparum* proteome identified 1289 proteins, with 931 and 645 proteins in the gametocytes and gametes, respectively (Lasonder et al., 2002). Of the proteins identified in the sexual stages, 315 were specific to gametocytes and 97 were specific to gametes, although the study was limited to asexual and sexual stages of the *Plasmodium* lifecycle (Lasonder et al., 2002).

P. falciparum Gametocyte EXported Protein-5 (PfGEXP5) is exported to the infected host erythrocyte cytoplasm at only 14 hours post-invasion (Tibúrcio et al., 2015). Additionally, two highly abundant gametocyte-specific proteins, Pfs16 and Pfg27, are upregulated 24-30 hours post-invasion and are among the early markers of sexual conversion (Bruce et al., 1994; Eksi et al., 2005). Pfmdv-1/peg3, Pfpeg4, Pfg14.744 and Pfg14.748 are other gametocyte-specific proteins which are upregulated 30-40 hours post-invasion (Silvestrini et al., 2005). In a genome-wide molecular characterisation study, comparison of the *P. falciparum* gametocyte and trophozoite proteomes revealed an enrichment of the gametocyte-exported proteins (GEXPs) in early gametocytes (Silvestrini et al., 2010). Constituting a tenth of the early-gametocyte enriched proteome, the GEXPs uncovered the importance of protein export in early gametocytogenesis (Silvestrini et al., 2010).

Stage V gametocytes are arrested in the G0 phase of the cell cycle and activation of gametogenesis occurs almost instantaneously, when gametocytes encounter a change in environmental conditions within the mosquito midgut. Hence, a full complement of proteins required for gametogenesis are pre-synthesised in these stages (Florens et al., 2002), such as tubulin and P230 which are involved in cell cycle regulation and DNA processing (Sinden, 2009). Energy production within gametocytes relies on the mitochondrial tricarboxylic acid (TCA) cycle and enzymes required for this are abundant in gametocytes (Khan et al., 2005).

1.2.3.6 Sexual differences

Microgametocytes and macrogametocytes become morphologically discernible late into their development, but the molecular differentiation of the sexes precedes visible sexual dimorphism. A proteomic analysis of *P. berghei* identified that males and females share only 69 of the 406 gametocyte-specific proteins identified in the study (Khan et al., 2005). The first transcriptomic analysis of *P. falciparum* male and female gametocytes was coupled to proteomic analysis, and identified male-specific enrichment of proteins involved in DNA replication, axoneme formation and chromatin organisation, hallmarks of microgametogenesis (Lasonder et al., 2016). In contrast, the proteins found to be abundant in females included those that were required for zygote formation and post-fertilisation energy, lipid and protein metabolism (Lasonder et al., 2016).

Male-specific proteins include the most abundant cytoplasmic protein, α-tubulin II (Sinden, 2009), the serine/threonine mitogen-activated protein kinase 2 (MAP2) and multiple axoneme-associated proteins, consistent with the formation of flagellated microgametes (Khan et al., 2005). In contrast, female specific proteins include Pfs47 which has a role in fertilisation (Schaijk et al., 2006), the osmiophilic body-protein Pfg377 (Silvestrini, Alano, and Williams, 2000) and NIMA-related kinase (NEK4) which is required for meiosis and zygote development (Khan et al., 2005).

1.2.3.7 Translational Repression

A hallmark feature of female gametocyte development is the translational repression of transcripts, which are translated following gametogenesis and fertilisation. An integrated transcriptomic and proteomic study of *P. falciparum* sexual stages found 512 maternal transcripts were repressed in female gametocytes (Lasonder et al., 2016). In *P. berghei*, translationally quiescent mRNA associates with messenger ribonucleoprotein particles (mRNP) within which the translational repressors, DDX6 class RNA helicase DOZI (development of zygote inhibited) and Sm-like protein CITH (homolog of worm CAR-I and fly Trailer Hitch) are also found (Guerreiro et al., 2014; Mair et al., 2010). In *P. falciparum*, Pumilio and fem-3 binding factor 2 (Puf2) translationally represses *pfs25* and *pfs28* by binding to the Puf-binding

elements (PBEs) in the untranslated regions (UTRs) of the genes (Miao et al., 2013).

1.2.3.8 Gametogenesis

Upon reaching maturity, the newly deformable stage V gametocytes enter the host circulation where they become transmissible to a feeding female *Anopheles* mosquito. Once transmitted, stage V gametocytes encounter a change in conditions within the mosquito midgut which triggers gametogenesis, the process by which male and female gametes are formed. Experimental emulation of these conditions has permitted the extensive study of gametogenesis *in vitro* (Figure 1.6). Encountering the mosquito metabolite xanthurenic acid (Billker et al., 1998), a rise in pH and a decrease in temperature to 20-25°C, gametocytes are activated to form either microgametes or macrogametes in processes which are highly divergent (Billker et al., 1997). Microgametogenesis, or male gamete formation, is remarkably complex and rapid, being deemed one of the fastest eukaryotic cell transformations known. The formation of fertilisation-competent female gametes, or macrogametes, requires considerably less cellular reorganisation in comparison.

1.2.3.9 Microgametogenesis

The formation of eight haploid microgametes from a single microgametocyte is achieved in only 15-20 minutes and involves numerous cellular transformations which occur simultaneously; events include the rounding up of the falciform microgametocyte (for *P. falciparum*), three rounds of DNA replication which alternate with three endomitotic divisions, egress from the host erythrocyte and the nucleation and elongation of eight axonemes which emerge as flagellated haploid microgametes (Sinden, 2009; Sinden et al., 2010). The spatial and temporal resolution available with bright-field, fluorescence and electron microscopy have been central to shaping all existing insights into microgametogenesis (Sinden, Canning, and Spain, 1976; Andreadaki et al., 2018; Bertiaux et al., 2021; Sinden et al., 1978). Pioneering electron microscopy studies were the first to resolve the complex processes of gametogenesis (Figure 1.6), utilising fixed *P. falciparum* (Sinden et al., 1978), *P. berghei* (Billker et al., 2002) and *P. yoelii* (Sinden, Canning, and Spain, 1976) gametocytes, with the latter two

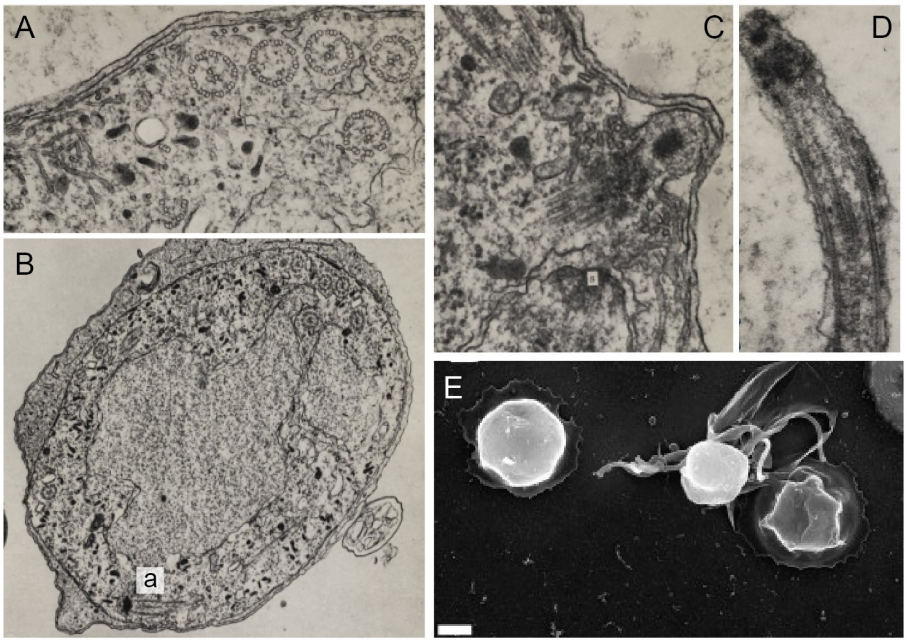


Figure 1.6: Electron micrographs from landmark studies of microgametogenesis. (A-D) Transmission electron micrographs of *P. yoelii* parasites during microgametogenesis (images from Sinden, Canning, and Spain, 1976). (A) Cross-section of developing axonemes with the characteristic 9+2 organisation of microtubules and (B) axoneme long-section (a). (C) Tip of microgamete emerging from a microgametocyte, with visible passage of the basal body and axoneme and (D) fully emerged, free motile microgamete. (E) Scanning electron micrograph of *P. berghei* exflagellation, with the parasite remaining in close contact with the erythrocyte from which it emerged (image from Billker et al., 2004).

species being most predominantly studied. Among the many developments occurring during *P. falciparum* microgametogenesis is the morphological transformation from falciform to round (Sinden et al., 1978), not occurring in species such as *P. berghei* in which the round morphology is adopted during gametocytogenesis (Billker et al., 2002). Prior to activation of microgametogenesis, a single microtubule organising centre (MTOC) is aligned at the cytoplasmic face of the nuclear pore (Sinden et al., 2010; Sinden et al., 1978). The intranuclear body (INB) with embedded kinetochores can be found at the nuclear face of this pore, structurally linking the machinery required to assemble the key structures of the developed microgamete; the genome and flagellum (Sinden et al., 2010). Activation stimulates the transformation of the MTOC to two orthogonal tetrads of basal bodies, from which axonemes are nucleated and elongated (Sinden, Canning, and Spain, 1976; Sinden

et al., 2010; Sinden et al., 1978). Large quantities of cytoplasmic tubulin, one of the most abundant microgametocyte proteins, are rapidly polymerised to microtubules within the developing microgametocyte (Rawlings et al., 1992). Assembled with the canonical '9+2' organisation of microtubules, axonemes rapidly elongate and coil around the nucleus within the parasite cytoplasm, until fully developed at an average length of 14 μm (Sinden et al., 2010).

Occurring simultaneously to the substantial cytoskeletal rearrangement, three rounds of DNA replication transform the haploid genome (1n) to octoploid (8n). Replication alternates with three rounds of endomitosis, with concurrent segregation of the eight basal bodies occurring with each division (Sinden, Canning, and Spain, 1976; Sinden et al., 2010; Sinden et al., 1978). This synchronous segregation allows each of the eight basal bodies to attach to each of the resulting eight spindle poles, where a hemi-spindle is localised and attached to the 14 chromosomes of the microgamete haploid genome (Sinden et al., 2010). Emergence of microgametes occurs upon full axoneme elongation and DNA replication at $\sim$15 minutes post-activation, in a process termed exflagellation. Upon exflagellation, the tip of a fully developed axoneme aligns at the periphery of the parasite cell body and carries the haploid genome through the cell surface, emerging in rapid glycolysis-powered motion (Sinden et al., 2010). Comprised of only an axoneme, nucleus and plasma membrane, the motile microgametes are notoriously simple in composition and able to fertilise macrogametes (Sinden et al., 2010).

Egress from the host erythrocyte occurs within a few minutes of activation via an 'inside-out' mechanism, with disintegration of the PVM preceding rupture of the host erythrocyte (Andreadaki et al., 2018). The mechanism and molecular basis of gametocyte egress has been widely studied using *P. berghei* (Andreadaki et al., 2018; Olivieri et al., 2015; Ponzi et al., 2009; Deligianni et al., 2013; Talman et al., 2011). A stepwise model of *P. berghei* gametocyte egress has been described based on observations using live immunolabelling and brightfield microscopy: i) the PVM and host erythrocyte membranes swell, ii) the PVM ruptures and vesiculates, iii) an erythrocyte membrane pore forms, with the pore most commonly localising towards PVM vesicles (seen with both males and females) and in some instances, localising

towards the parasite (females) and iv) the host erythrocyte vesiculates to permit emergence of the parasite (Andreadaki et al., 2018). An inside-out mechanism of egress has also been reported in *P. falciparum* (Sologub et al., 2011). Reverse genetics has revealed the importance of osmiophillic body proteins Pfg377 (Koning-Ward et al., 2008), MDV-1/PEG3 (Ponzi et al., 2009) and PbGEST (Talman et al., 2011) in gametocyte egress. PPLP2 (Deligianni et al., 2013) and merozoite-TRAP (MTRAP) (Kehrer, Frischknecht, and Mair, 2016; Bargieri et al., 2016) are also required for egress. Whilst MDV/PEG3, PbGEST and MTRAP are required for both sexes, Pfg377 and PPLP2 demonstrate female and male-specific roles, respectively.

1.2.3.10 Macrogametogenesis

Although the morphological transformation of macrogametogenesis is considerably less complex than microgametogenesis, the process is associated with a drastic molecular transformation as translational repression is lifted (Sinden, 2009). *P. falciparum* macrogametocytes initially round up from a falciform to round morphology, as microgametocytes do when activated (Sinden et al., 1978). A reduction in the cytoplasmic density, specifically a reduction in osmiophilic body number and density of ER cisternae, is also observed (Sinden et al., 1978). Emergence from the host erythrocyte prepares macrogametes for fertilisation by a motile haploid microgamete (Sinden et al., 1978).

1.2.3.11 Signalling cascade

The events that ensue as gametogenesis is initiated occur in rapid succession in the mosquito midgut and require tight orchestration by a signalling cascade, which is summarised in Figure 1.7 (Bennink, Kiesow, and Pradel, 2016). Xanthurenic acid, a mosquito secretory product, stimulates gametocyte membrane-associated guanylyl cyclase activity (Muhia et al., 2001) and subsequently activates the phosphoinositol pathway (Sinden, 2009). Activation of guanylyl cyclase α (GCα) results in cyclic guanosine monophosphate (cGMP) synthesis, dependent on Mg^{2+}/Mn^{2+} (Muhia et al., 2001). In *P. falciparum*, levels of cGMP are regulated by the cGMP-hydrolysing phosphodiesterases (PDEs) α-δ, with PDEδ being required for game-

togenesis (Taylor, McRobert, and Baker, 2008). cGMP subsequently activates the cGMP-dependent protein kinase G (PKG) which acts upstream of intracellular Ca^{2+} (McRobert et al., 2008). A recent study identified that the multipass membrane protein important for calcium mobilization-1 (ICM1) is phosphorylated by PKG and is crucial for calcium mobilisation (Balestra et al., 2021).

A downstream increase in cytosolic Ca^{2+} occurs at around ten seconds post-activation (Billker et al., 2004; Bennink, Kiesow, and Pradel, 2016) and is critical to the regulation of gametogenesis. Phosphoinositide-specific phospholipase C (PI-PLC) activity is both stimulated by and responsible for downstream Ca^{2+} mobilisation, suggesting a crucial Ca^{2+} feedback mechanism in gametogenesis (Bennink, Kiesow, and Pradel, 2016; Raabe et al., 2011). Once stimulated, PI-PLC is linked to phosphatidylinositol-(4,5)-bisphosphate (PIP2) hydrolysis into inositol-(1,4,5)-trisphosphate (IP3) and diacylglycerol (DAG) (Martin, Jett, and Schneider, 1994). The opening of calcium channels in the ER is then triggered by IP3. PKG additionally regulates Ca^{2+} levels by mediating phosphatidylinositol 4-phosphate (PI4P) synthesis which is linked to PIP2 production. Ca^{2+}-dependent protein kinases (CDPKs) then regulate gametogenesis, with CDPK1 translationally activating repressed mRNAs in females (Sebastian et al., 2012). CDPK4 is considered the master regulator of microgametogenesis, with roles in initiating genome replication, mediating mitotic spindle assembly and activating microgamete motility (Fang et al., 2017). An array of other proteins then regulate replication, cytoskeletal reorganisation, chromatin condensation and exflagellation (Bennink, Kiesow, and Pradel, 2016).

1.2.3.12 Mosquito stages

Commencing with the transmission of gametocytes upon a bloodmeal, the sequential developmental transformations that ensue within the mosquito vector are considerably conserved across *Plasmodium* spp. (Baton and Ranford-Cartwright, 2005).

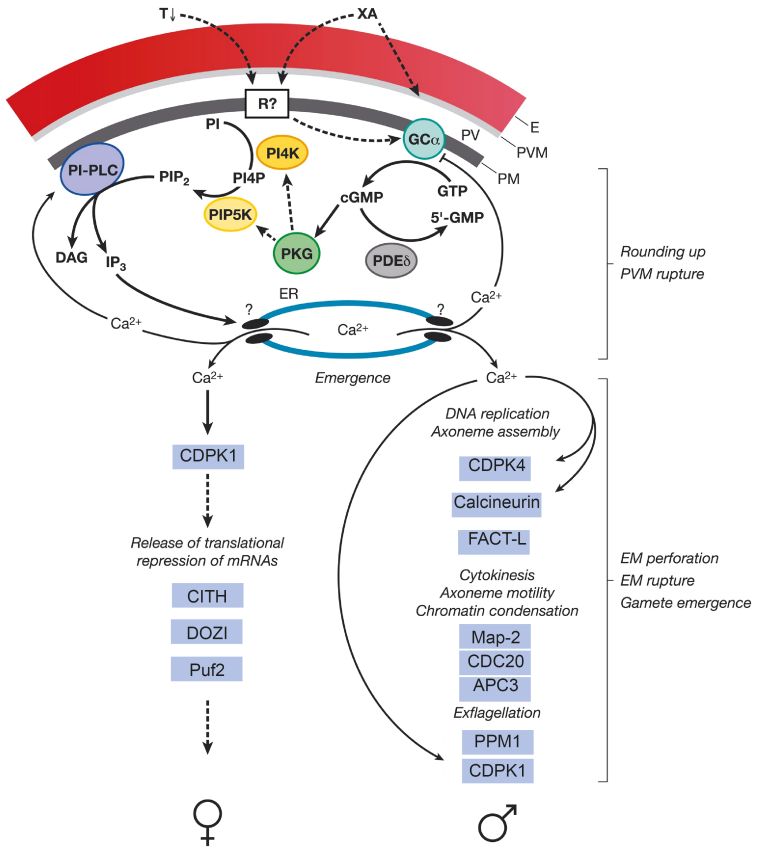


Figure 1.7: Signalling pathways involved in regulation of gametogenesis. The receptor (R) which translates the activation signals (xanthurenic acid (XA), pH drop and temperature (T) rise) is unresolved but activates the phosphoinositol pathway. Cyclic guanosine monophosphate (cGMP) activates protein kinase G (PKG), which acts upstream of Ca^{2+}. Ca^{2+} is needed by Ca^{2+}-dependent protein kinases (CDPKs), including master regulator of microgametogenesis, CDPK4. Parasitophorous vacuole (PV), parasitophorous vacuole (PVM), erythrocyte (E), erythrocyte membrane (EM), cell division cycle protein 20 (CDC20), homolog of worm CAR-I and fly Trailer Hitch (CITH), diacylglycerol (DAG), development of zygote inhibited (DOZI), facilitates chromatin transcription protein L (FACT-L), guanylyl cyclase (GC), guanosine monophosphate (5'-GMP), inositol triphosphate (IP3), Mitogen-activated protein kinase 2 (Map-2), phosphodiesterase (PDE), phosphatidyl-1D-myo-inositol (PI), phosphatidylinositol 4-kinase (PI4K), phosphatidylinositol 4-phosphate (PI4P), phosphatidylinositol-4,5-bisphosphate (PIP2), phosphatidylinositol 4-phosphate 5-kinase (PIP5K), phosphoinositide-specific phospholipase C (PI-PLC), metallo-dependent protein phosphatase 1 (PPM1), Pumilio/FBF (fem-3 binding factor) family protein 2 (Puf2). Figure adapted from Bennink, Kiesow, and Pradel, 2016.

Fertilisation

The complex developmental cycle within the *Anopheles* vector is initiated with gametogenesis and immediately followed with the fertilisation of microgametes and macrogametes, forming diploid zygotes. Meiotic recombination between genomes occurs during the sexual reproduction stage of the *Plasmodium* lifecycle and facilitates evolutionary adaptation, consequently representing the point at which resistance can emerge or spread (Bechtsi and Waters, 2017). Fertilisation commences with gamete attachment when a microgamete reaches a macrogamete, for which there is no evidence of directed movement, or chemotaxis (Sinden, 1983b). Gamete membranes fuse, mediated by HAP2/GCS1, and the haploid microgamete passes into the cytoplasm of the female (Sinden et al., 2010). The microgamete nucleus crosses a macrogamete ER channel prior to fusing with its nucleus (Aikawa et al., 1984), followed by endomeiotic replication and formation of a spherical zygote (Baton and Ranford-Cartwright, 2005).

Ookinete development

Transformation of the extracellular sessile zygote into an elongated motile ookinete occurs ∼10-25 hours post-gamete fusion, depending on the *Plasmodium* spp. in question (Angrisano et al., 2012). Firstly, polarisation of the zygote nucleus into a cone shape occurs, with the apical complex forming at the apex of the nucleus (Baton and Ranford-Cartwright, 2005; Aikawa et al., 1984). Many concentric polar rings develop at the centre of the apical complex prominence, surrounded by the plasma membrane and IMC (Gass, 1979). These form what is known as the ookinete pellicle, which is surrounded by a dense surface coat (Baton and Ranford-Cartwright, 2005). Microtubules elongate from the pellicle and the subpellicular network is formed. The morphological transformation from zygote to ookinete includes an intermediate retort-form parasite (Baton and Ranford-Cartwright, 2005). The conserved architecture of the apical and pellicular complexes mediate ookinete gliding motility, permitting migration out of the central blood bolus prior to midgut colonisation (Angrisano et al., 2012).

Oocyst and sporozoite formation

Upon invasion of the midgut epithelium, ookinetes transform to spherical oocysts by rounding up beneath the basal lamina where they are encapsulated by a thick extracellular capsule (Baton and Ranford-Cartwright, 2005). An upregulation of DNA replication and protein synthesis machinery ensues as parasites enter sporogony, during which thousands sporozoites are produced over 10-14 days (Angrisano et al., 2012). Once sporozoites have migrated to the salivary glands, entry is mediated with parasite proteins thrombospondin-related anonymous protein (TRAP), TRAP-related protein (TREP), circumsporozoite protein (CSP) and apical membrane antigen/erythrocyte binding-like protein (MAEBL) (Graumans et al., 2020). Salivary gland proteins Saglin, CSP-binding protein (CSPBP) and salivary gland surface protein 1 (SGS1) are among the best characterised host proteins involved in the process (Graumans et al., 2020). Sporozoites migrate to the secretory cavity and salivary duct where they await inoculation into a mammalian host upon a bloodmeal, completing the *Plasmodium* lifecycle (Graumans et al., 2020; Pimenta, Touray, and Miller, 1994).

1.2.3.13 'Omics' and AI for *Plasmodium* life cycle study

Technological advances in research have given rise to the 'omics' approaches, revolutionising the study of genes, RNA, proteins and metabolites in biological organisms. The rise of 'omics' and 'multi-omics', that is the combination of multiple 'omic' methods, has transformed malaria research (Zhou, Varol, and Efferth, 2021). For example, a recent genomic study (Zhang et al., 2018) exploited the AT-rich *P. falciparum* genome to generate 38,000 mutants by applying high-throughput *piggyBac* transposon insertional mutagenesis and quantitative insertion site sequencing (QIseq). By generating the mutagenesis scores, a rank of the dispensability of a given gene, the study identified 2680 genes essential to the ABS stages, thereby identifying potential antimalarial drug targets (Zhang et al., 2018).

Another recent landmark study utilised single-cell RNA sequencing (scRNA-seq) to map the transcriptomic profiles of parasites across the *Plasmodium* lifecycle, predominantly in *P. berghei* (Howick et al., 2019). A reference dataset was assembled,

termed the Malaria Cell Atlas, which is accessible to the malaria research community (Howick et al., 2019). A follow-up *P. falciparum* study elucidated the transcriptional signatures of the transmission stages (Real et al., 2021).

As well as the 'omics' revolution, high-throughput study of *Plasmodium* imaging data has been transformed by application of machine learning. One study described a semi-supervised machine learning approach which ordered *Plasmodium* asexual developmental stages, based on morphological differences exhibited in fluorescence imaging data (Ashdown et al., 2020). Trained by a combination of human and machine-labelled data, the approach was utilised in a high-throughput screen of drugged ABS parasites, identifying morphologically abhorrent parasites (Ashdown et al., 2020). Routine culture of *Plasmodium* relies on microscopic examination of thin blood smears, and a recent study utilised machine-learning to detect and stage asexual-infected erythrocytes of blood smear images (Davidson et al., 2021). An accessible web-based tool, called PlasmoCount, was developed from the study for routine use in the malaria community (Davidson et al., 2021).

1.3 Malaria treatment strategies

Resistance threatens the existing malaria armamentarium, hence necessitating the agenda to discover and develop new antimalarial treatments (Drugs, 2011). Developed by the not-for-profit Medicines for Malaria Venture (MMV), the characteristics required of antimalarial drug candidates have been defined (Figure 1.8). The criteria for novel candidates can be categorised into the target candidate profile (TCP) or the target product profile (TPP), as described by Burrows et al., 2013; Burrows et al., 2017. Whilst TCPs describe the type of individual molecule, or more specifically the parasite stage targeted by the molecule, TPPs represent the final formulated product which may encompass multiple candidates (Burrows et al., 2013; Burrows et al., 2017).

As summarised in Figure 1.8, drug candidates targeting the symptomatic ABS (TCP-1) and asymptomatic stages (TCP-3-5), and mosquito-targeted endectocides (TCP-6) are sought after (Burrows et al., 2017). There are two existing TPPs;

TPP-1 addresses malaria case management and TPP-2 focuses on chemoprotection. In the case of SM management, the priority is rapid treatment of the symptomatic stages (TCP-1) and for cases of acute uncomplicated malaria, treatment should be supplemented with molecules to prevent transmission (TCP-5) and relapse (TCP-3) (Burrows et al., 2017). Chemoprotection would be achieved by treating both the symptomatic erythrocytic and pre-erythrocytic stages, vital during epidemics or for travellers (Burrows et al., 2017). Single encounter radical cure and post-treatment prophylaxis, or SERCaP, describes the most favourable antimalarial formulation that would eliminate the entire parasite reservoir of an infected individual in a single treatment. Depending on the *Plasmodium* spp. responsible for infection, SERCaP eliminates the ABS reservoir whilst also targeting gametocytes or hypnozoites (Drugs, 2011). Of the existing antimalarials, the chosen drug and route of administration (oral or parenteral) are selected according to the nature of the case; considerations made include whether patients are pregnant, whether the malaria case is severe or uncomplicated, and frequencies of drug resistance, which is higher with *P. falciparum* relative to other species (Phillips et al., 2017).

1.3.1 Antimalarial drugs

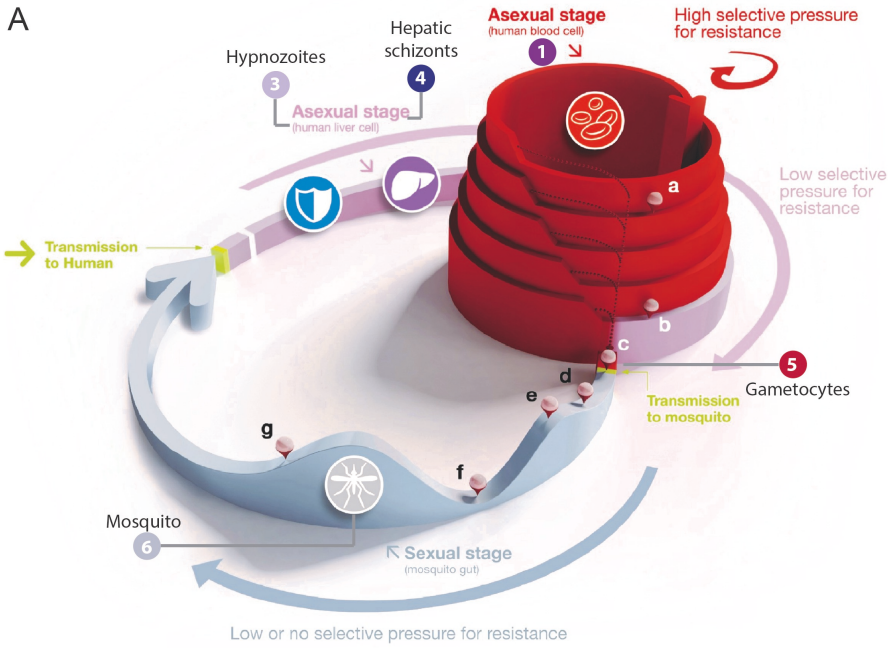
1.3.1.1 Artemisinin combination therapies

ACTs remain the frontline antimalarial treatment, particularly for cases of uncomplicated *P. falciparum* malaria (Phillips et al., 2017). The combination therapy is comprised of a fixed-dose of an artemisinin derivative and quinine derivative, specifically a 4-aminoquinoline or aminoalcohol, with various combinations available (Phillips et al., 2017; World Health, 2015).

1.3.1.2 Artemisinin and derivatives

Artemisinin was first isolated from a Chinese medicinal herb, *Artemisia annua*, by Tu YouYou in 1971, for which she was rewarded a Nobel Prize (Tse, Korsik, and Todd, 2019). The semi-synthetic derivatives of artemisinin (ARTs), dihydroartemisinin (DHA), artesunate and artemether, are approved for use in com-

A



B

TCP key

	TCP	Lifecycle stage	Therapeutic purpose	Notes
●	TCP-1	Asexual blood stages	Relieve symptoms	Active against ACT-resistant strains
●	TCP-3	Hypnozoites	Prevent relapse	Safety improvements to primaquine/ tafenoquine
●	TCP-4	Hepatic schizonts	Provide chemoprotection	Active at equal/ reduced dose to TCP-1
●	TCP-5	Gametocytes	Block transmission	Low dose
●	TCP-6	Insect vector	Block transmission (endectocides)	Low dose

TPPs

TPP Purpose TCPs addressed	Notes
TPP-1 Case management TCP-1, TCP-3, TCP-5	Severe malaria: single parenteral formulation of single TCP-1 compound Uncomplicated malaria: 2+ molecules targeting TCP-1, TCP-5 & TCP-3
TPP-2 Chemoprotection TCP-1, TCP-4	For migration and epidemics, combination of treatments to prevent emerging infections

Figure 1.8: Profiles for antimalarial drug candidates. (A) 3D depiction of the population sizes of each *Plasmodium* life-cycle stage, with corresponding selective pressures. The (a) asexual blood stage represents the peak in parasite population, with markedly lower parasite numbers in the (b) hepatic, (c) gametocyte, (d) gamete, (e) ookinete, (f) oocyst and (g) sporozoite stages. (B) The corresponding target candidate profiles (TCPs) and target product profiles (TPPs). Figure adapted from Duffey et al., 2021 and Leroy et al., 2014.

bination therapy, whereas the high lipophilicity of artemisinin deems it an unfavourable treatment option (Phillips et al., 2017). ARTs exhibit short *in vivo* half-lives, thereby necessitating administration with a partner drug. Combination therapy is hence crucial in preventing recrudescence and the subsequent development of antimalarial resistance (Tilley et al., 2016).

The mode of action (MoA) by which artemisinin derivatives inhibit *Plasmodium* is widely debated. One theory is that the activation of the ART endoperoxide bridge generates a carbon-centred radical able to bind parasite proteins (Tilley et al., 2016). ART activation is thought to be catalysed by iron derived from haem, that is released from haemoglobin digestion. The precise cellular target(s) of activated ARTs are yet to be completely characterised, although it is believed that ART-induced parasite death may arise from a general disruption to various pathways (Tilley et al., 2016). The hypothesis that the inhibitory activity of ARTs is pleiotropic in nature has been corroborated by chemical proteomics studies, which have identified a broad range of interacting partners with clickable ARTs (Ismail et al., 2016; Wang et al., 2015). Many potential targets have been studied, including EXP1 (Lisewski et al., 2014), *Pf*PI3K (Mbengue et al., 2015) and *Pf*ATP6 (Shandilya et al., 2013). However, given ART-mediated disruption to parasite membranes, oxidative damage, increase in protein ubiquitination and ART accumulation in lipid bodies, there is evidence that widespread damage occurs with ART treatment, as opposed to a single cellular target (Tilley et al., 2016).

ART resistance is associated with a reduction in the rate of parasite clearance and the genetic determinant of this resistance has been associated with several mutations in the *P. falciparum* Kelch13 (K13) propeller domain (Ariey et al., 2014). The impact of ART resistance on the transmissibility of *P. falciparum* has additionally been tested, with various K13 mutants demonstrating a reduction in ART sensitivity in mosquito feeds and microgametogenesis-based assays, relate to wild-type parasites (Witmer et al., 2020). K13 is involved in the endocytosis of haemoglobin from host erythrocytes and a reduction of this activity thereby disrupts ART activation, which is mediated by products of haemoglobin degradation (Birnbaum et al., 2020). However, the molecular function of K13 and the mechanism of resistance is still

widely debated, as is the case with ART activity (Tilley et al., 2016). Resistant lines depict varying levels of resistance to DHA, with C580Y, I543T, R539T and Y493H mutations being identified (Ariey et al., 2014).

1.3.1.3 4-aminoquinolines and aminoalcohols

The plasma half-lives of ART derivatives are only a few hours in comparison to the longer-term half-lives of the 4-aminoquinolines and amino-alcohols, of over four days (Phillips et al., 2017). Hence, amodiaquine, piperaquine and pyronaridine, the 4-aminoquinolines, and mefloquine or lumefantrine, the amino-alcohols, are suitable ART partner drugs (Phillips et al., 2017). The quinolines are associated with an accumulation of toxic free haem in parasites by preventing haem polymerisation and disposal of food vacuole polymers to the parasite cytoplasm (Kaur et al., 2010). The emergence of resistance to piperaquine in the Greater Mekong subregion (Amato et al., 2017), where artemisinin resistance is also found, threatens the efficacy of ACTs.

1.3.1.4 Alternative drugs

Quinine was the first chemically purified antimalarial treatment, initially isolated from cinchona tree bark in 1820 (Tse, Korsik, and Todd, 2019). However, since the emergence of resistance to quinine, it is now only utilised in instances where ART derivatives are unavailable to treat cases of SM (Tse, Korsik, and Todd, 2019). Chloroquine is now recommended to treat cases of uncomplicated *P. vivax* malaria and pregnant women infected with *P. vivax*, *P. ovale* or *P. malariae*, but is also threatened by emerging resistance (Phillips et al., 2017).

To prevent relapse and block transmission, the 8-aminoquinoline, primaquine is also administered alongside the frontline treatment, although there are shortcomings of this drug. A 14-day course of treatment is required with primaquine and is associated with severe haemolysis in glucose-6-phosphate dehydrogenase (G6PD) deficient patients (White, 2011). The recent approval of 8-aminoquinoline, tafenoquine or Krintafel, has been engineered for improved metabolic stability, preventing relapse with a single dosage rather than the prolonged course required of primaquine (Watson, Nekkab, and White, 2021). Active against the pre-erythrocytic liver-stages,

symptomatic ABS and transmissible gametocytes, tafenoquine is a promising new antimalarial (Frampton, 2018). Although it remains elusive, it has been hypothesised that tafenoquine inhibits haematin polymerisation and disrupts mitochondrial function (Frampton, 2018). However, like primaquine, tafenoquine is associated with haemolysis in G6PD-deficient patients (Watson, Nekkab, and White, 2021). Primaquine and tafenoquine remain the only approved drugs to treat *P. vivax* relapse (Phillips et al., 2017).

Chemoprotection of individuals travelling to areas of high endemicity or areas recently declared free of malaria is crucial (Phillips et al., 2017). The combination of proguanil and atovaquone, sold as Malarone^{TM}, serves as chemoprotection to non-immune travellers (Wells, Huijsduijnen, and Van Voorhis, 2015). The two compounds act by varying MoAs but exhibit a synergistic effect (Srivastava and Vaidya, 1999). Whilst atovaquone inhibits the cytochrome bc_1 complex and thus prevents mitochondrial electron transport, proguanil acts as a dihydrofolate reductase (DHFR) inhibitor (Tse, Korsik, and Todd, 2019). Atovaquone potently inhibits ookinete and oocyst development in the mosquito vector (Davies et al., 1989) and interestingly, atovaquone-resistance is not heritable, as the mutations that arise in ABS parasites deem them as sterile for transmission (Goodman et al., 2016; Delves, Angrisano, and Blagborough, 2018). Mefloquine is an alternative gold-standard treatment for chemoprotection, although associated with a small risk (11.9 cases per 10,000 treatments) of adverse neuropsychiatric side effects (Wells, Huijsduijnen, and Van Voorhis, 2015; Lee et al., 2017).

Chemoprevention entails treatment of populations, including asymptomatic carriers, to combat seasonal malaria (Phillips et al., 2017). Sulfadoxine–pyrimethamine and amodiaquine has been effective in chemoprevention campaigns in regions threatened by recurring malaria (Phillips et al., 2017).

1.3.2 Drug discovery pipeline

Building on the successes and learning from the drawbacks of existing antimalarials, the key traits required of novel hit compounds entering the developmental pipeline is clear. Firstly, drugs targeting the symptomatic ABS parasites should exert a

rapid clearance of the parasite reservoir whilst maintaining an active plasma concentration for a prolonged period, ideally lasting a week (Wells, Huijsduijnen, and Van Voorhis, 2015). There is increased attention on optimising the *in vivo* half-lives of newly discovered compounds, given the shortcomings of ART derivatives (Burrows et al., 2017; Wells, Huijsduijnen, and Van Voorhis, 2015). Additionally, given the resistance to sulfadoxine–pyrimethamine, alternative compounds that target the pre-erythrocytic forms and therefore provide chemoprotection are required (Wells, Huijsduijnen, and Van Voorhis, 2015).

Moving towards eradication, novel antimalarials able to break the cycle of transmission by compromising viability of the sexual stage gametocytes are key (Burrows et al., 2017). Mass drug administration campaigns are also central to eradication, requiring compounds able to both treat symptomatic patients and eliminate the parasite reservoir of asymptomatic patients (Wells, Huijsduijnen, and Van Voorhis, 2015). Finally, SERCaP would entail elimination of the dormant hypnozoites and although tafenoquine shows great promise, safety concerns threaten its use (Burrows et al., 2017). By accelerating the rate of discovery, the advent of high-throughput screening, whether phenotypic or target-based, has transformed the drug developmental pipeline (See Figure 1.9).

1.3.3 Vector control

Responsible for 68% of averted malaria cases from 2000 and 2015, vector control by administration of LLINs and IRS have substantially impacted the malaria landscape (Bhatt et al., 2015). Persistent use of these control measures, particularly the pervasive use of pyrethroids, have unfortunately given rise to insecticide resistance in *Anopheles* mosquitos (Ojuka et al., 2015; Toé et al., 2014). There has been a consequent acceleration in trialling insecticides with activity against pyrethroid-resistant mosquitos, importantly aiming to identify compounds with novel MoAs which can be formulated in combination with other insecticides (N'Guessan et al., 2016; Ngufor et al., 2014). Insecticide deployment strategies are also being explored with ongoing research into spraying technologies, slow-release from wall linings and seasonal release of compounds (Phillips et al., 2017).

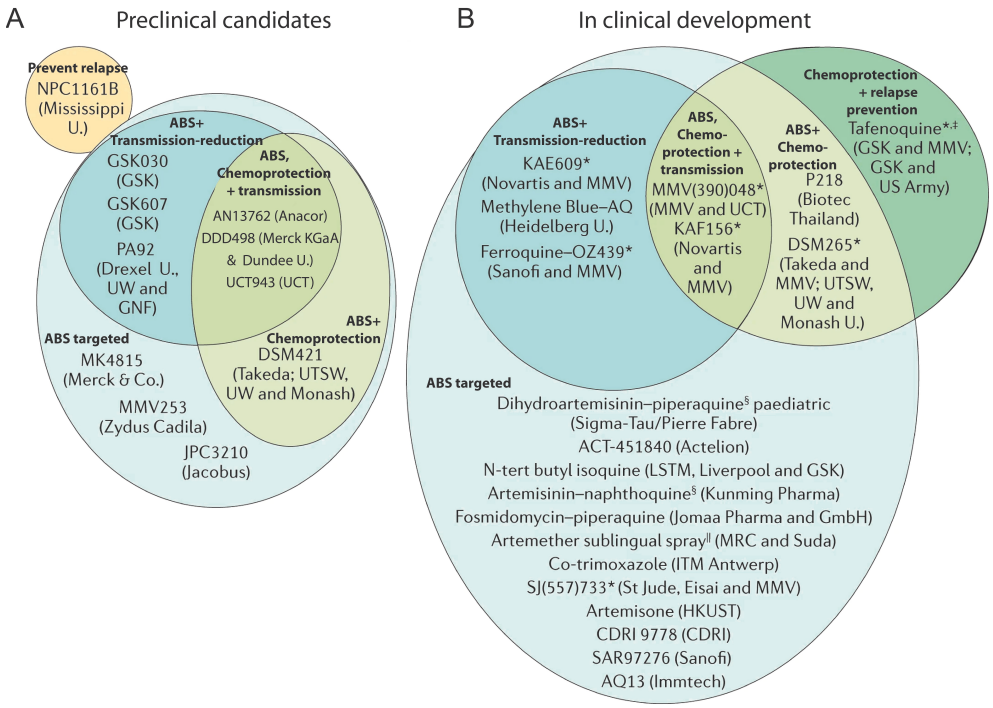


Figure 1.9: The antimalarial drug pipeline. (A) Preclinical candidates and (B) compounds in clinical development are listed, along with the institutes in which they were discovered. Candidates include those that *aim to be formulated in a combination treatment as a single-exposure radical cure, ‡target relapse, §represent novel three-day ACTs and ‖treat severe malaria. Figure adapted from Phillips et al., 2017.

There has been great innovation in research around vector control in recent years. A genetic approach which has gained significant traction in the field is gene drive-modification of mosquitos (Windbichler et al., 2011). Gene drive technology biases inheritance of a given genetic modification, so it is transmitted to progeny at a super-Mendelian frequency (Nolan, 2021). Applying the concept to malaria control, gene drives may facilitate inheritance of a gene that disrupts mosquito viability or fertility, or generate mosquitos unable to transmit malaria (Windbichler et al., 2011; Nolan, 2021; Raban, Marshall, and Akbari, 2020).

Another recently tested approach to malaria control is the application of anti-malarials to bed nets and mosquito sugar baits (Paton et al., 2019). This potential tool was experimentally emulated using an adapted format of the gold-standard standard membrane feeding assay (SMFA) and known inhibitor of ookinete and oocyst formation, atovaquone (Paton et al., 2019). It was found that *P. falciparum* transmission was blocked in *Anopheles gambiae* mosquitoes upon tarsal exposure (by the mosquito legs) to atovaquone and other cytochrome *b* inhibitors (Paton et al., 2019). Mathematical modelling of malaria transmission dynamics predicted that administration of antimalarial-impregnated mosquito nets would reduce malaria prevalence (Paton et al., 2019). These technologies are under continued development and are gaining widespread attention by leaders in the field, showing great promise as a future means of malaria control (Paton et al., 2019).

1.3.4 Vaccines

Malaria vaccines can be categorised into pre-erythrocytic, whole sporozoite, blood stage, placental and transmission blocking vaccines (Duffy and Patrick Gorres, 2020). Mosquirix™, the peptide RTS,S and proprietary adjuvant ASO1E, is the most advanced of vaccines to date, having undergone vigorous clinical testing. RTS,S is a pre-erythrocytic vaccine integrating a *P. falciparum* CSP fragment, comprised of a central repeat and C-terminal regions fused to a hepatitis B surface antigen (Duffy and Patrick Gorres, 2020). There are efficacy concerns with RTS,S and although the partial protection imparted by the vaccine would be valuable to malaria control, alternative vaccines are highly sought after (Wells, Huijsduijnen, and Van Voorhis,

2015; Duffy and Patrick Gorres, 2020). Alternative pre-erythrocytic vaccines which have been advanced to clinical testing are the CSP-based R21, full-length CSP candidates and viral-vectored candidates, including those targeted to CSP (Duffy and Patrick Gorres, 2020). Also, under trial are various whole sporozoite vaccines, produced by harvesting and attenuating *P. falciparum* sporozoites (PfSPZ) and administered by venous inoculation (Duffy and Patrick Gorres, 2020; Seder et al., 2013). Methods of PfSPZ attenuation include radiation attenuation, chemoattenuation and genetic attenuation (Duffy and Patrick Gorres, 2020).

Blood-stage vaccines candidates include PfRH5 and the AMA1-RON2 complex. Transmission-blocking vaccines can be categorised into three broad approaches: i) pre-fertilisation gametocyte and gamete proteins, ii) mosquito stage (gamete, zygote and ookinete) proteins and iii) mosquito-derived antigens associated with midgut epithelium penetration (Delves, Angrisano, and Blagborough, 2018). Pre-fertilisation antigens P48/45, P230 and HAP2 and post-fertilisation antigens P25 and P28 are considered a priority due to the reproducible efficacy and immunity in transmission-blocking (Delves, Angrisano, and Blagborough, 2018).

1.4 The antimalarial screening landscape

By drastically accelerating the rate of discovery, drug screening has revolutionised the drug discovery and development field and can be categorised into target-based and phenotypic approaches. Target-based screening, or reverse pharmacology, utilises genomics and recombinant technology to study a target protein of interest. Small molecular chemical libraries are screened against the proposed target with biochemical assays or to test for high affinity binding. This approach requires both a fully validated drug target and follow-up tests to determine if hits exert a pharmacological effect *in vitro* (Lage et al., 2018; Flannery, Chatterjee, and Winzeler, 2013). In contrast, the phenotypic approach, also referred to as cell-based screening or forward pharmacology, entails testing chemical libraries in assays with a cell viability or phenotype-based readout. Although target and MoA deconvolution of hits identified in phenotypic screens is required, this approach uniquely facilitates the discovery of

compounds with novel biological activity (Lage et al., 2018; Flannery, Chatterjee, and Winzeler, 2013).

With the rise of antimalarial resistance, drugs with novel chemotypes and previously unexplored *Plasmodium* targets are crucial. Whilst the discovery of ABS-targeted compounds remains a priority, it is important to also target interventions towards other *Plasmodium* stages when aiming for elimination (Flannery, Chatterjee, and Winzeler, 2013; Yahiya et al., 2019). Advancements to *in vitro* culture techniques, liquid handling, robotic automation, assay miniaturisation and high content imaging have facilitated the plethora of antimalarial phenotypic screening data that has emerged in recent years (Flannery, Chatterjee, and Winzeler, 2013; Yahiya et al., 2019), with some key screens summarised in Figure 1.10. Screening initiatives at academic institutions are often enabled by access to molecular libraries from the pharmaceutical and chemical vendor industries. Depending on the *Plasmodium* stage in question, various assays are deployed and often performed in collaboration with other institutions in the case of large-scale screens (Yahiya et al., 2019). Results are deposited in the chEMBL Neglected Tropical Disease archive (Gaulton et al., 2017).

1.4.1 Asexual blood stage screens (TCP-1)

1.7 million compounds of the Genomics Institute of the Novartis Research Foundation (GNF) Chemical Library were screened against *P. falciparum* in the first major ABS screen, yielding 6000 hit compounds (Plouffe et al., 2008). One landmark screen performed by GlaxoSmithKline tested two million compounds (Gamo et al., 2010), identifying >13,500 potent hits which were later developed into the Tres Cantos antimalarial compound set (TCAMS), initiating further screens with this library (Crowther et al., 2016; Miguel-Blanco et al., 2017; Gomez-Lorenzo et al., 2018). Other *P. falciparum* ABS screening initiatives include those against the 250,000-compound Griffiths University library (Avery et al., 2014) and 300,000-compound St. Jude Children's Research Hospital (SJCRH) chemical library (Guiguemde et al., 2010). The potent spirondolone KAE609, or Cipargamin (White et al., 2014b), was yielded in an ABS screen and is currently under development, exemplifying the

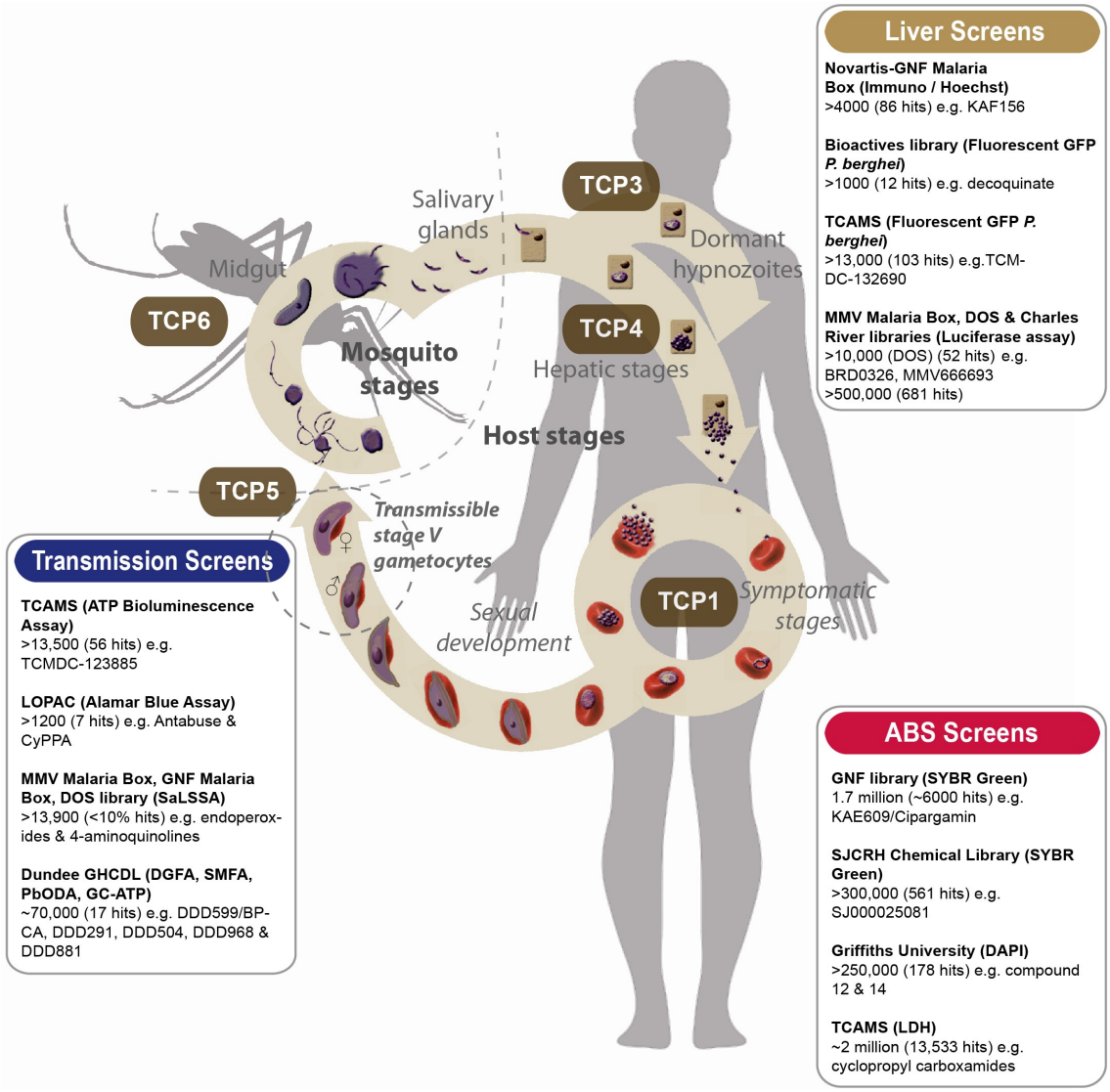


Figure 1.10: The antimalarial phenotypic screening landscape and corresponding TCPs of the *Plasmodium* life cycle. Phenotypic screening has predominantly focussed on the asexual blood stages (TCP-1), the pre-erythrocytic stages (TCPs 3-4) and the sexual stages (TCP-5), in search for candidates treating symptoms, providing chemoprotection and blocking transmission, respectively. Exemplar screens are listed as the compound library, assay(s) performed, library size, the number of hits identified and examples of notable hits. Figure adapted from Yahiya et al., 2019.

benefit of phenotypic screening.

1.4.2 Pre-erythrocytic screens (TCPs 3-4)

In search for compounds able to inhibit relapse (TCP-3) or with chemoprophylactic activity (TCP-4), robust *in vitro* assays have enabled liver-stage screens, which have otherwise been challenged by the requirement to develop infective sporozoites. Although screening for TCP-3 activity has advanced, scarce *P. vivax* hypnozoite models have limited the discovery of alternative treatments to primaquine and tafenoquine. A low-throughput *in vivo* imaging-based assay with rhesus monkeys and *P. cynomolgi* was the leading platform for hypnozoitocidal drug testing, until an *in vitro* alternative was developed (Dembele et al., 2011). The *in vitro* model utilises *P. cynomolgi* sporozoites and primary monkey hepatocytes (Dembele et al., 2011), and enabled discovery of the multi-stage inhibitor KAI407 (Zeeman et al., 2014). Another notable output of the *in vitro* culture of *P. cynomolgi*–infected *M. fascicularis* primary hepatocytes was the elucidation of a 'wake-and-kill' phenotype of TM2-115, an inhibitor of histone methyltransferase (Dembélé et al., 2014). TM2-115 was found to accelerate hypnozoite activation, making them susceptible to inhibition (Dembélé et al., 2014).

Screening for pre-erythrocytic TCP-4 activity is substantially more advanced than testing for TCP-3 activity, with various high-content imaging and luciferase-based assays available for study. The imidazolopiperazine scaffold of KAF156, a multi-stage inhibitor of the asexual, liver and transmission stages, was discovered in a screen of the Novartis-GNF library (Meister et al., 2011) and with subsequent lead development into KAF156, the compound has now entered clinical trials (White et al., 2016). Numerous high-throughput liver-stage screens have now been published: i) 1037 existing drugs were screened against *P. berghei*, yielding a multi-stage mitochondrial bc_1 complex-inhibitor, decoquinate (Cruz et al., 2012), ii) the MMV malaria box and Broad Institute Diversity-Oriented Synthesis library were screened in a luciferase-based assay (Swann et al., 2016), iii) 103 multi-stage active hits were identified in a screen of the TCAMS library (Raphemot et al., 2015) and iv) 600 hits were identified in a screen of half a million compounds from Charles River

(Antonova-Koch et al., 2018).

1.4.3 Transmission blocking (TCP-5) screens and assays

Breaking the cycle of *Plasmodium* transmission is critical to the eradication agenda, broadening protection from the infected individual to the uninfected population (Burrows et al., 2017). Parasite transmission from the vertebrate to the mosquito hinges on the viability of sexual stage gametocytes. Characterised by their markedly complex development, gametocytes uniquely exist over multiple morphological forms and as two sexes, providing multiple avenues for treatment. Evolution of gametocyte-targeted drug resistance would occur at a considerably lower rate than ABS-targeted medicines, given gametocytes represent a non-replicative population bottleneck, comprising only a small percentage of the total parasite population in an infected individual (Delves et al., 2018). Transmission screening initiatives have centred around improvements to *in vitro* culture of *P. falciparum* gametocytes (Delves et al., 2016; Duffy et al., 2016). Despite the sexual stages not being amenable to the customary proliferation or DNA replication markers of viability, being non-replicative in nature, multiple markers of viability have been developed (Duffy and Avery, 2013; Buchholz et al., 2011; Adjalley et al., 2011; Peatey et al., 2011).

One exemplar transmission-focused screen was performed against the MMV malaria box and utilised two high-throughput assays to profile for immature and mature gametocytocidal activity (Duffy and Avery, 2013). The readout of both assays was obtained by confocal fluorescence microscopy, measuring either the expression of pfs16-Luc-GFP, a gametocyte specific marker, or a marker of mitochondrial function, MitoTracker Red (Duffy and Avery, 2013). Multiple studies have taken similar approaches, including those that have performed assays with flow cytometry (Peatey et al., 2011; Buchholz et al., 2011) and luminescence-based (Adjalley et al., 2011) readouts. In a study conducted by GSK and MMV, improvements to the mass production and purification of gametocytes and an ATP bioluminescence-based assay enabled the screening of 17 gold-standard antimalarial compounds (Lelièvre et al., 2012) and the TCAMS library (Almela et al., 2015). Additional assays of gametocyte viability with varying readouts have been developed; these include col-

orimetric screening assays i) measuring parasite lactate dehydrogenase (pLDH) activity (D'Alessandro et al., 2013) and ii) use of oxidoreduction indicator alamarBlue (Tanaka and Williamson, 2011) as markers of gametocyte metabolic activity, iii) the use of fluorescent acridine orange to measure gametocytaemia and gametogenesis-induced rounding up (Lucantoni et al., 2015) and iv) the Saponin-lysis Sexual Stage Assay (SaLSSA) which measures mitochondrial membrane potential using Mito-Tracker Red (Plouffe et al., 2016).

1.4.3.1 Standard Membrane Feeding Assay

Drug interventions targeted towards immature gametocytes will be clinically unfavourable, given only stage V gametocytes are transmissible and may already be present in circulation at the point of treatment. Crucially, the *in vivo* transmission-blocking activity of gametocytocidal hits must be validated with the standard membrane feeding assay (SMFA) additionally to tests of gametocyte viability (Churcher et al., 2012; Delves and Sinden, 2010). The gold-standard SMFA determines the transmissibility of mature gametocytes by measuring the prevalence and intensity of a mosquito infection, specifically the presence and number of oocysts, respectively (Churcher et al., 2012). Drug-treated mature gametocytes are fed to *Anopheline* mosquitos via an artificial membrane and following an appropriate developmental period, mosquito midguts are dissected to measure oocyst development (Churcher et al., 2012). In the context of drug screening, the laborious, expensive and low throughput experimental conditions of the SMFA limits its use in high-throughput campaigns.

1.4.3.2 Sex and stage specificity

Overcoming the limitations of the SMFA, an assay which determines gamete formation as a measure of the functional viability of stage V gametocytes *in vitro* has been developed (Ruecker et al., 2014). The dual gamete formation assay (DGFA) is uniquely adaptable to provide the sex (male and/or female) and stage (gametocyte and/or gamete) specificity of transmission-blocking hits, is amenable to high-throughput screening and importantly predicts inhibitory activity found in the

SMFA (Ruecker et al., 2014; Delves et al., 2019). The scope and significance of the results which can be derived from the DGFA are summarised in Figure 1.11.

For the purpose of drug screening, the DGFA can be performed in 384-well screening plates in which test compounds are dispensed, either as single or multiple doses, along with negative DMSO and positive gentian violet controls (Delves et al., 2016; Ruecker et al., 2014). Mature gametocytes meeting a cut-off exflagellation rate, a marker of culture viability, are plated with test compounds (Delves et al., 2016). Cultures are incubated with compounds from 0-48 hours, critically maintaining a 37°C temperature during plate handling and incubation, to avoid premature activation of gametogenesis. Following compound incubation, gametogenesis of treated gametocytes is induced with ookinete media containing Cy3-conjugated anti-Pfs25 antibody (Ruecker et al., 2014). Microscopy is utilised to measure the male and female gamete formation counts per well, which are subsequently converted to either a percentage of inhibition or half-maximal inhibitory concentration (IC_{50}) of each test-compound, relative to controls. The DGFA readout varies with sex: male gamete formation is measured as the number of exflagellation centres from time-lapses acquired by brightfield microscopy, and female gamete formation is measured with single-image fluorescence microscopy to measure Pfs25 expression, a marker of female egress. Stage-specificity can be determined with varying formats of the DGFA in which compounds are incubated with gametocytes, and are either present ('carry-over') or removed ('wash-out') from samples when measuring gametogenesis, or alternatively gametocytes are not incubated with compounds but added at the point of activation ('add-in'). Throughput is maximised by automated dispense of test compounds, automated microscopy and analysis and miniaturisation to 384-well plate-based format (Delves et al., 2016; Ruecker et al., 2014).

The DGFA and assays determining capacity to block gametogenesis have revealed that males demonstrate an increased susceptibility to inhibition (Delves et al., 2013) and many existing antimalarials exert transmission-blocking activity (Delves et al., 2013; Delves et al., 2012b). Given the increased susceptibility of males to drug treatment and skewed gametocyte sex ratio (∼3-5 females:1 male), viability-based assays fail to identify all gametocytocidal hits (Delves et al., 2013). In combination

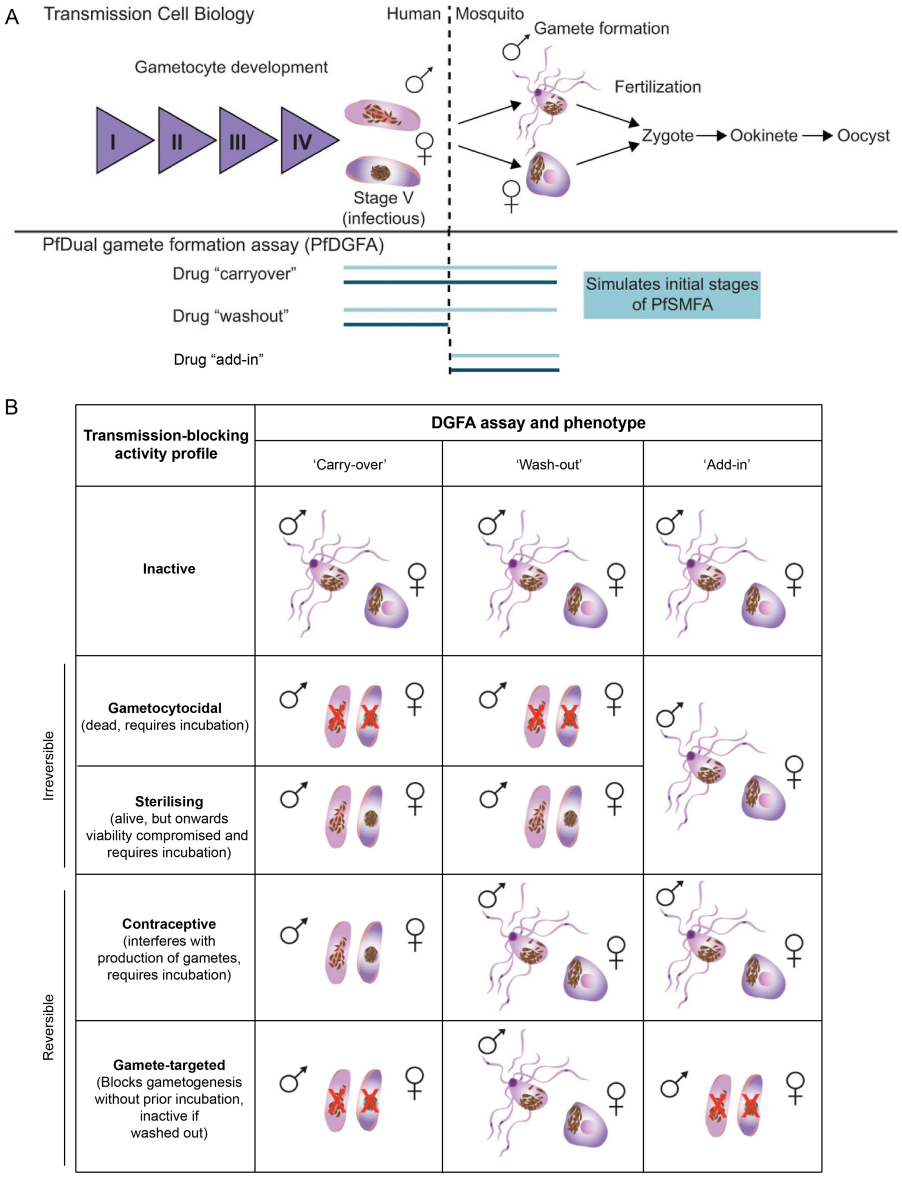


Figure 1.11: Scope, phenotype and activity profiles derived from the DGFA. The gametogenesis readout of hits in the carry-over, wash-out and add-in formats of the DGFA provides an indication of the compound profile. **DDD01035881** falls under the 'gamete-targeted' bracket, specifically blocking male gamete formation (microgametogenesis). Figure adapted from (Ruecker et al., 2014).

with the SMFA and various assays of viability, a high throughput screen was recently performed with a focus on the transmission-blocking activity determined in the DGFA (Delves et al., 2018). Details of the screen follow in Chapter 1.5.

1.5 The Global Health Chemical Diversity Library screen

Addressing the requirement for transmission-blocking antimalarials, a recent large-scale screening campaign was performed between Imperial College London and GSK Tres Cantos, exemplifying the benefit of collaboration between industry and academia (Delves et al., 2018). Mitigating the traditional screening framework in which ABS-activity is prioritised and transmission-blocking activity is measured as a secondary benefit, the screen took a transmission-centred approach. Compiled by the Dundee University Drug Discovery Unit (DDU), the 68,689-compound unbiased Global Health Chemical Diversity Library (GHCDL) was screened against various stages of *Plasmodium*, primarily filtered based on activity in the *Pf*DGFA (Figure 1.12). GHCDL compounds are structurally dissimilar to existing antimalarials and display lead-like physicochemical properties. Clustered in groups of 3-14 structurally similar molecules, structure-activity relationships of active hits could be intrinsically determined by screening against GHCDL compounds (Delves et al., 2018).

1.5.1 GHCDL screening framework

To primarily profile the GHCDL based on transmission-blocking activity, compounds were initially tested in the *Pf*DGFA carry-over format, with a 48-hour incubation at 2 μM. 24 hits with IC_{50}s < 10 μM were yielded which were further profiled for cytotoxic activity against human HepG2 cells, with 22 demonstrating $< 50\%$ inhibition at 10 μM. Of the original 24 hits, 19 were male-specific, three were female-specific and two had dual-activity against both sexes. The GHCDL was simultaneously screened in the LDH assay (Gamo et al., 2010) as a measure of ABS-targeted activity, prioritising hits with IC_{50}s < 2 μM (Delves et al., 2018).

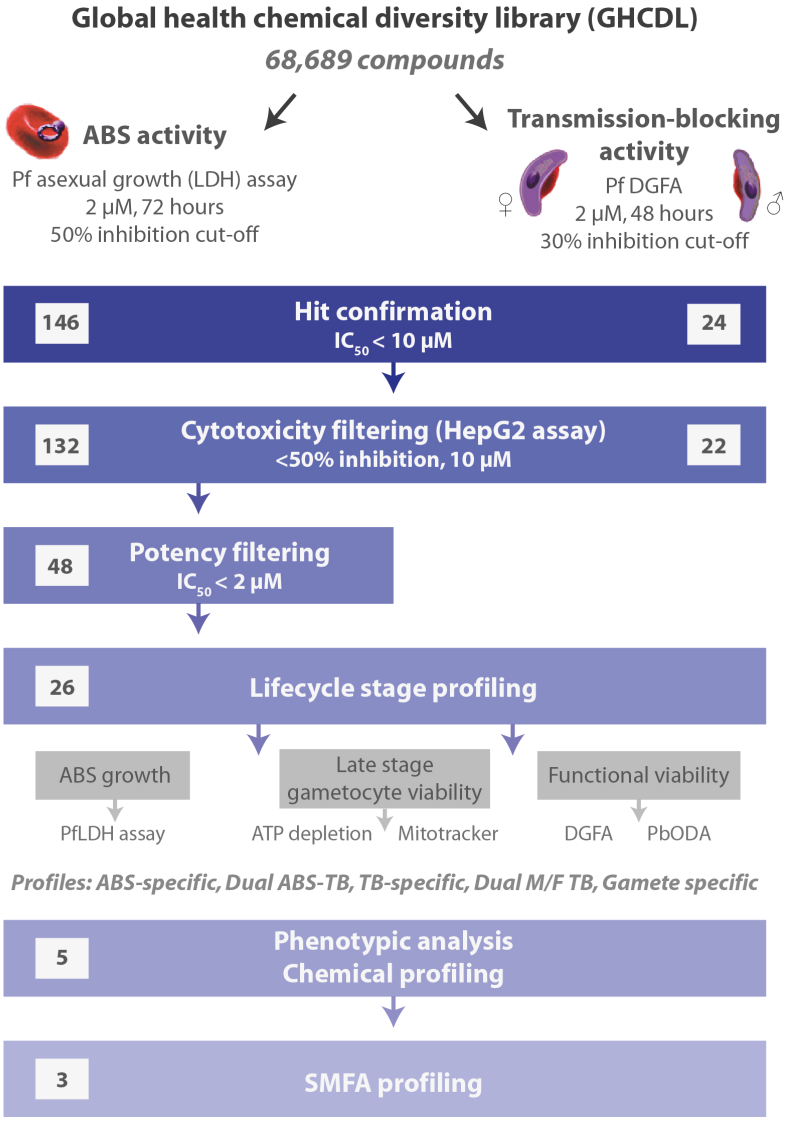


Figure 1.12: GHCDL screen workflow. The GHCDL screen progression cascade, which was performed by Delves et al., 2018 in parallel against *P. falciparum* asexual and sexual stages, predominantly filtering hits for transmission-blocking activity in the DGFA. Figure adapted from Delves et al., 2018.

Hits were further biologically profiled utilising various assays to assign stage-specificity, assessing whether activity was targeted to the *P. falciparum* ABS parasites, *P. falciparum* sexual stages (specifically the male and female mature gametocytes or gametes) or early *P. berghei* mosquito stages. Additionally to the ABS LDH assay (Gamo et al., 2010) and DGFA (Ruecker et al., 2014), stage IV/V gametocyte metabolic viability was determined with the late-stage gametocyte ATP depletion (Almela et al., 2015) and mitotracker (Plouffe et al., 2016) assays. Additionally, onwards *P. berghei* mosquito development was measured with the *Pb* ookinete development assay (*Pb*ODA) (Ruecker et al., 2014; Delves et al., 2012a). Hits were found to have diverse activity profiles, with transmission-specific, male gamete-specific, dual ABS-gametocyte and asexual-specific compounds being identified. Interestingly, no transmission-blocking hits were active against the liver stages in the *P. berghei* luciferase sporozoite HepG2 invasion assay, likely due to the divergences in cell biology of these stages (Swann et al., 2016). Five male-active hits were prioritised due to their favourable potency and activity profiles, and their phenotypic impact during microgametogenesis was determined by imaging immunofluorescence-labelled gametocytes treated with hit compounds (Delves et al., 2018).

1.5.2 Chemical profiling

Favourable hits were re-sourced for chemical profiling and drug metabolism and pharmacokinetics (DMPK) analysis. Unexpectedly, three of the five hits were found to be inactive in the *Pf*DGFA when re-synthesised; two compounds were found to be prone to oxidation and it was found that the structure of the third GHCDL-derived compound differed from the re-synthesised compound, determined by NMR and LCMS. The three compounds were found to be chemically unfavourable and the two remaining hits, dual asexual-gametocyte (both male and female) inhibiting compound **DDD01245291** and male gamete-targeted **DDD01035881**, were prioritised for further study. DMPK analysis of **DDD01245291** revealed a suitable aqueous solubility (> 250 μM) and satisfactory mouse liver microsome clearance rate (4.2 ml min^{-1} g^{-1} liver). However, the compound was limited by its poor bioavailability in the parallel artificial membrane permeability assay (PAMPA) with

a membrane permeability of 5.9 nm s^{-1}. **DDD01035881** showed a suitable DMPK profile, with a favourable aqueous solubility (>250 μM) and no mouse liver microsome metabolism (< 0.5 ml min^{-1} g^{-1} liver), making it a priority for further study (Delves et al., 2018).

1.5.3 *In vivo* transmission-blocking activity

The transmission blocking efficacy of **DDD01245291** and **DDD01035881** was determined using an adapted *Pf*SMFA with a luciferase oocyst readout (Vos et al., 2015). **DDD01245291** was tested in 'indirect mode', treating gametocytes with 10 μM compound for 24-hours, prior to mosquito feeding in the absence of compound. The infection prevalence of **DDD01245291**-treated parasites was strongly inhibited. Due to its male gamete-targeted activity, **DDD01035881** was tested in 'direct mode', in which there was no prior compound incubation with gametocytes, but 10 μM compound was present during the mosquito feed. A complete block in transmission, in both oocyst prevalence and intensity, was determined with **DDD01035881** treatment (Delves et al., 2018).

Using *P. berghei* infected mice, **DDD01245291** and **DDD01035881** *in vivo* transmission blocking activity was evaluated. 24 hours prior to a mosquito feed, mice were treated with a 50 mg kg^{-1} intraperitoneal (IP) dose of compounds. Asexual parasitaemia was not impacted by **DDD01245291**, but gametocytaemia was considerably reduced. The *in vivo* effects of **DDD01245291** were less notable relative to its *Pf*SMFA and *in vitro* activity, and was a probable result of its poor membrane solubility. Reduction in oocyst production was not deducible due to the unusually high baseline oocyst levels in controls (Delves et al., 2018).

DDD01035881 administration 24 hours prior to a feed did not reduce oocyst development and as expected from its gamete-targeted activity, did not reduce ABS parasitaemia or gametocytaemia. However, a complete block of transmission was measured when administered 30 minutes prior to a feed. Pharmacokinetic analysis was performed and a **DDD01035881** plasma half-life of around 90 minutes was measured in naïve mice (Delves et al., 2018).

Stage	**Assay**	**Incubation (h)**	**Activity**	
Liver stages	*Pb* Liver Invasion	48h	IC_{50} (μM)	Not converged
	Recombinant luciferase	48h		>50
ABS	*Pf*LDH	72h		17.52
Gametocytes	*Pf* Late stage ATP	72h		>10
	Pf Stage V Mito	72h		>25
Gametes	*Pf*DGFA	24h carryover		Male: 0.26, Female: >12.5
		48h carry-over		Male: 0.70, Female: >12.5
		48h wash-out		Male: >12.5, Female: >12.5
		0h add-in		Male: 0.19, Female: >10
Ookinetes	*Pb*ODA	24h		0.11
Human safety profile	Human HepG2	48h	TOX_{50} (μM)	>50

Table 1.1: **DDD01035881** activity profile. Assays performed by Delves et al., 2018 as part of the published GHCDL screen.

1.5.4 The N-4HCS compounds

Notably, six potent compounds which specifically targeted the male gamete were found to share a common *N*-((4-hydroxychroman-4-yl)methyl)-sulphonamide (N-4HCS) scaffold, including **DDD01035881** (Delves et al., 2018). The **DDD0103-5881** activity profile, defined in the GHCDL screen, is summarised in Table 1.1. The male-gamete specificity of the N-4HCS hits was apparent from the potent inhibition of exflagellation in the *Pf*DGFA carry-over and add-in, notably not requiring any prior compound incubation with gametocytes for activity. Additionally, the inactivity of N-4HCS compounds in the *Pf*DGFA wash-out and against ABS parasites corroborated its male-gamete targeted activity. Consistent with N-4HCS inhibition of exflagellation, these compounds were found to inhibit *P. berghei* ookinete development (Delves et al., 2018). The potent transmission-blocking activity demonstrated in the DGFA, SMFA and against *P. berghei*-infected mice without any compound incubation deem **DDD01035881** and N-4HCS analogues interesting avenues of study. With suitable formulation and improved stability, **DDD01035881** may become an important starting point for antimalarial development. Uncovering the mode by which N-4HCS compounds exert an instant inhibitory effect to microgametogenesis has the potential to reveal novel observations of this remarkable biological process.

1.6 Aims and hypotheses

Gains made in malaria control continue to be threatened by the spread of drug and insecticide resistance and now, as the COVID-19 pandemic may further jeopardise progress, it is more important than ever to identify novel treatment strategies. Combined vector and parasite control measures, measured by the success of insecticides and ACTs, have been pivotal to progress against malaria. Here, we focus on parasite development within the vector itself by developing a compound, **DDD01035881**, able to halt host-to-vector transmission.

By following a traditional drug development pipeline, the work presented in this thesis aims to develop an in depth understanding of the target, mode of action, phenotype, chemical characteristics and safety profile of **DDD01035881**, maximising its success in preclinical testing. Furthermore, we aim to facilitate future transmission-blocking drug discovery by devising a novel method of phenotypic characterisation. The overarching aims of this thesis are to:

1. Test the potency and safety of the male gamete-targeted N-4HCS compound series in a hit-to-lead development study; and

2. Identify and validate the cellular target(s) of N-4HCS compounds; and

3. Characterise the N-4HCS cellular phenotype and corresponding mode of action in *P. falciparum*; and

4. Develop an accessible live-cell fluorescence microgametogenesis imaging workflow with future applications in drug discovery.

Chapter 2

Materials and methods

2.1 Materials and reagents

*PfDyn*GFP/*P47*mCherry parasites (Lasonder et al., 2016) were generously donated by Edwin Lasonder (Plymouth University, Plymouth, UK), Richard Bartfai and colleagues (Radboud University, Nijmegen, The Netherlands). *Pf2004*/164-tdTom parasites (Brancucci et al., 2015) were kindly donated by Nicolas Brancucci, Matthias Marti and colleagues (Harvard T.H. Chan School of Public Health, Boston, Massachusetts, USA).

Compound **1294** (Doggett et al., 2014) was generously provided by Wesley C. Van Voorhis and colleagues (University of Washington, Seattle, Washington, USA). Compound **ML10** was kindly donated by David A. Baker (London School of Hygiene & Tropical Medicine, London, UK), Simon A. Osbourne (LifeArc, Stevenage, UK) and colleagues (Baker et al., 2017). Compounds **DDD01035881**, **(-)-DDD01035881**, **(+)-DDD01035881**, **DDD01028076**, **(-)-DDD01028076**, **(+)-DDD01028076** and **1-8** were synthesised and kindly provided by Charlie Saunders, Oliver J. Fischer, Ainoa Rueda-Zubiaurre and Xiaojun Hu (Imperial College London, UK), see Rueda-Zubiaurre et al., 2019. Azido-TAMRA/biotin capture reagent (AzTB) was synthesised and generously donated by Edward Tate and colleagues (Imperial College London, UK), see Wright et al., 2015.

Mouse anti-Pfs16 clone 32F717:B02 (Moelans, 1995) was kindly donated by Robert Sauerwein and colleagues (Radboud University, Nijmegen, The Netherlands).

Rabbit anti-Pfg377 (Ishino et al., 2020) was generously donated by Tomoko Ishino and colleagues (Ehime University, Toon, Ehime, Japan).

The CL-1000 Ultraviolet Crosslinker (UVP) was kindly shared by members of the Dallman lab (Imperial College London, UK) for photoaffinity labelling.

2.2 *In vitro* culture of *Plasmodium falciparum*

P. falciparum strains NF54, *PfDyn*GFP/*P47*mCherry (Lasonder et al., 2016) and *Pf*2004/164-tdTom (Brancucci et al., 2015) were cultured as previously described (Delves et al., 2016). Asexual blood stage parasites were maintained at 0.5-5% total parasitaemia in RPMI-1640 media with 25mM HEPES (Life Technologies), supplemented with 300 μg/ml L-glutamine, 50 μg/ml hypoxanthine (Sigma) and 10% A+ human serum (Interstate Blood-Bank). *Pf*2004/164-tdTom parasite culture media was further supplemented with 4nM WR 99210. Parasites were cultured in human O+ or A+ erythrocytes (NHS National Blood Service) at 4% (NF54 and *PfDyn*GFP/*P47*mCherry) or 5% (*Pf*2004/164-tdTom) haematocrit supplemented with heparin (Sigma-Aldrich) to a final concentration of 30 units/ml. Parasite cultures were maintained at 37°C under 3% O_2/5% CO_2/92% N_2 gas (BOC Special Gases) and media was replaced daily.

Unless otherwise stated, gametocytes were induced at 3% asexual blood stage parasitemia and 4% haematocrit, in media supplemented with 2.78 mg/ml sodium bicarbonate, 2 mg/ml D-glucose, 150 μg/ml L-glutamine, 50 μg/ml hypoxanthine, 5% A+ human serum and 5% AlbuMAX II (Life Technologies). Gametocytes were cultured to stage V maturity by replacing media daily without dilution or addition of new erythrocytes for 14 days following induction, strictly maintaining parasites at 37°C to ensure viability and prevent activation of gametogenesis. Exflagellation rates were determined as a measure of gametocyte viability and maturity on day 14 post-induction. Microgametogenesis was activated by combination of equal volumes of gametocyte culture and ookinete media (RPMI 1640 with 25 mM HEPES supplemented with 50 μg/ml hypoxanthine, 2 g/l sodium bicarbonate and 100 μM xanthurenic acid, stored at 4°C). To count exflagellation rates relative to erythro-

cyte density at 15 minutes post-activation. Exflagellation was counted using a Nikon Leica DC500 microscope and a haemocytometer (VWR).

2.3 *P. falciparum* Male Gamete Formation Assay

The male gamete formation assay (MGFA) was adapted from the previously described dual gamete formation assay (Ruecker et al., 2014). The MGFA was performed for the identification of active analogues of the male-specific **DDD01035881**, which acts immediately upon microgametogenesis activation. Hence, the MGFA was performed with a male-specific readout and no compound preincubation with gametocytes. Compounds of interest, prepared as 10 mM stock solutions, were dispensed in serial dilutions into black flat-bottom 384-well plates (Greiner) with the HP D300 Digital Dispenser. Initial dose responses were tested from 40 nM to 25 μM, followed by lower targeted concentration ranges for compounds with an $IC_{50} < 1000$ nM. Plates contained 0.25% DMSO (Honeywell) and 20 μM **DDD01028076** negative and positive single point controls, respectively, and each well was normalised to 0.25% DMSO. Stage V *P. falciparum* NF54 gametocytes with $\geqq 0.3\%$ exflagellation were diluted to 25 million erythrocytes/ml with prewarmed culture media to a total of 25 ml. To activate gametogenesis, 10 μl ookinete media was dispensed into each well of the plates followed by 50 μl dilute gametocyte culture. To aid activation, plates were cooled by incubating them at 4°C for 4 minutes, followed by 28°C for 5 minutes.

Plates were transferred to a Nikon Eclipse Ti inverted microscope to capture exflagellation events in each well. Using the JOBS module of NIS elements, autofocus was used to determine a suitable z-coordinate at which 10-frame time-lapses were acquired. Time-lapses were acquired at 4 frames/sec under phase contrast, at x4 objective and 1.5x zoom. Exflagellation events appeared as areas of perturbation to the erythrocyte monolayer in time-lapses.

Using the open-source Icy Bioimage Analysis software (Chaumont et al., 2012), exflagellation events in each time-lapse were quantified with a semi-automated algorithm. The algorithm was designed to recognise exflagellation events over back-

ground based on the circularity, size and pixel intensity of erythrocyte monolayer perturbations. The percentage inhibition of exflagellation, relative to positive (C1) and negative (C2) controls, was determined for each data point. Only data with a Z′ factor $\geqq 0.4$ was used. Percentage inhibition was calculated with the following equation:

$$\%\, inhibition = 100 - \left(\left(\frac{test\, compound - C1}{C2 - C1}\right) \times 100\right) \tag{2.1}$$

Dose response data was used to determine the IC_{50} of studied compounds in GraphPad Prism version 8 with the "log(inhibitor) vs response-variable slope (four parameters)" function. All reported IC_{50} values are depicted as an average of biological replicates ± standard error, derived from dose response curves with $R^2 \geqq 0.95$. The assay was performed with $n \geqq 3$ and $n \geqq 2$ biological and technical replicates, respectively.

2.4 HepG2 Viability

2.4.1 HepG2 cell culture

Commercially sourced HepG2 cells (ATCC HB-8065) were maintained in Dulbecco's modified Eagle medium (Sigma) supplemented with 1% L-glutamine (Sigma), 1% penicillin-streptomycin solution (Sigma) and 10% fetal bovine serum (Sigma). Cells were grown in 1 $\mu g/cm^2$ collagen (Gibco by Life Technologies) coated flasks and detached with trypsin (Gibco) for counting using FastRead slides (Immune Systems).

2.5 Alamar Blue viability assay

To determine HepG2 viability under N-4HCS treatment, HepG2 cells were diluted to 2.2×10^5 cells/ml in complete culture medium. 1 $\mu g/cm^2$ collagen-coated black 96-well plates (Greiner) were prewarmed and washed with phosphate-buffered saline (PBS) prior to plating of 100 μl of diluted HepG2 cells. Plated cells were then maintained at 37°C and 5% CO_2.

HepG2 cells were left to grow for 24 h prior to treatment with 10 μM compounds. Plates were normalised to 0.5% DMSO and contained 0.5% DMSO (Honeywell) or 50 μM doxorubicin (Sigma) negative and positive controls, respectively. Blanks of HepG2, media ± Alamar Blue (Thermo Fisher) and empty wells were incorporated into each plate. Plates were incubated at 37°C and 5% CO_2 for 48 h prior to addition of Alamar Blue. Upon addition of Alamar Blue, plates were further incubated for 2.5 h at 37 °C and fluorescence of each well was measured using a Tecan infinite M200 Pro, with excitation at 560 nm and emission at 590 nm. HepG2 viability was determined as the percentage of viable cells using the following equation:

$$\%\, viability = \left(\frac{test\, compound - blank}{DMSO\, control - blank} \right) \times 100 \tag{2.2}$$

Results depicted were derived from n $\geqq$ 3 biological replicates, with an average Z' factor of 0.65 for each replicate.

2.6 Target identification and validation

2.6.1 Photoaffinity labelling of live gametocytes

For target identification by nLC-MS/MS, parasites were treated with either 0.25% DMSO, 10 μM probe **8** only or a combination of 10 μM probe **8** and 10 μM parent molecule **7**. For validation by in-gel fluorescence and western blot, dose response samples were also obtained by treating parasites with either 0.25% DMSO or 2.5 μM, 5 μM or 10 μM probe **8**. Live stage V *P. falciparum* NF54 gametocytes with $\geqq$ 0.3% exflagellation were treated with the appropriate treatment conditions, normalised to 0.25% DMSO, for 10 minutes at 37°C. Treated parasites were irradiated with UV light at 254 nm for 10 minutes using a CL-1000 Ultraviolet Crosslinker (UVP) before purification of gametocytes by density barrier isolation. All experiments were performed with n $\geqq$ 3 biological replicates.

2.6.2 Gametocyte purification by density barrier isolation

Stage V gametocytes were isolated with Nycoprep 1.077 density gradient media (Axis-Shield). 10 ml of mature stage V gametocyte culture was added dropwise to 5 ml prewarmed Nycoprep 1.077 and centrifuged at 500 x *g* for 20 minutes at 37°C (brake applied). The gametocyte interface was collected and washed in prewarmed culture media at 800 x *g* for 5 minutes at 37°C (brake applied). Media was removed to obtain a pure gametocyte pellet which was then treated with 200 μl ookinete media to activate gametogenesis. Gametogenesis was halted by addition of 0.01% saponin at 4°C for 5 minutes before centrifugation at 17,000 x *g* for 5 minutes at 4°C, to lyse erythrocytes. The supernatant was removed and the cell pellet was washed a further 4 times in 0.01% saponin (Sigma) before a final wash in PBS to obtain a pure gametocyte pellet. The pellet was snap frozen in liquid nitrogen and stored at -80°C.

2.6.3 Cell lysis by sonication

For photoaffinity labelling, treated gametocyte pellets were resuspended in lysis buffer (1% Triton-X100 / 150 mM NaCl / 10 mM Tris /cOmplete™ ULTRA EDTA-free Protease Inhibitor Cocktail at pH 7.5 in H2O) before sonication (60% amplitude (2 s pulse, 2 s rest), 3 minutes). Cell lysate was centrifuged at 17,000 x *g* for 20 minutes at 4°C and protein concentration of each sample was determined using the Pierce™ BCA Protein Assay Kit, following the manufacturer's instructions. A NanoDrop™ 2000 spectrophotometer was used to measure absorbance, using BSA as a protein standard. 100 μl gametocyte lysate was prepared at 0.5-1 mg/ml in PBS for cycloaddition and protein precipitation.

2.6.4 CuAAC and protein precipitation

For copper catalysed azide-alkyne cycloaddition (CuAAC) of gametocyte lysate, a click reaction master mix was prepared by combination of the following reagents in order:

1. 0.1 mM AzTB (Wright et al., 2015) capture reagent (1 vol of 10 mM DMSO

stock)

2. 1 mM $CuSO_4$ (2 vol of 50 mM H_2O stock)

3. 1 mM Tris(2-carboxyethyl)phosphine hydrochloride (TCEP) (2 vol of 50 mM H_2O)

4. 0.1 mM TBTA (1 vol of 10 mM DMSO stock)

A mock catalyst mix was prepared for negative click control samples, in which the $CuSO_4$ catalyst was replaced by H_2O. Either the click reaction or mock catalyst master mixes were added to gametocyte lysate, adding 6 μl per 100 μl lysate. Samples were gently vortexed and incubated for 1 hour at RT with moderate shaking. To quench the CuAAC reaction, EDTA was added at a final concentration of 5 mM from a 500 mM stock in H_2O. For nLC-MS/MS-based identification, proteins were precipitated by addition of 4 volumes MeOH, 1 volume chloroform and 3 volumes H_2O. For in-gel fluorescence and western blot, proteins were precipitated by addition of 2 volumes MeOH, 0.5 volumes chloroform and 1 volume H_2O. Precipitated proteins were centrifuged at 17,000 x g for 2 minutes at 4°C. The protein interface was isolated by decanting the chloroform and MeOH/H_2O layers and was washed with 4 volumes MeOH, sonicated until dissolved and stored at -80°C for at least 20 minutes. Each sample was then centrifuged at 17,000 x g for 5 minutes at 4°C. MeOH was decanted and the protein pellet was left to air dry for 5 minutes. Protein was resolubilised in 2% SDS, sonicated and dissolved in PBS up to a final concentration of 0.2% SDS. 10μl of the crude lysate and CuAAC treated protein was set aside for analysis by in-gel fluorescence and western blot.

2.6.5 nLC-MS/MS sample pulldown

Sample preparation steps for target identification by nLC-MS/MS were performed together with Dr. Charlie Saunders (Chapters 2.6.5-2.6.8), who in collaboration with the Tate Lab (Imperial College London) designed the following proteomics aspect of the experiment. For nLC-MS/MS analysis, samples were incubated with Neutravidin Agarose beads to minimise background signal. Beads were derivatised

by centrifugation at 7000 rpm for 4 minutes at RT, washing with 100 mM triethylammonium bicarbonate (TEAB) 5 times and incubating with 100 mM TEAB, 25 mM $NaBH_3CN$ and 0.2% formaldehyde for 1 hour at RT, with moderate shaking. 1% ethanolamine in 100 mM TEAB was used to quench the reaction, before washing beads with 50 mM HEPES, pH 8.0 3 times and 0.2% SDS in HEPES (50 mM, pH 8.0) twice. Protein samples were added to derivatised beads and incubated for 2 hours at RT with moderate shaking. Beads were centrifuged at 7000 rpm for 4 minutes at RT, supernatant was removed and beads were washed with 0.2% SDS in HEPES (50 mM, pH 8.0) and 50mM HEPES, pH 8.0.

2.6.6 Digestion and TMT labelling

LysC and trypsin digestion was subsequently performed. LysC in 50mM HEPES, pH 8.0, was incubated with samples for 1 hour at 37°C to elute protein from beads. Eluted protein was obtained by retaining the supernatant obtained from centrifugation of samples at 6000 rpm for 4 min at RT, beads were washed at 50 mM HEPES, pH 8.0. Supernatants of each sample were combined and incubated with 5 mM TCEP and 10 mM chloroacetamide (CAA) for 10 min at RT. Samples were digested with 20 μg/100ul trypsin in 50mM HEPES, pH 8.3, incubating overnight at 37°C.

9-plex TMT labelling of samples was performed for MS analysis. TMT reagents (Thermo Fisher Scientific, MA) in acetonitrile were added to samples in a 1:1 volume ratio and incubated for 2 hours at RT, with moderate shaking. 5% hydroxylamine was added to samples to quench the reaction, prior to combination of all samples and 45°C centrifugal evaporation.

2.6.7 nLC-MS/MS preparation and acquisition

Subsequent proteomics sample preparation steps were performed by Dr. Charlie Saunders. To briefly summarise, desalting and 3-layer fractionation was performed before peptide separation on Acclaim PepMap RSLC column (Thermo Fisher Scientific). nLC-MS/MS data acquisition was performed with an QExactive mass spectrometer coupled to an easy nLC-1000 via an easy spray source (Thermo Fisher

Scientific).

2.6.8 Proteome Database Search and Analysis

Raw nLC-MS/MS data was analysed by Dr. Charlie Saunders in MaxQuant version 1.6.1.0 (Cox and Mann, 2008), using Andromeda to search against the Uniprot *P. falciparum* NF54 proteome (UniProt, 2019). Subsequent proteomics data analysis was performed together with Dr. Charlie Saunders using Perseus version 1.6.5.0 (Kulak et al., 2014). Corrected reporter intensity values were inputted into Perseus and filtered, removing rows based on reverse and contaminant columns. Filtered TMT data was $\log_2$ transformed before subtracting the median values of each column to normalise data. Identified groups were retained only if displaying 2 valid values within each triplicate condition. 2-sample t-tests (Permutation-based FDR = 0.10; S0 = 0.15) were performed and data was analysed according to either their $\log_2$-transformed fold change enrichment between samples or statistical significance.

2.7 Target validation by photoaffinity labelling

2.7.1 Streptavidin-based enrichment

For target validation by in-gel fluorescence (IGF) and immunoblot, clicked and precipitated protein samples (prepared as described in Chapter 2.6.4) were incubated with Pierce^{TM} streptavidin coated magnetic beads. Magnetic beads were prewashed 3 times by addition of 0.2% SDS in PBS, moderately shaking samples and magnet partitioning. Using 300 μl beads per 1 mg total protein, samples were added to beads and incubated with moderate shaking for 2 h at RT. Samples were partitioned with a magnet to retain the flow-through protein for analysis. To elute enriched protein, beads were washed 3 times with 0.2% SDS, once with 0.1% Tween-20 in H_2O and then incubated with 0.1 M glycine, pH 2.0 at RT for 5 minutes with moderate shaking. 2 x sample loading buffer was added to protein samples which were then boiled at 95°C for 10 minutes. Samples were centrifuged at 17,000 x g for 10 minutes at RT and eluate retained for separation by gel electrophoresis.

2.7.2 Separation by gel glectrophoresis and fluorescence detection

Crude lysate, clicked protein, flow-through and eluate samples were separated on SDS-PAGE gels (NuPage 4-12% Bis-Tris gels (Novex)) at 200 V for 40 minutes. An FLA 5000 biomolecular imager was used to detect IGF of TAMRA-labelled proteins before immunoblotting.

2.7.3 Immunoblot

SDS-PAGE gels were transferred to nitrocellulose membranes using the iBlot 2 Gel Transfer Device with a pre-programmed voltage method of 20 V for 1 minute, 23 V for 4 minutes and 25 V for 2 minutes. Membranes were blocked in 5% skimmed milk in PBS-T (0.1% Tween-20 in PBS) for 1 h at RT and then incubated with primary antibody, prepared in blocking solution. Membranes were washed 3 times with PBS-T, at 5 minutes per wash, before incubating with secondary antibody in 5% skimmed milk blocking solution for 1 h at RT. Membranes were washed a further 3 times with PBS-T before developing using ECL (Amersham) and imaging. The primary antibodies used here included 1:800 mouse anti-Pfs16 clone 32F717:B02 (Moelans, 1995) and 1:1000 rabbit anti-Pfg377 (Ishino et al., 2020). Goat anti-rabbit or goat anti-mouse horseradish peroxidase (HRP) were used as secondary antibodies. Densitometric analysis was used to measure band intensity in ImageJ, which has been reported as relative to DMSO controls.

2.8 Target validation by CETSA

2.8.1 Production of parasite cell lysate

Stage V *P. falciparum* NF54 gametocyte culture with exflagellation $\geqq$ 0.3% was purified as described in 2.6.2. To obtain stage I-III gametocyte protein, *P. falciparum* NF54 gametocyte cultures with $>$ 1% gametocytaemia were prepared on 4 days post-induction of sexual conversion, which contained residual asexual parasites which were yet to commit to sexual conversion or crash. To obtain mixed asexual parasite

protein, cultures were checked for > 5% asexual parasitemia before purification. Suitable gametocyte or asexual cultures were centrifuged at 800 x *g* for 5 minutes at 37°C (brake applied) and media was removed. Erythrocytes in the cultures were lysed by addition of 0.01% saponin at 37°C for 10 minutes and the culture was centrifuged at 17,000 x *g* for 5 minutes at 37°C. The supernatant was removed and the 0.01% saponin wash was repeated 4 times, followed by a final wash in PBS before removing the supernatant. The resulting cell pellet was snap frozen in liquid nitrogen before storing at -80°C.

2.8.2 Cellular Thermal Shift Assay

The cellular thermal shift assay (CETSA) was performed as previously described (Jafari et al., 2014). The thermal shifts of Pfs16 and Pfg377, derived from activated stage V gametocytes and stage I-III gametocytes, were obtained and analysed by immunoblot. Lysis buffer (1% Triton-X100 / 10 mM Tris / 150 mM NaCl / cOmplete™ ULTRA EDTA-free Protease Inhibitor Cocktail at pH 7.5 in H2O) was added to parasite pellets for 30 min at 4°C before centrifugation at 17,000 x *g* for 30 minutes at 4°C to obtain soluble the protein fraction.

2.8.2.1 Melting curve

Soluble proteins were treated with either 1% DMSO or 100 μM **DDD01035881**, or analogues, and then split into 10 μl aliquots. Aliquots were incubated at RT for 3 minutes before thermally challenging over a temperature gradient for 5 minutes, using a BioRad C1000 Touch™ Thermal Cycler. An initial temperature gradient of 50-100°C was applied before subsequently applying a targeted temperature gradient, over a minimum of 11 points, to extrapolate a T_m. Protein aliquots were then incubated at 4°C for 3 minutes before centrifugation at 17,000 x *g* for 30 minutes at 4°C. Aggregated proteins were discarded and the supernatant was prepared for separation by gel electrophoresis and visualisation by immunoblot, as described in 2.7.2 and 2.7.3, respectively.

2.8.2.2 Isothermal Dose Response

DDD01035881 was dispensed into 384 well-plates over a 15-point serial dilution from 1 nM to 100 μM before addition of 10 μl cell lysate. Using data from the melting curve, a single temperature in which Pfs16 was stabilised under **DDD01035881** treatment but mostly aggregated under DMSO treatment was derived. After 10 minutes incubation with **DDD01035881** at RT, treated protein was then thermally challenged at the selected temperature of 78.4°C for 5 minutes. Proteins were then incubated at 4°C for 3 minutes before isolating soluble proteins by centrifugation at 17,000 x g for 30 minutes at 4°C. Proteins in the supernatant were separated by gel electrophoresis and Pfs16 was detected by immunoblot, as described in 2.7.3.

2.8.2.3 T_{Agg} extrapolation and dose response

CETSA data was analysed as previously described (Jafari et al., 2014). The band intensity of each data point of Pfs16 and Pfg377 labelled immunoblots was determined by densitometric analysis, carried out in ImageJ. To obtain a melt-curve, data was normalised by setting the lowest (A) and highest (B) band intensity values as 0 and 100%, respectively. The band intensity of each data point (Band x) was converted to a relative intensity using the highest and lowest values with the following equation:

$$Relative\,band\,intensity\,(\%) = \frac{Band\,x - A}{B - A} \times 100 \tag{2.3}$$

To obtain a melt curve and extrapolate a T_{Agg} value, the Boltzmann Sigmoid equation in GraphPad Prism version 8.0 was used to fit normalised data. Statistical significance was calculated using an unpaired two tailed t-test in GraphPad Prism.

To obtain a dose response curve, normalised data was analysed with the saturation binding curve (one site binding rectangular hyperbola) function in GraphPad Prism.

2.9 *Pf*2004/164-tdTomato sexual conversion assay

2.9.1 *Pf*2004/164-tdTomato parasite preparation

The rate of *Pf*2004/164-tdTomato sexual conversion under N-4HCS treatment was measured using a previously described assay (Brancucci et al., 2015). *Pf*2004/164-tdTomato asexual parasites (>2% ring-stage parasitemia) were synchronised to a 24-hour post-invasion (h.p.i.) window using 5% Sorbitol (Sigma). To synchronise to ring stage parasites, cultures were centrifuged at 800 x *g* for 5 minutes and the media was removed before addition of 16 pellet volumes of 5% Sorbitol. After a 5-minute incubation at 37°C, parasites were centrifuged at 800 x *g* for 5 minutes and the supernatant was removed and replaced with culture media. To further synchronise parasites to an 8-hour window of 16-24 h.p.i, cultures were Sorbitol-treated again 16 hours later, within the same intraerythrocytic developmental cycle. To prepare parasites for the plate-based assay, cultures were washed with fresh culture media and diluted to 0.3% parasitemia and 2.5% haematocrit.

2.9.2 N-4HCS treatment

Sexual conversion rates of *Pf*2004/164-tdTomato parasites were measured under three N-4HCS treatment conditions including i) 48 h compound exposure from the point of induction (carry-over), ii) compound removal after 24-hours (wash-out) and iii) compound treatment 24-hours post-induction (add-in). Parasites were treated with either 25 μM of N-4HCS compounds **DDD01035881**, **DDD01028076**, **(-)-DDD01028076**, **(+)-DDD01028076** or DMSO as a negative control. Compounds were dispensed into round bottom 96-well plate using a HP D300 digital dispenser and all samples were normalised to 0.25% DMSO. Positive controls treated with 20 μM choline were included in plates and were prepared by diluting in choline-treated media prior to plating.

For 48 h carry-over and wash-out treatment, 220 μl diluted culture was dispensed into pre-treated plates for induction of sexual conversion. At 24 h post-induction,

the culture media of carry-over samples was replaced by centrifugation of plates at 800 x g for 5 min. Spent media was removed and replaced with fresh culture media which was treated with 25 μM of N-4HCS compounds or controls, to match conditions at induction. For wash-out samples, plates were centrifuged at 800 x g for 5 min and 200 μl drugged media was replaced with fresh culture media at 24 h post-induction. The wash step was repeated twice.

For add-in samples, 220 μl diluted culture was plated directly into untreated plates to induce conversion. At 24 h post-induction, media was removed and replaced with fresh culture media treated with 25 μM of N-4HCS compounds or controls.

2.9.3 Conversion rate by flow cytometry

To determine the parasitemia of treated samples by flow cytometry, 10 μl of each sample was stained with 1:5000 SYBR-Green in PBS at 48 h post-induction. After a 20-minute incubation at 37°C, samples were washed twice with PBS before quantification by flow cytometry. Cells were excited at 488 nm and emission read between 515 and 545 nm. 100, 000 events were acquired per condition using a BD Fortessa flow cytometer. To measure gametocytaemia, 10 μl of each sample was prepared for flow cytometry 48 h after quantifying parasitaemia. Samples were stained with 1:5000 SYBR-Green in PBS. tdTomato was detected with the 561 nm laser and 586/16 filter and SYBR-Green was detected with the 488 nm laser and 530/30 filter, capturing a total of 400,000 events per sample.

Data was analysed in FlowJo version 10 according to the published assay (Brancucci et al., 2015). Plots of tdTom fluorescence and SYBR-Green fluorescence were generated and uninfected erythrocyte (double-negative), asexual parasite (SYBR-Green positive) and gametocyte (SYBR-Green/tdTom double-positive) populations were gated. The same gates were applied to all samples from each run. Sexual conversion rates of samples were then determined based on the initial parasitaemia (proportion of parasitised erythrocytes) and resulting gametocytaemia (proportion of gametocyte-infected erythrocytes), with the following equation:

$$Sexual\,conversion\,rate = \frac{gametocytemia}{parasitemia\,48h\,post\,induction} \tag{2.4}$$

2.10 DDD01035881 activity window

2.10.1 Activated microgametocyte treatment

To induce gametogenesis of *P. falciparum* NF54 gametocytes, 5 volumes of mature culture was added to 1 volume of ookinete media at RT. For t = 0 minute treatment samples, ookinete media was pre-treated with 5 μM **DDD01035881**, 25 μM **ML10** or 5 μM **1294** prior to gametocyte addition. To determine activity windows of compounds during microgametogenesis, gametocytes were activated in the absence of compound and 5μM **DDD01035881**, 5μM **1294** and 25μM **ML10** were added to activated gametocyte culture (normalised to 0.25% DMSO) at varying time points post-activation.

DDD01035881 reversibility was determined by activating gametocytes with ookinete media pre-treated with **DDD01035881** and centrifuging at 1 or 6 minutes post-activation. Supernatant was removed and replaced with fresh untreated ookinete medium. This wash step was repeated 3 times to remove all residual **DDD01035881**.

2.10.2 Exflagellation rate quantification

To calculate the percentage exflagellation relative to erythrocyte density, total exflagellation events and erythrocytes were quantified per 1 ml of culture. Density and exflagellation was quantified by phase contrast microscopy using a haemocytometer at 25 minutes post-activation. The exflagellation rates were then converted to rates relative to DMSO controls. For **DDD01035881** reversibility counts, the exflagellation rates of **DDD01035881**-treated gametocytes was calculated as relative to washed DMSO controls to account for loss to exflagellation by centrifugation.

2.11 Phenotypic characterisation by microscopy

2.11.1 Parasite treatment and fixation for immunofluorescence assays

To prepare parasites for immunofluorescence staining and microscopy, *P. falciparum* NF54 mature stage V gametocytes were treated under various compound conditions and fixed with paraformaldehyde to a final concentration of 4% in PBS. To obtain timelapses of microgametogenesis, parasites were treated with 0.25% DMSO, 5 μM **DDD01035881**, 1 μM **1294** and 25 μM **ML10** (normalised to 0.25% DMSO) were immediately activated with ookinete medium and fixed at time increments up to 25 minutes post-activation. To determine perturbations to exflagellation at 25 minutes post-activation under staggered **DDD01035881** treatment, parasites were treated as described in 2.10.1 before fixing at 25 minutes post-activation. For phenotypic analysis of GHCDL-derived compounds **DDD01255968**, **DDD01249504** and **DDD01245291**, gametocytes were treated with 5 μM compound for 48 hours before inducing microgametogenesis and fixing at time increments up to 25 minutes post-activation. Any samples fixed at t = 0 minutes, relative to activation, were fixed with prewarmed paraformaldehyde to prevent activation of gametogenesis.

2.11.2 Immunofluorescence labelling

Flat bottom 24-well plates were loaded with 13 mm glass coverslips and coated with poly-L-lysine (Sigma) for 24 hours at RT. Poly-L-lysine (Sigma) was removed and coverslips were washed once with PBS. Fixed gametocyte samples were loaded onto coverslips and left to adhere at 4 °C overnight. Coverslips with adhered parasites were washed once in PBS before permeabilization with 0.1% Triton-X100 in PBS for 15 minutes. Triton-X100 was removed from coverslips which were subsequently washed with PBS 3 times before blocking with 10% fetal bovine serum (FBS) in PBS for 30 minutes. The FBS blocking solution was removed and replaced with primary antibodies, prepared in 10% FBS, for 1 hour. Primary antibodies and dilutions used for immunofluorescence assays (IFAs) were 1:800 mouse anti-Pfs16 clone

32F717:B02, 1:500 mouse anti-alpha tubulin clone DM1A (Sigma) and 1:1000 rabbit anti-Glycophorin A clone EPR8200 (Abcam). Primary antibody solutions were removed by washing coverslips 3 times with PBS before addition of secondary antibodies and fluorescent dyes for 45 minutes, protecting samples from light. Secondary antibodies used here include anti-mouse or anti-rabbit Alexa Fluor 488 (Thermo-Fisher), anti-mouse or anti-rabbit Alexa Fluor 594 (Thermo-Fisher), all prepared at a 1:500 dilution in 10% FBS. 5μg/ml Wheat Germ Agglutinin (WGA)-633 and 10nM 4',6-diamidino-2-phenylindole (DAPI) were added simultaneously to secondary antibodies to stain the host erythrocyte and parasite DNA, respectively. Coverslips were washed with PBS 3 times to remove unbound antibody and stains. To prepare samples for microscopy, coverslips were mounted onto glass slides (VWR) with VectaShield mountant (Vector Laboratories) and sealed.

A Nikon Eclipse Ti-E inverted widefield microscope was used to acquire images with pre-programmed channels in NIS Elements v4.20 software. All images were acquired at x100 magnification, capturing through Z in 0.2 μm increments from above and below the cell. Images were analysed using Icy Bioimage Analysis (version 2.1.0.0) software (Chaumont et al., 2012). The pre-programmed EpiDEMIC plugin (Soulez et al., 2012) in Icy (Chaumont et al., 2012) was used to deconvolve images over 50 iterations and 2 loops, applying the relevant channel wavelengths. All images represent the maximum intensity projections of images acquired through Z.

2.11.3 Electron microscopy

To prepare samples for electron microscopy, stage V *P. falciparum* NF54 gametocytes were purified by density barrier isolation using NycoPrep 1.077. Stage V pure gametocytes were subsequently treated with 0.25% DMSO or 5μM **DDD01035881** (normalised to 0.25% DMSO) and added to ookinete medium to activate gametogenesis. Perturbances to exflagellation were studied by fixing activated samples at 25 minutes post-activation in 4% high EM grade paraformaldehyde / 2.5% glutaraldehyde / 0.1% tannic acid in 0.1 M sodium cacodylate buffer (pH 7.2) for 3 hours at RT, with rotary mixing. Fixed cells were washed with 0.1 M sodium cacodylate 3 times, at 20 minutes per wash, before treating with 1% osmium tetroxide in 0.1 M

sodium cacodylate for 2 hours at RT.

The following staining steps were performed by Dr. Silvia Haase (Baum Lab). Cells were washed with 0.1 M sodium cacodylate and subsequently stained with 1% uranyl acetate for 1 hour at RT. Stained samples, dehydrated in ethanol series, were embedded in epoxy resin (TAAB) and a Leica EM UC7 ultramicrotome was used to cut 70 nm sections. Using manufacturer instructions, sections were contrasted with Uranyless (TAAB) and 3% Reynolds lead citrate (TAAB) for 2 minutes and 1 minute, respectively. A JEOL JEM-1400Plus TEM (120 kV) was used to acquire images of sections, using a Ruby Camera (2 K × 2 K).

2.12 Ploidy determination by flow cytometry

2.12.1 Sample preparation

Quantification of *PfDyn*GFP/*P47*mCherry microgametocyte ploidy during microgametogenesis was determined as previously described (Fang et al., 2017). The ploidy of *PfDyn*GFP/*P47*mCherry and *P. falciparum* NF54 gametocytes with $> 0.3\%$ exflagellation was determined, with NF54 being used as a control. Gametocytes were purified by density barrier isolation using NycoPrep 1.077 and resuspended in suspended activation (SA) medium (RPMI-1640 with 25 mM HEPES (Life Technologies) supplemented with 5% fetal bovine serum and 4 mM sodium bicarbonate, pH 7.2). SA medium was used to prevent premature activation of microgametogenesis during RT staining steps. Samples were then treated with either 0.25% DMSO or 5 μM **DDD01035881** (normalised to 0.25% DMSO). Treated and untreated gametocyte samples were prepared at t = 0-minutes or t = 15-minutes relative to activation of gametogenesis. To prepare t = 15-minute samples, gametocytes were activated with ookinete medium. To halt gametogenesis at 15 minutes post-activation, gametocytes were treated with ice-cold PBS and maintained at 4°C. T = 0-minute samples were simultaneously prepared by adding gametocytes directly to ice-cold PBS, skipping the activation step. Samples were centrifuged at 300 x *g* for 2 minutes at 4°C, supernatant was removed and replaced with fresh PBS at 4°C. Samples were stained with 1:2000 Vybrant™ DyeCycle™ Violet (Thermo-Fisher) for 30 min at

4°C. Unstained controls of each *PfDyn*GFP/*P47*mCherry and *P. falciparum* NF54 sample were also prepared. Additional stained and unstained erythrocyte samples were prepared.

2.12.2 Flow cytometry

DNA content of Vybrant™ DyeCycle™ Violet-stained *PfDyn*GFP/*P47*mCherry and *P. falciparum* NF54 gametocytes was quantified by flow cytometry, using a BD Fortessa flow cytometer. 100,000 events were acquired per sample. Microgametocyte populations were gated based on GFP positivity, from which Vybrant™ DyeCycle™ Violet staining histograms were derived. Populations with a 1N, 2N, 4N or 8N genome were gated and analysed with the proliferation tool in FlowJo 10.6.1 software. Microgametocyte populations were grouped based on ploidy to compare DMSO and **DDDD01035881**-treated samples.

2.13 Live-cell fluorescence imaging of microgametogenesis

2.13.1 Live gametocyte staining

Stage V *P. falciparum* gametocytes with $> 0.3\%$ exflagellation were stained for live-cell fluorescence imaging of microgametogenesis. Gametocytes were stained with 500 nM SiR-tubulin (Spirochrome) for 3 hours at 37°C. 30 minutes prior to imaging, gametocytes were stained with 5 μg/ml wheat germ agglutinin (WGA) conjugated to AlexaFluor633 (Invitrogen) and 500 nM Vybrant™ DyeCycle™ Violet at 37°C. Samples were protected from light and maintained strictly at 37°C to prevent premature activation of gametogenesis.

In preparation for microscopy, 140 μl of ookinete medium was added to the wells of an Ibidi 8-well μ-Slide and slides were pre-positioned on the microscope stage. To activate gametogenesis, 6 μl stained gametocyte culture was added directly to the ookinete medium treated slides at RT.

2.13.2 Live widefield microscopy of microgametogenesis

Microgametogenesis was imaged using a Nikon Ti2-E widefield microscope and Prime 95B sCMOS camera (Photometrics). The triggered multi-wavelength LED and static quad band filter cube were used to trigger acquisition both through Piezo Z-stage movement and in alternation between wavelengths. Images were acquired using a x100 Plan Apo 1.4 numerical aperture (NA) oil objective in 0.2 μm steps through Z, with Cy5 and DAPI filter sets, using NIS Elements v4.20 software. All time-lapses were captured through time with 'no delay', at 34 ms exposure time.

To capture the early developmental stages of microgametogenesis, stage V males were identified based on SiR-Tubulin stained mitotic spindles. Early development was captured in 4 dimensions, both through Z and T, alternating between fluorescence and brightfield microscopy to minimise the effects of phototoxicity. Microgametogenesis events were captured until parasites were deemed unviable, subsequently identifying alternate viable parasites to capture microgamete emergence, or exflagellation. Timelapses of exflagellation were captured continually through time at a single Z slice.

2.13.2.1 Timelapse deconvolution

All timelapses were deconvolved using Icy Bioimage Analysis version 2.0.1.0 software (Chaumont et al., 2012). Early microgametogenesis 4D (3D+t) timelapses were deconvolved using a custom-made automated Protocol, designed for this study by Dr. David Gaboriau (FILM facility, Imperial College London). The automated algorithm was designed to batch deconvolve each time frame using the inbuilt EpiDEMIC deconvolution bloc (Soulez et al., 2012), a plugin designed to deconvolve 3D images. In EpiDEMIC (Soulez et al., 2012), individual channels and corresponding wavelengths were specified, and images were deconvolved in 50 iterations, over 2 loops. Deconvolved data was converted to 3D projections of volume-rendered data or 2D maximum intensity projections.

2.13.2.2 Timelapse analysis

For staining intensity and circularity analysis, raw 3D data was transformed to 2D maximum intensity projections and individual cells were defined as a custom region of interest (ROI) in NIS Elements v4.20. SiR-tubulin and Vybrant™ DyeCycle™ Violet staining intensity of individual cells was measured using the time-measurement tool and was reported here in arbitrary units. The circularity of individual cells was measured with the Automated Measurement tool and derived from the perimeter and area of individual cells. Cells were characterised based on increasing circularity as a shape measure value from 0-1, with a value of 1 representing a circle. Egress phenotypes were determined with manual observation and calculated as a percentage of the total population, under a given treatment condition.

Icy (Chaumont et al., 2012) was used to measure the DNA segregation angle. SiR-tubulin staining was used to select frames from 4D timelapses, obtaining images of parasites depicting; a spindle, newly nucleated axonemes or developed axonemes. Selected frames were oriented in three dimensions, optimally aligning parasites to measure the angle of segregrated DNA, relative to basal body tetrads. Maximum intensity projections of optimally oriented frames were generated and the 'angle helper' tool was utilised to measure angles between DNA and basal body tetrads, which were previously identified and marked.

All data was processed and statistically analysed using GraphPad Prism, version 8.0.

Chapter 3

Lead development of the N-4HCS series

3.1 Introduction

The advent of phenotypic screening has drastically accelerated the rate of antimalarial hit discovery and importantly has facilitated the identification of compounds with novel chemotypes and modes of action. A recent screen of the 68,689-compound Global Health Chemical Diversity Library (GHCDL) exemplifies the scale at which screening campaigns can now be performed, given the substantial strides made in maximising assay throughput (Delves et al., 2018). Centred around the discovery of inhibitors of *Plasmodium* host-to-vector transmission, specifically the sexual stage gametocytes, the GHCDL screen identified a range of hits with diverse activity profiles. Notably, a set of compounds sharing an *N*-((4-hydroxychroman-4-yl)methyl)-sulphonamide (N-4HCS) scaffold were found to potently and immediately block microgametogenesis, requiring no prior compound incubation with *in vitro* gametocytes (Delves et al., 2018). Of the N-4HCS compounds, **DDD01035881** (Figure 3.1) was found to the be most potent in the Dual Gamete Formation Assay (DGFA) (Delves et al., 2018).

Whilst phenotypic screening initiates the drug discovery pipeline, substantial study of the chemical and biological characteristics of small molecule hits is required prior to their clinical testing. Adhering to common drug developmental frameworks,

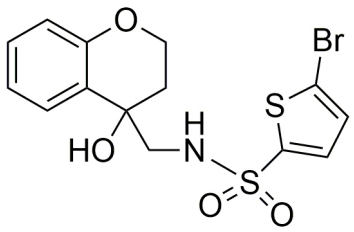


Figure 3.1: **DDD01035881** structure. The most potent N-4HCS compound identified in the GHCDL-screen (Delves et al., 2018) and the structural basis of the SAR study (Rueda-Zubiaurre et al., 2019).

hit identification is frequently followed by lead development in which the potency, safety profile and metabolic stability of hits are studied and optimised. Elucidation of the structure-activity relationship (SAR) of a compound reveals the functional groups that are either essential or dispensable to its biological activity. Additionally, SAR knowledge can enable future target identification studies by uncovering regions of a compound structure which are amenable to the addition of linker groups required for photoaffinity labelling. Although structural analogues of **DDD01035881** with the N-4HCS scaffold were tested in the GHCDL screen, few analogues were available and thus provided limited SAR insights.

In this chapter, I used an adapted microgamete-specific format of the DGFA to measure the potency of **DDD01035881** analogues designed and synthesised by medicinal chemists at Imperial College London to study the compound SAR. Additionally, I tested the impact of changing functional groups on the N-4HCS scaffold on mammalian cell viability. Results of this chapter have been published (Rueda-Zubiaurre et al., 2019).

3.2 Results

3.2.1 Microgamete Formation Assay

To test the potency of N-4HCS analogues synthesised by our medicinal chemist collaborators, an adapted format of the Dual Gamete Formation Assay (DGFA) was performed here. The DGFA was designed to test the transmission-blocking potency of antimalarial compounds by testing the capacity of gametocytes to form male and female gametes as a measure of functional viability (Ruecker et al., 2014), as outlined in Chapter 1.4.3.2. Given the specific microgamete-targeted activity of the N-4HCS compounds, the assay was performed solely with a microgamete readout without prior compound incubation ('add-in' format). The scope and workflow of the assay is summarised in Figure 3.2 and will henceforth be referred to as the Microgamete Formation Assay (MGFA).

Functional viability of stage V microgametocytes, specifically the ability to form microgametes, was tested in a phenotypic assay with a readout measured by phase contrast microscopy. N-4HCS analogues were first dispensed into black flat-bottom 384-well plates in serial dilutions, with single-dose controls included across plates. DMSO was plated as a negative control and 20 µM **DDD01028076**, a microgamete-targeted N-4HCS compound derived from the GHCDL, acted as a positive control. Ookinete medium was used to emulate conditions of the mosquito midgut and was dispensed into N-4HCS-treated well plates, followed immediately by viable stage V NF54-strain *P. falciparum* gametocyte culture. Following short 4°C and 28°C incubations to encourage gametogenesis, plates were immediately transferred to wide-field microscope stages for automated data capture. Ten-frame time-lapses of each well were acquired to capture any inhibitory effects to microgametogenesis. At ∼15 minutes post-activation, the process of microgametogenesis is characteristically concluded with the rapid emergence of motile haploid microgametes, in a process referred to as exflagellation. Within an erythrocyte monolayer, exflagellating microgametes adhere to neighbouring erythrocytes and appear as regions of disruption, which are measured and quantified with automated image analysis in the MGFA.

To calculate the potency of N-4HCS analogues, exflagellation rates derived from

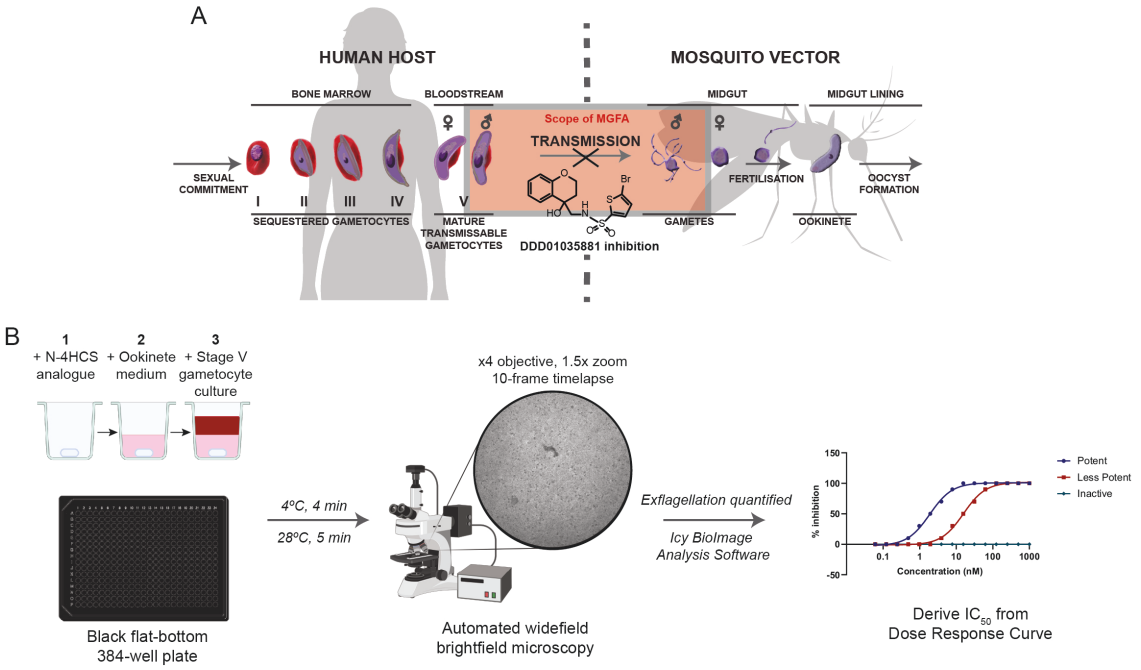


Figure 3.2: Microgamete formation assay (MGFA). (A) Scope of the MGFA and **DDD01035881** inhibitory activity relative to the transmission-stages of *P. falciparum*. Figure adapted from Rueda-Zubiaurre et al., 2019. (B) The MGFA workflow. Phase-contrast microscopy is used to obtain the readout of plate-based assay. Time-lapses capturing exflagellation are acquired and automated image analysis is used to quantify exflagellation. Inhibition rates of exflagellation are used to generate dose-response curves, from which (IC_{50}) values are derived.

image analysis can be converted to percentage inhibition values relative to positive and negative controls. Dose-response curves can be plotted from inhibition rates, from which half-maximal inhibitory concentration (IC_{50}) values can be derived and directly compared between N-4HCS analogues as a measure of potency.

3.2.2 Insights into N-4HCS SAR

Medicinal chemists of the Fuchter, Barnard and Tate groups (Imperial College London) sought to study the N-4HCS SAR by synthesising a range of compounds with altered structural characteristics. Functional groups modified here can be broadly categorised into the following: the aromatic ring, sulphonamide linker, core scaffold (chromane oxygen, cycle size and presence/position of hydroxyl group) and separation of enantiomeric pairs (Rueda-Zubiaurre et al., 2019). Over 70 analogues were tested and published, yielding hits with IC_{50}s in the nanomolar concentration range

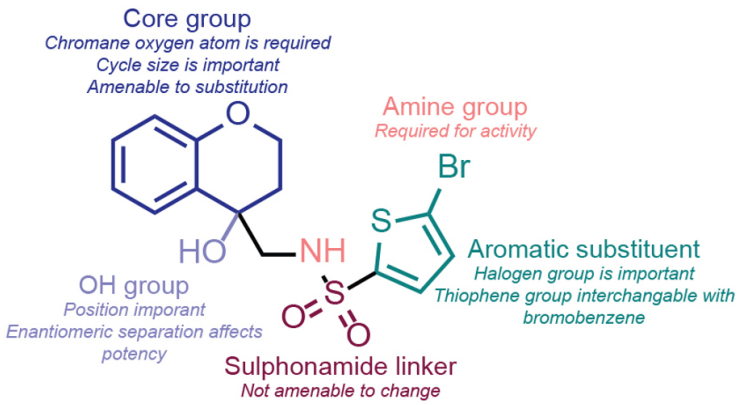


Figure 3.3: Summary of N-4HCS structure activity relationship (SAR). To determine whether modifications to the N-4HCS scaffold were tolerated, activity of analogues were tested in the MGFA. Compounds were designed and synthesised by medicinal chemists of the Fuchter, Barnard and Tate Groups at Imperial College London (Rueda-Zubiaurre et al., 2019).

(Rueda-Zubiaurre et al., 2019). Activity of a subset of N-4HCS compounds synthesised as part of this study which were both utilised throughput this thesis and for further safety profiling are listed in Table 3.1.

Given the author contributed to the biological aspect of this study, the chemistry will not be discussed in detail, but the full results have been published (Rueda-Zubiaurre et al., 2019). Summarised in Figure 3.3, the most significant findings of the study were:

1. Limited modifications could be made to the **aromatic substituent**. The thiophene group of **DDD01035881** was interchangeable with a phenyl group, which could withstand removal of the halogen atom but was favoured by its presence. Halogen atom positioning impacted activity.

2. The **sulphonamide linker** was required for activity.

3. The **core scaffold** was not amenable to much modification, although introduction of a fluorine atom was tolerated. Expansion or contraction of the cycle size and removal of the oxygen atom within the core scaffold reduced activity.

4. The **hydroxyl (OH) group** in the core scaffold was important for activity, but was susceptible to some substitutions.

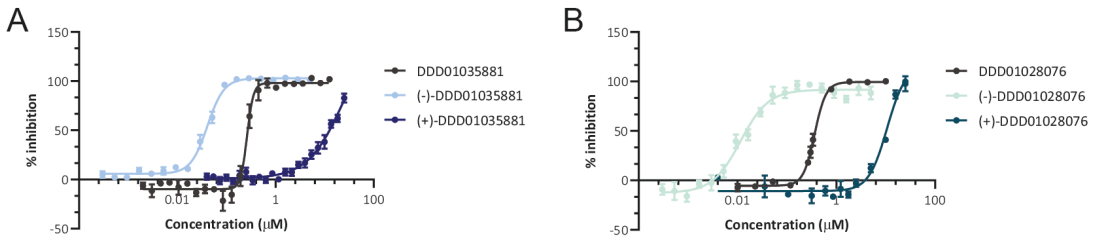


Figure 3.4: Impacts of stereochemistry on N-4HCS activity. Dose-response curves depicting MGFA-derived activity of N-4HCS enantiomers and racemic mixtures. Chiral resolution of **DDD01035881** and **DDD01028076** revealed a notable difference in activity between each of the two enantiomers and the racemic mixtures. Points depict the average percentage inhibition (%) of exflagellation ± standard error of the mean (SEM), derived from between three and eight biological replicates of the MGFA, with a minimum of two technical replicates. Synthesis and chiral resolution of compounds was performed by Dr. Ainoa Rueda-Zubiaurre and Mr. Oliver J. Fischer (Rueda-Zubiaurre et al., 2019).

5. The **absolute stereochemistry** of the most potent N-4HCS compounds impacted activity, with chiral resolution demonstrating a difference in activity between the racemic mixtures and two separated enantiomers (Figure 3.4).

Interestingly, whilst it was found that newly synthesised **DDD01028076** and the screen-derived compound stock shared a similar IC_{50}, newly synthesised **DDD01035881** was found to be more potent than the original value measured in the screen (Table 3.1). This difference in activity may arise due to the inherent variability of the MGFA and the improved purity of the newly synthesised **DDD01035881** stock. As depicted by the dose response curves in Figure 3.4 and IC_{50}s in Table 3.1, separation of the enantiomers of **DDD01035881** and **DDD01028076** resulted in a notable difference in activity. Specifically, there was a three-fold and seven-fold increase in potency between the racemic mixture and most potent enantiomers of **DDD01035881** and **DDD01028076**, respectively. Additionally, there was a 20-fold and 100-fold difference between separated enantiomers of **DDD01035881** and **DDD01028076**, respectively, with the (-) isomer being the most potent in both cases (Figure 3.4).

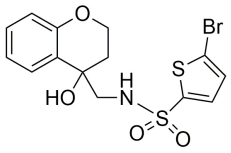
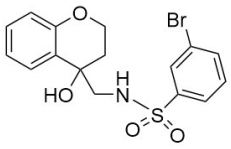
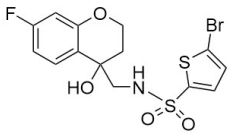
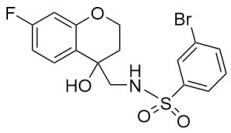
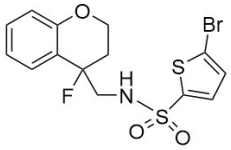
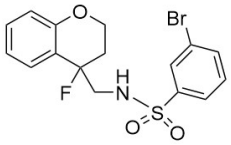
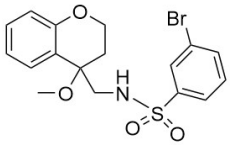
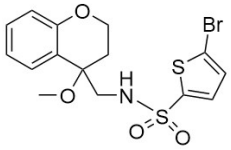
Structure	Compound	IC_{50} (nM)
	**DDD01035881**	292±38*/130±30†
	(-)-DDD01035881	46±5
	(+)-DDD01035881	>1000
	**DDD01028076**	367±34*/344±71†
	(-)-DDD01028076	18±3
	(+)-DDD01028076	2861±325
	**1**	364±47
	**2**	79±41
	**3**	1231±108
	**4**	945±192
	**5**	149±24
	**6**	354±22

Table 3.1: Structures and MGFA IC_{50}s of notable N-4HCS analogues. IC_{50} values are expressed as the average ± standard error of the mean (SEM) and were derived from curves with an $R^2 \geqq 0.95$. Data was obtained from between three and eight biological replicates and a minimum of two technical replicates. *IC_{50}s derived from the GHCDL screen (Delves et al., 2018) versus †IC_{50}s derived from the SAR study (Rueda-Zubiaurre et al., 2019). Design, synthesis and chiral resolution of compounds was performed by Dr. Ainoa Rueda-Zubiaurre, Dr. Charlie N. Saunders, Mr. Oliver J. Fischer and Mr. Xiaojun Hu (Rueda-Zubiaurre et al., 2019).

3.2.3 Safety profiling

To conclude lead development, the safety profiles of potent N-4HCS hits synthesised for the SAR study were elucidated. N-4HCS compounds were selected for safety testing based both on potency in the MGFA and structural diversity; hits of high potency were tested due to their favourable activity profiles and compounds of varying structural characteristics were tested to determine if viability is compromised with specific functional groups. A plethora of assays are available to measure the cytotoxic and viability-compromising effects of drug treatment. Here, the assay utilised in the GHCDL screen was performed to enable a direct comparison between safety profiles of N-4HCS compounds synthesised for the SAR study and those sourced for the screen (Delves et al., 2018).

Utilising a resazurin-based alamarBlue^{TM} cell viability indicator, the viability of human HepG2 cells, an immortal cell line derived from a hepatocellular carcinoma, was measured under N-4HCS treatment. The alamarBlue^{TM} assay measured the reducing power of viable cells by utilising the cell-permeable, non-fluorescent and non-toxic resazurin. Resazurin is reduced to the highly fluorescent and red-coloured compound resofurin in metabolically active cells, which is detectable by fluorescence and absorbance-based measures. HepG2 cells were treated with 10 μM N-4HCS compounds for 48 hours, prior to addition of alamarBlue^{TM}. The fluorescence of treated cells was then measured in a plate-based assay that was validated with the positive control, doxorubicin. Doxorubicin binds DNA-associated enzymes and intercalates DNA base pairs to exert its cytotoxic effect, and is widely used as a chemotherapy drug (Tacar, Sriamornsak, and Dass, 2013).

The viability of cells under N-4HCS treatment was subsequently measured, relative to a negative DMSO control. Treatment with any of the tested N-4HCS compounds did not compromise the metabolic viability of HepG2 cells, with each treatment demonstrating a significant difference in percentage viability compared to doxorubicin treatment (Figure 3.5). As the N-4HCS compounds tested in the GHCDL screen were also found not to demonstrate unfavourable toxicity in the HepG2 resazurin-based assay (Delves et al., 2018), the structural changes explored were not detrimental to the safety profile. This suggests that, as well as favourable

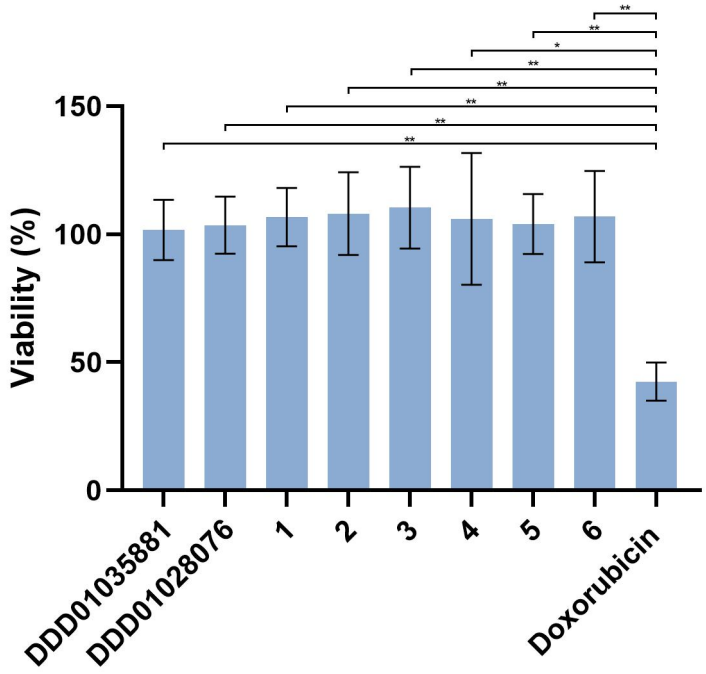


Figure 3.5: HepG2 Viability under N-4HCS treatment. Viability (%) of HepG2 cells was determined using the resazurin-based alamarBlue™ assay. Values are expressed as average viability (%) ± standard deviation and were derived from three biological replicates, performed with a minimum of two technical replicates. Statistical significance was tested using a two-tailed unpaired *t*-test (*p $<$ 0.05; **p $<$ 0.01). Design and synthesis of compounds was performed by Dr. Ainoa Rueda-Zubiaurre and Mr. Xiaojun Hu (Rueda-Zubiaurre et al., 2019).

potency in the MGFA, **DDD01035881**, **DDD01028076** and compounds **3-8** display favourable safety in human cells, thus deeming them suitable for drug development.

3.3 Discussion

Development of novel transmission-blocking antimalarials is crucial to the eradication agenda and though phenotypic screening has accelerated discovery, hits require significant development before progressing through the drug pipeline. The aim of this chapter was to develop the most robust GHCDL-screen derived hit **DDD01035881** and compounds of the same N-4HCS scaffold to display lead-like properties in an SAR study. By applying a suitable format of the DGFA with a solely male-readout and no prior compound incubation, referred to as the MGFA, the potency of N-4HCS analogues synthesised by collaborators were tested here. The full results of this study have been published (Rueda-Zubiaurre et al., 2019).

Multiple potent hits were tested in this SAR study, including compounds with MGFA IC_{50}s in the nanomolar concentration range. Chiral resolution of N-4HCS hits **DDD01035881** and **DDD01028076**, compounds which were initially described in the GHCDL screen (Delves et al., 2018), revealed that a single enantiomer displayed up to an 100-fold improvement in activity relative to its racemic mixture counterpart. Additionally, to further progress potent N-4HCS compounds by measuring their safety, a subset of these hits were tested against the immortal human HepG2 cell line. The metabolic viability of HepG2 cells was not compromised when treated with any of the tested N-4HCS compounds, suggesting the compounds exert a parasite-specific inhibition of microgametogenesis.

The ideal administration profile of a novel transmission-blocking antimalarial has been defined as a single low-dose treatment (Burrows et al., 2017) and improving the potency of drug candidates is key to addressing this; the greater the potency of a drug, the lower the dose required for sufficient efficacy. Given the safety concerns associated with the currently approved transmission-blocking drugs primaquine and tafenoquine, a key characteristic required of novel drug candidates is a favourable safety profile (Burrows et al., 2017). Here, the N-4HCS scaffold has been developed by improving potency without impacting safety against human cells, testing a repertoire of N-4HCS analogues. KAE609, a potent asexual and sexual-stage antimalarial, was identified in a high-throughput phenotypic screen (Plouffe et al., 2008)

and following hit-to-lead development (Yeung et al., 2010) has subsequently entered clinical trials (White et al., 2014b). The spirondolone KAE609 thus demonstrates that lead development by SAR is a crucial step in the development pipeline.

Although potent hits were derived from this SAR study, it also became evident that the compound was not amenable to many structural modifications. This observation points to a potential tight binding pocket of the cellular target and therefore necessitates follow-up target deconvolution. To begin to test this hypothesis, the SAR study lays the groundwork for synthesis of N-4HCS analogues which are amenable to photoaffinity labelling of the *P. falciparum* proteome for target identification. Hit-to-lead development within this chapter has therefore aided future drug development programmes, whilst simultaneously preparing the study for further progression down the drug development pipeline.

Chapter 4

N-4HCS target identification

4.1 Introduction

Although phenotypic screening supersedes target-based screening in its ability to identify drug candidates with novel chemotypes and activity profiles, the cellular target(s) and modes of action of hits require elucidation. Confirmation of a parasite-specific cellular target and mode of action would maximise the chances of success in clinical testing.

One common approach to identify the target of an antimalarial hit is the forward genetics method of *in vitro* evolution and whole genome analysis, or IVIEWGA (Luth et al., 2018). IVIEWGA involves the exposure of parasites to sublethal concentrations of the antimalarial compound in question, to act as a selective pressure, until yielding parasites which are resistant to the compound. Whole genome sequencing is subsequently performed to compare resistant and parental clones, enabling the identification of the genetic determinant of resistance and suspected drug target(s) (Luth et al., 2018). Given the sexual stage gametocytes are non-replicative, generation of resistant mutants from repeated antimalarial exposure is not feasible. Hence, an alternative approach to IVIEWGA is required in transmission-blocking drug target deconvolution.

Chemical proteomics is a branch of chemical biology with applications in target deconvolution (Wright and Sieber, 2016). In small molecule target identification, chemical proteomics involves synthesis of chemical probes able to covalently bind

to drug target(s) upon irradiation with light. Chemical probes, referred to as photoaffinity probes, are designed to incorporate three key structural groups; i) the specificity unit, comprised of the structural elements of the drug candidate required for target engagement and *in vitro* activity, ii) the photoreactive moiety which enables photo-induced covalent binding to cellular target(s) and iii) the reporter or identification tag which is required for detection of probe-tagged proteins. Direct incorporation of a bulky reporter tag, for example a fluorescent dye or partner of the biotin-avidin binding event, may impede cell-permeability and target binding. Hence, it is often favourable to indirectly incorporate a reporter group by integrating an alkyne or azide group into the photoaffinity probe which can be later conjugated to a reporter tag by click chemistry (Smith and Collins, 2015). Using a photoaffinity probe to bind a cellular target is a chemical proteomics method referred to as photoaffinity labelling (PAL) and enables identification of a drug target.

Guided by the knowledge acquired in the GHCDL screen and SAR study, PAL of the *P. falciparum* gametocyte proteome was performed with the aim to deconvolve the cellular target of the N-4HCS series in this chapter. Given the evidence obtained in the GHCDL screen that the N-4HCS series imparts a microgamete-specific inhibition of transmission, we sought to identify a cellular target consistent with this phenotype. Additionally, label-free proteomics techniques were used to validate the specificity of PAL findings. Crucially, this chapter progresses the N-4HCS development pipeline from hit discovery and lead development to target identification and validation, pathing the way towards complete characterisation of the compound series. The findings reported in this chapter are currently available in pre-print form (Yahiya et al., 2021b).

4.2 Results

4.2.1 Proteome-wide photoaffinity labelling

4.2.1.1 N-4HCS photoaffinity probe

To facilitate target identification, we sought to synthesise a photoaffinity probe by drawing on the knowledge of the N-4HCS SAR, working alongside our medicinal chemist colleagues. Incorporation of bulky linkers were found to detriment potency in the MGFA and considerable optimisation was required to synthesise molecules required for PAL. Probe **8** and parent molecule **7** retained nanomolar to micromolar activity in the MGFA and were utilised in this study (Table 4.1). N-4HCS-analogue **DDD01028076** (Table 4.1) was derivatised based on regions shown to be amenable to modification, yielding probe **8** which incorporated an aryl azide moiety and alkyne handle onto the N-4HCS scaffold. Additionally, parent molecule **7** was synthesised as a control and active competitor. To closely mimic the biological activity of probe **8**, the structure of parent molecule **7** was designed to resemble the probe without the clickable and photoactivatable groups. Synthesis and chemical design was performed by Dr. Charlie Saunders, a PhD student based in our group, the Baum Lab, and Tate Group (Department of Chemistry, Imperial College London).

4.2.1.2 Photoaffinity labelling workflow

Utilising the photoaffinity probe **8**, PAL of the *P. falciparum* proteome was performed to identify gametocyte-specific cellular target(s), as outlined in Figure 4.1. Live *P. falciparum* NF54-strain stage V gametocytes of suitable viability ($> 0.3\%$ exflagellation or $> 1.5\%$ gametocytaemia) were treated to obtain three samples, treated with either: i) 10 μM probe **8**, ii) a combination of 10 μM parent molecule **7** and 10 μM probe **8** or iii) DMSO. Samples were treated for 10 minutes, strictly maintaining 37°C to prevent premature activation of gametogenesis. Treated samples were subsequently irradiated at 254nm for 10 minutes, allowing the photoreactive aryl azide moiety of probe **8** to form a reactive nitrene intermediate, able to covalently bind to protein target(s). Whilst irradiation of gametocytes solely in

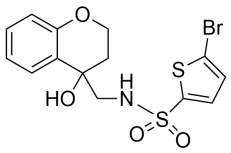
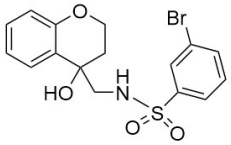
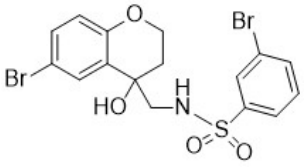
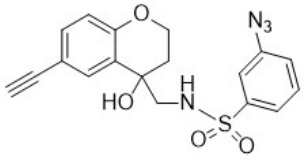
Structure	Compound	IC_{50} (nM)
	**DDD01035881**	292±38*/130±30†
	(-)-DDD01035881	46±5
	(+)-DDD01035881	>1000
	**DDD01028076**	367±34*/344±71†
	(-)-DDD01028076	18±3
	(+)-DDD01028076	2861±325
	**7**	785±48
	**8**	3981±211

Table 4.1: Structures and MGFA-derived IC_{50}s of GHCDL N-4HCS hits and derivatives for target identification and validation. **DDD01035881** and **DDD01028076** were first discovered in the GHCDL screen and were the structural basis from which parent molecule **7** and probe **8** were synthesised. Synthesis and chiral resolution was performed by Dr. Charlie Saunders, Mr. Oliver Fischer and Dr. Ainoa Zubiaurre. IC_{50} values are expressed as the average ± standard error of the mean (SEM), derived from dose-response curves with an $R^2 \geqq 0.95$. Data was obtained from between three and eight biological replicates and at least two technical replicates. *IC_{50}s derived from the GHCDL screen (Delves et al., 2018) versus †IC_{50}s derived from the SAR study (Rueda-Zubiaurre et al., 2019).

the presence of probe **8** permits photo-crosslinking, co-treatment with the parent molecule **7** is performed as a competition control. In the presence of the more potent parent molecule, probe **8** would be out-competed such that the target binding site would be occupied by molecule **7**. Given the parent molecule and DMSO are not amenable to photo-crosslinking or click chemistry, the target would not be enriched in subsequent pulldown experiments in these samples.

To isolate stage V gametocytes from uninfected erythrocytes and asexual parasites, treated and irradiated samples were purified by density barrier isolation. Given the microgamete-specific activity of N-4HCS compounds, isolated stage V gameto-

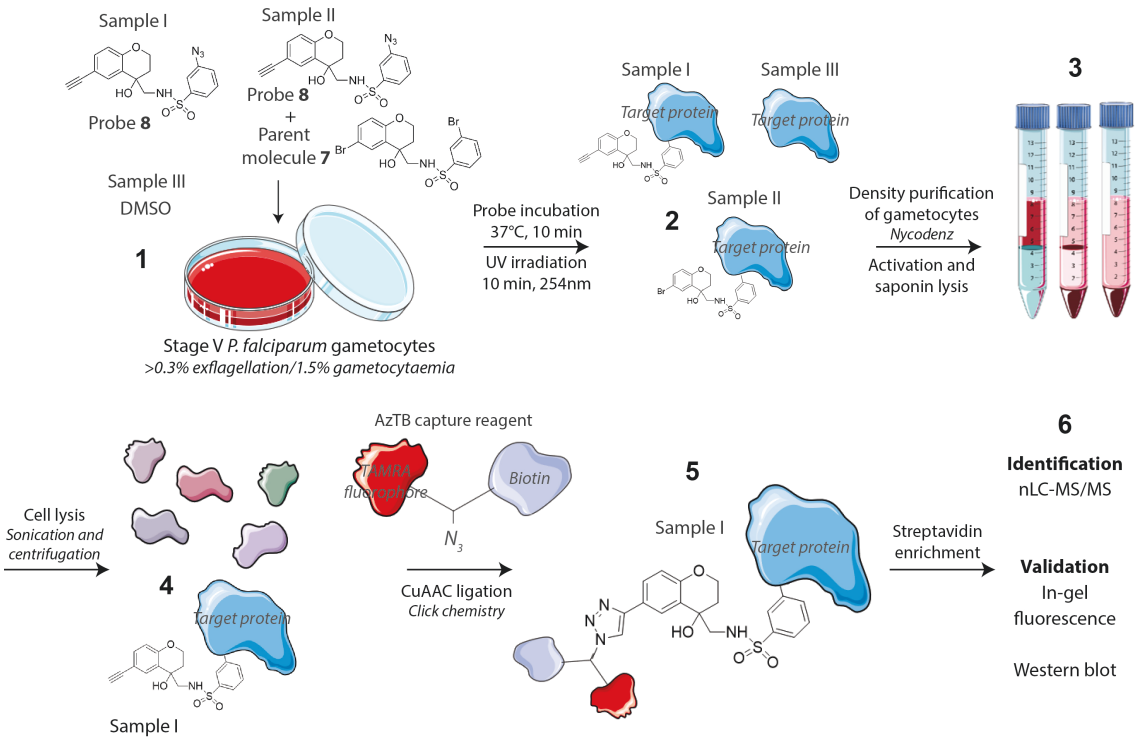


Figure 4.1: Photoaffinity labelling for N-4HCS target identification. **(1)** Three samples were obtained in triplicate with live *P. falciparum* NF54-strain stage V gametocytes by treating with either (I) probe, (II) a combination of probe and parent molecule or (III) DMSO. **(2)** Samples were incubated with compounds and irradiated to either (I) photo-crosslink probe to cellular target protein(s), (II) out-compete probe with parent molecule or (III) leave target protein(s) unbound with DMSO-treatment. Treated gametocytes were subsequently **(3)** purified by density barrier isolation and **(4)** lysed. **(5)** Probe **8**-crosslinked proteins in the gametocyte lysate were ligated to capture reagent azido-TAMRA/biotin (AzTB) by performing a CuAAC reaction, **(6)** permitting downstream enrichment and analysis by either nLC-MS/MS, in-gel fluorescence or western blot.

cytes were activated to induce gametogenesis and saponin-treated to lyse host erythrocytes, obtaining pure gametocytes. Gametocyte pellets were lysed and lysate was ligated to azido-TAMRA/biotin (AzTB), a capture reagent which is equipped with a tetramethylrhodamine (TAMRA) fluorophore for visualisation and a biotin moiety for enrichment (Broncel et al., 2015; Wright et al., 2015). A copper (I)-catalyzed alkyne–azide cycloaddition (CuAAC) reaction was performed to ligate AzTB to the alkyne handle of probe **8**-bearing crosslinked proteins. Crosslinked and ligated proteins could then be enriched for target identification by nano-scale liquid chromatographic tandem mass spectrometry (nLC-MS/MS), performed by

members of the Tate lab, or target validation using in-gel fluorescence or western blot.

4.2.2 N-4HCS target identification by PAL

To identify crosslinked and AzTB-ligated proteins, which include the hypothesised N-4HCS cellular target(s), samples were first enriched with Neutravidin agarose beads and prepared for TMT labelling. Subsequent nLC-MS/MS analysis was performed by members of the Tate lab. Peptides enriched in probe-treated, competition control and DMSO control samples were quantified, yielding 129 protein hits. The specific probe-protein interaction profile was determined by excluding hits enriched under DMSO treatment from the 129 identified hits. Protein hits enriched in DMSO controls were considered a result of non-specific binding and upon comparison of probe **8** and DMSO treated fractions, 20 protein hits were found to be positively enriched as a specific result of probe-labelling (Figure 4.2 and Appendix A). Subsequent comparison of proteins enriched in samples treated solely with probe **8** and a combination of probe **8** and parent molecule **7** was performed to confirm specificity of probe and protein interactions. Negatively enriched proteins yielded from comparing these fractions represented proteins out-competed by parent molecule **7** (Figure 4.1). Nine proteins were found to be negatively enriched when compared this way (Figure 4.2 and Appendix A) and of these hits, six were additionally identified in the initial comparison between DMSO and probe treated samples (Table 4.2). The six identified hits represent potential N-4HCS target protein(s) and thus the function and stage-specificity of these hits were further analysed.

4.2.3 PAL protein hits

Among the six enriched hits were four proteins which are expressed in the symptomatic asexual blood stages of *Plasmodium*, and hence were not specific to the sexual stage gametocytes. Given the extensive study in the GHCDL screen and within this thesis confirming microgamete-specificity of the N-4HCS series, these hits were a likely result of non-specific binding, a drawback of PAL. An example

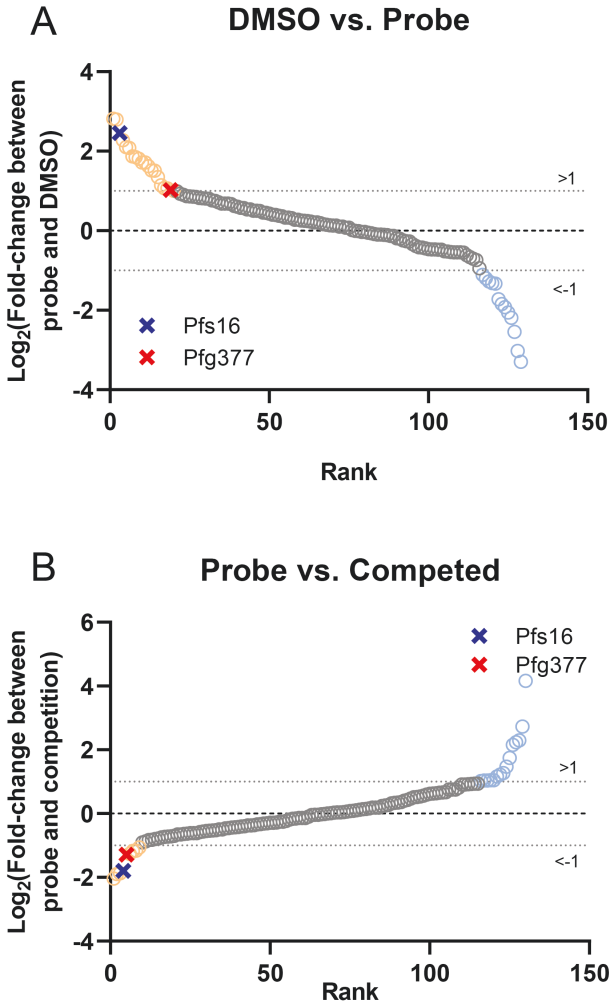


Figure 4.2: N-4HCS target identification by proteome-wide photoaffinity labelling (PAL). PAL was performed on stage V *P. falciparum* gametocytes and enriched proteins were pulled down and identified by nLC-MS/MS, utilising TMT-labelling. Comparison of (A) DMSO and probe **8**-treated samples and (B) probe **8** and competed (combined probe **8** and parent molecule **7** treatment) samples was measured as the $\log_2$-transformed fold change (Log_2FC) in protein enrichment. Depicted as S-plots, proteins (circles) were ranked according to the Log_2FC between average enrichment of samples, from three biological replicates. The probe-protein specific interaction profile is displayed as orange circles, specifically representing positively enriched proteins ($Log_2FC > 1$) in (A) and negatively enriched proteins ($Log_2FC <$ -1) in (B). Blue circles represent negatively enriched proteins ($Log_2FC <$ -1) in (A) and positively enriched proteins ($Log_2FC > 1$) in (B). Gametocyte specific hits Pfs16 and Pfg377 are denoted as blue and red crosses, respectively. Positively enriched hits in A are summarised in Table A1 and negatively enriched hits in B are listed in Table A2 in Appendix A. The combined profile of enrichment (positive enrichment in A and negative enrichment in B) is summarised in Table 4.2.

is RAB1B which is found to localise adjacent to the early asexual blood stage ER, with a role in ER-to-Golgi transport (Quevillon et al., 2003; Taku et al., 2020). Study of *Rab1B* deemed this gene essential to asexual growth (Zhang et al., 2018), which was found to be unaffected by N-4HCS treatment in the GHCDL screen, as summarised in Table 1.1 (Delves et al., 2018). Similarly, inhibition of the 60S ribosomal protein L26 is highly unlikely to result in a transmission-specific block in parasite viability and is a probable artefact of non-specific binding following photoactivation. Inhibitors of spermidine synthase have been found to inhibit asexual growth (Sprenger et al., 2015; Dufe et al., 2007), as expected from the erythrocytic schizogony-specificity enzyme (Haider et al., 2005). Finally, the V-type proton ATPase enzyme is involved in maintenance of the cytosolic pH in parasites (Schalkwyk et al., 2010), with evidence of function in erythrocytic schizogony (Hayashi et al., 2000; Auparakkitanon and Wilairat, 2006; Bray, Howells, and Ward, 1992). Again, the inactivity of the N-4HCS series in *in vitro* asexual growth assays reported in the GHCDL screen (Delves et al., 2018), point to the likely non-specific binding of these proteins.

Of the six hits identified, the gametocyte-specific 16kDa *P. falciparum* parasitophorous vacuole membrane protein Pfs16 (PlasmoDB ID, PF3D7_0406200) was found to be most positively enriched upon comparison of DMSO and probe-treated samples (Table 4.2). Furthermore, the *P. falciparum* female gametocyte protein Pfg377 (PlasmoDB ID, PF3D7_1250100) was additionally enriched. Notably, Pfs16 and Pfg377 were the only hits identified with specific expression and function during the sexual stages of *Plasmodium*.

4.2.4 Sexual stage-specific hits

Given the gametocyte-specificity of hits Pfs16 and Pfg377, these proteins were further studied in this thesis. Although Pfs16 is known to be an early marker of *Plasmodium* sexual conversion, little is known of the protein function. Comprised of 157 amino acids, the protein contains a signal peptide and transmembrane domain, and is known to localise to the PVM. Significantly, targeted gene disruption of *Pfs16* is associated with a block in microgametogenesis (Kongkasuriyachai, Fujioka,

	DMSO vs. probe 8				Probe 8 vs. competition			
Rank	**Colloquial Name**	**Protein ID**	**P value**	**Log_2 FC**	**Colloquial Name**	**Protein ID**	**P value**	**Log_2 FC**
1	***Pfs16**	**PF3D7_0406200.1-p1**	**0.0701**	**2.45809**	Spermidine Synthase	PF3D7_1129000.1-p1	0.1552	-2.0397
2	Spermidine Synthase	PF3D7_1129000.1-p1	0.1058	2.27369	60S Ribsomal Protein L26	PF3D7_0312800.1-p1	0.0051	-1.8946
3	RAB-1B (Ras related protein)	PF3D7_0512600.1-p1	0.0314	2.08532	RAB-1B (Ras related protein)	PF3D7_0512600.1-p1	0.0177	-1.8675
4	60S Ribsomal Protein L26	PF3D7_0312800.1-p1	0.0423	1.71633	***Pfs16**	**PF3D7_0406200.1-p1**	**0.3069**	**-1.7926**
5	V-type Proton ATPase	PF3D7_1311900.1-p1	0.0567	1.34692	****Pfg377**	**PF3D7_1250100.1-p1**	**0.1180**	**-1.2868**
6	****Pfg377**	**PF3D7_1250100.1-p1**	**0.4615**	**1.02634**	V-type Proton ATPase	PF3D7_1311900.1-p1	0.0201	-1.1617

Table 4.2: Probe-protein interaction profile determined by nLC-MS/MS analysed photoaffinity labelling. Proteins listed both were positively enriched in comparison of DMSO and probe **8**-treated samples and negatively enriched when comparing probe **8**-treated and competition (combined probe **8** and parent molecule **7**-treatment). Hits, including *Pfs16 and **Pfg377, are ranked by log_2-transformed fold change (Log_2FC) between the average enrichment of samples, derived from three biological replicates. Protein hits not enriched in both conditions were omitted as non-specific interactions and the full list of hits can be found in Appendix A. P values were obtained by performing a student's *t*-test.

and Kumar, 2004), consistent with the N-4HCS compound phenotype. In contrast, despite Pfg377 being exclusively expressed during the sexual stages, the protein is female-specific and thus inconsistent with the microgamete-targeted activity of the N-4HCS series. In *P. falciparum*, Pfg377 is associated with osmiophilic bodies which are membrane-bound vesicles involved in parasite egress during gametogenesis (Koning-Ward et al., 2008). Validation of the specificity of Pfs16 and Pfg377 enrichment ensued.

4.2.5 Pfs16 and Pfg377 target validation by PAL

To validate the nLC-MS/MS identification of Pfs16 and Pfg377 as binding partners of the N-4HCS series, in-gel fluorescence (IGF) coupled to western blot analysis was utilised in follow-up PAL experiments. Following the general format outlined in Figure 4.1, live stage V gametocytes were treated with increasing concentrations of probe **8**. Whilst the initial PAL experiment was performed at a single concentration of probe and parent molecule, the preliminary identification of Pfs16 and Pfg377 was validated here by determining whether enrichment of these hits occurred in a probe **8**-dose-dependent manner. Live stage V gametocytes were treated with increasing doses of probe **8** or a single dose of DMSO prior to photo-crosslinking to cellular target(s). Additionally, UV and click controls were obtained by treating samples with a single concentration of probe **8** but omitting the irradiation step or copper catalyst required for the CuAAC reaction, respectively. Treated cells were purified, lysed and ligated to AzTB as outlined in Figure 4.1. AzTB-ligated proteins were subsequently enriched using streptavidin-coated magnetic beads. The presence of TAMRA in AzTB permitted detection of enriched proteins by IGF.

Analysis of samples by IGF revealed a probe **8** concentration-dependent pulldown of a protein between 15 and 20kDa in size (Figure 4.3A), likely corresponding to the 16kDa protein Pfs16. Densitometric analysis revealed an increased enrichment of the protein with increasing doses of probe **8**, relative to DMSO controls (Figure 4.3B). Importantly, enrichment was shown to be CuAAC-dependent as the 15-20kDa band was only minimally detected in click controls. Detection of the protein band in the UV control signified an irradiation-independent irreversible binding of probe **8** to the

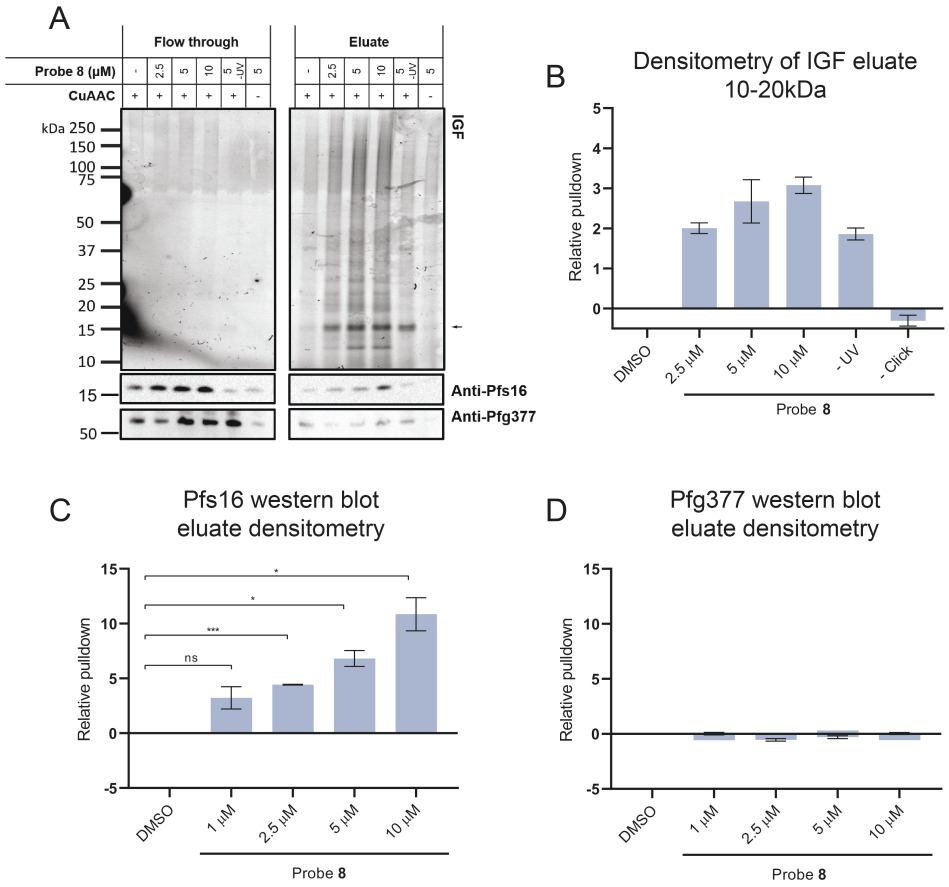


Figure 4.3: Pfs16 and Pfg377 target validation by photoaffinity labelling. Validation of Pfs16 and Pfg377 enrichment by nLC-MS/MS was validated by PAL, performed by live gametocyte treatment with probe **8**, AzTB conjugation and streptavidin-based enrichment. Probe **8**-concentration dependent pulldown was measured from 1-10 μM. (A) IGF and western blots of proteins identified in both flow-through and enriched samples are depicted. The presence of a copper catalyst in the click chemistry-ligation of AzTB is denoted as CuAAC, with the CuAAC (-) sample representing the click control. A UV control (-UV) was additionally obtained. A 15-20kDa protein was abundantly TAMRA-labelled (arrow) in the enriched (eluate) sample and likely corresponds to Pfs16. Pfs16 and Pfg377 specific antibodies were used to label corresponding western blots. (B) The band intensity, relative to DMSO, of the eluted 15-20kDa protein band by IGF in (A) was measured by densitometry. Average pulldown values were derived from three biological replicates and error bars denote SEM. Corresponding (C) Pfs16 and (D) Pfg377-labelled western blots of enriched (eluate) samples were analysed by densitometry to obtain band intensities relative to DMSO (relative pulldown). Values represent the average relative pulldown from three biological replicates and error bars denote the SEM. Unpaired two-tailed t-tests were performed to derive significant differences in relative pulldown (*** ($p < 0.001$), * ($p < 0.05$) and ns ($p \geqq 0.05$)).

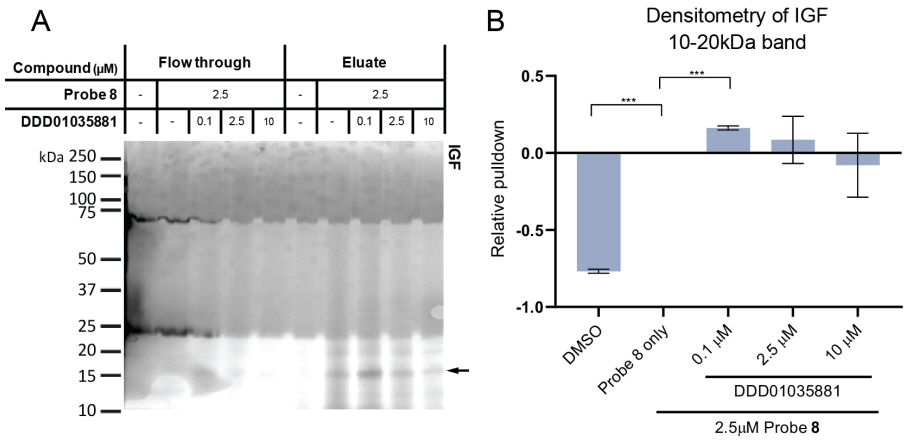


Figure 4.4: Photoaffinity labelling validation by probe **8** and **DDD01035881** competition. PAL was performed with live gametocytes by cotreatment with probe **8** and GHCDL compound **DDD01035881**. Following AzTB conjugation and streptavidin-based enrichment, (A) IGF of flow through and enriched (eluate) proteins was measured. A notable 15-20kDa protein band (arrow) was identified in the eluate and analysed by densitometry to measure relative pulldown, compared to a probe **8**-only control. Average relative pulldown values were derived from two-three biological replicates and error bars denote SEM. Unpaired two-tailed *t*-tests were performed to measure significance (*** ($p < 0.001$)).

protein of interest (Figure 4.3A-B). Modification of the N-4HCS scaffold to obtain the photoaffinity probe **8** may, therefore, reduce the reversibility of binding that is otherwise seen in **DDD01035881** and analogues, independently of photoactivation.

The Pfs16 and Pfg377-specificity of enrichment was then measured by immunoblot and densitometry, using antibodies specific to the proteins (Moelans, 1995; Ishino et al., 2020). Pulldown of Pfs16 was found to correlate with probe **8** concentration, being significantly enriched with 2.5, 5 and 10 μM of probe **8** relative to DMSO (Figure 4.3C). In contrast, Pfg377 was not significantly enriched in the presence of probe **8** relative to DMSO controls (Figure 4.3D). This observation supported our hypothesis that Pfg377 was likely enriched due to non-specific binding. The dose-dependent pulldown of Pfs16 provided strong evidence of this protein being the N-4HCS cellular target and the association of Pfs16 with microgametogenesis further corroborated our hypothesis.

Additional support of the Pfs16 engagement with N-4HCS compounds was sought by repetition of the PAL competition experiments, analysing Pfs16 enrichment by

IGF. Gametocytes were treated with a combination of probe **8** and the original GHCDL-derived compound, **DDD01035881**. In the presence of the more potent parent molecule **DDD01035881**, probe **8** would theoretically be outcompeted, subsequently reducing the extent of target protein pulldown. As depicted in Figure 4.4, IGF revealed the enrichment of a 15-20kDa protein band, likely representing Pfs16. The relative pulldown of the 15-20kDa protein was reduced in the presence of increasing concentrations of **DDD01035881**. However, it should be noted that in the presence of 0.1 μM **DDD01035881**, the pulldown was significantly higher than in probe-only controls, which likely corresponded to the variability in the experiment (Figure 4.4B).

Interestingly, pulldown of the 15-20kDa protein was not significantly reduced in the presence of 2.5 or 10 μM **DDD01035881**, relative to samples treated solely with probe **8** (Figure 4.4B). Given the irreversible binding activity of **DDD01035881**, it is highly plausible that irradiation of live stage V gametocytes in the presence of both probe **8** and **DDD01035881** may favour photo-crosslinking of probe **8** to the protein target(s). It was therefore unsurprising that the competition was not of significance here.

Although successful competition of Pfs16-binding was observed in the original nLC-MS/MS identification experiments, probe **8** treatment was outcompeted by parent molecule **7**, the structure of which closely mimics that of the photoaffinity probe. Parent molecule **7** binding characteristics were therefore more likely to mirror those of the probe **8**, potentially overcoming the irreversibility of **DDD01035881** as previously discussed. Therefore, co-treatment with parent molecule **7** may feasibly result in a more significant competition than **DDD01035881**. Importantly, these results pointed to specific probe-mediated pulldown of a protein which likely corresponds to Pfs16.

4.2.6 Label-free target validation of Pfs16 and Pfg377

Although PAL is a valuable tool in small molecule target identification, nonspecific crosslinking to abundant proteins besides the cellular target(s) can limit its reliability. This necessitates validation of the interactions identified by PAL, to discern

specific binding over background labelling (Smith and Collins, 2015). As nonspecific labelling arises from the formation of reactive intermediates during photoactivation, label-free validation utilising compounds lacking photoreactive groups is crucial to the identification of false-positive results. Here, I sought to ascertain the specificity of Pfs16 and Pfg377 binding to the N-4HCS series by performing the label-free Cellular Thermal Shift Assay (CETSA).

4.2.6.1 Cellular thermal shift assay

The underlying premise of CETSA is based on the biophysical principle that proteins are thermally stabilised when ligand-bound (Jafari et al., 2014; Martinez Molina et al., 2013). In the context of small molecule drugs, cellular target(s) are stabilised by drug binding and measurement of this stabilisation has applications in target discovery (Jafari et al., 2014; Martinez Molina et al., 2013). Although thermal shift assays are widely applied to purified proteins, CETSA investigates thermal stabilisation in complex environments such as live cells, tissues and cell lysates and thus preserves biologically relevant traits of drug binding, such as cellular localisation and post-translational modifications (Jafari et al., 2014).

Application of this principal in a practical setting entails treatment of cells or lysate with either the compound-of-interest or a vehicle control. Treated samples are then thermally challenged over a range of temperatures to irreversibly aggregate the cellular target(s), which can be removed with centrifugation for detection of the remaining soluble protein. Thermally challenged proteins can be separated and detected by gel electrophoresis and western blot, respectively. Densitometry of western blots permits quantitative measure of protein aggregration, enabling generation of protein melting curves and extrapolation of the temperature at which a protein aggregates, referred to as T_{Agg}. A positive shift in the thermal stability of a protein, specifically an increase in T_{Agg}, between vehicle control and compound-of-interest indicates stabilisation by compound binding.

To determine if Pfs16 and Pfg377 are thermally stabilised in the presence of N-4HCS compounds, CETSA was performed with cell lysate and detected by western blot as outlined in Figure 4.5. Stage V *P. falciparum* NF54-strain gametocytes

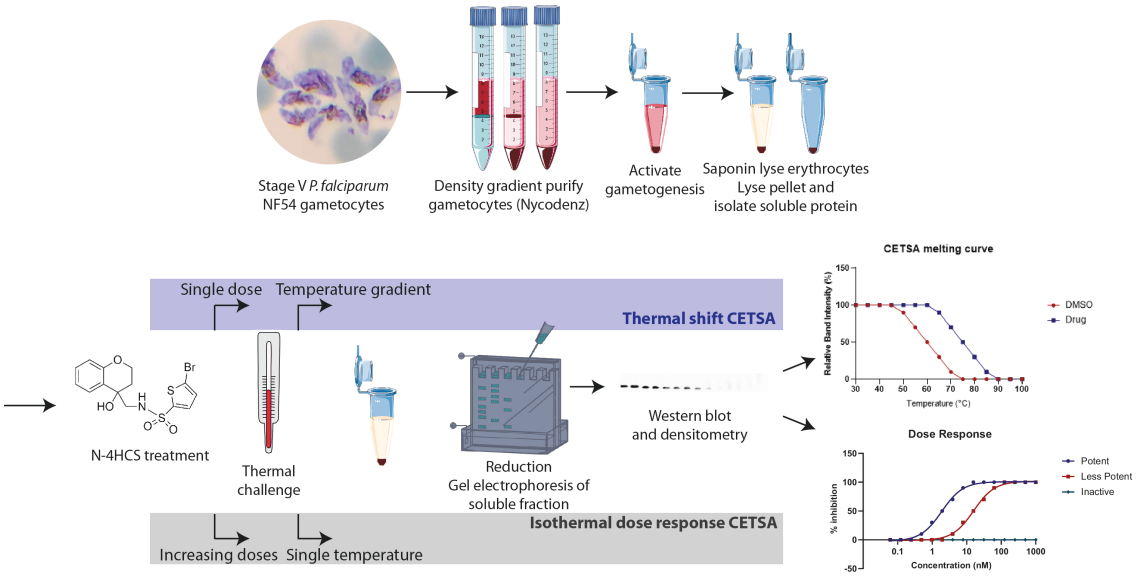


Figure 4.5: The cellular thermal shift assay workflow. Stage V *P. falciparum* NF54-strain gametocytes are purified by density barrier isolation and activated prior to saponin lysis of erythrocytes. The soluble fraction of the resulting gametocyte lysate is obtained for the cellular thermal shift assay (CETSA). To derive melting curves for the thermal shift format of the assay, lysate is drug-treated at a single dose and thermally challenged over a temperature gradient. To derive dose-response curves in the isothermal dose response (ITDR) format of CETSA, lysate is treated with varying drug concentrations and thermally challenged at a single temperature which is derived from the corresponding melt curve. For both formats of CETSA, centrifugation is utilised to remove the aggregated (by drug-stabilisation) protein and soluble protein is separated by gel-electrophoresis. Western blot and densitometry is performed to obtain either melting curves, from which temperatures of aggregation (T_{Agg}s) are derived, or a drug dose-response curve. Shifts in thermal stability by increased T_{Agg}, relative to DMSO, signify drug engagement and are validated by dose-response.

were purified by density gradient isolation and activated to induce gametogenesis. Saponin lysis of isolated gametocytes was performed at 4°C to both halt gamete formation and lyse erythrocytes. Gametocyte lysate was then obtained according to the lysis conditions utilised in the PAL identification study, using a lysis buffer containing 1% Triton-X100 which is sufficient for solubilisation of PVM proteins, such as Pfs16. To perform the thermal shift format of CETSA (Figure 4.5), soluble gametocyte protein was treated with either DMSO, to act as the vehicle control, or **DDD01035881** and thermally challenged over a gradient of temperatures. In contrast, the isothermal dose response format of CETSA was performed at a single

temperature but varying concentrations of compound. Soluble protein was isolated by centrifugation and separated by gel electrophoresis prior to western blot-based detection, using antibodies specific to Pfs16 (Moelans, 1995) and Pfg377 (Ishino et al., 2020). Densitometric analysis of western blots was performed to determine the band intensity of each thermally challenged sample for generation of melting and dose response curves.

4.2.6.2 Pfs16 and Pfg377 thermal stabilisation

Thermal challenge of gametocyte lysate over a temperature gradient was performed to generate Pfs16 and Pfg377 melting curves, from which T_{Agg}s were extrapolated. To optimise the conditions applied in the thermal shift format of the assay, Pfs16 aggregation was measured using DMSO-treated lysate from activated stage V gametocyte culture (Figure 4.6). Initial tests found that with a three minute thermal challenge and 20 minute centrifugation, Pfs16 did not aggregate in a temperature gradient from 51.6-100°C (Figure 4.6). Increasing the duration of thermal challenge to five minutes and centrifugation of challenged samples to 30 minutes resulted in aggregation of Pfs16 (Figure 4.6), and these conditions were henceforth applied in CETSA experiments.

Treatment of soluble gametocyte protein fractions with **DDD01035881** resulted in a positive shift in the melting curve of Pfs16 relative to the DMSO melting curve, as depicted in Figure 4.8. Melting curves were generated by densitometric analysis of western blots, with representative blots depicted in Figure 4.7. Comparison of T_{Agg}s revealed a significant difference in relative band intensity between DMSO and **DDD01035881**-treated fractions at 91°C ($p < 0.001$). This result signified a **DDD01035881**-mediated thermal stabilisation of Pfs16, suggesting that the N-4HCS series bound and stabilised this protein in activated mature gametocytes. Crucially, this finding confirmed that Pfs16 binding occurred independently of photo-crosslinking and thus validated the specificity of the PAL enrichment of Pfs16. This further corroborated Pfs16 as the likely cellular target of the N-4HCS series.

Additionally, the melting curves of Pfs16 were obtained from mature gametocyte

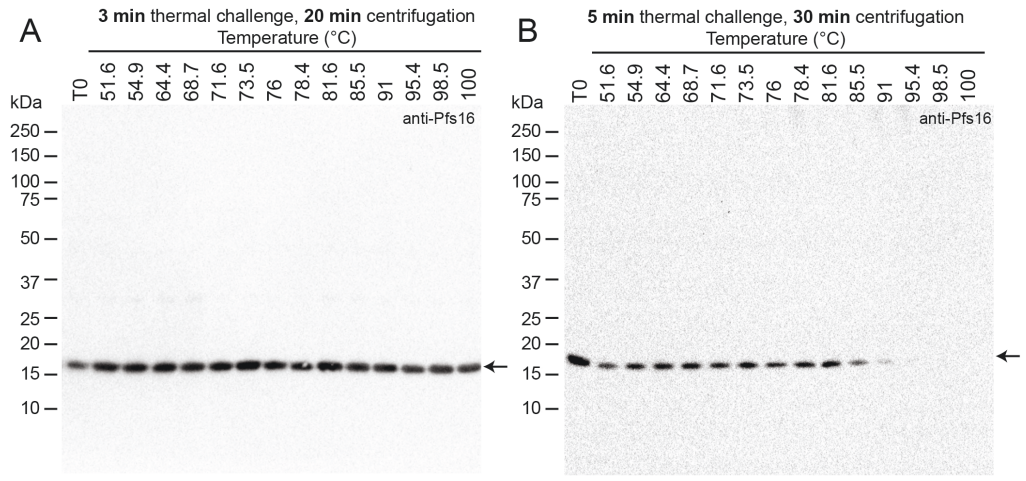


Figure 4.6: Optimisation of conditions for CETSA. Aggregation of Pfs16 was required to generate melting curves and was optimised using DMSO-treated activated stage V gametocyte lysate, analysed by Pfs16-labelled western blots. (A) Three-minute thermal challenge and 20 minute centrifugation demonstrated no aggregation from 51.6-100°C. (B) An increase in the thermal challenge and centrifugation duration to five and 30 minutes, respectively, resulting in aggregation of Pfs16 at 91°C. T0 controls represent untreated stage V gametocyte lysate which was not thermally challenged.

lysate treated with the separated enantiomers of GHCDL-compound **DDD010280-76**, **(-)-DDD01028076** and **(+)-DDD01028076** (Figure 4.9). A clear shift in the curves of both compounds relative to the DMSO curve were found, with both compounds displaying a significant difference in relative band intensity compared to DMSO at 85.5°C ($p < 0.05$). Although there is an >100-fold difference in the *in vitro* activity between these enantiomers, this difference in potency was not reflected in CETSA. This finding was expected given CETSA was performed by treating lysate with 100 μM N-4HCS compounds to ensure maximal binding to target protein(s). The thermal stabilisation of Pfs16 with **(-)-DDD01028076** and **(+)-DDD01028076** supported that compounds of the N-4HCS series bind the protein in a label-free setting.

In contrast, Pfg377 was not stabilised by **DDD01035881** treatment in the thermal shift format of CETSA, as shown in Figure 4.8. This observation further supported the hypothesis that Pfg377 enrichment in the nLC-MS/MS analysed PAL experiment was a false-positive result, arising from non-specific binding. Evidence

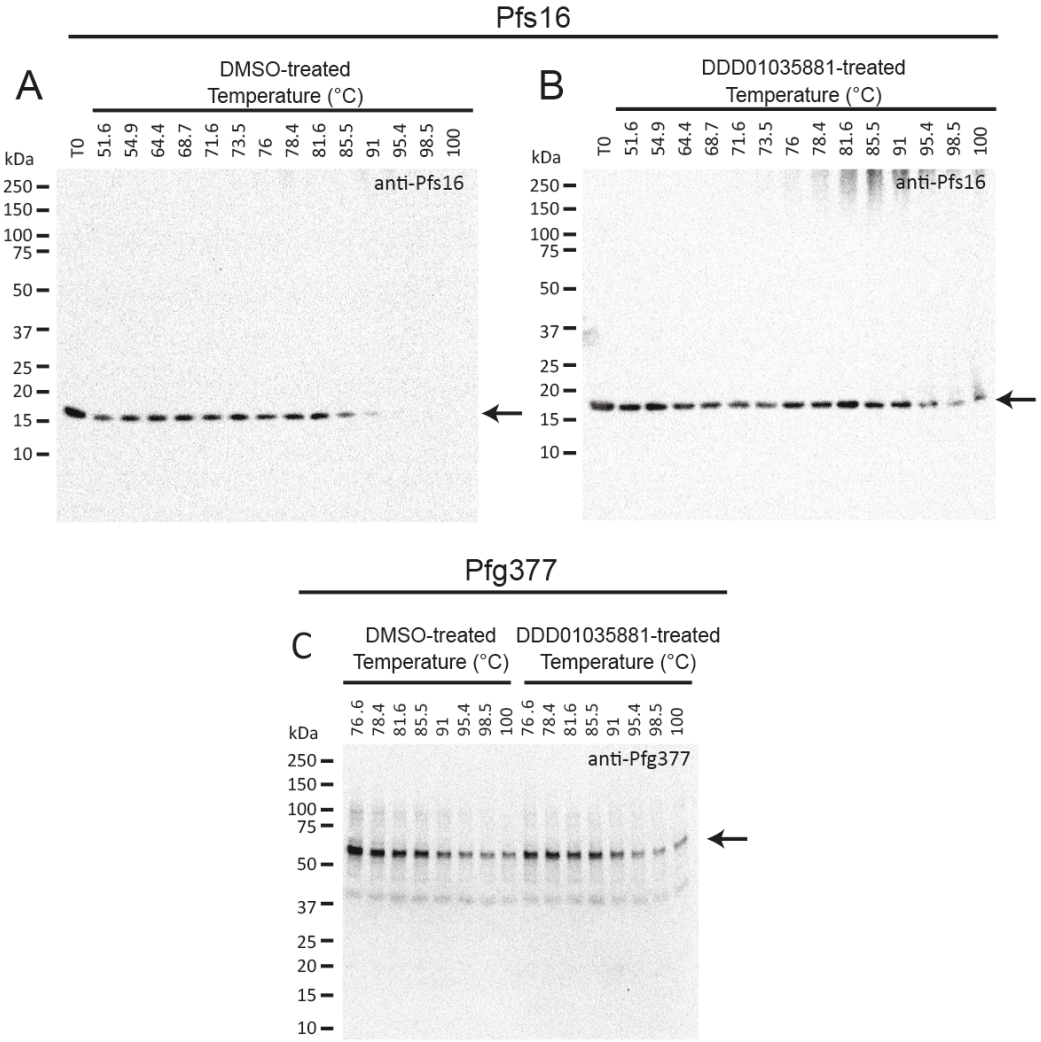


Figure 4.7: Full CETSA western blots utilised to derive protein melting curves. CETSA was performed with stage V activated gametocyte lysate to obtain (A-B) Pfs16 and (C) Pfg377-labelled western blots, using varying temperature ranges. The 16kDa protein band (arrow), corresponding to Pfs16, was analysed by densitometry to obtain (A) DMSO and (B) **DDD01035881** melting curves, and corresponding T_{Agg} values. (C) A Pfg377-labelled band between 50-75kDa in size (arrow) was analysed by densitometry to generate and compare DMSO and **DDD01035881** melting curves and T_{Agg} values. T0 refers to untreated stage V gametocyte controls.

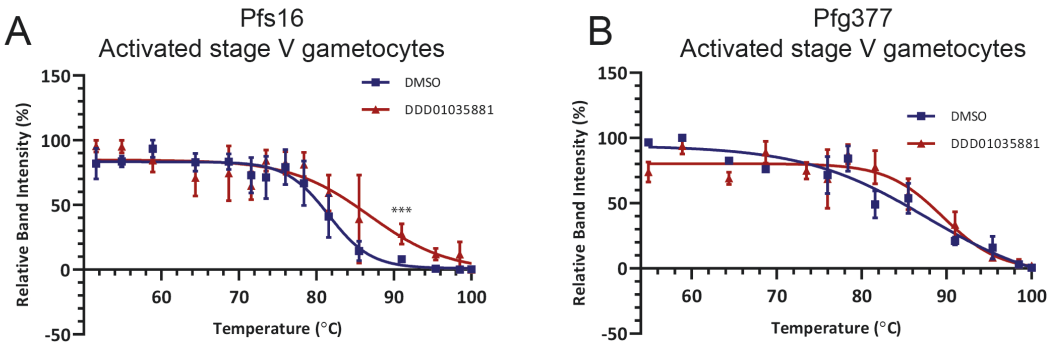


Figure 4.8: Label-free CETSA validation of Pfs16 and Pfg377 binding. Melting curves of (A) Pfs16 and (B) Pfg377 were generated by densitometric analysis of western blots depicted in Figure 4.7, with relative intensities being normalised to the highest and lowest band values. Comparison of DMSO and **DDD0135881** curves were used as validation of N-4HCS binding and stabilisation of the two proteins identified by PAL. Average band intensity at each temperature was plotted and error bars represent the SEM of three biological replicates. An unpaired two-tailed *t*-test found a statistically significant difference in the band intensity of DMSO and **DDD01035881**-treated fractions at 91°C (*** $p < 0.001$).

obtained from label-free CETSA additionally supported the in-gel fluorescence PAL validation experiment described in Chapter 4.2.5. Importantly, Pfg377 served as a suitable a protein control to these validation experiments.

4.2.6.3 Isothermal dose response

Positive shifts in melting curves identified by CETSA are traditionally validated by the isothermal dose response (ITDR) format of CETSA, in which soluble protein is treated with serial dilutions of compound but thermally challenged with a single temperature. Compound stabilisation with increasing compound concentrations would be indicative of drug binding. The temperature applied in ITDR-CETSA is selected based on the differential stabilisation of a given protein between DMSO and drug-treated protein fractions. Specifically, this is extrapolated from melting curves as a temperature at which the protein is aggregated with DMSO treatment (minimal band intensity) but stabilised by drug (relatively increased band intensity). ITDR-CETSA is therefore solely applicable to proteins demonstrating a positive thermal shift and was hence only applied to Pfs16 in this study.

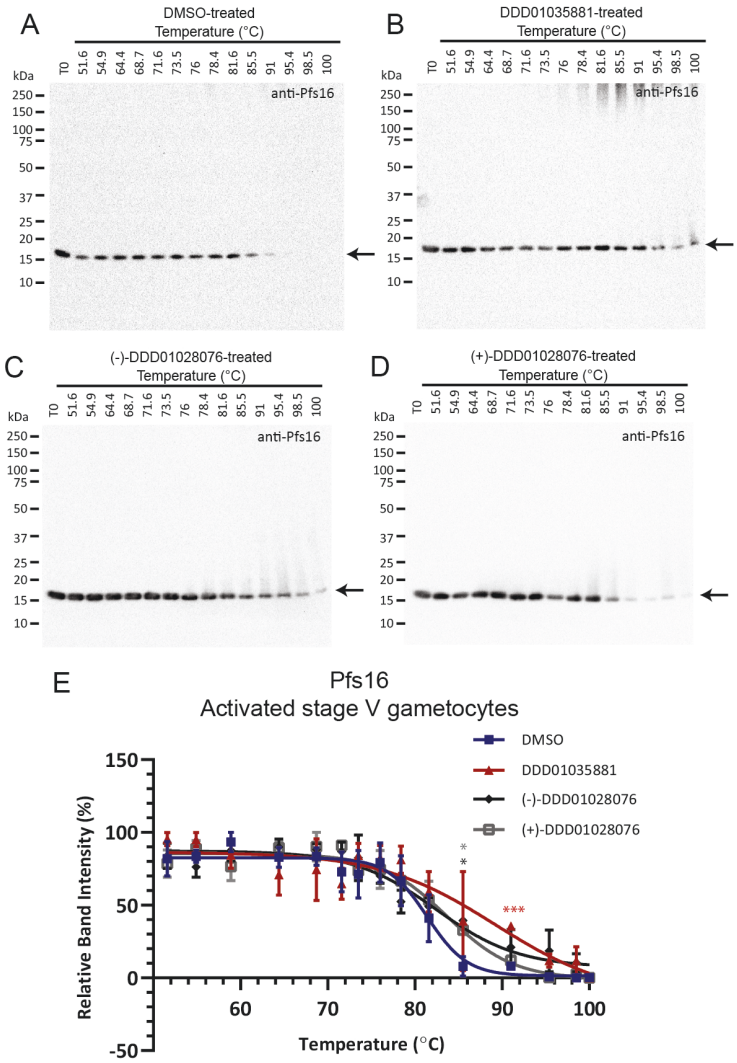


Figure 4.9: Pfs16 CETSA melting curves under N-4HCS treatment. Stage V gametocyte lysate was treated with either (A) DMSO, (B) **DDD01035881** or separated enantiomers of **DDD01028076**, (C) **(-)-DDD01028076** or (D) **(+)-DDD01028076**, to obtain (E) Pfs16 CETSA melting curves. (A-D) DMSO and N-4HCS compound-treated lysate was thermally challenged in a gradient from 51.6-100°C and Pfs16 aggregation was detected by western blot, measuring the band intensity of the 16kDa Pfs16 bands (arrows). T0 refers to untreated stage V gametocyte controls. (E) Densitometry values from western blots (A-D) were converted to relative band intensity to generate melting curves. Points and error bars represent the average relative band intensity and SEM of three biological replicates. respectively. Statistically significant differences between band intensities was measured with an unpaired two-tailed t-test. Significant differences were found between DMSO and **DDD01035881** at 91°C (*** $p < 0.001$) and between DMSO and both **(-)-DDD01028076** and (D) **(+)-DDD01028076** at 85.5°C (* $p < 0.05$).

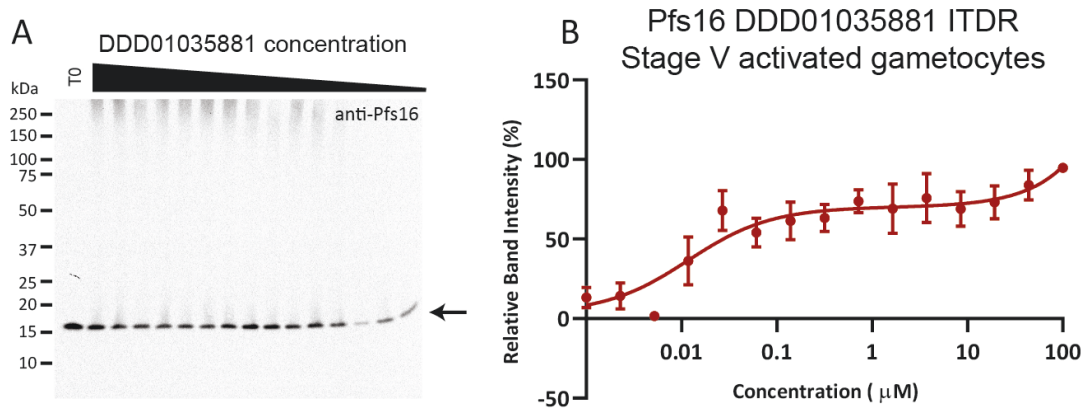


Figure 4.10: Isothermal dose response (ITDR) CETSA of Pfs16 and **DDD01035881**. The thermal shift of Pfs16 under **DDD01035881** treatment, depicted in Figures 4.8 and 4.9, was validated by measuring Pfs16 aggregation at 78.4°C with increasing **DDD01035881** concentrations (1 nM-100 μM). (A) Densitometry of Pfs16-labelled western blots was measured to obtain the Pfs16 band intensity (arrow) of each sample and converted to relative band intensity, enabling generation of (B) a dose response curve of **DDD01035881**. T0 refers to untreated stage V gametocyte controls. Average band intensity was plotted and error bars represent the SEM of four biological replicates.

ITDR-CETSA of Pfs16 was performed at 78.4°C, treating activated stage V gametocyte lysate with **DDD01035881** from 1 nM to 100 μM. A **DDD01035881**-concentration dependent stabilisation of Pfs16 was observed (Figure 4.10), corroborating the thermal shift observed in Figure 4.8. Notably, Pfs16 engagement was identified in nLC-MS/MS-analysed PAL and validated by in-gel fluorescence and western blot-based PAL, and both thermal shift and ITDR-CETSA. Combined evidence obtained here and the consistency of N-4HCS activity with Pfs16 expression strongly supports our hypothesis that the protein is bound by the N-4HCS compound series. Additionally, non-specific binding of N-4HCS compounds to Pfg377 was confirmed by both CETSA and gel-based PAL. As a female-specific protein, Pfg377 was inconsistent with our understanding that **DDD01035881** specifically inhibits microgametogenesis. Combining medicinal chemistry, chemical proteomics and chemical biology, this chapter has progressed N-4HCS development from lead optimisation to identification and validation of Pfs16 as the cellular target.

4.3 Discussion

Identification of hits demonstrating transmission-blocking activity in the GHCDL screen (Delves et al., 2018) crucially addressed the need to discover novel antimalarial candidates, as sustained success of the artemisinin combination therapies is threatened by resistance. Compounds of the N-4HCS series, discovered in the GHCDL screen, uniquely block microgametogenesis without requiring any incubation with gametocytes. Prior to this study, knowledge of the N-4HCS series was solely phenotypic and the cellular target(s) required deconvolution. Following lead development (Rueda-Zubiaurre et al., 2019), outlined in Chapter 3 of this thesis, the *P. falciparum* cellular target was identified and validated in this chapter.

Here, six proteins were identified as interactors of an N-4HCS probe by chemical proteomics and of these six hits, Pfs16 and Pfg377 were prioritised for validation due to their gametocyte-specific expression in *P. falciparum*. By using in-gel fluorescence and western blot-based analysis of photoaffinity labelled *P. falciparum* gametocytes, the Pfs16 interaction was validated whilst Pfg377 was found to be a false positive result. Further corroborating this finding, label-free validation by the Cellular Thermal Shift Assay (CETSA), which has proven to be highly valuable in antimalarial drug discovery (Dziekan et al., 2019; Dziekan et al., 2020), revealed a dose-dependent thermal stabilisation of Pfs16 by **DDD01035881**. Crucially, this showed that N-4HCS compounds bind to Pfs16 independently of photoactivation. In contrast, Pfg377 was not thermally stabilised by **DDD01035881**, providing further evidence of the non-specific enrichment of the protein in the initial study.

Pfs16 is known as one of the earliest markers of sexual conversion (Bruce et al., 1994; Kongkasuriyachai, Fujioka, and Kumar, 2004; Lanfrancotti et al., 2007) and targeted gene disruption of *Pfs16* is associated with a block in microgametogenesis (Kongkasuriyachai, Fujioka, and Kumar, 2004), consistent with the phenotype of N-4HCS compounds. The biological relevance of Pfs16 to N-4HCS activity combined with identification and validation of binding here, provided strong evidence that this protein is the cellular target of these compounds. Pfg377, in contrast, is female specific (Koning-Ward et al., 2008) and thus inconsistent with the male-specific

N-4HCS activity. Highly reactive intermediates formed with photoactivation are prone to bind non-specifically to abundant proteins and given the high expression of Pfg377 in stage V females (Severini et al., 1999) and the female biased sex-ratio in gametocytes (1 male for every 3-5 females), false-positive enrichment is probable.

Multistage-active drugs primaquine and tafenoquine exert an inhibitory effect on the transmissible gametocytes (Frampton, 2018), but alternatives are sought after given the safety concerns associated with these treatments. Crucial to avoiding the same safety concerns and resistance mechanisms of existing drugs, compounds with unexplored modes of action are required. As there is little selective pressure for resistance with the non-replicative gametocytes, a population bottleneck in the *Plasmodium* lifecycle, these stages are a desirable target for drug intervention. Currently, no existing antimalarials target the gametocyte-specific protein Pfs16, making the N-4HCS compounds a great starting point for transmission-blocking drug development. Though the function of Pfs16 remains elusive, the 16kDa, 157-amino acid protein is known to localise to the parasitophorous vacuole membrane (Bruce et al., 1994).

Deconvolving the cellular target of the N-4HCS series was a crucial step in the development pipeline, but further study was required to gain a comprehensive understanding of the compound mode of action. Knowledge that the N-4HCS compounds bind Pfs16 to likely exert a downstream inhibitory effect to microgametogenesis permitted tailored analysis of the compound phenotype. As Pfs16 is known as an early marker of sexual conversion with a role in microgametogenesis, detailed phenotypic analysis of N-4HCS compound effects to these processes followed this study.

Chapter 5

Phenotypic characterisation of the N-4HCS series

5.1 Introduction

To overcome the declining efficacy of existing antimalarials and to move towards malaria elimination and eradication, new drugs able to block the cycle of transmission are key. In line with this, compounds with the N-4HCS scaffold were discovered to potently block host-to-vector transmission of *Plasmodium* by compromising male gametocyte viability prior to this study (Delves et al., 2018). To advance the N-4HCS pipeline, hit-to-lead development by medicinal chemistry (Rueda-Zubiaurre et al., 2019) and target identification by chemical proteomics were pursued. Pfs16, a 16kDa parasitophorous vacuole membrane (PVM) protein specific to the sexual stages of *Plasmodium*, was found to be bound by N-4HCS compounds. To further validate Pfs16 as an N-4HCS cellular target and gain a detailed understanding of the mode of action (MoA), the aim of this chapter was to deconvolve the precise cellular phenotype of the N-4HCS compounds.

Combined knowledge of the Pfs16 expression pattern and microgametogenesis-targeted activity of the N-4HCS compounds enabled tailored study of the compound series MoA. As Pfs16 is one of the earliest markers of sexual conversion (Kongkasuriyachai, Fujioka, and Kumar, 2004), localises to the PVM (Baker et al., 1994) and plays a role in microgametogenesis (Kongkasuriyachai, Fujioka, and Kumar,

2004), the impact of the N-4HCS series on these processes and traits were studied here. Sustained expression of Pfs16 from the initial stages of sexual development up until stage V maturity suggested N-4HCS compounds may impart an additional inhibitory effect to early gametocytes. Various cell and chemical biology techniques were used to explore this hypothesis.

Additionally, the precise mode by which microgametogenesis is interrupted required deconvolution. As described in Chapter 1.2.3.9, gametocytes are activated to produce gametes in the mosquito midgut following a blood meal. The process of male gamete formation, or microgametogenesis, is characteristically rapid and complex. Activation of male gametocytes triggers a morphological transformation, host erythrocyte-egress, three rounds of DNA replication with alternating rounds of endomitosis and a drastic cytoskeletal rearrangement (Sinden, 2009). The cytoskeletal transformations are markedly complex and involves the nucleation and elongation of axonemes. Upon full development, axonemes emerge from the microgametocyte cell body along with a haploid genome, in an explosive process called exflagellation (Sinden et al., 2010). Being so complex, there are multiple avenues for inhibition of microgametogenesis and a range of techniques were used to elucidate which of the processes were interrupted by N-4HCS compounds.

Chemical biology, flow cytometry, high-resolution widefield fluorescence and electron microscopy (EM) techniques were used to study the specific impact of N-4HCS treatment on *Plasmodium*. Crucially, it was found that N-4HCS inhibition was consistent with the previously reported targeted gene disruption of *Pfs16* (Kongkasuriyachai, Fujioka, and Kumar, 2004). Here we found that N-4HCS compounds bind to Pfs16 to solely inhibit microgametogenesis, without impacting early sexual development.

5.2 Results

The aim of this chapter was to elucidate the precise mode of action by which the N-4HCS series inhibits *Plasmodium* transmission by binding to Pfs16. Work was guided by the knowledge that Pfs16 is expressed from the initial stages of sexual conversion up to the fully developed transmissible stage V gametocytes. Hence, it was sought to study the impact of N-4HCS compounds on gametocytogenesis and early gametocyte development. Additionally, we aimed to identify the specific processes during microgametogenesis which are are impeded by N-4HCS treatment. The results of this chapter are currently submitted as an online pre-print (Yahiya et al., 2021b).

5.2.1 N-4HCS impact to gametocytogenesis

The impact of N-4HCS treatment on gametocytogenesis and early gametocyte development was explored by performing the *in vitro* *Pf*2004/164-tdTom sexual conversion assay. Findings were then validated with the cell lysate-based Cellular Thermal Shift Assay (CETSA), to determine if N-4HCS compounds bind to Pfs16 in the early stages of gametocyte development.

5.2.1.1 *Pf*2004/164-tdTom sexual conversion assay

To quantify the rate of sexual conversion under N-4HCS treatment, a well-established assay using a transgenic *P. falciparum* line was performed (Brancucci et al., 2015). The transgenic *Pf*2004/164-tdTomato line was produced to enable gametocyte detection upon sexual conversion and was done so by those who designed the assay (Brancucci et al., 2015). Developers of the assay and parasite line opted to use the recently culture-adapted *P. falciparum* strain *Pf*2004, an isolate from Ghana, due to its susceptibility to environmental stimuli for gametocyte induction (Brancucci et al., 2015). Upon conversion to sexual stage gametocytes, *Pf*2004/164-tdTomato parasites express the fluorescent reporter tandem Tomato (tdTom), driven by the promoter of gametocyte-specific *etramp10.3*. By staining parasites with nucleic acid stain, SYBR green, flow cytometry is used to quantify and compare the initial

asexual parasitaemia of parasites to the subsequent gametocytaemia, enabling the calculation of a sexual conversion rate (Brancucci et al., 2015). The assay was applied to address the question of whether N-4HCS compounds can impede viability of the early sexual stages.

The workflow of the *Pf*2004/164-tdTomato sexual conversion assay performed in this chapter is described in Figure 5.1. Successive rounds of asexual *Pf*2004/164-tdTomato parasite synchronisation were performed by treatment with sorbitol, over four intraerythrocytic development cycles (IDCs). Repeated synchronisation brought parasites to a narrow developmental window, permitting synchronous sexual conversion without the need to remove gametocytes produced in preceding IDCs. Stage synchronised asexual parasites were then seeded into 96-well plates at high parasitaemia in the presence of spent medium, conditions which induce gametocyte production. Sexual conversion inhibitor choline was utilised as a positive control in the assay and N-4HCS compounds were added at varying times across the assay, to assess disruptions to both conversion and early gametocyte development. Following a round of asexual replication (an IDC), parasites were stained with SYBR green at 28 hours post-invasion (h.p.i.) to measure parasitaemia by flow cytometry. At 66 h.p.i., parasites were stained with SYBR green to determine gametocytaemia, measured as double-positive tdTomato expression and SYBR green staining. Impediments to conversion were determined with varying assay formats, to test various hypotheses:

1. **Carry-over format**. Prolonged N-4HCS treatment, added from the point of gametocyte induction to test for inhibition to sexual conversion.

2. **Wash-out format**. N-4HCS treatment at the point of induction, followed by compound removal 24 hours post-induction, to test for reversibility of any inhibitory effects to sexual conversion.

3. **Add-in format**. N-4HCS treatment 24 hours post-induction to measure the impact on early gametocyte development.

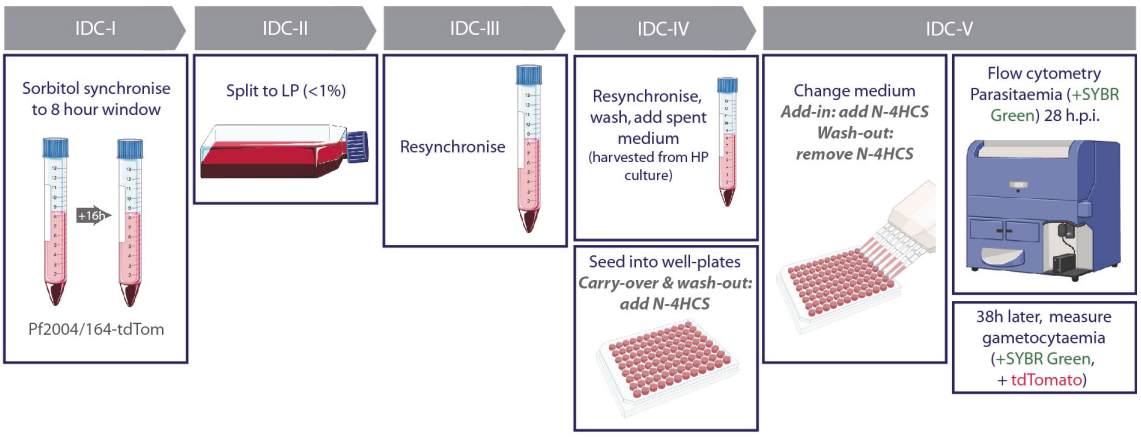


Figure 5.1: *Pf*2004/164-tdTom sexual conversion assay workflow. Sexual conversion rates of *Pf*2004/164-tdTom parasites can be determined using a previously described protocol (Brancucci et al., 2015), performed over five intraerythrocytic developmental cycles (IDCs). During IDC-I, *Pf*2004/164-tdTom asexual blood stage parasites are synchronised to an 8-hour age window, over two successive sorbitol synchronisation steps performed 16 hours apart. Parasites are maintained at a low asexual parasitaemia (LP; <1%) during IDC-II, prior to resynchronisation at IDC-III. At IDC-IV, parasites are further synchronised, and gametocytogenesis is induced using spent media which was harvested from high parasitaemia (HP) cultures. Induced parasites are seeded into 96-well plates and treated with N-4HCS compounds for the carry-over and wash-out formats of the assay, which probe for impacts to sexual conversion. During the final IDC (IDC-V), N-4HCS compounds are removed (wash-out) or added (add-in) to probe for reversibility to sexual conversion effects or inhibition of early gametocyte development, respectively. Following incubation, parasites are stained with SYBR-Green to determine parasitaemia by flow cytometry at 28 h.p.i. (hours post-invasion). Gametocytaemia is measured at 66 h.p.i., measuring SYBR-green and tdTomato double-positive cells, enabling calculation of sexual conversion rates. Some images were sourced and adapted from BioRender.com (2021).

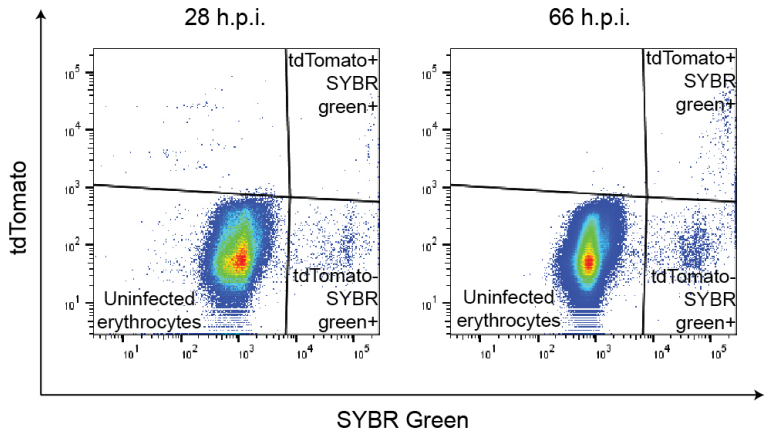


Figure 5.2: *Pf*2004/164-tdTom flow cytometry gating strategy to measure sexual conversion. SYBR-Green intensity (x axis) and tdTomato intensity (y axis) of stained *Pf*2004/164-tdTom parasites was measured by flow cytometry. Parasitaemia (SYBR-Green positive population) was measured at 28 hours post invasion (h.p.i.) and gametocytaemia (SYBR-Green and tdTomato double-positive population) was measured at 66 h.p.i. and values were used to calculate a sexual conversion rate. Cell populations were gated to identify uninfected erythrocytes, asexual blood stage (ABS) parasites and gametocytes, and the same gates were applied to corresponding samples at 28 h.p.i. and 66 h.p.i.

N-4HCS impact to *Pf*2004/164-tdTom sexual conversion

Flow cytometry measurements of asexual parasitaemia and gametocytaemia enabled calculation of sexual conversion rates of parasites treated with **DDD01035881**, **DDD01028076**, **(-)-DDD01028076**, **(+)-DDD01028076** or DMSO, under the carry-over, wash-out and add-in formats of the *Pf*2004/164-tdTom sexual conversion assay. Under each of the three assay formats and with each N-4HCS compound, relative sexual conversion rates of *Pf*2004/164-tdTom parasites were not significantly reduced compared to DMSO controls. This result suggested that the N-4HCS compounds did not exert an inhibitory effect to either early gametocyte development or sexual conversion. As sexual conversion was not inhibited by N-4HCS treatment, the insignificant impact to conversion rates upon removal of compounds in the wash-out format of the assay were expected. These results revealed that N-4HCS compounds specifically inhibited microgametogenesis without impacting gametocytogenesis or gametocyte development. As work outlined in this thesis revealed that the microgametogenesis-blocking N-4HCS compounds likely target Pfs16, a protein

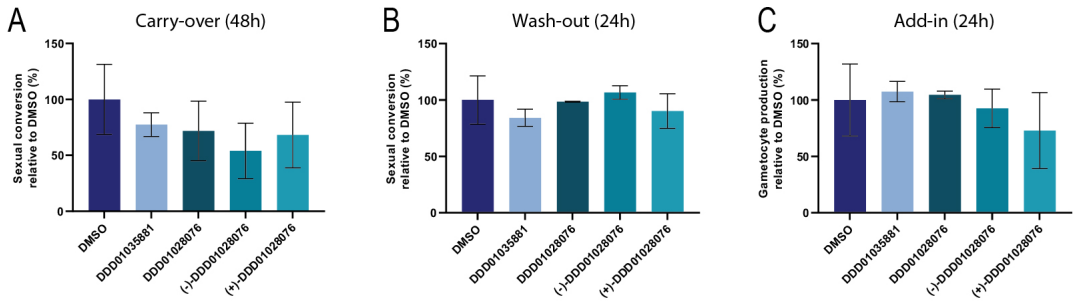


Figure 5.3: Relative sexual conversion and gametocyte production rates of N-4HCS-treated *Pf*2004/164-tdTom parasites. Sexual conversion was measured from flow cytometry-based quantification of gametocytaemia relative to initial parasitaemia and are depicted as percentage conversion or gametocyte production rates, relative to DMSO controls. Parasites were treated with either DMSO, **DDD01035881**, **DDD01028076**, **(-)-DDD01028076** or **(+)-DDD01028076** to measure (A) the impact to sexual conversion, (B) reversibility of any impact to conversion and (C) the effect on early gametocyte development. Error bars represent the SEM of two biological replicates. No significant differences were measured between negative DMSO controls and any N-4HCS compound in the (A) carry-over, (B) wash-out or (C) add-in formats in unpaired two-tailed *t*-tests.

expressed from the onset of sexual conversion, results here point to a varied role of the protein across parasite development.

5.2.1.2 Pfs16 and Pfg377 thermal stabilisation in stage I-III gametocytes

To validate the observation that N-4HCS compounds do not impede sexual conversion of *Pf*2004/164-tdTom parasites, we sought to determine whether the compounds bind to the identified cellular target, Pfs16, in the early stages of gametocyte development. By performing the Cellular Thermal Shift Assay (CETSA) on lysate derived from *P. falciparum* NF54-strain stage I-III gametocyte culture, Pfs16 engagement with **DDD01035881** was measured. Additionally, the assay was used to validate engagement with Pfg377, which was initially identified in a proteome-wide target identification study and later found to interact with N-4HCS compounds due to non-specific binding.

Performing CETSA as outlined in Chapter 4.2.6.1 and Figure 4.5, early gametocyte lysate was treated with either DMSO or a single concentration of **DDD010358-81** before thermally challenging over a gradient of temperatures. It was first vali-

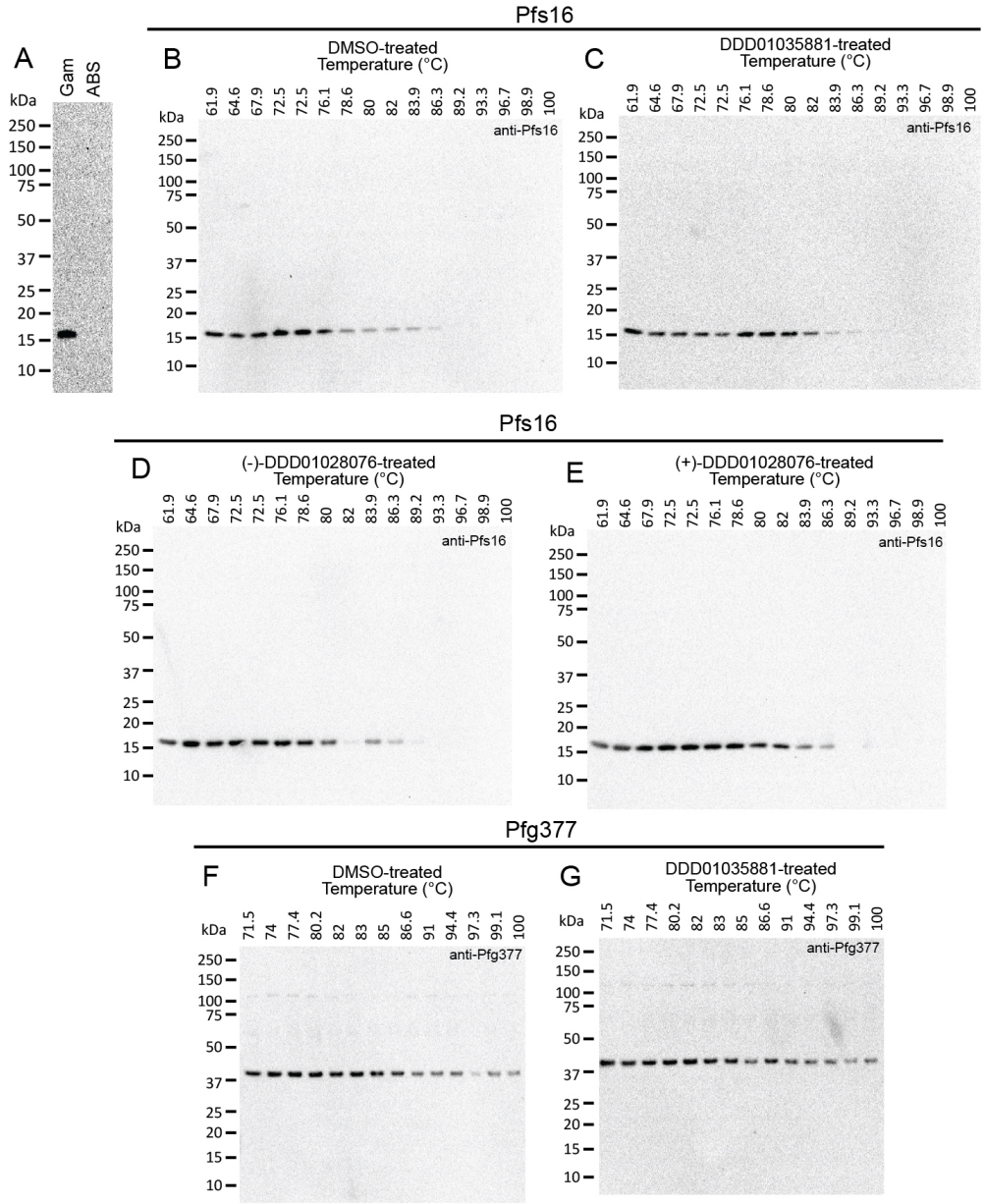


Figure 5.4: *P. falciparum* stage I-III gametocyte cellular thermal shift assay-derived western blots. (A) Pfs16 expression measured by western blot using cell lysate derived from asexual blood stage (ABS) parasites or stage V gametocytes (Gam). Anti-Pfs16 antibodies were used to validate that Pfs16 was expressed in gametocytes, but not ABS. Lysate of mixed ABS and stage I-III gametocytes was subsequently used to measure thermal stabilisation of Pfs16 when treated with (B) DMSO, (C) **DDD01035881**, (D) **(-)-DDD01028076** or (E) **(+)-DDD01028076** and thermally challenged from 61.9-100 °C. Pfg377 thermal stabilisation under (F) DMSO or (G) **DDD01035881** treatment was measured from 71.5-100 °C. Western blots were analysed by densitometry to measure band intensity and derive Pfs16 and Pfg377 melting curves.

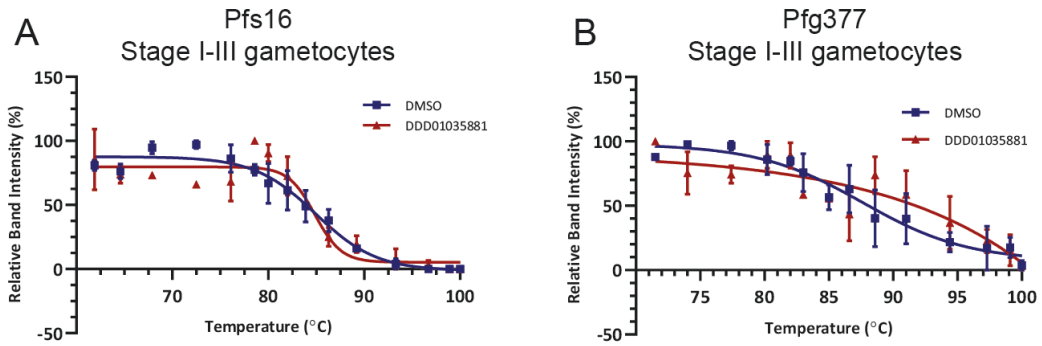


Figure 5.5: CETSA melting curves of Pfs16 and Pfg377 using *P. falciparum* stage I-III gametocyte lysate. Melting curves of (A) Pfs16 and (B) Pfg377 were generated by densitometric analysis of western blots, with representative blots depicted in Figures 5.4B, C, F and G. Relative band intensities were normalised to the highest and lowest band values. Melting curves were generated by plotting average band intensities and SEM, derived from three biological replicates. No statistically significant difference between DMSO and DDD01035881-treated lysate was measured at any temperature with either Pfs16 or Pfg377 when performing unpaired two-tailed *t*-tests.

dated that Pfs16 was not expressed in ABS, as determined by western blot-based labelling of lysate derived from asexual parasites (Figure 5.4A). Validating the gametocyte-specific expression of Pfs16 assured any thermal stabilisation of Pfs16 measured by CETSA would not amount from residual ABS within cell lysate. Hence, this enabled the generation of stage I-III gametocyte lysate for CETSA without the need to purify cultures to remove residual asexual parasites, which can be experimentally complex. CETSA was subsequently performed on lysate derived from *in vitro* culture containing a mix of all asexual stages and stages I-III gametocytes. Following thermal challenge, aggregated protein was removed and the remaining soluble protein was separated and detected by gel electrophoresis and western blot. Western blots were then labelled using antibodies specific to Pfs16 (Moelans, 1995) and Pfg377 (Ishino et al., 2020), with examples of full blots in Figure 5.4B-E.

Densitometric analysis of Pfs16 and Pfg377 labelled-western blots enabled the generation of melting curves for both proteins (Figure 5.5). Interestingly, Pfs16 thermal stabilisation was markedly higher in stage I-III gametocytes (Figure 5.5A) relative to stage V gametocytes (Figure 4.8). The discrepancy in thermal stability is a probable result of post-translational modification of Pfs16, varying between

gametocyte stages. Neither Pfs16 nor Pfg377 were thermally stabilised in the presence of **DDD01035881** relative to DMSO controls, with no shift in the melting curves or significant difference in relative band intensity at any given temperature (Figure 5.5). Additionally, Pfs16 melting curves under **(-)-DDD01028076** and **(+)-DDD01028076** treatment were generated and no significant difference in band intensity was measured with either compound, at any temperature (Figure 5.6).

Although no notable shift in the Pfs16 melting curve or final temperature of aggregation was measured with N-4HCS treatment, observation of the resulting western blots suggests stabilisation of Pfs16 commenced at a lower temperature in DMSO compared to N-4HCS-treated samples (Figure 5.4B-E). It could be hypothesised that Pfs16 may in fact be bound by N-4HCS compounds in early gametocytes, but not arising in a phenotypic impact in these stages. Further validation by structural analysis of N-4HCS-bound Pfs16 or identification of the specific residues bound by the compounds may shed light on this inconclusive result.

These findings suggested Pfg377 was not bound and stabilised by N-4HCS compounds during early gametocyte development. Given Pfg377 was found to not interact with N-4HCS compounds in target validation experiments (Chapter 4), this finding was consistent with previous observations. Combined analysis conclusively confirm that the binding of N-4HCS compounds to Pfs16 does not result in inhibition of sexual conversion or early gametocyte development, though further analysis of the binding characteristics at this stage is warranted.

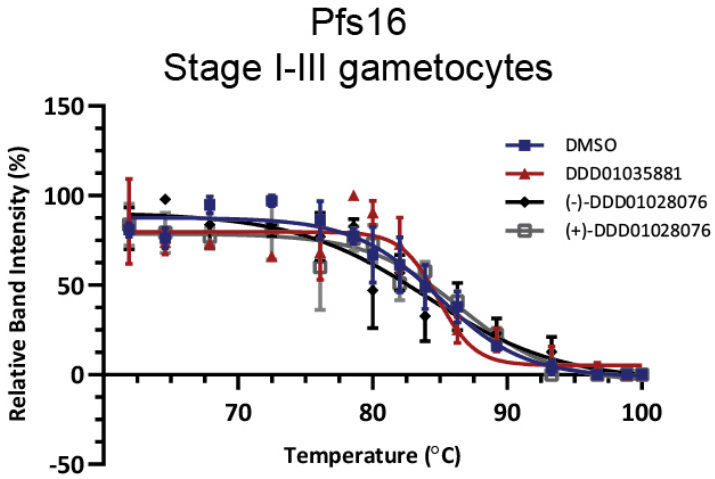


Figure 5.6: CETSA melting curves of N-4HCS-treated Pfs16. Melting curves of Pfs16 using lysate derived from *P. falciparum* stage I-III gametocytes treated with DMSO, **DDD01035881**, **(-)-DDD01028076** or **(+)-DDD01028076**. Curves were generated by densitometric analysis of western blots (representative blots in Figures 5.4B-E), from which relative band intensities were measured and normalised to the highest and lowest values. Points represent average band intensities and SEM of three biological replicates. Unpaired two-tailed *t*-tests were performed between DMSO and N-4HCS relative band intensities, finding no statistical significance with any compound at any temperature.

5.2.2 N-4HCS phenotype during microgametogenesis

Elucidating that N-4HCS compounds specifically inhibit mature microgametocyte viability, it was next sought to define the cellular phenotype of **DDD01035881** and N-4HCS analogues during microgametogenesis, utilising microscopy and flow cytometry.

5.2.2.1 The DDD01035881 activity window is consistent with Pfs16 function

Evidence of potent N-4HCS activity in both the Dual Gamete Formation Assay (DGFA) carry-over and add-in formats revealed that the compounds inhibit microgametogenesis without requiring any prior incubation with gametocyte culture (Delves et al., 2018). It could hence be hypothesised that N-4HCS activity may be sustained when treating gametocytes beyond activation of gametogenesis. To explore this hypothesis, we sought to define the activity window and reversibility of N-4HCS parent compound **DDD01035881**, using phase contrast microscopy.

By experimentally emulating the conditions of the mosquito midgut, using a xanthurenic acid-containing medium maintained at a low temperature and high pH relative to parasite culture, stage V *P. falciparum* NF54-strain gametocytes were activated. Gametocytes were activated in the absence of N-4HCS treatment and **DDD01035881** was subsequently added in time increments (0, 0.5, 1, 2, 4, 6, 8, 10, 15 and 25 minutes post-activation) up the point of exflagellation, the process of microgamete emergence. Phase contrast microscopy was then used to quantify the rate of exflagellation of samples at 25 minutes post-activation. Exflagellation rates were calculated relative to DMSO controls, and it was found that **DDD01035881** potently inhibited exflagellation and retained its inhibitory activity up to six minutes post-activation (Figure 5.7A). A statistically significant difference in exflagellation rate was observed between DMSO and **DDD01035881**-treated samples within this active window. Interestingly, the PVM, within which Pfs16 resides in stage V gametocytes, is known to rupture during parasite egress, which occurs from four-to-six minutes post-activation (Andreadaki et al., 2018). Hence, the six-minute microgametogenesis activity window of **DDD01035881** coincides with the presence of Pfs16

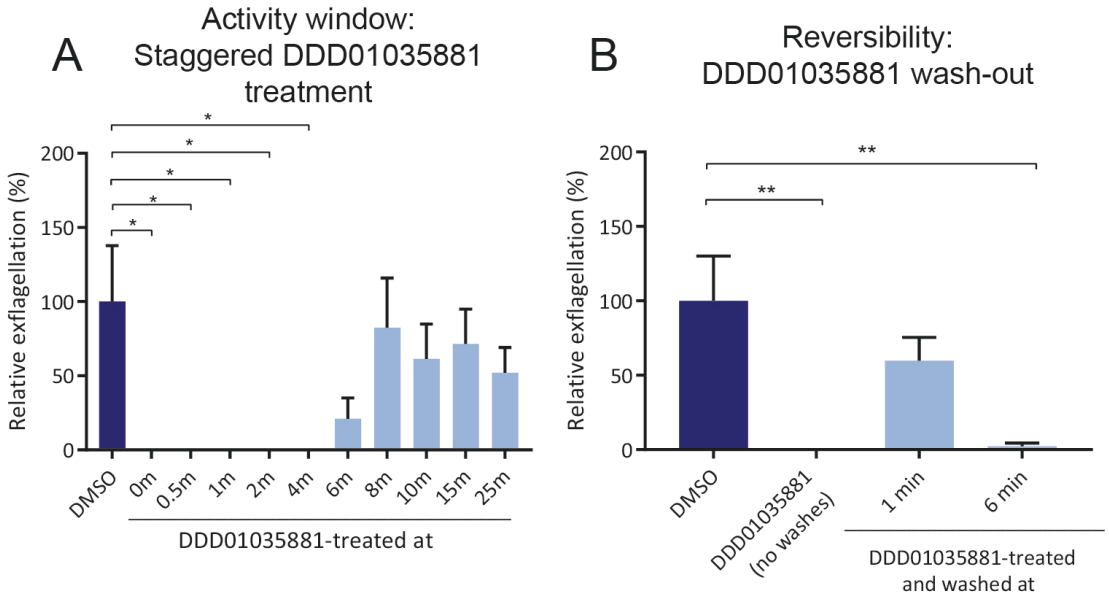


Figure 5.7: **DDD01035881** activity window and reversibility during microgametogenesis. *P. falciparum* NF54-strain gametocyte exflagellation rates were quantified relative to DMSO controls when (A) activated in the absence of compound and treated with 5 μM **DDD01035881** at the stated timepoints or (B) pre-treated with DMSO or 5 μM **DDD01035881**, activated and washed at the stated timepoints, with the exception of the positive control (**DDD01035881** treated without washing). Exflagellation was then quantified at 25 minutes post-activation and rates are depicted as average values derived from five to six biological replicates. Error bars represent the SEM and an unpaired two-tailed t-test was performed to measure statistical significance (denoted as * ($p < 0.05$) and ** ($p < 0.01$)).

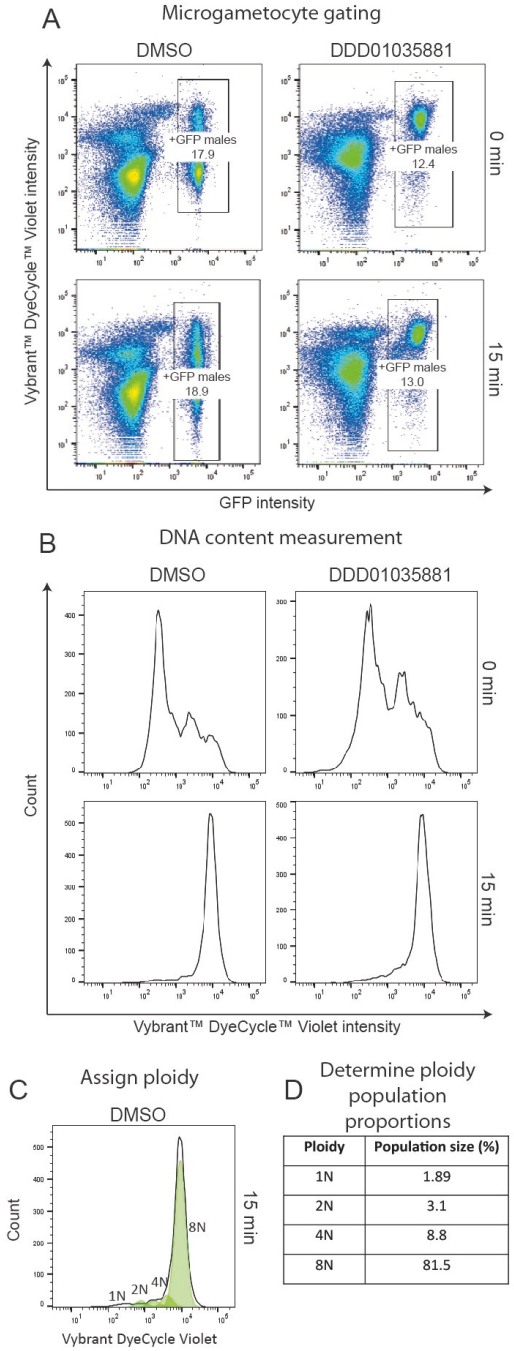
in gametocytes and activity is lost beyond expulsion of the PVM and protein. The consistency of the activity window of **DDD01035881** with Pfs16 function both provides further validation of the protein as the true cellular target of N-4HCS compounds and provides insights into the specific mode of action.

We next sought to determine the reversibility of **DDD01035881** inhibition during its six-minute activity window. Stage V *P. falciparum* gametocytes were activated in the presence of **DDD01035881** and subsequently washed to remove **DDD01035881** at one and six-minutes post-activation. Exflagellation was counted at 25 minutes post-activation and the rates at which samples exflagellated were calculated relative to DMSO controls. **DDD01035881** removal at one-minute post-activation was found to restore exflagellation and hence suggested that compound activity was reversible during its activity window (Figure 5.7B). In contrast, inhibition of exflagellation was retained when removing **DDD01035881** at six-minutes post-activation, with a significant reduction in exflagellation compared to DMSO controls. As **DDD01035881** lost activity at this point (Figure 5.7A), this finding was consistent with the N-4HCS activity window and Pfs16 function. Observations made here suggested that **DDD01035881** binds reversibly to Pfs16 prior to its expulsion during microgametogenesis, with binding resulting in a downstream inhibition of microgamete emergence.

5.2.2.2 Microgametocyte DNA replication is not inhibited by N-4HCS treatment

Microgametogenesis involves multiple cellular transformations in a short period of time (10-15 minutes), including three rounds of DNA replication in which the haploid parasite genome is replicated to an octoploid genome. **DDD01035881** was found to rapidly inhibit microgametogenesis within a six-minute activity window, during which gametocyte genome replication occurs. Therefore, we next sought to elucidate the impact of **DDD01035881** on gametocyte ploidy during microgametogenesis.

To measure microgametocyte ploidy during gametogenesis, an established flow cytometry protocol was performed here (Fang et al., 2017). A transgenic *P. falciparum* line, *Pf*DynGFP/*P47*mCherry, with GFP-expressing male and mCherry-



Ploidy	Population size (%)
1N	1.89
2N	3.1
4N	8.8
8N	81.5

Figure 5.8: Gating strategy to measure ploidy of *Pf*DynGFP/*P47*mCherry microgametocytes. Ploidy of DMSO or **DDD01035881**-treated microgametocytes at 0 and 15 minutes post-activation was measured by flow cytometry, using Vybrant™ DyeCycle™ Violet to stain DNA. (A) Male *Pf*DynGFP/*P47*mCherry gametocytes were gated as the GFP-positive population. (B) Histograms of Vybrant™ DyeCycle™ Violet intensity of gated males were generated. (C) To further gate male gametocytes into 1N, 2N, 4N or 8N populations, the FlowJo proliferation model was applied and (D) relative populations (%) were quantified.

expressing female gametocytes was generously donated to us for the purpose of this study (Lasonder et al., 2016). Dr. Edwin Lasonder and colleagues described generation of the double transgenic line (Lasonder et al., 2016), first producing the male-specific *PfDyn*GFP line by stable integration of the pDynGFP construct into *P. falciparum* NF54 parasites, with *gfp* under control of the promoter region of the dynein heavy chain protein gene. The *PfDyn*GFP line was subsequently transfected with a pPFCENv2-*PfP47*mCherry construct, with mCherry under control of the *PfP47* promotor region, generating the GFP-male and mCherry-female expressing line (Fang et al., 2017).

Donated transgenic parasites were cultured to stage V gametocyte maturity and stained with Vybrant™ DyeCycle™ Violet, a dye used for live-cell quantification of DNA content. Vybrant™ DyeCycle™ Violet is cell permeable and binds to double-stranded DNA, emitting a fluorescent signal which is proportional to the mass of DNA and hence permited ploidy quantification by flow cytometry. Microgametocyte ploidy was measured at 0 and 15 minutes post-activation of gametogenesis, under both DMSO and **DDD01035881** treatment to measure the impact of **DDD01035881** on DNA replication. Measured by flow cytometry, microgametocytes were gated as the double-positive GFP and Vybrant™ DyeCycle™ Violet population (Figure 5.8). Discrete microgametocyte populations with 1N, 2N, 4N and 8N genomes were then measured and compared at 0 and 15 minutes post-activation of gametogenesis (Figure 5.8).

Under DMSO treatment, most stage V microgametocytes (0 minutes relative to activation of gametogenesis) were found to have a 1N genome, as DNA replication was yet to commence. Microgametocyte populations with 2N, 4N and 8N genomes were also measured at this timepoint, though these populations were considerably less abundant (Figure 5.9). As DNA replication occurs following activation, the 2N, 4N and 8N populations were likely present due to selective gene amplification (Janse et al., 1988) or premature activation of gametogenesis within these samples. A clear difference in the ploidy of microgametocyte populations was measured at 15 minutes post-activation, at which point three rounds of DNA replication were expected to have occurred. Microgametocytes with an 8N genome were most abundant

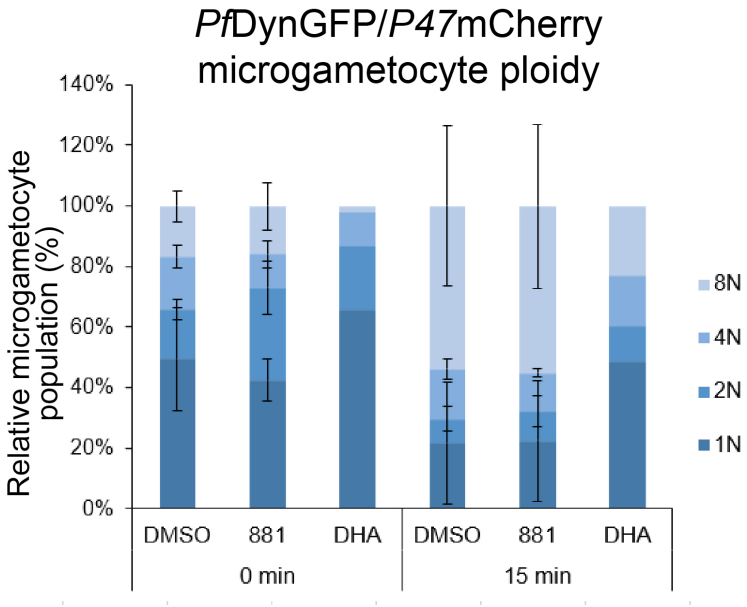


Figure 5.9: *Pf*DynGFP/*P47*mCherry microgametocyte ploidy under drug treatment. The relative Vybrant™ DyeCycle™ Violet-stained DNA content of *Pf*DynGFP/*P47*mCherry microgametocytes at 0 and 15 minutes post-activation of microgametogenesis, treated with DMSO, **DDD01035881** (denoted as 881) or artemisinin-derivative DHA. Ploidy (1N, 2N, 4N or 8N) was measured by flow cytometry, as described with DMSO and **DDD01035881** examples in Figure 5.8. Error bars of DMSO and **DDD01035881** (881) samples depict the SEM of three biological replicates. N = 1 samples were obtained with DHA treatment as a proof-of-concept positive control, due to time constraints.

in DMSO-treated samples at 15 minutes, signifying three rounds of DNA replication (Figure 5.9). Relatively smaller gametocyte populations with a 1N, 2N and 4N genome were also measured at 15 minutes post-activation (Figure 5.9). As a remarkably complex process, microgametogenesis is prone to error (Sinden et al., 2010) and the presence of populations without an 8N genome were expected to arise due to failed activation or DNA replication.

Interestingly, **DDD01035881**-treated microgametocyte populations were not significantly different in their distribution compared to DMSO controls. At 0 minutes post-activation, **DDD01035881**-treated microgametocytes with a 1N genome were most abundant, whereas the 8N population was most abundant at 15 minutes (Figure 5.9). The artemisinin derivative dihydroartemisinin (DHA), which is known to block exflagellation (Leba et al., 2015), was used as positive control to validate this finding. Under DHA treatment at 15 minutes post-activation, microgametocytes with a 1N genome remained the most abundant of populations (Figure 5.9) and thus suggested DHA blocks DNA replication. In contrast, **DDD01035881** activity appeared to be independent of DNA replication. Binding of **DDD01035881** to Pfs16 thus did not result in a downstream defect to DNA replication during microgametogenesis. Should the binding interaction between **DDD01035881** and Pfs16 be responsible for the potent block to microgametogenesis observed *in vitro*, this finding suggested that Pfs16 does not play a role in replication.

5.2.2.3 DDD01035881 cellular phenotype

As **DDD01035881** activity has been specifically associated with microgametogenesis, independent of DNA replication or gametocytogenesis, the precise cellular phenotype was next elucidated. Using traditional immunofluorescence and EM techniques, the specific structural changes to microgametocytes under **DDD01035881** were observed.

5.2.2.4 Microgametogenesis

To assess perturbances to microgametogenesis in the presence of **DDD01035881**, we initially sought to resolve the cellular processes occurring during microgameto-

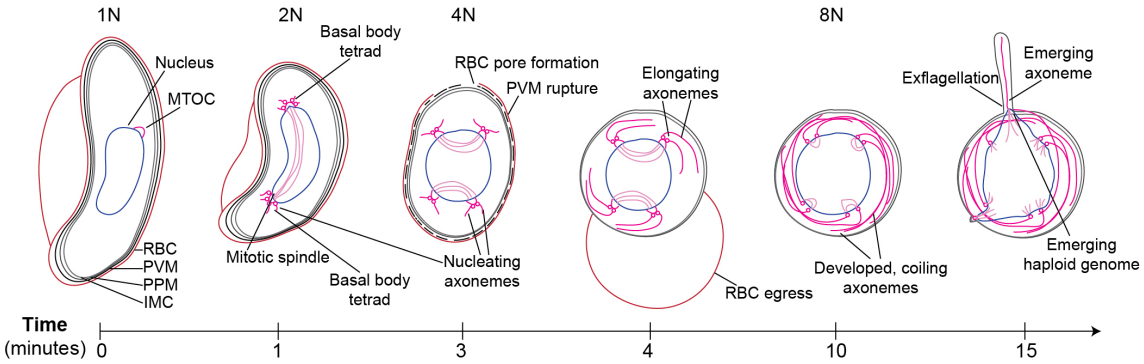


Figure 5.10: *P. falciparum* microgametogenesis. Schematic diagram depicting the various morphological transformations occurring as eight haploid microgametes form from a single microgametocyte in only 15 minutes. Prior to activation (0 minutes), microgametocytes are falciform in morphology before rounding-up, reaching maximal circularity between four to six minutes post activation. At 0 minutes, microgametocytes have a four-layer membrane (comprised of the red blood cell (RBC) membrane, parasitophorous vacuole membrane (PVM), parasitophorous plasma membrane (PPM) and inner membrane complex (IMC)), from which parasites egress by vesiculation of the PVM and emergence from the host RBC at around six minutes post-activation. A single microtubule organising centre (MTOC) transforms to two tetrads of basal bodies, the sites from which axonemes nucleate, elongate and coil around the parasite until emerging during exflagellation at 15 minutes. Three rounds of DNA replication transform the haploid (1N) genome to octoploid (8N), with each genome replication alternating with a round of endomitotic division.

genesis without drug treatment, using microscopy. In just 15-20 minutes, single microgametocytes are transformed to eight motile haploid microgametes upon encountering an environmental change in the mosquito midgut. Host erythrocyte egress, cytoskeletal rearrangement and DNA replication are all hallmarks of microgametogenesis and are summarised in Figure 5.10.

As outlined in detail in Chapter 1.2.3.9, prior to gametogenesis activation a single microtubule organising centre (MTOC) is found in close proximity to a microgametocyte nuclear pore and rapidly transforms to two orthogonal tetrads of basal bodies when activated. Axonemes nucleate and elongate from basal bodies, eventually coiling around the microgametocyte cell body until poised for emergence as microgametes. Simultaneously to these cytoskeletal transformations, the microgametocyte genome replicates from haploid to octoploid over three rounds of replication. DNA replication alternates with three rounds of endomitosis, with basal

bodies segregating at each endomitotic division. Close alignment of basal bodies to the nucleus enables each microgamete to emerge at ∼15 minutes post-activation in the process of exflagellation, carrying a haploid genome along with its developed axoneme. A concurrent 'inside-out' mechanism of host erythrocyte egress occurs in the early stages of microgametogenesis, which involves the vesiculation and rupture of the PVM prior to parasite expulsion from an erythrocyte pore (Andreadaki et al., 2018). Using fixed DMSO-treated stage V gametocytes, both widefield fluorescence and electron microscopy (EM) were used to define the structural characteristics of developing microgametes.

Immunofluorescence time course of microgametogenesis

P. falciparum NF54-strain stage V gametocytes were activated and fixed at various time-points across microgametogenesis to obtain a time course of microgamete development. Immunofluorescence labelling of fixed parasites and visualisation by widefield fluorescence microscopy was performed to define specific traits of developing microgametes, with a focus on the cytoskeleton, DNA and host erythrocyte (Figure 5.11). The microgametocyte cytoskeleton was labelled using antibodies specific to α-tubulin II, revealing a transformation from falciform at 0 minutes to rounded by four minutes (Figure 5.11). Additionally, α-tubulin II staining showed the formation of a mitotic spindle spanning the length of the parasite body at two minutes, with basal body tetrads forming at the extreme ends of the spindle (Figure 5.11). Axonemes were shown to nucleate from basal bodies at four minutes, lengthening by eight minutes when they coiled around the cell body. Host erythrocytes were visualised using antibodies specific to glycophorin A, a sialoglycoprotein of the erythrocyte membrane. Egress was shown to occur between four and eight minutes post-activation. DAPI staining revealed an increase in DNA content from 0 minutes onwards, peaking at ten minutes, indicating three rounds of replication were complete by this stage. Although it is well established that exflagellation commences at ∼15 minutes-post activation, parasites were fixed at 25 minutes post-activation to capture full microgamete emergence with α-tubulin II staining (Figure 5.11).

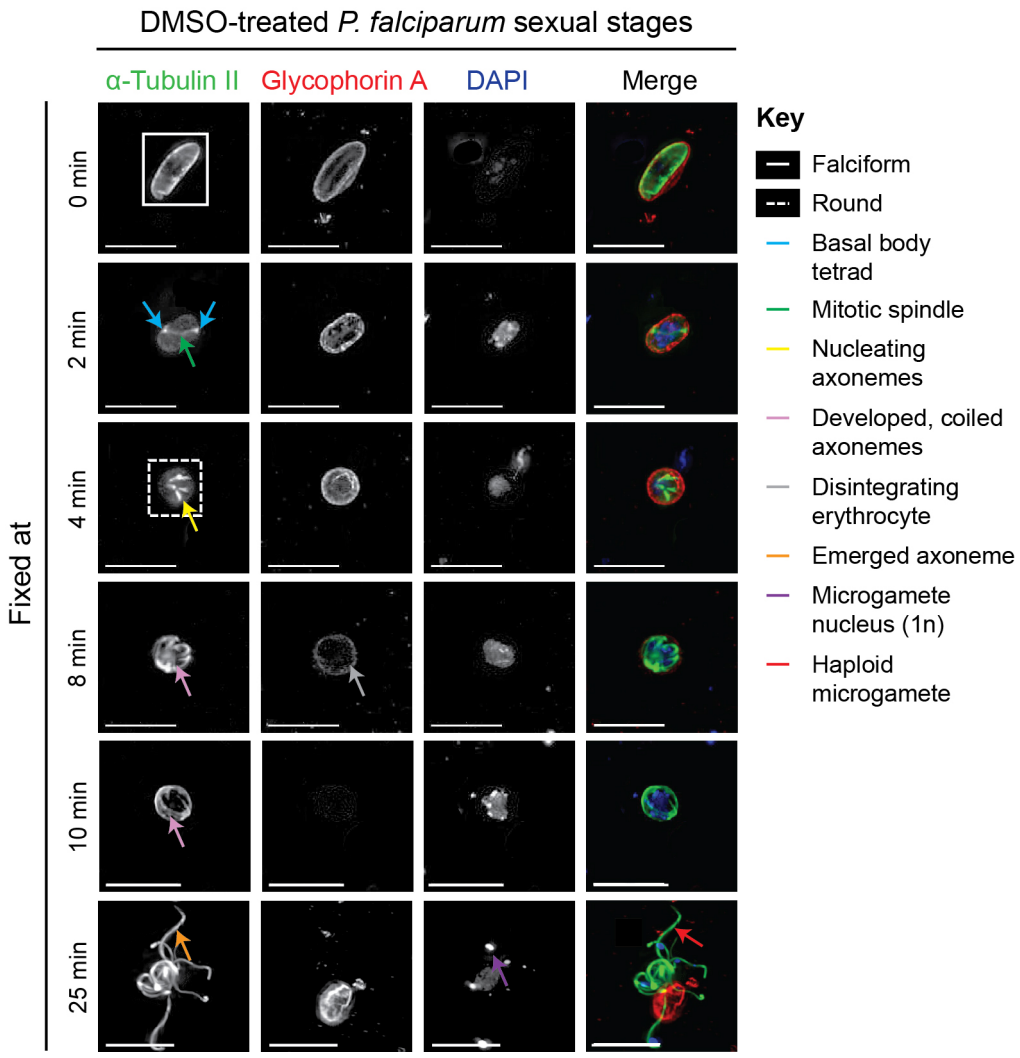


Figure 5.11: Immunofluorescence time-course of *P. falciparum* microgametogenesis. *P. falciparum* NF54-strain gametocytes were treated with DMSO to enable comparison to N-4HCS treated parasites, activated to induce microgametogenesis and fixed at the stated time-points. Individual channels of the α-tubulin II-labelled cytoskeleton (green), glycophorin A-labelled host erythrocyte (red) and DAPI-stained DNA (blue) are depicted alongside merged channels. Significant cellular transformations are labelled with a key. Scale bars = 10 μm.

Microgametogenesis at an ultrastructural level

EM has been pivotal to obtaining ultrastructural insights into microgametogenesis (Billker et al., 2002; Sinden et al., 1978; Sinden, Canning, and Spain, 1976) and here we sought to determine the finer details of **DDD01035881**-induced perturbances to microgamete formation using this technique. To first establish a baseline of microgametogenesis development without **DDD01035881**, DMSO-treated stage V *P. falciparum* NF54-strain gametocytes were activated and fixed at 25 minutes post-activation before staining and imaging by EM (Figure 5.12).

DMSO-treated microgametocytes were observed in preparation for microgamete emergence (exflagellation) at 25 minutes post-activation. The characteristic '9+2' organisation of microtubules was visualised (Figure 5.12A), as fully developed axonemes formed and coiled around the microgametocyte nucleus (Figure 5.12C). Coordination of the notably complex process of microgametogenesis can give rise to errors in development (Sinden et al., 2010) and this was observed as instances of incorrect microtubule orientation (Figure 5.12B). Microgametes were poised for exflagellation, as developed axonemes and the parasite nucleus were seen in close alignment and oriented at the microgametocyte cell periphery (Figure 5.12D). Located at the parasite nucleus centriolar plaque, the basal body and associated sphere and granule were observed to position towards the plasmalemma (Figure 5.12D). Intranuclear spindles and condensed chromatin were visualised within the nucleus alongside these structures (Figure 5.12D). These cellular traits have been extensively described (Sinden, Canning, and Spain, 1976) and combined, enable axonemes to emerge though the perikinetosomal basket with a haploid genome as microgametes.

As well as structures required for exflagellation, EM revealed the ultrastructure of other cellular traits seen specifically in *Plasmodium* gametocytes and parasites. For example, a flattened extension of the host erythrocyte referred to as the Laveran's bib was visualised (Figure 5.13A). The Laveran's bib is known to form as the region of the host cell not occupied by the parasite and hosts exported proteins (Ingmundson et al., 2014). Additionally, membranous whorls referred to as Garnham bodies were observed with varying morphologies (Figure 5.13B-C). Garnham bodies form in gametocyte-infected host erythrocytes and are thought to protect parasites

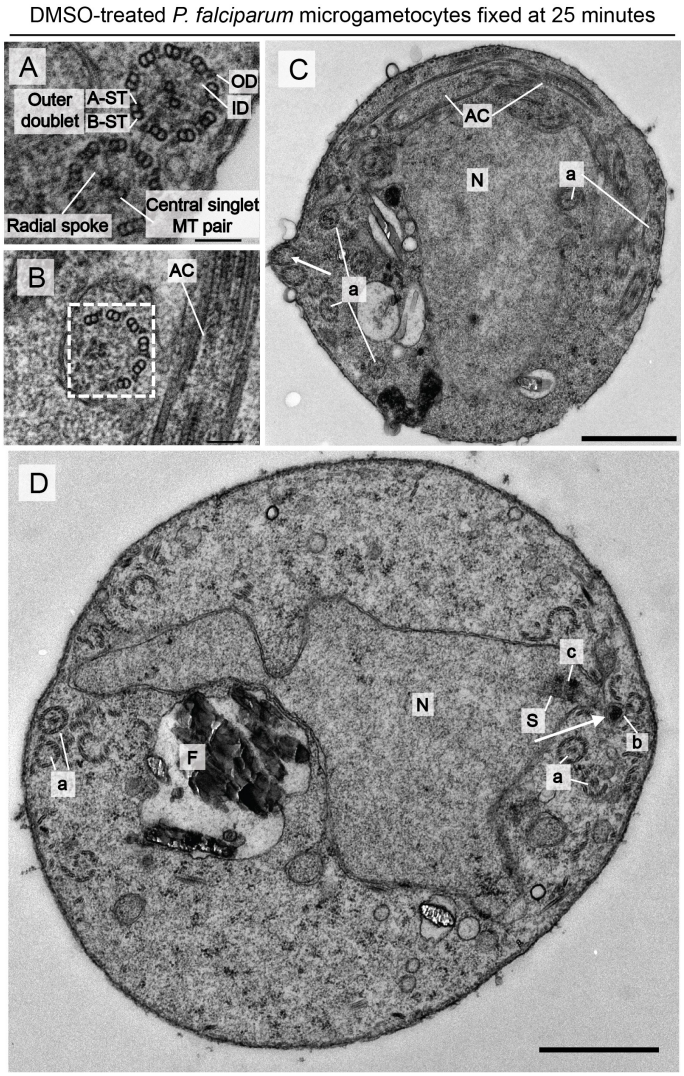


Figure 5.12: *P. falciparum* microgametogenesis imaged by electron microscopy. *P. falciparum* gametocytes were activated, fixed at 25 minutes post-activation and imaged by EM. (A) Axonemes adopt the '9+2' microtubule (MT) arrangement, in which radial spokes space the outer doublets, comprised of A and B subtubules (A-ST and B-ST), from the inner central singlet MT pair. Outer dynein (OD) and inner dynein (ID) arms are visible. Scale bar = 100nm. (B) Microgametogenesis is prone to error, as depicted by the incomplete '9+2' MT arrangement, alongside an axoneme cross-section (AC). Scale bar = 100nm. (C) Axonemes (a) at the microgametocyte cell periphery coil around the nucleus (N), as seen by the numerous axoneme cross sections. Scale bar = 1 μm. (D) A microgamete in preparation for exflagellation, as axonemes align towards the parasite plasmalemma to emerge through the perikinetosomal basket (b). A basal body and sphere and granule (arrow) closely associate with the nucleus (N). Intranuclear spindles (S) and condensed chromatin (c) are visible within the nucleus, ready for emerging microgametes to carry a haploid genome through the cell. A food vacuole (F) is positioned by the nucelus. Scale bar = 1 μm.

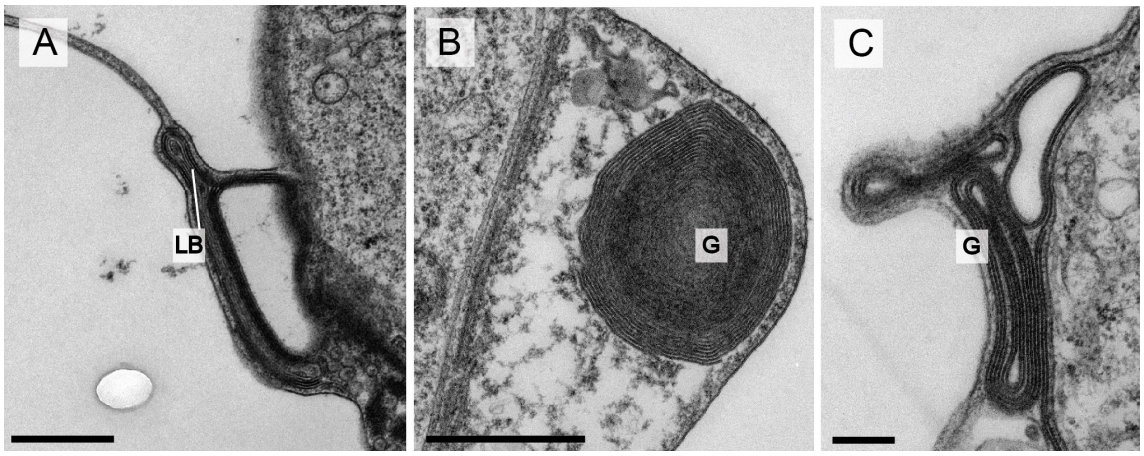


Figure 5.13: Ultrastructure of *P. falciparum* gametocyte cellular traits. Characteristic traits of intraerythrocytic gametocytes including the (A) Laveran's bib (LB) and (B-C) Garnham bodies (G). Scale bars: A = 500nm, B = 200nm and C = 500nm.

from ferriprotoporphyrin IX (FP) toxicity by storing haemozoin in these structures (Orjih, 2012).

5.2.2.5 DDD01035881 cellular phenotype during microgametogenesis

Combined observations made by widefield fluorescence and electron microscopy were used to establish a baseline of microgametogenesis development, enabling the identification of perturbances under **DDD01035881** treatment.

DDD01035881 impact to the cytoskeleton, egress and DNA replication

As **DDD01035881** was found to retain activity in a six-minute window following activation of gametogenesis, it was hypothesised that treatment at varied time-points throughout this window may result in varied cellular phenotypes. To explore this hypothesis, *P. falciparum* NF54-strain stage V gametocytes were activated in the absence of **DDD01035881** and then treated with the compound at differing time-points, relative to activation. Activated and **DDD01035881**-treated parasites were fixed at 25 minutes post-activation, the point at which microgametes fully emerge in DMSO-control conditions. Immunofluorescence labelling and staining of the parasite cytoskeleton, parasite DNA and host erythrocyte were performed prior to imaging by widefield fluorescence microscopy (Figure 5.14).

DMSO-control parasites were seen to exflagellate at 25 minutes post-activation, whereas **DDD01035881**-induced perturbances to microgametogenesis were observed up to five minutes post-activation. Morphological phenotypes varied according to the time-point at which microgametocytes were treated with **DDD01035881**, relative to activation. The failure to exflagellate with **DDD01035881** treatment resulted in three distinct phenotypes, observed in parasites treated in time-points between i) 0 and 0.5, ii) one and two or iii) four and five minutes post-activation (Figure 5.14).

DDD01035881 treatment from 0-0.5 minutes blocked cytoskeletal rearrangement by preventing mitotic spindle formation and axoneme nucleation and elongation, as made evident with immunofluorescence labelling of α-tubulin II. Parasites succeeded in morphologically transforming from falciform to rounded with treatment at these time-points. The egress phenotype was mixed, with some parasites remaining intraerythrocytic and some succeeding in egress, as evident with glycophorin A staining (Figure 5.14). DAPI staining of treated parasites revealed a similar DNA content to DMSO-control parasites (Figure 5.14), suggesting replication was not impeded, consistent with previous findings (Figure 5.9).

In contrast, **DDD01035881** treatment from one-to-two minutes post-activation resulted in the parasite cytoskeleton adopting a 'figure-of-eight' morphology (Figure 5.14). No axonemes or mitotic spindles were apparent with treatment at these time-points and the egress phenotype was mixed. Erythrocyte vesiculation was observed in both instances of successful and failed egress. Remnants of erythrocytic vesicles remained in close association with the parasite in the case of egress, which has previously been described in wild-type parasites (Andreadaki et al., 2018). **DDD01035881**-treatment from one-to-two minutes did not impact DNA replication, and DAPI-stained DNA was observed in one or both sides of the 'figure-of-eight' (Figure 5.14).

Phenotypes of microgametocytes treated with **DDD01035881** from four-to-five minutes post-activation resembled the one-to-two minute phenotype, differing in some traits. Although the 'figure-of-eight' cytoskeletal structure was additionally observed in these time-points, the phenotype differed in the formation of truncated

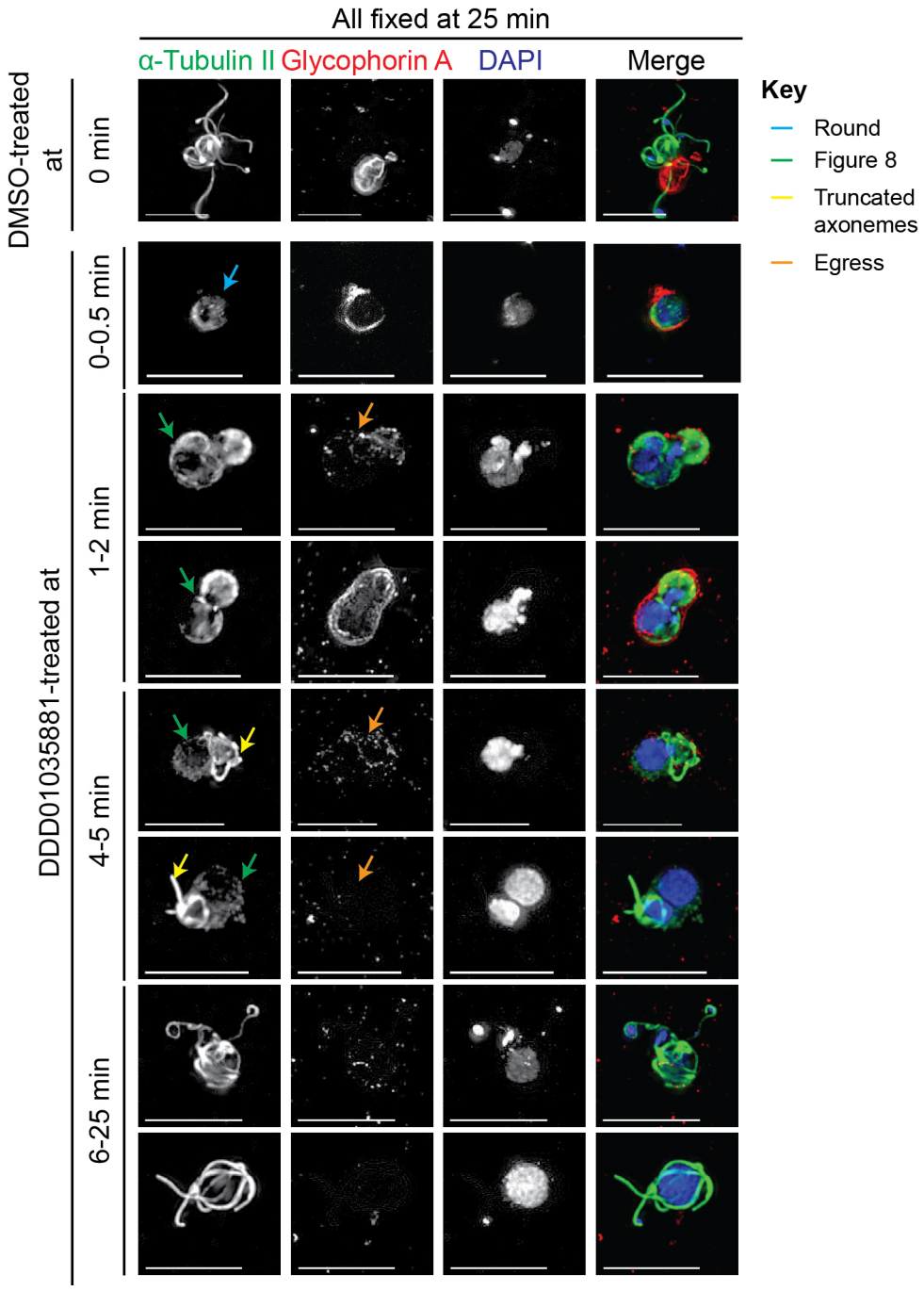


Figure 5.14: **DDD01035881** phenotype during microgametogenesis by immunofluorescence. *P. falciparum* NF54-strain gametocytes were activated, treated with DMSO or **DDD01035881** at the stated timepoints and fixed at 25 minutes post-activation. Individual channels of the α-tubulin II-labelled cytoskeleton (green), glycophorin A-labelled host erythrocyte (red) and DAPI-stained DNA (blue) are depicted alongside merged channels. Notable phenotypic traits are denoted with a key. Scale bars = 10 μm.

axonemes from one end of the parasite (Figure 5.14). Interestingly, the truncated axonemes formed from the side of the 'figure-of-eight' which was both smaller in size and displayed a greater level of α-tubulin II staining. Egress and erythrocyte vesiculation was observed in parasites which were treated at four-to-five minutes (Figure 5.14). DNA replication was not inhibited with **DDD01035881**-treatment at these time-points (Figure 5.14).

Treating activated microgametocytes with **DDD01035881** beyond six minutes post-activation failed to inhibit microgametogenesis, with exflagellation occurring as per the DMSO controls (Figure 5.14). Though exflagellation was observed with treatment beyond six minutes, the onwards viability of resulting microgametes was not determined. Combined, these observations of the **DDD01035881** cellular phenotype suggested that the mode of action by which N-4HCS compounds inhibited microgametogenesis was associated with cytoskeletal rearrangement. Having defined an interaction between **DDD01035881** and Pfs16, these findings correlated Pfs16 with a likely function in the cytoskeletal transformation required for microgamete formation.

DDD01035881 effect to Pfs16 expression during microgametogenesis

Using immunofluorescence labelling coupled to widefield fluorescence microscopy, we next aimed to elucidate the precise impact of **DDD01035881** on Pfs16 distribution during microgametogenesis. Pfs16 is widely utilised as a marker of the gametocyte PVM (Baker et al., 1994), a membrane known to vesiculate prior to erythrocyte disintegration during microgametogenesis (Andreadaki et al., 2018). Using antibodies specific to Pfs16, immunofluorescence image time-courses of Pfs16 distribution during microgametogenesis were compiled. *P. falciparum* NF54-strain stage V gametocytes, treated either with **DDD01035881** or DMSO prior to activation, were fixed at various time-points (Figure 5.15).

In DMSO control parasites, Pfs16 was distributed around the entirety of stage V microgametocytes at 0 minutes relative to activation (Figure 5.15). In preparation for egress, the cellular distribution of Pfs16 was seen to transform by either capping to a single side of the microgametocyte or localising to a concentrated 'pore' at $\sim$5.5

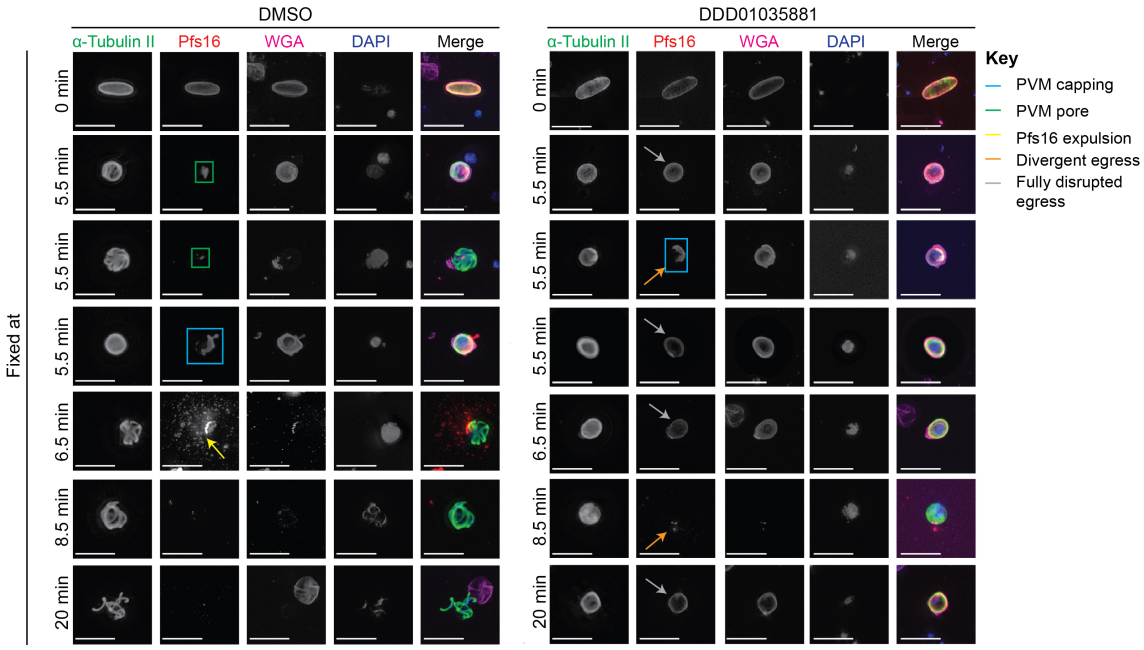


Figure 5.15: **DDD01035881** disruption to Pfs16 and the PVM during microgametogenesis. *P. falciparum* NF54-strain gametocytes were treated with DMSO or **DDD01035881**, activated, fixed at the stated time-points and labelled by immunofluorescence for imaging. Individual channels of the α-tubulin II-labelled cytoskeleton (green), Pfs16 labelling of the PVM (red), WGA-labelled host erythrocyte (far red) and DAPI-stained DNA (blue) are depicted alongside merged channels. Notable phenotypic traits are denoted with a key. Scale bars = 10 μm.

minutes post-activation. This transformation of the PVM and Pfs16 distribution preceded egress from the host erythrocyte, which was labelled with the lectin wheat germ agglutinin (WGA) conjugated to a fluorophore. Following host erythrocyte egress at 6.5 minutes, expulsion of Pfs16-labelled vesicles from a single side of the parasite was observed. Upon full parasite egress from the PVM and erythrocyte at 8.5 minutes, Pfs16 labelling was minimal and vesicles were not found associated with the developing microgametocyte. Pfs16 was not detected on exflagellating microgametes, imaged at 20 minutes post-activation (Figure 5.15). Crucially, we found Pfs16 expression and association with the parasite to occur in the early stages of microgametogenesis, as the protein was expelled from 6.5 minutes (Figure 5.15).

Comparatively to DMSO control parasites, Pfs16 expression was distinctly different in **DDD01035881**-treated microgametocytes during egress (Figure 5.15). PVM distribution, defined by Pfs16 expression, adopted two precise phenotypes with **DDD01035881** treatment; i) divergent or ii) fully disrupted egress. In the divergent egress phenotype, egress was successful but differed from DMSO controls as PVM capping was evident, but Pfs16 vesiculation and expulsion was not detected (Figure 5.15). Many microgametocytes were imaged to have fully egressed from 8.5 minutes post-activation, with no WGA and minimal Pfs16 staining, which we propose resulted from this divergent phenotype. In contrast, parasites adopting the fully disrupted egress phenotype retained full Pfs16 and WGA expression from 0-20 minutes post-activation, as neither the PVM nor the host erythrocyte vesiculated or disintegrated (Figure 5.15).

Observations made here demonstrate that **DDD01035881** binding to Pfs16 directly impacted expulsion of the protein, which corresponds to PVM disintegration, during microgametogenesis.

Ultrastructural DDD01035881 phenotype

To resolve the **DDD01035881** cellular phenotype at an ultrastructural level, microgametocytes pre-treated with compound, activated and fixed at 25 minutes-post-activation were imaged by EM. Dr. Silvia Haase and Dr. Gema Vizcay-Barrena prepared and imaged samples which were treated, fixed and analysed by the author

of this thesis.

DMSO-treated control parasites were observed in preparation for exflagellation at 25 minutes post-activation, as developed axonemes and the parasite nucleus oriented towards the gametocyte plasmalemma (Figure 5.16A). In contrast, **DDD01035881**-treated parasites displayed no axoneme nucleation, which was otherwise observed in DMSO controls as the '9+2' microtubule arrangement (Figure 5.16B). Although immunofluorescence labelling of α-tubulin II enabled us to initially observe the **DDD01035881**-induced impediment to cytoskeletal transformation (Figure 5.14), EM revealed a complete block in axoneme assembly at an ultrastructural level (Figure 5.16B). **DDD01035881** was previously shown not to impact DNA replication (Figure 5.9) and observations by EM showed that treatment additionally disrupted the structural integrity of the microgametocyte nucleus (Figure 5.16B). Similarly, the structure of the food vacuole was compromised by **DDD01035881**. Numerous haemozoin-containing vacuoles were dispersed across the microgametocyte cytosol (Figure 5.16B), which was consistent with published observations of lines with targeted gene disruption of *Pfs16* (Kongkasuriyachai, Fujioka, and Kumar, 2004). Notably, the consistency in these EM findings supported our notion that Pfs16 is targeted and inhibited by N-4HCS compounds such as **DDD01035881**.

EM added further detail to the observation that **DDD01035881** either disrupted the ordinary mechanism of egress during microgametogenesis or blocked it altogether. Whilst full egress under **DDD01035881** treatment can be seen in Figure 5.16B, egress was entirely blocked in Figure 5.16C. The **DDD01035881**-induced failed egress phenotype demonstrated in Figure 5.16C showed the retention of the gametocyte four-layer membrane, comprised of the erythrocyte membrane, PVM, parasite plasma membrane (PPM) and inner membrane complex (IMC). In contrast, only the PPM and IMC remained after full microgametocyte egress in control parasites (Figure 5.16D).

Combined, EM provided insights into the ultrastructure of **DDD01035881**-inhibited microgametocytes, displaying disruptions to axoneme assembly, egress and food vacuole and nucleus structure. Fitting with published observations of *Pfs16* targeted gene disruption (Kongkasuriyachai, Fujioka, and Kumar, 2004), these find-

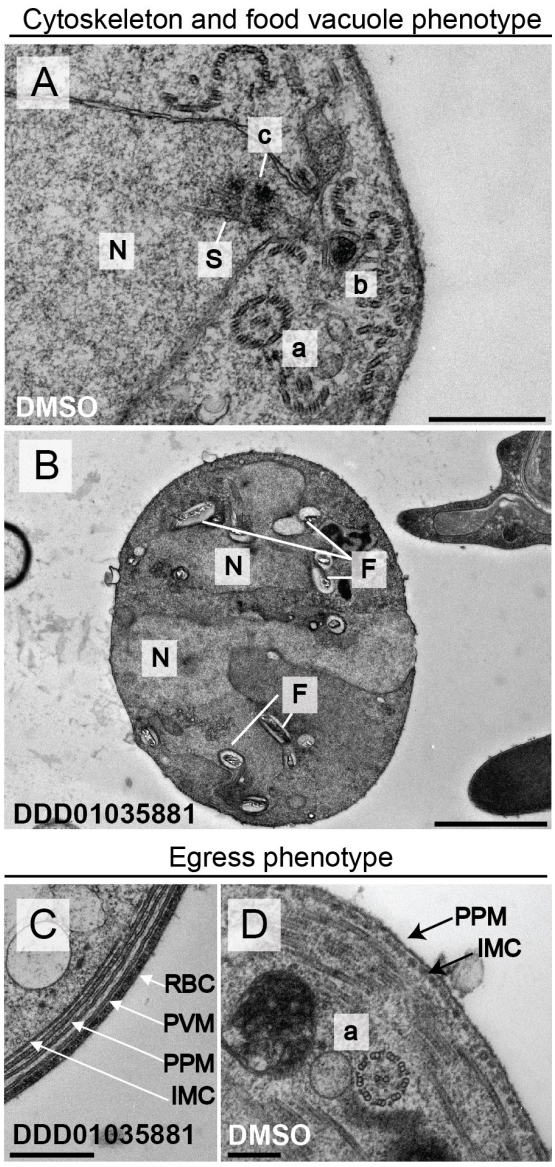


Figure 5.16: Ultrastructural **DDD01035881** phenotype during microgametogenesis. DMSO or **DDD01035881**-treated *P. falciparum* NF54-strain stage V gametocytes were activated, fixed at 25 minutes post-activation and imaged by EM. (A) Under DMSO-treatment, axonemes (a) prepare for emergence through the perikinetosomal basket (b). Condensed chromatin (c) is visible as microgametes prepare to emerge with a haploid genome, carried from the nucleus (N) and driven by intranuclear spindles (S). Scale bar = 500nm. (B) **DDD01035881**-treated microgametocyte which has emerged from the host erythrocyte, displaying compromised nuclear (N) structural integrity and fragmented food vacuoles (F). Scale bar = 2 μm. (C) Characteristic four-layer membrane of an **DDD01035881**-treated microgametocyte which has failed to egress. Red blood cell membrane (RBC), parasitophorous vacuole membrane (PVM), parasite plasma membrane (PPM) and inner membrane complex (IMC). Scale bar = 500nm. (D) DMSO-treated microgametocyte following egress. Scale bar = 200nm.

ings supported Pfs16 as a cellular target of **DDD01035881**. Given the limited knowledge of Pfs16 function, **DDD01035881** is a valuable tool in uncovering new insights into the protein.

5.2.3 Inhibition of microgametogenesis regulators

Gametogenesis is tightly regulated with a signalling cascade, as outlined in Chapter 1.2.3.11. Pfs16 is required for microgametogenesis and **DDD01035881** potently inhibits the process in a six-minute window which coincides with microgametogenesis regulation. Beyond this knowledge, the interplay between Pfs16, **DDD01035881** and microgametogenesis regulators remains elusive. To place Pfs16 and **DDD01035881** inhibition in the context of the signalling cascade, inhibitors of known regulators of microgametogenesis were studied here.

Protein kinase G

Cyclic guanosine monophosphate (cGMP)-dependent protein kinase G (PKG) regulates microgametogenesis by acting upstream of Ca^{2+}. The serine/threonine PKG controls intracellular Ca^{2+} levels by regulating phosphoinositide metabolism (Brochet et al., 2014; Balestra et al., 2021). A series of compounds targeting PKG recently demonstrated activity against merozoite egress and gametocyte transmission (Baker et al., 2017). Of this series, **ML10** was reported as the most potent and as highly specific to PKG, with a nanomolar IC_{50} value (Baker et al., 2017). Here, we treated *P. falciparum* NF54-strain stage V gametocytes with **ML10** to elucidate the cellular phenotype and activity window of the compound.

To determine the window of PKG function during microgametogenesis, gametocytes were activated in the absence of compound and then treated with PKG-inhibitor **ML10** at various time-points up the point of exflagellation. Exflagellation was subsequently quantified at 25 minutes post-activation and upon comparison to DMSO controls, relative rates of exflagellation were calculated. **ML10** significantly blocked exflagellation up to eight minutes post-activation, losing activity at ten minutes (Figure 5.17A). In comparison to DMSO, relative exflagellation was reduced by **ML10** treatment at 15 and 25 minutes post-activation, the timepoints at which

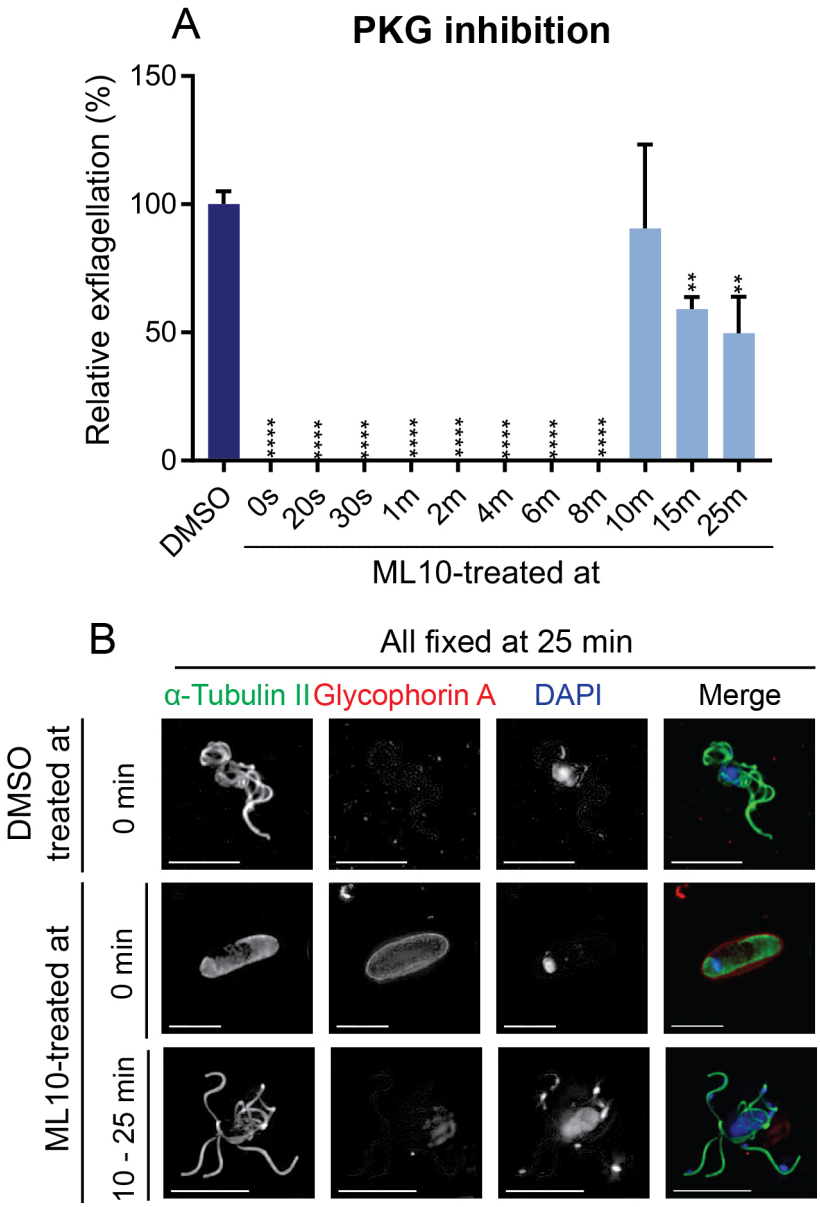


Figure 5.17: PKG inhibition phenotype during *P. falciparum* microgametogenesis. (A) Microgametogenesis activity window of PKG-inhibitor, **ML10**, determined by activation of *P. falciparum* NF54-strain gametocytes in the absence of compound, treatment at the stated timepoints and quantification of exflagellation at 25 minutes-post activation. Exflagellation rates, relative to DMSO controls, are depicted as average values derived from three biological replicates and error bars represent the SEM. Unpaired two-tailed *t*-tests were performed to measure statistical significance (denoted as ** ($p < 0.01$) and **** ($p < 0.0001$)). (B) **ML10** cellular phenotype during microgametogenesis by immunofluorescence. *P. falciparum* gametocytes were activated, treated with DMSO or **ML10** at the stated timepoints and fixed at 25 minutes post-activation. The α-tubulin II-labelled cytoskeleton (green), glycophorin A-labelled host erythrocyte (red) and DAPI-stained DNA (blue) individual channels are shown alongside merged channels. Scale bars = 10 μm.

microgametes emerge (Figure 5.17A). This result suggested that **ML10** either impeded microgamete release from the parasite cell body or reflected the biological error in the process, with exflagellation rates being prone to variation.

Immunofluorescence labelling of parasites treated with **ML10** prior to activation and fixed at 25 minutes post-activation was performed to elucidate the cellular phenotype. Fluorescence microscopy revealed that microgametocytes remained falciform and intraerythrocytic, failed to replicate DNA and did not display mitotic spindle or axoneme assembly when treated with **ML10** (Figure 5.17B). In contrast, exflagellation was observed in DMSO-treated control parasites. The cellular phenotype resembled the morphology of stage V microgametocytes prior to activation, suggesting that all morphological developments during microgametogenesis were blocked by **ML10**. The active window of **ML10** was validated by additionally treating parasites beyond ten minutes post-activation, finding exflagellation to occur as per the DMSO controls (Figure 5.17B).

Sustained activity of **ML10** for eight minutes following activation suggested that PKG-mediated mobilisation of Ca^{2+} is required throughout microgametogenesis, up until the late developmental stages. Beyond eight minutes post-activation of microgametogenesis, DNA replication, egress and the bulk of cytoskeletal rearrangement is complete. Combined observations made by immunofluorescence-labelling of **ML10**-treated microgametocytes and the activity window revealed that PKG plays a crucial role in regulating multiple transformations required of microgametogenesis. PKG-inhibition is markedly divergent from **DDD01035881** activity which exerts inhibition over a six-minute window, with a differing cellular phenotype. This finding confirmed that **DDD01035881** activity is unlikely to target PKG and suggested that function of the probable cellular target, Pfs16, differs from PKG.

Calcium-dependent protein kinase 4

Upon calcium mobilisation, a myristoylated isoform of Ca^{2+}-dependent protein kinase 4 (CDPK4) is activated, enabling the enzyme to regulate multiple processes during microgametogenesis. Labelled as the master regulator of microgametogenesis, CDPK4 plays three crucial roles in i) initiating the first genome replication

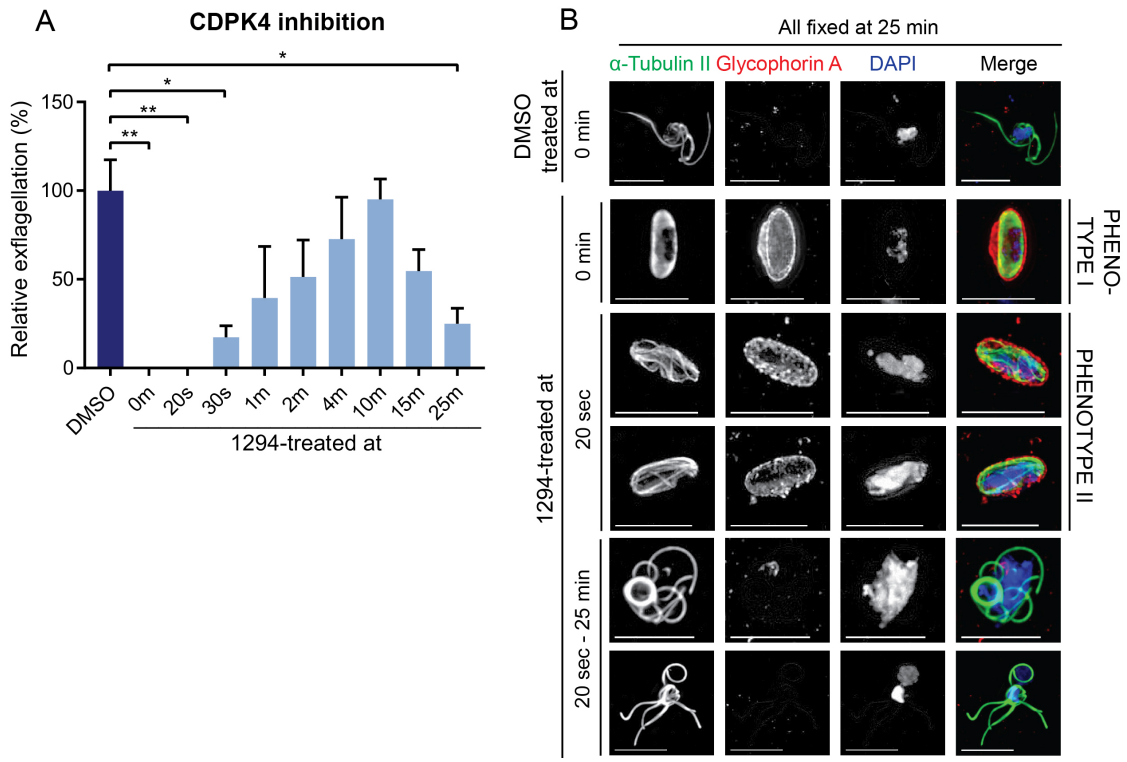


Figure 5.18: CDPK4 inhibition phenotype during *P. falciparum* microgametogenesis. (A) The activity window of CDPK4-inhibitor, **1294**, was determined by activation of *P. falciparum* NF54-strain stage V gametocytes in the absence of compound, followed by **1294**-treatment at the stated timepoints. Exflagellation of samples was then quantified at 25 minutes-post activation, and rates relative to DMSO controls were calculated. Rates are depicted as average values derived from three biological replicates, error bars represent the SEM and significant differences between DMSO and treated samples were measured using an unpaired two-tailed *t*-tests (denoted as * ($p < 0.05$) and ** ($p < 0.01$)). (B) **1294** cellular phenotype by immunofluorescence labelling of treated parasites. *P. falciparum* gametocytes were activated, treated with either **1294** or DMSO at the stated timepoints and fixed at 25 minutes post-activation. α-tubulin II-labelled cytoskeletons (green), glycophorin A-labelled host erythrocytes (red) and DAPI-stained DNA (blue) are depicted as individual channels, alongside merged channels. Scale bars = 10 μm.

upon activation, ii) regulating mitotic spindle assembly and iii) activating microgamete motility, which is performed by a non-myristoylated isoform of CDPK4 (Fang et al., 2017). Potent bumped-kinase inhibitor **1294** was found to selectively inhibit *Plasmodium* CDPK4 over mammalian kinases, by capitalising on a small serine gatekeeper residue in the CDPK4 active site (Ojo et al., 2014). **1294** was shown to block exflagellation (Fang et al., 2017) and here, we aimed to study the compound activity window and cellular phenotype.

P. falciparum NF54-strain stage V gametocytes were activated in the absence of compound and treated with **1294** at various time-points, to calculate relative exflagellation rates at 25 minutes post-activation. A narrow active window of only 20-30 seconds was measured with **1294**, as the compound significantly blocked exflagellation if treating gametocytes at 0 or 20 seconds post-activation (Figure 5.18A). Exflagellation was restored from 30 seconds post-activation, though the difference between DMSO and **1294**-treated gametocyte exflagellation rates remained significant until one minute post-activation (Figure 5.18A). Consistent with published observations that CDPK4 plays an early role in mitotic spindle assembly and initiation of DNA replication (Fang et al., 2017), the narrow activity window suggests these processes are regulated within the first 20 seconds of activation. Also fitting with the published role of CDPK4 in microgamete flagellar motility (Fang et al., 2017), a significant difference in exflagellation rate was measured between DMSO controls and gametocytes treated with **1294** at 25 minutes post-activation (Figure 5.18A).

Precise cellular traits arising from **1294**-treatment were then determined by immunofluorescence labelling of microgametocytes during microgametogenesis. Gametocytes were activated, **1294**-treated at various timepoints, fixed at 25 minutes and stained to assess perturbances to exflagellation. Two distinct phenotypes were found upon **1294** treatment: i) if treated at the onset of gametogenesis (0 minutes post-activation), parasites resembled stage V microgametocyte morphology, failing to round-up, egress, replicate DNA or assemble axonemes or ii) if treated at 20 seconds post-activation, microgametocytes remained falciform and intraerythrocytic, but were able to replicate DNA and assemble axonemes which coiled around the

falciform gametocyte body (Figure 5.18B). Beyond 20 seconds, exflagellation was found to occur as per the DMSO controls.

The narrow 20-second active window and cellular phenotype of **1294** differed significantly from that of **DDD01035881**. Divergent phenotypes of **DDD01035881** and **1294** fit existing knowledge of the two compounds and their cellular targets. For example, whilst CDPK4 is required to initiate the first round of DNA replication during microgametogenesis, we found **DDD01035881** does not impact microgametocyte ploidy. Findings here thus suggested that Pfs16 and CDPK4 have discrete roles during microgametogenesis. Hence, **DDD01035881** is unlikely to inhibit CDPK4, supporting Pfs16 as a cellular target.

Microtubule inhibitors

Having elucidated the cellular phenotype of **DDD01035881** to find the compound impacts cytoskeletal rearrangement, specifically inhibiting mitotic spindle and axoneme assembly, we next sought to compare the phenotype to known inhibitors of microtubules. Canonical microtubule inhibitor, colchicine, and actin microfilament inhibitor, cytochalasin B, were studied. For complete inhibition of microgametogenesis by colchicine and cytochalasin B, gametocytes required 48-hour preincubation with the compounds. Hence, it was not possible to obtain activity windows of gametocytes treated with the compounds following activation of microgametogenesis. However, MSc student Ms. Sarah Jordan performed immunofluorescence labelling of colchicine and cytochalasin B-treated microgametocytes. Given the detailed phenotypic analysis was performed by Ms. Jordan, the precise results will not be described in this thesis. Briefly, a notable observation was that the cellular phenotypes of these microtubule inhibitors differed from that of **DDD01035881**. This finding supported Pfs16 as a probable target of **DDD01035881**, suggesting that the inhibition of cytoskeletal rearrangement likely arises from an indirect downstream effect of binding to Pfs16 rather than direct inhibition of microtubules.

5.2.4 GHCDL hit phenotypes

Characterisation of the **DDD01035881** phenotype during microgametogenesis followed its discovery in the high throughput screen of the Global Health Chemical Diversity Library (GHCDL), reported by Delves et al., 2018. After extensive lead development and deconvolution of the cellular target, we have obtained a detailed understanding of N-4HCS compound activity. Whilst **DDD01035881** was the most potent of GHCDL hits, other compounds with varying activity profiles were discovered in the screen. Here, to facilitate future deconvolution of the cellular target(s) and modes of action of GHCDL hit compounds, we used immunofluorescence staining to elucidate the cellular phenotypes of the hits during microgametogenesis. The developmental pipeline presented in this thesis present a framework for development of these hits. Results of this study have been previously submitted in candidature for an MRes in Drug Discovery and Development at Imperial College London.

Compounds **DDD01255968** and **DDD01249504** were found to be male gametocyte-specific in the GHCDL screen, inhibiting exflagellation in the dual gamete formation assay (DGFA) carry-over and wash-out formats (Delves et al., 2018). **DDD01255968** was additionally active in the add-in format of the DGFA. In contrast, **DDD01245291** exhibited dual activity against both male and female gametocytes and asexual blood stage parasites, additionally blocking transmission in the *P. falciparum* standard membrane feeding assay (*Pf*SMFA), as reported by Delves et al., 2018. The male IC_{50}s of **DDD01255968**, **DDD01249504** and **DDD01245291** are listed in Figure 5.19B.

Cellular phenotypes of **DDD01255968**, **DDD01249504** and **DDD01245291** were studied here. *P. falciparum* NF54-strain stage V gametocytes were treated and incubated with the hit compounds, activated to induce gametogenesis, fixed at various timepoints and stained for microscopy. Immunofluorescence staining of the host erythrocyte and parasite cytoskeleton was performed using antibodies specific to glycophorin A and α-tubulin II, and DNA was stained with DAPI.

DDD01255968 displayed a distinct cellular phenotype in which a large mass of tubulin-stained parasite material was found to lie adjacent to the gametocyte, within the host erythrocyte (Figure 5.19C). This extension of parasite material was evident

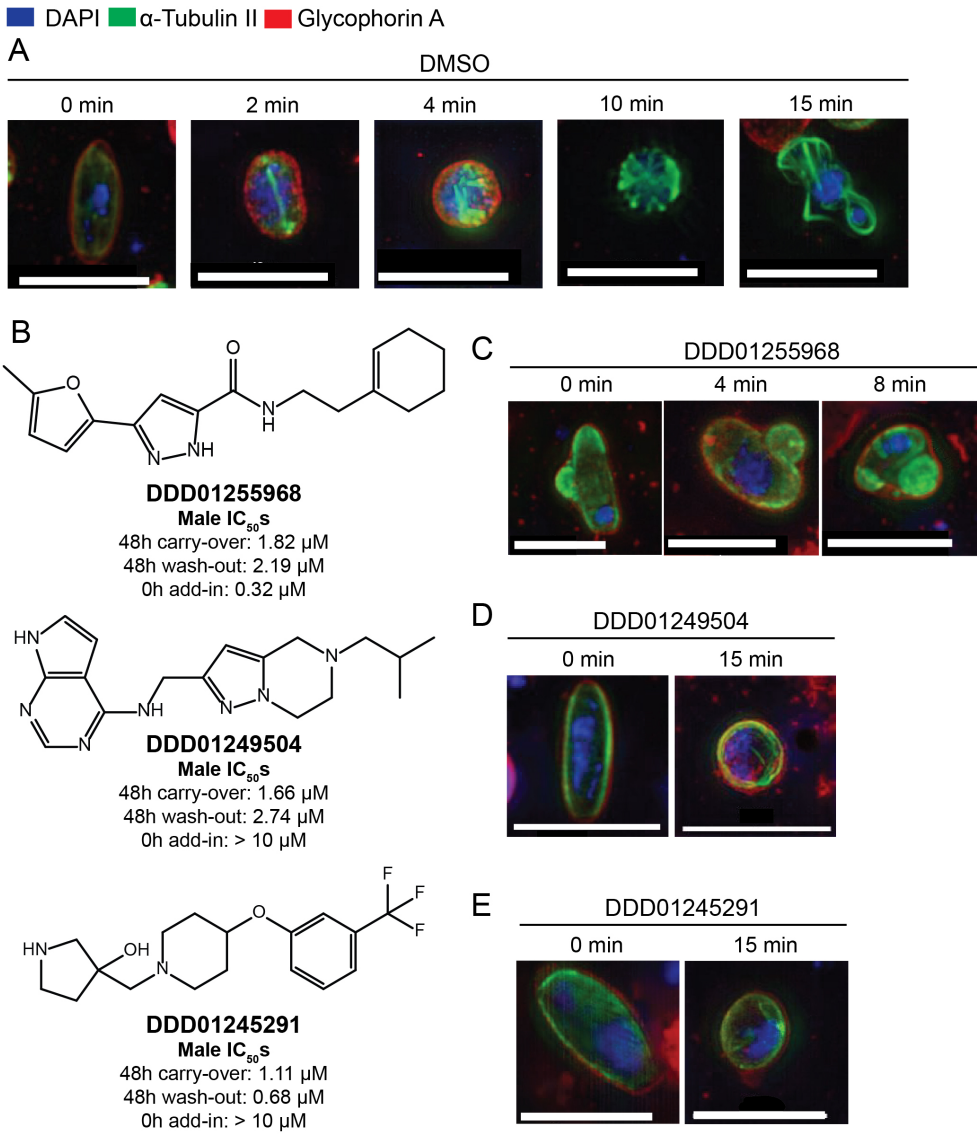


Figure 5.19: Cellular phenotypes of GHCDL compounds during microgametogenesis by immunofluorescence. (A) *P. falciparum* NF54-strain gametocytes were treated with DMSO, activated and fixed at the stated timepoints to create a time-course of microgametogenesis. (B) Structures of GHCDL-derived compounds **DDD01255968**, **DDD01249504** and **DDD01245291** and corresponding male IC_{50} values measured in the published screen, derived from varying formats of the DGFA (Delves et al., 2018). Cellular phenotypes of gametocytes treated with either (C) **DDD01255968**, (D) **DDD01249504** or (E) **DDD01245291** during microgametogenesis. Merged channels of the α-tubulin II-labelled cytoskeleton (green), glycophorin A-labelled host erythrocyte (red) and DAPI-stained DNA (blue) are depicted in A, C, D and E. Scale bars = 10 μm.

prior to activation, following 48-hour treatment with compound. Cytoskeletal rearrangement was largely prohibited under **DDD01255968** treatment, with no evidence of mitotic spindle or axoneme assembly but some rounding-up of the originally falciform gametocyte. DNA replication and host erythrocyte egress was inhibited by **DDD01255968** (Figure 5.19C). No further progression of gametocyte morphology was visible beyond the phenotype observed at eight minutes post-activation.

DDD01249504 treatment resulted in a cellular phenotype which resembled that of **DDD01035881**, with regards to microgametocyte morphology (Figure 5.19D). Whilst microgametocytes were able to transform from falciform to round, parasites remained intraerythrocytic. By 15 minutes post-activation, some DNA replication and microtubule polymerisation was observed, unlike with **DDD01035881**. Few axonemes appeared to nucleate and elongate, though these appeared less dense and fewer in number compared to DMSO controls.

Finally, **DDD01245291**-treated microgametocytes depicted little progression beyond rounding up during microgametogenesis (Figure 5.19E). Parasites remained intraerythrocytic, failed to form mitotic spindles or axonemes and did not fully replicate DNA, similarly to **DDD01035881**.

Importantly, observations of the GHCDL compound phenotypes combined with knowledge of their activity profiles in the initial screen may guide future study of target(s) and modes of action.

5.3 Discussion

Building on the identification of Pfs16 as a cellular target of the N-4HCS series, detailed phenotypic analysis of the microgamete-targeted compound series was performed in this chapter. Utilising flow cytometry of transgenic *P. falciparum* lines and the cellular thermal shift assay combined with phase contrast, widefield fluorescence and electron microscopy, the precise phenotypic impact of **DDD01035881** on *Plasmodium* was elucidated.

N-4HCS compounds were found to specifically block microgametogenesis without impacting sexual conversion or early gametocyte development. **DDD01035881** activity was observed to be uniquely rapid, blocking microgametogenesis without incubation and retaining activity within the first six minutes of microgamete development. Knowledge of this activity window, combined with Pfs16 expression at the PVM and observations that this membrane was expelled beyond six minutes of microgametogenesis activation, corroborated **DDD01035881** binding to Pfs16. Widefield fluorescence and electron microscopy revealed a clear **DDD01035881**-mediated inhibition of mitotic spindle and axoneme assembly. These observations suggested that Pfs16 played an early role in regulating these transformations during microgametogenesis, a role which was found to be divergent from known regulators of microgametogenesis, PKG and CDPK4.

Although the phenotypic impact of **DDD01035881** on microgametogenesis was fitting with studies of *Pfs16* targeted gene disruption (Kongkasuriyachai, Fujioka, and Kumar, 2004), the insignificant impact to early gametocyte development under **DDD01035881**-treatment was inconsistent. This discrepancy may arise due to the site in which **DDD01035881** binds to Pfs16 to exert its inhibitory effect. Findings of a study on protein trafficking across the parasitophorous vacuole (PV) to the PVM during *P. falciparum* gametocyte development corroborated this hypothesis (Eksi and Williamson, 2011). The study aimed to define the amino acid (AA) domains of Pfs16 essential to PVM targeting, retention and capping, using various Pfs16-GFP constructs to track GFP localisation in reporter lines expressing distinct regions of the protein (Eksi and Williamson, 2011). The study found evidence of a

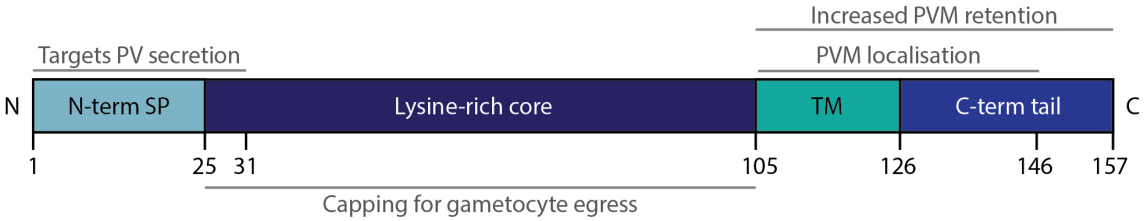


Figure 5.20: Predicted Pfs16 domain structure alignment. The 157 amino acid protein Pfs16 contains an N-terminal signal peptide (SP), lysine-rich core, transmembrane domain (TM) and C-terminal tail enriched in charged amino acids. Eksi and Williamson, 2011 performed detailed analysis of the different regions of Pfs16 using GFP fusion proteins, and defined the regions of the protein required to target secretion to the parasitophorous vacuole (PV), parasitophorous vacuole membrane (PVM) targeting and retention and capping during gametocyte egress, depicted here in grey.

dual role of Pfs16, with different regions required for PVM capping during gametogenesis compared to earlier roles in PVM targeting and retention (summarised in Figure 5.20). The AAs between the Pfs16 transmembrane domain and N-terminal secretory signal were found to be essential to capping during gametogenesis egress, but contrastingly were not essential to PVM targeting (Eksi and Williamson, 2011). The 53 C-terminal AAs, containing a conserved PVM motif, were sufficient for PVM targeting and retention (Eksi and Williamson, 2011). Given the conservation of a motif within this region of Pfs16 among PVM proteins, it is unlikely to be bound by the sexual stage-specific N-4HCS compounds which were not found to interact with any other PVM proteins. Of the 53 C-terminal AAs, 42 AAs were defined as the specific signal for PVM targeting, and contained 20 of the 31 C-terminal tail AAs and 22 AAs of the transmembrane domain (Eksi and Williamson, 2011). Additionally, the remaining 11 C-terminal AA were shown to increase PVM retention, independent of targeting (Eksi and Williamson, 2011). The region of Pfs16 involved specifically in capping during gametogenesis egress, without a role in PVM targeting and retention, is likely to correspond to the **DDD01035881**-binding site. Importantly, the findings of the study which support a dual role of Pfs16 (Eksi and Williamson, 2011), provide rationale to the observation that N-4HCS compounds inhibit gametogenesis independently of gametocytogenesis.

Additionally, an immunoelectron microscopy-based study on the subcellular lo-

calisation of Pfs16 found its expression in the Garnham bodies and membranes surrounding the food vacuole and cytosome (Baker et al., 1994). As Garnham bodies are known to host material exported by the parasite (Orjih, 2012) and may form from PVM budding (Baker et al., 1994), Pfs16 localisation at these bodies is unsurprising. Ingestion of host cell cytoplasm is mediated by the cytosome, a transitory invagination of the PVM, forming food vacuoles in which haemozoin crystals reside (Baker et al., 1994). The localisation of Pfs16 at these vacuoles is consistent with our ultrastructural observation that increased food vacuoles were found dispersed across the **DDD01035881**-treated parasite cytosol. The dispersed food vacuoles likely arise from a downstream effect of compound binding to the membranes of these structures.

Challenged by the inability to perform *in vitro* evolution and whole genome analysis (IVIEWGA) with the non-replicatative sexual stages of *Plasmodium*, the precise target and mode of action of transmission blocking N-4HCS compounds was explored with chemical proteomics combined with conventional microscopy and flow cytometry techniques. To further validate the N-4HCS interaction with Pfs16 and explore the hypothesis that binding occurs in the region of Pfs16 which is involved in PVM capping, future structural investigation is required. Additionally, changes to the N-4HCS phenotypic activity upon altering the expression levels of Pfs16 may provide further genetic evidence to corroborate the results of this chapter. Given the elusive function of Pfs16, biochemical validation reporting inhibition to Pfs16 activity in the presence of N-4HCS compounds is currently not feasible. Identification of the specific residues bound by the compounds should, however, be prioritised for further study. This chapter concluded the developmental pipeline of a GHCDL-derived microgametogenesis blocking compound series with phenotypic characterisation, following on from discovery, lead development and target identification. Collectively, findings reported in this thesis may guide further development and clinical testing of the N-4HCS series. Results of this chapter were concluded by phenotypically characterising alternative GHCDL compounds to guide future investigations into the cellular targets and modes of action, crucially facilitating the development of these hits.

Chapter 6

Live-cell imaging of *P. falciparum* microgametogenesis

6.1 Introduction

As demonstrated throughout this thesis, microgametogenesis represents a remarkably rapid and complex developmental process which occurs as *Plasmodium* parasites transition from a vertebrate to mosquito host. Uptake during a mosquito bloodmeal triggers the onset of male (micro) and female (macro) gamete formation, or gametogenesis (See Chapter 1.2.3.8). Discussed in Chapter 1.2.3.9, the transformation of a single microgametocyte to eight haploid motile microgametes is an explosive transformation in which the 22.9 Mb genome is replicated, the parasite cytoskeleton undergoes significant reorganisation and parasites egress from their host erythrocyte, all occurring simultaneously in only ∼15 minutes (Sinden, 2009). Replication of the microgametocyte genome from haploid to octoploid is one of the fastest eukaryotic DNA replication events that exists. In stark contrast, macrogamete formation (Chapter 1.2.3.10) simply involves a morphological transformation and host erythrocyte-egress (Guttery et al., 2015; Andreadaki et al., 2018). Given the increased susceptibility of microgametocytes to drug inhibition compared to macrogametocytes (Delves et al., 2013) and the uniquely complex cellular biology of microgametogenesis, the process represents an interesting avenue of study.

Microscopy remains the gold-standard technique for uncovering the cellular traits

associated with microgametogenesis, commonly relying on the activation and fixation of *in vitro* gametocyte culture. Electron microscopy studies have defined the stepwise series of events now known to occur during the formation of microgametes, at an ultrastructural level (Billker et al., 2002; Sinden, Canning, and Spain, 1976; Sinden et al., 2010; Sinden et al., 1978). Traditional fluorescence microscopy techniques have also been widely implemented in studies of microgametogenesis and drug discovery. For example, the high-throughput screen of the GHCDL library from which the N-4HCS compounds were derived, reported the immunofluorescence labelling of fixed gametocytes to define the perturbances to microgametogenesis imparted by transmission-blocking hits (Delves et al., 2018). This premise was applied in Chapter 5 of this thesis to define the phenotypes of various inhibitors of microgametogenesis. The recent advent of ultrastructure expansion microscopy (U-ExM) was shown to bridge fluorescence and electron microscopy, superseding the respective resolution and technical limitations of these traditional approaches (Bertiaux et al., 2021). U-ExM has proven utility in the study of microgametogenesis, recently being shown to resolve the structures of axonemes, mitotic spindles and subpellicular microtubules (Bertiaux et al., 2021). Spatial resolution available from electron and fluorescence microscopy techniques have been crucial to our understanding of the fine cellular biology of microgametogenesis. However, these techniques rely on fixed parasite samples and thus fail to fully resolve the dynamic nature of events occurring during microgamete formation.

Live-cell microscopy is crucial to improve the temporal characterisation of microgametogenesis. Challenged by the speed at which microgametogenesis occurs, live-cell microscopy of microgamete development has been relatively less common than studies utilising fixed parasites. Despite these challenges, live brightfield imaging of exflagellation has proven to provide temporal resolution of microgametogenesis, without being impacted by the phototoxicity associated with fluorescence microscopy. The dual gamete formation assay (DGFA), utilised in the GHCDL screen (Delves et al., 2018), capitalises on the adherence of emerging microgametes to neighbouring erythrocytes during exflagellation, which is measured by low-resolution brightfield microscopy (Ruecker et al., 2014). However, the limits to spatial reso-

lution by brightfield imaging mean microtubules, DNA replication and the precise mechanisms of egress are not resolvable. Improved spatial resolution by live-cell fluorescence microscopy of microgametogenesis has also been previously explored, to study the phenotypes of transgenic *P. berghei* lines (Wall et al., 2018; Zeeshan et al., 2021). Insights made by these studies take advantage of high temporal and spatial resolution, evading the antibody staining steps required of fixed parasite imaging, but are limited by the complex generation of transgenic parasite lines.

Here we sought to develop a live-cell fluorescence imaging workflow of microgametogenesis which is widely accessible to the malaria community, utilising commercially available stains, widefield fluorescence microscopy and open-access software for analysis. Traditional live-cell brightfield microscopy and fluorescence microscopy was performed to acquire both 2D and 3D data through time. Unique acquisition of 4D data (3D+t) provided high spatiotemporal resolution which enabled us to precisely define the dynamic events encompassing microgametogenesis, using the most virulent malaria parasite, *P. falciparum*. Crucially, the findings outlined in this chapter evaded the need for complex generation of transgenic cell lines or specialised equipment and was proven to have applications in drug discovery.

6.2 Results

Resolution of the stepwise cellular transformations occurring during microgametogenesis (Figure 6.1) have been limited by poor spatial resolution, the complex generation of transgenic parasites or fixed parasite protocols. Here, we have devised a live-cell *P. falciparum* NF54-strain microgametogenesis imaging workflow that is translatable to other research labs, utilising both 2D and 3D microscopy in real-time. Visualisation and volumetric analysis of the complex egress, cytoskeletal and DNA replication events were proven to have applications in the phenotypic characterisation of both known and unexplored inhibitors of the process. Results outlined in this chapter are accessible in an online open-access pre-print (Yahiya et al., 2021a).

6.2.1 Development of a live-cell fluorescence imaging protocol

6.2.1.1 Stain optimisation

Selective testing of commercially available DNA, cytoskeletal and erythrocyte membrane dyes was first performed to develop an accessible live-cell protocol. It was found that the silicon-rhodamine (SiR) derivative SiR-DNA and commonly used 4',6-diamidino-2-phenylindole (DAPI) were unsuitable, failing to stain live *P. falciparum* microgametocyte DNA effectively. In contrast, the cell-permeable dye Vybrant™ DyeCycle™ Violet effectively stained live stage V microgametocyte DNA. Vybrant™ DyeCycle™ Violet binds double-stranded DNA and subsequently emits a fluorescent signal which correlates to DNA mass, with applications in the measurement of microgametocyte ploidy by flow cytometry, as shown in Chapter 5.2.2.2 and previous studies (Fang et al., 2017). Optimisation revealed 500 nM Vybrant™ DyeCycle™ Violet was suitable for observation of replication by microscopy.

As the microgametocyte cytoskeleton undergoes drastic transformation, a suitable microtubule stain was sought after and SiR-tubulin was found to be highly suited to this study. SiR-tubulin is an SiR-derivative conjugated to chemotherapy

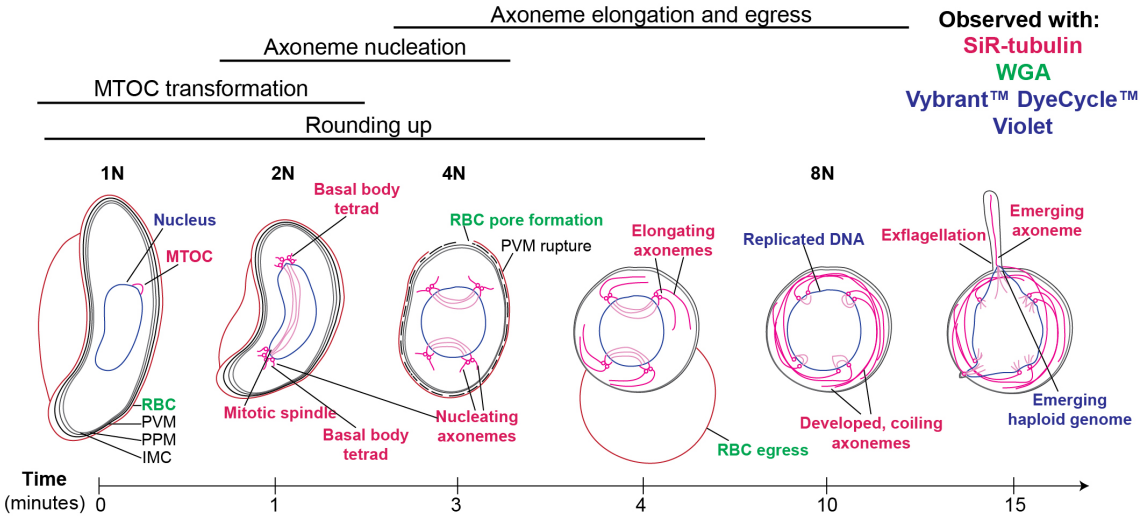


Figure 6.1: Cellular events encompassed by microgametogenesis. A schematic summarising the currently accepted model of microgametogenesis and the transformations which were observed here with SiR-tubulin, WGA and Vybrant™ DyeCycle™ Violet staining. Various cytoskeletal transformations are observed during microgametogenesis; including morphological rounding up from falciform, microtubule organising centre (MTOC) transformation and axoneme nucleation and elongation, which were observed with SiR-tubulin staining of microtubules. Three rounds of DNA replication transform the 1N genome to 8N, and DNA content can be monitored with Vybrant™ DyeCycle™ Violet. Parasites egress from the host erythrocyte and parasitophorous vacuole membrane (PVM), transforming the four-layer membrane comprised of the erythrocyte membrane (or red blood cell membrane, RBC), PVM, parasite plasma membrane (PPM) and inner membrane complex (IMC). Erythrocyte egress was monitored here with WGA staining.

drug docetaxel (Dubois et al., 1995) and this non-toxic far-red fluorogenic probe was found here to bind specifically to microgametocyte microtubules. Crucially, SiR-tubulin demonstrated suitable photostability during live-cell fluorescence microscopy. With optimisation, it was found that staining live stage V *P. falciparum* gametocytes with 500 nM SiR-tubulin for three hours enabled us to discern males from females and effectively resolve mitotic spindles, basal body tetrads and axonemal microtubules.

Staining the host erythrocyte was vital to uncovering the mechanisms of host-erythrocyte egress during microgametogenesis. Here, we found that 5 μg/ml of lectin wheat-germ agglutinin conjugated to AlexaFluor488 efficiently stained the host erythrocyte membrane. Frequently used in fixed parasite imaging (Ashdown

et al., 2020), here we found that WGA demonstrated suitable photostability and was hence effective in live-cell fluorescence microscopy. Importantly, egress, DNA replication and cytoskeletal rearrangement was not impacted by WGA staining, confirming it as non-toxic. Combining stains, development of the parasite cytoskeleton, DNA and host erythrocyte traits were visualised to dissect and develop the existing model of microgametogenesis (Figure 6.1).

Step one of our workflow involved staining live stage V *P. falciparum* NF54-strain gametocytes with a combination of 500 nM Vybrant™ DyeCycle™ Violet, 500 nM SiR-tubulin and 5 μg/ml WGA-488 (Figure 6.2). To study the cellular phenotypes of microgametogenesis-inhibitors here, compounds were added alongside stains for a three-hour incubation. To prevent premature activation of gametogenesis, parasites were stained and strictly maintained at 37°C prior to imaging.

6.2.1.2 Live-cell widefield microscopy

To acquire time-lapses of microgametogenesis, gametogenesis was activated at the microscope for immediate image acquisition, in step two of our workflow (Figure 6.2). Activation was performed by experimental emulation of mosquito midgut conditions, using a xanthurenic-acid treated medium which was used at room temperature and maintained at pH 7.4, referred to as "ookinete media". With optimisation, it was found that the direct addition of treated and labelled gametocytes to slides loaded with ookinete-media and prepositioned at the widefield microscope, permitted suitable time-lapse acquisition.

Step three of the workflow was the identification of male parasites for live-cell microgametogenesis time-lapse acquisition (Figure 6.2). Upon activation, a single microtubule organising centre (MTOC) transforms to two orthogonal tetrads of basal bodies (Sinden, 2009). By SiR-tubulin staining, this process was visualised as the transformation of a punctate spot of SiR-tubulin-staining into a mitotic spindle spanning the length of the parasite body, before axonemes were seen to nucleate from the basal bodies located at the poles of the spindle. Given the extremely rapid turnaround between activation and MTOC transformation, microgametocytes were predominantly identified by mitotic spindle-staining. Mitotic spindles appeared at

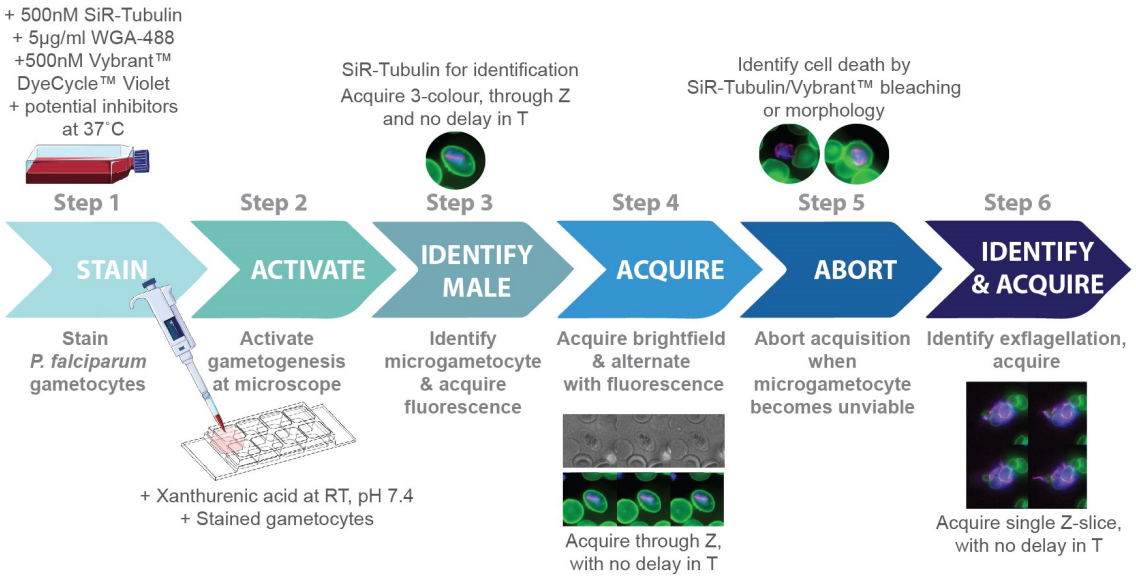


Figure 6.2: Live-cell fluorescence imaging of *P. falciparum* microgametogenesis workflow. Prior to analysis, the imaging workflow was encompassed in six steps. Microgametocytes were first stained (step one) before activation at the microcrope, to facilitate immediate acquisition (step two). Microgametocytes were subsequently identified based on microtubule traits (step three) before immediate and alternating acquisition (step four). Acquisition was aborted when parasites were deemed unviable (step five) before further identification and acquisition of males undergoing the later stages of exflagellation (step six).

around one-minute post-activation and indicated that a round of DNA replication was complete, with the initiation of the first genome replication being reported to occur within 20 seconds of activation (Fang et al., 2017).

Following microgametocyte identification, step four of the workflow entailed the acquisition of real-time 3D (4D) time-lapses of early microgametogenesis (Figure 6.2). Acquisition was alternated between fluorescence and brightfield imaging to maximise microgametocyte viability, which was otherwise compromised by the phototoxic effects imparted by continual fluorescence microscopy. Three-colour fluorescent time-lapses were first acquired, with a maximum of ten time-frames being captured by fluorescence microscopy to further prolong parasite viability. To monitor morphological transformations, time-lapse acquisition was switched to brightfield imaging. Following the observation of further development in brightfield, such as changes to the erythrocyte in preparation for egress, a further ten frames were acquired by fluorescence microscopy until the full early stages of microgametogenesis

were captured. Both brightfield and fluorescence time-lapses were acquired in 4D (3D+t) at the early stages, which was crucial for detailed analysis of egress mechanisms and microtubule polymerisation. It was found that fluorescence imaging over 24-44 Z-slices, every one-to-three minutes, enabled acquisition from mitotic spindle formation to full axoneme development without compromising viability.

Although phototoxic effects were drastically minimised by the alternation between brightfield and fluorescence microscopy and reduced LED intensity, capturing development from activation through to exflagellation in a single parasite proved to be challenging. It was found that a marked reduction in magnification and LED intensity permitted time-lapse acquisition from activation to exflagellation, however the resulting resolution was too poor for valuable analysis. This limitation was circumvented by capturing the entire series of microgametogenesis events over two stages of development: i) the early stages of cytoskeletal rearrangement, egress and DNA replication and ii) the later stages of microgamete emergence, or exflagellation. Upon observation of cell-death, acquisition of early development was aborted (step 5, Figure 6.2) and alternative parasites poised for exflagellation were identified (step 6, Figure 6.2). Parasites preparing for exflagellation were identified by SiR-tubulin staining of fully developed axonemes which coiled around the microgametocyte cell body, and time-lapses were immediately acquired. Time-lapse acquisition of the later stages, specifically the rapid and explosive emergence of haploid microgametes, was undertaken with 2D microscopy through time. Capturing a single Z-slice was required as the dynamic motion of microgametes were not susceptible to 3D microscopy.

Crucially, the combination of brightfield and fluorescence time-lapses enabled us to visualise the formation of motile haploid microgametes from the early stages of endomitosis and mitotic spindle assembly through to the later stages of exflagellation. We were able to dissect microgametogenesis in its entirety, for the first time, by live-cell fluorescence microscopy using widely accessible tools and techniques.

6.2.2 Insights into microgametogenesis

Having developed a reproducible workflow for real-time acquisition of microgametogenesis in full, we used open access tools to analyse our observations. For the first time, we have attained 4D (3D+t) data of microgametogenesis, which uniquely provided volumetric information susceptible to observational and quantifiable analysis. Novel insights were made, building on the existing model of microgametogenesis which is summarised in Chapters 1.2.3.9 and Chapter 5.2.2.4, and Figure 6.1. Corresponding time-lapses of all images depicted in this Chapter have been made available, along with descriptions in Appendix B.

6.2.3 Cytoskeletal rearrangements

6.2.3.1 Microtubule polymerisation

Substantial transformation of the microgametocyte cytoskeleton occurs upon initiation of gametogenesis, with morphological transformation, mitotic spindle assembly, basal body formation and nucleation and elongation of axonemes all occurring in rapid succession. We resolved these processes using SiR-tubulin staining of parasite microtubules.

SiR-tubulin staining confirmed that the single MTOC transformed upon activation of gametogenesis, forming a mitotic spindle which lengthened across the microgametocyte cell body (Figure 6.3A). Subsequent formation of two tetrads of basal bodies at the extreme ends of the mitotic spindle was visualised, observed as regions of increased microtubule staining. Basal bodies have been described as the sites from which axonemes nucleate and elongate, witnessed here from as early as two-to-three minutes post-activation (Figure 6.3A). Generation of 3D projections of volume rendered data enabled close observation of axoneme assembly from basal body tetrads, which later elongated and coiled around the cell body (Figure 6.3B).

SiR-tubulin staining intensity was measured to quantify microtubule polymerisation during microgamete development, focussing on three distinct stages: microgametocytes with i) an assembled mitotic spindle, ii) newly nucleated axonemes and iii) fully developed axonemes. Images derived from live-cell fluorescence imaging

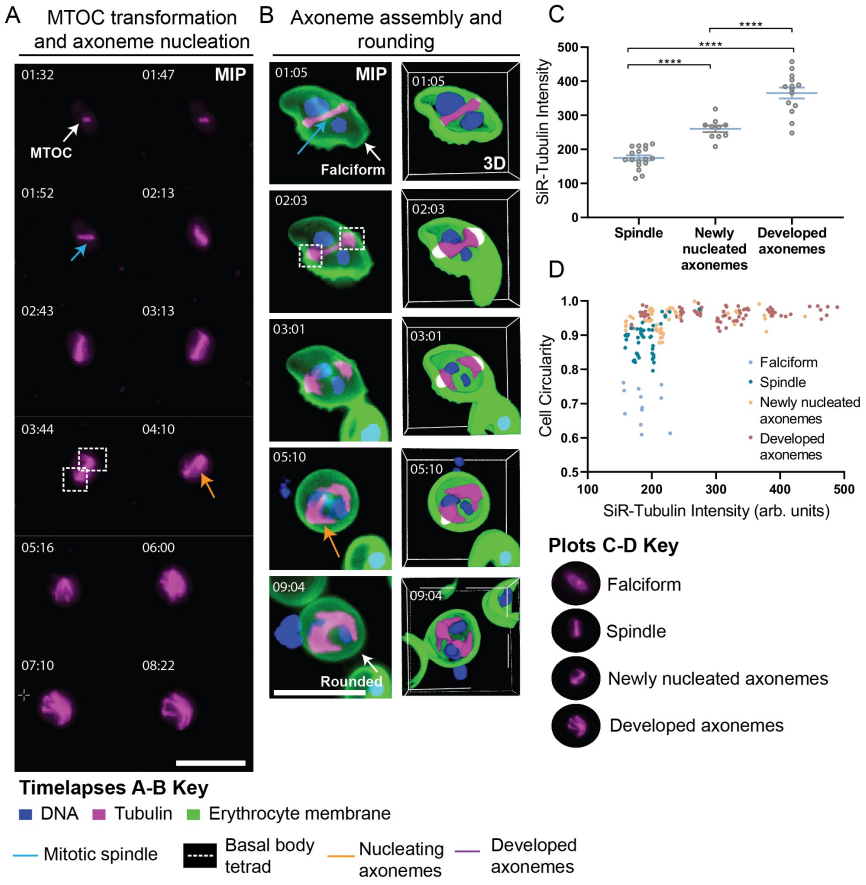


Figure 6.3: Cytoskeletal transformations of developing *P. falciparum* microgametes. Individual time-frames of microgametocytes acquired by live-cell fluorescence time-lapse microscopy depicting (A) SiR-tubulin-stained microtubules (magenta) and (B) SiR-tubulin-stained microtubules (magenta), Vybrant^{TM} DyeCycle^{TM} Violet-stained DNA (blue) and WGA-stained erythrocyte membranes (green). (A) Microtubule organising centre (MTOC) transformation into two basal body tetrads spaced across the parasite by a mitotic spindle. (B) The transformation from falciform to rounded is shown, along with axoneme nucleation and elongation from basal bodies. Maximum intensity projections (MIP) and 3D projections of volume rendered data (3D) are displayed. Scale bars = 10 μm. Time is depicted as minutes and seconds (mm:ss). Depicted images represent observations made from >10 biological replicates. (C) SiR-tubulin intensity (arbitrary units) derived from individual microgametocytes, assigned a developmental stage based on microtubule staining (see Plots C-D Key); spindle (n = 17), newly nucleated axonemes (n = 10) and developed axonemes (n = 14). A one-way ANOVA test with Tukey multiple comparisons was performed to measure the statistical significance of the difference between stain intensities (**** $p < .0001$) (D) SiR-tubulin intensity (arbitrary units) plotted against cell circularity. Each point represents individual microgametocytes assigned one of the four stages (see Plots C-D Key); falciform (n = 12), spindle (n = 46), newly nucleated axonemes (n = 48) and developed axonemes (n = 82).

of these early stages were manually assigned one of the three developmental stages and SiR-tubulin intensity was measured. Stained tubulin content significantly increased across each stage, signifying the rapid microtubule polymerisation between these stages (Figure 6.3C). Here, we demonstrated the retrieval of quantifiable data from our novel imaging platform, crucial for downstream characterisation of drug phenotypes.

6.2.3.2 Microgametocyte rounding

Unlike in rodent malaria, *P. falciparum* microgametogenesis entails a morphological transformation from falciform to round. SiR-tubulin combined with WGA staining of the host erythrocyte revealed the rounding up of microgametocytes, which was mirrored by the host cell (Figure 6.3B). Hence, we next aimed to study the relationship between microtubule polymerisation and the rounding up of microgametocytes. Based on the SiR-tubulin stained phenotype, individual cells were assigned one of four distinct developmental stages: microgametocytes which were i) falciform or displayed ii) mitotic spindles, iii) newly nucleated axonemes or iv) developed axonemes. The microtubule content and extent of parasite rounding was then measured as SiR-tubulin staining intensity and parasite cell circularity, respectively (Figure 6.3D). The cytoskeletal transformations which occurred at the onset of microgametogenesis, such as rounding up and mitotic spindle assembly, required little microtubule polymerisation. This conclusion was drawn as minimal changes to SiR-tubulin staining intensity were measured between falciform and mitotic spindle-containing parasites (Figure 6.3D). These stages did, however, display a greater range in cell circularity levels compared to the later microgametocyte stages, which reached maximum circularity upon axoneme nucleation. The bulk of microtubule polymerisation was found to occur in the later stages, which was evident as microgametocytes displaying newly nucleated or developed axonemes had the greatest SiR-tubulin content and variation (Figure 6.3D).

6.2.4 Changes to DNA during microgametogenesis

6.2.4.1 DNA segregation

DNA staining by Vybrant™ DyeCycle™ Violet was performed to measure the extent of DNA replication and behaviour of the microgametocyte nucleus. 3D projections of volume rendered data revealed the microgametocyte nucleus to segregate with DNA replication (Figure 6.4A), a novel observation which demonstrated the value of 4D data acquisition. Notably, segregated DNA appeared to localise at a perpendicular angle to the basal body tetrads, which formed at opposing spindle poles. To quantify this, microgametocytes displaying either a mitotic spindle, newly nucleated axonemes or developed axonemes were identified by SiR-tubulin staining, before measurement of the angles between basal body tetrads and segregated DNA of these parasites, defined here as the DNA segregation angle. Volumetric data proved to be valuable in this analysis, as parasites were optimally aligned through volume-rendered images prior to angle measurement. Between the three stages, there was no significant difference in the DNA segregation angle and values ranged from 60 to 90° (Figure 6.4C). Quantification of DNA segregation angles supported the initial observation that segregation aligned away from basal body tetrads and revealed that further DNA segregation was insignificant.

6.2.4.2 DNA replication

Replication of the haploid stage V microgametocyte genome to octoploid during microgametogenesis is notably rapid, with three rounds of replication occurring within ten minutes of activation. Vybrant™ DyeCycle™ Violet staining enabled the observation and quantification of microgametocyte DNA content, revealing an increase to DNA content in 3D projections of volume rendered data (Figure 6.4B). Supporting this observation, a significant increase in Vybrant™ DyeCycle™ Violet intensity was measured between the late and early stages of microgametogenesis (Figure 6.4C). In parasites with fully developed axonemes, a significantly greater extent of Vybrant™ DyeCycle™ Violet staining was measured in comparison to parasites with either a mitotic spindle or newly nucleated axonemes (Figure 6.4C).

Notably, data derived from this approach enabled quantification of DNA content using simple widefield microscopy. Although flow cytometry is traditionally utilised in studies of this nature, our approach permitted the simultaneous observation of DNA behaviour, such as segregation.

Egress

Novel insights into the mechanisms of egress implemented by microgametocytes were obtained from our 4D dataset. Spike formation of the host erythrocyte membrane was observed (Figure 6.5A-B) and resembled the process of echinocytosis, which has been reported to occur during merozoite invasion of erythrocytes (Blake, Haase, and Baum, 2020). Additionally, WGA staining revealed the formation of an erythrocyte pore from which microgametocytes emerged (Figure 6.5B). Prior to ejection from the host erythrocyte, developing microgametocytes aligned towards the erythrocyte periphery, until emerging via a single pole of the microgametocyte mitotic spindle (Figure 6.5B). Quantification of the proportion of microgametocytes depicting this phenotype revealed that pore formation and spindle-directed egress occurred in every instance of egress, unlike possible echinocytosis which was only observed in 40% of parasites (Figure 6.5C). Novel insights into microgametocyte egress suggested a probable role of echinocytosis and potential driving force coordinating spindle-directed egress. Crucially, this demonstrated the value of our imaging framework in dissecting cellular events encompassing microgametogenesis.

Exflagellation

Finalising the complex events leading to microgamete development is the explosive process of exflagellation, during which eight haploid microgametes emerge from the parasite body in rapid motion at ∼15 minutes post-activation. Exflagellation of microgametes ensues upon full axoneme development, with EM studies demonstrating the alignment of complex nuclear machinery and developed axonemes towards the parasite plasmalemma in preparation for emergence. During exflagellation, axonemes emerge through the cell surface along with a haploid genome, taken from

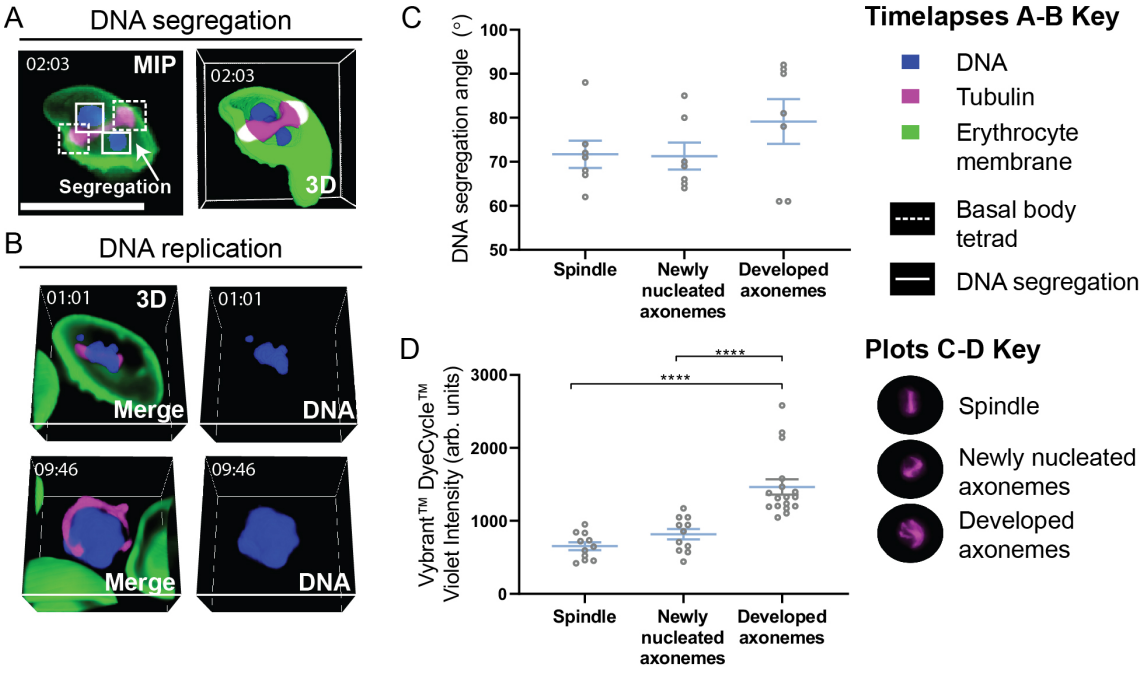


Figure 6.4: DNA segregation and replication during *P. falciparum* microgametogenesis. Individual time-frames of microgametocytes were acquired by live-cell fluorescence time-lapse microscopy. Images show SiR-tubulin-stained microtubules (magenta), Vybrant™ DyeCycle™ Violet-stained DNA (blue) and WGA-stained erythrocyte membranes (green), depicting DNA (A) segregation and (B) replication. (A) Both the maximum intensity projection (MIP) and 3D projections of volume rendered data (3D) are displayed. (B) 3D projections of volume rendered data (3D) are displayed of merged three-colour and DNA-only frames. Scale bars = 10 μm. Time is depicted as minutes and seconds (mm:ss). Depicted images represent observations made from >10 biological replicates. (C) Angles measured between basal body tetrads and segregated DNA (DNA segregation angles (°)) and (D) Vybrant™ DyeCycle™ Violet intensity (arbitrary units) of microgametocytes assigned with one of three developmental stages (see Plots C-D Key); spindle (C: n = 5, D: n = 11), newly nucleated axonemes (C: n = 5, D: n = 11) and developed axonemes (C: n = 5, D: n = 17). To measure the statistical significance, one-way ANOVA tests with Tukey multiple comparisons were performed (**** $p < .0001$).

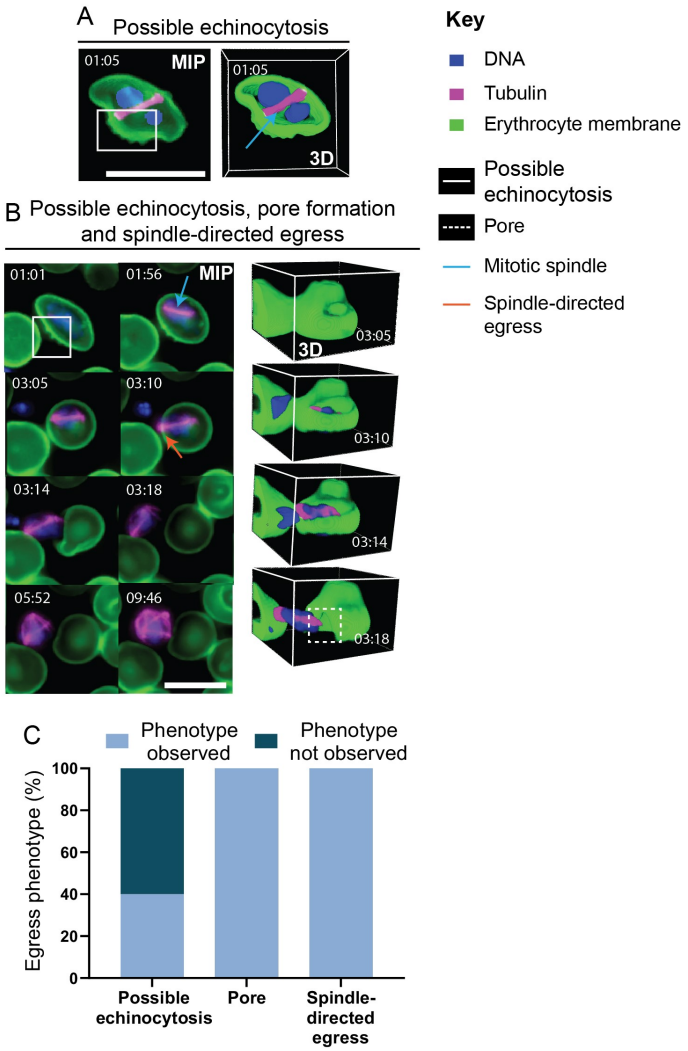


Figure 6.5: *P. falciparum* microgametogenesis erythrocyte egress mechanisms. Individual time-frames of microgametocytes acquired by live-cell fluorescence time-lapse imaging. Time-frames show SiR-tubulin-stained microtubules (magenta), Vybrant^{TM} DyeCycle^{TM} Violet-stained DNA (blue) and WGA-stained erythrocyte membranes (green). Images depict erythrocyte (A) possible echinocytosis and (B) possible echinocytosis, pore formation and spindle-directed egress. Maximum intensity projection (MIP) and 3D projections of volume rendered data (3D) are shown. Time is depicted as minutes and seconds (mm:ss). Scale bars = 10 μm. Images represent observations made from >7 biological replicates. (C) Mechanisms of egress observed in microgametocytes were measured and are depicted as the proportion (%) relative to all parasites successfully emerging from the host erythrocyte (n = 7).

the newly replicated octoploid genome. In stark contrast to the complexity of their development, the cellular composition of microgametes themselves is notably simple; comprised of only an axoneme, nucleus and plasma membrane (Sinden et al., 2010). Microgametes are subsequently poised for fertilisation of developed macrogametes, leading to zygote formation and further development within the mosquito. Being remarkably dynamic in nature, microscopic study of exflagellation would benefit from maximised spatiotemporal resolution, which we have explored here.

Following acquisition of the earlier developmental stages, the microscope stage was realigned to capture exflagellation of parasites not impacted by the phototoxicity imparted by continued fluorescence microscopy. Prior to time-lapse acquisition, parasites poised for exflagellation were identified either by SiR-tubulin-stained microtubules or motion by brightfield. Demonstrated by the rapid loss in motion following acquisition, exflagellating microgametes were particularly sensitive to LED phototoxicity and hence, identification by brightfield was favourable. 2D, three-colour fluorescence time-lapses revealed the emergence and motion of SiR-tubulin-stained emerging microgametes (Figure 6.6A). Microgametes were seen to emerge from the parasite cell body which was densely stained with Vybrant™ DyeCycle™ Violet, after three rounds of genome replication (Figure 6.6A).

As Z-acquisition was restricted by the dynamic motion of microgametes, we sought to develop alternative methods to attain volumetric data of exflagellation. One approach was to capture 3D, single time-frame images of exflagellating microgametes upon loss of motion (Figure 6.6B). Here, we observed microgametes to emerge and adhere to neighbouring WGA-stained erythrocytes (Figure 6.6B). Although viability of these parasites was compromised, the resulting volumetric data enabled close observation of microgamete localisation through space. Alternatively, intense regions of staining could be identified by generating 3D-intensity plots of staining, using 2D data acquired through time. Demonstrated here with SiR-tubulin intensity (Figure 6.6C), 3D-intensity plots revealed regions of dense microtubule staining which appeared from axoneme coiling, observations which otherwise rely on 4D imaging. As 3D-intensity plots may be generated through time, this method of analysis would enable users to monitor changes to density as microgametes continue

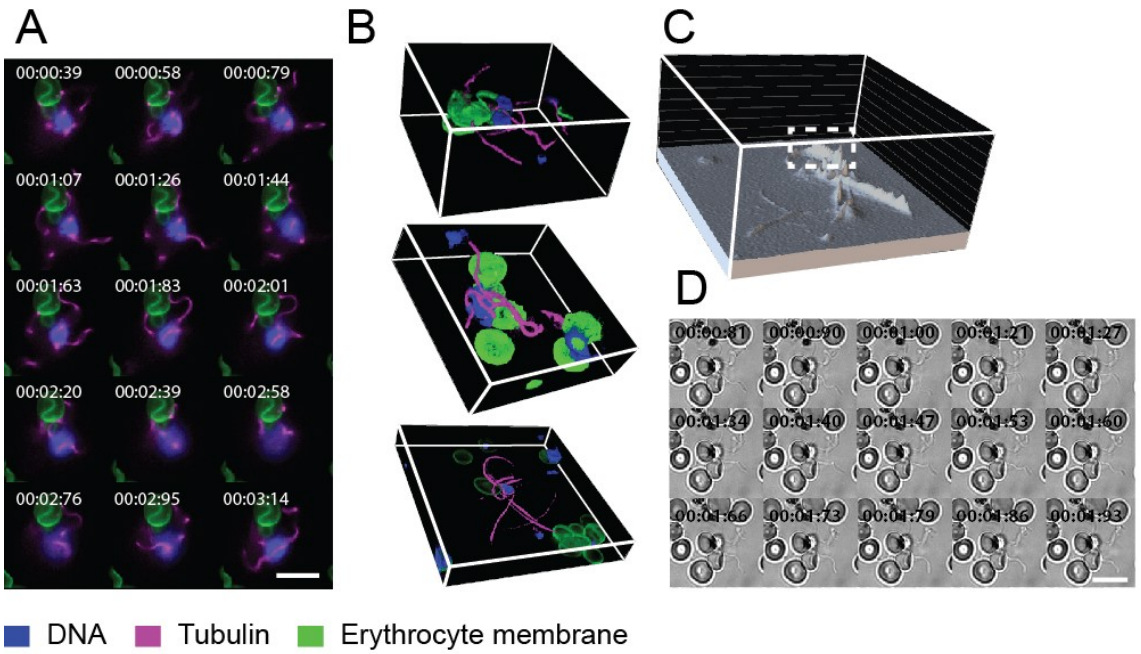


Figure 6.6: Emergence of *P. falciparum* microgametes by exflagellation. (A) Individual time-frames of microgametocytes acquired by 2D live-cell fluorescence time-lapse imaging. SiR-tubulin-stained microtubules (magenta), Vybrant™ DyeCycle™ Violet-stained DNA (blue) and WGA-stained erythrocyte membranes (green) are shown. (B) 3D projections of three-colour volume rendered data of exflagellating microgametocytes. (C) SiR-tubulin staining intensity depicted as a 3D intensity plot, revealing axoneme overlap (white dashed box) as densely stained regions. (D) 2D brightfield imaging of microgamete emergence. Scale bars = 10 μm. Time is depicted as minutes, seconds and milliseconds (mm:ss:ms). Depicted images represent observations made from >10 biological replicates.

to emerge.

Finally, brightfield imaging of exflagellation was performed, demonstrating microgamete rapid motion and adherence to neighbouring erythrocytes. Crucially, brightfield imaging of exflagellation enabled prolonged time-lapse acquisition compared to fluorescence microscopy, where viability of photosensitive parasites was otherwise compromised by LED exposure (Figure 6.6D).

6.2.5 Drug discovery application

Having developed a reproducible workflow for the combined 3D and 2D live-cell fluorescence imaging of microgametogenesis, we defined the cytoskeletal, DNA replication and egress events which occurred during microgamete development. Using these

observations as a reference for successful microgametogenesis, we next sought to define drug-induced perturbances using our workflow, with the aim to characterise the phenotypes of known and unknown inhibitors of microgametogenesis. Here, we used 4D data and quantitative analysis techniques to compare wild-type development to drugged parasites.

6.2.6 Live-cell phenotypes of known inhibitors

As described in Chapter 5.2.3, inhibitors of cell signalling regulators required to tightly synchronise microgametogenesis have been developed. Compounds ML10 (Baker et al., 2017) and 1294 (Doggett et al., 2014; Fang et al., 2017) demonstrate potent and immediate inhibition of microgametogenesis by targeting cyclic-GMP-dependent protein kinase G (PKG) and Ca^{2+}-dependent protein kinase 4 (CDPK4), respectively. Phenotypes of these compounds were previously studied using immunofluorescence labelling of fixed parasites undergoing microgametogenesis, outlined in Chapter 5.2.3. Here, we aimed to validate the applicability of our imaging approach to studies of drug phenotypes, by determining the reproducibility of fixed parasite studies.

6.2.6.1 Live-cell phenotype of PKG-inhibition

PKG is known to regulate Ca^{2+} levels during gametogenesis and is required for the morphological rounding up of *P. falciparum* falciform microgametocytes. Treatment with PKG-inhibitor, ML10, resulted in a clear block to microgametogenesis, arresting microgametocyte development prior to DNA replication and parasite rounding up (Figure 6.7A). Consistent with the phenotype observed by immunofluorescence staining in Chapter 5.2.3 and Figure 5.17, 4D data revealed that gametocytes remained falciform in morphology from the onset of gametogenesis through to the later stages, at which point wild-type parasites would be observed to exflagellate (Figure 6.7A). SiR-tubulin intensity was quantified at ten minutes post-activation, the point at which axoneme development and microtubule polymerisation was complete in wild-type conditions (Figure 6.8A). Under ML10-treatment, there was a significant reduction in SiR-tubulin intensity relative to untreated controls (Figure

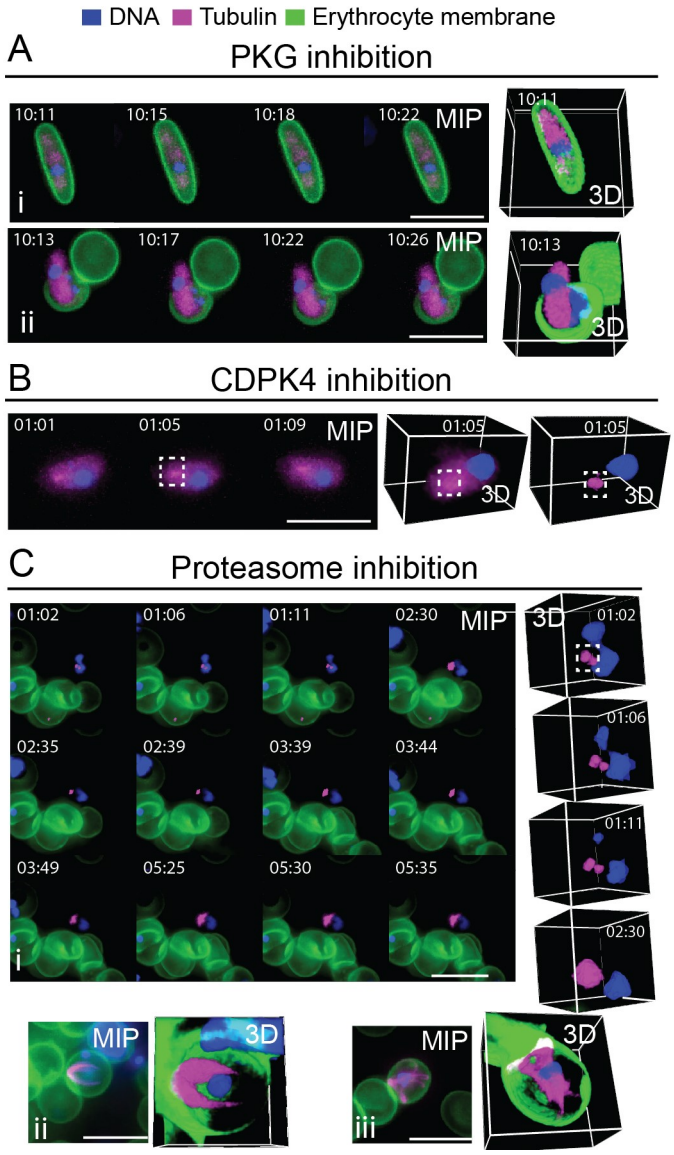


Figure 6.7: Microgametocyte cellular phenotypes upon PKG, CDPK4 and proteasome inhibition. Individual time-frames of microgametocytes acquired by 3D live-cell fluorescence time-lapse imaging. Images depict SiR-tubulin-stained microtubules (magenta), Vybrant^{TM} DyeCycle^{TM} Violet-stained DNA (blue) and WGA-stained erythrocyte membranes (green), showing both maximum intensity projection (MIP) and 3D projections of volume rendered data (3D). (A) ML10-inhibition of PKG, showing i) failed egress and ii) partial egress from the host erythrocyte. (B) 1294-inhibition of CDPK4 showing failed MTOC (white dashed box) transformation and stress-induced egress. (C) Proteasome inhibition by bortezomib displaying i) MTOC transformation to two small SiR-tubulin-stained foci (white dashed box) ii-iii) formation of truncated axonemes from one pole of the parasite. Time is depicted as minutes and seconds (mm:ss). Scale bars = 10 μm. Depicted images represent observations made from >10 biological replicates.

6.8A), which was consistent with the observed impediments to MTOC transformation, mitotic spindle assembly and axoneme formation (Figure 6.8A). Measurement of SiR-tubulin intensity throughout development, from one through to ten minutes post-activation, revealed that staining levels were retained at the level measured at one minute post-activation, matching untreated controls at this time-point (Figure 6.8B). To correlate the inhibition of microtubule polymerisation with the visualised disruption to rounding up, cell circularity of ML10-treated cells was measured and plotted against SiR-tubulin intensity (Figure 6.8C). As expected, microtubule staining remained at the minimal level observed in both treated and untreated parasites and ML10-treated parasites failed to reach the maximal level of circularity demonstrated by untreated controls.

Three distinct egress phenotypes were visualised upon initial inspection of 4D imaging data of ML10-treated microgametocytes (Figure 6.7A): parasites that i) failed to emerge, ii) partially emerged or iii) demonstrated full egress (not shown in Figure 6.7A) from the host-erythrocyte. Quantifying these observations, it was found that 50% of ML10-treated microgametocytes fully egressed, 42% failed and 8% depicted the partial-emergence phenotype (Figure 6.9A). Finally, the observed block to DNA replication was quantified as Vybrant™ DyeCycle™ Violet intensity at ten minutes post-activation, the time-point at which untreated controls had undergone three rounds of replication. ML10 was shown to significantly block DNA replication, relative to untreated controls (Figure 6.9B).

Combined, results demonstrated that PKG played an early role in the regulation of microgametogenesis, with inhibition by ML10 resulting in the downstream inhibition of DNA replication, rounding up and microtubule polymerisation. We have demonstrated the ability to observe and quantify a compound phenotype during microgametogenesis using our novel live-cell imaging framework, matching observations made with fixed parasite protocols whilst circumventing laborious immunofluorescence labelling steps.

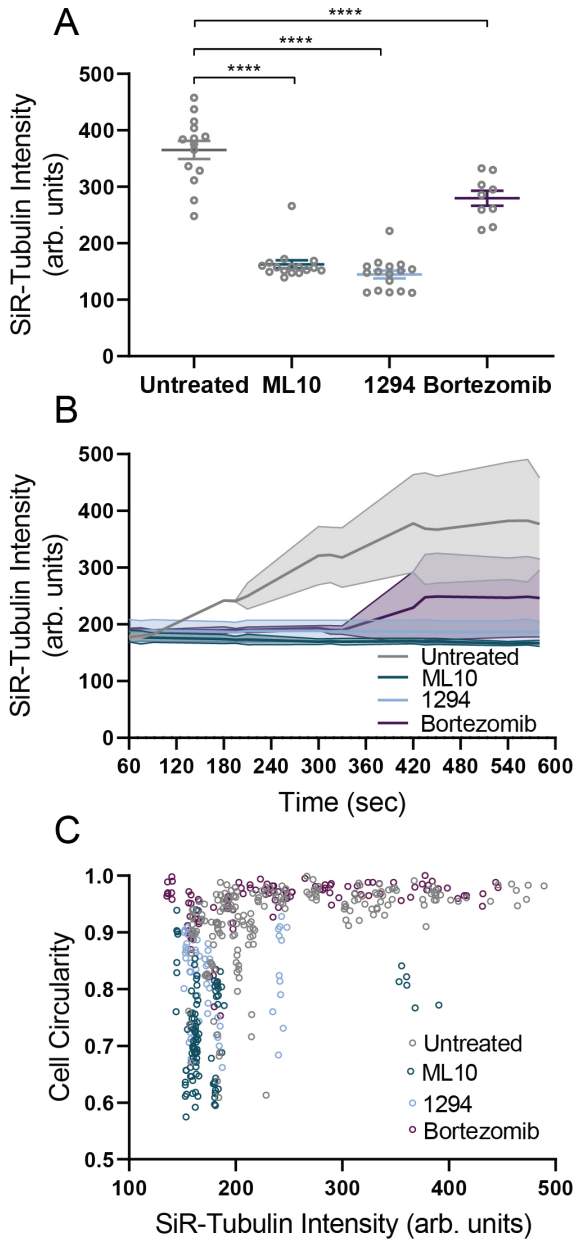


Figure 6.8: Microgametocyte microtubule polymerisation and morphological transformation under drug treatment. (A) SiR-tubulin intensity (arbitrary units) at ten minutes post-activation was measured in untreated ($n = 14$) and ML10 ($n = 16$), 1294 ($n = 16$) and bortezomib ($n = 9$) treated parasites. Statistical significance between untreated and drug-treated samples was determined by performing one-way ANOVA tests with Tukey multiple comparisons (**** $p < .0001$). (B) A continuum of SiR-tubulin staining (arbitrary units) of untreated ($n = 4$), ML10 ($n = 3$), 1294 ($n = 3$) and bortezomib ($n = 6$) treated microgametocytes. (C) Cell circularity and SiR-tubulin intensity (arbitrary units) across the entire developmental timeline of microgametogenesis, measured in individual cells which were untreated ($n = 188$) or treated with ML10 ($n = 106$), 1294 ($n = 58$) or bortezomib ($n = 105$).

6.2.6.2 Live-cell phenotype of CDPK4-inhibition

To further validate the applicability of our live-cell microscopy workflow to the study of drug phenotypes, we next dissected the impact of CDPK4-inhibition to microgametogenesis. Considered the master regulator of microgametogenesis, CDPK4 is involved in the initiation of genome replication, mitotic spindle assembly and microgamete motility. Bumped kinase inhibitor, 1294, has been reported to specifically and potently block this enzyme (Doggett et al., 2014; Fang et al., 2017) and the phenotype was studied by immunofluorescence staining of fixed gametocytes in Chapter 5.2.3 (Figure 5.18). Although the 1294-phenotype of fixed cells explored in Chapter 5.2.3 was studied by both treating gametocytes prior to and following activation (Figure 5.18), here we focused solely on the phenotype observed when pre-treating gametocytes.

Disruptions to microgametogenesis under 1294-treatment were observed by 4D imaging and revealed a visible block to cytoskeletal transformation (Figure 6.7B). The SiR-tubulin-stained MTOC failed to transform to basal body tetrads, subsequently preventing axoneme nucleation and elongation (Figure 6.7B). Quantification of SiR-tubulin staining intensity confirmed these observations, with 1294-treatment causing a clear block to microtubule polymerisation relative to untreated controls (Figure 6.8A). From one-to-ten minutes post-activation, the level of SiR-tubulin staining under 1294 treatment was retained at a level that matched untreated controls at one minute post-activation, suggesting little microtubule polymerisation occurred upon CDPK4-inhibition (Figure 6.8B). Correlation of these observations with cell circularity revealed that 1294-treated parasites failed to reach the maximum level of circularity observed in untreated controls, although slight rounding was measured. This suggested that CDPK4 plays a downstream role in complete microgametocyte rounding (Figure 6.8C).

Upon comparison of the egress phenotypes demonstrated by untreated and 1294-treated parasites, there was no notable difference to the level of full egress between samples (Figure 6.9A; 50% full egress with 1294-treatment, compared to 53% in untreated samples). However, it was found that pre-treatment with 1294 resulted in microgametocyte egress at the onset of microgametogenesis (Figure 6.7B). This

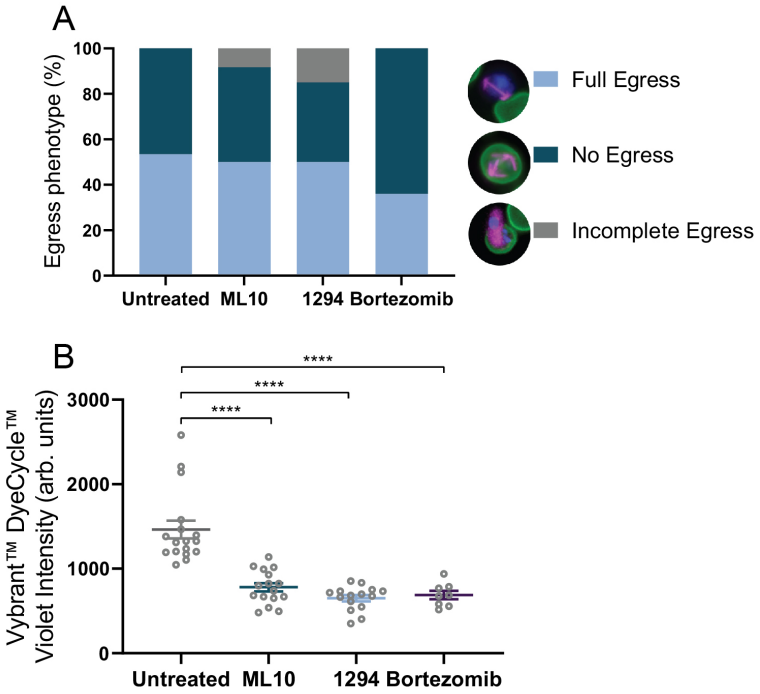


Figure 6.9: Microgametocyte egress and DNA replication under drug treatment. (A) Egress phenotypes of parasites at ten minutes post-activation, which were untreated (n = 58) or treated with ML10 (n = 25), 1294 (n = 20) or bortezomib (n = 24). (B) Vybrant™ DyeCycle™ Violet intensity (arbitrary units) at ten minutes post-activation of untreated (n = 17) or ML10 (n = 9), 1294 (n = 15) or bortezomib (n = 16) treated microgametocytes. The statistical significance of difference in DNA staining between untreated and drug-treated samples was measured with one-way ANOVA tests with Tukey multiple comparisons (**** $p < .0001$).

observation suggested CDPK4 inhibition may cause stress-induced egress prior to activation of gametogenesis, despite the fact that the final egress phenotype appeared insignificant. Additionally, the partial parasite emergence phenotype observed in PKG-inhibited parasites, was also observed in 15% of 1294-treated microgametocytes (Figure 6.9A). A significant block to DNA replication was also found, measured as Vybrant™ DyeCycle™ Violet intensity at ten-minutes post-activation (Figure 6.9B).

Further validating the applicability of our live-cell fluorescence imaging workflow to studies of transmission-blocking drugs, the CDPK4-inhibition phenotype visualised and quantified here was consistent with fixed parasite (Figure 5.18) and published observations (Fang et al., 2017). Given the relative simplicity and repro-

ducibility of results found with our live-cell workflow compared to traditional fixed parasite approaches, our framework is a promising tool for the reliable phenotypic characterisation of inhibitors which are yet to be explored in transmission-blocking drug discovery.

6.2.7 Proteasome inhibition during microgametogenesis

Having demonstrated that our imaging framework can provide novel insights into microgametogenesis and reproducibly define the phenotypes of known inhibitors of the cell signalling pathway, we next aimed to determine whether compounds of unknown activity could be studied. Currently unexplored for its activity during microgametogenesis, we sought to test bortezomib, an inhibitor of the proteasome. Bortezomib activity was recently described to arrest *Sulfolobus acidocaldarius* cells mid-division (Tarrason Risa et al., 2020) and is known to be active against eukaryote and euryarchaeota proteasomes (Adams et al., 1999; Chen et al., 2011; Fu et al., 2016). Interest in the proteasome as an antimalarial drug target (Xie et al., 2018) and proven activity of bortezomib against the symptomatic *Plasmodium* asexual stages (Reynolds et al., 2007) encouraged the study of this compound as a potential transmission-blocker. Here, we sought to identify whether bortezomib actively inhibits microgametogenesis, dissect any resulting perturbances and subsequently deduce a role of the proteasome in microgamete development, using our imaging framework.

Bortezomib was found to block microgametogenesis using our imaging workflow, visibly disrupting the formation of developed microgametes (Figure 6.7C). Dissection of the 4D imaging data revealed that bortezomib inhibited egress, and the nucleation and development of eight axonemes (Figure 6.7C). Whilst the MTOC was seen to transform to two punctate-foci of SiR-tubulin staining, mitotic spindles and basal body tetrads were not observed (phenotype i, Figure 6.7C). Depicted in Figure 6.7C as phenotypes i-iii, partial microtubule polymerisation was observed from a single pole of the parasite as truncated axonemes appeared to nucleate (phenotype i) and minimally elongate (phenotypes ii-iii). Quantification of SiR-tubulin staining intensity confirmed this observation, with a significant difference in intensity compared

to untreated controls at ten-minutes post-activation (Figure 6.8A). Consistent with the observation that some microtubule polymerisation occurred under bortezomib-treatment, but full axoneme development was blocked (Figure 6.7C), SiR-tubulin staining intensity was measured to increase from around six minutes post-activation but failed to reach the levels measured in untreated controls (Figure 6.8B). Measurement of cell circularity revealed that bortezomib-treated parasites were able to round-up, and varying levels of SiR-tubulin intensity of rounded cells were measured (Figure 6.8C).

Microgametocytes predominantly remained intraerythrocytic in the presence of bortezomib, with 64% of parasites failing to egress (Figure 6.9A). Additionally, Vybrant™ DyeCycle™ Violet intensity of bortezomib-treated microgametocytes at ten-minutes post-activation was significantly lower than untreated controls, signifying inhibition of DNA replication. Taken together, observations revealed that the proteasome regulates microgametogenesis, with bortezomib-mediated inhibition of the proteasome resulting in downstream disruptions to microtubule polymerisation and DNA replication. The proteasome is considered a desirable target of antimalarials inhibiting asexual replication and bortezomib has been explored as a potential drug candidate. Here, we show proteasome inhibition by bortezomib may additionally represent a desirable transmission-blocking intervention.

6.2.8 Novel insights by live-cell fluorescence microscopy

Our newly devised live-cell fluorescence imaging workflow enabled us to make some significant and novel observations on microgametogenesis, summarised in Figure 6.10. Firstly, we observed a level of possible echinocytosis and DNA segregation in untreated parasites (Figure 6.10A). With three varied egress phenotypes, PKG inhibition was found to prevent DNA replication, rounding up and microtubule polymerisation, such that ML10-treated parasites morphologically resembled stage V microgametocytes prior to activation of gametogenesis (Figure 6.10B). The cellular phenotype observed with inhibition of CDPK4 was similar to that of PKG, though minimal rounding-up was observed (Figure 6.10C). Crucially, we found the proteasome to be crucial in regulating DNA replication and microtubule polymeri-

sation during microgametogenesis, and the resulting phenotype of bortezomib is summarised in Figure 6.10D.

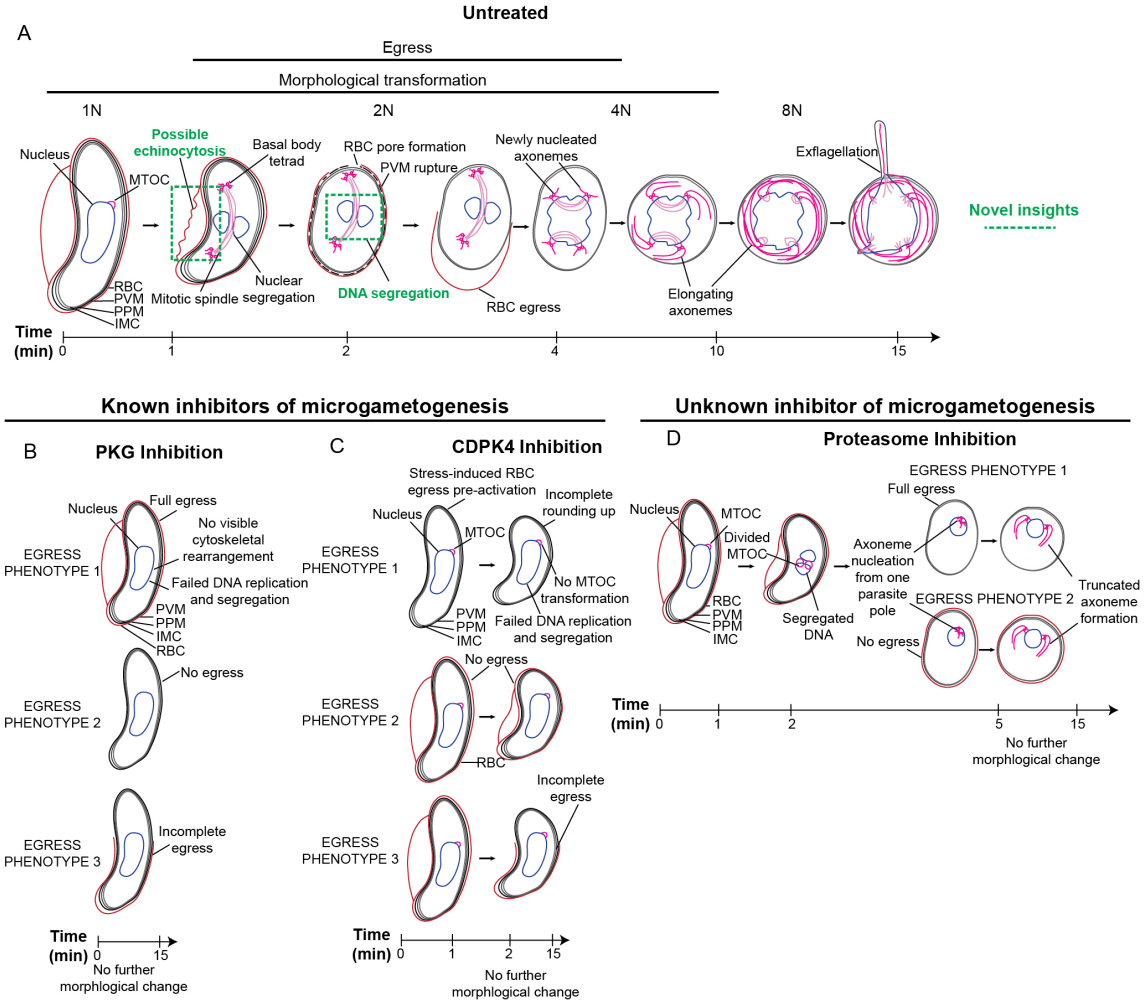


Figure 6.10: Novel observations on untreated and drug-treated microgametogenesis. Insights into DNA replication, cytoskeletal rearrangement and host erythrocyte egress during microgametogenesis were made using our newly devised live-cell fluorescence imaging framework. (A) Without drug-treatment, new insights into DNA segregation and changes to the erythrocyte membrane were revealed. Cellular phenotypes of (B) PKG, (C) CDPK4 and (D) proteasome inhibition were studied using drug treatment, and the various phenotypes are summarised in this schematic.

6.3 Discussion

In this chapter, a live-cell *P. falciparum* microgametogenesis imaging workflow was developed, combining traditional 2D fluorescence and brightfield time-lapse imaging techniques, with 3D fluorescence microscopy through time (4D imaging). Dynamic transformations encompassed in microgamete development were captured from the onset of activation up to exflagellation, visualising early development in 3D and explosive microgamete emergence in 2D. Evading the requirement for specialised equipment, complex staining steps and parasite fixation, our protocol was considerably less laborious than traditional EM and fluorescence approaches, requiring a short incubation of dyes with live-cells. Fundamentally, our approach utilised commercially available stains, widefield microscopy and open-access analysis tools, and is thus translatable to the wider malaria research community.

Utilising our new approach, we made novel observations to the behaviour of the parasite cytoskeleton, DNA and host-erythrocyte, with a cell-permeable fluorogenic probe, DNA dye and lectin, respectively. Optimisation of the workflow enabled prolonged acquisition of 3D data through time (4D data) in the early stages, from which volumetric data was retrieved and analysed. 4D imaging has recently gained traction in a study of asexual invasion, using lattice light-sheet microscopy to study the biophysics of the erythrocyte and PVM (Geoghegan et al., 2021). Here, we were able to deduce the relative localisation of segregated DNA and basal bodies during microgametogenesis from 4D data acquired with widefield microscopy. 3D projections of volume rendered data also enabled the detailed dissection of egress mechanisms. On occasion, we found the erythrocyte membrane to form spikes, resembling echinocytosis, in preparation for gametocyte egress followed by spindle-directed emergence from an erythrocyte pore. These findings built on a published study of *P. berghei* gametocyte egress, which described host erythrocyte swelling prior to PVM vesiculation and rupture (Andreadaki et al., 2018). Data derived from this study represents an important starting-point in the investigation of mechanisms of microgametocyte DNA segregation and the forces driving spindle-directed egress.

Crucially, we demonstrated the applicability of our protocol to phenotypic char-

acterisation of transmission-blocking drug candidates. The methodological approach proved to have utility in the study of compounds with both known and unknown activity against microgametogenesis. By studying the live-cell phenotypes of known inhibitors of PKG and CDPK4, we were able to reproduce observations previously made by immunofluorescence labelling of fixed cells. This importantly proved the workflow to reliably facilitate phenotypic characterisation and hence, we aimed to translate this into the study of an unexplored inhibitor of the proteasome, bortezomib. In doing so, we found the proteasome to be a crucial component of microgametogenesis regulation and bortezomib as an effective inhibitor. This observation suggested microgametogenesis relies on the regulation of functional protein levels and the degradation of misfolded proteins. With reported activity against the asexual stages (Reynolds et al., 2007), bortezomib has the potential to both treat the symptoms of malaria and block transmission, with a single molecule. Although bortezomib was selected for this study due to its remarkable phenotype in *Sulfolobus acidocaldarius* (Tarrason Risa et al., 2020), extensive study on parasite-specific proteasome inhibitors has been performed (Li et al., 2016; Yoo et al., 2018). For optimal clinical development, future study of optimally selective proteasome-inhibitors should follow this study. These findings thereby necessitate further development of proteasome inhibitors as transmission-blockers, including improvements to potency and *in vivo* mosquito feed testing.

Spatiotemporal resolution provided by the live-cell fluorescence imaging of *P. falciparum* microgametogenesis was achieved with simple, accessible techniques and importantly enabled real-time study of development. Here, we have focussed on characterising drug phenotypes of wild-type *P. falciparum* gametocytes, but the workflow is applicable to future studies of transgenic cell lines. Importantly, retrieval of volumetric or intensity information from our workflow would enable quantification of observed phenotypes of transgenic lines, as well as novel drugs, whilst avoiding parasite fixation. Incorporation of stains of parasite membranes, intracellular organelles and protein markers of sex provides the potential to uncover further insights into the remarkable process of microgametogenesis.

Chapter 7

Discussion

Any strides made in malaria control are threatened by the spread of resistance to the frontline artemisinin drugs and insecticides (World Health, 2020). Pervasive implementation of existing control strategies has resulted in the emergence of resistance (Tilley et al., 2016; Toé et al., 2014), and novel approaches to malaria control are, hence, highly sought after (Burrows et al., 2017). Targeting host-to-vector transmission by compromising the viability of the *Plasmodium* sexual-stage gametocytes has the added advantage of preventing the onward spread of malaria across the uninfected population (Burrows et al., 2017). Representing a population bottleneck which faces little selective pressure (Duffey et al., 2021; Delves et al., 2018), gametocytes are a desirable target of drug intervention. Primaquine and tafenoquine are currently the only approved transmission-blockers (Frampton, 2018; Phillips et al., 2017), additionally preventing *P. vivax* relapse (Phillips et al., 2017), but alternatives are crucial to address the safety concerns associated with these drugs (Burrows et al., 2017; Watson, Nekkab, and White, 2021).

Findings outlined in this thesis addressed the need for novel transmission-blocking antimalarial drugs by taking two approaches: i) following a traditional drug discovery pipeline to develop a transmission-blocking hit and ii) exploring drug phenotypic characterisation to aid future transmission-blocking drug development, utlising both established and novel workflows. In the first approach, a microgametogenesis-blocking compound was progressed from phenotypic screen-based hit discovery to lead development, which facilitated target identification and subsequent phenotypic

characterisation. In the second approach, alternative transmission-blocking hits discovered in the same phenotypic screen were phenotypically characterised using an established fixed-cell approach, to facilitate future developmental programmes of these compounds. Additionally, an accessible live-cell microscopy strategy was developed to aid future phenotypic characterisation of microgametogenesis-blocking drug candidates.

7.1 The developmental pipeline of *N*-4HCS compounds

Following discovery in a high throughput screen of the Global Health Chemical Diversity library (GHCDL), this thesis reported on the downstream development of microgamete-targeted *N*-((4-hydroxychroman-4-yl)methyl)-sulphonamide (N-4HCS) compounds (Delves et al., 2018). High-throughput screening campaigns are highly valuable to antimalarial drug discovery, with increasing reports of studies against the various stages of the *Plasmodium* lifecycle, beyond the symptomatic asexual stages (Yahiya et al., 2019). In contrast to hypothesis or target-driven discovery, phenotypic screening has the benefit of identifying compounds with novel chemotypes and modes of action, but hits require extensive characterisation following discovery (Lage et al., 2018; Flannery, Chatterjee, and Winzeler, 2013). Here, activity of various N-4HCS analogues were thoroughly characterised in a range of studies. Firstly, hit-to-lead development was performed in a collaborative study with medicinal chemist colleagues. Here, we tested the potency of N-4HCS analogues, synthesised by our colleagues, in a structure activity relationship study and yielded potent hits with nanomolar activity and favourable safety profiles (Rueda-Zubiaurre et al., 2019). Secondly, chemical proteomics techniques were utilised to identify and validate the *P. falciparum* sexual stage-specific protein, Pfs16, as a cellular target of N-4HCS compounds. Finally, in a phenotypic characterisation study, N-4HCS compounds were found to potently but reversibly block microgametogenesis in a six-minute activity window. Interestingly, N-4HCS compounds exclusively inhibited microgamete formation without impeding sexual conversion, early gametocyte development and

DNA replication.

Pfs16, a 16kDa parasitophorous vacuole membrane (PVM) protein, was identified as a promising cellular target of the N-4HCS compounds. As outlined in Chapter 5, studies on the targeted gene disruption of *Pfs16* (Kongkasuriyachai, Fujioka, and Kumar, 2004), cellular localisation of Pfs16 (Bruce et al., 1994; Baker et al., 1994; Lanfrancotti et al., 2007) and the protein domains crucial to PVM localisation and capping during gametogenesis (Eksi and Williamson, 2011) were consistent with the N-4HCS phenotype we observed during microgametogenesis. Most notably, a previous study described a mutant *P. falciparum* line expressing truncated Pfs16, which demonstrated an impairment to exflagellation (Kongkasuriyachai, Fujioka, and Kumar, 2004) which was fitting with the microgametogenesis-blocking activity of N-4HCS compounds. Parent compound **DDD01035881** demonstrated activity in the initial stages of microgametogenesis, the time-points at which the Pfs16-containing PVM remained associated with the gametocyte. **DDD01035881** activity halted following disintegration of the PVM and subsequent loss of Pfs16 expression, consistent with the hypothesis that N-4HCS may bind to Pfs16, subsequently disrupting gametocyte egress.

Although N-4HCS activity was largely consistent with the reported structure and function of Pfs16, it is worth highlighting aspects of the literature surrounding Pfs16 which may be perceived as inconsistent with our findings. As an example, N-4HCS activity did not impair sexual conversion or early gametocyte development, despite Pfs16 being considered an early marker of sexual conversion (Dechering et al., 1997). We hypothesise that the Pfs16 binding site of the N-4HCS compounds may account for this inconsistency, as the protein structure has previously been reported to have a dual role (Eksi and Williamson, 2011), as outlined in Chapter 5.3. Further to this, the initial GHCDL screen tested the transmissibility of both *P. falciparum* and *P. berghei* under N-4HCS treatment (Delves et al., 2018). As summarised in Chapter 1.5.3, **DDD01035881** potently blocked *in vivo* oocyst formation in both *P. falciparum* and *P. berghei*, with no impact to *P. berghei* asexual parasitaemia or gametocytaemia (Delves et al., 2018). Additionally, *P. falciparum* exflagellation and *P. berghei* ookinete formation were potently inhibited by **DDD01035881**

(Delves et al., 2018). Inconsistent with these observations, knockout of the putative, though divergent, Pfs16 orthologue expressed in rodent malaria parasite *P. berghei*, Pbg16 (PBANKA_1003900), was reported to neither impair gametocyte production, exflagellation nor ookinete formation (Deligianni et al., 2018). Oocyst formation was, however, reduced in the *Pbg16* knock-out and suggested Pbg16 has a role in the ookinete-to-oocyst transition (Deligianni et al., 2018).

There are two plausible explanations for the inconsistences between Pfs16 and Pbg16 function, relative to N-4HCS activity. Firstly, proteins expressed by the syntenic genes are notably divergent, with Pfs16 sharing <20% identical amino acids with Pbg16 and <30% overall similarity with orthologues expressed in other *Plasmodium* species (*P. chabaudii*, *P. yoelii*, *P. vivax* and *P. knowlesii*), as studied in Deligianni et al., 2018 and Niu et al., 2021. Minimal sequence similarity between species suggests N-4HCS compounds may feasibly exert a *P. falciparum*-specific effect and potentially not bind to Pfs16 orthologues expressed by other *Plasmodium* species. This theory would suggest the N-4HCS-mediated block in *P. berghei* transmission would occur by inhibition of an alternative cellular target, thereby warranting further study. Alternatively, N-4HCS compounds may still bind and inhibit Pbg16 to block transmission by an alternative mode of action, as Pbg16 may exhibit a different function to Pfs16. Despite the low sequence similarity, Pfs16 and Pbg16 share the predicted domain structure comprised of an N-terminal signal peptide, transmembrane domain and charged region at the C-terminus (Deligianni et al., 2018), suggesting N-4HCS binding potential may be conserved between the two proteins. Crucially, studies of *P. berghei* inhibition by **DDD01035881** in the GHCDL screen did not measure impediments to exflagellation, instead focussing on ookinete and oocyst formation. It is thus feasible N-4HCS compounds do not inhibit *P. berghei* transmission by compromising microgamete viability, as they do in *P. falciparum*. The difference in the phenotypic impact would be unsurprising given the difference in gametocyte development between species; whilst *P. falciparum* gametocytes mature to a falciform morphology in 10-12 days, *P. berghei* form rounded gametocytes in a 26-30 hour developmental period. Variations in gametocyte development may result in divergent roles of the PVM and mechanisms of egress between

these species. Supporting this, we observed instances of echinocytosis of the host-erythrocyte to occur during *P. falciparum* gametocyte egress in Chapter 6 of this thesis, which was not reported in a live-cell microscopy study of *P. berghei* gametocyte egress (Andreadaki et al., 2018). Although echinocytosis was not observed in all cases of parasite egress, the few instances point to a varied mechanism between species. Though these hypotheses may explain the inconsistencies in literature relative to our study, further structural investigation and elucidation of the impact to *P. berghei* is necessary.

Fundamentally, we found N-4HCS compounds interact with Pfs16 in *P. falciparum* gametocytes and exert potent inhibition of microgametogenesis within a six-minute active window. Though Pfs16 is not male-specific, it is well established that the mechanisms of gamete formation are hugely divergent between males and females (Sinden, 2009; Deligianni et al., 2011; Koning-Ward et al., 2008) and a sex-specific function of Pfs16 is highly probable. It has recently been reported that *P. falciparum* transmission was reduced in the presence of anti-Pfs16 polyclonal antibody, supporting Pfs16 as a viable target of both drug and vaccine-mediated malaria control (Niu et al., 2021). Transmission-blocking compounds are sought after, with various compounds being developed to address this (Ojo et al., 2014; Jennison et al., 2019). Our study describes Pfs16 as a potential transmission-blocking antimalarial-drug target using the N-4HCS compounds as a powerful tool to explore this for the first time.

7.2 Facilitation of transmission-blocking identification studies

Following development of the N-4HCS series, the study was concluded by defining the cellular phenotypes of alternative GHCDL-derived hits with varied activity profiles (Chapter 5). Elucidation of the phenotypic impact of these compounds may guide future investigation into their targets and modes of action, as demonstrated here with the study of N-4HCS compounds. Additionally, a live-cell fluorescence imaging platform was successfully developed and shown to be effective and repro-

ducible in drug phenotype characterisation studies, utilising CDPK4, PKG and proteasome inhibition as examples (Chapter 6). The framework was designed to be accessible to the wider malaria research community and, fundamentally, overcame the laborious fixed-cell protocols currently in place.

High-resolution imaging of live-cell *Plasmodium* development has been transformed by the advent of techniques such as lattice light-sheet (Geoghegan et al., 2021) and stimulated emission depletion (STED) microscopy (Schloetel et al., 2019). Furthermore, serial block-face scanning electron microscopy (SBF-SEM) was recently implemented in a study of the *P. falciparum* gametocyte inner membrane complex (IMC), combining super-resolution optical microscopy with 3D electron microscopy to study fixed cells (Parkyn Schneider et al., 2017). The costly and relatively inaccessible equipment required to perform these techniques limits their use in the wider research community. Additionally, the complex and lengthy protocols in place for fixed-cell studies limit the throughput required for drug discovery. Our widefield microscopy-based approach to live-cell imaging required minimal sample preparation, was amenable to high-throughput study and reproduced fixed-cell drug phenotypic characterisation studies. The combination of 3D and 2D live-cell fluorescence microscopy enabled us to capture microgametogenesis from early development through to late microgamete emergence. Most notably, we defined the proteasome as a viable target of transmission-blocking intervention for the first time, and found the proteasome-inhibitor, bortezomib, to demonstrate activity against microgamete formation. Given previous reports of bortezomib as a potent inhibitor of asexual development (Reynolds et al., 2007), we propose this drug is a desirable multi-stage inhibitor of *Plasmodium*.

7.3 Conclusions and future directions

Addressing the eradication agenda and increasing biological threats to malaria control, this thesis reported the identification of Pfs16 as a desirable target of *P. falciparum* transmission-blocking drug intervention and development of the N-4HCS series of compounds, viable antimalarial candidates to implement Pfs16-targeted

treatment. Combined biology, chemistry and chemical proteomics techniques were applied to establish the N-4HCS compounds as highly potent, parasite-specific and safe, poising them for further development and clinical testing. Further investigation into the Pfs16 structure and N-4HCS pharmacokinetic properties, impacts on other *Plasmodium* species and appropriate formulation and administration approaches are required to conclude drug development.

Uniquely targeting the development of microgametes in the mosquito midgut following gametocyte activation, the N-4HCS compounds present a novel avenue for treatment, which has otherwise been unexplored. Whilst more conventional approaches to transmission-blocking may be to sterilise the circulating mature gametocytes or sequestered immature gametocytes, these stages can be challenging to target with drug treatment. Targeting the stage V gametocytes, the transmissible stages of *Plasmodium*, would require optimal gametocytocidal drug concentrations to be exhibited with extreme longevity as infectious gametocytes can circulate for 20 days (Burrows et al., 2017). This is further complicated in drugs which require protracted compound-parasite exposure for effective inhibition of gametocyte viability. A multiple-dose regimen of highly stable compounds or intravenous administration may overcome this (Burrows et al., 2017). Alternatively targeting the earlier stages of gametocytes is challenged by the sequestration habits of these stages. Upon seeking treatment, infected patients may already contain gametocytes at any stage of maturation within their parasite reservoir, further complicating the approach to target commitment or early development.

To address these drawbacks of transmission-blocking, we have developed the N-4HCS compounds which distinctively prevent gametocyte viability beyond activation in the mosquito vector. Administration of N-4HCS compounds as drugs would require compound concentrations to be retained at a level which would be efficacious upon a mosquito bloodmeal (Burrows et al., 2017). Chemical development to increase compound half-lives or engineering compounds into nanoparticles for slow release (Kamaly et al., 2016) are feasible approaches to maximise longevity. An alternative approach has recently been explored in which antimalarial drugs are coupled to vector-targeted tools, such as bed nets and mosquito sugar baits (Paton

et al., 2019; Fiorenzano, Koehler, and Xue, 2017). Gaining a lot of traction in the malaria field, the study simulated the conditions of drug-impregnated mosquito bed nets using existing cytochrome *b*-targeted antimalarials (Paton et al., 2019). The study measured a potent block in *Plasmodium* development in the mosquito upon tarsal exposure (via the mosquito legs) to these antimalarials (Paton et al., 2019). N-4HCS compounds potently and immediately halt microgametogensis upon exposure to stage V gametocytes and are hence highly suited to bed net and bait-based delivery, a hypothesis we hope to test. Co-formulation of N-4HCS compounds with mosquito-targeted endectocides presents an innovative and desirable route to breaking the cycle of *Plasmodium* transmission, delivering our developed compounds as 'antimalarials for mosquitos'.

Collaboration and interdisciplinary science has been pivotal to combatting infectious diseases, with malaria and now, the ongoing COVID-19 pandemic, exemplifying this. Understanding the remarkable biology of the deadly *Plasmodium* parasite has enabled researchers to develop a plethora of translational tools to fight it. Here, at the interface of chemistry and biology, we have discovered and developed a safe, potent and unique transmission-blocking antimalarial candidate.

Bibliography

Abkarian, M. et al. (2011). "A novel mechanism for egress of malarial parasites from red blood cells". In: *Blood* 117.15, pp. 4118–24.

Adams, Julian et al. (1999). "Proteasome inhibitors: a novel class of potent and effective antitumor agents". In: *Cancer Research* 59.11, pp. 2615–2622.

Adjalley, Sophie H. et al. (2011). "Quantitative assessment of *Plasmodium falciparum* sexual development reveals potent transmission-blocking activity by methylene blue". In: *Proceedings of the National Academy of Sciences* 108.47, E1214.

Aikawa, M. et al. (1984). "New observations on gametogenesis, fertilization, and zygote transformation in *Plasmodium gallinaceum*". In: *J Protozool* 31.3, pp. 403–13.

Aingaran, M. et al. (2012). "Host cell deformability is linked to transmission in the human malaria parasite *Plasmodium falciparum*". In: *Cell Microbiol* 14.7, pp. 983–93.

Alano, P. et al. (1995). "*Plasmodium falciparum*: parasites defective in early stages of gametocytogenesis". In: *Exp Parasitol* 81.2, pp. 227–35.

Almela, Maria Jesus et al. (2015). "A new set of chemical starting points with *Plasmodium falciparum* transmission-blocking potential for antimalarial drug discovery". In: *PLOS ONE* 10.8, e0135139.

Amato, R. et al. (2017). "Genetic markers associated with dihydroartemisinin-piperaquine failure in *Plasmodium falciparum* malaria in Cambodia: a genotype-phenotype association study". In: *Lancet Infect Dis* 17.2, pp. 164–173.

Amino, R. et al. (2006). "Quantitative imaging of *Plasmodium* transmission from mosquito to mammal". In: *Nat Med* 12.2, pp. 220–4.

Andreadaki, Maria et al. (2018). "Sequential membrane rupture and vesiculation during *Plasmodium berghei* gametocyte egress from the red blood cell". In: *Scientific Reports* 8.1, p. 3543.

Angrisano, F. et al. (2012). "Malaria parasite colonisation of the mosquito midgut–placing the *Plasmodium* ookinete centre stage". In: *Int J Parasitol* 42.6, pp. 519–27.

Antonova-Koch, Yevgeniya et al. (2018). "Open-source discovery of chemical leads for next-generation chemoprotective antimalarials". In: *Science* 362.6419, eaat9446.

Ariey, F. et al. (2014). "A molecular marker of artemisinin-resistant *Plasmodium falciparum* malaria". In: *Nature* 505.7481, pp. 50–5.

Ashdown, G. W. et al. (2020). "A machine learning approach to define antimalarial drug action from heterogeneous cell-based screens". In: *Sci Adv* 6.39.

Ashley, Elizabeth A., Aung Pyae Phyo, and Charles J. Woodrow (2018). "Malaria". In: *The Lancet* 391.10130, pp. 1608–1621.

Auparakkitanon, S. and P. Wilairat (2006). "Antimalarial activity of concanamycin A alone and in combination with pyronaridine". In: *Southeast Asian J Trop Med Public Health* 37.4, pp. 619–21.

Avery, Vicky M. et al. (2014). "Screening and hit evaluation of a chemical library against blood-stage *Plasmodium falciparum*". In: *Malaria Journal* 13.1, p. 190.

Baer, Kerstin et al. (2007). "Release of hepatic *Plasmodium yoelii* merozoites into the pulmonary microvasculature". In: *PLOS Pathogens* 3.11, e171.

Baker, D. A. et al. (1994). "Subcellular localization of Pfs16, a *Plasmodium falciparum* gametocyte antigen". In: *Parasitology* 108.2, pp. 129–137.

Baker, David A. et al. (2017). "A potent series targeting the malarial cGMP-dependent protein kinase clears infection and blocks transmission". In: *Nature Communications* 8.1, p. 430.

Balestra, Aurélia C. et al. (2021). "Ca^{2+} signals critical for egress and gametogenesis in malaria parasites depend on a multipass membrane protein that interacts with PKG". In: *Science Advances* 7.13, eabe5396.

Bancells, C. et al. (2019). "Revisiting the initial steps of sexual development in the malaria parasite *Plasmodium falciparum*". In: *Nat Microbiol* 4.1, pp. 144–154.

Bargieri, Daniel Y. et al. (2016). "*Plasmodium* merozoite TRAP family protein is essential for vacuole membrane disruption and gamete egress from erythrocytes". In: *Cell Host & Microbe* 20.5, pp. 618–630.

Baruch, D. I. et al. (1995). "Cloning the *P. falciparum* gene encoding PfEMP1, a malarial variant antigen and adherence receptor on the surface of parasitized human erythrocytes". In: *Cell* 82.1, pp. 77–87.

Baton, Luke A. and Lisa C. Ranford-Cartwright (2005). "Spreading the seeds of million-murdering death*: metamorphoses of malaria in the mosquito". In: *Trends in Parasitology* 21.12, pp. 573–580.

Baum, J. et al. (2008a). "Host-cell invasion by malaria parasites: insights from *Plasmodium* and *Toxoplasma*". In: *Trends Parasitol* 24.12, pp. 557–63.

Baum, Jake et al. (2006a). "A conserved molecular motor drives cell invasion and gliding motility across malaria life cycle stages and other apicomplexan parasites *". In: *Journal of Biological Chemistry* 281.8, pp. 5197–5208.

Baum, Jake et al. (2006b). "Regulation of apicomplexan actin-based motility". In: *Nature Reviews Microbiology* 4.8, pp. 621–628.

Baum, Jake et al. (2008b). "A malaria parasite formin regulates actin polymerization and localizes to the parasite-erythrocyte moving junction during invasion". In: *Cell Host & Microbe* 3.3, pp. 188–198.

Bechtsi, D. P. and A. P. Waters (2017). "Genomics and epigenetics of sexual commitment in *Plasmodium*". In: *International Journal for Parasitology* 47.7, pp. 425–434.

Bennink, Sandra, Meike J. Kiesow, and Gabriele Pradel (2016). "The development of malaria parasites in the mosquito midgut". In: *Cellular Microbiology* 18.7, pp. 905–918.

Bertiaux, E. et al. (2021). "Expansion microscopy provides new insights into the cytoskeleton of malaria parasites including the conservation of a conoid". In: *PLoS Biol* 19.3, e3001020.

Bhatt, S. et al. (2015). "The effect of malaria control on *Plasmodium falciparum* in Africa between 2000 and 2015". In: *Nature* 526.7572, pp. 207–211.

Billker, O. et al. (1997). "The roles of temperature, pH and mosquito factors as triggers of male and female gametogenesis of *Plasmodium berghei in vitro*". In: *Parasitology* 115 (Pt 1), pp. 1–7.

Billker, O. et al. (1998). "Identification of xanthurenic acid as the putative inducer of malaria development in the mosquito". In: *Nature* 392.6673, pp. 289–292.

Billker, O. et al. (2002). "Azadirachtin disrupts formation of organised microtubule arrays during microgametogenesis of *Plasmodium berghei*". In: *J Eukaryot Microbiol* 49.6, pp. 489–97.

Billker, Oliver et al. (2004). "Calcium and a calcium-dependent protein kinase regulate gamete formation and mosquito transmission in a malaria parasite". In: *Cell* 117.4, pp. 503–514.

Birnbaum, Jakob et al. (2020). "A Kelch13-defined endocytosis pathway mediates artemisinin resistance in malaria parasites". In: *Science* 367.6473, p. 51.

Blake, Thomas C. A., Silvia Haase, and Jake Baum (2020). "Actomyosin forces and the energetics of red blood cell invasion by the malaria parasite *Plasmodium falciparum*". In: *PLOS Pathogens* 16.10, e1009007.

Brancucci, N. M. B. et al. (2014). "Heterochromatin protein 1 secures survival and transmission of malaria parasites". In: *Cell Host Microbe* 16.2, pp. 165–176.

Brancucci, Nicolas M. B. et al. (2015). "An assay to probe *Plasmodium falciparum* growth, transmission stage formation and early gametocyte development". In: *Nature Protocols* 10.8, pp. 1131–1142.

Brancucci, Nicolas M. B. et al. (2017). "Lysophosphatidylcholine regulates sexual stage differentiation in the human malaria parasite *Plasmodium falciparum*". In: *Cell* 171.7, 1532–1544.e15.

Bray, P. G., R. E. Howells, and S. A. Ward (1992). "Vacuolar acidification and chloroquine sensitivity in *Plasmodium falciparum*". In: *Biochem Pharmacol* 43.6, pp. 1219–27.

Bray, R. S. (1956). "Studies on malaria in chimpanzees. I. The erythrocytic forms of *Plasmodium reichenowi*". In: *J Parasitol* 42.6, pp. 588–92.

Brochet, M. et al. (2014). "Phosphoinositide metabolism links cGMP-dependent protein kinase G to essential Ca^{2+} signals at key decision points in the life cycle of malaria parasites". In: *PLoS Biol* 12.3, e1001806.

Brock, P. M. et al. (2016). "*Plasmodium knowlesi* transmission: integrating quantitative approaches from epidemiology and ecology to understand malaria as a zoonosis". In: *Parasitology* 143.4, pp. 389–400.

Broncel, Malgorzata et al. (2015). "Multifunctional reagents for quantitative proteome-wide analysis of protein modification in human cells and dynamic profiling of protein lipidation during vertebrate development". In: *Angewandte Chemie (International ed. in English)* 54.20, pp. 5948–5951.

Bruce, M. C. et al. (1990). "Commitment of the malaria parasite *Plasmodium falciparum* to sexual and asexual development". In: *Parasitology* 100 Pt 2, pp. 191–200.

Bruce, M. C. et al. (1994). "Cellular location and temporal expression of the *Plasmodium falciparum* sexual stage antigen Pfs16". In: *Mol Biochem Parasitol* 65.1, pp. 11–22.

Buchholz, Kathrin et al. (2011). "A high-throughput screen targeting malaria transmission stages opens new avenues for drug development". In: *The Journal of Infectious Diseases* 203.10, pp. 1445–1453.

Burrows, Jeremy N. et al. (2013). "Designing the next generation of medicines for malaria control and eradication". In: *Malaria Journal* 12.1, p. 187.

Burrows, Jeremy N. et al. (2017). "New developments in anti-malarial target candidate and product profiles". In: *Malaria Journal* 16.1, p. 26.

Chaumont, F. de et al. (2012). "Icy: an open bioimage informatics platform for extended reproducible research". In: *Nat Methods* 9.7, pp. 690–6.

Chen, D. et al. (2011). "Bortezomib as the first proteasome inhibitor anticancer drug: current status and future perspectives". In: *Curr Cancer Drug Targets* 11.3, pp. 239–53.

Chin, William et al. (1965). "A naturally acquired quotidian-type malaria in man transferable to monkeys". In: *Science* 149.3686, p. 865.

Churcher, Thomas S. et al. (2012). "Measuring the blockade of malaria transmission – an analysis of the standard membrane feeding assay". In: *International Journal for Parasitology* 42.11, pp. 1037–1044.

Clark, Ian A. and Lisa M. Alleva (2009). "Is human malarial coma caused, or merely deepened, by sequestration?" In: *Trends in Parasitology* 25.7, pp. 314–318.

Coleman, Bradley I. et al. (2014). "A *Plasmodium falciparum* histone deacetylase regulates antigenic variation and gametocyte conversion". In: *Cell Host & Microbe* 16.2, pp. 177–186.

Collins, Christine R. et al. (2013). "Malaria parasite cGMP-dependent protein kinase regulates blood stage merozoite secretory organelle discharge and egress". In: *PLOS Pathogens* 9.5, e1003344.

Cowman, Alan F., Drew Berry, and Jake Baum (2012). "The cellular and molecular basis for malaria parasite invasion of the human red blood cell". In: *Journal of Cell Biology* 198.6, pp. 961–971.

Cowman, Alan F. et al. (2016). "Malaria: biology and disease". In: *Cell* 167.3, pp. 610–624.

Cowman, Alan F. et al. (2017). "The molecular basis of erythrocyte invasion by malaria parasites". In: *Cell Host & Microbe* 22.2, pp. 232–245.

Cox, J. and M. Mann (2008). "MaxQuant enables high peptide identification rates, individualized p.p.b.-range mass accuracies and proteome-wide protein quantification". In: *Nat Biotechnol* 26.12, pp. 1367–72.

Crowther, Gregory J. et al. (2016). "Biochemical screening of five protein kinases from *Plasmodium falciparum* against 14,000 cell-active compounds". In: *PLOS ONE* 11.3, e0149996.

Cruz, Filipa P. da et al. (2012). "Drug screen targeted at *Plasmodium* liver stages identifies a potent multistage antimalarial drug". In: *The Journal of Infectious Diseases* 205.8, pp. 1278–1286.

D'Alessandro, Sarah et al. (2013). "A *Plasmodium falciparum* screening assay for anti-gametocyte drugs based on parasite lactate dehydrogenase detection". In: *Journal of Antimicrobial Chemotherapy* 68.9, pp. 2048–2058.

Das, S. et al. (2015). "Processing of *Plasmodium falciparum* merozoite surface protein MSP1 activates a spectrin-binding function enabling parasite egress from RBCs". In: *Cell Host Microbe* 18.4, pp. 433–44.

Dasgupta, Sabyasachi et al. (2014). "Membrane-wrapping contributions to malaria parasite invasion of the human erythrocyte". In: *Biophysical Journal* 107.1, pp. 43–54.

Davidson, Mira S. et al. (2021). "Automated detection and staging of malaria parasites from cytological smears using convolutional neural networks". In: *Biological Imaging*, pp. 1–22.

Davies, C. S. et al. (1989). "The causal prophylactic activity of the novel hydroxynaphthoquinone 566C80 against *Plasmodium berghei* infections in rats". In: *Acta Leidensia* 58.2, pp. 115–128.

Day, K. P. et al. (1998). "CD36-dependent adhesion and knob expression of the transmission stages of *Plasmodium falciparum* is stage specific". In: *Mol Biochem Parasitol* 93.2, pp. 167–77.

Dearnley, Megan K. et al. (2012). "Origin, composition, organization and function of the inner membrane complex of *Plasmodium falciparum* gametocytes". In: *Journal of Cell Science* 125.8, pp. 2053–2063.

Dechering, Koen J. et al. (1997). "Developmentally regulated expression of Pfs16, a marker for sexual differentiation of the human malaria parasite *Plasmodium falciparum*". In: *Molecular and Biochemical Parasitology* 89.2, pp. 235–244.

Deligianni, E. et al. (2013). "A perforin-like protein mediates disruption of the erythrocyte membrane during egress of *Plasmodium berghei* male gametocytes". In: *Cell Microbiol* 15.8, pp. 1438–55.

Deligianni, Elena et al. (2011). "Critical role for a stage-specific actin in male exflagellation of the malaria parasite". In: *Cellular Microbiology* 13.11, pp. 1714–1730.

Deligianni, Elena et al. (2018). "Sequence and functional divergence of gametocyte-specific parasitophorous vacuole membrane proteins in *Plasmodium* parasites". In: *Molecular and Biochemical Parasitology* 220, pp. 15–18.

Delves, M. J., F. Angrisano, and A. M. Blagborough (2018). "Antimalarial transmission-blocking interventions: past, present, and future". In: *Trends in Parasitology* 34.9, pp. 735–746.

Delves, M. J. et al. (2012a). "A high-throughput assay for the identification of malarial transmission-blocking drugs and vaccines". In: *Int J Parasitol* 42.11, pp. 999–1006.

Delves, Michael et al. (2012b). "The activities of current antimalarial drugs on the life cycle stages of *Plasmodium*: a comparative study with human and rodent parasites". In: *PLOS Medicine* 9.2, e1001169.

Delves, Michael et al. (2019). "Fueling open innovation for malaria transmission-blocking drugs: hundreds of molecules targeting early parasite mosquito stages". In: *Frontiers in Microbiology* 10, p. 2134.

Delves, Michael J. and Robert E. Sinden (2010). "A semi-automated method for counting fluorescent malaria oocysts increases the throughput of transmission blocking studies". In: *Malaria journal* 9, pp. 35–35.

Delves, Michael J. et al. (2013). "Male and female *Plasmodium falciparum* mature gametocytes show different responses to antimalarial drugs". In: *Antimicrobial agents and chemotherapy* 57.7, pp. 3268–3274.

Delves, Michael J. et al. (2016). "Routine in vitro culture of *P. falciparum* gametocytes to evaluate novel transmission-blocking interventions". In: *Nature Protocols* 11.9, pp. 1668–1680.

Delves, Michael J. et al. (2018). "A high throughput screen for next-generation leads targeting malaria parasite transmission". In: *Nature Communications* 9.1, p. 3805.

Dembele, Laurent et al. (2011). "Towards an *in vitro* model of *Plasmodium* hypnozoites suitable for drug discovery". In: *PLOS ONE* 6.3, e18162.

Dembélé, Laurent et al. (2014). "Persistence and activation of malaria hypnozoites in long-term primary hepatocyte cultures". In: *Nature Medicine* 20.3, pp. 307–312.

Dixon, Matthew W. A. and Leann Tilley (2021). "*Plasmodium falciparum* goes bananas for sex". In: *Molecular and Biochemical Parasitology* 244, p. 111385.

Dixon, Matthew W. A. et al. (2012). "Shape-shifting gametocytes: how and why does *P. falciparum* go banana-shaped?" In: *Trends in Parasitology* 28.11, pp. 471–478.

Doggett, J. S. et al. (2014). "Bumped kinase inhibitor 1294 treats established *Toxoplasma gondii* infection". In: *Antimicrob Agents Chemother* 58.6, pp. 3547–9.

Dondorp, Arjen M. et al. (2008). "The relationship between age and the manifestations of and mortality associated with severe malaria". In: *Clinical Infectious Diseases* 47.2, pp. 151–157.

Dos Santos Pacheco, Nicolas et al. (2020). "Evolution, composition, assembly, and function of the conoid in apicomplexa". In: *Trends in Parasitology* 36.8, pp. 688–704.

Drugs, The malERA Consultative Group on (2011). "A research agenda for malaria eradication: Drugs". In: *PLOS Medicine* 8.1, e1000402.

Dubois, Joëlle et al. (1995). "Fluorescent and biotinylated analogues of docetaxel: Synthesis and biological evaluation". In: *Bioorganic & Medicinal Chemistry* 3.10, pp. 1357–1368.

Dufe, V. T. et al. (2007). "Crystal structure of *Plasmodium falciparum* spermidine synthase in complex with the substrate decarboxylated S-adenosylmethionine and the potent inhibitors 4MCHA and AdoDATO". In: *J Mol Biol* 373.1, pp. 167–77.

Duffey, Maëlle et al. (2021). "Assessing risks of *Plasmodium falciparum* resistance to select next-generation antimalarials". In: *Trends in Parasitology* 37.8, pp. 709–721.

Duffy, Patrick E. and J. Patrick Gorres (2020). "Malaria vaccines since 2000: progress, priorities, products". In: *npj Vaccines* 5.1, p. 48.

Duffy, Sandra and Vicky M. Avery (2013). "Identification of inhibitors of *Plasmodium falciparum* gametocyte development". In: *Malaria journal* 12, pp. 408–408.

Duffy, Sandra et al. (2016). "Large-scale production of *Plasmodium falciparum* gametocytes for malaria drug discovery". In: *Nature Protocols* 11.5, pp. 976–992.

Dvorak, J. A. et al. (1975). "Invasion of erythrocytes by malaria merozoites". In: *Science* 187.4178, pp. 748–50.

Dvorin, Jeffrey D. et al. (2010). "A plant-like kinase in *Plasmodium falciparum* regulates parasite egress from erythrocytes". In: *Science* 328.5980, p. 910.

Dykes, Cherry L. et al. (2015). "Knockdown resistance (kdr) mutations in Indian Anopheles culicifacies populations". In: *Parasites & Vectors* 8.1, p. 333.

Dziekan, J. M. et al. (2019). "Identifying purine nucleoside phosphorylase as the target of quinine using cellular thermal shift assay". In: *Sci Transl Med* 11.473.

Dziekan, J. M. et al. (2020). "Cellular thermal shift assay for the identification of drug-target interactions in the *Plasmodium falciparum* proteome". In: *Nat Protoc.*

Eksi, S. and K. C. Williamson (2011). "Protein targeting to the parasitophorous vacuole membrane of *Plasmodium falciparum*". In: *Eukaryot Cell* 10.6, pp. 744–52.

Eksi, S. et al. (2005). "Identification of a subtelomeric gene family expressed during the asexual-sexual stage transition in *Plasmodium falciparum*". In: *Mol Biochem Parasitol* 143.1, pp. 90–9.

Eksi, S. et al. (2012). "*Plasmodium falciparum* gametocyte development 1 (Pfgdv1) and gametocytogenesis early gene identification and commitment to sexual development". In: *PLoS Pathog* 8.10, e1002964.

Fang, Hanwei et al. (2017). "Multiple short windows of calcium-dependent protein kinase 4 activity coordinate distinct cell cycle events during *Plasmodium* gametogenesis". In: *eLife* 6, e26524.

Faust, Christina and Andrew P. Dobson (2015). "Primate malarias: Diversity, distribution and insights for zoonotic *Plasmodium*". In: *One Health* 1, pp. 66–75.

Filarsky, M. et al. (2018). "GDV1 induces sexual commitment of malaria parasites by antagonizing HP1-dependent gene silencing". In: *Science* 359.6381, pp. 1259–1263.

Fiorenzano, J. M., P. G. Koehler, and R. D. Xue (2017). "Attractive toxic sugar bait (ATSB) for control of mosquitoes and its impact on non-target organisms: a review". In: *Int J Environ Res Public Health* 14.4.

Flannery, Erika L., Arnab K. Chatterjee, and Elizabeth A. Winzeler (2013). "Antimalarial drug discovery — approaches and progress towards new medicines". In: *Nature Reviews Microbiology* 11.12, pp. 849–862.

Florens, Laurence et al. (2002). "A proteomic view of the *Plasmodium falciparum* life cycle". In: *Nature* 419.6906, pp. 520–526.

Fong, Y. L., F. C. Cadigan, and G. R. Coatney (1971). "A presumptive case of naturally occurring *Plasmodium knowlesi* malaria in man in Malaysia". In: *Trans R Soc Trop Med Hyg* 65.6, pp. 839–40.

Frampton, J. E. (2018). "Tafenoquine: first global approval". In: *Drugs* 78.14, pp. 1517–1523.

Francia, Maria E. and Boris Striepen (2014). "Cell division in apicomplexan parasites". In: *Nature Reviews Microbiology* 12.2, pp. 125–136.

Frevert, U. et al. (2006). "Nomadic or sessile: can Kupffer cells function as portals for malaria sporozoites to the liver?" In: *Cell Microbiol* 8.10, pp. 1537–46.

Frischknecht, F. and K. Matuschewski (2017). "*Plasmodium* sporozoite biology". In: *Cold Spring Harb Perspect Med* 7.5.

Frénal, Karine et al. (2017). "Gliding motility powers invasion and egress in Apicomplexa". In: *Nature Reviews Microbiology* 15.11, pp. 645–660.

Fu, X. et al. (2016). "Ubiquitin-like proteasome system represents a eukaryotic-like pathway for targeted proteolysis in archaea". In: *mBio* 7.3.

Gamboa, D. et al. (2010). "A large proportion of *P. falciparum* isolates in the Amazon region of Peru lack pfhrp2 and pfhrp3: implications for malaria rapid diagnostic tests". In: *PLoS One* 5.1, e8091.

Gamo, Francisco-Javier et al. (2010). "Thousands of chemical starting points for antimalarial lead identification". In: *Nature* 465.7296, pp. 305–310.

Gass, R. F. (1979). "The ultrastructure of cultured *Plasmodium gallinaceum* ookinetes: a comparison of intact stages with forms damaged by extracts from blood fed, susceptible *Aedes aegypti*". In: *Acta Trop* 36.4, pp. 323–34.

Gaulton, Anna et al. (2017). "The ChEMBL database in 2017". In: *Nucleic Acids Research* 45.D1, pp. D945–D954.

Gautret, P. and A. Motard (1999). "Periodic infectivity of *Plasmodium* gametocytes to the vector. A review". In: *Parasite* 6.2, pp. 103–111.

Geoghegan, Niall D. et al. (2021). "4D analysis of malaria parasite invasion offers insights into erythrocyte membrane remodeling and parasitophorous vacuole formation". In: *Nature Communications* 12.1, p. 3620.

Gething, Peter W. et al. (2016). "Mapping *Plasmodium falciparum* mortality in Africa between 1990 and 2015". In: *New England Journal of Medicine* 375.25, pp. 2435–2445.

Gilson, P. R. and B. S. Crabb (2009). "Morphology and kinetics of the three distinct phases of red blood cell invasion by *Plasmodium falciparum* merozoites". In: *Int J Parasitol* 39.1, pp. 91–6.

Glushakova, S. et al. (2005). "Membrane transformation during malaria parasite release from human red blood cells". In: *Curr Biol* 15.18, pp. 1645–50.

Gomez-Lorenzo, Maria G. et al. (2018). "Functional screening of selective mitochondrial inhibitors of *Plasmodium*". In: *International Journal for Parasitology: Drugs and Drug Resistance* 8.2, pp. 295–303.

Goodman, C. D. et al. (2016). "Parasites resistant to the antimalarial atovaquone fail to transmit by mosquitoes". In: *Science* 352.6283, pp. 349–53.

Graumans, W. et al. (2020). "When is a *Plasmodium*-infected mosquito an infectious mosquito?" In: *Trends Parasitol* 36.8, pp. 705–716.

Guerreiro, Ana et al. (2014). "Genome-wide RIP-Chip analysis of translational repressor-bound mRNAs in the *Plasmodium* gametocyte". In: *Genome biology* 15.11, pp. 493–493.

Guiguemde, W. Armand et al. (2010). "Chemical genetics of *Plasmodium falciparum*". In: *Nature* 465.7296, pp. 311–315.

Guttery, David S. et al. (2015). "Commit and transmit: molecular players in *Plasmodium* sexual development and zygote differentiation". In: *Trends in Parasitology* 31.12, pp. 676–685.

Haider, N. et al. (2005). "The spermidine synthase of the malaria parasite *Plasmodium falciparum*: molecular and biochemical characterisation of the polyamine synthesis enzyme". In: *Mol Biochem Parasitol* 142.2, pp. 224–36.

Hale, Victoria L. et al. (2017). "Parasitophorous vacuole poration precedes its rupture and rapid host erythrocyte cytoskeleton collapse in *Plasmodium falciparum* egress". In: *Proceedings of the National Academy of Sciences of the United States of America* 114.13, pp. 3439–3444.

Hanssen, Eric et al. (2012). "Soft X-ray microscopy analysis of cell volume and hemoglobin content in erythrocytes infected with asexual and sexual stages of *Plasmodium falciparum*". In: *Journal of Structural Biology* 177.2, pp. 224–232.

Harvey, Katherine L., Paul R. Gilson, and Brendan S. Crabb (2012). "A model for the progression of receptor–ligand interactions during erythrocyte invasion by *Plasmodium falciparum*". In: *International Journal for Parasitology* 42.6, pp. 567–573.

Hayashi, M. et al. (2000). "Vacuolar H(+)-ATPase localized in plasma membranes of malaria parasite cells, *Plasmodium falciparum*, is involved in regional acidification of parasitized erythrocytes". In: *J Biol Chem* 275.44, pp. 34353–8.

Hliscs, Marion et al. (2015). "Organization and function of an actin cytoskeleton in *Plasmodium falciparum* gametocytes". In: *Cellular Microbiology* 17.2, pp. 207–225.

Howick, Virginia M. et al. (2019). "The malaria cell atlas: Single parasite transcriptomes across the complete *Plasmodium* life cycle". In: *Science* 365.6455, eaaw2619.

Ingmundson, Alyssa et al. (2014). "Feeling at home from arrival to departure: protein export and host cell remodelling during *Plasmodium* liver stage and gametocyte maturation". In: *Cellular Microbiology* 16.3, pp. 324–333.

Ishino, T. et al. (2020). "Observation of morphological changes of female osmiophilic bodies prior to *Plasmodium* gametocyte egress from erythrocytes". In: *Mol Biochem Parasitol* 236, p. 111261.

Ismail, H. M. et al. (2016). "Artemisinin activity-based probes identify multiple molecular targets within the asexual stage of the malaria parasites *Plasmodium falciparum* 3D7". In: *Proc Natl Acad Sci U S A* 113.8, pp. 2080–5.

Jafari, Rozbeh et al. (2014). "The cellular thermal shift assay for evaluating drug target interactions in cells". In: *Nature Protocols* 9.9, pp. 2100–2122.

Janse, C. J. et al. (1988). "DNA synthesis in gametocytes of *Plasmodium falciparum*". In: *Parasitology* 96.1, pp. 1–7.

Jennison, Charlie et al. (2019). "Inhibition of plasmepsin v activity blocks *Plasmodium falciparum* gametocytogenesis and transmission to mosquitoes". In: *Cell Reports* 29.12, 3796–3806.e4.

Josling, Gabrielle A. and Manuel Llinás (2015). "Sexual development in *Plasmodium* parasites: knowing when it's time to commit". In: *Nature Reviews Microbiology* 13.9, pp. 573–587.

Josling, Gabrielle A., Kim C. Williamson, and Manuel Llinás (2018). "Regulation of sexual commitment and gametocytogenesis in malaria parasites". In: *Annual Review of Microbiology* 72.1, pp. 501–519.

Josling, Gabrielle A. et al. (2020). "Dissecting the role of PfAP2-G in malaria gametocytogenesis". In: *Nature Communications* 11.1, p. 1503.

Kafsack, Björn F. C. et al. (2014). "A transcriptional switch underlies commitment to sexual development in malaria parasites". In: *Nature* 507.7491, pp. 248–252.

Kamaly, N. et al. (2016). "Degradable controlled-release polymers and polymeric nanoparticles: mechanisms of controlling drug release". In: *Chem Rev* 116.4, pp. 2602–63.

Kaur, Kirandeep et al. (2010). "Quinolines and structurally related heterocycles as antimalarials". In: *European Journal of Medicinal Chemistry* 45.8, pp. 3245–3264.

Kehrer, Jessica, Friedrich Frischknecht, and Gunnar R. Mair (2016). "Proteomic analysis of the *Plasmodium berghei* gametocyte egressome and vesicular bioID of osmiophilic body proteins identifies merozoite TRAP-like protein (MTRAP) as an essential factor for parasite transmission". In: *Molecular & cellular proteomics : MCP* 15.9, pp. 2852–2862.

Khan, Shahid M. et al. (2005). "Proteome analysis of separated male and female gametocytes reveals novel sex-specific *Plasmodium* biology". In: *Cell* 121.5, pp. 675–687.

Kongkasuriyachai, D., H. Fujioka, and N. Kumar (2004). "Functional analysis of *Plasmodium falciparum* parasitophorous vacuole membrane protein (Pfs16) during gametocytogenesis and gametogenesis by targeted gene disruption". In: *Mol Biochem Parasitol* 133.2, pp. 275–85.

Koning-Ward, T. F. de et al. (2008). "The role of osmiophilic bodies and Pfg377 expression in female gametocyte emergence and mosquito infectivity in the human malaria parasite *Plasmodium falciparum*". In: *Mol Microbiol* 67.2, pp. 278–90.

Kono, Maya et al. (2012). "Evolution and architecture of the inner membrane complex in asexual and sexual stages of the malaria parasite". In: *Molecular Biology and Evolution* 29.9, pp. 2113–2132.

Krettli, A. U. and L. A. Dantas (2000). "Which routes do *Plasmodium* sporozoites use for successful infections of vertebrates?" In: *Infect Immun* 68.5, pp. 3064–5.

Kulak, N. A. et al. (2014). "Minimal, encapsulated proteomic-sample processing applied to copy-number estimation in eukaryotic cells". In: *Nat Methods* 11.3, pp. 319–24.

Lage, Olga Maria et al. (2018). "Current screening methodologies in drug discovery for selected human diseases". In: *Marine drugs* 16.8, p. 279.

Lanfrancotti, Alessandra et al. (2007). "*Plasmodium falciparum*: mRNA co-expression and protein co-localisation of two gene products upregulated in early gametocytes". In: *Experimental parasitology* 116.4, pp. 497–503.

Lasonder, Edwin et al. (2002). "Analysis of the *Plasmodium falciparum* proteome by high-accuracy mass spectrometry". In: *Nature* 419.6906, pp. 537–542.

Lasonder, Edwin et al. (2016). "Integrated transcriptomic and proteomic analyses of *P. falciparum* gametocytes: molecular insight into sex-specific processes and translational repression". In: *Nucleic Acids Research* 44.13, pp. 6087–6101.

Leba, Louis-Jérôme et al. (2015). "Use of *Plasmodium falciparum* culture-adapted field isolates for *in vitro* exflagellation-blocking assay". In: *Malaria journal* 14, pp. 234–234.

Lee, K. S. et al. (2009). "*Plasmodium knowlesi* from archival blood films: further evidence that human infections are widely distributed and not newly emergent in Malaysian Borneo". In: *Int J Parasitol* 39.10, pp. 1125–8.

Lee, S. J. et al. (2017). "Adverse effects of mefloquine for the treatment of uncomplicated malaria in Thailand: A pooled analysis of 19, 850 individual patients". In: *PLoS One* 12.2, e0168780.

Lelièvre, Joël et al. (2012). "Activity of clinically relevant antimalarial drugs on *Plasmodium falciparum* mature gametocytes in an ATP bioluminescence "transmission blocking" assay". In: *PLOS ONE* 7.4, e35019.

Leroy, Didier et al. (2014). "Defining the biology component of the drug discovery strategy for malaria eradication". In: *Trends in Parasitology* 30.10, pp. 478–490.

Li, H. et al. (2016). "Structure- and function-based design of *Plasmodium*-selective proteasome inhibitors". In: *Nature* 530.7589, pp. 233–6.

Lim, Caeul et al. (2016). "Reticulocyte preference and stage development of *Plasmodium vivax* isolates". In: *The Journal of Infectious Diseases* 214.7, pp. 1081–1084.

Lisewski, A. M. et al. (2014). "Supergenomic network compression and the discovery of EXP1 as a glutathione transferase inhibited by artesunate". In: *Cell* 158.4, pp. 916–928.

Liu, Weimin et al. (2010). "Origin of the human malaria parasite *Plasmodium falciparum* in gorillas". In: *Nature* 467.7314, pp. 420–425.

Lopez-Rubio, Jose-Juan, Liliana Mancio-Silva, and Artur Scherf (2009). "Genome-wide analysis of heterochromatin associates clonally variant gene regulation with perinuclear repressive centers in malaria parasites". In: *Cell Host & Microbe* 5.2, pp. 179–190.

Lucantoni, Leonardo et al. (2015). "A simple and predictive phenotypic high content imaging assay for *Plasmodium falciparum* mature gametocytes to identify malaria transmission blocking compounds". In: *Scientific Reports* 5.1, p. 16414.

Luth, Madeline R. et al. (2018). "Using *in vitro* evolution and whole genome analysis to discover next generation targets for antimalarial drug discovery". In: *ACS Infectious Diseases* 4.3, pp. 301–314.

Mair, Gunnar R. et al. (2010). "Universal features of post-transcriptional gene regulation are critical for *Plasmodium* zygote development". In: *PLoS pathogens* 6.2, e1000767–e1000767.

Martin, S. K., M. Jett, and I. Schneider (1994). "Correlation of phosphoinositide hydrolysis with exflagellation in the malaria microgametocyte". In: *The Journal of parasitology* 80.3, pp. 371–378.

Martinez Molina, D. et al. (2013). "Monitoring drug target engagement in cells and tissues using the cellular thermal shift assay". In: *Science* 341.6141, pp. 84–7.

Mbengue, A. et al. (2015). "A molecular mechanism of artemisinin resistance in *Plasmodium falciparum* malaria". In: *Nature* 520.7549, pp. 683–7.

McRobert, Louisa et al. (2004). "Distinct trafficking and localization of STEVOR proteins in three stages of the *Plasmodium falciparum* life cycle". In: *Infection and Immunity* 72.11, pp. 6597–6602.

McRobert, Louisa et al. (2008). "Gametogenesis in malaria parasites is mediated by the cGMP-dependent protein kinase". In: *PLOS Biology* 6.6, e139.

Meister, Stephan et al. (2011). "Imaging of *Plasmodium* liver stages to drive next-generation antimalarial drug discovery". In: *Science* 334.6061, p. 1372.

Miao, Jun et al. (2013). "Puf mediates translation repression of transmission-blocking vaccine candidates in malaria parasites". In: *PLOS Pathogens* 9.4, e1003268.

Miguel-Blanco, Celia et al. (2017). "Hundreds of dual-stage antimalarial molecules discovered by a functional gametocyte screen". In: *Nature Communications* 8.1, p. 15160.

Moelans, Inge Irma Maria Dominique (1995). *Pfs16, a potential vaccine candidate against the human malaria parasite* Plasmodium falciparum. [Sl: sn].

Monerri, N. C. Silmon de et al. (2011). "Global identification of multiple substrates for *Plasmodium falciparum* SUB1, an essential malarial processing protease". In: *Infect Immun* 79.3, pp. 1086–97.

Morrissette Naomi, S. and L. David Sibley (2002). "Cytoskeleton of Apicomplexan Parasites". In: *Microbiology and molecular biology reviews* 66.1, pp. 21–38.

Mota, Maria M. et al. (2001). "Migration of *Plasmodium* sporozoites through cells before infection". In: *Science* 291.5501, p. 141.

Muhia, David K. et al. (2001). "The gametocyte-activating factor xanthurenic acid stimulates an increase in membrane-associated guanylyl cyclase activity in the human malaria parasite *Plasmodium falciparum*". In: *Molecular Microbiology* 42.2, pp. 553–560.

Naissant, Bernina et al. (2016). "*Plasmodium falciparum* STEVOR phosphorylation regulates host erythrocyte deformability enabling malaria parasite transmission". In: *Blood* 127.24, e42–e53.

Ngotho, Priscilla et al. (2019). "Revisiting gametocyte biology in malaria parasites". In: *FEMS Microbiology Reviews* 43.4, pp. 401–414.

Ngufor, Corine et al. (2014). "Olyset Duo® (a pyriproxyfen and permethrin mixture net): an experimental hut trial against pyrethroid resistant *Anopheles gambiae* and culex quinquefasciatus in southern benin". In: *PLOS ONE* 9.4, e93603.

Niu, Guodong et al. (2021). "Studies of the parasite-midgut interaction reveal *Plasmodium* proteins important for malaria transmission to mosquitoes". In: *Frontiers in Cellular and Infection Microbiology* 11, p. 458.

Nolan, Tony (2021). "Control of malaria-transmitting mosquitoes using gene drives". In: *Philosophical Transactions of the Royal Society B: Biological Sciences* 376.1818, p. 20190803.

N'Guessan, Raphael et al. (2016). "A chlorfenapyr mixture net Interceptor® G2 shows high efficacy and wash durability against resistant mosquitoes in West Africa". In: *PLOS ONE* 11.11, e0165925.

Ojo, Kayode K. et al. (2014). "A specific inhibitor of PfCDPK4 blocks malaria transmission: chemical-genetic validation". In: *The Journal of Infectious Diseases* 209.2, pp. 275–284.

Ojuka, P. et al. (2015). "Early biting and insecticide resistance in the malaria vector *Anopheles* might compromise the effectiveness of vector control intervention in Southwestern Uganda". In: *Malar J* 14, p. 148.

Olivieri, A. et al. (2015). "Distinct properties of the egress-related osmiophilic bodies in male and female gametocytes of the rodent malaria parasite *Plasmodium berghei*". In: *Cell Microbiol* 17.3, pp. 355–68.

Ondeto, Benyl M. et al. (2017). "Current status of insecticide resistance among malaria vectors in Kenya". In: *Parasites & Vectors* 10.1, p. 429.

Orjih, A. U. (2012). "Hemozoin accumulation in Garnham bodies of *Plasmodium falciparum* gametocytes". In: *Parasitol Res* 111.6, pp. 2353–9.

Parkyn Schneider, Molly et al. (2017). "Disrupting assembly of the inner membrane complex blocks *Plasmodium falciparum* sexual stage development". In: *PLOS Pathogens* 13.10, e1006659.

Paton, Douglas G. et al. (2019). "Exposing *Anopheles* mosquitoes to antimalarials blocks *Plasmodium* parasite transmission". In: *Nature* 567.7747, pp. 239–243.

Peatey, Christopher L. et al. (2011). "A high-throughput assay for the identification of drugs against late-stage *Plasmodium falciparum* gametocytes". In: *Molecular and Biochemical Parasitology* 180.2, pp. 127–131.

Phillips, Margaret A. et al. (2017). "Malaria". In: *Nature Reviews Disease Primers* 3.1, p. 17050.

Pimenta, Paulo F., Musa Touray, and Louis Miller (1994). "The journey of malaria sporozoites in the mosquito salivary gland". In: *Journal of Eukaryotic Microbiology* 41.6, pp. 608–624.

Pinzon-Ortiz, Consuelo et al. (2001). "The binding of the circumsporozoite protein to cell surface heparan sulfate proteoglycans is required for *Plasmodium* sporozoite attachment to target cells*". In: *Journal of Biological Chemistry* 276.29, pp. 26784–26791.

Plouffe, David et al. (2008). "*In silico* activity profiling reveals the mechanism of action of antimalarials discovered in a high-throughput screen". In: *Proceedings of the National Academy of Sciences* 105.26, p. 9059.

Plouffe, David M et al. (2016). "High-throughput assay and discovery of small molecules that interrupt malaria transmission". In: *Cell Host & Microbe* 19.1, pp. 114–126.

Pongponratn, E. et al. (2003). "An ultrastructural study of the brain in fatal *Plasmodium falciparum* malaria". In: *Am J Trop Med Hyg* 69.4, pp. 345–59.

Ponzi, Marta et al. (2009). "Egress of *Plasmodium berghei* gametes from their host erythrocyte is mediated by the MDV-1/PEG3 protein". In: *Cellular Microbiology* 11.8, pp. 1272–1288.

Pradel, G. and U. Frevert (2001). "Malaria sporozoites actively enter and pass through rat Kupffer cells prior to hepatocyte invasion". In: *Hepatology* 33.5, pp. 1154–65.

Prudêncio, Miguel, Ana Rodriguez, and Maria M. Mota (2006). "The silent path to thousands of merozoites: The *Plasmodium* liver stage". In: *Nature Reviews Microbiology* 4.11, pp. 849–856.

Prugnolle, Franck et al. (2010). "African great apes are natural hosts of multiple related malaria species, including *Plasmodium falciparum*". In: *Proceedings of the National Academy of Sciences* 107.4, p. 1458.

Prugnolle, Franck et al. (2013). "Diversity, host switching and evolution of *Plasmodium vivax* infecting African great apes". In: *Proceedings of the National Academy of Sciences* 110.20, p. 8123.

Quevillon, E. et al. (2003). "The *Plasmodium falciparum* family of Rab GTPases". In: *Gene* 306, pp. 13–25.

Raabe, A. C. et al. (2011). "Multiple roles for *Plasmodium berghei* phosphoinositide-specific phospholipase C in regulating gametocyte activation and differentiation". In: *Cell Microbiol* 13.7, pp. 955–66.

Raban, R. R., J. M. Marshall, and O. S. Akbari (2020). "Progress towards engineering gene drives for population control". In: *J Exp Biol* 223.Pt Suppl 1.

Ramdani, Ghania et al. (2015). "cAMP-Signalling Regulates Gametocyte-Infected Erythrocyte Deformability Required for Malaria Parasite Transmission". In: *PLoS pathogens* 11.5, e1004815–e1004815.

Raphemot, Rene et al. (2015). "Discovery of dual-stage malaria inhibitors with new targets". In: *Antimicrobial agents and chemotherapy* 60.3, pp. 1430–1437.

Rawlings, David J. et al. (1992). "α-Tubulin II is a male-specific protein in *Plasmodium falciparum*". In: *Molecular and Biochemical Parasitology* 56.2, pp. 239–250.

Real, Eliana et al. (2021). "A single-cell atlas of *Plasmodium falciparum* transmission through the mosquito". In: *Nature Communications* 12.1, p. 3196.

Reddy, K. Sony et al. (2015). "Multiprotein complex between the GPI-anchored CyRPA with PfRH5 and PfRipr is crucial for *Plasmodium falciparum* erythrocyte invasion". In: *Proceedings of the National Academy of Sciences* 112.4, p. 1179.

Reynolds, Jennifer M. et al. (2007). "Antimalarial activity of the anticancer and proteasome inhibitor bortezomib and its analog ZL3B". In: *BMC clinical pharmacology* 7, pp. 13–13.

Riglar, David T. et al. (2011). "Super-resolution dissection of coordinated events during malaria parasite invasion of the human erythrocyte". In: *Cell Host & Microbe* 9.1, pp. 9–20.

Ruecker, A. et al. (2014). "A male and female gametocyte functional viability assay to identify biologically relevant malaria transmission-blocking drugs". In: *Antimicrob Agents Chemother* 58.12, pp. 7292–302.

Ruecker, Andrea et al. (2012). "Proteolytic activation of the essential parasitophorous vacuole cysteine protease SERA6 accompanies malaria parasite egress from its host erythrocyte". In: *The Journal of biological chemistry* 287.45, pp. 37949–37963.

Rueda-Zubiaurre, A. et al. (2019). "Structure-activity relationship studies of a novel class of transmission blocking antimalarials targeting male gametes". In: *J Med Chem*.

Schaijk, B. C. van et al. (2006). "Pfs47, paralog of the male fertility factor Pfs48/45, is a female specific surface protein in *Plasmodium falciparum*". In: *Mol Biochem Parasitol* 149.2, pp. 216–22.

Schalkwyk, D. A. van et al. (2010). "Inhibition of *Plasmodium falciparum* pH regulation by small molecule indole derivatives results in rapid parasite death". In: *Biochem Pharmacol* 79.9, pp. 1291–9.

Schloetel, J. G. et al. (2019). "Guided STED nanoscopy enables super-resolution imaging of blood stage malaria parasites". In: *Sci Rep* 9.1, p. 4674.

Sebastian, Sarah et al. (2012). "A *Plasmodium* calcium-dependent protein kinase controls zygote development and transmission by translationally activating repressed mRNAs". In: *Cell Host & Microbe* 12.1, pp. 9–19.

Seder, R. A. et al. (2013). "Protection against malaria by intravenous immunization with a nonreplicating sporozoite vaccine". In: *Science* 341.6152, pp. 1359–65.

Severini, Carlo et al. (1999). "The production of the osmiophilic body protein Pfg377 is associated with stage of maturation and sex in *Plasmodium falciparum* gametocytes". In: *Molecular and Biochemical Parasitology* 100.2, pp. 247–252.

Shandilya, A. et al. (2013). "A plausible mechanism for the antimalarial activity of artemisinin: A computational approach". In: *Sci Rep* 3, p. 2513.

Silvestrini, F., P. Alano, and J. L. Williams (2000). "Commitment to the production of male and female gametocytes in the human malaria parasite *Plasmodium falciparum*". In: *Parasitology* 121.5, pp. 465–471.

Silvestrini, F. et al. (2012). "Differential adhesive properties of sequestered asexual and sexual stages of *Plasmodium falciparum* on human endothelial cells are tissue independent". In: *PLoS One* 7.2, e31567.

Silvestrini, Francesco et al. (2005). "Genome-wide identification of genes upregulated at the onset of gametocytogenesis in *Plasmodium falciparum*". In: *Molecular and Biochemical Parasitology* 143.1, pp. 100–110.

Silvestrini, Francesco et al. (2010). "Protein export marks the early phase of gametocytogenesis of the human malaria parasite *Plasmodium falciparum*". In: *Molecular & cellular proteomics : MCP* 9.7, pp. 1437–1448.

Silvie, O. et al. (2004). "A role for apical membrane antigen 1 during invasion of hepatocytes by *Plasmodium falciparum* sporozoites". In: *J Biol Chem* 279.10, pp. 9490–6.

Silvie, Olivier et al. (2003). "Hepatocyte CD81 is required for *Plasmodium falciparum* and *Plasmodium yoelii* sporozoite infectivity". In: *Nature Medicine* 9.1, pp. 93–96.

Sinden, R. E. (1982). "Gametocytogenesis of *Plasmodium falciparum in vitro*: an electron microscopic study". In: *Parasitology* 84.1, pp. 1–11.

— (1983a). "Sexual development of malarial parasites". In: *Adv Parasitol* 22, pp. 153–216.

— (1983b). "The cell biology of sexual development in *Plasmodium*". In: *Parasitology* 86 (Pt 4), pp. 7–28.

— (2009). "Malaria, sexual development and transmission: retrospect and prospect". In: *Parasitology* 136.12, pp. 1427–1434.

Sinden, R. E., E. U. Canning, and B. Spain (1976). "Gametogenesis and fertilization in *Plasmodium yoelii nigeriensis*: a transmission electron microscope study". In: *Proc R Soc Lond B Biol Sci* 193.1110, pp. 55–76.

Sinden, R. E. et al. (1978). "Gametocyte and gamete development in *Plasmodium falciparum*". In: *Proc R Soc Lond B Biol Sci* 201.1145, pp. 375–99.

Sinden, R. E. et al. (2010). "The flagellum in malarial parasites". In: *Current Opinion in Microbiology* 13.4, pp. 491–500.

Sinden, Robert E (1998). "Gametocytes and sexual development". In: *Malaria: Parasite Biology, Pathogenesis and Protection*, pp. 25–48.

Singh, B. et al. (2004). "A large focus of naturally acquired *Plasmodium knowlesi* infections in human beings". In: *Lancet* 363.9414, pp. 1017–24.

Sinha, Abhinav et al. (2014). "A cascade of DNA-binding proteins for sexual commitment and development in *Plasmodium*". In: *Nature* 507.7491, pp. 253–257.

Sinnis, P. et al. (1996). "Remnant lipoproteins inhibit malaria sporozoite invasion of hepatocytes". In: *Journal of Experimental Medicine* 184.3, pp. 945–954.

Smalley, M. E., S. Abdalla, and J. Brown (1981). "The distribution of *Plasmodium falciparum* in the peripheral blood and bone marrow of Gambian children". In: *Trans R Soc Trop Med Hyg* 75.1, pp. 103–5.

Smith, E. and I. Collins (2015). "Photoaffinity labeling in target- and binding-site identification". In: *Future Med Chem* 7.2, pp. 159–83.

Smith, T. G. et al. (2000). "Commitment to sexual differentiation in the human malaria parasite, *Plasmodium falciparum*". In: *Parasitology* 121 (Pt 2), pp. 127–33.

Sologub, Ludmilla et al. (2011). "Malaria proteases mediate inside-out egress of gametocytes from red blood cells following parasite transmission to the mosquito". In: *Cellular Microbiology* 13.6, pp. 897–912.

Soulez, Ferréol et al. (2012). "Blind deconvolution of 3D data in wide field fluorescence microscopy". In: *International Symposium on Biomedical Imaging*, CDROM.

Sprenger, J. et al. (2015). "Three-dimensional structures of *Plasmodium falciparum* spermidine synthase with bound inhibitors suggest new strategies for drug design". In: *Acta Crystallogr D Biol Crystallogr* 71.Pt 3, pp. 484–93.

Srivastava, I. K. and A. B. Vaidya (1999). "A mechanism for the synergistic antimalarial action of atovaquone and proguanil". In: *Antimicrobial agents and chemotherapy* 43.6, pp. 1334–1339.

Stewart, Michael J. and Jerome P. Vanderberg (1988). "Malaria sporozoites leave behind trails of circumsporozoite protein during gliding motility". In: *The Journal of Protozoology* 35.3, pp. 389–393.

Sturm, Angelika et al. (2006). "Manipulation of host hepatocytes by the malaria parasite for delivery into liver sinusoids". In: *Science* 313.5791, p. 1287.

Sultan, Ali A. et al. (1997). "TRAP is necessary for gliding motility and infectivity of *Plasmodium* sporozoites". In: *Cell* 90.3, pp. 511–522.

Sutherland, Colin J. (2016). "Persistent parasitism: the adaptive biology of malariae and ovale malaria". In: *Trends in Parasitology* 32.10, pp. 808–819.

Swann, Justine et al. (2016). "High-throughput luciferase-based assay for the discovery of therapeutics that prevent malaria". In: *ACS Infectious Diseases* 2.4, pp. 281–293.

Tacar, Oktay, Pornsak Sriamornsak, and Crispin R. Dass (2013). "Doxorubicin: an update on anticancer molecular action, toxicity and novel drug delivery systems". In: *Journal of Pharmacy and Pharmacology* 65.2, pp. 157–170.

Taku, I. et al. (2020). "Rab5b-associated Arf1 GTPase regulates export of N-myristoylated adenylate kinase 2 from the endoplasmic reticulum in *Plasmodium falciparum*". In: *Front Cell Infect Microbiol* 10, p. 610200.

Talman, Arthur M. et al. (2004). "Gametocytogenesis : the puberty of *Plasmodium falciparum*". In: *Malaria Journal* 3.1, p. 24.

Talman, Arthur M. et al. (2011). "PbGEST mediates malaria transmission to both mosquito and vertebrate host". In: *Molecular Microbiology* 82.2, pp. 462–474.

Tan, Michele S. Y. and Michael J. Blackman (2021). "Malaria parasite egress at a glance". In: *Journal of cell science* 134.5, jcs257345.

Tanaka, Takeshi Q. and Kim C. Williamson (2011). "A malaria gametocytocidal assay using oxidoreduction indicator, alamarBlue". In: *Molecular and Biochemical Parasitology* 177.2, pp. 160–163.

Tardieux, Isabelle and Jake Baum (2016). "Reassessing the mechanics of parasite motility and host-cell invasion". In: *Journal of Cell Biology* 214.5, pp. 507–515.

Tarrason Risa, Gabriel et al. (2020). "The proteasome controls ESCRT-III–mediated cell division in an archaeon". In: *Science* 369.6504, eaaz2532.

Taylor, Cathy J., Louisa McRobert, and David A. Baker (2008). "Disruption of a *Plasmodium falciparum* cyclic nucleotide phosphodiesterase gene causes aberrant gametogenesis". In: *Molecular Microbiology* 69.1, pp. 110–118.

Teboh-Ewungkem, Miranda I. and Gideon A. Ngwa (2021). "COVID-19 in malaria-endemic regions: potential consequences for malaria intervention coverage, morbidity, and mortality". In: *The Lancet Infectious Diseases* 21.1, pp. 5–6.

Thomson, J. G. and Andrew Robertson (1935). "The structure and development of *Plasmodium falciparum* gametocytes in the internal organs and peripheral circulation". In: *Transactions of The Royal Society of Tropical Medicine and Hygiene* 29.1, pp. 31–40.

Tibúrcio, Marta et al. (2012). "A switch in infected erythrocyte deformability at the maturation and blood circulation of *Plasmodium falciparum* transmission stages". In: *Blood* 119.24, e172–e180.

Tibúrcio, Marta et al. (2013). "Early gametocytes of the malaria parasite *Plasmodium falciparum* specifically remodel the adhesive properties of infected erythrocyte surface". In: *Cellular Microbiology* 15.4, pp. 647–659.

Tibúrcio, Marta et al. (2015). "Specific expression and export of the *Plasmodium falciparum* Gametocyte EXported Protein-5 marks the gametocyte ring stage". In: *Malaria journal* 14, pp. 334–334.

Tilley, L. et al. (2016). "Artemisinin action and resistance in *Plasmodium falciparum*". In: *Trends Parasitol* 32.9, pp. 682–696.

Toé, Kobié et al. (2014). "Increased pyrethroid resistance in malaria vectors and decreased bed net effectiveness, Burkina Faso". In: *Emerging Infectious Disease journal* 20.10, p. 1691.

Trager, W. and G. S. Gill (1992). "Enhanced gametocyte formation in young erythrocytes by *Plasmodium falciparum in vitro*". In: *The Journal of protozoology* 39.3, pp. 429–432.

Tse, Edwin G., Marat Korsik, and Matthew H. Todd (2019). "The past, present and future of anti-malarial medicines". In: *Malaria Journal* 18.1, p. 93.

UniProt, Consortium (2019). "UniProt: a worldwide hub of protein knowledge". In: *Nucleic Acids Res* 47.D1, pp. D506–D515.

Van Bortel, Wim et al. (2008). "The insecticide resistance status of malaria vectors in the Mekong region". In: *Malaria Journal* 7.1, p. 102.

Vanderberg, J. P. and U. Frevert (2004). "Intravital microscopy demonstrating antibody-mediated immobilisation of *Plasmodium berghei* sporozoites injected into skin by mosquitoes". In: *Int J Parasitol* 34.9, pp. 991–6.

Vaughan, A. M. and S. H. I. Kappe (2017). "Malaria parasite liver infection and exoerythrocytic biology". In: *Cold Spring Harb Perspect Med* 7.6.

Vaughan, A. M. et al. (2012). "Complete *Plasmodium falciparum* liver-stage development in liver-chimeric mice". In: *J Clin Invest* 122.10, pp. 3618–28.

Venugopal, Kannan et al. (2020). "*Plasmodium* asexual growth and sexual development in the haematopoietic niche of the host". In: *Nature Reviews Microbiology* 18.3, pp. 177–189.

Volz, Jennifer C et al. (2016). "Essential role of the PfRh5/PfRipr/CyRPA complex during *Plasmodium falciparum* invasion of erythrocytes". In: *Cell Host & Microbe* 20.1, pp. 60–71.

Vos, M. W. et al. (2015). "A semi-automated luminescence based standard membrane feeding assay identifies novel small molecules that inhibit transmission of malaria parasites by mosquitoes". In: *Sci Rep* 5, p. 18704.

Votýpka, Jan et al. (2017). "Apicomplexa". In: *Handbook of the Protists*. Ed. by John M. Archibald et al. Cham: Springer International Publishing, pp. 1–58.

Wall, R. J. et al. (2018). "*Plasmodium* APC3 mediates chromosome condensation and cytokinesis during atypical mitosis in male gametogenesis". In: *Sci Rep* 8.1, p. 5610.

Wang, J. et al. (2015). "Haem-activated promiscuous targeting of artemisinin in *Plasmodium falciparum*". In: *Nat Commun* 6, p. 10111.

Watson, James A., Narimane Nekkab, and Michael White (2021). "Tafenoquine for the prevention of *Plasmodium vivax* malaria relapse". In: *The Lancet Microbe* 2.5, e175–e176.

Weiss, Daniel J. et al. (2021). "Indirect effects of the COVID-19 pandemic on malaria intervention coverage, morbidity, and mortality in Africa: a geospatial modelling analysis". In: *The Lancet Infectious Diseases* 21.1, pp. 59–69.

Wells, Timothy N. C., Rob Hooft van Huijsduijnen, and Wesley C. Van Voorhis (2015). "Malaria medicines: a glass half full?" In: *Nature Reviews Drug Discovery* 14.6, pp. 424–442.

Wesseling, J. G. et al. (1989). "Stage-specific expression and genomic organization of the actin genes of the malaria parasite *Plasmodium falciparum*". In: *Mol Biochem Parasitol* 35.2, pp. 167–76.

White, Nicholas J. (2011). "Determinants of relapse periodicity in *Plasmodium vivax* malaria". In: *Malaria Journal* 10.1, p. 297.

White, Nicholas J. et al. (2014a). "Malaria". In: *The Lancet* 383.9918, pp. 723–735.

White, Nicholas J. et al. (2014b). "Spiroindolone KAE609 for falciparum and vivax malaria". In: *New England Journal of Medicine* 371.5, pp. 403–410.

White, Nicholas J. et al. (2016). "Antimalarial activity of KAF156 in falciparum and vivax malaria". In: *New England Journal of Medicine* 375.12, pp. 1152–1160.

Williams, J. L. (1999). "Stimulation of *Plasmodium falciparum* gametocytogenesis by conditioned medium from parasite cultures". In: *Am J Trop Med Hyg* 60.1, pp. 7–13.

Windbichler, Nikolai et al. (2011). "A synthetic homing endonuclease-based gene drive system in the human malaria mosquito". In: *Nature* 473.7346, pp. 212–215.

Witmer, Kathrin et al. (2020). "Transmission of artemisinin-resistant malaria parasites to mosquitoes under antimalarial drug pressure". In: *Antimicrobial Agents and Chemotherapy* 65.1, e00898–20.

World Health, Organization (2010). *Global report on antimalarial drug efficacy and drug resistance: 2000-2010*. Geneva: World Health Organization.

— (2015). *Guidelines for the treatment of malaria*. 3rd ed. Geneva: World Health Organization.

— (2019). *World malaria report 2019*. Geneva: World Health Organization.

— (2020). *World malaria report 2020: 20 years of global progress and challenges*. Geneva: World Health Organization.

World Health Organization. Roll Back, Malaria and Development United States. Agency for International (2000). *New perspectives : malaria diagnosis : report of a joint WHO/USAID informal consultation, 25-27 October 1999*. Geneva: World Health Organization.

Wright, M. H. and S. A. Sieber (2016). "Chemical proteomics approaches for identifying the cellular targets of natural products". In: *Natural Product Reports* 33.5, pp. 681–708.

Wright, M. H. et al. (2015). "Global analysis of protein N-myristoylation and exploration of N-myristoyltransferase as a drug target in the neglected human pathogen *Leishmania donovani*". In: *Chem Biol* 22.3, pp. 342–54.

Wunderlich, J., P. Rohrbach, and J. P. Dalton (2012). "The malaria digestive vacuole". In: *Front Biosci (Schol Ed)* 4, pp. 1424–48.

Xie, S. C. et al. (2018). "Target validation and identification of novel boronate inhibitors of the *Plasmodium falciparum* proteasome". In: *J Med Chem* 61.22, pp. 10053–10066.

Yahiya, S. et al. (2019). "The antimalarial screening landscape-looking beyond the asexual blood stage". In: *Curr Opin Chem Biol* 50, pp. 1–9.

Yahiya, Sabrina et al. (2021a). "4D live-cell imaging of microgametogenesis in the human malaria parasite *Plasmodium falciparum*". In: *bioRxiv*, p. 2021.07.28.454129.

Yahiya, Sabrina et al. (2021b). "*Plasmodium falciparum* protein Pfs16 is a target for transmission-blocking antimalarial drug development". In: *bioRxiv*, p. 2021.06.14.448287.

Yeoh, S. et al. (2007). "Subcellular discharge of a serine protease mediates release of invasive malaria parasites from host erythrocytes". In: *Cell* 131.6, pp. 1072–83.

Yeung, Bryan K. S. et al. (2010). "Spirotetrahydro β-carbolines (spiroindolones): a new class of potent and orally efficacious compounds for the treatment of malaria". In: *Journal of Medicinal Chemistry* 53.14, pp. 5155–5164.

Ying, Patrick et al. (1997). "The malaria circumsporozoite protein: interaction of the conserved regions I and II-plus with heparin-like oligosaccharides in heparan sulfate". In: *Experimental Parasitology* 85.2, pp. 168–182.

Yoo, Euna et al. (2018). "Defining the Determinants of Specificity of *Plasmodium* Proteasome Inhibitors". In: *Journal of the American Chemical Society* 140.36, pp. 11424–11437.

Zeeman, Anne-Marie et al. (2014). "KAI407, a potent non-8-aminoquinoline compound that kills *Plasmodium cynomolgi* early dormant liver stage parasites *in vitro*". In: *Antimicrobial Agents and Chemotherapy* 58.3, pp. 1586–1595.

Zeeshan, Mohammad et al. (2021). "Protein phosphatase 1 regulates atypical mitotic and meiotic division in *Plasmodium* sexual stages". In: *Communications Biology* 4.1, p. 760.

Zhang, M. et al. (2018). "Uncovering the essential genes of the human malaria parasite *Plasmodium falciparum* by saturation mutagenesis". In: *Science* 360.6388.

Zhou, Min, Ayşegül Varol, and Thomas Efferth (2021). "Multi-omics approaches to improve malaria therapy". In: *Pharmacological Research* 167, p. 105570.

Appendix A

Probe-protein interaction profile determined by nLC-MS/MS analysed photoaffinity labelling

DMSO vs. Probe 8					
Rank	**Enriched in Competed vs. Probe?**	**Colloquial Name**	**Protein ID**	**P value**	**Log_2 FC**
1	No	Thioredoxin 1	PF3D7_ 1457200.1-p1	0.0146	2.81975
2	No	Guanine exchange factor SEC12	PF3D7_ 1116400.1-p1	0.0588	2.7969
3	**Yes**	***Pfs16**	**PF3D7_ 0406200.1-p1**	**0.0701**	**2.45809**
4	Yes	Spermidine Synthase	PF3D7_ 1129000.1-p1	0.1058	2.27369
5	No	ER-resident calcium binding protein	PF3D7_ 1108600.1-p1	0.0064	2.10138
6	Yes	RAB-1B (Ras related protein)	PF3D7_ 0512600.1-p1	0.0314	2.08532
7	No	SURFIN 4.2	PF3D7_ 0424400.1-p1	0.0650	1.86738
8	No	Early Transcribed Membrane Protein 10.3	PF3D7_ 1016900.1-p1	0.1441	1.85326
9	No	Conserved Plasmodium protein unknown	PF3D7_ 1016100.1-p1	0.0215	1.81175
10	No	Actin1	PF3D7_ 1246200.1-p1	0.0490	1.71661
11	Yes	60S Ribsomal Protein L26	PF3D7_ 0312800.1-p1	0.0423	1.71633
12	No	Conserved Plasmodium protein unknown	PF3D7_ 1125600.1-p1	0.0074	1.62489
13	No	Signal Peptide Peptidase	PF3D7_ 1457000.1-p1	0.0007	1.51684
14	No	Conserved Plasmodium protein unknown	PF3D7_ 1429600.1-p1	0.2077	1.51165
15	Yes	V-type Proton ATPase	PF3D7_ 1311900.1-p1	0.0567	1.34692
16	No	Glyceraldehyde-3-phosphate dehydrogenase	PF3D7_ 1462800.1-p1	0.1464	1.14122
17	No	40S Ribosomal Protein S8e	PF3D7_ 1408600.1-p1	0.0756	1.0703
18	No	GAP45	PF3D7_ 1222700.1-p1	0.2073	1.06565
19	**Yes**	****Pfg377**	**PF3D7_ 1250100.1-p1**	**0.4615**	**1.02634**
20	No	Conserved Apicomplexan protein, unknown function	PF3D7_ 1105800.1-p1	0.3922	1.00096

Table A1: Full background-independent enrichment profile from nLC-MS/MS analysed photoaffinity labelling. All proteins listed were positively enriched when comparing DMSO and probe **8**-treated samples, and those additionally enriched in competed samples are indicated. Protein hits are ranked according to log_2-transformed fold change (Log_2FC) between average values of three biological replicates. Positive enrichment was determined by a Log_2FC value >1. P values were obtained by performing a student's *t*-test.

Competed vs. Probe 8					
Rank	**Enriched in DMSO vs. Probe?**	**Colloquial Name**	**Protein ID**	**P value**	**Log_2 FC**
1	Yes	Spermidine Synthase	PF3D7_1129000 .1-p1	0.1552	-2.0397
2	Yes	60S Ribsomal Protein L26	PF3D7_0312800 .1-p1	0.0051	-1.8946
3	Yes	RAB-1B (Ras related protein)	PF3D7_0512600 .1-p1	0.0177	-1.8675
4	**Yes**	***Pfs16**	**PF3D7_ 0406200. 1-p1**	**0.3069**	**- 1.7926**
5	**Yes**	****Pfg377**	**PF3D7_ 1250100. 1-p1**	**0.1180**	**- 1.2868**
6	No	FoP	PF3D7_0519700 .1-p1	0.1261	- 1.26247
7	No	Single Strand Telomeric DNA binding Protein GBP2	PF3D7_1006800 .1-p1	0.2826	- 1.17232
8	Yes	V-type Proton ATPase	PF3D7_1311900 .1-p1	0.0201	-1.1617
9	No	60S Ribsomal Protein L3	PF3D7_1027800 .1-p1	0.3531	- 1.06337

Table A2: Full competed protein profile from nLC-MS/MS analysed photoaffinity labelling. All protein hits listed were negatively enriched when comparing competed (combination treatment of probe **8** and parent molecule **7**) and probe **8**-treated samples. Hits additionally positively enriched over background (DMSO vs. probe **8**) are indicated. Proteins are ranked by log_2-transformed fold change (Log_2FC) between average values of three biological replicates, with Log_2FC values < -1 representing negative. Significance was determined using a student's *t*-test, with corresponding P values listed.

Appendix B

Description of supplementary time-lapses

1. Supplementary Video 1. SiR-tubulin (magenta) stained microtubules depicting MTOC transformation, mitotic spindle assembly, basal body formation and axoneme nucleation. Time-lapse to accompany Figure 6.3 A.

2. Supplementary Video 2. SiR-Tubulin-stained microtubules (magenta), WGA-488-stained host erythrocyte (green) and Vybrant™ DyeCycle™ Violet-stained DNA (blue) show axoneme assembly and rounding. Time-lapse to accompany Figure 6.3 B and 6.4 A. A 3D projection of volume rendered data and 2D maximum intensity projection (MIP) are shown.

3. Supplementary Video 3. SiR-Tubulin-stained microtubules (magenta), WGA-488-stained host erythrocyte (green) and Vybrant™ DyeCycle™ Violet-stained DNA (blue) show erythrocyte membrane perforation and pore formation, prior to spindle-directed egress of a microgametocyte. Time-lapse to accompany Figure 6.4 B and 6.5 B. A 3D projection of volume rendered data and 2D maximum intensity projection (MIP) are shown.

4. Supplementary Video 4. SiR-Tubulin-stained microtubules (magenta), WGA-488-stained host erythrocyte (green) and Vybrant™ DyeCycle™ Violet-stained DNA (blue) show microgametes emerging in the process of exflagellation. A single Z-slice (2D) time-lapse is depicted and accompanies Figure 6.6 A.

5. Supplementary Video 5. SiR-Tubulin-stained microtubules (magenta), WGA-488-stained host erythrocyte (green) and Vybrant™ DyeCycle™ Violet-stai-

ned DNA (blue) show emerging microgametes in a rotated view of a single time-frame captured in 3D. Accompaniment for Figure 6.6 B.

6. Supplementary Video 6. SiR-Tubulin-stained microtubules (magenta) show microgametes emerging in the process of exflagellation. A single Z-slice (2D) time-lapse is depicted.

7. Supplementary Video 7 .Microgametes emerging in the process of exflagellation, captured by brightfield as a single-slice (2D) time-lapse. Accompaniment for Figure 6.6 D.

8. Supplementary Video 8. SiR-Tubulin-stained microtubules (magenta), WGA-488-stained host erythrocyte (green) and Vybrant™ DyeCycle™ Violet-stained DNA (blue) show a cellular phenotype of ML10-mediated inhibition of PKG. Time-lapse to accompany Figure 6.7 A (phenotype i). A 3D projection of volume rendered data and 2D maximum intensity projection (MIP) are shown.

9. Supplementary Video 9. SiR-Tubulin-stained microtubules (magenta), WGA-488-stained host erythrocyte (green) and Vybrant™ DyeCycle™ Violet-stained DNA (blue) show a cellular phenotype of ML10-mediated inhibition of PKG. Time-lapse to accompany Figure 6.7 A (phenotype ii). A 3D projection of volume rendered data and 2D maximum intensity projection (MIP) are shown.

10. Supplementary Video 10. SiR-Tubulin-stained microtubules (magenta), WGA-488-stained host erythrocyte (green) and Vybrant™ DyeCycle™ Violet-stained DNA (blue) show a cellular phenotype of 1294-mediated inhibition of CDPK4. Time-lapse to accompany Figure 6.7 B. A 3D projection of volume rendered data and 2D maximum intensity projection (MIP) are shown.

11. Supplementary Video 11. SiR-Tubulin-stained microtubules (magenta), WGA-488-stained host erythrocyte (green) and Vybrant™ DyeCycle™ Violet-stained DNA (blue) show a cellular phenotype of 1294-mediated inhibition of

CDPK4. A 3D projection of volume rendered data and 2D maximum intensity projection (MIP) are shown.

12. Supplementary Video 12. SiR-Tubulin-stained microtubules (magenta), WGA-488-stained host erythrocyte (green) and Vybrant™ DyeCycle™ Violet-stained DNA (blue) show a cellular phenotype of bortezomib-mediated inhibition of the gametocyte proteasome. Time-lapse to accompany Figure 6.7 C (phenotype i). A 3D projection of volume rendered data and 2D maximum intensity projection (MIP) are shown.

13. Supplementary Video 13. SiR-Tubulin-stained microtubules (magenta), WGA-488-stained host erythrocyte (green) and Vybrant™ DyeCycle™ Violet-stained DNA (blue) show a cellular phenotype of bortezomib-mediated inhibition of the gametocyte proteasome. Time-lapse to accompany Figure 6.7 C (phenotype ii). A 3D projection of volume rendered data and 2D maximum intensity projection (MIP) are shown.

14. Supplementary Video 14. SiR-Tubulin-stained microtubules (magenta), WGA-488-stained host erythrocyte (green) and Vybrant™ DyeCycle™ Violet-stained DNA (blue) show a cellular phenotype of bortezomib-mediated inhibition of the gametocyte proteasome. Time-lapse to accompany Figure 6.7 C (phenotype iii). A 3D projection of volume rendered data and 2D maximum intensity projection (MIP) are shown.

Appendix C

A high throughput screen for next-generation leads targeting malaria parasite transmission

nature COMMUNICATIONS

ARTICLE

DOI: 10.1038/s41467-018-05777-2 OPEN

A high throughput screen for next-generation leads targeting malaria parasite transmission

Michael J. Delves[1], Celia Miguel-Blanco[1,2], Holly Matthews[1], Irene Molina[2], Andrea Ruecker[1], Sabrina Yahiya[1], Ursula Straschil[1], Matthew Abraham[3], María Luisa León[2], Oliver J. Fischer[4], Ainoa Rueda-Zubiaurre[4], Jochen R. Brandt[4], Álvaro Cortés[2], Anna Barnard[4], Matthew J. Fuchter[4], Félix Calderón[2], Elizabeth A. Winzeler[3], Robert E. Sinden[1], Esperanza Herreros[2], Francisco J. Gamo[2] & Jake Baum[1]

Spread of parasite resistance to artemisinin threatens current frontline antimalarial therapies, highlighting the need for new drugs with alternative modes of action. Since only 0.2–1% of asexual parasites differentiate into sexual, transmission-competent forms, targeting this natural bottleneck provides a tangible route to interrupt disease transmission and mitigate resistance selection. Here we present a high-throughput screen of gametogenesis against a ~70,000 compound diversity library, identifying seventeen drug-like molecules that target transmission. Hit molecules possess varied activity profiles including male-specific, dual acting male–female and dual-asexual-sexual, with one promising *N*-((4-hydroxychroman-4-yl)methyl)-sulphonamide scaffold found to have sub-micromolar activity in vitro and in vivo efficacy. Development of leads with modes of action focussed on the sexual stages of malaria parasite development provide a previously unexplored base from which future therapeutics can be developed, capable of preventing parasite transmission through the population.

[1] Department of Life Sciences, Imperial College London, Sir Alexander Fleming Building, Exhibition Road, South Kensington, London SW7 2AZ, UK. [2] Diseases of the Developing World (DDW), GlaxoSmithKline, 28760 Tres Cantos, Madrid, Spain. [3] School of Medicine, University of California San Diego, 9500 Gilman Drive 0760, La Jolla, CA 92093, USA. [4] Department of Chemistry, Imperial College London, Exhibition Road, South Kensington, London SW7 2AZ, UK. These authors contributed equally: Michael J. Delves, Celia Miguel-Blanco. Correspondence and requests for materials should be addressed to F.J.G. (email: francisco-javier.b.gamo@gsk.com) or to J.B. (email: jake.baum@imperial.ac.uk)

Success in reducing the burden of malaria disease since the turn of the millennium has seen the paradigm shift from control to one of regional elimination and eventual global eradication[1,2]. The coordinated roll-out of established measures has yielded substantial reductions in mortality and morbidity and helped to achieve elimination of malaria in 10 countries[3]. However, to ensure that these gains are maintained and accelerated, and in light of worrying emergence of multidrug-resistant malaria in Southeast Asia[4], new and innovative therapeutics are needed to prevent a potential reversal in numbers in the coming years.

At the heart of malaria disease incidence is spread of the *Plasmodium* parasite in the population via an infected *Anopheles* mosquito bite. Fundamental to this process is a switch in parasite biology from asexual replication to sexual development. Approximately 0.2–1% of asexual parasites undergo this alternative sexual developmental pathway to form mosquito-infectious male and female gametocytes[5]. Gametocytogenesis in *Plasmodium falciparum*, the species most deadly to humans, takes place over 10–12 days with the developing gametocytes, initially sequestered in the bone marrow, re-entering peripheral blood upon reaching maturity[6]. Mature gametocytes then maintain an arrested state awaiting uptake into the mosquito upon blood feeding. The consequence of this comparatively quiescent state is an insensitivity to most current antimalarials[7] leading to a situation whereby a patient can be readily cured of malarial symptoms (killing asexuals) but remain infectious to mosquitoes and as such able to perpetuate disease spread. Successful transmission itself requires uptake of both male and female gametocytes into the mosquito midgut, which immediately sense a change in local environment and rapidly differentiate into male and female gametes. Male gametogenesis involves three rapid rounds of endomitosis and assembly of eight motile, flagellated sperm-like gametes[8]. Female gametogenesis involves expression of translationally repressed mRNA stored at the gametocyte stage[9]. Fertilisation ensues in the midgut forming a motile zygote that migrates to and through the midgut epithelium before forming an oocyst, establishing an infected mosquito state. Transmission is a huge population bottleneck in the parasite life cycle with natural mosquito infections usually having only ~2–5 oocysts (compared to 10^{11} asexual parasites in an infected host)[10].

The concept of targeting sexual stages specifically, as a strategy to reduce malaria incidence, has received increased interest recently[11]. This follows emerging (re)appreciation that targeting the malaria parasite at the acute population bottleneck of transmission has potential benefits over asexually targeted therapeutics both as a means to break the cycle of infection but critically also as a barrier to the spread of drug-resistance alleles[11,12]. Conceptually, evolution of resistance to drugs specifically targeting the transmission stages will take far longer to develop than for conventional antimalarials, as selective pressure is only applied to the relatively small (non-replicating) gametocyte population compared to drugs targeting the ~10^{11} asexual parasites constantly replicating within a malarial host. Whilst quiescent in the human host, stage V gametocytes are poised for rapid onward development immediately upon mosquito blood-feeding, utilising distinct pathways to achieve their sex-specific roles during gametogenesis and fertilisation. Despite these observations, most current gametocyte assays utilise only an indicator of the metabolic viability of the gametocyte to determine compound activity and/or do not distinguish between male or female gametocytes e.g. mitotracker[7,13], luminescence[14,15], metabolic activity[16,17] or are limited to female gametogenesis[18]. In contrast, the *P. falciparum* Dual Gamete Formation Assay (Pf DGFA) uses male and female gamete formation as sensitive reporters of the functional viability (i.e. their ability to undergo further development) of both gametocytes individually and is highly predictive of transmission-blocking activity in the current laboratory gold standard transmission assay—the standard membrane-feeding assay (SMFA)[19]. Finally, whilst high-throughput screening (HTS) of millions of compounds in pharmaceutical libraries has populated the antimalarial development pipeline in the past decade, with promising new chemotypes targeting the disease-causing asexual stages[20–22], drug activity against other parasite stages have primarily only been considered when this property added extra value to existing identified molecules rather than essential properties in their own right. As such, very few studies have screened for sexual stage-specific activity without pre-filtering on asexual activity first[7].

Here we have undertaken HTS of a large unbiased chemical diversity library where the primary filter for hit identification is specifically the ability to target transmission itself, using the Pf DGFA. Profiling of selected hits revealed a diverse range of activities both dependent and independent of asexual activity and some showing gametocyte sex-specific activity. We show that exemplar molecules from each activity class appear to inhibit transmission by different mechanisms and that this directly translates into a blockade of mosquito transmission. In particular, we identify a novel *N*-((4-hydroxychroman-4-yl) methyl) sulphonamide (N-4HCS) scaffold that rapidly inhibits the process of male gamete formation in vitro and blocks transmission in vivo in a mouse model of malaria. The N-4HCS scaffold shows excellent chemical tractability, favourable physicochemical properties and promise for further development as a transmission-specific therapeutic that could be used in new antimalarial combination therapies.

Results

Gametocyte and asexual-targeted compounds within the GHCDL. The Global Health Chemical Diversity Library (GHCDL) comprises 68,689 compounds dissimilar to molecules already known to have antimalarial properties. All molecules possess lead-like physicochemical properties and are arranged into structurally similar clusters of between 3 and 14 compounds. The Pf DGFA measures the functional viability of Stage V male and female gametocytes as reported by their ability to form male and female gametes[23]. The GHCDL was screened in the Pf DGFA at 2 μM with a 48 h incubation prior to triggering gamete formation, yielding 24 hits with an IC_{50} < 10 μM (19 male-specific, 3 female-specific, 2 dual-active) (Fig. 1). Of these, 22 hits showed <50% inhibition at 10 μM against human HepG2 cells (i.e. are non-toxic) (Supplementary Data 1). Of note, six of the male-specific compounds possessed a similar N-4HCS core structure.

In parallel the GHCDL was screened against asexual blood stages at 2 μM over a 72 h incubation using lactate dehydrogenase activity as a surrogate readout for parasite growth. Screening yielded 146 hits with an IC_{50} < 10 μM; 132 of which showed <50% inhibition at 10 μM against human HepG2 cells (chemically classified in 16 clusters and 97 singletons) (Supplementary Data 2). For prioritisation, only asexual-active compounds with an IC_{50} < 2 μM were progressed for downstream characterisation (48 in total).

Multistage biological profiling of hit compounds. Independent stocks of 26 of the most potent commercially available hit compounds from both gametocyte and asexual screens, were studied in detail in seven profiling assays (Fig. 2a and Supplementary Data 3) to assess whether they targeted asexual parasite stages, mature gametocytes, male or female gametocytes, male or female gametes or, alternatively, interfered with early mosquito stage development in the rodent malaria parasite *Plasmodium berghei* (or any combination of above). Combining data gave several different activity profiles: gamete-targeted (7 compounds that

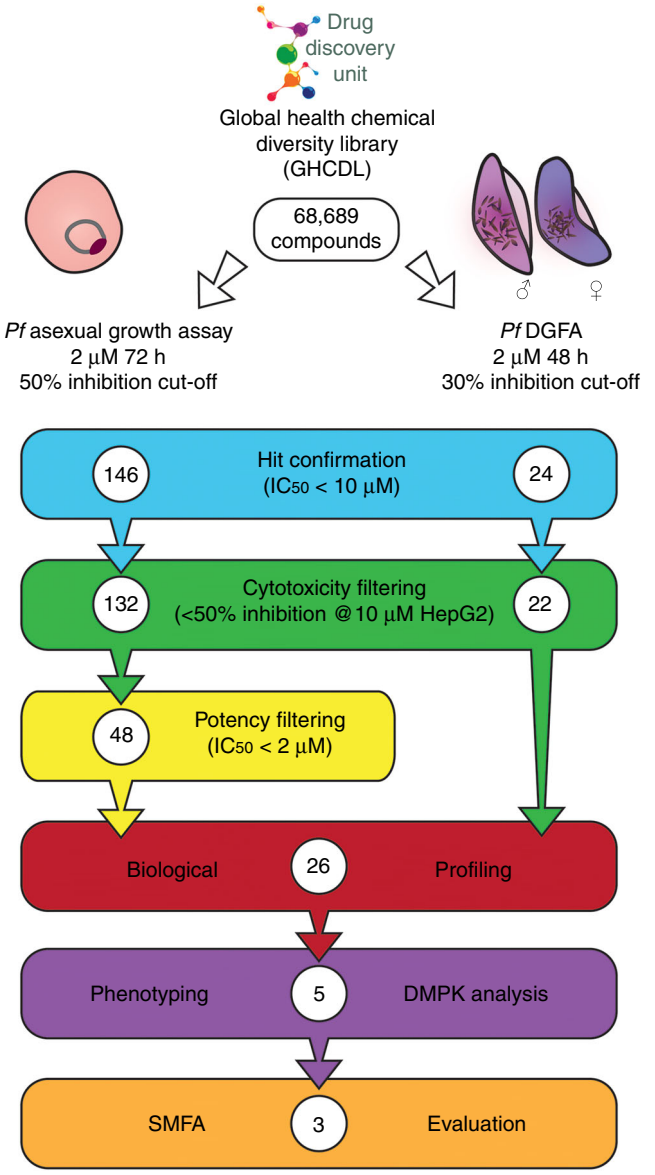


Fig. 1 Screening progression cascade. The Global Health Chemical Diversity Library (GHCDL) was screened in parallel against *Plasmodium falciparum* asexual stage and male and female gametocyte. Actives were reconfirmed and cytotoxic compounds removed. Asexual hits were further filtered based upon potency and 26 compounds selected for further profiling based upon potency and commercial availability. Five compounds with different transmission-blocking properties were further investigated for activity phenotype against male gametogenesis and their physiochemical properties (DMPK) investigated. Activity of three molecules was confirmed by standard membrane-feeding assay (SMFA)

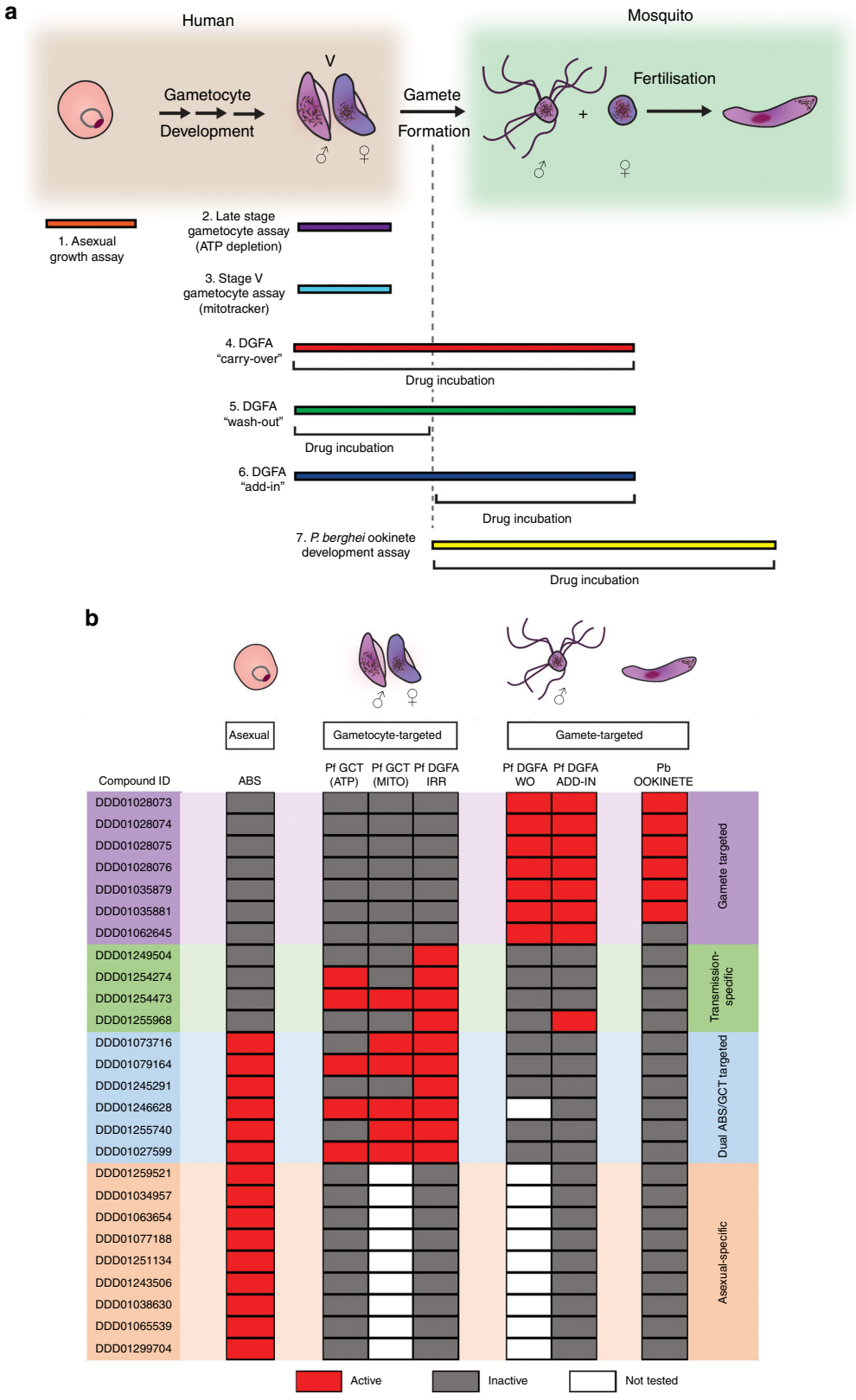
showed a male-specific gamete-targeted profile), transmission-specific (4 compounds male gametocyte-specific and irreversible), dual asexual-gametocyte targeted (6 compounds, all active against asexual, male and female gametocytes, and were irreversible) and asexual-specific (9 compounds) (Fig. 2b).

The gamete-targeted compounds all specifically inhibited exflagellation (male gamete formation). Moreover, the six N-4HCS compounds comprising most of this category also inhibited *P. berghei* ookinete development (consistent with having prevented exflagellation). The remaining gamete-targeted compound, DDD01062645, was inactive in the ookinete assay possibly indicating specificity for *P. falciparum*. Most of the transmission-specific compounds targeted the male gametocyte specifically, the exception being DDD01254473 that was more potent against female gametocytes than males. It showed reproducible submicromolar activity in the GC-ATP and mitotracker assays, suggesting that DDD01254473 may inhibit a fundamental metabolic pathway more essential to female gametocyte viability than males. Additionally, DDD01255968 also affected male gamete formation, suggesting it may either show polypharmacology or target a biological process common to both stages but absent in asexuals. Five compounds identified in the Pf DGFA primary screen were found to have weak micromolar asexual activity (thus did not meet hit potency criteria in the asexual screen) and so were re-classified as dual asexual/transmission active compounds. Similarly, asexual-specific DDD01027599 showed activity against gametocytes and was also reclassified. Interestingly all but one (DDD01246628) dual asexual/transmission active compounds affected both male and female gametocytes in the Pf DGFA. Coupled to their asexual activity, it is therefore likely that they target biological pathways fundamental for survival in the human host. Supporting this hypothesis, five of the six compounds in the category were also active in one or both of the gametocyte viability assays.

We investigated whether hit compounds could inhibit liver stage invasion and growth in an established *P. berghei* luciferase sporozoite HepG2 invasion assay[24]. Only one compound, DDD01243506, showed submicromolar activity against *P. berghei* liver stage invasion at a similar level to its activity against asexuals (Pb liver $IC_{50} = 0.52$ μM; HepG2 $TOX_{50} \geq 50$ μM; Recombinant luciferase $IC_{50} \geq 50$ μM; Pf asexual $IC_{50} = 0.66$ μM, Supplementary Data 3). Indeed, no Pf DGFA-active compounds showed specific activity against liver stages, presumably either due to fundamental differences in cell biology between different parasite stages or species-specific differences between *P. falciparum* and *P. berghei*.

To fully evaluate the power of the screening pipeline and to understand how the profiling categories could translate into transmission-blocking therapeutics, five compounds were selected for further study based upon potency and profile (Fig. 3): DDD01027599 (DDD599/BPCA) and DDD01245291 (DDD291) representing asexual and Pf DGFA dual-stage actives, respectively; DDD01249504 (DDD504) and DDD01255968 (DDD968) representing male-specific and gametocyte-specific actives, respectively; and finally, DDD01035881 (DDD881), one of the N-4HCS cluster representing male gamete-specific actives. In summary, our screening efforts identified 17 confirmed transmission blocking and 9 asexual targeting leads for further development.

Phenotypic impact of compounds on male gametogenesis. In vitro evolution followed by whole-genome analysis is the primary approach currently used for understanding how compounds act in malaria parasites[25]. As it is not currently feasible to generate resistant mutants to compounds that are only active in the gametocyte stage (resistance generation requires extensive rounds of replication in the presence of compound), phenotypic immunofluorescence assays were performed to evaluate compound activity on male gamete formation. Gametocytes treated with 10 μM of each compound were sampled at 0, 2, 3, 4, 6, 8, 10, and 20 min post induction of gamete formation before imaging (Fig. 4). Individual male cells were then extracted from the images and analysed for shape and haploid chromosome number/DNA content to quantitatively measure the progression of DNA replication ($n = 198$–668 cells) (Fig. 5a).



Each of the five compounds arrested male gametogenesis but showed distinct morphological failures suggesting distinct modes of action (Fig. 4b–g). DDD599/BPCA-treated gametocytes rounded up after induction but most cells did not replicate their DNA and none exflagellated (Figs. 4c and 5d). Cells frequently showed irregular and distorted tubulin fibres that did not associate with the generally small condensed nucleus. At the last observed time point (20 min post induction), a proportion of cells had commenced DNA replication, possessing microtubule fibres resembling the initial round of endomitosis of the DMSO control and an increase in DNA content (Fig. 5b). Most DDD291-treated male gametocytes also arrested after rounding up (Figs. 4f and 5e).

Fig. 2 Profiling the transmission blocking properties of selected compounds. **a** 26 compounds were profiled in seven assays that interrogate different ranges of parasite cell biology (represented by position and length of coloured bars). Ability to prevent asexual replication was tested by asexual growth assay[20]. Ability to inhibit the metabolic viability of stage IV/V gametocytes (Pf GCT) was tested by late stage gametocyte ATP depletion assay (ATP)[43] and stage V gametocyte by mitotracker assay (MITO)[7]. By varying compound incubation period, the carry-over/wash-out (WO)/add-in Pf DGFA assays permit discrimination between gametocyte- and gamete-targeted activity[23]. The *P. berghei* ookinete development assay[37] tests activity against early mosquito stage parasites and cross-reactivity to *P. berghei*. **b** Table summarising outcome of compound profiling. Compounds fell into four categories: gamete-targeted (purple); transmission-specific (gametocyte-targeted, green); dual asexual/gametocyte targeted (blue); asexual-specific (orange). Red blocks indicate compound was active in respective assay (IC_{50} > highest assay concentration: 12.5 μM asexual; 10 μM ATP; 25 μM MITO; 12.5 μM WO; 10 μM Add-in; >12.5 μM Pb Ookinete), grey indicates inactive and white indicates not tested. The exception being the Pf DGFA columns: compounds that were irreversible (IRR), e.g. active in carry-over and wash-out (WO) were designated gametocyte-active; compounds that lost activity in wash-out format were designated gamete-active

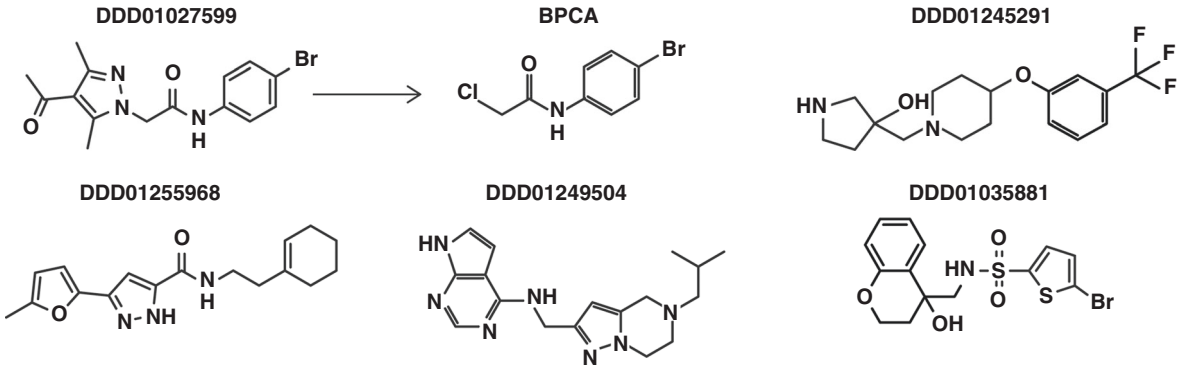


Fig. 3 Chemical structure of GHCDL compounds selected for further study. Five compounds showing a range of transmission-blocking activity at the profiling stage were selected for detailed study. DDD01027599 (found to actually be BPCA—see Supplementary Fig. 1-2) and DDD01245291 are active against gametocytes and asexuals; DDD01255968 and DDD01249504 are active specifically against male gametocytes; and DDD01035881 specifically targets male gamete formation

Microtubule staining showed some cells formed spindle fibres however these appeared disordered in the absence of DNA replication (Fig. 4f). Contrastingly, the first round of DNA replication of DDD504-treated male gametocytes appeared with similar kinetics to the DMSO control (Fig. 5b). However, the second and third divisions were delayed with a smaller proportion of cells reaching 8n. Interestingly, microtubule staining appeared to show that during DNA replication, the spindle poles do not separate and rotate into opposition, but cluster at one location rather than being evenly spaced out around the cell periphery. The few cells that do attempt exflagellation did not have properly segregated genomes and no organised flagellar structure (Fig. 4d). Most DDD968-treated male gametocytes did not replicate their DNA and remained with 1n genome copies (Fig. 5b). However, some cells successfully progressed to 8n with disordered appearing spindle fibres and resulted in an irregular-shaped cell possessing a large DNA-rich mass and intense large foci of tubulin-rich cytoplasm that distorted the overlying erythrocyte membrane (Figs. 4e and 5b, g). Finally, the gamete-targeted DDD881, like DDD291, permitted induced gametocytes to round up but only a few cells replicated their DNA and none exflagellated (Fig. 5b, h). In activated cells, the usually diffuse DNA of the gametocyte frequently appeared somewhat condensed with tubulin-rich accumulations at various points surrounding it (Fig. 4g). Although phenotypes do not define a precise mode of action, the distinct nature of each suggests very different cellular targets during male gametogenesis.

Preliminary chemical profiling, SAR and DMPK analysis. Having explored their effects on cell development, each compound was resynthesized either 'in house' or re-sourced commercially and their activity re-confirmed in the Pf DGFA (Supplementary Methods and Supplementary Fig. 1-4). Surprisingly freshly resynthesized DDD0504, DDD968 and DDD599 were all inactive in the Pf DGFA. DDD504 and DDD968 were hypothesised to be prone to oxidation and potency of both could be restored by aging the molecules (Supplementary Fig. 5). By ^{1}H-NMR, aged compounds appeared to be a mixture of different products and so the identity of the active metabolite(s) could not be resolved. However, preliminary analysis of DDD504 suggests that the most likely position for its oxidation is the 4-unsubstituted position in the pyrazole ring, as seen by the loss of the signal for that proton in the ^{1}H-NMR spectra upon aging (Supplementary Fig. 5). Consequently, study of both DDD504 and DDD968 was paused pending future identification of active component(s). The GHCDL-derived stock of DDD599 gave different LCMS and NMR spectra than resynthesized DDD599 and was positively identified as N-(4-bromophenyl)-2-chloroacetamide (BPCA) (Supplementary Fig. 1-2). When adjusted for correct molecular weight, BPCA was found to be almost identically active to GHCDL DDD599 (Asexual $IC_{50} = 0.80$ vs. 0.80 μM; Pf DGFA male $IC_{50} = 1.46$ vs. 1.38 μM; Pf DGFA female $IC_{50} = 10.98$ vs. 3.43 μM, respectively). We hypothesise that BPCA is a by-product of synthesis. Unsurprisingly, BPCA was reactive with nucleophiles (evidenced by being trapped by glutathione, Supplementary Table 1) and analogues lacking the reactive chlorine were inactive (Fig. 6). However, a broad range of activities was found amongst analogues containing the carbon potentially susceptible to nucleophilic attack with anti-parasite activity not correlated with general cytotoxicity. Substituting the bromine atom for a hydroxyl or hydroxymethyl group gave the highest parasite selectivity. No analogues of DDD291 were commercially available to conduct structure activity relationship (SAR) however drug metabolism and

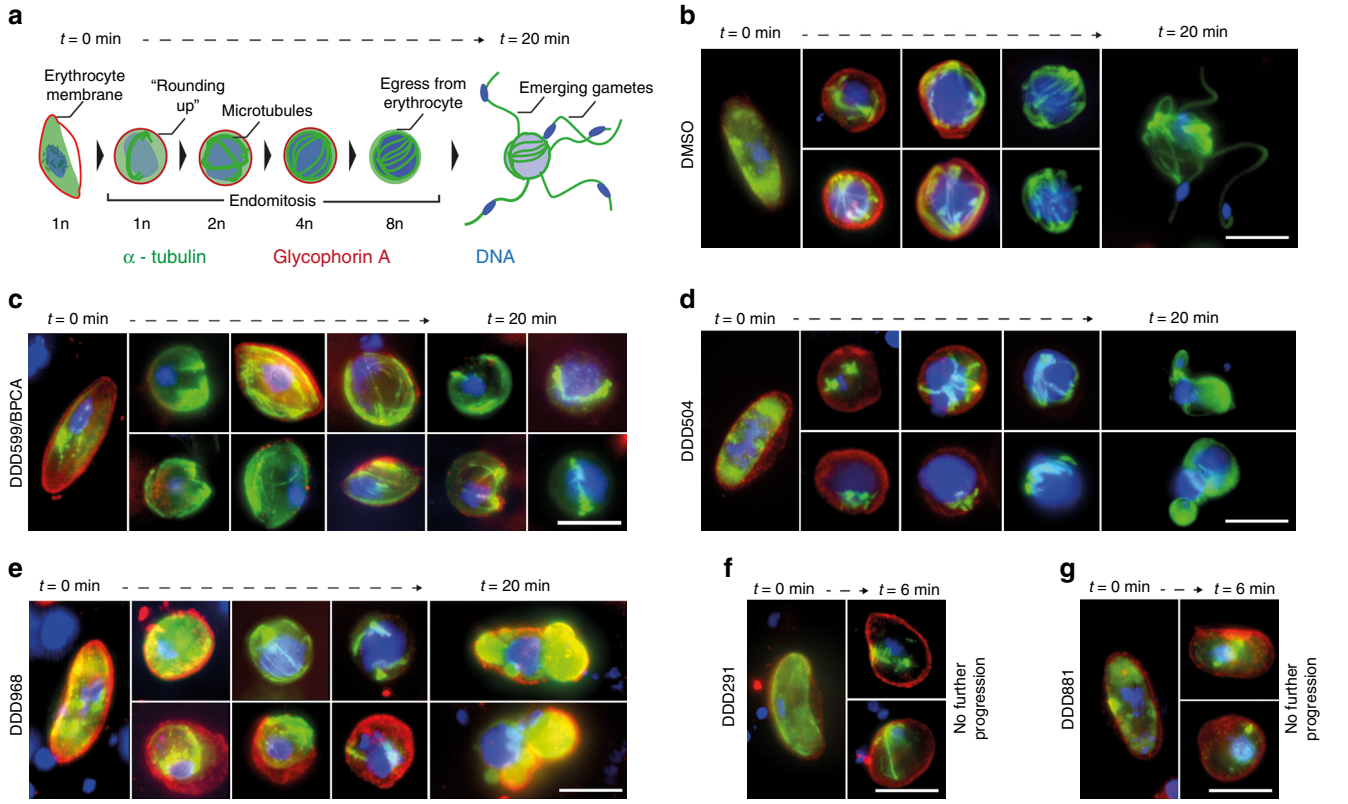


Fig. 4 Monitoring the effect of compound treatment on male gamete formation by IFA. Gametocytes were treated for 24 h with DMSO or 10 μM test compound and then gamete formation triggered by the addition of ookinete medium and reduction to room temperature. Aliquots were sampled at different time points and immediately fixed before being stained directly for α-tubulin (green), glycophorin A (red) and DNA via DAPI labelling (blue). Images show representative non-induced cells (0 min), representative cells during gamete formation progression (2–10 min), and representative cells showing the most advanced phenotype at 20 min. **a** Upon activation, male gametocytes initially round up before undergoing three endomitotic genome replications, egressing from the surrounding erythrocyte membrane and releasing up to eight flagellated gametes. **b** Images from left to right show DMSO-treated cells undergoing normal male gamete formation over 20 min. Male gametocytes initially have an elongated morphology with a faint nucleus, relatively homogenous tubulin distribution and are surrounded by an erythrocyte membrane. Upon induction of gametogenesis, cells round up and begin three rounds of endomitosis, with ordered microtubule spindle fibres and increasingly intense DNA staining. Towards the end of gametogenesis, the surrounding erythrocyte membrane is shed and up to eight microgametes emerge from the cell possessing a microtubule-rich flagellum and one replicated genome. **c** DDD599/BPCA-treated cells; **d** DDD504-treated cells; **e** DDD968-treated cells; **f** DDD291-treated cells; **g** DDD881-treated cells. Bars = 5 μm

pharmacokinetics (DMPK) analysis showed good aqueous solubility (>250 μM), acceptable mouse liver microsome clearance rate (4.2 ml min^{-1} g^{-1} Liver), but poor membrane permeability (5.9 nm s^{-1}) in the parallel artificial membrane permeability assay (PAMPA) suggesting oral bioavailability may be low. The sulphonamide R-group of DDD881 was found to be essential for activity and replacement with an amide group resulted in loss of function (Fig. 7 and Supplementary Text). The replacement of the R′-group thiophene ring with benzene was tolerated, and decoration with a single halogen atom enhanced activity (Fig. 7). DDD881 showed good aqueous solubility (>250 μM), with no detectable metabolism in mouse liver microsomes (<0.5 ml^{-1} min^{-1} g Liver) suggesting a suitably promising profile for in vivo efficacy studies.

Confirmation of transmission-blocking activity in mosquitos. Compound inhibition in the Pf DGFA accurately predicts inhibition of parasite transmission to the mosquito in the SMFA[23]. To directly measure the transmission-blocking efficacy of our identified hits, we used an established *P. falciparum* SMFA with a luciferase oocyst readout[26]. DDD599/BPCA and DDD291 were tested at 10 μM in indirect mode in which test compounds were incubated with gametocytes for 24 h before being fed to mosquitoes in the absence of compound and presence of oocysts assessed 8 days later (Fig. 8a and Supplementary Data 4). DDD291 and DDD599/BPCA blocked transmission strongly and gave mean normalised luciferase intensities similar to uninfected, unfed mosquitoes (1.37 and 5.27 arbitrary units, respectively; unfed = 1.12; DMSO-treated control = 88.77). Furthermore, the same pattern was observed with prevalence of infection (Fig. 8b), with no infected mosquitoes observed following DDD291 treatment and BPCA treatment reduced infection prevalence to 25.12% of the DMSO control. As DDD881 was found to exclusively target male gamete formation in the Pf DGFA and potency was lost if washed out, it was evaluated in the Pf SMFA at 10 μM in direct mode and consequently was added directly to the blood meal in the membrane feeder without any pre-exposure to gametocytes. Under these conditions DDD881 completely blocked transmission in two out of three replicates and a luciferase reading above uninfected background was only detected in 1 out of 69 mosquitoes in the third replicate (mean normalised luciferase intensity = 0.26; prevalence = 0.49% of DMSO control).

DDD291 and DDD881 were then evaluated for in vivo transmission-blocking activity in a mouse model of transmission. *P. berghei*-infected mice ($n = 2$ per compound) were given a single intraperitoneal (IP) dose of 50 mg kg^{-1} of DDD291 or

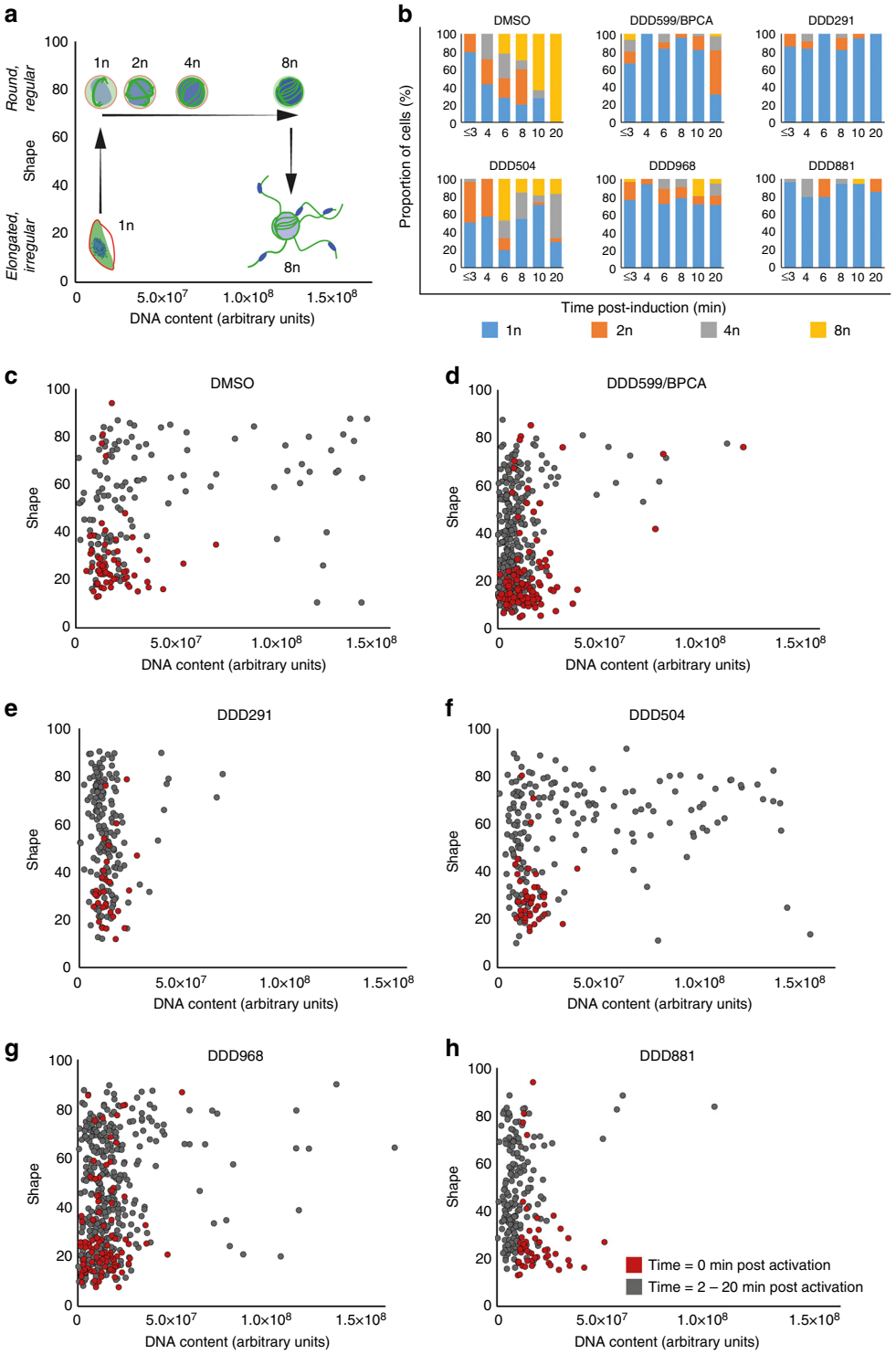


Fig. 5 Computer-aided quantification of male gamete formation from IFA images. Individual cells were extracted from IFA images stained for α-tubulin, glycophorin A and DNA from samples fixed between 0 and 20 min post induction of gamete formation ($n = 195$–668 cells per compound treatment). Cell shape (elongated/irregular vs. round) and haploid chromosome number (1nto 8n) were estimated from α-tubulin and DAPI staining (DNA content) respectively (arbitrary units). **a** Schematic diagram illustrating how cell shape and DNA content parameters vary over the course of male gamete formation. Initially gametocytes are elongated with 1n haploid chromosome number. Upon induction, they round up then undergo three rounds of DNA replication whilst maintaining a round shape. Finally, male gamete release (exflagellation) changes the shape of the cell whilst maintaining a high DNA content. **b** Genome copy number during gamete formation was estimated by benchmarking mean DAPI intensity with respect to the non-activated gametocytes at $t = 0$ min (1n) and exflagellating cells at $t = 10$–20 min (8n). DNA replication was compared between the DMSO control and five test compounds. **c**–**h** Graphs plotting the cell shape and DAPI intensity data for each individual cell analysed. Red dots show the initial distribution of cells before induction ($t = 0$ min). Grey dots show induced cells ($t = 2$–20 min)

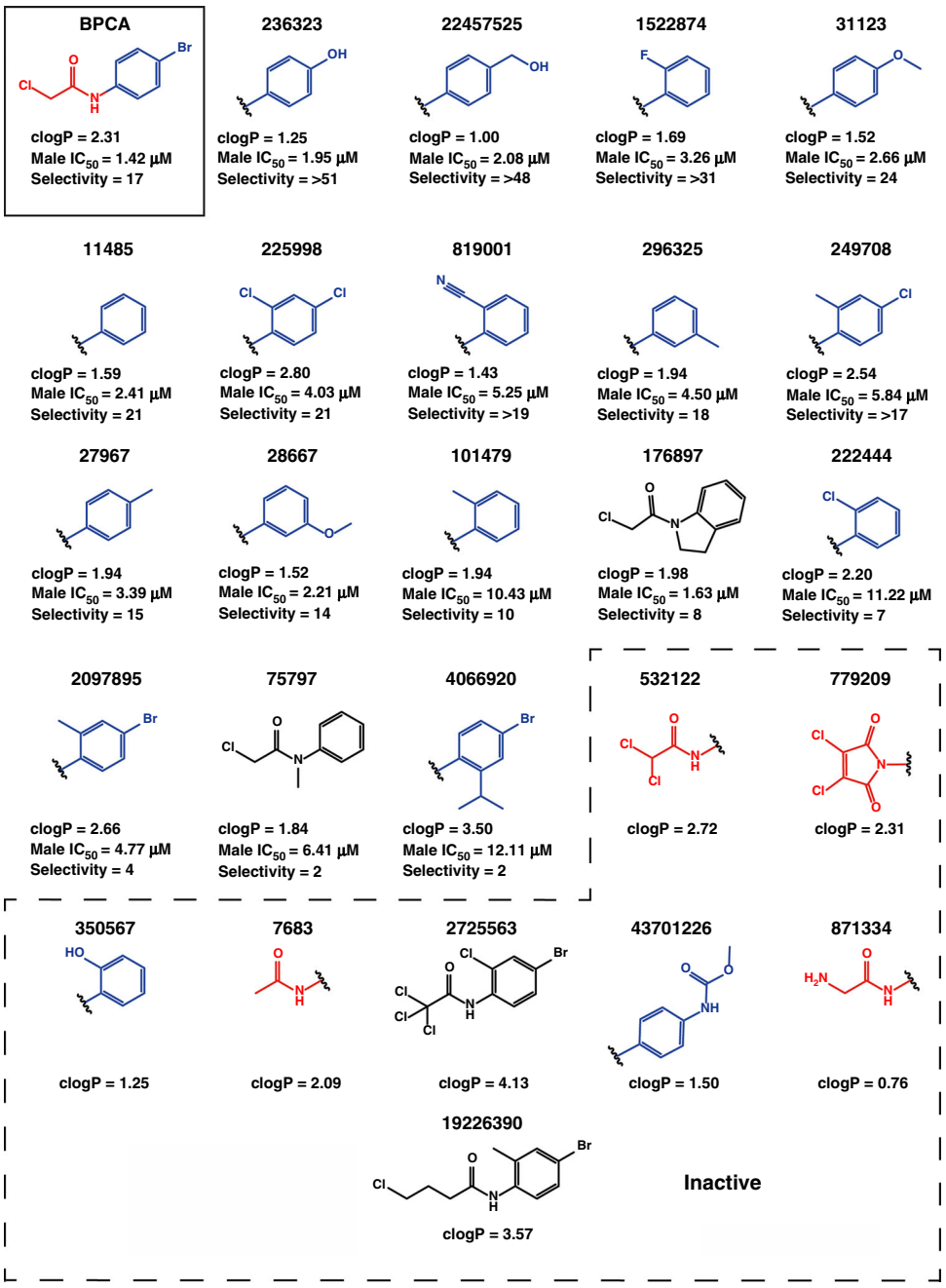


Fig. 6 Structure–activity relationship between BPCA/DDD599 and analogues. Activity in the Pf DGFA male readout and parasite selectivity compared to Tox_{50} in HepG2 cells shown. Red and blue groups indicate modifications to respective parts of the parent molecule. Black molecules are modified in both groups. Analogue IDs correspond to PubChem ID (https://pubchem.ncbi.nlm.nih.gov/)

DDD0881 on day 3 of infection, 24 h prior to mosquito feed. DDD881 was also administered similarly on day 4 of infection only 30 min prior to mosquito feed in a separate cohort of mice (Supplementary Data 5). Twenty-four-hour exposure to DDD291 did not affect asexual parasitaemia but suppressed gametocytaemia ~6-fold in both mice compared to vehicle-only controls (Fig. 9a, b), however due to the very high baseline gametocytaemia saturating mosquitoes (vehicle control groups had mean oocyst intensities of 246.3 and 281.0 oocysts per mosquito), it was not possible to measure a reduction in transmission at the oocyst level (Fig. 9c). DDD881 specifically targets male gametes therefore it was unsurprising that asexual parasitaemia and gametocytaemia were not impacted by treatment. If administered 24 h before mosquito feeding, DDD881 showed no transmission blocking efficacy at the oocyst level. However, if administered 30 min before the feed, a 99.6% blockade on oocyst intensity was observed. Supporting these observations, pharmacokinetic analysis of naïve mice dosed similarly with DDD881 showed that after an initial distribution phase, plasma concentrations remained stable at ~1000 ng ml^{-1} up to 120 min after dosing before being eliminated, with an approximate half-life of 90 min (Fig. 9d). Combined, these data suggest that, with improved stability or slow release, the N-4HCS scaffold could provide a potent starting point for future transmission-blocking antimalarials.

Discussion

Using transmission as the first screening filter yielded novel chemical scaffolds that were not identified in the parallel asexual

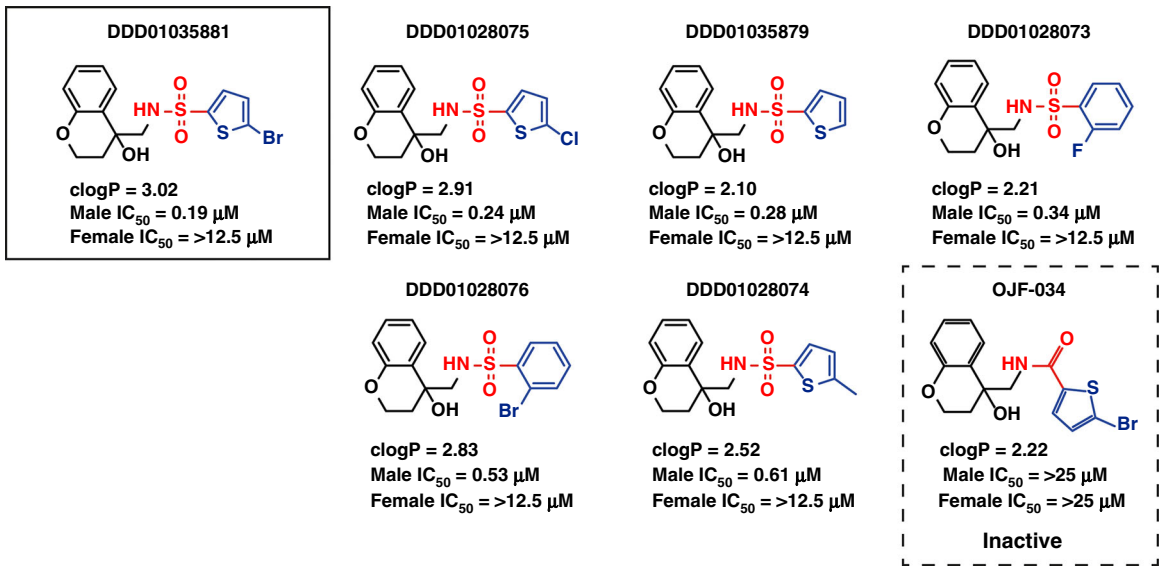


Fig. 7 Pf DGFA structure activity relationship between DDD01035881 and analogues. Red and blue groups indicate modifications to respective parts of the parent molecule. Analogue IDs correspond to molecules within the GHCDL with the exception of OJF-034 which was synthetised in-house

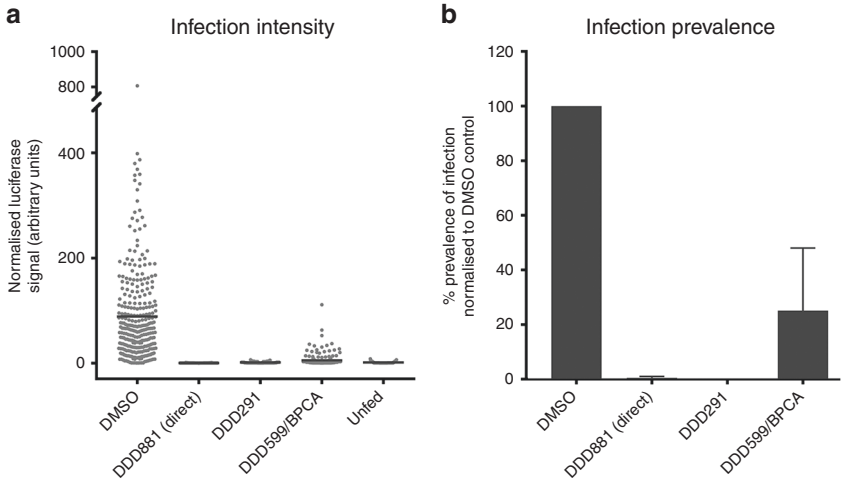


Fig. 8 Transmission-blocking efficacy of leads in *P. falciparum* SMFA. The predictive power of the Pf DGFA to identify transmission-blocking compounds was assessed by treating GFP/luciferase-expressing *P. falciparum* gametocytes for 24 h with DMSO, DDD291 or DDD599/BPCA and then feeding them to *A. stephensi* mosquitoes in indirect mode in which test compound is absent from the blood meal. As DDD881 targets gamete formation rather than gametocytes, membrane feeds with this compound were performed in direct mode, added directly to the blood meal with no prior incubation. **a** Normalised luciferase intensity from individual mosquitoes ($n = 56$–72 per condition per replicate) was compared to DMSO and unfed (uninfected) controls. Data combined from three independent biological replicate feeds. Grey dots indicate individual luciferase readout for individual mosquitoes and black bar shows the mean. **b** Calculated infection prevalence of mosquito feeds normalised to respective DMSO control. Error bars denote the standard error of the mean

screen and showed inhibition in mosquito transmission assays. This suggests that within the ~7 million compounds already screened by the research community for asexual activity and discarded, there are transmission-blocking molecules still waiting to be discovered. Male gametocytes are much more sensitive to antimalarial compounds than females[23,27]. Likely this is due to the rapid and complex nature of male gamete formation which provides more opportunities for intervention. This is further evidenced by the five distinct inhibition phenotypes of the five compounds studied here (Fig. 4), and also highlights the utility of phenotypic immunofluorescence to shed light on drug targets for which resistance selection is impractical. DDD599/BPCA is a small reactive molecule with poor parasite selectivity. Interestingly however, varying the bromophenyl group greatly affected both activity and parasite selectivity. DDD599/BPCA and analogues therefore may make promising tool molecules for covalent ligand discovery of essential proteins in the parasite genome[28]. DDD504 and DDD968 showed gametocyte-specific activity. Conceptually this class of sexual stage specific antimalarial would be partnered with a schizonticidal combination therapy to both cure malarial symptoms and prevent onward transmission to mosquitoes, effectively protecting both infected persons and the much larger population at risk of infection[11]. Both compounds showed striking phenotypes against male gamete formation (Fig. 4d) and work is now ongoing to identify the active component(s) within these unstable compounds to determine their suitability for further progression. In vitro, DDD291 showed low micromolar activity against asexuals, and both male and female gametocytes (Supplementary Data 3). Transmission was almost totally arrested by DDD291 in the Pf

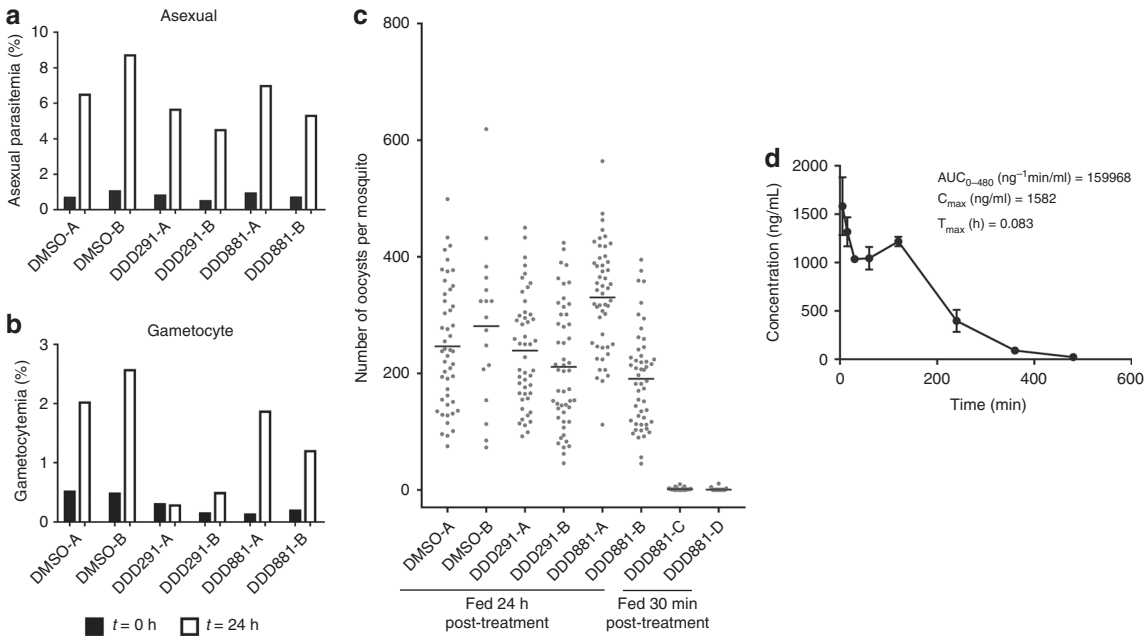


Fig. 9 In vivo transmission-blocking efficacy in *P. berghei* direct feeding assays. Eight phenylhydrazine-treated mice were infected with *P. berghei* constitutively expressing GFP. On day 3 of infection, they were assigned into four groups of two mice (DMSO A + B; DDD291 A + B; DDD881 A + B and C + D). Three groups received either 50 mg kg^{-1} DDD291, 50 mg kg^{-1} DDD881 or DMSO + vehicle control by IP injection. Prior to dosing and 24 h later, immediately before feeding *to A. stephensi* mosquitoes, **a** asexual parasitemia and **b** gametocytaemia were recorded. The fourth group received a 50 mg kg^{-1} DDD881 dose on day 4, 30 min prior to mosquito feed. **c** Seven days after feeding, mosquitoes were dissected ($n = 17$–52 per condition) and oocysts recorded by fluorescent microscopy and automated image analysis. Horizontal bars indicate the mean. **d** PK analysis of DDD881. BALB/c mice were dosed with 50 mg kg^{-1} DDD881 ($n = 3$) and plasma concentrations were monitored over time. After an initial distribution phase, DDD881 was eliminated with a half-life of ~90 min. Error bars denote the standard deviation

SMFA, however in vivo its effects were less pronounced. Likely the weak in vivo activity is linked to poor membrane solubility of this molecule which could be improved through SAR optimisation.

Of all hits, the N-4HCS scaffold shows the greatest promise as a new chemotype for transmission-specific antimalarial drug development. It is fast-acting, non-toxic and amenable to further medicinal chemistry. Its precise mode of action is unknown; however, it specifically targets early male gamete formation and arrests development before DNA replication. Several other molecules targeting male gamete formation are under development as potential therapeutics[29–31]. Clinical patients treated with current artemisinin-combination therapies (ACTs) even supplemented with a low dose of the only licenced transmission-blocking therapeutic, primaquine, are still infectious to mosquitoes for several days after treatment[32,33]. To immediately halt and maintain a block in transmission, administration of a DDD881-like molecule either with a longer half-life, reformulated for slow release, or administered over multiple doses, could close this transmission window between treatment and complete cure during which drug resistance is being selected for and could escape. Given the low toxicity to human cells and coupled to future improvements in bioavailability/longevity, N-4HCS could be used as a chemical vaccine in mass drug administration campaigns. We envision that in targeted malaria endemic areas, the entire population could be treated with intermittent curative doses of a conventional schizonticidal therapy during the dry season to disrupt the residual parasite reservoir in humans and then use maintenance dose(s) of a DDD881-like molecule to protect the mosquito population from being re-infected as the rainy season begins to suppress new incidences of malarial infection. Based on these findings, we believe further investigation of similar transmission-specific blocking antimalarials is clearly warranted.

Methods

Provision of the GHCDL and screening conditions. The Global Health Chemical Diversity Library (GHCDL) was compiled by Dundee University Drug Discovery Unit (DDU) comprising 68,689 compounds with lead-like properties enriched for chemotypes not known to have been previously screened against malaria parasites. The library was provided by DDU dissolved in 100% dimethylsulfoxide (DMSO) in screening-ready 384-well plates (781091, Greiner). Plates arrived frozen and were stored at −20 °C and only thawed immediately prior to use. Chemical structures for the GHCDL can be accessed via the ChEMBL Database[34]. The library was screened in the Pf DGFA with a single replicate at 2 µM with a 48 h pre-incubation of test compounds with stage V gametocytes prior to triggering the gamete formation readout. The initial hit rate was low and so a generous cut-off of >30% inhibition was used yielding 251 hits. Upon re-test in dose response, 24 compounds showed an $IC_{50} < 10$ µM. The GHCDL was also screened against asexual parasites with a single replicate at 2 µM over 72 h yielding 412 hits with a cut-off of >50% inhibition. Upon retest in dose response, 416 showed an $IC_{50} < 10$ µM. Compounds were clustered using the OSIRIS DataWarrior using the FragFP algorithm with a 0.8 cut-off.

Culture of *P. falciparum* asexual and sexual blood stages. *P. falciparum* NF54 strain (originally isolated from an imported malaria case in the Netherlands in the 1980s; BEI Resources, cat. no. MRA-1000) asexual and sexual stages culture was performed as previously described[35]. Gametocyte cultures were initiated at 1% asexual ring stage parasitaemia and 4% haematocrit in 40 ml final volume. To induce gametocyte production, complete culture medium (CM) (RPMI 1640 supplemented with 25 mM HEPES, 50 µg ml^{-1} hypoxanthine, 2 g l^{-1} $NaHCO_3$ and 10% pooled human male type A+ serum) was replaced daily for 14 days without fresh erythrocyte addition. Human serum was obtained from Interstate Blood Bank, A^+ serotype; no aspirin 2 h before drawing and no antimalarials 2 weeks before drawing. On day 14 after culture induction, gametocyte production was assessed by thin smear and Giemsa staining, and exflagellation accurately counted in a haemocytometer[35]. Gametocyte cultures with >0.2% exflagellation (compared to total erythrocyte cell number) were deemed acceptable for use in the Pf DGFA. Note, all human biological samples were sourced ethically and their research use was in accord with the terms of the informed consents under an IRB/EC approved protocol.

***P. falciparum* dual gamete formation assay (Pf DGFA)**. In screening mode, the assay was performed as described in Delves et al.[35] with a mean Z′ factor of 0.56 ± 0.14 (SD) (male) and 0.71 ± 0.17 (SD) (female). Pooled mature gametocyte cultures with the capacity to yield >0.2% exflagellation (of total cells) were diluted in CM to 14 million cells per ml and so that 700,000 cells were dispensed in 50 µl into each well of the warmed 384-well screening plates. Parasites were incubated in the plates with compounds for 48 h in a humidified chamber under 92%N_2/5% CO_2/3% O_2 gas mix before gamete formation was triggered by addition of 10 µl per well ookinete medium (RPMI 1640 supplemented with 25 mM HEPES, 50 µg ml^{-1} hypoxanthine, 2 g l^{-1} $NaHCO_3$, 100 µM xanthurenic acid) containing 0.5 µg ml^{-1} anti-Pfs25 clone 4B7 (BEI Resources, cat. no. MRA-315) conjugated to the fluorophore Cy3 (GE Healthcare), and also by cooling the plate at 4 °C for 4 min and then a further 5 min at 28 °C. Exflagellation was recorded immediately by brightfield microscopy using a Nikon Ti-E widefield microscope at ×4 objective, ×1.5 zoom, recording a 10-frame video time-lapse over 2 s for each well. Afterwards, plates were incubated in the dark at 28 °C for a further 24 h to allow female gametes to maximally express Pfs25 on their surface. Female gamete formation was recorded by single-image fluorescence microscopy using the same microscope and magnification as above. Exflagellation and female gamete formation were quantified by specific algorithms designed with the open-source ICY Image Analysis software[36]. Data were normalised to the percentage of inhibition of the biological response by using positive (12 µM Gentian Violet, Ctrl2) or negative (0.5% DMSO, Ctrl1) controls following Eq. (1) described below:

$$\%\text{Inhibition} = 100 - (((\text{test compound} - \text{Ctrl2})/(\text{Ctrl1} - \text{Ctrl2})) \times 100) \quad (1)$$

Assay performance statistics, such as signal to background ratio, Z′ and robust 3×SD activity cut-off were calculated using templates in ActivityBase XE (IDBS, Guilford, Surrey, UK). Hit population analysis and visualisation were conducted using Spotfire DecisionSite (Spotfire, Inc., Somerville, Massachusetts). The pIC_{50} ($-\log IC_{50}$) values were obtained using the ActivityBase XE nonlinear regression function in the full curve analysis bundle. In screening mode, the Pf DGFA achieved a mean Z′ factor of 0.56 ± 0.14 (SD) (male) and 0.71 ± 0.17 (SD) (female).

In profiling mode, the Pf DGFA was performed in 96-well plates[23] in wash-out and add-in formats to aid manual manipulation steps. In the wash-out format, gametocytes were incubated for 24 h with test compounds in round-bottomed 96 well plates and then culture medium replaced three times over 6 h, to remove as much of the compound as possible from the well. Gametocytes were then rapidly transferred to a flat bottomed 96-well plate containing ookinete medium and anti-Pfs25 to trigger gametogenesis and then imaged and quantified as above (in the absence of test compound), hence gametogenesis was assayed in the absence of compound. In add-in format, gametocytes were added directly to flat-bottomed 96-well plates containing test compounds, ookinete medium and anti-Pfs25. Gametogenesis was triggered simultaneously with compound treatment hence only the process of gametogenesis was exposed to compound.

Whole-cell time extended asexual growth assay. Asexual activity was assayed via *Plasmodium* lactate dehydrogenase activity (pLDH), a surrogate of asexual parasite growth[20]. Cultures of 3D7 strain (BEI Resources, cat. no. MRA-102) asexual blood stages at 0.25% parasitaemia and 2% haematocrit, in RPMI-1640 supplemented with 5% Albumax and 150 µM hypoxanthine, were dispensed into 384-well plates (25 µl per well) containing the test compounds. 2 µM artesunate and DMSO were used as the positive and negative controls, respectively. Parasites were incubated for 72 h at 37 °C, under 5% CO_2/5% O_2/90% N_2 and then frozen at −70 °C. Plates were warmed at RT and 70 µl per well of reaction solution (100 mM sodium L-lactate, 100 mM 3-acetylpyridine adenine dinucleotide (APAD), 125 µM NitroBlue tetrazolium (NBT), 200 µl ml^{-1} diaphorase, 0.5% tween 20, 100 mM Tris-HCl pH 8) were added. After plate mixing, NBT reduction was measured by absorbance at 650 nm using Envision (Perkin Elmer).

Gametocytocidal ATP-based bioluminescence assay (GC-ATP). The metabolic viability of late stage gametocytes was determined using a gametocyte ATP bioluminescence assay[16]. Stage IV–V 3D7 gametocyte cultures were double-purified by density gradient sedimentation over NycoPrep® followed by magnetic isolation. Then, parasites (50 µl per well containing 12,500 gametocytes) were added to compound pre-dispensed 384-well plates (781091, Greiner) and incubated at 37 °C for 48 h under 5% CO_2/3% O_2/92% N_2. BacTiter-Glo® kit (G8231, Promega) was used to determine the ATP levels of viable parasites according to manufacturer's instructions. After reagent addition (50 µl per well), luminescence of the plates was measured using a microplate reader (HTS counter Victor, Wallac).

Gametocytocidal MitoTracker-based viability assay. As another independent assessment of the metabolic viability of compound-treated stage V gametocytes, the Saponin-lysis Sexual Stage Assay (SaLSSA) was employed[7]. A volume of 100 nl of test compounds were pre-dispensed in 384-well plates (781091-2B, Greiner) in 12-point dose response (25 µM to 1.41×10^{-4} µM), prior to the addition of synchronous NF54 stage V gametocytes (40 µl at 0.70% gametocytaemia). Assay plates were then incubated for 72 h in a low oxygen environment (92% N_2, 5% CO_2, 3% O_2) before a 10 µl MitoTracker Red CMXRos (2.5 µM) and saponin solution (0.13%w/v) was added. Plates were returned to 37 °C for 1 h to allow for complete red blood cell lysis, after which viable gametocytes were detected using an Operetta high-content imaging system. Analysis was performed using the Harmony package software, with potency calculated relative to puromycin (positive control) and DMSO (negative control).

***P. berghei* ookinete development assay (Pb ODA)**. All mouse procedures were performed in accordance with the UK Animals (Scientific Procedures) Act (PPL 70/7185) and approved by the Imperial College Animal Welfare and Ethical Review Body (AWERB). The ability of test compounds to inhibit *P. berghei* early mosquito stage development was tested in the Ookinete Development Assay[37] with a few exceptions. Anaesthetised 6- to 8-week-old female Tucks Ordinary (TO) mice infected with *P. berghei* strain CTRPpGFP[38] were rapidly exsanguinated by cardiac puncture and 500 µl of blood diluted in 25 ml of ookinete medium supplemented with 20% foetal bovine serum. Immediately the blood/medium mixture was dispensed by multichannel pipette into 384 well plates containing pre-plated test compounds. 10 µM cycloheximide and DMSO were used as the positive and negative controls, respectively. Plates were stored in the dark in a humidified incubator at 18 °C for 24 h. Ookinete production was imaged by fluorescence microscopy of GFP expression under the ookinete-specific CTRP promoter using a Nikon Ti-E widefield microscope and ×10 objective. Ookinete production was quantified using ICY and percentage inhibition calculated as above with reference to positive and negative controls.

Determination of compound activity profile. Compounds were classified as asexual-specific if they showed IC_{50}s < 12.5 µM in the asexual assay but no activity in any other profiling assay. Compounds were classified as dual asexual-gametocyte targeted if they possessed asexual activity as above but also an IC_{50} < 12.5 µM against male or female gametocytes in the 48 h Pf DGFA carry-over format and maintained potency after washing out in the wash-out format and had no activity in the add-in format. Compounds were classified as transmission-specific if they were inactive up to 20 µM against asexual parasites but showed IC_{50}s < 12.5 µM against male or female gametocytes in the 48 h Pf DGFA carry-over format and maintained potency after washing out in the wash-out format and had no activity in the add-in format (with the exception of DDD968 which was also active in the add-in format). Compounds were classified as gamete-targeted if they were inactive against asexuals up to 20 µM but showed IC_{50}s < 12.5 µM against male or female gametocytes in the 48 h Pf DGFA carry-over format and also activity >12.5 µM in the add-in format but became inactive if washed-out.

***P. falciparum* SMFA**. SMFAs were performed commercially by TropiQ Health Sciences (Nijmegen, The Netherlands)[26]. Cultures of mature stage V gametocytes of *P. falciparum* expressing a GFP-Luciferase fusion protein under the control of the *hsp70* promoter were treated with DMSO or 10 µM of test compound for 24 h (indirect mode). They were then mixed with uninfected erythrocytes and pelleted. The cell pellet was resuspended in human serum to form the blood meal and fed to *Anopheles stephensi* mosquitoes. For direct feeding, gametocytes did not receive pre-exposure to test compounds and test compound was added directly to the blood meal immediately prior to mosquito feeding. Eight days after infection, mosquitoes were individually processed and their lysate assessed for luciferase activity in comparison to uninfected mosquitoes.

***P. berghei* mosquito feeding assays**. Six- to eight-week female T0 mice were treated with phenylhydrazine 3 days prior to intraperitoneal (IP) inoculation with 100 µl of mouse blood infected with the constitutively GFP expressing *P. berghei* 507 strain[39]. On day 3 after infection, thin blood smears were taken from tail blood to quantify parasitaemia and gametocytaemia. Mice were divided randomly into groups of two, received IP injections of 50 mg kg^{-1} of test compounds or vehicle control (33% DMSO in dH_2O) and fed to *Anopheles stephensi* mosquitoes 24 h later. The exception was two mice that were dosed with DDD01035881 on day 4 of infection only 30 min prior to mosquito feeding. Twenty-four hours after feeding, unfed mosquitoes were removed and remaining mosquitoes maintained for a further 9 days on sucrose solution. Mosquito midguts were then dissected, imaged and oocysts quantified by semi-automated computer analysis[40].

Hep G2 cytotoxicity assay. Actively growing HepG2 human cells (85011430, European Collection of Authenticated Cell Cultures) were detached from the culture surface with trypsin and counted using a Cellometer (Nexcelom). Then, 12 ml of culture per plate required were prepared at a density of 1.0×10^5 cells per ml using Minimum Essential Medium (41090, GIBCO) supplemented with 10% foetal bovine serum (10106–169, GIBCO) and 1% NEAA solution (11140–035, GIBCO). Cells were seeded (25 µl per well) in 384-well plates (781098, Greiner) with pre-stamped compounds and controls (DMSO and Doxorubicin 50 µM) (125 nl per well) using a WellMate dispenser (Thermo Scientific). Cells were incubated at 37 °C and 5% CO_2 in a humidified incubator for 48 h. After incubation, 5 µl of Resazurin (R7017, Sigma) per well (45 µM final concentration) were added and plates were kept at 37 °C for 3.5–4 h. Plates were then read on Pherastar LS plate reader (BMG)

and percentage of inhibition for each test compound was calculated using Eq. (2):

$$\%\text{Inhibition} = 100 - (((\text{TEST COMPOUND} - \text{BLANK})/(\text{DMSO control} - \text{BLANK})) \times 100) \quad (2)$$

TOX_{50}s were calculated using ActivityBase templates.

***P. berghei* liver stage assay**. Compound inhibition of *P. berghei* sporozoite liver infection was assessed in a high-throughput luciferase assay[24]. 1536-well plates (789173-F, Greiner Bio-One) were pre-seeded with 5 µl HepG2-A16-CD81^{EGFP} cells grown in DMEM (11965–092, Invitrogen) containing 10% FBS (35–011-CV, Corning) and 1× Pen Strep Glutamine (10378–016, Invitrogen). Then, 50 nl of compound in DMSO was dispensed in 12-point serial dilution dose-response format (50 µM to 2.82×10^{-4} µM), and incubated overnight.*A. stephensi* mosquitoes infected with *P. berghei*-ANKA-GFP-Luc-SM_{CON} (Pb-Luc)[41] sporozoites bearing the antifolate-resistance-conferring *Toxoplasma gondii* dihydrofolate reductase-thymidylate synthase selectable marker, pyR2. After dissection, ~1000 sporozoites in 5 µl screening media (DMEM, 11965–092, Invitrogen; 5% FBS, 35–011-CV, Corning; 5x Pen Strep Glutamine, 10378–016, Invitrogen) were added per well and incubated for 48 h (37 °C, 5% CO_2). Bioluminescence was measured using an EnVision microplate reader (Perkin Elmer), following the addition of 2 µl per well of Bright-Glo™ (Promega). Compound toxicity against HepG2 cells was determined in parallel by measuring cellular ATP levels reported by luciferase activity. Methods were similar to the *P. berghei* liver stage assay, except for the addition of CellTiter-Glo® (Promega) as a detection reagent. DMSO (0.5%) was used as a negative control in both assays, with Atovaquone (5 µM) and Puromycin (10 µM) acting as positive controls in the *P. berghei* and toxicity assays, respectively.

Recombinant luciferase inhibition assay. A counter-screen to the *P. berghei* liver stage assay was run against recombinant luciferase (*Photinus pyralis*) to measure the intrinsic bioluminescence inhibition from select compounds. Briefly, compounds were plated in 12-point serial dose response (50–2.82×10^{-4} µM) in 1536-well opaque-bottom plates (789173-F, Greiner Bio-One). A 20 pM QuantiLum® Recombinant Luciferase (E1701, Promega) containing solution was made in screening media (DMEM, 11965–092, Invitrogen; 5% FBS, 35–011-CV, Corning; 5x Pen Strep Glutamine, 10378–016, Invitrogen), and 8 µl were added to each well. After 1 h incubation at room temperature, 2 µl of Bright-Glo™ (E2610, Promega) were dispensed per well, and bioluminescence was immediately measured using the EnVision microplate reader (PerkinElmer). DMSO (0.5%) and Luciferase Inhibitor-2 (9.8 µM) (119114, MilliporeSigma) served as negative and positive controls, respectively.

Immunofluorescence staining and modelling of exflagellation. Day 14 gametocyte culture was divided into 4 ml aliquots and treated either with DMSO or 10 µM test compound. After 24 h, 500 µl aliquots of the non-activated gametocytes were fixed in an equal volume of 8% paraformaldehyde (PFA) warmed to 37 °C to generate Time = 0 min ($t = 0$) samples. Gamete formation was induced in the remainder of the cultures by cooling to RT and addition of 500 µl ookinete medium. At $t = 2$, 3, 4, 6, 8, 10, and 20 min 500 µl of culture was removed and immediately fixed in equal volume of 8% PFA at room temperature for 15 min. Fixed cells were diluted in PBS and allowed to settle onto poly-L-lysine-coated glass coverslips overnight. The next day, cells were washed in PBS, permeabilized in 0.1% Triton X-100 and blocked in PBS + 10% FBS. Cells were stained with mouse anti-alpha tubulin (Sigma) clone DM1A (1:500 dilution) and rabbit anti-Glycophorin A (Abcam) clone EPR8200 (1:1000 dilution). Staining was visualised with anti-mouse Alexa448 and anti-rabbit Alexa555 (Thermo-Fisher) both at 1:1000 dilution. Coverslips were mounted onto glass slides with VectaShield mountant (Vector Laboratories) containing 4′,6-diamidino-2-phenylindole (DAPI) to visualise cellular DNA. Cells were imaged at random (n = 195–668 cells per test compound) using a Nikon Ti-E widefield microscope using a × 100 objective lens and taken in 0.2 µm slice z-stack images to capture the whole cell. All images were converted to maximum intensity projections in NIS Elements v4.20 and all further image processing performed in ICY. Individual cells were manually selected and automatically extracted from each image using the Active Contours plugin gated to the tubulin staining. Using the ROI Statistics plugin, the following parameters were calculated for each cell and exported to MS Excel: Cell area, Cell roundness, Cell elongation, and Average intensity of blue channel (DNA). In the DMSO control image collection, it was found that Cell roundness and Cell elongation were proportional and excellent discriminators of falciform-shaped non-activated gametocytes and round activated gametocytes. Outlier cells from the curve were all exflagellating (Supplementary Fig. 6). These two parameters were combined as a ratio of roundness:elongation to produce the parameter Cell shape. Cellular DNA content was estimated by multiplying the average pixel intensity of the blue channel (after subtracting the background intensity of an empty area in the same parent image) with the total cell area.

Generation of active DDD504 and DDD698 by aging. Freshly synthesised powder was dissolved to 30 mM in DMSO and aged for 10 days at room temperature in the light or 10 days at 37 °C in the dark with tube caps opened every 2 days to allow air to circulate. In the light, potency of DDD504 was restored giving an IC_{50} of 381 nM (compared to the untreated compound and compound incubated in the dark at 37 °C that were inactive). Contrastingly, light did not affect DDD986, however restoration of activity appeared to be linked to temperature as prolonged incubation at 37 °C yielded greater activity than when incubated at room temperature (IC_{50} = 5.85 and 15.9 µM, respectively).

DMPK and compound stability analysis. DMPK analyses were performed by the Dundee University Drug Discovery Unit and BPCA/DDD599 stability analysis were undertaken by chemists at GlaxoSmithKline using in-house, standardised approaches[42].

Code availability. All computer codes used to analyse the data in this study are available from the corresponding authors upon reasonable request.

Data availability. The data that support the findings of this study are available from the corresponding authors upon reasonable request.

Received: 24 May 2018 Accepted: 26 July 2018
Published online: 18 September 2018

References

1. Alonso, P. L. et al. A research agenda to underpin malaria eradication. *PLoS Med.* **8**, e1000406 (2011).
2. Hemingway, J. et al. Tools and strategies for malaria control and elimination: what do we need to achieve a grand convergence in malaria? *PLoS Biol.* **14**, e1002380 (2016).
3. World Health Organization. *World Malaria Report 2017* http://www.who.int/malaria/publications/world-malaria-report-2017/report/en/ (WHO, Geneva, 2017).
4. Imwong, M., Hien, T. T., Thuy-Nhien, N. T., Dondorp, A. M. & White, N. J. Spread of a single multidrug resistant malaria parasite lineage (PfPailin) to Vietnam. *Lancet Infect. Dis.* **17**, 1022–1023 (2017).
5. Sinden, R. E. Sexual development of malarial parasites. *Adv. Parasitol.* **22**, 153–216 (1983).
6. Joice, R. et al. *Plasmodium falciparum* transmission stages accumulate in the human bone marrow. *Sci. Transl. Med.* **6**, 244re245 (2014).
7. Plouffe, D. M. et al. High-throughput assay and discovery of small molecules that interrupt malaria transmission. *Cell Host Microbe* **19**, 114–126 (2016).
8. Sinden, R. E., Canning, E. U., Bray, R. S. & Smalley, M. E. Gametocyte and gamete development in *Plasmodium falciparum*. *Proc. R. Soc. Lond. B Biol. Sci.* **201**, 375–399 (1978).
9. Mair, G. R. et al. Regulation of sexual development of *Plasmodium* by translational repression. *Science* **313**, 667–669 (2006).
10. Sinden, R. E. A biologist's perspective on malaria vaccine development. *Hum. Vaccin.* **6**, 3–11 (2010).
11. Burrows, J. N. et al. New developments in anti-malarial target candidate and product profiles. *Malar. J.* **16**, 26 (2017).
12. Burrows, J. N., van Huijsduijnen, R. H., Mohrle, J. J., Oeuvray, C. & Wells, T. N. Designing the next generation of medicines for malaria control and eradication. *Malar. J.* **12**, 187 (2013).
13. Duffy, S. & Avery, V. M. Identification of inhibitors of *Plasmodium falciparum* gametocyte development. *Malar. J.* **12**, 408 (2013).
14. D'Alessandro, S. et al. A chemical susceptibility profile of the *Plasmodium falciparum* transmission stages by complementary cell-based gametocyte assays. *J. Antimicrob. Chemother.* **71**, 1148–1158 (2016).
15. Lucantoni, L., Fidock, D. A. & Avery, V. M. Luciferase-based, high-throughput assay for screening and profiling transmission-blocking compounds against *Plasmodium falciparum* gametocytes. *Antimicrob. Agents Chemother.* **60**, 2097–2107 (2016).
16. Lelievre, J. et al. Activity of clinically relevant antimalarial drugs on *Plasmodium falciparum* mature gametocytes in an ATP bioluminescence "transmission blocking" assay. *PLoS One* **7**, e35019 (2012).
17. Tanaka, T. Q. & Williamson, K. C. A malaria gametocytocidal assay using oxidoreduction indicator, alamarBlue. *Mol. Biochem. Parasitol.* **177**, 160–163 (2011).
18. Miguel-Blanco, C. et al. Imaging-based high-throughput screening assay to identify new molecules with transmission-blocking potential against *Plasmodium falciparum* female gamete formation. *Antimicrob. Agents Chemother.* **59**, 3298–3305 (2015).

19. Colmenarejo, G. et al. Predicting transmission blocking potential of anti-malarial compounds in the Mosquito Feeding Assay using *Plasmodium falciparum* Male Gamete Inhibition Assay. *Sci. Rep.* **8**, 7764 (2018).
20. Gamo, F. J. et al. Thousands of chemical starting points for antimalarial lead identification. *Nature* **465**, 305–310 (2010).
21. Guiguemde, W. A. et al. Chemical genetics of *Plasmodium falciparum*. *Nature* **465**, 311–315 (2010).
22. Plouffe, D. et al. In silico activity profiling reveals the mechanism of action of antimalarials discovered in a high-throughput screen. *Proc. Natl Acad. Sci. USA* **105**, 9059–9064 (2008).
23. Ruecker, A. et al. A male and female gametocyte functional viability assay to identify biologically relevant malaria transmission-blocking drugs. *Antimicrob. Agents Chemother.* **58**, 7292–7302 (2014).
24. Swann, J. et al. High-throughput luciferase-based assay for the discovery of therapeutics that prevent malaria. *ACS Infect. Dis.* **2**, 281–293 (2016).
25. Cowell, A. N. et al. Mapping the malaria parasite druggable genome by using in vitro evolution and chemogenomics. *Science* **359**, 191–199 (2018).
26. Vos, M. W. et al. A semi-automated luminescence based standard membrane feeding assay identifies novel small molecules that inhibit transmission of malaria parasites by mosquitoes. *Sci. Rep.* **5**, 18704 (2015).
27. Delves, M. J. et al. Male and female *Plasmodium falciparum* mature gametocytes show different responses to antimalarial drugs. *Antimicrob. Agents Chemother.* **57**, 3268–3274 (2013).
28. Backus, K. M. et al. Proteome-wide covalent ligand discovery in native biological systems. *Nature* **534**, 570–574 (2016).
29. Jones, I. W. et al. Sexual development of malaria parasites is inhibited in vitro by the neem extract azadirachtin, and its semi-synthetic analogues. *FEMS Microbiol. Lett.* **120**, 267–273 (1994).
30. Ojo, K. K. et al. Transmission of malaria to mosquitoes blocked by bumped kinase inhibitors. *J. Clin. Invest.* **122**, 2301–2305 (2012).
31. Pino, P. et al. A multistage antimalarial targets the plasmepsins IX and X essential for invasion and egress. *Science* **358**, 522–528 (2017).
32. Bousema, T. et al. Revisiting the circulation time of *Plasmodium falciparum* gametocytes: molecular detection methods to estimate the duration of gametocyte carriage and the effect of gametocytocidal drugs. *Malar. J.* **9**, 136 (2010).
33. Dicko, A. et al. Primaquine to reduce transmission of *Plasmodium falciparum* malaria in Mali: a single-blind, dose-ranging, adaptive randomised phase 2 trial. *Lancet Infect. Dis.* **16**, 674–684 (2016).
34. CHEMBL. University of Dundee, Gates Library screen for HepG2 cell viability (CHEMBL3507680). Preprint at https://doi.org/10.6019/CHEMBL3507680 (2018).
35. Delves, M. J. et al. Routine in vitro culture of *P. falciparum* gametocytes to evaluate novel transmission-blocking interventions. *Nat. Protoc.* **11**, 1668–1680 (2016).
36. de Chaumont, F. et al. Icy: an open bioimage informatics platform for extended reproducible research. *Nat. Methods* **9**, 690–696 (2012).
37. Delves, M. J. et al. A high-throughput assay for the identification of malarial transmission-blocking drugs and vaccines. *Int. J. Parasitol.* **42**, 999–1006 (2012).
38. Vlachou, D. et al. in vivo analysis of malaria ookinete locomotion and mosquito midgut invasion. *Cell Microbiol.* **6**, 671–685 (2004).
39. Janse, C., Ramesar, J. & Waters, A. High-efficiency transfection and drug selection of genetically transformed blood stages of the rodent malaria parasite *Plasmodium berghei*. *Nat. Protoc.* **1**, 346–356 (2006).
40. Delves, M. J. & Sinden, R. E. A semi-automated method for counting fluorescent malaria oocysts increases the throughput of transmission blocking studies. *Malar. J.* **9**, 35 (2010).
41. Franke-Fayard, B. et al. Murine malaria parasite sequestration: CD36 is the major receptor, but cerebral pathology is unlinked to sequestration. *Proc. Natl Acad. Sci. USA* **102**, 11468–11473 (2005).
42. Baragana, B. et al. A novel multiple-stage antimalarial agent that inhibits protein synthesis. *Nature* **522**, 315–320 (2015).
43. Almela, M. J. et al. A new set of chemical starting points with *Plasmodium falciparum* transmission-blocking potential for antimalarial drug discovery. *PLoS One* **10**, e0135139 (2015).

Acknowledgements

We thank Didier Leroy, Omar Vandal, Richard Elliott and other members of the Bill & Melinda Gates Foundation sponsored Gametocyte Targeting Consortium for fruitful discussions and guidance in development of a high-throughput DGFA. We thank members of the Dundee University Drug Discovery Unit for provision of screen-ready assay plates and helpful discussions regarding compound identity and activity. We thank the National Health Service Blood and Transplant (UK) and Biobank of Castilla y León, Banc de Sang i Teixits and Centro de Transfusiones de Madrid (Spain) as providers of human red blood cell concentrate. We thank Koen Dechering and Angelika Sturm for help with SMFAs and Kevin Read for help with DMPK and PK/PD work. The following reagent was obtained through MR4 as part of the BEI Resources Repository, NIAID, NIH: *Plasmodium falciparum* anti-Pfs25 MAb 4B7, MRA-28, deposited by D. C. Kaslow. This work was funded by the Bill & Melinda Gates Foundation, grant OPP1043501 (M.J. D., E.H. and J.B.). J.B. is supported by an Investigator Award from Wellcome (100993/Z/13/Z). A.R.-Z. acknowledges Alfonso Martín Escudero Foundation for a postdoctoral fellowship.

Author contributions

M.J.D., C.M.-B., H.M., A.R., U.S., S.Y., O.J.F., I.M., M.L.L., A.B., M.F., F.C., R.E.S., E.H., F.J.G and J.B. designed all experiments. M.J.D., C.M.-B., H.M., A.R., U.S., S.Y., O.J.F., I.M., A.R.-Z., J.R.B. and M.L.L. performed experiments. M.A. and E.A.W. designed and performed the liver stage and mitotracker gametocyte experiments. All authors contributed to manuscript preparation. M.J.D., C.M.-B., F.J.G. and J.B. wrote the manuscript.

Additional information

Supplementary Information accompanies this paper at https://doi.org/10.1038/s41467-018-05777-2.

Competing interests: The authors declare no competing interests.

Reprints and permission information is available online at http://npg.nature.com/reprintsandpermissions/

Publisher's note: Springer Nature remains neutral with regard to jurisdictional claims in published maps and institutional affiliations.

Open Access This article is licensed under a Creative Commons Attribution 4.0 International License, which permits use, sharing, adaptation, distribution and reproduction in any medium or format, as long as you give appropriate credit to the original author(s) and the source, provide a link to the Creative Commons license, and indicate if changes were made. The images or other third party material in this article are included in the article's Creative Commons license, unless indicated otherwise in a credit line to the material. If material is not included in the article's Creative Commons license and your intended use is not permitted by statutory regulation or exceeds the permitted use, you will need to obtain permission directly from the copyright holder. To view a copy of this license, visit http://creativecommons.org/licenses/by/4.0/.

© The Author(s) 2018

Appendix D

The antimalarial screening landscape—looking beyond the asexual blood stage

Available online at www.sciencedirect.com

ScienceDirect

Current Opinion in Chemical Biology

The antimalarial screening landscape—looking beyond the asexual blood stage

Sabrina Yahiya[1], Ainoa Rueda-Zubiaurre[2], Michael J Delves[3], Matthew J Fuchter[2] and Jake Baum[1]

In recent years, the research agenda to tackle global morbidity and mortality from malaria disease has shifted towards innovation, in the hope that efforts at the frontiers of scientific research may re-invigorate gains made towards eradication. Discovery of new antimalarial drugs with novel chemotypes or modes of action lie at the heart of these efforts. There is a particular interest in drug candidates that target stages of the malaria parasite lifecycle beyond the symptomatic asexual blood stages. This is especially important given the spectre of emerging drug resistance to all current frontline antimalarials. One approach gaining increased interest is the potential of designing novel drugs that target parasite passage from infected individual to feeding mosquito and back again. Action of such therapeutics is geared much more at the population level rather than just concerned with the infected individual. The search for novel drugs active against these stages has been helped by improvements to *in vitro* culture of transmission and pre-erythrocytic parasite lifecycle stages, robotic automation and high content imaging, methodologies that permit the high-throughput screening (HTS) of compound libraries for drug discovery. Here, we review recent advances in the antimalarial screening landscape, focussed on transmission blocking as a key aim for drug-treatment campaigns of the future.

Addresses
[1] Department of Life Sciences, Imperial College London, Sir Alexander Fleming Building, Exhibition Road, South Kensington, London SW7 2AZ, UK
[2] Department of Chemistry, Imperial College London, Molecular Sciences Research Hub, White City Campus, Wood Lane, London W12 OBZ, UK
[3] London School of Hygiene and Tropical Medicine, Keppel Street, London WC1E 7HT, UK

Corresponding author: Baum, Jake (jake.baum@imperial.ac.uk)

Current Opinion in Chemical Biology 2019, **50**:1–9

This review comes from a themed issue on **Next Generation Therapeutics**

Edited by **Yimon Aye** and **Paul J Hergenrother**

For a complete overview see the Issue and the Editorial

Available online 12th March 2019

https://doi.org/10.1016/j.cbpa.2019.01.029

1367-5931/© 2019 The Authors. Published by Elsevier Ltd. This is an open access article under the CC BY license (http://creativecommons.org/licenses/by/4.0/).

Introduction

Incredible progress has been made in reducing the global malaria burden since the declaration of the UN Millennium Development Goals in 2000. However, in recent years, progress has stalled, with incidence and death rates from malaria no longer declining [1]., Commitment to these goals triggered a spike in global funding and interest, resulting in an increased implementation of artemisinin combination therapies (ACTs), insecticide treated bed nets (ITNs) and indoor residual spraying (IRS) which was pivotal in addressing the global burden of malaria disease [2]. Parasite resistance to artemisinin, its derivatives and partner drugs [3] and mosquito resistance to insecticides are, therefore, key challenges to get reduction of malarial incidence back on track. It is increasingly acknowledged that a focus on innovation, and not just implementation of the current antimalarial armamentarium, is required to overcome these challenges [4•,5]. New drugs, with novel chemical structures and new modes of action (MoA), will likely be a key component of such innovation [5].

Many groups active in antimalarial drug discovery, coordinate their work within a framework of molecule type [target candidate profiles (TCP)], meaning the lifecycle stage which is compromised by the drug, and medicine class (target product profiles (TPP)], the final drug formulation defined as a combination of TCPs, developed by the not-for-profit Medicines for Malaria Venture, MMV [6••] (Table 1). Sought after characteristics include activity against asymptomatic stages (TCP3-5), endectocides targeting the mosquito (TCP-6) and symptomatic asexual blood stages (ABS), classified as TCP-1 (Table 1). Profiles meet different needs such as medicines for clinical case management, chemoprotection for travellers, and those aimed at breaking population transmission. Protection of the uninfected population is crucial for eventual local elimination of transmission, and can be achieved by either targeting the mosquito (via vector control, bite-prevention or endectocides) or via compounds with transmission blocking activity [6••]. One long-sought goal for optimal treatment formulation is the administration of a Single Encounter Radical Cure and Prophylaxis (SERCaP), removing blood parasitemia and the longer-lived parasite reservoir from patients for both radical cure and elimination of future transmission, all in one go [5].

Drug Discovery by screening

In recent years, great emphasis has been placed on high-throughput screening (HTS) of large compound libraries,

Table 1

Classifications of Medicines for Malaria Venture TCP and TPPs

Target Candidate Profiles

Profile	*Plasmodium* lifecycle stage target	Notes
TCP1 Symptomatic treatment	Asexual blood stages	Active against resistant strains of *Plasmodium*
TCP3 Anti-relapse	Dormant liver-stage hypnozoites	Improved safety compared to primaquine and tafenoquine
TCP4 Chemoprotection	Hepatic schizonts	Effective at equal/lower dose to TCP1 treatment
TCP5 Transmission blocking	Gametocytes/Gametes	Low dose, less than TCP1 treatment
TCP6 Transmission blocking	Insect vector (endectocides)	Low dose, less than TCP1 treatment

Target Product Profiles

Profile	TCPs Addressed	Notes
TPP1 Case Management	TCP1 TCP3 TCP5 TCP6	Single or multiple treatment medicines for treatment of: Severe malaria (TCP1) Uncomplicated malaria and preventative treatment (TCP1) Relapsing malaria (TCP3) Asymptomatic stages for population protection (TCP5 & 6)
TPP2 Chemoprotection	TCP1 TCP4	In the case of epidemics or for migratory populations

to find novel therapeutics having a new MoA, combined with improvement of existing compounds through medicinal chemistry and structure activity relationship (SAR) studies. High-throughput screens (HTS) are generally categorised into two types: target-specific assays (usually biochemical) or whole-cell (phenotypic) tailored to meet the different TCP/TPP criteria [7]. Given the breadth in the literature of both, here we centre our discussion on phenotypic (specifically cellular) screens, with a particular focus on *P. falciparum*, the most virulent parasite causing malaria in humans [8].

Although *in vitro* culture of *P. falciparum* is routine, automation, liquid handling and high-throughput imaging have played key roles in recent advancements in HTS capacity [7]. This has been markedly helped by efforts from the chemical vendor industry and pharma to provide access of compound libraries to smaller institutions and academic research groups, permitting testing on a massive scale, often with millions of compounds. Combined with assay miniaturisation, this has led to development of robust, inexpensive, and reproducible screens, typically utilising 384- or 1536-well plate-based formats [7,9]. To date, the vast majority of screening campaigns have centred on ABS. Recently, however, this has expanded to transmission and pre-erythrocytic stages, including development of screening platforms for sporozoites [10], sexual stage gametocytes [11••], gametes [12], ookinetes [13] and liver stages [14]. In either context, parasite cultures are incubated with compounds of interest and parasite survival is determined as an assay readout. Structures and activity of antimalarial compounds derived from such phenotypic screens are then deposited in the chEMBL Neglected Tropical Disease archive [15].

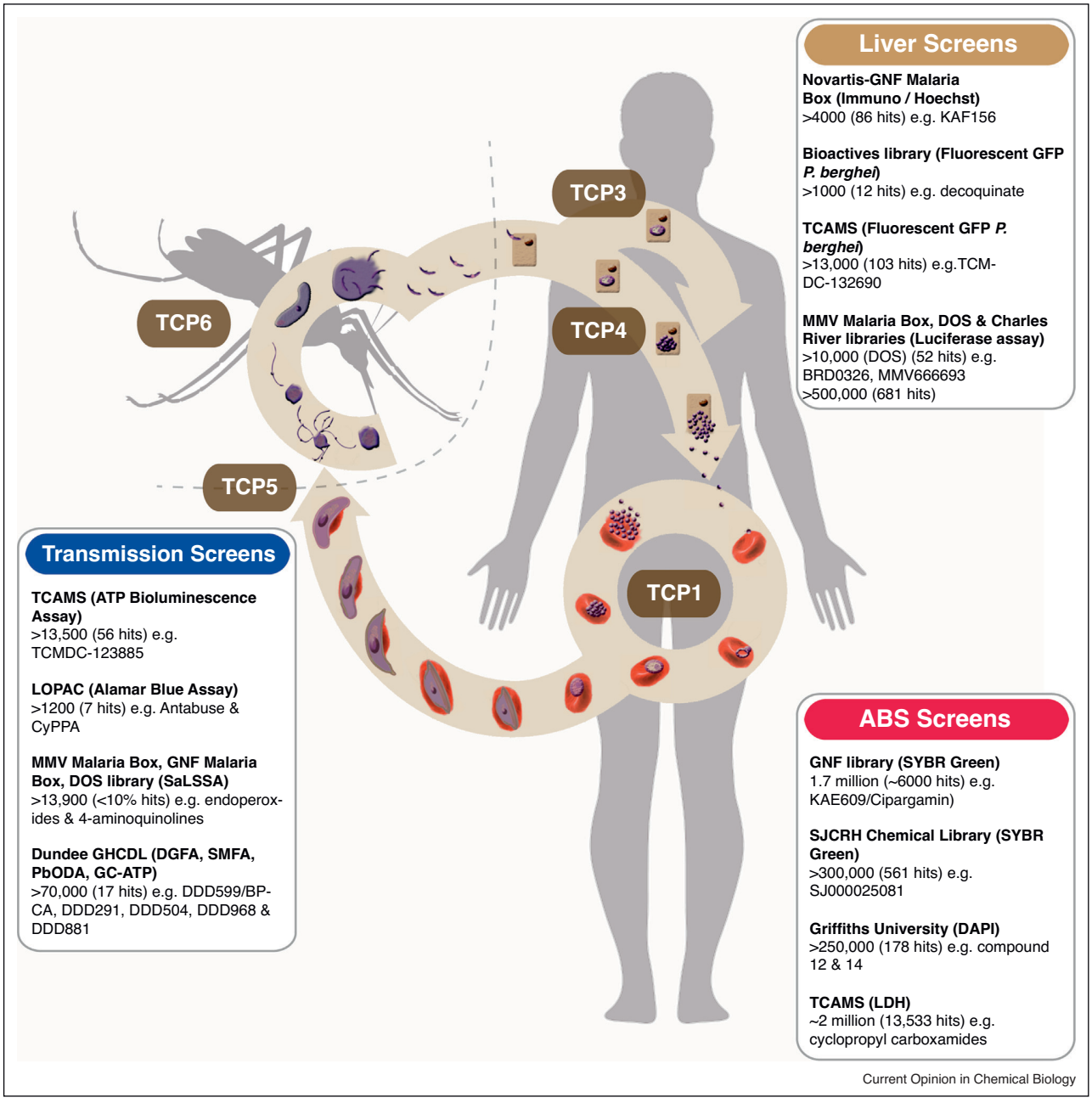
Asexual Blood Stage (ABS) screens

Novel compounds targeting asexual blood stages (under the umbrella of TCP-1) have long been seen as a priority in antimalarial research, being the causative agent of symptoms associated with malaria [6••]. The first *P. falciparum* ABS screen (indeed the first major HTS) tested 1.7 million compounds from the Genomics Institute of the Novartis Research Foundation (GNF) Chemical Library, identifying ~6000 hits [16]. Similar screens followed using 300 000 compounds of the St. Jude Children's Research Hospital (SJCRH) chemical library [17]; 250 000 compounds from the Griffiths University library [18]; and, possibly the largest study, from GlaxoSmithKline who screened almost 2 million compounds [19]. This latter screen yielded an enriched library of >13 500 future potential antimalarials, called the Tres Cantos antimalarial compound set (TCAMS) that has since seeded several other screens (for example, Refs. [20–23]). The numerous asexual blood stage screens performed to date, each using very different methodologies (Figure 1), have identified thousands of hits, some of which have progressed to developmental antimalarials, such as the spirondolone KAE609 (Cipargamin, Figure 2) [24].

Liver stage screens

Beyond ABS, in recent years, the search for novel antimalarials has pushed for drugs targeting other stages of the parasite lifecycle. *Plasmodium* hepatic forms have recently gained significant traction due to improved

Figure 1



The Plasmodium parasite lifecycle highlighting notable cell-based screens and Target Candidate Profiles (TCP) for developmental drugs.
The *Plasmodium* lifecycle occurs in stages between a mosquito vector and vertebrate host covering many different sites for drug intervention. Inoculation of motile sporozoites during the female *Anopheles* mosquito bloodmeal commences the asymptomatic liver stage. Exclusively to *P. vivax* and *P. ovale*, a proportion of liver-stage parasites form dormant hypnozoites (TCP3). Rupture of hepatic schizonts (TCP4) releases small merozoite forms that initiate the symptomatic stages (ABS, TCP1) made up of cycles of erythrocyte invasion, replication and release. A proportion of ABS parasites, rather than divide, commit to sexual differentiation to form the transmissible male and female gametocytes (TCP5), developing over 8–12 days (for *P. falciparum*), likely in the bone marrow, through morphologically distinct stages with sexual dimorphism most apparent at the mature stage V. Upon uptake to the mosquito during a bloodmeal, gametogenesis (formation of mature gametes), is induced rapidly (~10–15 min). This follows environmental cues in the mosquito midgut, including a rise in pH, drop in temperature and the presence of xanthurenic acid, a mosquito-derived excretory product. Gametogenesis commences with the rounding up of both male and female gametocytes and their egress from the host erythrocyte. Male gamete formation, or exflagellation, is a remarkably rapid and tightly regulated process. The process includes three rounds of DNA replication alternating with endomitotic division, followed by the release of eight motile haploid male gametes. Fusion of male and female gametes ensues, leading to formation of a motile zygote that eventually colonizes the mosquito midgut, reseeding the vector for a new

culture techniques, opening up possibilities for finding drugs with causal chemoprophylaxis against liver stages (TCP4) and those that may target the dormant hypnozoite stage (unique to *P. vivax* and *P. ovale* species) classified as TCP3 [25]. Targeting either form hits a natural bottleneck in the parasite lifecycle, and, therefore, a powerful way to reduce the probability of drug resistance developing [26]. One challenge remaining, however, is the need for complete parasite development in the mosquito, required to obtain infective sporozoites to seed assays, and the poor rates of *in vitro* hepatocyte infectivity. Relatively robust assays are starting to emerge for *in vitro* development [14,27], suggesting a turning point in liver stage screening studies. Liver stage screens are often focused on smaller libraries of commercially available compounds with known activity against the asexual blood stages.

One of the first liver-stage screens (Novartis-GNF Malaria Box) identified a lead imidazolopiperazine scaffold. This screen was performed using immunolabelled parasites to determine the ratio of parasitemia to host nuclei, using a high-content imaging system [28]. Lead optimisation yielded a drug candidate, KAF156 (Figure 2) [28], which is not only active against ABS and liver stages, but also blocks parasite transmission. KAF156 is currently undergoing clinical trials [29••]. Another focused screen tested 1037 existing drugs, also by high-content imaging, to detect fluorescent murine malaria parasite, *P. berghei*, liver stages, identifying decoquinate, a compound with activity against the parasite mitochondrial bc_1 complex [30]. Two additional screens worth noting used the TCAMS library, to identify 103 hits with dual inhibitory activity against blood and liver stages [23] and an ultra-HTS format luciferase-based assay, that tested both an open access library of small molecules with confirmed activity against *P. falciparum* ABS (the MMV malaria box) and a Diversity-Oriented Synthesis library from the Broad Institute [31] (Figure 1). Very recently, a landmark screen of half a million compounds from Charles River [66••], consisting of small molecules with an average weight of 369 Daltons, found more than 600 hits with sub-micromolar IC_{50}s using a plate-based *P. berghei* assay (and validating assays with *P. vivax* and *P. falciparum*) similar to that developed in [31]. Hits included mitochondrial inhibitors and several others with potentially novel modes of action.

Although these screens have advanced the pre-erythrocytic targeting pipeline, at present, the only existing liver-stage targeted drugs in use and suited to targeting the hypnozoite stages are primaquine and tafenoquine (Figure 2). Both, however, are also associated with intravascular haemolysis in glucose-6-phosphate dehydrogenase (G6PD)-deficient patients [32]. The absence of an accepted *P. vivax* hypnozoite model is in part to blame for the limited anti-hypnozoite antimalarial discovery. The most robust platform for screening was, until recently, a low throughput *in vivo* imaging assay using *P. cynomolgi* and rhesus monkeys. An *in vitro* improvement to this using *P. cynomolgi* sporozoites and primary monkey hepatocytes [33] has successfully identified a hypnozoitocidal compound, KAI407 (Figure 2), that besides targeting the ABS is active against both liver developing parasites and hypnozoites [34]. Further advances in culture protocols and use of humanized mouse models add to the tool base towards the hoped-for radical cure treatment that would eliminate liver stages [35,36]. Although not yet adapted to an HTS format, one such assay [35,36] allowed for the identification of a compound, TM2-115, (Figure 2) a proposed *Plasmodium* histone methyltransferase inhibitor [37] with a unique "wake and kill" phenotype.

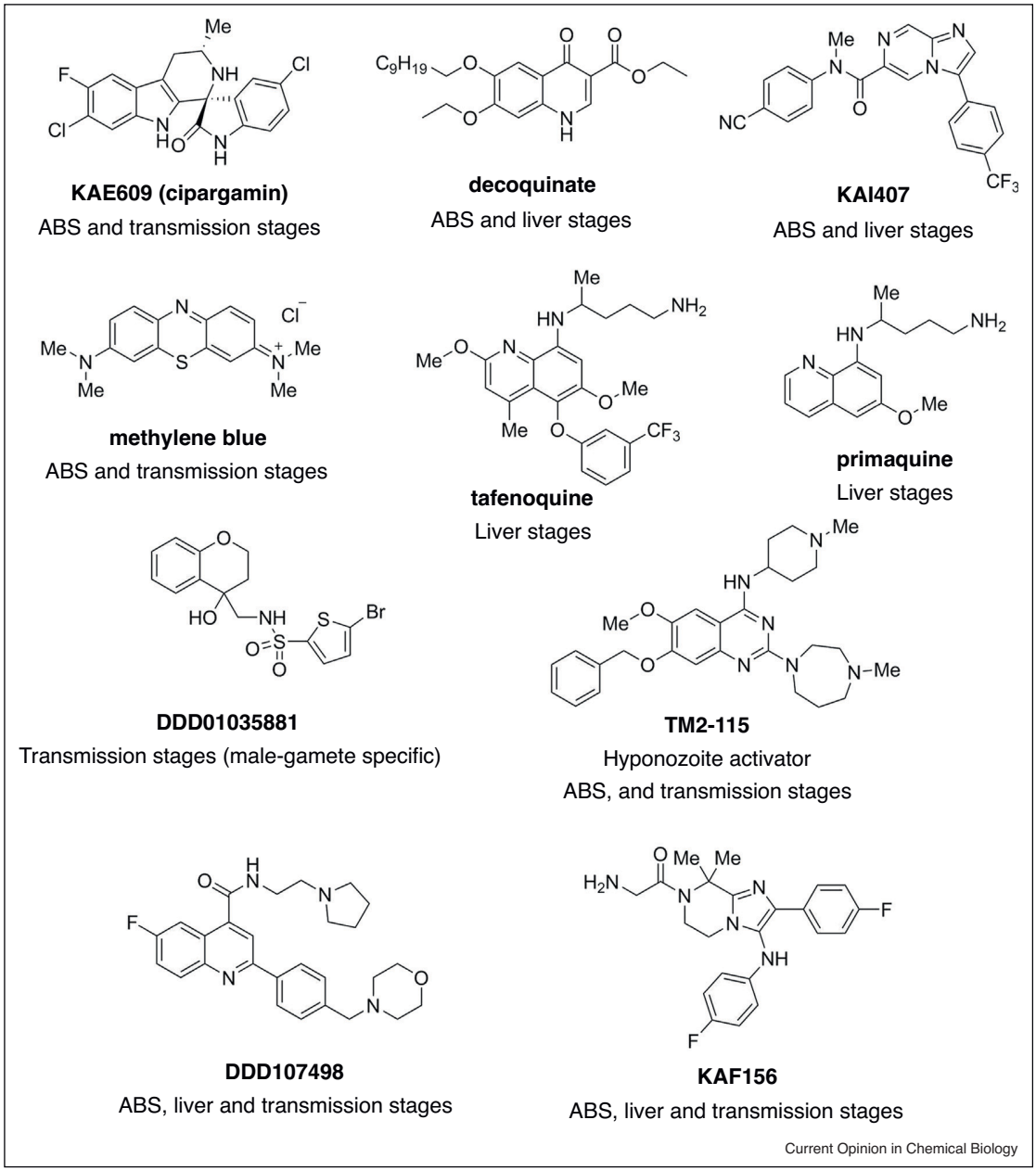
Transmission blocking assays

Beyond liver stages, there is a growing awareness of the potential for targeting parasite transmission, diverting away from simply treating symptomatic (or pre-symptomatic) forms of parasite infection. Targeting transmission has long been seen as a critical step towards meeting the demanding goals of an eradication agenda [38]. Although billions of parasites may circulate an infected individual during asexual stages, only 0.2–1% are thought to commit to sexual development and, therefore, are responsible for transmission, constituting a massive lifecycle bottleneck [39]. This stage is permissive for transmission to the mosquito upon uptake of a blood meal, making them a viable transmission blocking drug target [39].

Drug targeting strategies focussed on transmission centre on two areas, either breaking transmission by targeting the mosquito vector itself (using endecticides such as Ivermectin [40•]), classified as TCP6 (recently reviewed in [41]), or targeting the *Plasmodium* sexual stages, blocking gametocyte or gamete development, classified as TCP5 [6••]. By stopping onward transmission, each is orientated towards protecting the wider population rather than the individual [42]. Although several platforms for discovering transmission blocking drugs have been developed (Figure 1), advances in screening for compounds

(Figure 1 Legend Continued) round of human infection [39]. Notable ABS cellular screens include those against the GNF Library; SJCRH (identifying hits with 50% inhibitory activity (IC50) of $\leq$2 μM); Griffiths University library (identifying hits for physicochemical and chemical diversity analysis) and TCAMS from GSK. Screens against the asymptomatic liver stages include screens of the Novartis-GNF Malaria Box (potent against ABS stages); bioactives library of commercially sourced compounds in clinical or pre-clinical development; TCAMS library (hits with dual blood and liver-stage activity) and the ultra-HTS of the MMV Malaria Box, DOS and most-recently Charles River libraries (hits with submicromolar exoerythrocytic stage activity). Transmission blocking screens to find drugs that block parasite transmission, compromising gametocyte or gamete viability, include those against the TCAMS library; LOPAC library using alamarBlue; MMV Malaria Box, GNF library and DOS library (using SaLSSA) and the Dundee GHCDL (using the DGFA).

Figure 2



Notable frontline antimalarials with targets throughout the lifecycle.
Selected antimalarials with activity against different stages of the parasite lifecycle. "Me" denotes methyl groups. KAE609 is a PfATP4 inhibitor which shows fast parasite clearance and transmission-blocking potential and is currently undergoing phase II clinical trials. Decoquinate is a dual-stage antimalarial (ABS and liver) with activity against the parasite mitochondrial bc1 complex. Primaquine and tafenoquine are the only liver-stage targeted compounds with the ability to kill hypnozoites in use despite their side effects. KAI407 is a hypnozoitocidal compound identified using *P. cynomolgi* sporozoites and primary monkey hepatocytes that targets the ABS and developing liver stage parasites as well. TM2-115 is a putative histone methyltransferase inhibitor with activity against both asexual and sexual stages, and the ability to induce dormant liver stages to resume their maturation. Methylene blue is a classical antimalarial showing transmission-blocking activity regardless of assay read-out and can thus be used as positive control in screening campaigns. DD01035881 is a male-gamete formation inhibitor identified from the GHCDL screen. KAF156 is a drug candidate with activity against ABS, liver and sexual stages, which was developed through the optimisation of a hit identified in one of the first liver stage screens. DDD107498 is a eEF2 inhibitor with activity across all parasite stages. Primaquine, Tafenoquine and DDD1035881 are used as racemates.

targeting sexual development have been boosted by improvements to *in vitro* culture protocols for *P. falciparum* gametocytes [43•,44•,45•]. Being non-replicative developmental stages, however, gametocytes are not amenable to traditional DNA replication or cell proliferation markers, which has meant other measures of viability, including mitochondrial activity or fluorescent protein expression are required. Control compounds often used in such assays include classical antimalarials such as methylene blue (Figure 2), a compound in phase II trials which is consistently found to be active against transmission, though with ranging IC_{50} values (e.g. 12–490 nM). Artemisinin endoperoxides have generally proven inactive (>1 μM) against mature gametocytes.

One of the first gametocyte-centred screens used the MMV malaria box, aimed at the identification of dual asexual-sexually active drug candidates. Gametocytaemia was determined following expression of a transgenic gametocyte-specific protein pfs16-Luc-GFP marker, with cell viability determined using Mitotracker Red, a reporter of mitochondrial function [46]. Other studies have used similar strategies as a base for drug screening [47–49]. In parallel to these efforts, a group from GlaxoSmithKline developed a methodologically improved ATP bioluminescent assay, using reduction in ATP as a marker of cell injury and death [50]. Using this method, the group tested 17 gold-standard compounds with known antimalarial activity on purified stage IV–V gametocytes, before cytotoxicity and specificity tests with HepG2 cells. A follow-up screen examined dual activity of the TCAMS library against stage V gametocytes [51]. Towards an improved signal-to-noise ratio, required for HTS, several groups have developed colorimetric readouts for gametocyte viability. This includes parasite lactate dehydrogenase (pLDH) [52] and alamarBlue [53] as indicators of metabolic activity. Two recent large-scale screens are also worth highlighting, including the use of acridine orange (AO) to measure gametocytaemia and rounding-up post-activation as a marker of viability, adapted to 384-well format from researchers at the Istituto Superiore di Sanità in Rome [54] and, most recently, the Saponin-lysis Sexual Stage Assay (SaLSSA) from the University of California San Diego School of Medicine. [11••]. This latter assay utilises synchronised gametocytes and involves an *in situ* erythrocyte saponin-lysis before MitoTracker Red staining, highlighting parasites with an active mitochondrial membrane potential. Because it can work at low magnification, this automated high content imaging platform has been developed to 1534-well capacity and has been used effectively with several drug libraries [11••] (Figure 1).

Sex specificity and viability

One of the key challenges, however, to drug discovery of the transmission stages, is the *in vivo* validation of hits. Most screens to date, validate any newly discovered hits with the Standard Membrane Feeding Assay (SMFA) [55] to determine onwards viability. Although widely considered the gold-standard for transmission blocking activity, the assay is extremely low-throughput. It involves treatment of gametocyte culture before feeding to malaria-susceptible *Anopheline* mosquitos using an artificial membrane. Mosquito midguts are then dissected 7–10 days after feeding and oocyst abundance is counted by microscopy to determine viability [56]. Attempts to increase throughput have been made and hold great promise if robustness and reproducibility in mosquito-feeds can be achieved [57]. What use of the SMFA demonstrates is that viability of the sexual stages is not the same thing as capacity to transmit (i.e. gametocytaemia does not equate with transmission). For example, it is clear that many exemplar transmission-blocking drugs like primaquine do not affect the presence of viable (but transmission-incompetent) gametocytes in peripheral blood [58••]. Meeting this challenge head on, a very different approach to transmission screening is to explore the effect of drugs not on gametocytes but on the developing gametes, mimicking their transformation in the mosquito midgut *ex vivo* without the limitations of the SMFA. *P. falciparum* notably has a female-biased sex ratio, with a range of ratios of between ~3 and 5 females for every 1 male [59,60]. Combined with the fact that males exhibit an increased susceptibility to known antimalarials despite the greater abundance of females [59], has prompted development of assays that capture both male and female development independently. One of the most successful of these is the Dual Gamete Formation Assay (DGFA) [12,59], which measures male and female gametogenesis via automated imaging. Male gamete formation is signified by formation of 'exflagellation centres' as male gametes adhere to neighbouring erythrocytes; female gamete formation is detected by immunostaining of a surface protein expressed at the gamete surface upon egress. In measuring these two features, the assay provides a sex-specific gametocyte viability readout and has been developed to plate-based format [12]. Similar male-only [61] and female-only assays have also been developed [62]. Because of each entity's focus on gamete formation, stage V gametocyte viability is encompassed in each assay since it is the only stage that will develop further upon triggering gametogenesis. The assay has proven to be a powerful high-throughput proxy for transmission and there is good evidence of a linear correlation between sex-specific gamete assays and SMFA activity [12,63]. However, a key caveat that remains with each of these assays is the viable production of *in vitro*-derived stage V *P. falciparum* gametocytes that are competent for exflagellation and onward transmission to mosquitoes [43•].

Advancement of the DGFA to 384-well plate format recently permitted an HTS of the University of Dundee Global Health Chemical Diversity Library (GHCDL), in which the DGFA was undertaken in parallel to ABS and other transmission blocking assays to discern compounds with varying activity profiles. The joint study between Imperial College London and GlaxoSmithKline [64••] is

the largest transmission blocking focussed screen carried out to date on a non-biased library (i.e. a library unrelated to ABS activity). Numerous hits were identified displaying asexual-specific, dual asexual-sexual stage, sexual stage-specific and, for the first time, gamete-specific targeted activity. Of note, male specific, dual male-female gametocyte and male gamete only targeted compounds were also discovered. Among hits, several belonged to a cluster sharing an *N*-((4-hydroxychroman-4-yl)methyl)-sulphonamide scaffold, which shows promise for future transmission-only drug development (Figure 2).

The GHCDL screen, like many others, demonstrated the power of combining multiple platforms to find novel scaffolds with both new modes of action and multi-stage activity. A good example of the latter was the discovery of DDD107498, a translation elongation factor 2 (eEF2)-targeted compound (Figure 2) identified from the Dundee protein kinase scaffold library, which shows multiple activity against ABS, liver stages and male and female gamete formation [65]. Though many groups favour the clinical development of a multi-stage drug, one caution with this approach is the challenge that selection for parasite resistance will be amplified by its multiple points of sensitivity across the lifecycle (presuming it has a single pharmacological mode of action across the lifecycle). Combined formulations with drugs targeting different processes in different stages, in particular transmission, may be preferable in this case (as it has been with viral and bacterial infections), not only blocking transmission but protecting partner drugs from resistance development [64••].

Conclusions

Application of HTS technologies to the liver and the sexual stages of *Plasmodium* are receiving an increasing interest as a necessary addition to efforts in antimalarial drug discovery. Innovation in technologies and novel modes of action becomes increasingly important in an era of emerging ACT resistance and the plateau in declining malaria incidence. Advances in screening for drugs that act along each step of the parasite lifecycle (from ABS to transmission and back again) have advanced significantly in recent years with development of assays testing activity at each stage. Though these phenotypic screens exhibit clear advantages over target-based approaches in their scope, they also raise challenges in drug mode of action identification. However, by combining forces with medicinal chemistry to undertake detailed SAR of hits, the prospect of developing new lifecycle orientated drugs with new modes of action becomes increasingly feasible.

Acknowledgements

We apologise to the numerous researchers in the field whose work we were unable to discuss given the limited scope of a single review. Work in the Baum laboratory is supported by funding from Wellcome (Investigator Award 100993/Z/13/Z) and previous support from the Bill & Melinda Gates Foundation (OPP1043501). S.Y. is supported by a PhD from the UK Engineering and Physical Sciences Research Council (EPSRC). A.R-Z. acknowledges Alfonso Martin Escudero Foundation for a postdoctoral fellowship.

References and recommended reading

Papers of particular interest, published within the period of review, have been highlighted as:

- • of special interest
- •• of outstanding interest

1. **World malaria report 2017**. *Press Release*. 2017.

2. Bhatt S, Weiss DJ, Cameron E, Bisanzio D, Mappin B, Dalrymple U, Battle KE, Moyes CL, Henry A, Eckhoff PA *et al.*: **The effect of malaria control on plasmodium falciparum in Africa between 2000 and 2015**. *Nature* 2015, **526**:207-211.

3. Anthony MP, Burrows JN, Duparc S, Moehrle JJ, Wells TN: **The global pipeline of new medicines for the control and elimination of malaria**. *Malar J* 2012, **11**:316.

4. • Griffin JT, Bhatt S, Sinka ME, Gething PW, Lynch M, Patouillard E, Shutes E, Newman RD, Alonso P, Cibulskis RE, Ghani AC: **Potential for reduction of burden and local elimination of malaria by reducing plasmodium falciparum malaria transmission: a mathematical modelling study**. *Lancet Infect Dis* 2016, **16**:465-472.
This paper utilises as mathematical model of *P. falciparum* transmission to predict the effect of multiple intervention methods to malaria incidence and mortalities from 2015-2030. The study concludes that an innovative intervention scenario of seasonal chemoprotection and long-lasting insecticide treated nets would reduce mortality and incidence at a much greater extent than sustaining or accelerating current approaches.

5. Rabinovich RN, Drakeley C, Djimde AA, Hall BF, Hay SI, Hemingway J, Kaslow DC, Noor A, Okumu F, Steketee R *et al.*: **Malera: an updated research agenda for malaria elimination and eradication**. *PLoS Med* 2017, **14**:e1002456.

6. •• Burrows JN, Duparc S, Gutteridge WE, Hooft van Huijsduijnen R, Kaszubska W, Macintyre F, Mazzuri S, Mohrle JJ, Wells TNC: **New developments in anti-malarial target candidate and product profiles**. *Malar J* 2017, **16**:26.
This review reports the latest TCPs and TPPs which have evolved from an increased understanding of the challenges faced with current antimalarial treatments. Goals to find medicines for chemoprotection and novel ABS and transmission blocking drugs are reinforced in this paper. A novel mosquito-killing profile, or endectocides, was also introduced here.

7. Flannery EL, Chatterjee AK, Winzeler EA: **Antimalarial drug discovery - approaches and progress towards new medicines**. *Nat Rev Microbiol* 2013, **11**:849-862.

8. White NJ, Pukrittayakamee S, Hien TT, Faiz MA, Mokuolu OA, Dondorp AM: **Malaria**. *Lancet* 2014, **383**:723-735.

9. Hovlid ML, Winzeler EA: **Phenotypic screens in antimalarial drug discovery**. *Trends Parasitol* 2016, **32**:697-707.

10. Hegge S, Kudryashev M, Smith A, Frischknecht F: **Automated classification of plasmodium sporozoite movement patterns reveals a shift towards productive motility during salivary gland infection**. *Biotechnol J* 2009, **4**:903-913.

11. •• Plouffe DM, Wree M, Du AY, Meister S, Li F, Patra K, Lubar A, Okitsu SL, Flannery EL, Kato N *et al.*: **High-throughput assay and discovery of small molecules that interrupt malaria transmission**. *Cell Host Microbe* 2016, **19**:114-126.
This study introduces a novel HTP assay, SaLSSA, to test for transmission blocking activity of compounds. The paper reports on a HTS of a ~14,000 compound library, identifying hits with solely transmission blocking activity and hits with dual activity against sexual, asexual and liver stages.

12. Ruecker A, Mathias DK, Straschil U, Churcher TS, Dinglasan RR, Leroy D, Sinden RE, Delves MJ: **A male and female gametocyte functional viability assay to identify biologically relevant malaria transmission-blocking drugs**. *Antimicrob Agents Chemother* 2014, **58**:7292-7302.

13. Delves MJ, Ramakrishnan C, Blagborough AM, Leroy D, Wells TN, Sinden RE: **A high-throughput assay for the identification of**

malarial transmission-blocking drugs and vaccines. *Int J Parasitol* 2012, **42**:999-1006.

14. Roth A, Maher SP, Conway AJ, Ubalee R, Chaumeau V, Andolina C, Kaba SA, Vantaux A, Bakowski MA, Luque RT *et al.*: **A comprehensive model for assessment of liver stage therapies targeting plasmodium vivax and plasmodium falciparum**. *Nat Commun* 2018, **9**:1837.

15. Gaulton A, Hersey A, Nowotka M, Bento AP, Chambers J, Mendez D, Mutowo P, Atkinson F, Bellis LJ, Cibrian-Uhalte E *et al.*: **The chembl database in 2017**. *Nucleic Acids Res* 2017, **45**:D945-D954.

16. Plouffe D, Brinker A, McNamara C, Henson K, Kato N, Kuhen K, Nagle A, Adrian F, Matzen JT, Anderson P *et al.*: **In silico activity profiling reveals the mechanism of action of antimalarials discovered in a high-throughput screen**. *Proc Natl Acad Sci U S A* 2008, **105**:9059-9064.

17. Guiguemde WA, Shelat AA, Bouck D, Duffy S, Crowther GJ, Davis PH, Smithson DC, Connelly M, Clark J, Zhu F *et al.*: **Chemical genetics of plasmodium falciparum**. *Nature* 2010, **465**:311-315.

18. Avery VM, Bashyam S, Burrows JN, Duffy S, Papadatos G, Puthukkuti S, Sambandan Y, Singh S, Spangenberg T, Waterson D, Willis P: **Screening and hit evaluation of a chemical library against blood-stage plasmodium falciparum**. *Malar J* 2014, **13**:190.

19. Gamo FJ, Sanz LM, Vidal J, de Cozar C, Alvarez E, Lavandera JL, Vanderwall DE, Green DV, Kumar V, Hasan S *et al.*: **Thousands of chemical starting points for antimalarial lead identification**. *Nature* 2010, **465**:305-310.

20. Crowther GJ, Hillesland HK, Keyloun KR, Reid MC, Lafuente-Monasterio MJ, Ghidelli-Disse S, Leonard SE, He P, Jones JC *et al.*: **Biochemical screening of five protein kinases from plasmodium falciparum against 14,000 cell-active compounds**. *PLoS One* 2016, **11**:e0149996.

21. Miguel-Blanco C, Molina I, Bardera AI, Diaz B, de Las Heras L, Lozano S, Gonzalez C, Rodrigues J, Delves MJ, Ruecker A *et al.*: **Hundreds of dual-stage antimalarial molecules discovered by a functional gametocyte screen**. *Nat Commun* 2017, **8**:15160.

22. Gomez-Lorenzo MG, Rodriguez-Alejandre A, Moliner-Cubel S, Martinez-Hoyos M, Bahamontes-Rosa N, Gonzalez Del Rio R, Rodenas C, Fuente J, Lavandera JL, Garcia-Bustos JF, Mendoza-Losana A: **Functional screening of selective mitochondrial inhibitors of plasmodium**. *Int J Parasitol Drugs Drug Resist* 2018, **8**:295-303.

23. Raphemot R, Lafuente-Monasterio MJ, Gamo-Benito FJ, Clardy J, Derbyshire ER: **Discovery of dual-stage malaria inhibitors with new targets**. *Antimicrob Agents Chemother* 2015, **60**:1430-1437.

24. White NJ, Pukrittayakamee S, Phyo AP, Rueangweerayut R, Nosten F, Jittamala P, Jeeyapant A, Jain JP, Lefevre G, Li R *et al.*: **Spiroindolone kae609 for falciparum and vivax malaria**. *N Engl J Med* 2014, **371**:403-410.

25. Campo B, Vandal O, Wesche DL, Burrows JN: **Killing the hypnozoite-drug discovery approaches to prevent relapse in plasmodium vivax**. *Pathog Glob Health* 2015, **109**:107-122.

26. Mazier D, Renia L, Snounou G: **A pre-emptive strike against malaria's stealthy hepatic forms**. *Nat Rev Drug Discov* 2009, **8**:854-864.

27. March S, Ng S, Velmurugan S, Galstian A, Shan J, Logan DJ, Carpenter AE, Thomas D, Sim BK, Mota MM *et al.*: **A microscale human liver platform that supports the hepatic stages of plasmodium falciparum and vivax**. *Cell Host Microbe* 2013, **14**:104-115.

28. Meister S, Plouffe DM, Kuhen KL, Bonamy GM, Wu T, Barnes SW, Bopp SE, Borboa R, Bright AT, Che J *et al.*: **Imaging of plasmodium liver stages to drive next-generation antimalarial drug discovery**. *Science* 2011, **334**:1372-1377.

29. •• White NJ, Duong TT, Uthaisin C, Nosten F, Phyo AP, Hanboonkunupakarn B, Pukrittayakamee S, Jittamala P, Chuthasmit K, Cheung MS *et al.*: **Antimalarial activity of kaf156 in falciparum and vivax malaria**. *N Engl J Med* 2016, **375**:1152-1160.

Following one of the first screens against liver stages, this paper reports on a phase 2 clinical trial of the potent imidazolopiperazine hit, KAF156. Trials demonstrated no evident safety concerns with KAF156 and confirmed antimalarial activity against *P. falciparum* and *P. vivax*, including artemisinin resistant strains.

30. da Cruz FP, Martin C, Buchholz K, Lafuente-Monasterio MJ, Rodrigues T, Sonnichsen B, Moreira R, Gamo FJ, Marti M, Mota MM *et al.*: **Drug screen targeted at plasmodium liver stages identifies a potent multistage antimalarial drug**. *J Infect Dis* 2012, **205**:1278-1286.

31. Swann J, Corey V, Scherer CA, Kato N, Comer E, Maetani M, Antonova-Koch Y, Reimer C, Gagaring K, Ibanez M *et al.*: **High-throughput luciferase-based assay for the discovery of therapeutics that prevent malaria**. *ACS Infect Dis* 2016, **2**:281-293.

32. Watson J, Taylor WRJ, Bancone G, Chu CS, Jittamala P, White NJ: **Implications of current therapeutic restrictions for primaquine and tafenoquine in the radical cure of vivax malaria**. *PLoS Negl Trop Dis* 2018, **12**:e0006440.

33. Dembele L, Gego A, Zeeman AM, Franetich JF, Silvie O, Rametti A, Le Grand R, Dereuddre-Bosquet N, Sauerwein R, van Gemert GJ *et al.*: **Towards an in vitro model of plasmodium hypnozoites suitable for drug discovery**. *PLoS One* 2011, **6**:e18162.

34. Zeeman AM, van Amsterdam SM, McNamara CW, Voorberg-van der Wel A, Klooster EJ, van den Berg A, Remarque EJ, Plouffe DM, van Gemert GJ, Luty A *et al.*: **Kai407, a potent non-8-aminoquinoline compound that kills plasmodium cynomolgi early dormant liver stage parasites in vitro**. *Antimicrob Agents Chemother* 2014, **58**:1586-1595.

35. Dembele L, Franetich JF, Lorthiois A, Gego A, Zeeman AM, Kocken CH, Le Grand R, Dereuddre-Bosquet N, van Gemert GJ, Sauerwein R *et al.*: **Persistence and activation of malaria hypnozoites in long-term primary hepatocyte cultures**. *Nat Med* 2014, **20**:307-312.

36. Mikolajczak SA, Vaughan AM, Kangwanrangsan N, Roobsoong W, Fishbaugher M, Yimamnuaychok N, Rezakhani N, Lakshmanan V, Singh N, Kaushansky A *et al.*: **Plasmodium vivax liver stage development and hypnozoite persistence in human liver-chimeric mice**. *Cell Host Microbe* 2015, **17**:526-535.

37. Malmquist NA, Moss TA, Mecheri S, Scherf A, Fuchter MJ: **Small-molecule histone methyltransferase inhibitors display rapid antimalarial activity against all blood stage forms in plasmodium falciparum**. *Proc Natl Acad Sci U S A* 2012, **109**:16708-16713.

38. Sinden RE: **Developing transmission-blocking strategies for malaria control**. *PLoS Pathog* 2017, **13**:e1006336.

39. Angrisano F, Tan YH, Sturm A, McFadden GI, Baum J: **Malaria parasite colonisation of the mosquito midgut–placing the plasmodium ookinete centre stage**. *Int J Parasitol* 2012, **42**:519-527.

40. • Smit MR, Ochomo EO, Aljayyoussi G, Kwambai TK, Abong'o BO, Chen T, Bousema T, Slater HC, Waterhouse D, Bayoh NM *et al.*: **Safety and mosquitocidal efficacy of high-dose ivermectin when co-administered with dihydroartemisinin-piperaquine in kenyan adults with uncomplicated malaria (ivermal): a randomised, double-blind, placebo-controlled trial**. *Lancet Infect Dis* 2018, **18**:615-626.

This paper addresses the short mosquitocidal effect of a single dose of ivermectin, reporting a clinical trial of a high-dose 3-day treatment regime with the endectocide alongside a standard ACT. The suitable efficacy and tolerability of the treatment shows great promise for administration of this drug.

41. Chaccour CJ, Kobylinski KC, Bassat Q, Bousema T, Drakeley C, Alonso P, Foy BD: **Ivermectin to reduce malaria transmission: a research agenda for a promising new tool for elimination**. *Malar J* 2013, **12**:153.

42. Leroy D, Campo B, Ding XC, Burrows JN, Cherbuin S: **Defining the biology component of the drug discovery strategy for malaria eradication**. *Trends Parasitol* 2014, **30**:478-490.

43. • Delves MJ, Straschil U, Ruecker A, Miguel-Blanco C, Marques S, Dufour AC, Baum J, Sinden RE: **Routine in vitro culture of p. Falciparum gametocytes to evaluate novel transmission-blocking interventions**. *Nat Protoc* 2016, **11**:1668-1680.
This 15-day protocol was developed for routine maintenance of *in vitro P. falciparum* gametocyte culture for the HTP screening of compound libraries and low throughput SMFA in a robust and reproducible manner. Routine culture maintenance for these assays is vital in testing for drug efficacy to break the cycle of transmission from host to vector.

44. • Brancucci NM, Goldowitz I, Buchholz K, Werling K, Marti M: **An assay to probe plasmodium falciparum growth, transmission stage formation and early gametocyte development**. *Nat Protoc* 2015, **10**:1131-1142.
This paper describes an assay for drug efficacy determination against *P. falciparum* ABS replication, gametocytogenesis and early gametocyte maturation. The study reports an 11-day protocol utilising flow-cytometry to determine post-treatment proliferation and sexual conversion.

45. • Duffy S, Loganathan S, Holleran JP, Avery VM: **Large-scale production of plasmodium falciparum gametocytes for malaria drug discovery**. *Nat Protoc* 2016, **11**:976-992.
This paper outlines a 16-day protocol to develop highly synchronous gametocyte culture for transmission blocking drug discovery campaigns. Magnetic separation is used to purify haemozoin-containing parasites for great young RBC levels, decreased haematocrit and increased parasitemia.

46. Duffy S, Avery VM: **Identification of inhibitors of plasmodium falciparum gametocyte development**. *Malar J* 2013, **12**:408.

47. Adjalley SH, Johnston GL, Li T, Eastman RT, Ekland EH, Eappen AG, Richman A, Sim BK, Lee MC, Hoffman SL, Fidock DA: **Quantitative assessment of plasmodium falciparum sexual development reveals potent transmission-blocking activity by methylene blue**. *Proc Natl Acad Sci U S A* 2011, **108**:E1214-1223.

48. Buchholz K, Burke TA, Williamson KC, Wiegand RC, Wirth DF, Marti M: **A high-throughput screen targeting malaria transmission stages opens new avenues for drug development**. *J Infect Dis* 2011, **203**:1445-1453.

49. Peatey CL, Spicer TP, Hodder PS, Trenholme KR, Gardiner DL: **A high-throughput assay for the identification of drugs against late-stage plasmodium falciparum gametocytes**. *Mol Biochem Parasitol* 2011, **180**:127-131.

50. Lelievre J, Almela MJ, Lozano S, Miguel C, Franco V, Leroy D, Herreros E: **Activity of clinically relevant antimalarial drugs on plasmodium falciparum mature gametocytes in an atp bioluminescence "transmission blocking" assay**. *PLoS One* 2012, **7**:e35019.

51. Almela MJ, Lozano S, Lelievre J, Colmenarejo G, Coteron JM, Rodrigues J, Gonzalez C, Herreros E: **A new set of chemical starting points with plasmodium falciparum transmission-blocking potential for antimalarial drug discovery**. *PLoS One* 2015, **10**:e0135139.

52. D'Alessandro S, Silvestrini F, Dechering K, Corbett Y, Parapini S, Timmerman M, Galastri L, Basilico N, Sauerwein R, Alano P, Taramelli D: **A plasmodium falciparum screening assay for anti-gametocyte drugs based on parasite lactate dehydrogenase detection**. *J Antimicrob Chemother* 2013, **68**:2048-2058.

53. Tanaka TQ, Williamson KC: **A malaria gametocytocidal assay using oxidoreduction indicator, alamarblue**. *Mol Biochem Parasitol* 2011, **177**:160-163.

54. Lucantoni L, Silvestrini F, Signore M, Siciliano G, Eldering M, Dechering KJ, Avery VM, Alano P: **A simple and predictive phenotypic high content imaging assay for plasmodium falciparum mature gametocytes to identify malaria transmission blocking compounds**. *Sci Rep* 2015, **5**:16414.

55. Churcher TS, Blagborough AM, Delves M, Ramakrishnan C, Kapulu MC, Williams AR, Biswas S, Da DF, Cohuet A, Sinden RE: **Measuring the blockade of malaria transmission–an analysis of the standard membrane feeding assay**. *Int J Parasitol* 2012, **42**:1037-1044.

56. Li T, Eappen AG, Richman AM, Billingsley PF, Abebe Y, Li M, Padilla D, Rodriguez-Barraquer I, Sim BK, Hoffman SL: **Robust, reproducible, industrialized, standard membrane feeding assay for assessing the transmission blocking activity of vaccines and drugs against plasmodium falciparum**. *Malar J* 2015, **14**:150.

57. Vos MW, Stone WJ, Koolen KM, van Gemert GJ, van Schaijk B, Leroy D, Sauerwein RW, Bousema T, Dechering KJ: **A semi-automated luminescence based standard membrane feeding assay identifies novel small molecules that inhibit transmission of malaria parasites by mosquitoes**. *Sci Rep* 2015, **5**:18704.

58. •• Dicko A, Brown JM, Diawara H, Baber I, Mahamar A, Soumare HM, Sanogo K, Koita F, Keita S, Traore SF *et al.*: **Primaquine to reduce transmission of plasmodium falciparum malaria in mali: A single-blind, dose-ranging, adaptive randomised phase 2 trial**. *Lancet Infect Dis* 2016, **16**:674-684.
This paper outlines a phase 2 clinical trial of primaquine combined with a standard ACT treatment, finding a single dose to be efficacious and safe in male patients without G6PD deficiency.

59. Delves MJ, Ruecker A, Straschil U, Lelievre J, Marques S, Lopez-Barragan MJ, Herreros E, Sinden RE: **Male and female plasmodium falciparum mature gametocytes show different responses to antimalarial drugs**. *Antimicrob Agents Chemother* 2013, **57**:3268-3274.

60. Robert V, Sokhna CS, Rogier C, Ariey F, Trape JF: **Sex ratio of plasmodium falciparum gametocytes in inhabitants of dielmo, senegal**. *Parasitology* 2003, **127**:1-8.

61. Lozano S, Gamallo P, Gonzalez-Cortes C, Presa Matilla JL, Fairhurst RM, Herreros E, Amaratunga C, Rodrigues J: **Gametocytes from k13-propeller mutant plasmodium falciparum clinical isolates demonstrate reduced susceptibility to dihydroartemisinin in the male gamete exflagellation inhibition assay**. *Antimicrob Agents Chemother* 2018.

62. Miguel-Blanco C, Lelievre J, Delves MJ, Bardera AI, Presa JL, Lopez-Barragan MJ, Ruecker A, Marques S, Sinden RE, Herreros E: **Imaging-based high-throughput screening assay to identify new molecules with transmission-blocking potential against plasmodium falciparum female gamete formation**. *Antimicrob Agents Chemother* 2015, **59**:3298-3305.

63. Colmenarejo G, Lozano S, Gonzalez-Cortes C, Calvo D, Sanchez-Garcia J, Matilla JP, Leroy D, Rodrigues J: **Predicting transmission blocking potential of anti-malarial compounds in the mosquito feeding assay using plasmodium falciparum male gamete inhibition assay**. *Sci Rep* 2018, **8**:7764.

64. •• Delves MJ, Miguel-Blanco C, Matthews H, Molina I, Ruecker A, Yahiya S, Straschil U, Abraham M, Leon ML, Fischer OJ *et al.*: **A high throughput screen for next-generation leads targeting malaria parasite transmission**. *Nat Commun* 2018, **9**:3805.
This paper reports on the first HTP screen against a non-biased library, the Dundee GHCDL, to determine transmission blocking activity using the DGFA. The ABS/transmission blocking, sex-specific and gametocyte or gamete targeted activity was determined by using a range of assays; hits demonstrated a range of profiles, with one particular compound scaffold of interest displaying male gamete specific activity.

65. Baragana B, Hallyburton I, Lee MC, Norcross NR, Grimaldi R, Otto TD, Proto WR, Blagborough AM, Meister S, Wirjanata G *et al.*: **A novel multiple-stage antimalarial agent that inhibits protein synthesis**. *Nature* 2015, **522**:315-320.

66. •• Antonova-Koch Y, Meister S, Abraham M, Luth MR, Ottilie S, Lukens AK, Sakata-Kato T, Vanaerschot M, Owen E, Rodriguez JCJ *et al.*: **Open-source discovery of chemical leads for next-generation chemoprotective antimalarials**. *Science* 2018, **362**:eaat9446-10.
This recent landmark paper represents a watershed moment in liver stage drug screening by testing more than 500,000 compounds to find new potential drugs targeting the pre-erythrocytic stages. Although undertaken primarily in *Plasmodium berghei*, validation in *P. vivax* and *P. falciparum* demonstrates the assay's power as a route to new drugs with new modes of action against both major forms of malaria disease.

Appendix E

Structure-Activity Relationship Studies of a Novel Class of Transmission Blocking Antimalarials Targeting Male Gametes

Journal of Medicinal Chemistry

Article

Cite This: J. Med. Chem. 2020, 63, 2240−2262

pubs.acs.org/jmc

Structure−Activity Relationship Studies of a Novel Class of Transmission Blocking Antimalarials Targeting Male Gametes

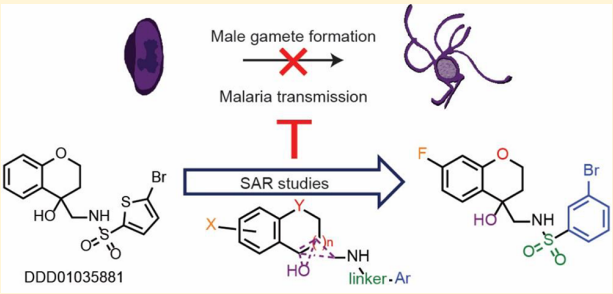
Ainoa Rueda-Zubiaurre,[†] Sabrina Yahiya,[‡] Oliver J. Fischer,[†] Xiaojun Hu,[†] Charlie N. Saunders,[†] Sachi Sharma,[†] Ursula Straschil,[‡] Junting Shen,[†] Edward W. Tate,[†] Michael J. Delves,[‡,§] Jake Baum,*[,‡] Anna Barnard,*[,†] and Matthew J. Fuchter*[,†]

[†]Department of Chemistry, Imperial College London, Molecular Sciences Research Hub, White City Campus, Wood Lane, London W12 0BZ, United Kingdom

[‡]Department of Life Sciences, Imperial College London, London SW7 2AZ, United Kingdom

Supporting Information

ABSTRACT: Malaria is still a leading cause of mortality among children in the developing world, and despite the immense progress made in reducing the global burden, further efforts are needed if eradication is to be achieved. In this context, targeting transmission is widely recognized as a necessary intervention toward that goal. After carrying out a screen to discover new transmission-blocking agents, herein we report our medicinal chemistry efforts to study the potential of the most robust hit, DDD01035881, as a male-gamete targeted compound. We reveal key structural features for the activity of this series and identify analogues with greater potency and improved metabolic stability. We believe this study lays the groundwork for further development of this series as a transmission blocking agent.



INTRODUCTION

Malaria is one of the leading causes of infant mortality in the developing world, with nearly half a million children dying each year. It is caused by a eukaryotic protozoan parasite from the genus *Plasmodium*, of which *P. falciparum* is the most lethal. The parasite is transmitted to humans by the bite of a female *Anopheles* mosquito.[1] Upon transmission, parasites invade hepatocytes and replicate, eventually being released into the bloodstream. The released parasites then invade erythrocytes to replicate asexually through a 48 h cycle during which all symptoms of the disease arise. A small percentage (0.2−1%) of parasites commit to sexual development, likely sequestered in the bone marrow, where they further develop through five morphological stages (Figure 1).[2,3] Mature, stage V, male and female gametocytes are then released into the bloodstream where they remain relatively dormant, until being taken up by a mosquito during a subsequent blood meal, instigating host to vector transmission. Following feeding, gametocytes in the blood bolus become activated in the mosquito midgut, with male forms developing through a rapid 15−20 min process of DNA replication and endomitosis to form 8 flagellated male gametes (a process termed exflagellation). Females in parallel round up and emerge from the infected red blood cell membrane. Fusion between gametes occurs within 24 h, generating a motile zygote (called an ookinete), which traverses the midgut lining to eventually form an oocyst on the midgut wall. The oocyst goes through rounds of meiosis generating haploid parasite invasive forms, called sporozoites, which migrate to the mosquito salivary glands, ready to infect the next human, and therefore are responsible for the vector to host transmission of the disease.[4]

Immense progress has been made from 2000 to 2015 in the reduction of the global malaria burden,[5] because of the implementation of artemisinin combination therapies to reduce parasite numbers together with the use of insecticide treated bed nets (ITNs) and indoor residual spraying (IRS) targeting the transmission of the disease.[6] However, the emergence of resistance (both to insecticides and to frontline chemotherapeutics, including artemisinin and related compounds) threatens the gains made.[7,8] If further progress is to be achieved toward eventual eradication of malaria, new drugs with new modes of action, including those able to stop disease transmission, will be needed.[9,10] Transmission is a particularly attractive target for chemotherapeutic intervention since it represents a key parasite population bottleneck, compared with asexual stages, with only tens of sexual stage parasites responsible for transmission.[11] Due to the low numbers of sexual stage parasites at a given time and the fact that they are nonreplicating stages, the development of resistance to transmission-blocking drugs is predicted to be less likely.

Special Issue: Women in Medicinal Chemistry

Received: June 5, 2019
Published: September 6, 2019

ACS Publications © 2019 American Chemical Society

DOI: 10.1021/acs.jmedchem.9b00898
J. Med. Chem. 2020, 63, 2240−2262

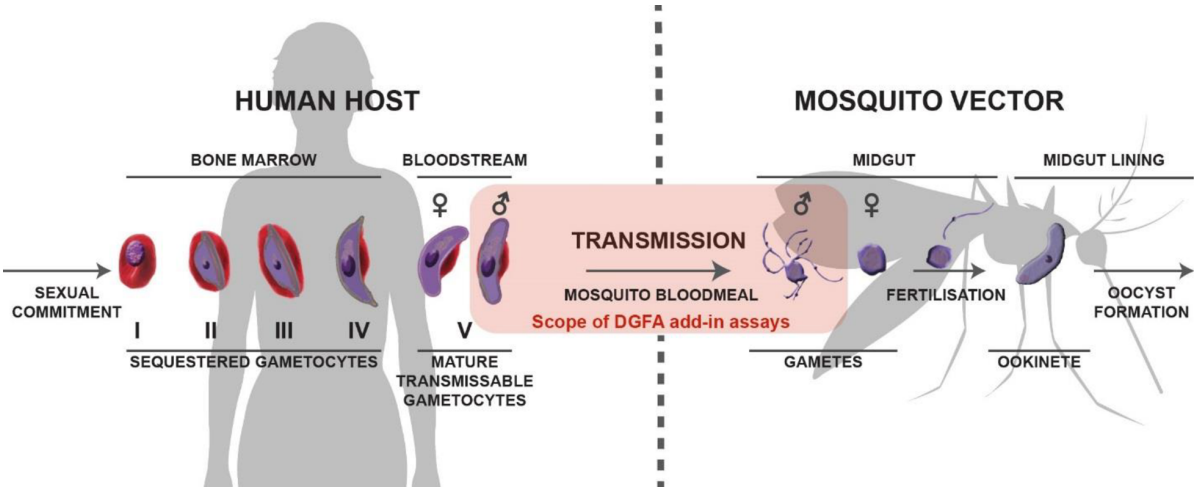
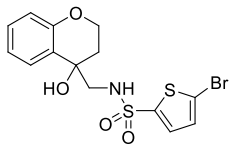


Figure 1. Host to vector transmission of *Plasmodium*. Following the commitment to sexual differentiation, gametocytes mature over five distinct morphological stages (I–V), maintaining quiescence from stages I–IV. Upon reaching maturation, stage V gametocytes withdraw from sequestration, entering the human bloodstream ready for transmission. In the event of a mosquito blood meal, male and female gametocytes rapidly transform into either eight flagellated male microgametes or a single female macrogamete in the mosquito midgut. The fertilization of haploid male and female gametes commences the onward progression of the parasite lifecycle. Zygotes (ookinetes) traverse the mosquito midgut lining, leading to the eventual formation and migration of sporozoites to the salivary glands. The in vitro DGFA add-in (pink box) measures male gametocyte viability as the rate of exflagellation, or male gamete formation.

Additionally, the blockade of transmission provides a means to limit the spread of the expanding artemisinin drug-resistant strains.[10]

Over the past decade a large amount of research has been devoted to the development of biochemical assays for the identification of compounds that target parasite transmission.[12] While these efforts have provided new assays amenable to high-throughput screening (HTS), most of them only assess gametocyte viability; in contrast to the standard membrane feeding assay (SMFA),[13] which evaluates the effectiveness of potential transmission-blocking drugs in vivo by studying changes in the numbers of oocysts in the mosquito midgut. Despite being considered the gold standard and efforts to increase its throughput,[14] the SMFA remains a costly and low-throughput method, making it unsuitable for large scale compound identification campaigns. To address this challenge, a dual gamete formation assay (DGFA)[15] was recently developed, which is amenable to HTS, emulating the conditions of the mosquito midgut in microtiter plate format in order to assess gametocyte development into gametes at scale. The DGFA has a sex-specific readout that allows for the identification of compounds with dual asexual–sexual, non-differentiating sexual and sex-specific activity, enabling identification of compounds that target aspects of biology unique to male and/or female gametocytes and gametes.[16] Recently, some of us reported the use of the DGFA to screen a 70 000-compound Global Health Chemical Diversity Library (GHCDL) from the University of Dundee.[17] The study represented the first example of a HTS campaign for the discovery of transmission-blocking agents carried out on a nonbiased chemical library where transmission was the primary filter.

The most robust hit identified from this screen was compound DDD01035881 (Figure 2). DDD01035881 is a fast acting, nontoxic male-gamete targeted compound with an in vitro EC_{50} value of approximately 200 nM and an in vivo inhibition of oocyst formation higher than 99%, as determined



DDD01035881

Figure 2. Structure of male-gamete targeted hit DDD01035881 identified in the GHCDL screen.[17]

using the SMFA when the compound was added 30 min before the mosquito feed at 10 μM.[17] The molecular target(s) of DDD01035881 is unknown. Five analogues of DDD01035881 were reported in the initial disclosure,[17] which provided limited information on the structure–activity relationships (SAR) of this series, none of which had improved characteristics over the hit. Here we report a detailed medicinal chemistry study of this chemotype, exploring its potential for usage as a male-gamete targeted compound. We reveal key structure determinants for the activity of this series and identify compounds that are more potent than DDD01035881 and have improved metabolic stability. We believe this work should enable the further progression of this series as a transmission blocking therapy.

RESULTS AND DISCUSSION

Taking into consideration the structure of hit compound DDD01035881 and initially reported analogues (Figure S1), we decided to perform further SAR studies in order to assess the structural requirements for transmission-blocking activity. A summary of the features explored within this study is shown Figure 3.

In order to study the effect of the bromothiophene substituent, a synthetic route was developed, starting from 4-chromanone (Scheme 1). The addition of trimethylsilyl cyanide provided the protected cyanohydrin **1**, which after

DOI: 10.1021/acs.jmedchem.9b00898
J. Med. Chem. 2020, 63, 2240–2262

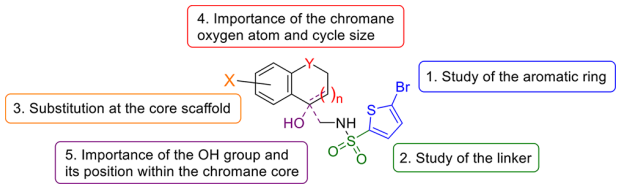


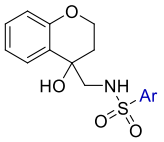
Figure 3. Structural features considered of interest for the SAR study of DDD01035881.

reduction using lithium aluminum hydride (LAH) yielded the necessary amino alcohol **2** in quantitative yield. Treatment of amine **2** with the sulfonyl chloride of the desired aromatic substituent afforded the first series of compounds **3**–**14**. Compounds **3** and **4** are newly synthesized batches of DDD01035881 and DDD01028076 from the original report.[17]

Compounds **3**–**14** were evaluated using the DGFA, and the results are shown in Table 1. The EC_{50} value obtained for compound **4** is in agreement with the data from the HTS, while derivative **3** shows a slight improvement when compared to the initial value,[17] which could be explained due to experimental variability inherent to the DGFA assay coupled with differences in compound purity. Compound **5**, where the bromine atom has been moved to position 3 of the thiophene ring, maintains the activity of **3**. Movement of the bromine atom within a phenyl rather than thiophene ring has more impact however. For example, changing from the *ortho*-position in **4** to *meta*- in **6** resulted in a >2.5-fold improvement in the activity, while the presence of a bromine atom at the *para*-position in **7** produced a complete loss of activity. Derivatives **8**–**10** containing a chlorine atom instead of a bromine atom show a similar trend. Removal of the halogen entirely does not result in a large decrease in activity (compound **11**), while introduction of an electron withdrawing group such as a ketone at the *meta*-position is not tolerated (compound **14**). In agreement with what was observed for halo-substitution, introduction of other groups at the *para*-position seems to be detrimental, regardless of their electronic properties (compounds **12** and **13**). Taken together, these data suggest there is limited space available within this region of the binding pocket of the (unknown) target(s), particularly once the ring is expanded to a six-membered ring, with the *para*-position being particularly sensitive to substitution.

As both 5-bromothiophene and *meta*-halobenzene rings in derivatives **3**, **6**, and **9** were able to produce the desired biological activity, we selected one of each for further SAR studies, specifically compounds **3** and **6** to maintain the identity of the halogen atom. To evaluate the importance of the sulfonamide linker, we synthesized derivatives **15**–**19**, where the sulfonamide had been either methylated or replaced by an amide or amine group (Scheme 2). Treatment of **6** with

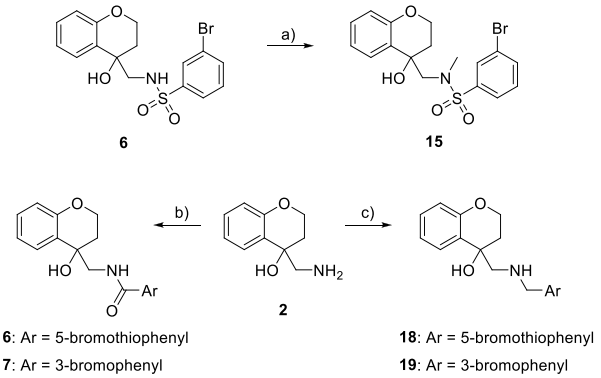
Table 1. Modifications in the Aromatic Ring (Ar)



Compound	Ar	EC_{50} (nM)[a]	Compound	Ar	EC_{50} (nM)[a]
DDD01035881 **3**		292±38 (200 nM[b]) 130±30	**9**		118±27
DDD01028076 **4**		367±34 (530 nM[b]) 344±71	**10**		> 10000
5		212±91	**11**		470±21
6		128±10	**12**		> 25000
7		> 5000	**13**		> 25000
8		> 1000	**14**		> 20000

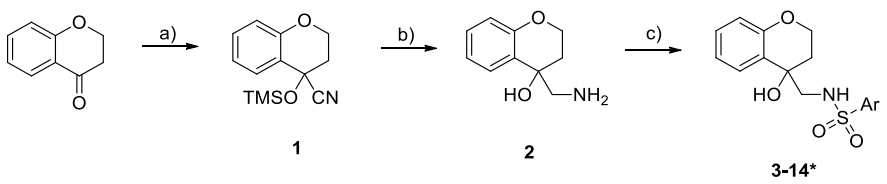
[a]Biological evaluation was carried out using the DGFA under the specific "add-in" format. Compounds were incubated at variable concentrations with fresh gametocytes, and their ability to impair exflagellation of male gametes was determined. Values below 1 μM are expressed as the mean ± SEM obtained from between three and eight biological replicates, each carried out in at least duplicate. [b]Value reported from initial HTS study.[17]

Scheme 2. Study of the Sulfonamide Linker[a]



[a]Reagents and conditions: (a) MeI, K_2CO_3, DMF, 50 °C, 4 h, 80%; (b) ArCOOH, EDC, HOBt, Et_3N, DCM/DMF, rt, 16 h, 55–68%; (c) ArCHO, 2-picoline borane, MeOH, rt, 24 h, 10–50%.

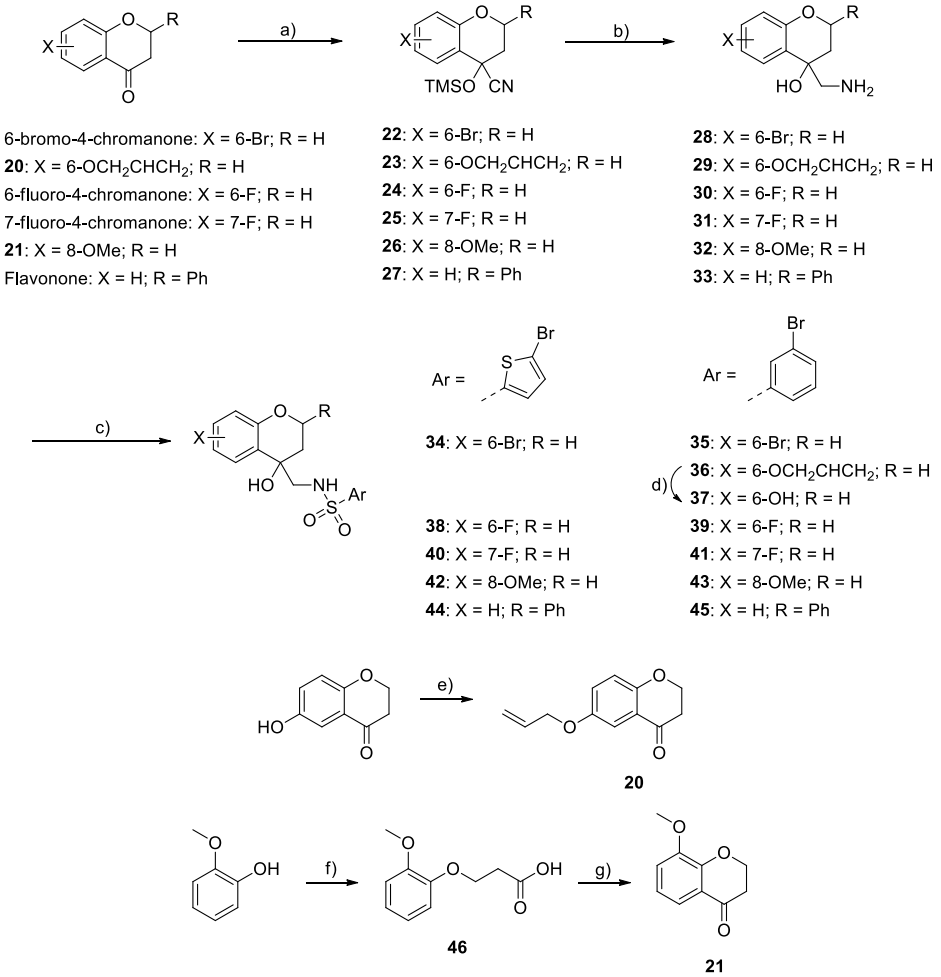
Scheme 1. Study of Different Aromatic Substituents for the Sulfonamide[a]



[a]Reagents and conditions: (a) TMSCN, ZnI_2, DCM, rt, 16 h, quant; (b) LAH, THF, rt, 16 h, quant; (c) $ArSO_2Cl$, Et_3N, DCM, rt, 16 h, 4–74%. *Ar groups can be reviewed in Table 1.

DOI: 10.1021/acs.jmedchem.9b00898
J. Med. Chem. 2020, 63, 2240–2262

Scheme 3. Study of Substitution in the Core Chromane Scaffold[a]



[a]Reagents and conditions: (a) TMSCN, ZnI_2, DCM, rt, 16 h, 65−91%; (b) LAH, THF, rt, 16 h, 23−70%; (c) $ArSO_2Cl$, Et_3N, DCM, rt, 16 h, 28−90%; (d) $Pd(PPh_3)_4$, K_2CO_3, MeOH, reflux, 16 h, 75%; (e) allyl bromide, K_2CO_3, acetone, reflux, 16 h, 85%; (f) 3-bromopropionic acid, NaH, DMF, rt, 16 h, 17%; (g) Eaton's reagent, rt, 16 h, 88%.

methyl iodide in the presence of potassium carbonate as base yielded methylsulfonamide **15** in good yield. Preparation of amides **16** and **17** was performed from coupling of amino alcohol **2** to the desired carboxylic acid, in moderate yields, under standard coupling conditions of *N*-(3-dimethylamino-propyl)-*N*′-ethylcarbodiimide hydrochloride (EDC) and 1-hydroxybenzotriazole (HOBt) in the presence of an excess of triethylamine. Amines **18** and **19** were synthesized by reductive amination of the desired aromatic aldehyde using amino alcohol **2** as the amine source. Picoline borane complex was selected as the reducing agent[18] in the absence of acetic acid, to prevent elimination of the labile benzylic hydroxyl group.

All the attempted modifications to the linker resulted in inactive compounds (Table S1). This highlights the importance of the sulfonamide group for activity. Interestingly, the fact that methylation of the sulfonamide in compound **15** renders loss of activity suggests that the NH group might be involved in a hydrogen-bonding interaction.

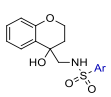
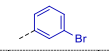
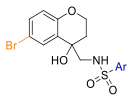
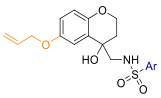
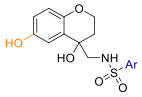
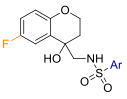
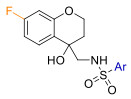
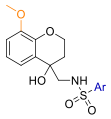
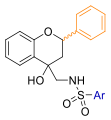
Next, we conducted a preliminary study of substitution of the chromane ring. Substituents were selected based on commercial availability of the reagents and synthetic feasibility.

As depicted in Scheme 3, the desired compounds were prepared from the corresponding 4-chromanones, following an identical synthetic route to that shown in Scheme 1. In the case of compound **37** with a free phenol group, commercially available 6-hydroxy-4-chromanone was protected with allyl bromide to avoid cross reactivity. Allylated derivative **36** was biologically tested but also used to prepare phenol **37** by removal of the allyl chain in the presence of $Pd(PPh_3)_4$ and potassium carbonate. 8-Methoxy-4-chromanone **21** was prepared from 2-methoxyphenol as previously described[19] but changing the reagent employed for the ring-closing Friedel−Crafts acylation from polyphosphoric acid (PPA) to Eaton's reagent. The latter is preferred over PPA as it overcomes acknowledged practical issues associated with the handling of PPA such as its strong viscosity, difficulties in the reaction workup, or the need for extremely high temperatures.[20] This alteration allowed us to increase the reported yield of 50−88%.

All synthesized analogues resulted in a significant loss of activity, with the exception of fluorinated derivatives **38**−**41** (Table 2). Compounds **39** and **41** even show a slight improvement in potency over **6**. Once again, these results

DOI: 10.1021/acs.jmedchem.9b00898
J. Med. Chem. 2020, 63, 2240−2262

Table 2. Study of Substitution in the Core Scaffold

Compound	Core Scaffold	Ar	EC_{50} (nM)[a]
3			130±30
6			128±10
34			> 1000
35			785±48
36			> 25000
37			> 10000
38			196±19
39			83±13
40			364±47
41			79±18
42			> 25000
43			> 25000
44			> 25000
45			> 25000

[a]Biological evaluation was carried out using the DGFA under the specific "add-in" format. Compounds were incubated at variable concentrations with fresh gametocytes, and their ability to impair exflagellation of male gametes was determined. Values below 1 μM are expressed as the mean ± SEM obtained from between three and eight biological replicates, each carried out in at least duplicate.

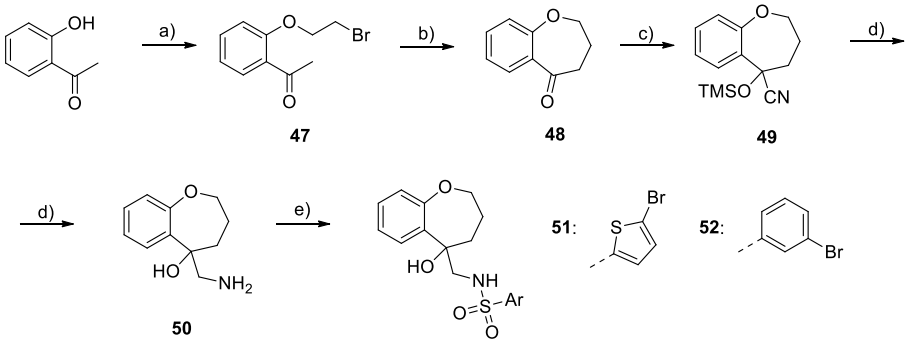
suggest the binding site of this series within the target(s) to be reasonably confined. Indeed, in contrast to other substituents, fluorine is very similar in size to hydrogen, which could explain why analogues **38**−**41** retain activity. It should be highlighted that fluorine is widely used within drug discovery to improve permeability by increasing lipophilicity and to address pharmacokinetic issues such as oxidative metabolism,[21] the latter being interesting in the context of this work (vide infra).

To further investigate the size constrains of the binding site, we next evaluated the outcome of modifying the size of the dihydropyran ring. Derivatives **51** and **52** with a seven-member ring or analogues **54** and **55** containing a dihydrofuran were devised. The former analogues were synthesized from commercially available 2-hydroxyacetophenone (Scheme 4). Alkylation of the phenol with 1,2-dibromoethane, followed by enolate formation with sodium hydride and in situ ring closure by nucleophilic substitution of the bromine, provided the necessary ketone **48**. Treatment of **48** with trimethylsilyl cyanide, followed by reduction with LAH as described for previous analogues, yielded amino alcohol **50**. Amino alcohol **50** was reacted with the desired sulfonyl chlorides to afford benzoxepine derivatives **51** and **52**.

Preparation of dihydrofuran analogues **54** and **55** initiated from 3-coumaranone, following the same synthetic route shown for 4-chromanones. However, the typical conditions used for the formation of the cyanohydrin (trimethylsilyl cyanide in the presence of catalytic zinc iodide) were unsuccessful, providing complex reactions mixtures. We speculate that lability of this scaffold to the Lewis acid was at fault, and thus we attempted a different protocol that used potassium carbonate as a catalyst instead.[22] Unfortunately, these conditions also did not afford the desired cyanohydrin. Finally, the use of potassium phthalimide as a catalyst in the absence of solvent provided mild enough conditions to allow for the formation of the desired cyanohydrin,[23] which was reduced immediately due to stability issues to yield amino alcohol **53** (Scheme 5). Treatment of **53** with the corresponding sulfonyl chlorides afforded final compounds **54** and **55**.

Expanding or contracting the central core resulted in a loss of activity (Table S2), being much more pronounced in the case of the seven-member ring analogues **51** and **52** (EC_{50} > 25 μM vs 1 > EC_{50} > 5 μM for **54** and **55**). These results are in agreement with our previous data suggesting a small binding

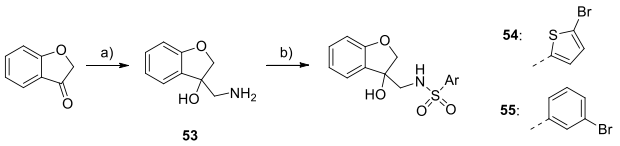
Scheme 4. Synthesis of the Extended Core Scaffold Analogues[a]



[a]Reagents and conditions: (a) 1,2-dibromoethane, K_2CO_3, ACN, reflux, 16 h, 34%; (b) NaH, THF, 0 °C to rt, 16 h, 77%; (c) TMSCN, ZnI_2, DCM, rt, 16 h, 97%; (d) LAH, THF, rt, 16 h, 35%; (e) $ArSO_2Cl$, Et_3N, DCM, 0 °C to rt, 16 h, 38−63%.

DOI: 10.1021/acs.jmedchem.9b00898
J. Med. Chem. 2020, 63, 2240−2262

Scheme 5. Synthesis of the Reduced Core Scaffold Analogues[a]



[a]Reactants and reagents: (a) (i) TMSCN, potassium phthalimide, rt, 16 h; (ii) LAH, THF, rt, 16 h, 35% (over two steps); (b) $ArSO_2Cl$, Et_3N, DCM, 0 °C to rt, 16 h, 51−53%.

site within the target(s). The drop in activity observed for the smaller derivatives **54** and **55** suggests that the geometry and size of the six-member ring are important for activity.

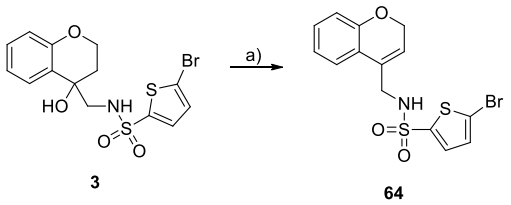
Given that alteration in ring size was not tolerated, we evaluated whether the oxygen atom within the chromane scaffold was important for activity. We therefore prepared analogues **60** and **61** with a methylene unit, and **62** and **63** with sulfur replacing the oxygen. Scheme 6 shows the synthetic route used to obtain these derivatives, which is identical to that shown previously in Scheme 1.

While compounds **60** and **61**, with no heteroatom at all, displayed a complete loss of activity, derivatives **62** and **63**, with a sulfur atom replacing the oxygen, showed a more moderate loss (EC_{50} > 25 μM and 1 > EC_{50} > 5 μM, respectively, Table S3). This result is suggestive that polarity in this region of the series is important to retain activity. The loss of activity in the sulfur derivatives versus the oxygen derivatives can possibly be explained by the lower electronegativity of this element when compared to oxygen. Alternatively, it might just be that the larger size of sulfur is nonoptimal.

The final region of the series for exploration was the quaternary hydroxyl group. Given that this moiety is at a benzylic position, it could present a potential stability issue. To study this, we took compound **3** and submitted it to acidic conditions in order to get the product of the E1 elimination reaction, **64** (Scheme 7).

The resulting alkene was found to be completely inactive in the DGFA assay (Table 3), suggesting that the hydroxyl group is required for transmission-blocking activity. An alternative option, however, would be that the geometry of the compound imposed by the alkene is not favored. To investigate this further, we designed the saturated dehydroxylated analogues **68** and **69** and derivatives **73** and **74** where the hydroxyl group was methylated. As a final comparator, we designed compounds **76** and **77**, where a fluorine atom replaced the hydroxyl group.

Scheme 7. Removal of the Hydroxyl Group in Compound 3[a]



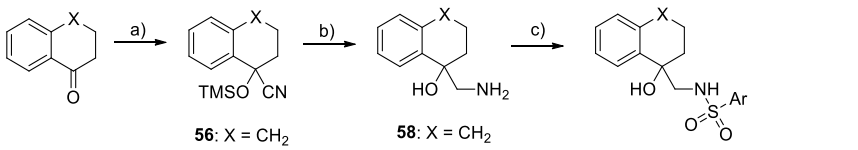
[a]Reagents and conditions: (a) $BF_3{\cdot}Et_2O$, DCM, 0 °C, 1 h, 11%.

For the preparation of analogues **68** and **69**, we attempted to follow a similar strategy to the one shown in Scheme 7, followed by reduction of the alkene. Unfortunately, the yields were very low, and the conditions were not reproducible upon scale up. Therefore, we followed an alternate synthetic route (Scheme 8). Wittig reaction of 4-chromanone with methoxymethylenetriphenylphosphine, prepared in situ by deprotonation of the corresponding phosphonium salt with butyllithium, yielded methyl vinyl ether **65** in good yield (86%). Cleavage of the methyl group using perchloric acid afforded aldehyde **66**, which was directly used in the next step for the formation and in situ reduction of the corresponding oxime to provide amine **67**. Amine **67** was converted to **68** and **69** using the previously established chemistry.

Analogues **73** and **74** were accessed from amino alcohol **2** by protection of the amine followed by methylation of the hydroxyl group. Cleavage of the Boc protecting group from **71** and coupling to the corresponding sulfonyl chlorides gave the final compounds **73** and **74** (Scheme 9). It is worth noting that the Boc group required removal using tetrabutylammonium fluoride (TBAF) in refluxing THF,[24] as compound **71** showed lability to commonly used acidic deprotection conditions (including TFA and HCl). Fluorinated derivatives **76** and **77** were obtained by replacement of the hydroxyl group in **2** by a fluorine atom using diethylaminosulfur trifluoride (DAST), followed by coupling of amine **75** to the desired sulfonyl chlorides.

As shown in Table 3, the loss of activity observed for derivative **64** following elimination of the hydroxyl group does not seem to be due to the different geometry enforced by the alkene. Instead, it seems that the absence of the polar hydroxyl group is the issue, with saturated analogues **68** and **69** also giving a complete loss of biological activity. Interestingly, the methylated derivatives **73** and **74** retain comparable activity, which indicates that the hydroxyl group is not acting as a

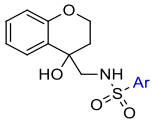
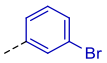
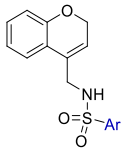
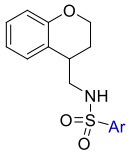
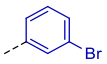
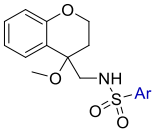
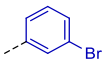
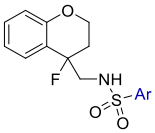
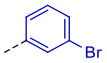
Scheme 6. Study of the Importance of the Oxygen Atom[a]



[a]Reagents and conditions: (a) TMSCN, ZnI_2, DCM, rt, 16 h, 45%−quant; (b) LAH, THF, rt, 16 h, 70−91%; (c) $ArSO_2Cl$, Et_3N, DCM, rt, 16 h, 33−75%.

DOI: 10.1021/acs.jmedchem.9b00898
J. Med. Chem. 2020, 63, 2240−2262

Table 3. Study of the Importance of the Hydroxyl Group

Compound	Core Scaffold	Ar	EC_{50} (nM)[a]
3			130±30
6			128±10
64			> 25000
68			> 10000
69			> 10000
73			354±22
74			149±24
76			>1000
77			945±192

[a]Biological evaluation was carried out using the DGFA under the specific "add-in" format. Compounds were incubated at variable concentrations with fresh gametocytes, and their ability to impair exflagellation of male gametes was determined. Values below 1 μM are expressed as the mean ± SEM obtained from between three and eight biological replicates, each carried out in at least duplicate.

hydrogen-bond donor in the target(s). Finally, exchange of the hydroxyl group with a fluorine atom in analogues **76** and **77** gives a 7-fold decrease in activity when compared with the corresponding hydroxylated counterparts.

As a final analysis of the importance of the hydroxyl group, we designed structurally isomeric compounds. Specifically, we elected to study compounds **78** and **79**, in which the hydroxyl group had been retained at the benzylic position but the sulfonamide moved to the adjacent carbon. We also selected derivatives **80** and **81** with both substituents moved to the adjacent carbon. The preparation of these analogues was envisioned through a common intermediate, alkene **82**, by hydroboration−oxidation or epoxidation and ring opening, respectively (Figure 4).

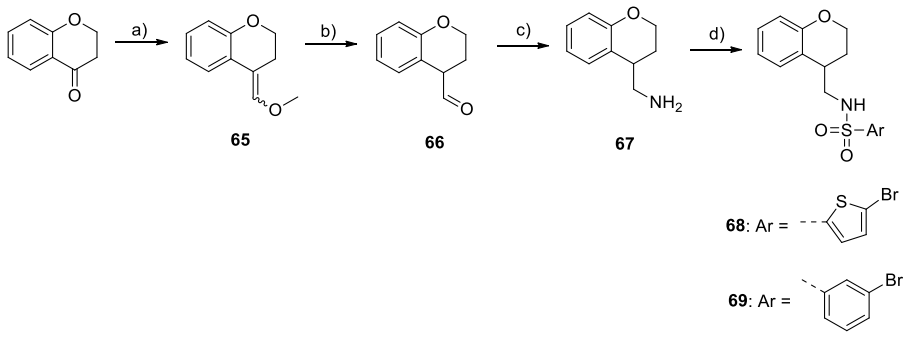
The synthesis of intermediate **82** was carried out by conjugate addition of 2-hydroxybenzaldehyde to acrylonitrile followed by an intramolecular aldol condensation[25] to yield **83** (Scheme 10). Reduction of nitrile **83** and Boc protection of the resulting amine gave product **82**.

Hydroboration−oxidation of alkene **82** was attempted using standard conditions, but complex reaction mixtures were obtained (Scheme 11). Careful following of the reaction by thin layer chromatography (TLC) showed that the oxidation step using hydrogen peroxide was responsible for the observed decomposition, while the hydroboration step appeared to occur cleanly. Therefore sodium perborate was used as an oxidant instead,[26] which after some reaction optimization gave the desired anti-Markovnikov alcohol **85** in moderate yield (49%), showing the expected *anti*-stereochemistry as a result of the *syn*-addition of the borane to the double bond (Scheme 11). Surprisingly, the corresponding Markovnikov analogue **86** was also isolated in 27% yield. Since the latter is the product needed for the preparation of compounds **80** and **81**, we progressed **86** instead of performing the planned epoxide formation.

Boc deprotection of compound **85** had to be optimized for reaction temperature and time in order to avoid elimination of the benzylic alcohol to return unsaturated amine **84**. However, epimerization at the benzylic position could not be completely avoided, and the desired amino alcohol was obtained as an inseparable 3:1 mixture of the *anti*- and *syn*-isomers **87a** and **87b** as a result (Scheme 12). The mixture was treated with the corresponding sulfonyl chlorides, and the resulting *anti*- and *syn*-isomers **78a**,**b** and **79a**,**b** could be separated by flash chromatography.

With the conditions from removal of the Boc group optimized, derivatives **80** and **81** were prepared from **86** following a similar synthetic route (Scheme 13).

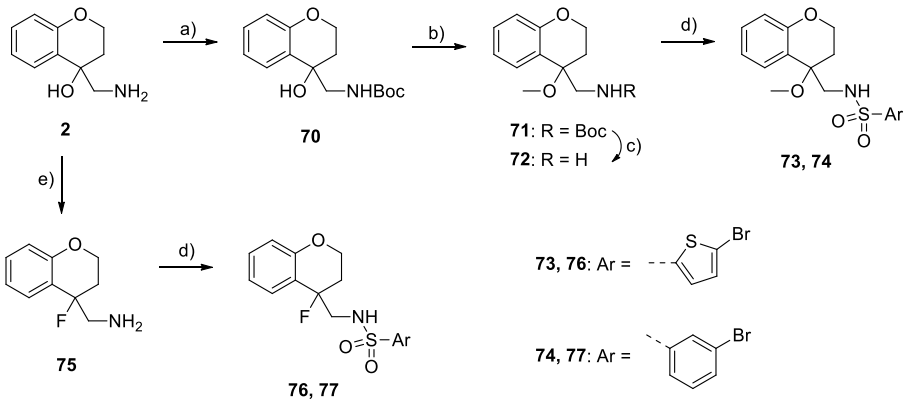
Scheme 8. Preparation of the Dehydroxylated Derivatives[a]



[a]Reagents and conditions: (a) (methoxymethyl)triphenylphosphonium chloride, BuLi, THF, −78 °C to rt, 16 h, 86%; (b) 70% $HClO_4$, Et_2O, 0 °C to rt, 45 min, quant; (c) (i) NH_2OH·HCl, EtOH, rt, 45 min; (ii) Zn, HCl, rt, 15 min, 33%; (d) $ArSO_2Cl$, Et_3N, DCM, rt, 16 h, 43−68%.

DOI: 10.1021/acs.jmedchem.9b00898
J. Med. Chem. 2020, 63, 2240−2262

Scheme 9. Synthesis of Alkylated and Fluorinated Analogues[a]



[a]Reagents and conditions: (a) Boc_2O, Et_3N, DCM, 0 °C to rt, 5 h, quant; (b) MeI, K^{t}OBu, THF, 0 °C to rt, 2 h, 70%; (c) 1 M TBAF in THF, reflux, 16 h, 39%; (d) $ArSO_2Cl$, Et_3N, DCM, rt, 16 h, 44−84%; (e) DAST, DCM, −78 °C to rt, 3 h, 31%.

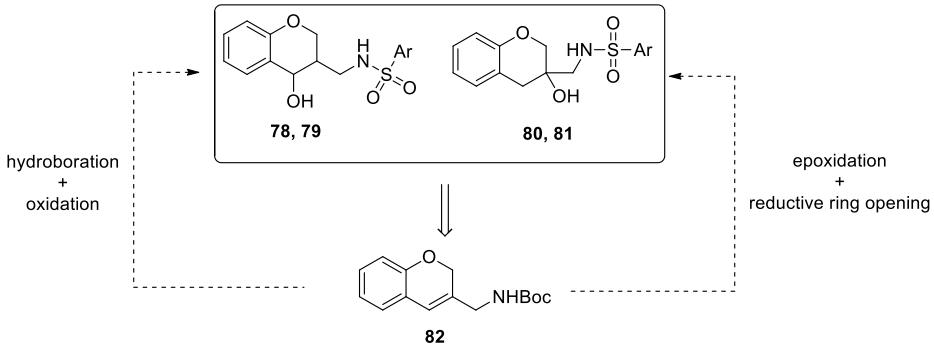
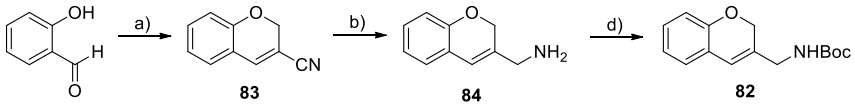


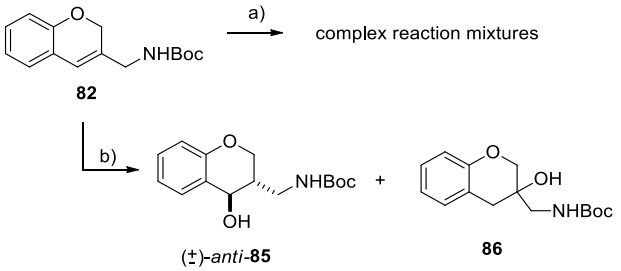
Figure 4. Schematic representation of the synthetic plan for the preparation of final compounds **78**−**81**.

Scheme 10. Synthesis of the Necessary Intermediate for the Preparation of Final Compounds 78−81[a]



[a]Reagents and conditions: (a) acrylonitrile, DABCO, 90 °C, 16 h, 74%; (b) LAH, $AlCl_3$, Et_2O, 0 °C to rt, 2 h, 56%; (c) Boc_2O, Et_3N, DCM, 0 °C to rt, 5 h, 83%.

Scheme 11. Hydroboration−Oxidation of 82[a]



[a]Reagents and conditions: (a) (i) 1 M BH_3·THF, 0 °C to rt, 2 h; (ii) H_2O_2, NaOH, H_2O, 0 °C to rt, 16 h; (b) (i) 1 M BH_3·THF, 0 °C to rt, 2 h; (ii) $NaBO_3$·$4H_2O$, H_2O, rt, 2 h, 27−49%.

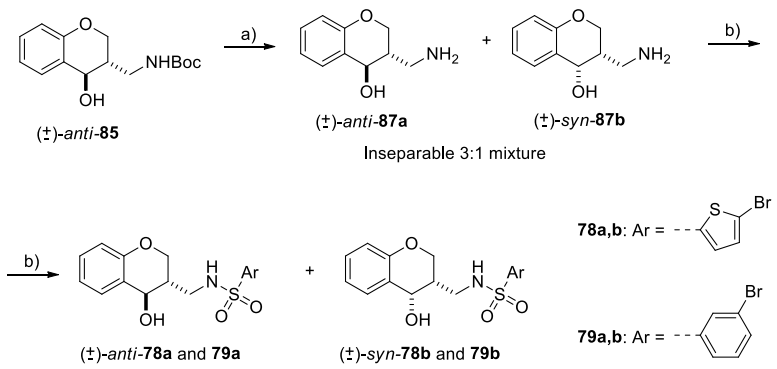
All six isomeric analogues were completely inactive (EC_{50} > 25 μM, Table S4), verifying the importance of the positioning of these substituents in the scaffold. While the relatively tight SAR displayed by this series is a challenge for ongoing medicinal chemistry, it may point to specificity for a given target(s) rather than promiscuous activity.

Up to this point, all compounds had been tested as racemic mixtures. To establish the role of absolute stereochemistry, we performed chiral resolution on a few of the most active derivatives. We selected the initial hit DDD01035881 (**3**) together with the bromobenzene analogue **6**, one of the fluorinated compounds (**41**), and methoxylated derivative **74**. Table 4 shows the results of this analysis, which demonstrates that one enantiomer is significantly more active than the other. In all cases, the (−) isomer is the active enantiomer. This result again suggests a specific biological interaction to underpin the activity of this series and showcases compounds with a potency of 18−59 nM. While it would be ideal to assign the absolute stereochemistry of the active enantiomer, all attempts of crystallization have been unsuccessful thus far.

In vivo studies carried out on the original hit DDD01035881 provided a half-life of ∼90 min for this compound.[17] Taking into consideration the parasite lifecycle stage in which this scaffold intervenes, namely, male gamete development in the

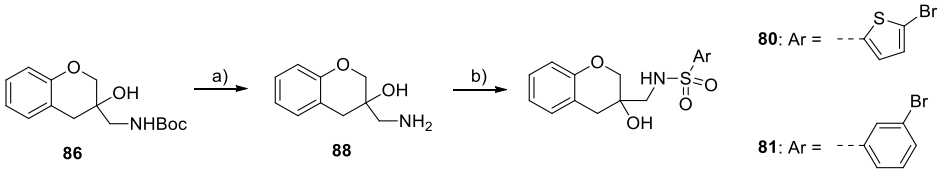
DOI: 10.1021/acs.jmedchem.9b00898
J. Med. Chem. 2020, 63, 2240−2262

Scheme 12. Preparation of Final Compounds 78a,b and 79a,b[a]



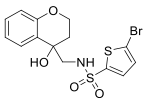
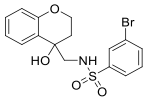
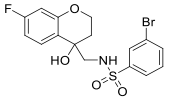
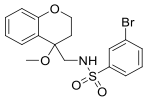
[a]Reagents and conditions: (a) TFA, DCM, 0 °C, 30 min, 57%; (b) $ArSO_2Cl$, Et_3N, DCM, rt, 16 h, 77−93%.

Scheme 13. Preparation of Final Compounds 80 and 81[a]



[a]Reagents and conditions: (a) TFA, DCM, 0 °C, 30 min, 33%; (b) $ArSO_2Cl$, Et_3N, DCM, rt, 16 h, 15−70%.

Table 4. Study of the Activity of the Enantiomeric Pairs

Compound	Core Scaffold	EC_{50} (nM)[a]	Enantiomer	EC_{50} (nM)[a]
3		130±30	(-)-3	46±5
			(+)-3	>1000
6		128±10	(-)-6	18±3
			(+)-6	>2000
41		79±18	(-)-41	51±13
			(+)-41	>1000
74		149±24	(-)-74	59±8
			(+)-74	>2000

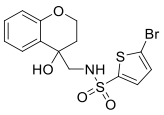
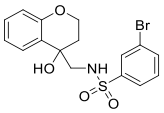
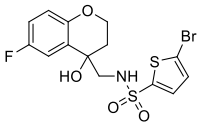
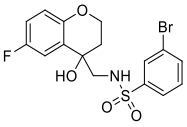
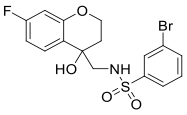
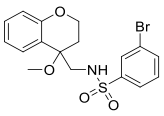
[a]Biological evaluation was carried out using the DGFA under the specific "add-in" format. Compounds were incubated at variable concentrations with fresh gametocytes, and their ability to impair exflagellation of male gametes was determined. Values below 1 μM are expressed as the mean ± SEM obtained from between three and eight biological replicates, each carried out in at least duplicate.

mosquito midgut, longer circulation time would be required for the compound to be taken up by the mosquito. We hypothesized that the thiophene ring in the initial hit **3** might be one of the causes for the fast metabolism.[27] For that reason, we decided to carry out in vitro metabolic stability studies on the most active compounds **6**, **39**, **41**, and **74**, all bearing the bromobenzene ring instead. Additionally, compound **3** and its fluorinated analogue (**38**) were included for comparison. Table 5 shows the intrinsic clearance values (CL_{int}) and half-lives ($t_{1/2}$) obtained for compounds **3**, **6**, **38**, **39**, **41**, and **74** when incubated with mouse liver microsomes. Surprisingly, changing the bromothiophene group to a bromobenzene ring does not impart metabolic stability: compound **6** is not detectable after 5 min of incubation with the microsomes, and bromobenzene derivative **39** has a reduced half-life of almost a minute when compared to its bromothiophene analogue (**38**). Compound **74** has a half-life comparable to that of compound **3**, suggesting that the hydroxyl group is also not important for microsomal metabolism. Interestingly, fluorinated derivatives **38**, **39**, and **41** show a considerable improvement in stability, with almost a 4-fold reduction in microsomal clearance for compounds **38** and **41** versus compound **3**. This result may suggest that the chromane aromatic ring is a soft spot for oxidative metabolism. Oxidation of electron rich aromatic rings by cytochrome P450 (CYP450) to produce the corresponding phenol is well-known, and fluorine is very commonly used to hamper such processes.[21] Oxidation normally occurs at the more electron rich positions, i.e., *ortho* and *para* with respect to activating substituents, the latter being the most commonly found. In the case of compound **41**, the most stable fluorinated analogue under microsomal metabolism, the fluorine atom is at *para* with respect to the alkyl chain and at *meta* with regard to the more activating ether substituent. Despite this, **41** shows a similar half-life as its analogue **39** where the fluorine atom is in *para* to the ether oxygen. This may suggest that the increased microsomal stability of the fluorinated derivatives stems from general electronic tuning of the chromane ring rather than blocking a specific metabolic soft spot on the aromatic ring.

The toxicity of four representative analogues against a human HepG2 cell line was evaluated as previously described.[17] No cytotoxicity was observed for any of the assayed compounds after 48 h of incubation when compared to the drug doxorubicin, which was used as positive control (Table S5).

DOI: 10.1021/acs.jmedchem.9b00898
J. Med. Chem. 2020, 63, 2240−2262

Table 5. Metabolic Stability Data for Compounds 3, 6, 38, 39, 41, and 74 in Mouse Microsomes

Compound	Core Scaffold	EC_{50} (nM)[a]	CL_{int} (μL/min/mg protein)[b]	$t_{1/2}$ (min)[b]
3		130±30	1130	1.23
6		128±10	N/A[c]	N/A[c]
38		196±19	298	4.65
39		83±13	355	3.90
41		79±18	291	4.76
74		149±24	1310	1.06

[a]Biological evaluation was carried out using the DGFA under the specific "add-in" format. Compounds were incubated at variable concentrations with fresh gametocytes, and their ability to impair exflagellation of male gametes was determined. Values below 1 μM are expressed as the mean ± SEM obtained from between three and eight biological replicates, each carried out in at least duplicate. [b]Values expressed as the mean from two to four experiments. [c]Metabolism was too fast to determine accurate values.

CONCLUSIONS

This study aimed to further explore the early medicinal chemistry of DDD01035881, the most robust hit identified from a 70 000-compound Global Health Chemical Diversity Library (GHCDL) screen using the DGFA assay.[17] The ultimate aim of this project is to further the progression of compounds that can stop the transmission of malaria. In addition to a clearer understanding of the SAR of this series, we have identified a compound (**41**) with improved metabolic stability over the original hit and have clearly defined the active enantiomer of this series. While this certainly bodes well for further optimization, ultimately a long circulating half-life will be required in order for the optimized compound to reach its biological target in the mosquito. We note that drug delivery techniques may be another approach to extend the circulating half-life of this series. Taking advantage of the different environment found in the vector, namely, the decrease in temperature to 28 °C, temperature-controlled release from a drug delivery system may be possible, an approach more commonly exploited for hyperthermia.[28] A final approach may be to use an optimized compound from this series as part of long-lasting ITNs or IRS. It has been recently shown that the antimalarial atovaquone can interrupt the parasite lifecycle completely in the mosquito, after exposure of the *Anopheles* female to a glass surface coated with the drug.[29] This is an exciting study that opens new avenues for the development of transmission-blocking agents through perturbing biology in the mosquito rather than the human host.

EXPERIMENTAL SECTION

Chemistry. Unless otherwise stated, the starting materials, reagents, and solvents were purchased as high-grade commercial products from Sigma-Aldrich, Acros, Alfa-Aesar, Fluorochem, TCI, or VWR. Solvents were either purchased anhydrous or dried by passing them through activated alumina columns using a Pure Solv Micro 100 Liter solvent purification system. All reactions were performed under nitrogen atmosphere.

Analytical thin-layer chromatography was run on Merck silica gel plates (Kieselgel 60 F-254), with detection by UV light (λ = 254 and 365 nm), ninhydrin or phosphomolybdic acid solutions in ethanol, or $KMnO_4$ (aqueous, aq). Products were purified by flash chromatography on glass column with silica gel type 60 (particle size 40−63 μm from Fluorochem). Optical rotation [α] was measured on a Bellingham and Stanley ADP 440+ polarimeter using a LED light source (interference filter, λ = 589 nm) with a 0.5 dm path length; concentrations (c) are given as g/100 mL. Nuclear magnetic resonance (NMR) spectra were recorded on a Bruker Avance III 400 MHz (^{1}H, 400 MHz; ^{13}C, 101 MHz; ^{19}F, 377 MHz) instrument at room temperature (rt) at the NMR core facility at Imperial College London. Chemical shifts (δ) are expressed in parts per million relative to internal tetramethylsilane; coupling constants (J) are in hertz (Hz). The following abbreviations are used to describe peak patterns when appropriate: s (singlet), d (doublet), t (triplet), q (quartet), qt (quintet), m (multiplet), app (apparent), and br (broad). High resolution mass spectrometry (HRMS) spectra were recorded on a

DOI: 10.1021/acs.jmedchem.9b00898
J. Med. Chem. 2020, 63, 2240−2262

Micromass Autospec Premier and Micromass LCT Premier spectrometer in electrospray ionization (ESI) mode at Imperial College London mass spectrometry core facility. For all final compounds, purity was determined by high-performance liquid chromatography coupled to mass spectrometry (HPLC−MS) using a Waters 2767 system. Separation was achieved using a XBridge C18 (5 μm, 4.6 mm × 100 mm) column, equipped with an XBridge C18 guard column (5 μm, 4.6 mm × 20 mm). The gradient mobile phase consisted of A (95:5 H_2O/acetonitrile [ACN]) and B (5:95 H_2O/ACN) with 0.1% formic acid as solvent modifier. Purity of tested compounds was at least 95%, unless stated otherwise. Spectra were acquired in positive or negative ionization mode from 100 to 1000 m/z and in UV mode (scan 190−700 nm). MS analysis was performed with an ESI source. Chiral resolution of selected compounds was performed by HPLC using either a PerkinElmer series 200 or an Agilent Thecnologies 1200 series system. Separation was achieved using a Chiralcel OD-H or a Chiralpack IE-3 column, with the corresponding guard columns. The mobile phase consisted of an isocratic gradient of hexane and isopropanol.

All compound spectra are freely available at https://doi.org/10.14469/hpc/5733.

General Procdures. A. Cyanohydrin Formation. To a stirred solution of the corresponding ketone (1 equiv) in dry DCM (3 mL/mmol) at 0 °C, ZnI_2 was added (0.02 equiv) followed by trimethylsylil cyanide (1.5 equiv). The resulting mixture was allowed to warm up to rt and stirred at that temperature overnight. The reaction was diluted with DCM, washed with a saturated (sat.) solution of $NaHCO_3$, dried over $MgSO_4$, filtered, and evaporated under reduced pressure. The crude product was used in the next step without further purification.

B. Cyanohydrin Reduction. To a stirred solution of the corresponding cyanohydrin (1 equiv) in anhydrous THF (4 mL/mmol) at 0 °C, a 1 M solution of LAH in THF (2 equiv) was added dropwise, and the resulting mixture was allowed to warm up to rt and stirred at that temperature overnight. The reaction was cooled down to 0 °C and worked up according to the Fieser procedure. The crude was purified by flash chromatography using the appropriate eluent to afford the corresponding amino alcohol.

C. Sulfonamide Formation. To a stirred solution of the corresponding amino alcohol (1 equiv) in dry DCM (4 mL/mmol) at 0 °C, triethylamine (2.5 equiv) was added dropwise. Then, a solution of the desired sulfonyl chloride (1.1 equiv) in dry DCM (4 mL/mmol) was added and the reaction mixture was allowed to warm up to rt and stirred for 5 h. Water was added, and the mixture was extracted with DCM (2×), dried over $MgSO_4$, filtered, and evaporated under reduced pressure. The crude was purified by flash chromatography using the appropriate eluent to afford the desired product.

D. Synthesis of *N*-((4-Hydroxychroman-4-yl)methyl)amides. To a solution of the corresponding carboxylic acid (1.1 equiv), EDC (1.5 equiv), and HOBt (1.5 equiv) in dry DMF (5 mL/mmol of EDC/HOBt) at 0 °C, a solution of the corresponding amino alcohol (1 equiv) in dry DCM (4 mL/mmol) was added followed by triethylamine (5 equiv). The mixture was stirred at 0 °C for 30 min and then allowed to warm up to rt and stirred overnight. The reaction mixture was then diluted with DCM and washed with 5% LiCl (aq, 3×) and brine, dried over $MgSO_4$, filtered, and evaporated under reduced pressure. The crude product was purified by flash chromatography using the appropriate eluent to afford the desired product.

E. Synthesis of *N*-((4-Hydroxychroman-4-yl)methyl)amines. To a solution of 4-(aminomethyl)chroman-4-ol (1 equiv) in dry MeOH (15 mL/mmol), the corresponding aldehyde (1 equiv) was added, and the solution was stirred for 15 min at rt before 2-picoline borane complex (1.2 equiv) was added portionwise. After stirring for 25 h, the reaction was dried over $MgSO_4$, filtered, and evaporated under reduced pressure. The crude product was purified by flash chromatography using the appropriate eluent to afford the desired product.

4-((Trimethylsilyl)oxy)chromane-4-carbonitrile (1). Following general procedure A, cyanohydrin **1** was obtained from 4-chromanone (2.00 g, 13.3 mmol) in quantitative yield (3.3 g) as a colorless oil. ^{1}H NMR (400 MHz, $CDCl_3$) δ 7.56 (dd, J = 7.8, 1.6 Hz, 1H), 7.31−7.26 (m, 1H), 6.98 (td, J = 7.8, 1.2 Hz, 1H), 6.84 (dd, J = 8.3, 1.1 Hz, 1H), 4.45−4.26 (m, 2H), 2.52−2.30 (m, 2H), 0.17 (s, 9H). ^{13}C NMR (101 MHz, $CDCl_3$) δ 153.7, 131.5, 128.8, 121.2, 120.9, 117.7, 65.7, 61.4, 36.4, 1.3. Spectra available at https://doi.org/10.14469/hpc/5801.

4-(Aminomethyl)chroman-4-ol (2). Following general procedure B, amino alcohol **2** was obtained from cyanohydrin **1** (3.30 g, 13.3 mmol) in quantitative yield (2.4 g) as a pale-yellow oil. Column chromatography: DCM/7 N NH_3 in MeOH, 10:0 to 9:1. ^{1}H NMR (400 MHz, $CDCl_3$) δ 7.42 (dd, J = 7.8, 1.7 Hz, 1H), 7.18 (ddd, J = 8.2, 7.3, 1.7 Hz, 1H), 6.95−6.91 (m, 1H), 6.83 (dd, J = 8.2, 1.2 Hz, 1H), 4.30−4.20 (m, 2H), 3.07 (d, J = 13.1 Hz, 1H), 2.95 (d, J = 13.0 Hz, 1H), 2.12−2.02 (m, 2H). ^{13}C NMR (101 MHz, MeOD) δ 156.2, 130.2, 127.9, 127.5, 121.6, 118., 68.7, 64.2, 51.0, 33.8. HRMS (ESI) calcd for $[M + H]^+$ $C_{10}H_{13}NO_2$ 180.1025, found 180.1024. Spectra available at https://doi.org/10.14469/hpc/5802.

5-Bromo-*N*-((4-hydroxychroman-4-yl)methyl)thiophene-2-sulfonamide (3). Following general procedure C, sulfonamide **3** was obtained from amino alcohol **2** (90 mg, 0.50 mmol) and 3-bromobenzenesulfonyl chloride (90 mg, 0.50 mmol) in 52% yield (105 mg) as a white solid. Column chromatography: hexane/EtOAc, 4:1. ^{1}H NMR (400 MHz, $CDCl_3$) δ 7.35−7.29 (m, 2H), 7.20 (ddd, J = 8.3, 7.2, 1.7 Hz, 1H), 7.06 (d, J = 3.9 Hz, 1H), 6.90 (td, J = 7.6, 1.2 Hz, 1H), 6.83 (dd, J = 8.3, 1.2 Hz, 1H), 5.27 (t, J = 6.6 Hz, 1H, NH), 4.29−4.14 (m, 2H), 3.33 (d, J = 6.5 Hz, 2H), 2.36 (ddd, J = 14.1, 6.3, 3.5 Hz, 1H), 2.29 (br s, 1H, OH), 2.03 (ddd, J = 14.1, 8.1, 4.3 Hz, 1H). ^{13}C NMR (101 MHz, $CDCl_3$) δ 154.7, 141.5, 132.4, 130.6, 130.2, 126.4, 125.0, 121.1, 120.2, 117.5, 68.4, 63.4, 51.6, 33.0. HRMS (ESI) calcd for $[M - H]^-$ $C_{14}H_{13}NO_4S_2Br$ 401.9469, found 401.9469. Spectra available at https://doi.org/10.14469/hpc/5803.

Chiral resolution was performed on a Chiralcel OD-H column using an isocratic gradient of hexane/isopropanol, 8:2, to yield (−)-**3** and (+)-**3**.

(+)-**3**: $[\alpha]_D^{20}$ = +48° (c = 0.125, MeOH).

(−)-**3**: $[\alpha]_D^{20}$ = −48° (c = 0.125, MeOH).

2-Bromo-*N*-((4-hydroxychroman-4-yl)methyl)benzenesulfonamide (4). Following general procedure C, sulfonamide **4** was obtained from amino alcohol **2** (90 mg, 0.50 mmol) and 2-bromobenzenesulfonyl chloride (141 mg, 0.55 mmol) in 67% yield (132 mg) as a white solid. Column chromatography: hexane/EtOAc, 4:1. ^{1}H NMR (400 MHz, $CDCl_3$) δ 8.10 (dd, J = 7.6, 1.9 Hz, 1H), 7.76 (dd, J = 7.5, 1.6 Hz, 1H), 7.47 (td, J = 7.5, 1.5 Hz, 1H), 7.42 (td, J = 7.5, 1.9 Hz, 1H), 7.32 (dd, J = 7.8, 1.6 Hz, 1H), 7.18 (ddd, J = 8.4, 7.3, 1.6 Hz, 1H), 6.88 (td, J = 7.8, 1.1 Hz, 1H), 6.82 (dd, J = 8.3, 1.0 Hz, 1H), 5.55 (br t, J = 6.2 Hz, 1H), 4.30−4.15 (m, 2H), 3.20 (dd, J = 6.7, 3.9 Hz, 2H), 2.43 (ddd, J = 14.1, 6.5, 3.7 Hz, 1H), 2.05 (m, 2H). ^{13}C NMR (101 MHz, $CDCl_3$) δ 154.7, 138.6, 135.2, 134.0, 131.7, 130.1, 128.0, 126.4, 125.0, 121.0, 119.8, 117.4, 68.3, 63.4, 51.5, 33.0. HRMS (ESI) calcd for $[M - H]^-$ $C_{16}H_{15}NO_4SBr$ 395.9905, found 395.9912. Spectra available at https://doi.org/10.14469/hpc/5804.

3-Bromo-*N*-((4-hydroxychroman-4-yl)methyl)thiophene-2-sulfonamide (5). Following general procedure C, sulfonamide **5** was obtained from amino alcohol **2** (90 mg, 0.50 mmol) and 3-bromothiophene-2-sulfonyl chloride (144 mg, 0.55 mmol) in 60% yield (111 mg) as a white solid. Column chromatography: hexane/EtOAc, 4:1. ^{1}H NMR (400 MHz, $CDCl_3$) δ 7.50 (d, J = 5.3 Hz, 1H), 7.33 (dd, J = 7.8, 1.6 Hz, 1H), 7.18 (ddd, J = 8.6, 7.3, 1.6 Hz, 1H), 7.11 (d, J = 5.3 Hz, 1H), 6.89 (td, J = 7.8, 1.1 Hz, 1H), 6.81 (dd, J = 8.3, 1.0 Hz, 1H), 5.63 (t, J = 6.6 Hz, 1H, NH), 4.29−4.13 (m, 2H), 3.31 (d, J = 6.7 Hz, 2H), 2.44−2.32 (m, 2H), 2.03 (ddd, J = 14.0, 8.0, 4.3 Hz, 1H). ^{13}C NMR (101 MHz, $CDCl_3$) δ 154.7, 135.8, 132.7, 131.2, 130.1, 126.4, 124.9, 121.0, 117.5, 113.4, 68.3, 63.4, 51.6, 32.9. HRMS (ESI) calcd for $[M - H]^-$ $C_{14}H_{13}NO_4S_2Br$ 401.9469, found 401.9476. Spectra available at https://doi.org/10.14469/hpc/5805.

DOI: 10.1021/acs.jmedchem.9b00898
J. Med. Chem. 2020, 63, 2240−2262

3-Bromo-*N*-((4-hydroxychroman-4-yl)methyl)benzenesulfonamide (6). Following general procedure C, sulfonamide **6** was obtained from amino alcohol **2** (90 mg, 0.50 mmol) and 3-bromobenzenesulfonyl chloride (141 mg, 0.55 mmol) in 42% yield (82 mg) as a white solid. Column chromatography: hexane/EtOAc, 4:1. ^{1}H NMR (400 MHz, $CDCl_3$) δ 7.98 (t, J = 1.9 Hz, 1H), 7.75 (ddd, J = 7.9, 1.7, 1.1 Hz, 1H), 7.71 (ddd, J = 8.2, 1.9, 1.0 Hz, 1H), 7.39 (t, J = 7.9 Hz, 1H), 7.29 (dd, J = 7.8, 1.7 Hz, 1H), 7.19 (ddd, J = 8.6, 7.3, 1.7 Hz, 1H), 6.88 (td, J = 7.6, 1.2 Hz, 1H), 6.82 (dd, J = 8.4, 1.2 Hz, 1H), 5.23 (dd, J = 8.1, 4.9 Hz, 1H, NH), 4.31−4.11 (m, 2H), 3.39−3.15 (m, 2H), 2.37 (ddd, J = 14.0, 6.3, 3.5 Hz, 1H), 2.31 (br s, 1H, OH), 2.02 (ddd, J = 14.0, 8.3, 4.4 Hz, 1H). ^{13}C NMR (101 MHz, $CDCl_3$) δ 154.7, 141.9, 136.0, 130.9, 130.2, 130.0, 126.4, 125.6, 125.0, 123.4, 121.0, 117.5, 68.5, 63.5, 51.4, 32.9. HRMS (ESI) calcd for $[M - H]^-$ $C_{16}H_{15}NO_4SBr$ 395.9905, found 395.9914. Spectra available at https://doi.org/10.14469/hpc/5806.

Chiral resolution was performed on a Chiralcel OD-H column using an isocratic gradient of hexane/isopropanol, 8:2 to yield (−)-**6** and (+)-**6**.

(−)-**6**: $[\alpha]_D^{20}$ = −87° (c = 0.53, DCM).

(+)-**6**: $[\alpha]_D^{20}$ = +68° (c = 0.41, DCM).

4-Bromo-*N*-((4-hydroxychroman-4-yl)methyl)benzenesulfonamide (7). Following general procedure C, sulfonamide **7** was obtained from amino alcohol **2** (90 mg, 0.50 mmol) and 3-bromobenzenesulfonyl chloride (141 mg, 0.55 mmol) in 54% yield (107 mg) as a white solid. Column chromatography: hexane/EtOAc, 4:1. ^{1}H NMR (400 MHz, $CDCl_3$) δ 7.66 (app d, J = 8.8 Hz, 2H), 7.62 (app d, J = 8.9 Hz, 2H), 7.25 (dd, J = 7.5, 1.9 Hz, 1H), 7.16 (ddd, J = 8.8, 7.3, 1.6 Hz, 1H), 6.84 (td, J = 7.7, 1.2 Hz, 1H), 6.79 (dd, J = 8.3, 1.1 Hz, 1H), 5.47 (t, J = 6.6 Hz, 1H, NH), 4.23−4.08 (m, 2H), 3.32−3.13 (m, 2H), 2.66 (s, 1H, OH), 2.31 (ddd, J = 14.0, 6.3, 3.5 Hz, 1H), 1.98 (ddd, J = 13.8, 8.2, 4.3 Hz, 1H). ^{13}C NMR (101 MHz, $CDCl_3$) δ 154.6, 138.8, 132.6, 130.1, 128.6, 127.9, 126.4, 125.0, 121.0, 117.4, 68.4, 63.4, 51.4, 32.8. HRMS (ESI) calcd for $[M - H]^-$ $C_{16}H_{15}NO_4SBr$ 395.9905, found 395.9915. Spectra available at https://doi.org/10.14469/hpc/5807.

2-Chloro-*N*-((4-hydroxychroman-4-yl)methyl)benzenesulfonamide (8). Following general procedure C, sulfonamide **8** was obtained from amino alcohol **2** (90 mg, 0.50 mmol) and 2-chlorobenzenesulfonyl chloride (0.093 mL, 0.55 mmol) in 53% yield (93 mg) as a white solid. Column chromatography: hexane/EtOAc, 4:1. ^{1}H NMR (400 MHz, $CDCl_3$) δ 8.09−8.00 (m, 1H), 7.58−7.48 (m, 2H), 7.41 (ddd, J = 8.5, 6.6, 2.1 Hz, 1H), 7.30 (dd, J = 7.8, 1.5 Hz, 1H), 7.17 (ddd, J = 8.6, 7.4, 1.6 Hz, 1H), 6.86 (td, J = 7.6, 1.0 Hz, 1H), 6.80 (dd, J = 8.3, 0.9 Hz, 1H), 5.53 (t, J = 6.6 Hz, 1H, NH), 4.28−4.11 (m, 2H), 3.27−3.11 (m, 2H), 2.43−2.37 (m, 2H), 2.02 (ddd, J = 13.8, 8.0, 4.3 Hz, 1H). ^{13}C NMR (101 MHz, $CDCl_3$) δ 154.7, 137.0, 134.0, 131.8, 131.4, 131.4, 130.1, 127.4, 126.4, 125.0, 121.0, 117.4, 68.3, 63.4, 51.5, 32.9. HRMS (ESI) calcd for $[M - H]^-$ $C_{16}H_{15}NO_4SCl$ 352.0410, found 352.0412. Spectra available at https://doi.org/10.14469/hpc/5808.

3-Chloro-*N*-((4-hydroxychroman-4-yl)methyl)benzenesulfonamide (9). Following general procedure C, sulfonamide **9** was obtained from amino alcohol **2** (90 mg, 0.50 mmol) and 3-chlorobenzenesulfonyl chloride (0.083 mL, 0.55 mmol) in 57% yield (101 mg) as a white solid. Column chromatography: hexane/EtOAc, 4:1. ^{1}H NMR (400 MHz, $CDCl_3$) δ 7.83 (t, J = 1.9 Hz, 1H), 7.72 (app d, J = 7.8 Hz, 1H), 7.56 (ddd, J = 8.0, 1.8, 0.9 Hz, 1H), 7.46 (t, J = 7.9 Hz, 1H), 7.30 (dd, J = 7.7, 1.7 Hz, 1H), 7.19 (ddd, J = 8.6, 7.3, 1.7 Hz, 1H), 6.89 (td, J = 7.5, 1.2 Hz, 1H), 6.82 (dd, J = 8.3, 1.2 Hz, 1H), 5.13 (dd, J = 8.4, 4.6 Hz, 1H, NH), 4.31−4.13 (m, 2H), 3.38−3.21 (m, 2H), 2.39 (ddd, J = 14.0, 6.3, 3.4 Hz, 1H), 2.18 (br s, 1H, OH), 2.02 (ddd, J = 13.2, 8.6, 4.7 Hz, 1H). ^{13}C NMR (101 MHz, $CDCl_3$) δ 154.7, 141.7, 135.6, 133.1, 130.7, 130.2, 127.2, 126.4, 125.2, 125.0, 121.0, 117.5, 68.5, 63.5, 51.5, 32.9. HRMS (ESI) calcd for $[M - H]^-$ $C_{16}H_{15}NO_4SCl$ 352.0410, found 352.0406. Spectra available at https://doi.org/10.14469/hpc/5809.

4-Chloro-*N*-((4-hydroxychroman-4-yl)methyl)benzenesulfonamide (10). Following general procedure C, sulfonamide **10** was obtained from amino alcohol **2** (90 mg, 0.50 mmol) and 4-chlorobenzenesulfonyl chloride (120 mg, 0.55 mmol) in 20% yield (28 mg) as a white solid. Column chromatography: hexane/EtOAc, 4:1. ^{1}H NMR (400 MHz, $CDCl_3$) δ 7.81−7.75 (m, 2H), 7.53−7.46 (m, 2H), 7.29 (dd, J = 7.8, 1.6 Hz, 1H), 7.20 (ddd, J = 8.8, 7.3, 1.6 Hz, 1H), 6.89 (td, J = 7.7, 1.2 Hz, 1H), 6.83 (dd, J = 8.3, 1.1 Hz, 1H), 4.98 (dd, J = 8.4, 4.6 Hz, 1H), 4.30−4.15 (m, 2H), 3.37−3.21 (m, 2H), 2.39 (ddd, J = 14.0, 6.3, 3.5 Hz, 1H), 2.17−1.97 (m, 2H). ^{13}C NMR (101 MHz, $CDCl_3$) δ 154.7, 139.5, 138.5, 130.2, 129.7, 128.6, 126.3, 125.1, 121.1, 117.5, 68.5, 63.5, 51.5, 33.0. HRMS (ESI) calcd for $[M - H]^-$ $C_{16}H_{15}NO_4SCl$ 352.0410, found 352.0405. Spectra available at https://doi.org/10.14469/hpc/5810.

***N*-((4-Hydroxychroman-4-yl)methyl)benzenesulfonamide (11).** Following general procedure C, sulfonamide **11** was obtained from amino alcohol **2** (50 mg, 0.28 mmol) and benzenesulfonyl chloride (0.04 mL, 0.31 mmol) in 74% yield (66 mg) as a white solid. Column chromatography: DCM/1% NH_4OH in MeOH, 98:2. ^{1}H NMR (400 MHz, $CDCl_3$) δ 7.88−7.81 (m, 2H), 7.63−7.57 (m, 1H), 7.56−7.50 (m, 2H), 7.29 (dd, J = 7.8, 1.6 Hz, 1H), 7.20 (ddd, J = 8.3, 7.3, 1.7 Hz, 1H), 6.92−6.86 (m, 1H), 6.83 (dd, J = 8.3, 1.1 Hz, 1H), 4.86 (dd, J = 8.1, 4.9 Hz, 1H, NH), 4.30−4.14 (m, 2H), 3.37−3.19 (m, 2H), 2.40 (ddd, J = 14.0, 6.4, 3.5 Hz, 1H), 2.06−1.97 (m, 2H, OH, $^1/_2CH_2$). ^{13}C NMR (101 MHz, $CDCl_3$) δ 154.8, 139.9, 133.0, 130.1, 129.4, 127.1, 126.4, 125.2, 121.0, 117.5, 68.5, 63.5, 51.5, 33.0. HRMS (ESI) calcd for $[M - H]^-$ $C_{16}H_{16}NO_4S$ 318.0800, found 318.0806. Spectra available at https://doi.org/10.14469/hpc/5811.

***N*-((4-Hydroxychroman-4-yl)methyl)-4-methoxybenzenesulfonamide (12).** Following general procedure C, sulfonamide **12** was obtained from amino alcohol **2** (90 mg, 0.50 mmol) and 4-methoxybenzenesulfonyl chloride (114 mg, 0.55 mmol) in 30% yield (52 mg) as a white solid. Column chromatography: hexane/EtOAc, 4:1. ^{1}H NMR (400 MHz, $CDCl_3$) δ 7.76 (d, J = 8.9 Hz, 2H), 7.29 (dd, J = 7.8, 1.6 Hz, 1H), 7.17 (ddd, J = 8.3, 7.2, 1.7 Hz, 1H), 6.96 (d, J = 8.9 Hz, 2H), 6.87 (td, J = 7.6, 1.2 Hz, 1H), 6.80 (dd, J = 8.2, 1.2 Hz, 1H), 5.07 (t, J = 6.7 Hz, 1H, NH), 4.26−4.11 (m, 2H), 3.86 (s, 3H), 3.22 (d, J = 6.9 Hz, 2H), 2.39−2.33 (m, 2H), 2.00 (ddd, J = 14.0, 8.3, 4.0 Hz, 1H). MS: m/z (ES) 348 $[M - H]^-$. ^{13}C NMR (101 MHz, $CDCl_3$) δ 163.1, 154.7, 131.3, 130.0, 129.3, 126.4, 125.3, 120.9, 117.4, 114.5, 68.4, 63.5, 55.8, 51.5, 33.0. HRMS (ESI) calcd for $[M - H]^-$ $C_{17}H_{18}NO_5S$ 348.0906, found 348.0910. Spectra available at https://doi.org/10.14469/hpc/5812.

4-Cyano-*N*-((4-hydroxychroman-4-yl)methyl)benzenesulfonamide (13). Following general procedure C, sulfonamide **13** was obtained from amino alcohol **2** (90 mg, 0.50 mmol) and 4-cyanobenzenesulfonyl chloride (112 mg, 0.55 mmol) in 65% yield (111 mg) as a white solid. Column chromatography: hexane/EtOAc, 4:1. ^{1}H NMR (400 MHz, $CDCl_3$) δ 7.95 (d, J = 8.2 Hz, 2H), 7.82 (d, J = 8.3 Hz, 2H), 7.30 (dd, J = 7.5, 1.9 Hz, 1H), 7.20 (ddd, J = 8.6, 7.3, 1.6 Hz, 1H), 6.89 (td, J = 7.5, 1.2 Hz, 1H), 6.83 (dd, J = 8.3, 1.1 Hz, 1H), 5.51 (dd, J = 8.4, 4.5 Hz, 1H, NH), 4.34−4.14 (m, 2H), 3.44−3.18 (m, 2H), 2.51 (s, 1H, OH), 2.37 (ddd, J = 14.0, 6.1, 3.4 Hz, 1H), 2.04 (ddd, J = 13.3, 8.6, 4.7 Hz, 1H). ^{13}C NMR (101 MHz, $CDCl_3$) δ 154.7, 144.3, 133.2, 130.2, 127.7, 126.3, 124.9, 121.0, 117.5, 117.4, 116.6, 68.5, 63.4, 51.5, 32.9. HRMS (ESI) calcd for $[M - H]^-$ $C_{17}H_{15}N_2O_4S$ 343.0753, found 343.0748. Spectra available at https://doi.org/10.14469/hpc/5813.

3-Acetyl-*N*-((4-hydroxychroman-4-yl)methyl)benzenesulfonamide (14). Following general procedure C, sulfonamide **14** was obtained from amino alcohol **2** (71 mg, 0.40 mmol) and 3-acetylbenzenesulfonyl chloride (120 mg, 0.50 mmol) in 4% yield (6.3 mg) as a white solid. Column chromatography: hexane/EtOAc, 4:1. ^{1}H NMR (400 MHz, $CDCl_3$) δ 8.40 (t, J = 1.8 Hz, 1H), 8.16 (app d, J = 7.8 Hz, 1H), 8.03 (app d, J = 7.8 Hz, 1H), 7.65 (t, J = 7.8 Hz, 1H), 7.29 (dd, J = 7.8, 1.7 Hz, 1H), 7.19 (ddd, J = 8.6, 7.3, 1.6 Hz, 1H), 6.88 (td, J = 7.6, 1.2 Hz, 1H), 6.83 (dd, J = 8.3, 1.2 Hz, 1H), 5.04 (dd, J = 8.7, 4.4 Hz, 1H, NH), 4.34−4.15 (m, 2H), 3.40−3.16 (m, 2H), 2.65 (s, 3H), 2.41 (ddd, J = 14.0, 6.2, 3.5 Hz, 1H), 2.04 (ddd, J = 13.4, 8.1, 4.4 Hz, 1H), 1.61 (s, 1H, OH). ^{13}C NMR (101 MHz, $CDCl_3$) δ 196.6, 154.7, 141.0, 138.1, 132.3, 131.2, 130.2, 129.9, 126.8, 126.3, 125.0, 121.0, 117.5, 68.5, 63.5, 51.5, 33.0, 26.9. HRMS (ESI)

DOI: 10.1021/acs.jmedchem.9b00898
J. Med. Chem. 2020, 63, 2240−2262

calcd for $[M - H]^-$ $C_{18}H_{18}NO_5S$ 360.0906, found 360.0887. Spectra available at https://doi.org/10.14469/hpc/5814.

3-Bromo-*N*-((4-hydroxychroman-4-yl)methyl)-*N*-methylbenzenesulfonamide (15). To a stirred suspension of sulfonamide **6** (40 mg, 0.10 mmol) and K_2CO_3 (48 mg, 0.35 mmol) in DMF (1.5 mL), methyl iodide (14 μL, 0.20 mmol) was added dropwise and the solution heated to 50 °C for 4 h. The mixture was diluted with EtOAc, washed with water (3×) and brine, dried over $MgSO_4$, filtered, and evaporated under reduced pressure. The resulting crude product was purified by flash chromatography (hexane/EtOAc, 3:1) to afford methylated sulfonamide **15** as a pale brown oil (36 mg, 80%). ^{1}H NMR (400 MHz, $CDCl_3$) δ 7.90 (t, *J* = 1.8 Hz, 1H), 7.72 (ddd, *J* = 8.0, 1.9, 1.0 Hz, 1H), 7.68 (ddd, *J* = 7.9, 1.7, 1.0 Hz, 1H), 7.40 (t, *J* = 7.9 Hz, 1H), 7.38 (dd, *J* = 7.8, 1.6 Hz, 1H), 7.20 (ddd, *J* = 8.3, 7.3, 1.7 Hz, 1H), 6.91 (ddd, *J* = 7.7, 7.3, 1.2 Hz, 1H), 6.84 (dd, *J* = 8.3, 1.1 Hz, 1H), 4.37−4.26 (m, 2H), 3.62 (d, *J* = 14.5 Hz, 1H), 3.11 (dd, *J* = 14.5, 0.7 Hz, 1H), 2.94 (s, 3H), 2.57 (ddd, *J* = 14.0, 5.5, 3.1 Hz, 1H), 2.33 (s, 1H, OH), 2.10 (dddd, *J* = 13.9, 9.4, 4.4, 0.8 Hz, 1H). ^{13}C NMR (101 MHz, $CDCl_3$) δ 154.4, 139.3, 136.0, 130.8, 130.3, 129.9, 126.7, 126.2, 126.0, 123.4, 120.9, 117.4, 70.0, 63.8, 58.6, 38.3, 33.2. HRMS, found 456.0117 ($C_{18}H_{19}NO_6S^{79}Br$, $[M - OH + HCO_2H]^+$, requires 456.0116). Spectra available at https://doi.org/10.14469/hpc/5815.

5-Bromo-*N*-((4-hydroxychroman-4-yl)methyl)thiophene-2-carboxamide (16). Following general procedure D, amide **16** was obtained from amino alcohol **2** (80 mg, 0.45 mmol) and 5-bromo-2-thiophenecarboxylic acid (104 mg, 0.55 mmol) in 55% yield (81 mg) as a white solid. ^{1}H NMR (400 MHz, MeOD) δ 7.55−7.48 (m, 2H), 7.19−7.12 (m, 2H), 6.91 (td, *J* = 7.8, 1.2 Hz, 1H), 6.77 (dd, *J* = 8.2, 1.1 Hz, 1H), 4.35−4.18 (m, 2H), 3.84 (d, *J* = 14.0 Hz, 1H), 3.62 (d, *J* = 14.0 Hz, 1H), 2.12 (ddd, *J* = 14.0, 6.4, 3.2 Hz, 1H), 2.00 (m, ddd, *J* = 13.2, 9.1, 4.2 Hz, 1H). ^{13}C NMR (101 MHz, MeOD) δ 163.7, 155.9, 141.8, 132.3, 130.2 130.1, 128.2, 127.6, 121.55, 119.2, 117.8, 70.0, 64.6, 49.6, 49.4, 49.2, 49.0, 48.8, 34.2. HRMS (ESI) calcd for $[M - H]^-$ $C_{15}H_{13}NO_3SBr$ 365.9756, found 365.9771. Spectra available at https://doi.org/10.14469/hpc/5822.

3-Bromo-*N*-((4-hydroxychroman-4-yl)methyl)benzamide (17). Following general procedure D, amide **17** was obtained from amino alcohol **2** (134 mg, 0.75 mmol) and 3-bromobenzoic acid (165 mg, 0.82 mmol) in 68% yield (184 mg) as a white solid. ^{1}H NMR (400 MHz, MeOD) δ 7.99 (app s, 1H), 7.78 (dd, *J* = 7.8, 0.9 Hz, 1H), 7.69 (dd, *J* = 8.0, 0.9 Hz, 1H), 7.53 (dd, *J* = 7.8, 1.3 Hz, 1H), 7.38 (t, *J* = 7.9 Hz, 1H), 7.20−7.11 (m, 1H), 6.91 (dd, *J* = 10.7, 4.4 Hz, 1H), 6.78 (d, *J* = 8.2 Hz, 1H), 4.35−4.27 (m, 1H), 4.23 (ddd, *J* = 10.5, 6.5, 3.7 Hz, 1H), 3.88 (d, *J* = 13.9 Hz, 1H), 3.68 (d, *J* = 13.9 Hz, 1H), 2.14 (ddd, *J* = 14.0, 6.5, 3.1 Hz, 1H), 2.02 (ddd, *J* = 13.2, 9.1, 4.0 Hz, 1H).^{13}C NMR (101 MHz, MeOD) δ 169.2, 155.9, 137.7, 135.6, 131.5, 131.4, 130.2, 128.2, 127.6, 127.2, 123.5, 121.5, 117.8, 70.0, 64.6, 49.8, 34.3. HRMS (ESI) calcd for $[M - H]^-$ $C_{17}H_{15}NO_3Br$ 360.0235, found 360.0229. Spectra available at https://doi.org/10.14469/hpc/5823.

4-((((5-Bromothiophen-2-yl)methyl)amino)methyl)-chroman-4-ol (18). Following general procedure E, amine **18** was obtained from amino alcohol **2** (90 mg, 0.50 mmol) and 5-bromothiophene-2-carbaldehyde (0.06 mL, 0.50 mmol) in 50% yield (89 mg) as a colorless oil. ^{1}H NMR (400 MHz, MeOD) δ 7.41 (dd, *J* = 7.8, 1.6 Hz, 1H), 7.16−7.09 (m, 1H), 6.94−6.85 (m, 2H), 6.75 (dd, *J* = 11.2, 2.5 Hz, 2H), 4.25−4.13 (m, 2H), 3.94, 3.90 (ABq, J_{AB} = 14.4 Hz, 2H), 2.92 (s, 2H), 2.36 (ddd, *J* = 13.9, 7.4, 4.2 Hz, 1H), 1.96 (ddd, *J* = 14.0, 6.7, 4.1 Hz, 1H). ^{13}C NMR (101 MHz, MeOD) δ 156.2, 147.6, 130.7, 130.0, 128.0, 127.9, 126.8, 121.5, 117.8, 111.7, 69.1, 64.3, 58.5, 49.6, 34.7. HRMS (ESI) calcd for $[M - H]^-$ $C_{15}H_{17}NO_2SBr$ 354.0163, found 354.0164. Spectra available at https://doi.org/10.14469/hpc/5824.

4-(((3-Bromobenzyl)amino)methyl)chroman-4-ol (19). Following general procedure E, amine **19** was obtained from amino alcohol **2** (90 mg, 0.50 mmol) and 3-bromobenzaldehyde (0.06 mL, 0.50 mmol) in 10% yield (18 mg) as a colorless oil. ^{1}H NMR (400 MHz, MeOD) δ 7.52 (s, 1H), 7.44−7.35 (m, 2H), 7.29 (d, *J* = 7.7 Hz, 1H), 7.23 (t, *J* = 7.7 Hz, 1H), 7.16−7.10 (m, 1H), 6.88 (td, *J* = 7.8, 0.9 Hz, 1H), 6.75 (dd, *J* = 8.3, 1.0 Hz, 1H), 4.27−4.11 (m, 2H), 3.80, 3.75 (ABq, *J* = 13.7 Hz, 2H), 2.94−2.82 (m, 2H), 2.36 (ddd, *J* = 14.0, 7.6, 4.1 Hz, 1H), 1.96 (ddd, *J* = 14.0, 6.8, 3.8 Hz, 1H). ^{13}C NMR (101 MHz, MeOD) δ 156.2, 144.0, 132.3, 131.2, 131.1, 130.0, 128.2, 128.0, 127.9, 123.4, 121.5, 117.8, 69.1, 64.3, 58.7, 54.2, 34.8. HRMS (ESI) calcd for $[M - H]^-$ $C_{17}H_{19}NO_2Br$ 348.0599, found 348.0606. Spectra available at https://doi.org/10.14469/hpc/5825.

6-(Allyloxy)chroman-4-one (20). To a suspension of 6-hydroxy-4-chromanone (0.83 g, 5.1 mmol) and K_2CO_3 (1.1 g, 7.6 mmol) in acetone (30 mL), allyl bromide (0.48 mL, 5.1 mmol) was added dropwise, and the reaction was refluxed for 24 h. The resulting mixture was diluted with EtOAc and washed with sat. NH_4Cl (3×). The combined aq layers were extracted with EtOAc (2×). Combined organic phases were washed with brine, dried over $MgSO_4$, and concentrated in vacuo. The crude product was purified by column chromatography (hexane/EtOAc, 9:1) to provide ketone **20** as a colorless oil (880 mg, 85%). ^{1}H NMR (400 MHz, $CDCl_3$) δ 7.23 (d, *J* = 3.2 Hz, 1H), 7.03 (dd, *J* = 9.0, 3.2 Hz, 1H), 6.82 (d, *J* = 9.0 Hz, 1H), 5.97 (ddt, *J* = 17.2, 10.5, 5.3 Hz, 1H), 5.35 (dq, *J* = 17.3, 1.6 Hz, 1H), 5.22 (dq, *J* = 10.5, 1.3 Hz, 1H), 4.45−4.40 (m, 4H), 2.72−2.69 (m, 2H). ^{13}C NMR (101 MHz, $CDCl_3$) δ 191.7, 156.5, 152.8, 132.9, 125.5, 121.0, 119.1, 117.7, 108.6, 69.2, 67.0, 37.6. HRMS (ESI) calcd for $[M + H]^+$ $C_{12}H_{13}O_3$ 205.0859, found 205.0860. Spectra available at https://doi.org/10.14469/hpc/5826.

8-Methoxychroman-4-one (21). Eaton's reagent (15 mL) was added dropwise to a flask containing carboxylic acid **46** (600 mg, 3.10 mmol), and the mixture was stirred at rt overnight. The reaction was quenched with sat. $NaHCO_3$, and the resulting mixture extracted with DCM (3×), dried over $MgSO_4$, filtered, and concentrated in vacuo to provide chromanone **21** as a yellow powder (480 mg, 88% yield). The spectroscopic data correspond with those previously reported.[19] ^{1}H NMR (400 MHz, $CDCl_3$) δ 7.52 (dd, *J* = 8.0, 1.6 Hz, 1H), 7.08 (dd, *J* = 8.0, 1.5 Hz, 1H), 6.98 (t, *J* = 8.0 Hz, 1H), 4.72−4.53 (m, 2H), 3.93 (s, 3H), 2.93−2.75 (m, 2H). ^{13}C NMR (101 MHz, $CDCl_3$) δ 191.8, 152.0, 149.0, 122.1, 120.9, 118.5, 116.8, 77.5, 77.2, 76.8, 67.8, 56.4, 37.8. HRMS (ESI) calculated for $[M + H]^+$ $C_{10}H_{10}O_3$ 179.0708, found 179.0715. Spectra available at https://doi.org/10.14469/hpc/5827.

6-Bromo-4-((trimethylsilyl)oxy)chromane-4-carbonitrile (22). Following general procedure A, cyanohydrin **22** was obtained from 6-bromo-4-chromanone (454 mg, 2 mmol) in 96% yield (626 mg) as an orange oil which was used in the next step without further purification. ^{1}H NMR (400 MHz, MeOD) δ 7.60 (d, *J* = 2.4 Hz, 1H), 7.43 (dd, *J* = 8.8, 2.4 Hz, 1H), 6.80 (d, *J* = 8.8 Hz, 1H), 4.44−4.24 (m, 2H), 2.47 (ddd, *J* = 13.1, 8.7, 4.4 Hz, 1H), 2.38 (ddd, *J* = 13.9, 5.5, 3.4 Hz, 1H), 0.21 (s, 9H). ^{13}C NMR (101 MHz, MeOD) δ 154.3, 135.3, 131.9, 124.5, 121.7, 120.9, 113.3, 66.7, 62.9, 36.9, 1.2. Spectra available at https://doi.org/10.14469/hpc/5828.

6-Fluoro-4-((trimethylsilyl)oxy)chromane-4-carbonitrile (24). Following general procedure A, cyanohydrin **24** was obtained from 6-fluorochroman-4-one (500 mg, 3.00 mmol) in 90% yield (718 mg) as a yellow oil and used in the next step without further purification. ^{1}H NMR (400 MHz, $CDCl_3$) δ 7.24 (dd, *J* = 8.6, 3.1 Hz, 1H), 6.99 (ddd, *J* = 9.1, 7.8, 3.1 Hz, 1H), 6.80 (dd, *J* = 9.1, 4.6 Hz, 1H), 4.38−4.27 (m, 2H), 2.43 (ddd, *J* = 13.6, 8.0, 4.5 Hz, 1H), 2.35 (ddd, *J* = 13.8, 5.7, 3.7 Hz, 1H), 0.23 (s, 9H). Spectra available at https://doi.org/10.14469/hpc/6020.

7-Fluoro-4-((trimethylsilyl)oxy)chromane-4-carbonitrile (25). Following general procedure A, cyanohydrin **25** was obtained from 7-fluorochroman-4-one (390 mg, 2.4 mmol) in 65% yield (405 mg) as a colorless oil. Column chromatography: hexane/DCM, 4:1. ^{1}H NMR (400 MHz, $CDCl_3$) δ 7.52 (dd, *J* = 8.7, 6.2 Hz, 1H), 6.71 (ddd, *J* = 8.7, 8.0, 2.6 Hz, 1H), 6.56 (dd, *J* = 10.0, 2.6 Hz, 1H), 4.40−4.28 (m, 2H), 2.46−2.32 (m, 2H), 0.18 (s, 9H). ^{13}C NMR (101 MHz, $CDCl_3$) δ 164.3 (d, *J* = 249.0 Hz), 155.0 (d, *J* = 12.7 Hz), 130.3 (d, *J* = 10.4 Hz), 120.9, 117.3 (d, *J* = 2.9 Hz), 108.6 (d, *J* = 22.4 Hz), 104.6 (d, *J* = 24.8 Hz), 65.2, 61.8, 36.2, 1.3. Spectra available at https://doi.org/10.14469/hpc/5829.

8-Methoxy-4-((trimethylsilyl)oxy)chromane-4-carbonitrile (26). Following general procedure A, cyanohydrin **26** was obtained

DOI: 10.1021/acs.jmedchem.9b00898
J. Med. Chem. 2020, 63, 2240−2262

from chromanone **21** (460 mg, 2.6 mmol) in 91% yield (652 mg) and was used in the next step without further purification. ^{1}H NMR (400 MHz, $CDCl_3$) δ 7.19 (dd, J = 7.8, 1.6 Hz, 1H), 6.94 (t, J = 7.9 Hz, 1H), 6.89 (dd, J = 8.1, 1.6 Hz, 1H), 4.48 (ddd, J = 11.5, 4.8, 4.0 Hz, 1H), 4.40 (ddd, J = 11.5, 9.8, 3.2 Hz, 1H), 3.88 (s, 3H), 2.48−2.36 (m, 2H), 0.17 (s, 9H). ^{13}C NMR (101 MHz, $CDCl_3$) δ 148.6, 143.4, 121.4, 121.1, 120.5, 120.4, 112.6, 65.5, 61.9, 56.2, 36.3, 1.3. Spectra available at https://doi.org/10.14469/hpc/5830.

2-Phenyl-4-((trimethylsilyl)oxy)chromane-4-carbonitrile (27). Following general procedure A, cyanohydrin **27** was obtained from flavonone (500 mg, 2.23 mmol) in 12% yield (90 mg) as a light yellow oil, which was used in the next step without further purification. ^{1}H NMR (400 MHz, $CDCl_3$) δ 7.58 (dd, J = 7.9, 1.6 Hz, 1H), 7.50−7.38 (m, 5H), 7.29 (ddd, J = 8.3, 7.3, 1.7 Hz, 1H), 7.07−7.03 (m, 1H), 6.92 (dd, J = 8.3, 1.0 Hz, 1H), 5.40 (dd, J = 12.1, 1.7 Hz, 1H), 2.67 (dd, J = 13.4, 1.8 Hz, 1H), 2.49 (dd, J = 13.4, 12.2 Hz, 1H), 0.30 (s, 9H). ^{13}C NMR (101 MHz, $CDCl_3$) δ 153.9, 139.1, 131.1, 129.0, 128.9, 127.6, 126.4, 122.6, 121.8, 121.4, 117.6, 75.9, 67.1, 43.9, 1.5. Spectra available at https://doi.org/10.14469/hpc/5831.

4-(Aminomethyl)-6-bromochroman-4-ol (28). Following general procedure B, amino alcohol **28** was obtained from cyanohydrin **22** (652 mg, 2 mmol) in 23% yield (115 mg) as a colorless oil. Column chromatography: DCM/7 N NH_3 in MeOH, 98:2. ^{1}H NMR (400 MHz, MeOD) δ 7.57 (d, J = 2.5 Hz, 1H), 7.27 (dt, J = 7.1, 3.6 Hz, 1H), 6.72 (t, J = 7.5 Hz, 1H), 4.31−4.17 (m, 2H), 2.94, 2.90 (ABq, J_{AB} = 13.6 Hz, 2H), 2.23 (ddd, J = 14.1, 6.6, 3.6 Hz, 1H), 1.98 (ddd, J = 14.0, 8.1, 4.2 Hz, 1H). ^{13}C NMR (101 MHz, MeOD) δ 155.2, 132.8, 130.7, 130.7, 119.9, 113.3, 69.3, 64.6, 51.5, 33.0. HRMS (ESI) calcd for $[M + H]^+$ $C_{10}H_{13}NO_2Br$ 258.0130, found 258.0134. Spectra available at https://doi.org/10.14469/hpc/5832.

6-(Allyloxy)-4-(aminomethyl)chroman-4-ol (29). Following general procedures A and B, amino alcohol **29** was obtained from ketone **20** (640 mg, 3.0 mmol) in 70% yield over two steps (630 mg). Column chromatography: DCM/7 N NH_3 in MeOH, 10:0 to 9:1. ^{1}H NMR (400 MHz, MeOD) δ 7.00 (d, J = 2.9 Hz, 1H), 6.77 (dd, J = 8.9, 3.0 Hz, 1H), 6.70 (d, J = 8.9 Hz, 1H), 6.04 (ddt, J = 17.2, 10.5, 5.2 Hz, 1H), 5.38 (app dq, J = 17.3, 1.6 Hz, 1H), 5.23 (app dq, J = 10.7, 1.4 Hz, 1H), 4.48 (dt, J = 5.1, 1.4 Hz, 2H), 4.20−4.11 (m, 2H), 2.90 (q, J = 13.6 Hz, 2H), 2.18 (ddd, J = 14.0, 7.0, 4.0 Hz, 1H), 1.94 (ddd, J = 14.0, 7.1, 4.2 Hz, 1H). ^{13}C NMR (101 MHz, MeOD) δ 153.9, 150.3, 135.2, 128.4, 118.5, 117.39, 117.35 113.5, 70.4, 69.6, 64.2, 51.8, 33.8. HRMS (ESI) calcd for $[M + H]^+$ $C_{13}H_{18}NO_3$ 236.1282, found 236.1287. Spectra available at https://doi.org/10.14469/hpc/5833.

4-(Aminomethyl)-6-fluorochroman-4-ol (30). Following general procedure B, amino alcohol **30** was obtained from cyanohydrin **24** (718 mg, 2.70 mmol) in 48% yield (253 mg) as a yellow solid. Column chromatography: DCM/10% NH_4OH in MeOH, 8:2. ^{1}H NMR (400 MHz, MeOD) δ 7.15 (dd, J = 9.6, 3.1 Hz, 1H), 6.90 (ddd, J = 9.0, 8.0, 3.1 Hz, 1H), 6.77 (dd, J = 9.0, 4.8 Hz, 1H), 4.25−4.15 (m, 2H), 2.95 (d, J = 13.5 Hz, 1H), 2.89 (d, J = 13.6 Hz, 1H), 2.21 (ddd, J = 14.1, 6.6, 3.9 Hz, 1H), 1.97 (ddd, J = 14.0, 7.5, 4.4 Hz, 1H). ^{13}C NMR (101 MHz, MeOD) δ 156.9 (d, J = 236.6 Hz), 128.0 (d, J = 6.2 Hz), 117.6 (d, J = 7.8 Hz), 115.3 (d, J = 23.6 Hz), 112.4 (d, J = 23.6 Hz), 67.9, 63.1, 50.1, 31.9. Spectra available at https://doi.org/10.14469/hpc/6021.

4-(Aminomethyl)-7-fluorochroman-4-ol (31). Following general procedure B, amino alcohol **31** was obtained from cyanohydrin **25** (400 mg, 1.5 mmol) in 27% yield (80 mg) as a yellow oil. Column chromatography: DCM/7 N NH_3 in MeOH, 99:1 to 9:1. ^{1}H NMR (400 MHz, $CDCl_3$) δ 7.37 (dd, J = 8.7, 6.6 Hz, 1H), 6.64 (ddd, J = 8.4, 2.6 Hz, 1H), 6.53 (dd, J = 10.2, 2.6 Hz, 1H), 4.31−4.18 (m, 2H), 3.02 (d, J = 13.0 Hz, 1H), 2.92 (d, J = 13.0 Hz, 1H), 2.04 (t, J = 5.6 Hz, 2H). ^{13}C NMR (101 MHz, $CDCl_3$) δ 163.1 (d, J = 245.8 Hz), 156.2 (d, J = 12.2 Hz), 128.2 (d, J = 10.1 Hz), 122.4 (d, J = 2.4 Hz), 108.2 (d, J = 21.8 Hz), 104.0 (d, J = 24.2 Hz), 67.5, 63.9, 50.8, 33.5. HRMS (ESI) calcd for $[M + H]^+$ $C_{10}H_{12}FNO_2$ 198.0930, found 198.0930. Spectra available at https://doi.org/10.14469/hpc/5834.

4-(Aminomethyl)-8-methoxychroman-4-ol (32). Following general procedure B, amino alcohol **32** was obtained from cyanohydrin **26** (600 mg, 2.2 mmol) in 34% yield (154 mg) as a white powder. Column chromatography: DCM/7 N NH_3 in MeOH, 95:5 to 9:1. ^{1}H NMR (400 MHz, $CDCl_3$) δ 7.04 (dd, J = 7.9, 1.5 Hz, 1H), 6.89 (t, J = 8.0 Hz, 1H), 6.80 (dd, J = 8.0, 1.4 Hz, 1H), 4.40−4.27 (m, 2H), 3.87 (s, 3H), 3.07 (d, J = 13.1 Hz, 1H), 2.94 (d, J = 13.1 Hz, 1H), 2.14−2.02 (m, 2H). ^{13}C NMR (101 MHz, $CDCl_3$) δ 148.5, 144.5, 127.0, 120.3, 118.3, 110.7, 67.9, 63.9, 56.1, 50.9, 33.5. HRMS (ESI) calcd for $[M + H]^+$ $C_{11}H_{15}NO_3$ 210.1130, found 210.1126. Spectra available at https://doi.org/10.14469/hpc/5835.

4-(Aminomethyl)-2-phenylchroman-4-ol (33). Following general procedure B, amino alcohol **33** was obtained from cyanohydrin **27** (85 mg, 0.26 mmol) in 61% yield (41 mg) as a white solid after trituration of the crude with diethyl ether. ^{1}H NMR (400 MHz, MeOD) δ 7.49−7.45 (m, 3H), 7.40−7.36 (m, 2H), 7.31 (ddd, J = 7.2, 3.6, 1.3 Hz, 1H), 7.18 (ddd, J = 8.3, 7.4, 1.7 Hz, 1H), 6.95 (td, J = 7.7, 1.1 Hz, 1H), 6.85 (dd, J = 8.2, 1.0 Hz, 1H), 5.15 (dd, J = 12.6, 1.9 Hz, 1H), 3.19 (d, J = 13.5 Hz, 1H), 3.08 (d, J = 13.5 Hz, 1H), 2.40 (dd, J = 13.9, 2.2 Hz, 1H), 2.17 (ddd, J = 13.7, 12.7, 0.8 Hz, 1H), 1.93 (s, 2H, NH_2). ^{13}C NMR (101 MHz, MeOD) δ 154.7, 140.9, 129.8, 129.0, 128.6, 127.0, 126.7, 126.5, 121.3, 117.1, 76.4, 68.9, 50.0, 40.1. HRMS (ESI) calcd for $[M + H]^+$ $C_{16}H_{18}NO_2$ 256.1338, found 256.1339. Spectra available at https://doi.org/10.14469/hpc/5836.

5-Bromo-*N*-((6-bromo-4-hydroxychroman-4-yl)methyl)-thiophene-2-sulfonamide (34). Following general procedure C, sulfonamide **34** was obtained from amino alcohol **28** (26 mg, 0.10 mmol) and 5-bromothiophene-2-sulfonyl chloride (40 mg, 1.5 mmol) in 83% yield (40 mg) as a white solid. Column chromatography: petroleum ether/Et_2O, 1:2. ^{1}H NMR (400 MHz, $CDCl_3$) δ 7.51 (d, J = 2.5 Hz, 1H), 7.37 (d, J = 4.0 Hz, 1H), 7.25 (dd, J = 8.8, 2.5 Hz, 1H), 7.16 (d, J = 4.0 Hz, 1H), 6.69 (d, J = 8.8 Hz, 1H), 4.29−4.15 (m, 2H), 3.31 (ddd, J = 9.4, 8.0, 7.6 Hz, 3H), 3.18 (d, J = 13.4 Hz, 1H), 2.31 (ddd, J = 14.1, 6.0, 3.8 Hz, 1H), 1.96 (ddd, J = 13.4, 8.3, 5.1 Hz, 1H). ^{13}C NMR (101 MHz, $CDCl_3$) δ 155.2, 144.2, 133.1, 132.0, 131.1, 129.6, 120.0, 119.9, 113.4, 68.6, 64.6, 52.7, 33.5. HRMS (ESI) calcd for $[M - H]^-$ $C_{14}H_{12}NO_4SBr_2$ 479.8574, found 479.8586. Spectra available at https://doi.org/10.14469/hpc/5837.

3-Bromo-*N*-((6-bromo-4-hydroxychroman-4-yl)methyl)-benzenesulfonamide (35). Following general procedure C, sulfonamide **35** was obtained from amino alcohol **28** (26 mg, 0.10 mmol) and 3-bromobenzenesulfonyl chloride (31 mg, 0.12 mmol) in 90% yield (43 mg) as a white solid. Column chromatography: petroleum ether/Et_2O, 1:2. ^{1}H NMR (400 MHz, MeOD) δ 7.98 (t, J = 1.8 Hz, 1H), 7.80 (app ddd, J = 7.8, 1.4, 1.0 Hz, 1H), 7.76 (app ddd, J = 8.1, 1.8, 0.9 Hz, 1H), 7.54−7.40 (m, 2H), 7.22 (dd, J = 8.8, 2.5 Hz, 1H), 6.68 (d, J = 8.8 Hz, 1H), 4.25−4.17 (m, 2H), 3.27 (d, J = 13.4 Hz, 1H), 3.11 (d, J = 13.4 Hz, 1H), 2.36−2.28 (m, 1H), 1.99−1.90 (m, 1H). ^{13}C NMR (101 MHz, MeOD) δ 155.2, 144.2, 136.5, 133.1, 132.0, 131.0, 130.6, 129.6, 126.6, 123.8, 119.8, 113.3, 68.7, 64.5, 52.5, 33.4. HRMS (ESI) calcd for $[M - H]^-$ $C_{16}H_{14}NO_4SBr_2$ 473.9010, found 473.9025. Spectra available at https://doi.org/10.14469/hpc/5838.

***N*-((6-(Allyloxy)-4-hydroxychroman-4-yl)methyl)-3-bromobenzenesulfonamide (36).** Following general procedure C, sulfonamide **36** was obtained from amino alcohol **29** (540 mg, 2.3 mmol) and 3-bromobenzenesulfonyl chloride (980 mg, 3.4 mmol) in 53% yield (558 mg). Column chromatography: hexane/EtOAc, 7:3. ^{1}H NMR (400 MHz, DMSO) δ 7.97 (t, J = 1.7 Hz, 1H), 7.88 (br s, 1H, OH), 7.84 (ddd, J = 8.0, 1.8, 0.9 Hz, 1H), 7.80 (ddd, J = 7.8, 1.4, 0.8 Hz, 1H), 7.53 (t, J = 7.9 Hz, 1H), 6.91 (d, J = 3.0 Hz, 1H), 6.75 (dd, J = 8.9, 3.0 Hz, 1H), 6.69 (d, J = 8.9 Hz, 1H), 6.00 (ddt, J = 17.2, 10.5, 5.2 Hz, 1H), 5.39−5.33 (m, 2H, NH, $^1/_2CH_2$=), 5.21 (dq, J = 10.5, 1.6 Hz, 1H), 4.49−4.40 (m, 2H), 4.13−4.06 (m, 2H), 3.13 (d, J = 13.3 Hz, 1H), 2.97 (d, J = 13.2 Hz, 1H), 2.19 (ddd, J = 13.8, 6.4, 3.6 Hz, 1H), 1.82 (ddd, J = 12.1, 7.5, 4.1 Hz, 1H). ^{13}C NMR (101 MHz, DMSO) δ 151.7, 148.2, 142.9, 135.1, 134.1, 131.3, 128.9, 127.3, 125.5, 122.0, 117.0, 116.8, 115.8, 112.9, 68.6, 67.1, 62.6, 51.1, 32.4. HRMS (ESI) calcd for $[M - H]^-$ $C_{19}H_{19}NO_5SBr$ 452.0167, found 454.0161. Spectra available at https://doi.org/10.14469/hpc/5839.

DOI: 10.1021/acs.jmedchem.9b00898
J. Med. Chem. 2020, 63, 2240−2262

3-Bromo-*N*-((4,6-dihydroxychroman-4-yl)methyl)benzenesulfonamide (37). To a solution of compound **36** (530 mg, 1.2 mmol) in MeOH (20 mL), $Pd(PPh_3)_4$ (135 mg, 0.3 mmol) was added and the mixture stirred for 10 min. K_2CO_3 (481 mg, 3.5 mmol) was then added, and the reaction was refluxed for 16 h. The resulting solution was concentrated in vacuo, taken up in DCM, washed with H_2O (3×), extracted with DCM (2×), washed with brine, dried over $MgSO_4$, and concentrated in vacuo. The crude product was purified by column chromatography (hexane/EtOAc, 1:1) to yield phenol **37** as a white solid (356 mg, 75%). ^{1}H NMR (400 MHz, DMSO) δ 8.84 (s, 1H, OH), 7.98 (t, J = 1.8 Hz, 1H), 7.87−7.82 (m, 2H, OH, CH), 7.80 (ddd, J = 7.8, 1.4, 0.9 Hz, 1H), 7.53 (t, J = 7.9 Hz, 1H), 6.71 (t, J = 1.5 Hz, 1H), 6.55 (d, J = 1.5 Hz, 2H), 5.33 (s, 1H, NH), 4.10−4.00 (m, 2H), 3.04 (dd, J = 13.1, 7.5 Hz, 1H), 2.88 (dd, J = 13.1, 4.9 Hz, 1H), 2.16 (ddd, J = 13.7, 6.5, 3.2 Hz, 1H), 1.81 (ddd, J = 13.3, 8.2, 3.8 Hz, 1H). ^{13}C NMR (DMSO-d_6) δ 150.6, 146.9, 142.8, 135.2, 131.4, 129.0, 127.4, 125.6, 122.1, 116.8, 116.0, 113.1, 67.1, 62.7, 51.3, 32.5. HRMS (ESI) calcd for $[M - H]^-$ $C_{16}H_{15}NO_5SBr$ 411.9854, found 411.9860. Spectra available at https://doi.org/10.14469/hpc/5840.

5-Bromo-*N*-((6-fluoro-4-hydroxychroman-4-yl)methyl)-thiophene-2-sulfonamide (38). Following general procedure C, sulfonamide **38** was obtained from amino alcohol **30** (48 mg, 0.24 mmol) and 5-bromothiophene-2-sulfonyl chloride (78 mg, 0.30 mmol) in 28% yield (29 mg) as a white solid. Reverse phase column chromatography: ACN/H_2O, 5:95. ^{1}H NMR (400 MHz, $CDCl_3$) δ 7.35 (d, J = 4.0 Hz, 1H), 7.08 (d, J = 4.0 Hz, 1H), 7.05 (dd, J = 9.0, 3.0 Hz, 1H), 6.92 (ddd, J = 9.0, 7.8, 3.1 Hz, 1H), 6.79 (dd, J = 9.0, 4.7 Hz, 1H), 4.97 (br s, 1H, NH), 4.25−4.14 (m, 2H), 3.29 (dd, J = 30.8, 13.0 Hz, 2H), 2.40 (ddd, J = 14.1, 5.9, 3.1 Hz, 1H), 2.03−1.96 (m, 2H). ^{13}C NMR (101 MHz, $CDCl_3$) δ 157.0 (d, J = 239.5 Hz), 150.7, 141.5, 132.4, 130.6, 126.0 (d, J = 6.1 Hz), 120.3, 118.6 (d, J = 7.8 Hz), 117.3 (d, J = 23.2 Hz), 112.6 (d, J = 23.6 Hz), 68.6, 63.6, 51.6, 32.8. HRMS (ESI) calcd for $[M - OH + H]^+$ $C_{14}H_{12}BrFNO_3S_2$ 403.9426, found 403.9420. Spectra available at https://doi.org/10.14469/hpc/6022.

3-Bromo-*N*-((6-fluoro-4-hydroxychroman-4-yl)methyl)-benzenesulfonamide (39). Following general procedure C, sulfonamide **39** was obtained from amino alcohol **30** (49 mg, 0.25 mmol) and 3-bromobenzenesulfonyl chloride (76 mg, 0.30 mmol) in 35% yield (37 mg) as a pale-yellow solid. Reverse phase column chromatography: ACN/H_2O, 5:95. ^{1}H NMR (400 MHz, $CDCl_3$) δ 7.99 (t, J = 1.8 Hz, 1H), 7.77 (ddd, J = 7.9, 1.7, 1.0 Hz, 1H), 7.73 (ddd, J = 8.0, 1.9, 1.0 Hz, 1H), 7.41 (t, J = 7.9 Hz, 1H), 7.01 (dd, J = 9.0, 3.0 Hz, 1H), 6.91 (ddd, J = 9.0, 7.8, 3.1 Hz, 1H), 6.78 (dd, J = 9.0, 4.7 Hz, 1H), 4.99 (s, 1H), 4.32−4.14 (m, 2H), 3.32 (dd, J = 13.2, 6.8 Hz, 1H), 3.19 (d, J = 13.9 Hz, 1H), 2.43 (ddd, J = 14.0, 5.8, 3.1 Hz, 1H), 2.19−1.88 (m, 2H). ^{13}C NMR (101 MHz, $CDCl_3$) δ 157.0 (d, J = 239.3 Hz), 155.8, 150.6, 141.7, 136.1, 131.0, 129.9, 126.0 (d, J = 6.4 Hz), 125.5, 123.4, 118.5 (d, J = 7.8 Hz), 117.1 (d, J = 23.3 Hz), 112.6 (d, J = 23.5 Hz), 68.7, 63.6, 51.4, 32.6. HRMS (ESI) calcd for $[M - OH + H]^+$ $C_{16}H_{14}BrFNO_3S$ 397.9862, found 397.9859. Spectra available at https://doi.org/10.14469/hpc/6023.

5-Bromo-*N*-((7-fluoro-4-hydroxychroman-4-yl)methyl)-thiophene-2-sulfonamide (40). Following general procedure C, sulfonamide **40** was obtained from amino alcohol **31** (35 mg, 0.2 mmol) and 5-bromothiophene-2-sulfonyl chloride (52 mg, 0.2 mmol) in 53% yield (40 mg) as a yellow powder. Column chromatography: pentane/EtOAc, 2:1. ^{1}H NMR (400 MHz, $CDCl_3$) δ 7.34 (d, J = 4.0 Hz, 1H), 7.31 (dd, J = 8.8, 6.4 Hz, 1H), 7.07 (d, J = 4.0 Hz, 1H), 6.63 (ddd, J = 8.6, 8.1, 2.6 Hz, 1H), 6.54 (dd, J = 10.1, 2.6 Hz, 1H), 5.12 (t, J = 6.5 Hz, 1H, NH), 4.30−4.18 (m, 2H), 3.38−3.25 (m, 2H), 2.37 (ddd, J = 14.1, 6.3, 3.4 Hz, 1H), 2.09−1.97 (m, 2H, OH, $^1/_2CH_2$). ^{13}C NMR (101 MHz, $CDCl_3$) δ 163.6 (d, J = 247.4 Hz), 156.1 (d, J = 12.4 Hz), 141.7, 132.4, 130.6, 127.9 (d, J = 10.1 Hz), 121.2 (d, J = 2.7 Hz), 120.3, 108.6 (d, J = 22.1 Hz), 104.5 (d, J = 24.3 Hz), 68.2, 63.9, 51.7, 33.0. ^{19}F NMR (377 MHz, $CDCl_3$) δ −110.8 (dd, J = 16.3, 7.9 Hz). HRMS (ESI) calcd for $[M - H]^-$ $C_{14}H_{13}BrFNO_4S_2$ 419.9375, found 419.9368. Spectra available at https://doi.org/10.14469/hpc/5841.

3-Bromo-*N*-((7-fluoro-4-hydroxychroman-4-yl)methyl)-benzenesulfonamide (41). Following general procedure C, sulfonamide **41** was obtained from amino alcohol **31** (35 mg, 0.2 mmol) and 3-bromobenzenesulfonyl chloride (51 mg, 0.2 mmol) in 53% yield (40 mg) as a white powder. Column chromatography: pentane/EtOAc, 2:1. ^{1}H NMR (400 MHz, $CDCl_3$) δ 7.98 (t, J = 1.8 Hz, 1H), 7.76 (ddd, J = 7.8, 1.6, 1.0 Hz, 1H), 7.72 (ddd, J = 8.0, 1.9, 1.0 Hz, 1H), 7.40 (t, J = 7.9 Hz, 1H), 7.28 (dd, J = 8.6, 6.3 Hz, 1H), 6.61 (ddd, J = 8.7, 8.0, 2.6 Hz, 1H), 6.53 (dd, J = 10.1, 2.6 Hz, 1H), 5.10 (dd, J = 8.2, 4.7 Hz, 1H, NH), 4.32−4.17 (m, 2H), 3.32−3.21 (m, 2H), 2.37 (ddd, J = 14.1, 6.2, 3.3 Hz, 1H), 2.14 (br s, 1H, OH), 2.06−1.95 (m, 1H). ^{13}C NMR (101 MHz, $CDCl_3$) δ 163.6 (d, J = 247.8 Hz), 156.1 (d, J = 12.4 Hz), 142.0, 136.1, 130.9, 130.0, 127.9 (d, J = 10.1 Hz), 125.6, 123.4, 121.2 (d, J = 3.0 Hz), 108.5 (d, J = 22.2 Hz), 104.4 (d, J = 24.5 Hz), 68.3, 63.9, 51.5, 32.9. ^{19}F NMR (377 MHz, $CDCl_3$) δ −110.93 (dd, J = 16.3, 7.9 Hz). HRMS (ESI) calcd for $[M - H]^-$ $C_{16}H_{15}BrFNO_4S$ 413.9811, found 413.9820. Spectra available at https://doi.org/10.14469/hpc/5842.

Chiral resolution was performed on a Chiralpack IE-3 column using an isocratic gradient of hexane/isopropanol, 7:3 to yield (−)-**41** and (+)-**41**.

(+)-**41**: $[\alpha]_D^{20}$ = +74° (c = 0.49, $CDCl_3$).

(−)-**41**: $[\alpha]_D^{20}$ = −82° (c = 0.41, $CDCl_3$).

5-Bromo-*N*-((4-hydroxy-8-methoxychroman-4-yl)methyl)-thiophene-2-sulfonamide (42). Following general procedure C, sulfonamide **42** was obtained from amino alcohol **32** (60 mg, 0.3 mmol) and 5-bromothiophene-2-sulfonyl chloride (84 mg, 0.3 mmol) in 67% yield (86 mg) as a yellow powder. Column chromatography: hexane/EtOAc, 1:1. ^{1}H NMR (400 MHz, $CDCl_3$) δ 7.34 (d, J = 4.0 Hz, 1H), 7.06 (d, J = 4.0 Hz, 1H), 6.95 (dd, J = 7.8, 1.7 Hz, 1H), 6.89 (t, J = 7.9 Hz, 1H), 6.83 (dd, J = 7.9, 1.7 Hz, 1H), 4.93 (dd, J = 7.2, 5.8 Hz, 1H, NH), 4.41−4.26 (m, 2H), 3.87 (s, 3H), 3.43−3.30 (m, 2H), 2.39 (ddd, J = 14.1, 6.6, 3.8 Hz, 1H), 2.10−1.98 (m, 2H, OH, $^1/_2CH_2$). ^{13}C NMR (101 MHz, chloroform-d) δ 148.6, 144.4, 141.6, 132.4, 130.6, 125.5, 120.7, 120.2, 117.7, 111.5, 68.3, 63.8, 56.1, 51.7, 32.9. HRMS (ESI) calcd for $[M - H]^-$ $C_{15}H_{16}BrNO_5S_2$ 431.9575, found 431.9583. Spectra available at https://doi.org/10.14469/hpc/5843.

3-Bromo-*N*-((4-hydroxy-8-methoxychroman-4-yl)methyl)-benzenesulfonamide (43). Following general procedure C, sulfonamide **43** was obtained from amino alcohol **32** (60 mg, 0.3 mmol) and 3-bromobenzenesulfonyl chloride (82 mg, 0.3 mmol) in 69% yield (86 mg) as a white powder. Column chromatography: hexane/EtOAc, 1:2. ^{1}H NMR (400 MHz, $CDCl_3$) δ 7.99 (t, J = 1.8 Hz, 1H), 7.77 (ddd, J = 7.8, 1.7, 1.0 Hz, 1H), 7.71 (ddd, J = 8.0, 1.9, 1.0 Hz, 1H), 7.40 (t, J = 7.9 Hz, 1H), 6.91 (dd, J = 7.8, 2.0 Hz, 1H), 6.87 (t, J = 7.8 Hz, 1H), 6.82 (dd, J = 7.7, 1.9 Hz, 1H), 4.85 (dd, J = 7.2, 5.5 Hz, 1H, NH), 4.44−4.23 (m, 2H), 3.87 (s, 3H), 3.39−3.19 (m, 2H), 2.39 (ddd, J = 14.1, 6.6, 3.7 Hz, 1H), 2.04 (ddd, J = 14.0, 7.8, 4.3 Hz, 1H), 1.98 (s, 1H, OH). ^{13}C NMR (101 MHz, chloroform-d) δ 148.6, 144.4, 141.9, 136.0, 130.9, 130.0, 125.62, 125.56, 123.3, 120.7, 117.7, 111.5, 68.4, 63.8, 56.1, 51.5, 32.9. HRMS (ESI) calcd for $[M - H]^-$ $C_{17}H_{18}BrNO_5S$ 426.0011, found 426.0011. Spectra available at https://doi.org/10.14469/hpc/5844.

5-Bromo-*N*-((4-hydroxy-2-phenylchroman-4-yl)methyl)-thiophene-2-sulfonamide (44). Following general procedure C, sulfonamide **44** was obtained from amino alcohol **33** (18 mg, 0.07 mmol) and 5-bromothiophene-2-sulfonyl chloride (20 mg, 0.08 mmol) in 28% yield (9.6 mg) as an off-white solid. Column chromatography: DCM/1% NH_4OH in MeOH, 98:2. ^{1}H NMR (400 MHz, $CDCl_3$) δ 7.52−7.48 (m, 2H), 7.44−7.40 (m, 3H), 7.37−7.33 (m, 2H), 7.27−7.23 (m, 1H), 7.05 (d, J = 4.0 Hz, 1H), 6.97 (td, J = 7.5, 1.1 Hz, 1H), 6.93 (dd, J = 8.3, 1.0 Hz, 1H), 5.23 (dd, J = 12.2, 1.8 Hz, 1H), 5.19 (br s, 1H, NH), 3.58 (d, J = 13.4 Hz, 1H), 3.30 (dd, J = 13.4, 1.6 Hz, 1H), 2.81 (dd, J = 13.7, 2.1 Hz, 1H), 2.02 (ddd, J = 13.8, 12.4, 1.7 Hz, 1H), 1.87 (br s, 1H, OH). ^{13}C NMR (101 MHz, $CDCl_3$) δ 154.6, 142.0, 140.3, 132.3, 130.6, 130.3, 128.8, 128.4, 126.5, 126.1, 125.6, 121.2, 120.1, 117.4, 76.3, 70.3, 51.8, 40.3. HRMS (ESI) calcd for $[M - H]^-$ $C_{20}H_{17}NO_4S_2Br$ 477.9782, found 477.9777. Spectra available at https://doi.org/10.14469/hpc/5847.

DOI: 10.1021/acs.jmedchem.9b00898
J. Med. Chem. 2020, 63, 2240−2262

3-Bromo-*N*-((4-hydroxy-2-phenylchroman-4-yl)methyl)-benzenesulfonamide (45). Following general procedure C, sulfonamide **45** was obtained from amino alcohol **33** (15 mg, 0.060 mmol) and 3-bromobenzenesulfonyl chloride (16 mg, 0.064 mmol) in 12% yield (3.3 mg) as a pale yellow solid. Column chromatography: DCM/1% NH_4OH in MeOH, 98:2. ^1H NMR (400 MHz, $CDCl_3$) δ 8.02 (t, J = 1.8 Hz, 1H), 7.79 (ddd, J = 7.8, 1.7, 1.0 Hz, 1H), 7.70 (ddd, J = 8.0, 1.9, 1.0 Hz, 1H), 7.52−7.49 (m, 2H), 7.44−7.31 (m, 5H), 7.26−7.21 (m, 1H), 6.98−6.92 (m, 2H), 5.25 (dd, J = 12.2, 1.7 Hz, 1H), 5.12 (br s, 1H, NH), 3.59−3.54 (m, 1H), 3.22 (d, J = 12.7 Hz, 1H), 2.84 (dd, J = 13.7, 2.1 Hz, 1H), 2.01 (ddd, J = 13.9, 12.5, 1.7 Hz, 1H), 1.85 (br s, 1H, OH). ^{13}C NMR (101 MHz, $CDCl_3$) δ 154.6, 142.3, 140.4, 136.0, 130.9, 130.3, 129.9, 128.8, 128.3, 126.5, 126.1, 125.6, 125.5, 123.4, 121.2, 117.4, 76.3, 70.4, 51.6, 40.3. HRMS (ESI) calcd for $[M - H]^-$ $C_{22}H_{19}NO_4SBr$ 472.0218, found 472.0224. Spectra available at https://doi.org/10.14469/hpc/5846.

3-(2-Methoxyphenoxy)propanoic Acid (46).[19] A solution of 2-methoxyphenol (2.7 mL, 24 mmol) in DMF (10 mL) was added dropwise to a suspension of NaH (60% suspension in mineral oil, 2.9 g, 72 mmol) in DMF (20 mL). After stirring for 1.5 h, a solution of 3-bromopropionic acid (3.7 g, 24 mmol) in anhydrous DMF (10 mL) was added dropwise, and the solution was stirred at rt overnight. The reaction was quenched with MeOH, acidified with 1 M HCl (pH ∼ 3), and extracted with EtOAc (3×). The combined organic phases were washed with 5% LiCl (2×) and brine, dried over $MgSO_4$, and concentrated in vacuo. The crude was redissolved in EtOAc and extracted with sat. $NaHCO_3$. The aqueous layer was acidified with 1 M HCl (pH 1), and the resulting precipitate was collected by filtration, washed with H_2O, and dried to provide acid **46** as a white solid (824 mg, 17% yield), which was used in the next step without further purification. The spectroscopic data correspond with those previously reported.[19] ^1H NMR (400 MHz $CDCl_3$) δ 6.99−6.89 (m, 4H), 4.31 (t, J = 6.5 Hz, 2H), 3.85 (s, 3H), 2.91 (t, J = 6.5 Hz, 2H). ^{13}C NMR (101 MHz, $CDCl_3$) δ 176.1, 150.0, 148.0, 122.3, 121.2, 114.8, 112.4, 64.8, 56.2, 34.5. HRMS (ESI) calcd for $[M + H]^+$ $C_{10}H_{12}O_4$ 196.0736, found 196.0740. Spectra available at https://doi.org/10.14469/hpc/5855.

1-(2-(2-Bromoethoxy)phenyl)ethanone (47). To a stirred suspension of 1-(2-hydroxyphenyl)ethanone (0.5 mL, 4.2 mmol) and K_2CO_3 (1.16 g, 8.40 mmol) in ACN, 1,2-dibromoethane (4.0 mL, 41.6 mmol) was added and the mixture heated at reflux overnight. Water was added and the mixture extracted with EtOAc, dried over $MgSO_4$, filtered, and evaporated under reduced pressure. The crude was purified by flash chromatography (pentane/EtOAc, 100:0 to 95:5) to provide ketone **47** as a pale yellow solid (350 mg, 34% yield). The spectroscopic data correspond with those previously reported.[30] ^1H NMR (400 MHz, $CDCl_3$) δ 7.76 (dd, J = 7.7, 1.8 Hz, 1H), 7.46 (ddd, J = 8.4, 7.4, 1.8 Hz, 1H), 7.04 (td, J = 7.7, 0.9 Hz, 1H), 6.91 (d, J = 8.3 Hz, 1H), 4.41 (t app, J = 5.8 Hz, 2H), 3.72 (t app, J = 5.8 Hz, 2H), 2.69 (s, 3H). ^{13}C NMR (101 MHz, $CDCl_3$) δ 199.8, 157.4, 133.7, 130.8, 128.8, 121.7, 112.4, 68.4, 32.4, 29.0. HRMS (ESI) calcd for $[M - H]^-$ $C_{10}H_{12}O_2Br$ 243.0021, found 243.0031. Spectra available at https://doi.org/10.14469/hpc/5856.

3,4-Dihydrobenzo[b]oxepin-5(2*H*)-one (48). A solution of ketone **47** (350 mg, 1.43 mmol) in the minimum amount of anhydrous THF was added dropwise to a suspension of NaH (60% in mineral oil, 115 mg, 2.87 mmol) in dry THF (3.6 mL) at 0 °C, and the resulting mixture was allowed to stir at rt overnight. The mixture was cooled down to 0 °C, and water was carefully added until no reaction was observed. The mixture was diluted with water, neutralized with 2 N HCl (aq), extracted with EtOAc (2×), dried over $MgSO_4$, filtered, and evaporated under reduced pressure. The crude was purified by flash chromatography (pentane/EtOAc, 95:5 to 85:15) to provide ketone **48** as a colorless oil (179 mg, 77% yield). The spectroscopic data correspond with those previously reported.[31] ^1H NMR (400 MHz, $CDCl_3$) δ 7.77 (dd, J = 7.8, 1.5 Hz, 1H), 7.45−7.41 (m, 1H), 7.12−7.06 (m, 2H), 4.24 (t, J = 6.6 Hz, 2H), 2.90 (t, J = 6.9 Hz, 2H), 2.22 (p, J = 6.7 Hz, 2H). ^{13}C NMR (101 MHz, $CDCl_3$) δ 200.9, 162.2, 133.9, 129.7, 129.3, 123.0, 121.0, 73.0, 40.8, 26.6. HRMS (ESI) calcd for $[M + H]^+$ $C_{10}H_{11}O_2$ 163.0759, found 163.0751. Spectra available at https://doi.org/10.14469/hpc/5857.

5-((Trimethylsilyl)oxy)-2,3,4,5-tetrahydrobenzo[*b*]oxepine-5-carbonitrile (49). Following general procedure A, cyanohydrin **49** was obtained from ketone **48** (150 mg, 0.92 mmol) in 97% yield (145 mg) as a white solid. Column chromatography: pentane to pentane/EtOAc, 98:2. ^1H NMR (400 MHz, $CDCl_3$) δ 7.62 (dd, J = 7.8, 1.7 Hz, 1H), 7.29 (td, J = 7.6, 1.6 Hz, 1H), 7.14 (td, J = 7.6, 1.3 Hz, 1H), 7.04 (dd, J = 7.9, 1.2 Hz, 1H), 4.19 (ddd, J = 9.7, 5.4, 3.6 Hz, 1H), 3.85 (ddd, J = 11.8, 8.7, 2.7 Hz, 1H), 2.32−2.12 (m, 4H), 0.22 (s, 9H). ^{13}C NMR (101 MHz, CDCl3) δ 158.2, 133.2, 130.6, 127.4, 124.0, 122.9, 120.5, 73.7, 72.6, 40.2, 26.9, 1.2. HRMS (ESI) calcd for $[M + ACN + Na]^+$ $C_{16}H_{22}N_2O_2SiNa$ 325.1348, found 325.1340. Spectra available at https://doi.org/10.14469/hpc/5858.

5-(Aminomethyl)-2,3,4,5-tetrahydrobenzo[*b*]oxepin-5-ol (50). Following general procedure B, amino alcohol **50** was obtained from cyanohydrin **49** (200 mg, 0.76 mmol) in 35% yield (52 mg). Column chromatography: 0−10% of EtOAc/EtOH 3:1 in pentane. ^1H NMR (400 MHz, $CDCl_3$) δ 7.63 (dd, J = 7.7, 1.8 Hz, 1H), 7.18 (td, J = 7.6, 1.8 Hz, 1H), 7.10 (td, J = 7.5, 1.4 Hz, 1H), 6.97 (dd, J = 7.8, 1.4 Hz, 1H), 4.38 (dtd, J = 12.0, 3.7, 1.3 Hz, 1H), 3.58 (td, J = 11.9, 1.9 Hz, 1H), 3.38 (d, J = 12.2 Hz, 1H), 2.85 (d, J = 12.2 Hz, 1H), 2.22−2.10 (m, 1H), 2.09−2.03 (m, 1H), 1.95 (dd, J = 13.4, 3.7 Hz, 1H), 1.82−1.75 (m, 1H). ^{13}C NMR (101 MHz, $CDCl_3$/MeOD, 9:1) δ 157.0, 137.6, 128.6, 127.4, 123.9, 122.1, 75.6, 73.0, 47.7, 37.1, 26.5. HRMS (ESI) calcd for $[M + H]^+$ $C_{11}H_{16}NO_2$ 194.1181, found 194.1185. Spectra available at https://doi.org/10.14469/hpc/5859.

5-Bromo-*N*-((5-hydroxy-2,3,4,5-tetrahydrobenzo[b]oxepin-5-yl)methyl)thiophene-2-sulfonamide (51). Following general procedure C, sulfonamide **51** was obtained from amino alcohol **50** (25 mg, 0.13 mmol) and 5-bromothiophene-2-sulfonyl chloride (37 mg, 0.14 mmol) in 63% yield (34 mg) as a yellow solid. Column chromatography: 15−30% EtOAc/EtOH 3:1 in pentane. ^1H NMR (400 MHz, $CDCl_3$) δ 7.52 (dd, J = 7.8, 1.7 Hz, 1H), 7.25 (d, J = 4.0 Hz, 1H), 7.22 (td, J = 7.6, 1.7 Hz, 1H), 7.11 (td, J = 7.6, 1.3 Hz, 1H), 6.99 (d, J = 4.0 Hz, 1H), 6.95 (dd, J = 7.9, 1.2 Hz, 1H), 5.00 (dd, J = 7.7, 4.8 Hz, 1H, NH), 4.31 (ddd, J = 11.3, 3.8, 2.7 Hz, 1H), 3.67−3.60 (m, 2H), 3.31 (dd, J = 12.5, 4.7 Hz, 1H), 2.65 (s, 1H, OH), 2.27−2.15 (m, 2H), 1.89−1.81 (m, 2H). ^{13}C NMR (101 MHz, $CDCl_3$) δ 157.3, 141.2, 136.7, 132.5, 130.5, 129.4, 126.8, 124.5, 122.6, 120.2, 75.8, 73.1, 49.5, 37.0, 26.5. HRMS (ESI) calcd for $[M - H]^-$ $C_{15}H_{15}BrNO_4S_2$ 415.9626, found 415.9634. Spectra available at https://doi.org/10.14469/hpc/5860.

3-Bromo-*N*-((5-hydroxy-2,3,4,5-tetrahydrobenzo[*b*]oxepin-5-yl)methyl)benzene-sulfonamide (52). Following general procedure C, sulfonamide **52** was obtained from amino alcohol **50** (25 mg, 0.13 mmol) and 3-bromobenzenesulfonyl chloride (36 mg, 0.14 mmol) in 38% yield (20 mg) as a white solid. Column chromatography: 15−30% EtOAc/EtOH 3:1 in pentane. ^1H NMR (400 MHz, $CDCl_3$) δ 7.91 (t, J = 1.8 Hz, 1H), 7.69 (ddd, J = 7.9, 1.5, 1.0 Hz, 1H), 7.66 (ddd, J = 8.0, 1.8, 1.0 Hz, 1H), 7.51 (dd, J = 7.8, 1.7 Hz, 1H), 7.33 (t, J = 7.9 Hz, 1H), 7.20 (td, J = 7.6, 1.7 Hz, 1H), 7.10 (td, J = 7.6, 1.3 Hz, 1H), 6.94 (dd, J = 7.8, 1.2 Hz, 1H), 4.85 (dd, J = 8.1, 4.7 Hz, 1H, NH), 4.33−4.29 (m, 1H), 3.66−3.58 (m, 2H), 3.23 (dd, J = 12.6, 4.7 Hz, 1H), 2.61 (s, 1H, OH), 2.25−2.16 (m, 2H), 1.88−1.81 (m, 2H). ^{13}C NMR (101 MHz, $CDCl_3$) δ 157.2, 141.5, 136.7, 135.9, 130.8, 130.0, 129.5 126.8, 125.7, 124.4, 123.3, 122.6, 75.9, 73.1, 49.3, 37.0, 26.5. HRMS (ESI) calcd for $[M - H]^-$ $C_{17}H_{17}BrNO_4S$ 410.0062, found 410.0055. Spectra available at https://doi.org/10.14469/hpc/5861.

3-(Aminomethyl)-2,3-dihydrobenzofuran-3-ol (53). To a flask containing benzofuran-3(2*H*)-one (500 mg, 3.73 mmol) and potassium phthalimide (17 mg, 0.09 mmol), trimethylsylil cyanide (0.60 mL, 4.47 mmol) was added, and the resulting mixture was stirred at rt overnight. Water was then added, and the mixture was extracted with EtOAc (2×), dried over $MgSO_4$, filtered, and evaporated under reduced pressure to yield the intermediate cyanohydrin, which due to stability issues was directly submitted to general procedure B to provide amino alcohol **53** in 35% yield over two steps (202 mg). ^1H NMR (400 MHz, $CDCl_3$) δ 7.32 (dd, J = 7.5,

DOI: 10.1021/acs.jmedchem.9b00898
J. Med. Chem. 2020, 63, 2240−2262

0.8 Hz, 1H), 7.27−7.23 (m, 1H), 6.94 (td, J = 7.4, 0.7 Hz, 1H), 6.86 (d, J = 8.1 Hz, 1H), 4.43 (s, 2H), 3.13 (d, J = 12.9 Hz, 1H), 3.04 (d, J = 12.9 Hz, 1H). ^{13}C NMR (101 MHz, $CDCl_3$) δ 160.5, 130.6, 129.8, 123.7, 121.1, 110.8, 81.2, 80.3, 49.3. HRMS (ESI) calcd for $[M + H]^+$ $C_9H_{12}NO_2$ 166.0868, found 166.0866. Spectra available at https://doi.org/10.14469/hpc/5862.

5-Bromo-*N*-((3-hydroxy-2,3-dihydrobenzofuran-3-yl)-methyl)thiophene-2-sulfonamide (54). Following general procedure C, sulfonamide **54** was obtained from amino alcohol **53** (50 mg, 0.30 mmol) and 5-bromothiophene-2-sulfonyl chloride (86 mg, 0.33 mmol) in 50% yield (60 mg) as a yellow solid. Column chromatography: 5−10% EtOAc/EtOH 3:1 in pentane. ^{1}H NMR (400 MHz, $CDCl_3$) δ 7.37 (d, J = 4.0 Hz, 1H), 7.32−7.28 (m, 2H), 7.09 (d, J = 4.0 Hz, 1H), 6.95 (td, J = 7.5, 0.8 Hz, 1H), 6.88 (dd, J = 8.7, 0.9 Hz, 1H), 5.02 (t, J = 6.0 Hz, 1H, NH), 4.57 (d, J = 10.7 Hz, 1H), 4.42 (d, J = 10.6 Hz, 1H), 3.47 (dd, J = 12.6, 5.1 Hz, 1H), 3.37 (dd, J = 12.7, 7.2 Hz, 1H), 2.31 (s, 1H, OH). ^{13}C NMR (101 MHz, $CDCl_3$) δ 160.5, 141.2, 132.7, 131.6, 130.7, 127.8, 123.8, 121.4, 120.5, 111.2, 81.1, 79.7, 50.1. HRMS (ESI) calcd for $[M - H]^-$ $C_{13}H_{11}BrNO_4S_2$ 387.9313, found 387.9320. Spectra available at https://doi.org/10.14469/hpc/5863.

3-Bromo-*N*-((3-hydroxy-2,3-dihydrobenzofuran-3-yl)-methyl)benzenesulfonamide (55). Following general procedure C, sulfonamide **55** was obtained from amino alcohol **53** (50 mg, 0.30 mmol) and 3-bromobenzenesulfonyl chloride (84 mg, 0.33 mmol) in 52% yield (60 mg) as a white solid. Column chromatography: 5−10% EtOAc/EtOH 3:1 in pentane. ^{1}H NMR (400 MHz, $CDCl_3$) δ 8.00 (t, J = 1.8 Hz, 1H), 7.78 (ddd, J = 7.9, 1.5, 0.9 Hz, 1H), 7.73 (ddd, J = 8.0, 1.7, 0.9 Hz, 1H), 7.42 (t, J = 7.9 Hz, 1H), 7.31−7.27 (m, 2H), 6.93 (td, J = 7.6, 0.6 Hz, 1H), 6.87 (d, J = 8.4 Hz, 1H), 5.00 (br s, 1H, NH), 4.55 (d, J = 10.7 Hz, 1H), 4.40 (d, J = 10.7 Hz, 1H), 3.39 (dd, J = 12.5, 3.5 Hz, 1H), 3.31 (dd, J = 12.5, 6.4 Hz, 1H), 2.36 (s, 1H, OH). ^{13}C NMR (101 MHz, $CDCl_3$) δ 160.5, 141.5, 136.2, 131.6, 130.9, 130.1, 127.9, 125.7, 123.8, 123.4, 121.4, 111.2, 81.1, 79.8, 50.0. HRMS (ESI) calcd for $[M - H]^-$ $C_{15}H_{13}BrNO_4S$ 381.9749, found 381.9753. Spectra available at https://doi.org/10.14469/hpc/5864.

1-((Trimethylsilyl)oxy)-1,2,3,4-tetrahydronaphthalene-1-carbonitrile (56). Following general procedure A, cyanohydrin **56** was obtained from 3,4-dihydronaphthalen-1(2*H*)-one (200 mg, 1.37 mmol) in quantitative yield (335 mg) and was used in the next step without further purification. ^{1}H NMR (400 MHz, $CDCl_3$) δ 7.67−7.63 (m, 1H), 7.29−7.24 (m, 2H), 7.13−7.10 (m, 1H), 2.89−2.77 (m, 2H), 2.34 (ddd, J = 12.9, 8.3, 3.3 Hz, 1H), 2.20 (ddd, J = 12.5, 9.2, 3.3 Hz, 1H), 2.11−1.92 (m, 2H), 0.21 (s, 9H). Spectra available at https://doi.org/10.14469/hpc/5865.

4-((Trimethylsilyl)oxy)thiochromane-4-carbonitrile (57). Following general procedure A, cyanohydrin **57** was obtained from thiochroman-4-one (200 mg, 1.22 mmol) in 45% yield (145 mg) as a pale-yellow oil, which and was used in the next step without further purification. ^{1}H NMR (400 MHz, $CDCl_3$) δ 7.71 (dd, J = 8.1, 1.4 Hz, 1H), 7.25−7.21 (m, 1H), 7.15−7.11 (m, 2H), 3.32 (ddd, J = 12.8, 11.3, 3.3 Hz, 1H), 3.02 (ddd, J = 12.8, 6.1, 3.6 Hz, 1H), 2.64 (ddd, J = 13.4, 6.1, 3.3 Hz, 1H), 2.36 (ddd, J = 13.5, 11.3, 3.6 Hz, 1H), 0.11 (s, 9H). ^{13}C NMR (101 MHz, $CDCl_3$) δ 133.3, 130.8, 130.0, 129.4, 127.1, 124.4, 121.2, 68.9, 36.0, 21.1, 1.1. Spectra available at https://doi.org/10.14469/hpc/5866.

1-(Aminomethyl)-1,2,3,4-tetrahydronaphthalen-1-ol (58). Following general procedure B, amino alcohol **58** was obtained from cyanohydrin **56** (300 mg, 1.2 mmol) in 91% yield (195 mg) as a colorless oil. Column chromatography: DCM/1% NH_4OH in MeOH, 10:0 to 9:1. ^{1}H NMR (400 MHz, $CDCl_3$) δ 7.52−7.50 (m, 1H), 7.22−7.16 (m, 2H), 7.09−7.07 (m, 1H), 2.98, 2.97 (ABq, J = 13.4 Hz, 2H), 2.87−2.72 (m, 5H, OH, NH_2, CH_2), 2.08−2.03 (m, 1H), 1.93−1.72 (m, 3H). ^{13}C NMR (101 MHz, $CDCl_3$) δ 139.6, 137.3, 129.1, 127.8, 126.5, 126.4, 71.2, 49.6, 33.6, 29.5, 19.9. HRMS (ESI) calcd for $[M + H]^+$ $C_{11}H_{16}NO$ 178.1232, found 178.1237. Spectra available at https://doi.org/10.14469/hpc/5867.

4-(Aminomethyl)thiochroman-4-ol (59). Following general procedure B, amino alcohol **59** was obtained from cyanohydrin **57** (130 mg, 0.55 mmol) in 70% yield (70 mg) as a white solid. Column chromatography: EtOAc/1% NH_4OH in MeOH, 99:1 to 95:5. ^{1}H NMR (400 MHz, $CDCl_3$) δ 7.58−7.56 (m, 1H), 7.12−7.06 (m, 3H), 3.10 (dd, J = 12.1, 4.1 Hz, 1H), 3.03 (dt, J = 12.6, 4.8 Hz, 1H), 2.92, 2.96 (ABq, J = 12.9 Hz, 2H), 2.30 (ddd, J = 13.5, 5.0, 4.1 Hz, 1H), 2.22−2.10 (m, 2H, OH, $^1/_2CH_2$). ^{13}C NMR (101 MHz, $CDCl_3$) δ 138.2, 133.2, 127.7, 126.43, 126.37, 124.3, 70.6, 49.2, 33.2, 23.4. HRMS (ESI) calcd for $[M + H]^+$ $C_{10}H_{14}NOS$ 196.0796, found 196.0798. Spectra available at https://doi.org/10.14469/hpc/5868.

5-Bromo-*N*-((1-hydroxy-1,2,3,4-tetrahydronaphthalen-1-yl)methyl)thiophene-2-sulfonamide (60). Following general procedure C, sulfonamide **60** was obtained from amino alcohol **58** (30 mg, 0.17 mmol) and 5-bromothiophene-2-sulfonyl chloride (49 mg, 0.19 mmol) in 39% yield (27 mg) as a yellow solid. Column chromatography: 5−10% EtOAc/EtOH 3:1 in pentane. ^{1}H NMR (400 MHz, $CDCl_3$) δ 7.45−7.43 (m, 1H), 7.31 (d, J = 3.9 Hz, 1H), 7.23−7.17 (m, 2H), 7.11−7.09 (m, 1H), 7.04 (d, J = 3.9 Hz, 1H), 5.17 (dd, J = 8.3, 3.7 Hz, 1H, NH), 3.30 (dd, J = 12.7, 8.8 Hz, 1H), 3.17 (dd, J = 12.7, 4.0 Hz, 1H), 2.87−2.73 (m, 2H), 2.36−2.31 (m, 1H), 2.05 (br s, 1H, OH), 1.90−1.74 (m, 3H). ^{13}C NMR (101 MHz, $CDCl_3$) δ 141.9, 139.3, 137.5, 132.2, 130.5, 129.3, 128.2, 126.6, 126.4, 119.9, 72.4, 52.0, 34.2, 29.5, 20.1. HRMS (ESI) calcd for $[M - H]^-$ $C_{15}H_{15}BrNO_3S_2$ 399.9677, found 399.9669. Spectra available at https://doi.org/10.14469/hpc/5869.

3-Bromo-*N*-((1-hydroxy-1,2,3,4-tetrahydronaphthalen-1-yl)methyl)benzenesulfonamide (61). Following general procedure C, sulfonamide **61** was obtained from amino alcohol **58** (30 mg, 0.17 mmol) and 3-bromobenzenesulfonyl chloride (47 mg, 0.19 mmol) in 75% yield (50 mg) as a white solid. Column chromatography: 5−10% EtOAc/EtOH 3:1 in pentane. ^{1}H NMR (400 MHz, $CDCl_3$) δ 7.98 (app s, 1H), 7.76 (d, J = 7.8 Hz, 1H), 7.70 (d, J = 8.0 Hz, 1H), 7.41 (d, J = 7.8 Hz, 1H), 7.37 (d, J = 7.9 Hz, 1H), 7.22−7.16 (m, 2H), 7.11−7.08 (m, 1H), 5.02 (dd, J = 8.5, 3.7 Hz, 1H, NH), 3.27 (dd, J = 12.8, 8.8 Hz, 1H), 3.10 (dd, J = 12.8, 4.0 Hz, 1H), 2.86−2.73 (m, 2H), 2.36−2.31 (m, 1H), 1.95 (br s, 1H, OH), 1.91−1.69 (m, 3H). ^{13}C NMR (101 MHz, $CDCl_3$) δ 142.1, 139.4, 137.6, 135.8, 130.8, 130.0, 129.3, 128.2, 126.6, 126.3, 125.6, 123.3, 72.4, 51.8, 34.2, 29.5, 20.1. HRMS (ESI) calcd for $[M - H]^-$ $C_{17}H_{17}BrNO_3S$ 394.0113, found 394.0120. Spectra available at https://doi.org/10.14469/hpc/5870.

5-Bromo-*N*-((4-hydroxythiochroman-4-yl)methyl)-thiophene-2-sulfonamide (62). Following general procedure C, sulfonamide **62** was obtained from amino alcohol **59** (30 mg, 0.15 mmol) and 5-bromothiophene-2-sulfonyl chloride (44 mg, 0.17 mmol) in 43% yield (27 mg) as a yellow solid. Column chromatography: pentane/EtOAc, 7:3 to 1:1. ^{1}H NMR (400 MHz, $CDCl_3$) δ 7.51 (dd, J = 7.7, 1.0 Hz, 1H), 7.31 (d, J = 4.0 Hz, 1H), 7.17−7.05 (m, 3H), 7.03 (d, J = 4.0 Hz, 1H), 5.06 (dd, J = 8.7, 3.2 Hz, 1H, NH), 3.40 (dd, J = 13.0, 9.1 Hz, 1H), 3.20 (td, J = 12.7, 3.7 Hz, 1H), 3.10 (dd, J = 13.0, 3.5 Hz, 1H), 2.98 (dt, J = 13.1, 4.6 Hz, 1H), 2.62 (ddd, J = 13.4, 4.7, 3.9 Hz, 1H), 2.12 (br s, 1H, OH), 2.03 (td, J = 12.7, 4.0 Hz, 1H). ^{13}C NMR (101 MHz, $CDCl_3$) δ 141.4, 136.4, 133.6, 132.4, 130.6, 128.6, 126.7, 126.3, 124.7, 120.2, 71.6, 50.3, 32.7, 23.1. HRMS (ESI) calcd for $[M - H]^-$ $C_{14}H_{13}BrNO_3S_3$ 417.9241, found 417.9250. Spectra available at https://doi.org/10.14469/hpc/5871.

3-Bromo-*N*-((4-hydroxythiochroman-4-yl)methyl)benzenesulfonamide (63). Following general procedure C, sulfonamide **63** was obtained from amino alcohol **59** (30 mg, 0.15 mmol) and 3-bromobenzenesulfonyl chloride (42 mg, 0.17 mmol) in 33% yield (23 mg) as a white solid. Column chromatography: pentane/EtOAc, 7:3 to 1:1. ^{1}H NMR (400 MHz, $CDCl_3$) δ 7.96 (t, J = 1.8 Hz, 1H), 7.74 (ddd, J = 7.8, 1.5, 1.0 Hz, 1H), 7.69 (ddd, J = 8.0, 1.8, 0.9 Hz, 1H), 7.48 (dd, J = 7.8, 1.1 Hz, 1H), 7.37 (t, J = 7.9 Hz, 1H), 7.21−6.94 (m, 3H), 5.03 (dd, J = 8.5, 3.0 Hz, 1H, NH), 3.37 (dd, J = 13.1, 9.1 Hz, 1H), 3.21 (td, J = 12.7, 3.7 Hz, 1H), 3.07−2.92 (m, 2H), 2.63 (ddd, J = 13.4, 4.8, 3.8 Hz, 1H), 2.14 (s, 1H, OH), 2.02 (td, J = 12.6, 4.1 Hz, 1H). ^{13}C NMR (101 MHz, $CDCl_3$) δ 141.7, 136.4, 136.0, 133.6, 130.9, 130.0, 128.6, 126.6, 126.3, 125.6, 124.6, 123.4, 71.6, 50.2, 32.6, 23.1. HRMS (ESI) calcd for $[M - H]^-$ $C_{16}H_{15}BrNO_3S_2$ 411.9677,

DOI: 10.1021/acs.jmedchem.9b00898
J. Med. Chem. 2020, 63, 2240−2262

found 411.9683. Spectra available at https://doi.org/10.14469/hpc/5872.

***N*-((2*H*-Chromen-4-yl)methyl)-5-bromothiophene-2-sulfonamide (64).** Borontrifluoride diethyl etherate (0.05 mL, 0.4 mmol) was dissolved in dry DCM (1 mL) and added to a stirred solution of compound **3** (40 mg, 0.1 mmol) in dry DCM (1 mL) under N_2 at 0 °C. The reaction mixture was stirred for 1h at 0 °C. Sat. $NaHCO_3$ (aq.) was added and the mixture was diluted with DCM. The organic layer was separated and the aqueous layer was extracted with DCM (3×). The combined organic fractions were then washed with brine, dried and concentrated *in vacuo*. The crude product was purified by preparative HPLC (H_2O/ACN 50:50 to 2:98, 30 min) to give **64** as a white solid (4.3 mg, 0.011 mmol, 11%). ^{1}H NMR (400 MHz, MeOD) δ 7.37 (d, J = 4.0 Hz, 1H), 7.18 (dd, J = 7.7, 1.5 Hz, 1H), 7.15 (d, J = 4.0 Hz, 1H), 7.11 (td, J = 7.8, 1.5 Hz, 1H), 6.87 (td, J = 7.6, 1.2 Hz, 1H), 6.73 (dd, J = 8.1, 1.0 Hz, 1H), 5.79 (t, J = 3.7 Hz, 1H), 4.68 (dt, J = 3.5, 1.3 Hz, 2H), 3.94 (dd, J = 2.7, 1.3 Hz, 2H). ^{13}C NMR (101 MHz, MeOD) δ 155.6, 133.3, 131.9, 130.8, 130.3, 124.4, 122.33, 122.26, 120.0, 116.9, 66.1, 44.9 (two signals missing due to low quantity). HRMS (ESI) calcd for $[M - H]^-$ $C_{14}H_{11}NO_3S_2Br$ 383.9364, found 383.9364. Spectra available at https://doi.org/10.14469/hpc/5873.

4-(Methoxymethylene)chromane (65).[32] To a stirred suspension of (methoxymethyl)triphenylphosphonium chloride (5.2 g, 15 mmol) in anhydrous THF (100 mL) at −78, *n*BuLi (2.5 M in toluene, 6.1 mL) was added dropwise. The resulting red mixture was allowed to stir at −78 °C for 30 min and at rt for additional 30 min. The mixture was cooled down to −78 °C before a solution of 4-chromanone (1.5 g, 10 mmol) in anhydrous THF (20 mL) was slowly added. The mixture was stirred at that temperature for 30 min and then allowed to warm up to rt and stirred overnight. The reaction mixture was poured into water, extracted with EtOAc (3×), dried over $MgSO_4$, filtered, and evaporated under reduced pressure. The crude was purified by flash chromatography (pentane/EtOAc, 99:1) to provide alkene **65** in 86% yield (1.5 g) as a colorless oil containing a mixture of the *Z*/*E* isomers which were not assigned. ^{1}H NMR (400 MHz, $CDCl_3$, isomer 1 (*1*)/isomer 2 (*2*), 3:1) δ 8.09 (dd, J = 7.9, 1.6 Hz, $1H_1$), 7.34−7.32 (m, $1H_2$), 7.11−7.02 (m, $1H_1$, $1H_2$), 6.90 (ddd, J = 8.0, 7.3, 1.3 Hz, $1H_1$), 6.86−6.81 (m, 3H, $1H_1$, $2H_2$), 6.65 (t, J = 1.6 Hz, $1H_2$), 6.03 (t, J = 1.2 Hz, $1H_1$), 4.23−4.21 (m, $2H_1$), 4.18−4.15 (m, $1H_2$), 3.76 (s, $3H_1$), 3.74 (s, $3H_2$), 2.69−2.66 (m, $1H_2$), 2.48−2.45 (m, $2H_1$). ^{13}C NMR (101 MHz, $CDCl_3$) δ 153.61 (*2*), 153.56 (*1*), 143.8 (*1*), 141.2 (*2*), 128.9 (*1*), 127.6 (*1*), 127.1 (*2*), 121.9 (*2*), 121.4 (*2*), 120.9 (*2*), 120.5 (*1*), 117.6 (*2*), 116.6 (*1*), 109.1 (*2*), 106.0 (*1*), 67.2 (*1*), 66.0 (*2*), 60.6 (*1*), 60.3 (*2*), 28.1 (*1*), 23.0 (*2*). HRMS (FTMS) calcd for $[M + H]^+$ $C_{11}H_{13}O_2$ 177.0910, found 177.0909. Spectra available at https://doi.org/10.14469/hpc/5880.

Chromane-4-carbaldehyde (66). To a stirred solution of methyl ether **65** (760 mg, 4.31 mmol) in Et_2O (15 mL) at 0 °C, perchloric acid (70% in water, 4.74 mL) was added dropwise, and the mixture was allowed to stir at rt for 45 min. The reaction mixture was quenched with sat. $NaHCO_3$ (43 mL), and the mixture was extracted with Et_2O (2×), dried over $MgSO_4$, filtered, and evaporated under reduced pressure to afford aldehyde **66** in quantitative yield (699 mg) as a colorless oil which was used straight away due to instability issues. ^{1}H NMR (400 MHz, $CDCl_3$) δ 9.74 (br s, 1H), 7.23−7.19 (m, 2H), 6.97 (td, J = 7.6, 1.1 Hz, 1H), 6.89 (br d, J = 8.2 Hz, 1H), 4.24 (dddd, J = 11.2, 4.8, 3.6, 0.9 Hz, 1H), 4.00 (ddd, J = 11.2, 10.1, 2.6 Hz, 1H), 3.61 (t, J = 5.1 Hz, 1H), 2.44 (dddd, J = 14.0, 4.9, 4.5, 2.7 Hz, 1H), 2.10 (tddd, J = 10.6, 6.3, 3.6, 0.7 Hz, 1H). Spectra available at https://doi.org/10.14469/hpc/5881.

Chroman-4-ylmethanamine (67). Aldehyde **66** (699 mg, 4.31 mmol) and hydroxylamine hydrochloride salt (360 mg, 5.17 mmol) were dissolved in EtOH (3 mL) and stirred at rt for 45 min. HCl (1.5 mL, 17.2 mmol) was added dropwise followed by zinc (705 mg, 10.8 mmol), which was added portionwise. The mixture was stirred for 15 min and then carefully quenched using ammonium hydroxide (30% in water, 1.3 mL) and 8 M NaOH (2 mL). The reaction mixture was extracted with DCM (2×). The combined organic layers were extracted with 1 M HCl, and the organic layer was discarded. The aqueous layer was basified with 8 M NaOH and extracted with Et_2O (2×). The combined organic layers were dried over $MgSO_4$, filtered, and evaporated under reduced pressure to provide amine **67** in 33% yield (229 mg) as a pale-yellow oil which was used in the next step without further purification. ^{1}H NMR (400 MHz, $CDCl_3$) δ 7.16 (d, J = 7.7 Hz, 1H), 7.13−7.09 (m, 1H), 6.87 (td, J = 7.5, 1.2 Hz, 1H), 6.82 (dd, J = 8.2, 1.2 Hz, 1H), 4.20−4.18 (m, 2H), 3.07 (dd, J = 12.7, 4.7 Hz, 1H), 2.92 (dd, J = 12.7, 8.3 Hz, 1H), 2.83 (dt, J = 13.5, 5.2 Hz, 1H), 2.11−2.05 (m, 1H), 2.03−1.97 (m, 1H). ^{13}C NMR (101 MHz, $CDCl_3$) δ 155.2, 129.2, 127.8, 123.9, 120.4, 117.1, 63.6, 47.2, 37.0, 25.1. HRMS (ESI) calcd for $[M + H]^+$ $C_{10}H_{14}NO$ 164.1075, found 164.1077. Spectra available at https://doi.org/10.14469/hpc/5882.

5-Bromo-*N*-(chroman-4-ylmethyl)thiophene-2-sulfonamide (68). Following general procedure C, sulfonamide **68** was obtained from amine **67** (30 mg, 0.18 mmol) and 5-bromothiophene-2-sulfonyl chloride (53 mg, 0.20 mmol) in 43% yield (30 mg) as pale-yellow oil. Column chromatography: 5−10% of (EtOAc/EtOH, 3:1) in pentane. ^{1}H NMR (400 MHz, $CDCl_3$) δ 7.35 (d, J = 4.0 Hz, 1H), 7.17−7.11 (m, 1H), 7.07 (d, J = 4.0 Hz, 1H), 7.03 (d, J = 7.6 Hz, 1H), 6.88−6.81 (m, 2H), 4.65 (t, J = 6.5 Hz, 1H, NH), 4.20−4.12 (m, 2H), 3.38−3.24 (m, 2H), 3.07−3.01 (m, 1H), 2.09−2.01 (m, 2H). ^{13}C NMR (101 MHz, $CDCl_3$) δ 155.4, 141.7, 132.4, 130.6, 128.8, 128.6, 121.4, 120.8, 120.2, 117.6, 63.2, 47.9, 33.8, 24.9. HRMS (ESI) calcd for $[M - H]^-$ $C_{14}H_{13}NO_3S_2Br$ 385.9520, found 385.9526. Spectra available at https://doi.org/10.14469/hpc/5874.

3-Bromo-*N*-(chroman-4-ylmethyl)benzenesulfonamide (69). Following general procedure C, sulfonamide **69** was obtained from amine **67** (30 mg, 0.18 mmol) and 3-bromobenzenesulfonyl chloride (51 mg, 0.20 mmol) in 68% yield (47 mg) as a colorless oil. Column chromatography: 5−10% of (EtOAc/EtOH, 3:1) in pentane. ^{1}H NMR (400 MHz, $CDCl_3$) δ 7.99 (t, J = 1.8 Hz, 1H), 7.77 (ddd, J = 7.9, 1.7, 1.0 Hz, 1H), 7.72 (ddd, J = 8.0, 1.9, 1.0 Hz, 1H), 7.40 (t, J = 7.9 Hz, 1H), 7.15−7.11 (m, 1H), 7.00 (dd, J = 7.7, 1.3 Hz, 1H), 6.84 (ddd, J = 14.5, 7.8, 1.1 Hz, 2H), 4.56 (t, J = 6.5 Hz, 1H, NH), 4.20−4.10 (m, 3H), 3.31−3.19 (m, 3H), 3.04−2.98 (m, 1H), 2.11−1.99 (m, 3H). ^{13}C NMR (101 MHz, $CDCl_3$) δ 155.4, 141.9, 136.0, 130.9, 130.1, 128.8, 128.6, 125.7, 123.4, 121.5, 120.7, 117.6, 63.2, 47.7, 33.9, 24.8. HRMS (ESI) calcd for $[M - H]^-$ $C_{16}H_{15}NO_3SBr$ 379.9956, found 379.9945. Spectra available at https://doi.org/10.14469/hpc/5875.

***tert*-Butyl ((4-Hydroxychroman-4-yl)methyl)carbamate (70).** To a stirred solution of amino alcohol **2** (365 mg, 2.00 mmol) in DCM (12 mL), Et_3N (0.6 mL, 4 mmol) was added dropwise. The resulting mixture was cooled down to 0 °C before di-*tert*-butyl dicarbonate (533 mg, 2.40 mmol) was added, and the mixture was stirred at rt for 5 h. Water was added and the mixture extracted with DCM (2×), dried over $MgSO_4$, filtered, and evaporated under reduced pressure to afford protected amine **70** in quantitative yield (559 mg) as a pale-yellow oil. ^{1}H NMR (400 MHz, $CDCl_3$) δ 7.43 (dd, J = 7.8, 1.4 Hz, 1H), 7.19 (ddd, J = 8.7, 7.4, 1.6 Hz, 1H), 6.94 (td, J = 7.7, 1.2 Hz, 1H), 6.83 (dd, J = 8.2, 1.1 Hz, 1H), 4.93 (br s, 1H, NH), 4.29−4.23 (m, 2H), 3.58−3.47 (m, 2H), 2.90 (br s, 1H, OH), 2.18−2.12 (m, 1H), 2.06−1.99 (m, 1H), 1.45 (s, 9H). ^{13}C NMR (101 MHz, $CDCl_3$) δ 157.2, 154.6, 129.6, 126.7, 126.1, 120.9, 117.2, 80.1, 69.1, 63.6, 49.7, 33.3, 28.5. HRMS (ESI) calcd for $[M + ACN + Na]^+$ $C_{17}H_{24}N_2O_4Na$ 343.1634, found 343.1630. Spectra available at https://doi.org/10.14469/hpc/5883.

***tert*-Butyl ((4-Methoxychroman-4-yl)methyl)carbamate (71).** Potassium *tert*-butoxide (125 mg, 1.11 mmol) was added portionwise to a flask containing anhydrous THF (3 mL) at 0 °C under nitrogen atmosphere, followed by a solution of Boc-protected amine **70** (259 mg, 0.93 mmol) in anhydrous THF (3 mL). After stirring for 15 min at 0 °C, iodomethane (0.09 mL, 1.40 mmol) was added and the mixture was allowed to stir at rt for 2 h. Water was slowly added and the mixture extracted with DCM (2×), dried over $MgSO_4$, filtered, and evaporated under reduced pressure. The crude was purified by flash chromatography (pentane/EtOAc, 95:5 to 9:1) to provide methyl ether **71** in 70% yield (191 mg) as a white solid. ^{1}H NMR (400 MHz, $CDCl_3$) δ 7.27−7.25 (m, 2H), 7.21−7.17 (m, 1H),

DOI: 10.1021/acs.jmedchem.9b00898
J. Med. Chem. 2020, 63, 2240−2262

6.92 (t, J = 7.2 Hz, 1H), 6.84 (dd, J = 8.2, 1.0 Hz, 1H), 4.96 (s, 1H), 4.30−4.25 (m, 2H), 3.68 (dd, J = 14.0, 8.8 Hz, 1H), 3.32 (ddd, J = 14.1, 3.8, 1.1 Hz, 1H), 3.03 (s, 3H), 2.30−2.23 (m, 1H), 1.88 (dt, J = 13.8, 3.4 Hz, 1H), 1.44 (s, 9H). ^{13}C NMR (101 MHz, $CDCl_3$) δ 156.5, 156.4, 129.5, 127.4, 122.4, 120.5, 117.2, 79.4, 74.4, 64.2, 50.2, 48.7, 28.5, 26.3. HRMS (ESI) calcd for $[M + ACN + Na]^+$ $C_{18}H_{26}N_2O_4Na$ 357.1790, found 357.1788. Spectra available at https://doi.org/10.14469/hpc/5884.

(4-Methoxychroman-4-yl)methanamine (72). TBAF (1 M in THF, 5 mL) was added dropwise to a solution of Boc-protected amine **71** (150 mg, 0.51 mmol) in anhydrous THF (3 mL), and the resulting mixture was stirred under reflux for 24 h. The reaction mixture was diluted with DCM, washed with sat. $NaHCO_3$, dried over $MgSO_4$, filtered, and evaporated under reduced pressure. The crude was purified by flash chromatography (DCM/10% NH_4OH in MeOH, 97:3) to provide amine **72** in 39% yield (38 mg) as a colorless oil. ^{1}H NMR (400 MHz, $CDCl_3$) δ 7.30 (dd, J = 7.8, 1.7 Hz, 1H), 7.19 (ddd, J = 8.3, 7.3, 1.7 Hz, 1H), 6.93 (td, J = 7.7, 1.2 Hz, 1H), 6.84 (dd, J = 8.2, 1.1 Hz, 1H), 4.30 (ddd, J = 11.2, 6.1, 4.1 Hz, 1H), 4.21 (ddd, J = 11.3, 9.3, 3.2 Hz, 1H), 3.10 (d, J = 14.9 Hz, 1H), 3.08 (s, 3H), 2.91 (d, J = 13.5 Hz, 1H), 2.29 (ddd, J = 13.6, 9.2, 4.0 Hz, 1H), 2.05 (ddd, J = 13.9, 6.1, 3.2 Hz, 1H). ^{13}C NMR (101 MHz, $CDCl_3$) δ 156.3, 129.3, 127.6, 123.1, 120.4, 117.2, 74.3, 64.1, 50.8, 50.4, 27.5. HRMS (ESI) calcd for $[M + H]^+$ $C_{11}H_{16}NO_2$ 194.1181, found 194.1187. Spectra available at https://doi.org/10.14469/hpc/5885.

5-Bromo-*N*-((4-methoxychroman-4-yl)methyl)thiophene-2-sulfonamide (73). Following general procedure C, sulfonamide **73** was obtained from amine **72** (15 mg, 0.080 mmol) and 5-bromothiophene-2-sulfonyl chloride (22 mg, 0.085 mmol) in 83% yield (27 mg) as a pale yellow solid. Column chromatography: pentane/EtOAc, 9:1. ^{1}H NMR (400 MHz, $CDCl_3$) δ 7.32 (d, J = 4.0 Hz, 1H), 7.22−7.17 (m, 2H), 7.05 (t, J = 3.3 Hz, 1H), 6.93−6.89 (m, 1H), 6.84 (dd, J = 8.1, 0.9 Hz, 1H), 5.10 (dd, J = 9.7, 2.3 Hz, 1H, NH), 4.31 (dt, J = 11.8, 4.3 Hz, 1H), 4.18 (td, J = 11.4, 2.6 Hz, 1H), 3.41 (dd, J = 12.7, 9.8 Hz, 1H), 3.19 (ddd, J = 12.7, 2.8, 1.4 Hz, 1H), 3.01 (s, 3H), 2.36−2.28 (m, 1H), 2.17 (ddd, J = 14.0, 4.3, 2.6 Hz, 1H). ^{13}C NMR (101 MHz, $CDCl_3$) δ 156.6, 141.9, 132.2, 130.5, 130.1, 127.2, 121.5, 120.8, 120.0, 117.5, 73.9, 64.1, 51.7, 50.3, 25.8. HRMS (ESI) m/z calcd for $[M - H]^-$ $C_{15}H_{15}NO_4S_2Br$ 415.9626, found 415.9632. Spectra available at https://doi.org/10.14469/hpc/5876.

3-Bromo-*N*-((4-methoxychroman-4-yl)methyl)benzenesulfonamide (74). Following general procedure C, sulfonamide **74** was obtained from amine **72** (15 mg, 0.080 mmol) and 3-bromobenzenesulfonyl chloride (22 mg, 0.085 mmol) in 84% yield (27 mg) as a white solid. Column chromatography: pentane/EtOAc, 9:1. ^{1}H NMR (400 MHz, $CDCl_3$) δ 7.98 (t, J = 1.8 Hz, 1H), 7.75 (ddd, J = 7.9, 1.6, 1.0 Hz, 1H), 7.70 (ddd, J = 8.0, 1.8, 1.0 Hz, 1H), 7.38 (t, J = 7.9 Hz, 1H), 7.19 (ddd, J = 8.3, 7.3, 1.7 Hz, 1H), 7.14 (dd, J = 7.8, 1.6 Hz, 1H), 6.89 (td, J = 7.8, 1.1 Hz, 1H), 6.83 (dd, J = 8.2, 1.0 Hz, 1H), 5.02 (dd, J = 9.7, 2.1 Hz, 1H, NH), 4.31 (dt, J = 11.8, 4.3 Hz, 1H), 4.18 (td, J = 11.5, 2.6 Hz, 1H), 3.39 (dd, J = 12.8, 9.9 Hz, 1H), 3.10 (ddd, J = 12.8, 2.6, 1.5 Hz, 1H), 3.00 (s, 3H), 2.35−2.27 (m, 1H), 2.18 (ddd, J = 14.0, 4.1, 2.7 Hz, 1H). ^{13}C NMR (101 MHz, $CDCl_3$) δ 156.6, 142.1, 135.9, 130.8, 130.0, 130.0, 127.2, 125.6, 123.3, 121.6, 120.8, 117.4, 74.1, 64.1, 51.6, 50.3, 25.6. HRMS (ESI) m/z calcd for $[M - H]^-$ $C_{17}H_{17}NO_4SBr$ 410.0062, found 410.0070. Spectra available at https://doi.org/10.14469/hpc/5877.

Chiral resolution was performed on a Chiralpack IE-3 column using an isocratic gradient of hexane/isopropanol, 85:25, to yield (−)-**74** and (+)-**74**.

(+)-**74**: $[\alpha]_D^{20}$ = +70° (c = 0.37, $CDCl_3$).

(−)-**74**: $[\alpha]_D^{20}$ = −77° (c = 0.30, CDCl3).

(4-Fluorochroman-4-yl)methanamine (75). To a stirred solution of amino alcohol **2** (356 mg, 1.99 mmol) in DCM (6 mL) at −78 °C, DAST (0.4 mL, 2.98 mmol) was added dropwise, and the resulting mixture was allowed to warm up to rt over 3 h. The mixture was diluted with DCM, washed with 1 M NaOH, dried over $MgSO_4$, filtered, and evaporated under reduced pressure. The crude was purified by flash chromatography (DCM/1% NH_4OH in MeOH, 98:2) to afford amine **75** in 31% yield (113 mg) as a colorless oil. ^{1}H NMR (400 MHz, $CDCl_3$) δ 7.43 (dt, J = 7.8, 1.4 Hz, 1H), 7.28−7.24 (m, 1H), 6.97 (t, J = 7.5 Hz, 1H), 6.88 (d, J = 8.3 Hz, 1H), 4.31−4.21 (m, 2H), 3.39 (dd, J = 13.9, 9.8 Hz, 1H), 3.05 (dd, J = 24.7, 13.9 Hz, 1H), 2.41−2.23 (m, 2H), 1.32 (s, 2H). ^{13}C NMR (101 MHz, $CDCl_3$) δ 155.5 (d, J = 3.2 Hz), 130.6 (d, J = 2.6 Hz), 127.0 (d, J = 2.5 Hz), 121.9 (d, J = 20.4 Hz), 121.0 (d, J = 1.9 Hz), 117.5, 90.8 (d, J = 173.7 Hz), 63.1 (d, J = 2.7 Hz), 49.3 (d, J = 30.4 Hz), 31.0 (d, J = 21.6 Hz). ^{19}F NMR (377 MHz, $CDCl_3$) δ −136.49 (tdd, J = 23.7, 17.5, 9.4 Hz). HRMS (ESI) calcd for $[M + H]^+$ $C_{10}H_{13}NOF$ 182.0981, found 182.0974. Spectra available at https://doi.org/10.14469/hpc/5886.

5-Bromo-*N*-((4-fluorochroman-4-yl)methyl)thiophene-2-sulfonamide (76). Following general procedure C, sulfonamide **76** was obtained from amine **75** (30 mg, 0.17 mmol) and 5-bromothiophene-2-sulfonyl chloride (48 mg, 0.18 mmol) in 44% yield (30 mg) as a pale yellow solid. Column chromatography: pentane/(EtOAc/EtOH, 3:1), 95:5 to 9:1. ^{1}H NMR (400 MHz, $CDCl_3$) δ 7.36 (d, J = 4.0 Hz, 1H), 7.31−7.27 (m, 2H), 7.08 (d, J = 4.0 Hz, 1H), 6.95 (t, J = 7.5 Hz, 1H), 6.89 (d, J = 8.6 Hz, 1H), 4.85 (dd, J = 8.6, 4.5 Hz, 1H, NH), 4.28−4.21 (m, 2H), 3.64 (ddd, J = 13.6, 8.8, 4.6 Hz, 1H), 3.45 (ddd, J = 27.2, 13.7, 8.9 Hz, 1H), 2.47−2.33 (m, 2H). ^{13}C NMR (101 MHz, $CDCl_3$) δ 154.0, 141.5, 132.6, 131.4 (d, J = 2.1 Hz), 130.7, 126.6 (d, J = 2.6 Hz), 121.2 (d, J = 1.5 Hz), 120.3 (d, J = 34.0 Hz), 117.8, 110.1, 89.8 (d, J = 176.6 Hz), 63.0 (d, J = 3.8 Hz), 50.0 (d, J = 30.2 Hz), 30.8 (d, J = 21.4 Hz). ^{19}F NMR (377 MHz, $CDCl_3$) δ −136.20 to −136.39 (m, 1F). HRMS (ESI) m/z calcd for $[M - H]^-$ $C_{14}H_{12}NO_3S_2BrF$ 403.9426, found 403.9431. Spectra available at https://doi.org/10.14469/hpc/5878.

3-Bromo-*N*-((4-fluorochroman-4-yl)methyl)benzenesulfonamide (77). Following general procedure C, sulfonamide **77** was obtained from amine **75** (30 mg, 0.17 mmol) and 3-bromobenzenesulfonyl chloride (46 mg, 0.18 mmol) in 61% yield (40 mg) as a white solid. Column chromatography: pentane/(EtOAc/EtOH, 3:1), 95:5 to 9:1. ^{1}H NMR (400 MHz, $CDCl_3$) δ 7.99 (t, J = 1.8 Hz, 1H), 7.77 (ddd, J = 7.9, 1.6, 1.0 Hz, 1H), 7.73 (ddd, J = 8.0, 1.7, 0.9 Hz, 1H), 7.42 (t, J = 7.9 Hz, 1H), 7.30−7.25 (m, 4H), 6.93 (t, J = 7.6 Hz, 1H), 6.88 (d, J = 8.1 Hz, 1H), 4.80 (dd, J = 8.6, 4.4 Hz, 1H, NH), 4.28−4.21 (m, 2H), 3.57 (ddd, J = 13.6, 8.9, 4.6 Hz, 1H), 3.43 (ddd, J = 27.3, 13.8, 8.9 Hz, 1H), 2.51−2.28 (m, 2H). ^{13}C NMR (101 MHz, $CDCl_3$) δ 155.4, 141.9, 136.2, 131.4 (d, J = 2.4 Hz), 131.0, 130.0, 126.6 (d, J = 3.1 Hz), 125.6, 123.5, 121,1, 120.3 (d, J = 20.3 Hz), 117.8, 110.1, 89.9 (d, J = 176.2 Hz), 63.0 (d, J = 4.0 Hz), 49.8 (d, J = 30.1 Hz), 30.7 (d, J = 21.4 Hz). ^{19}F NMR (377 MHz, $CDCl_3$) δ −136.60 − −136.79 (m, 1F). HRMS (ESI) m/z calcd for $[M - H]^-$ $C_{16}H_{14}NO_3SBrF$ 397.9862, found 397.9870. Spectra available at https://doi.org/10.14469/hpc/5879.

5-Bromo-*N*-(*anti*-(4-hydroxychroman-3-yl)methyl)-thiophene-2-sulfonamide (78a) and 5-Bromo-*N*-(*syn*-(4-hydroxychroman-3-yl)methyl)thiophene-2-sulfonamide (78b). Following general procedure C, sulfonamides **78a** and **78b** were obtained from a 3:1 mixture of **87a** and **87b** (25 mg, 0.14 mmol) and 5-bromothiophene-2-sulfonyl chloride (40 mg, 0.15 mmol) in 86% yield (12 mg) and 88% yield (37 mg) as yellow and white solids, respectively. Column chromatography: DCM/1% NH_4OH in MeOH, 99:1 to 98:2.

78a: ^{1}H NMR (400 MHz, MeOD) δ 7.35 (d, J = 4.0 Hz, 1H), 7.30 (dd, J = 7.7, 1.6 Hz, 1H), 7.18−7.13 (m, 2H), 6.91 (td, J = 7.5, 1.1 Hz, 1H), 6.75 (dd, J = 8.3, 1.0 Hz, 1H), 4.47 (d, J = 4.7 Hz, 1H), 4.28 (dd, J = 11.3, 2.8 Hz, 1H), 4.06 (dd, J = 10.9, 4.9 Hz, 1H), 2.99 (dd, J = 13.3, 6.5 Hz, 1H), 2.88 (dd, J = 13.3, 8.1 Hz, 1H), 2.14−2.07 (m, 1H). ^{13}C NMR (101 MHz, MeOD) δ 155.4, 143.8, 133.3, 132.0, 131.4, 130.3, 124.6, 121.8, 120.1, 117.5, 66.2, 65.1, 42.9, 41.9. HRMS (ESI) m/z calcd for $[M - H]^-$ $C_{14}H_{13}NO_4S_2Br$ 401.9469, found 401.9476.

78b: ^{1}H NMR (400 MHz, $CDCl_3$) δ 7.38 (d, J = 3.9 Hz, 1H), 7.28−7.22 (m, 8H), 7.08 (d, J = 4.0 Hz, 1H), 6.95 (td, J = 7.4, 1.1 Hz, 1H), 6.86 (dd, J = 8.2, 1.0 Hz, 1H), 5.21 (t, J = 6.4 Hz, 1H), 4.82 (s, 1H), 4.14−4.07 (m, 2H), 3.32 (dt, J = 13.3, 7.6 Hz, 1H), 3.24 (dt, J = 13.3, 5.4 Hz, 1H), 2.35−2.27 (m, 1H), 2.09−2.08 (m, 1H). ^{13}C NMR

DOI: 10.1021/acs.jmedchem.9b00898
J. Med. Chem. 2020, 63, 2240−2262

(101 MHz, $CDCl_3$) δ 154.3, 141.5, 132.5, 130.6, 130.4, 130.1, 123.3, 121.2, 120.2, 117.3, 65.3, 63.5, 42.1, 38.1. HRMS (ESI) m/z calcd for $[M - H]^-$ $C_{14}H_{13}NO_4S_2Br$ 401.9469, found 401.9473. Spectra available at https://doi.org/10.14469/hpc/5887 (a) and https://doi.org/10.14469/hpc/5888 (b).

3-Bromo-*N*-(*anti*-(4-hydroxychroman-3-yl)methyl)benzenesulfonamide (79a) and 3-Bromo-*N*-(*syn*-(4-hydroxychroman-3-yl)methyl)benzenesulfonamide (79b). Following general procedure C, sulfonamides **79a** and **79b** were obtained from a 3:1 mixture of **87a** and **87b** (25 mg, 0.14 mmol) and 3-bromobenzenesulfonyl chloride (39 mg, 0.15 mmol) in 93% yield (13 mg) and 77% yield (32 mg) as white solids. Column chromatography: DCM/1% NH_4OH in MeOH, 99:1 to 98:2.

79a: ^{1}H NMR (400 MHz, MeOD) δ 7.96 (t, J = 1.8 Hz, 1H), 7.79 (ddd, J = 3.0, 1.8, 1.0 Hz, 1H), 7.77 (ddd, J = 3.0, 1.8, 0.9 Hz, 1H), 7.48 (t, J = 7.9 Hz, 1H), 7.29 (dd, J = 7.6, 1.6 Hz, 1H), 7.15 (ddd, J = 8.6, 7.2, 1.4 Hz, 1H), 6.89 (td, J = 7.5, 1.2 Hz, 1H), 6.74 (dd, J = 8.2, 1.0 Hz, 1H), 4.45 (d, J = 4.9 Hz, 1H), 4.26 (dd, J = 11.3, 2.8 Hz, 1H), 4.03 (dd, J = 11.6, 5.0 Hz, 1H), 2.92 (dd, J = 13.4, 6.3 Hz, 1H), 2.81 (dd, J = 13.4, 8.2 Hz, 1H), 2.11−2.04 (m, 1H). ^{13}C NMR (101 MHz, MeOD) δ 155.4, 143.8, 136.6, 132.1, 131.4, 130.7, 130.2, 126.8, 124.6, 123.9, 121.8, 117.4, 66.2, 65.1, 42.7, 42.1. HRMS (ESI) m/z calcd for $[M - H]^-$ $C_{16}H_{15}NO_4SBr$ 395.9905, found 395.9907.

79b: ^{1}H NMR (400 MHz, $CDCl_3$) δ 8.03 (t, J = 1.8 Hz, 1H), 7.81 (ddd, J = 7.9, 1.7, 1.0 Hz, 1H), 7.72 (ddd, J = 8.0, 1.9, 1.0 Hz, 1H), 7.42 (t, J = 7.9 Hz, 1H), 7.28−7.21 (m, 8H), 6.94 (td, J = 7.4, 1.1 Hz, 1H), 6.85 (dd, J = 8.3, 0.9 Hz, 1H), 5.12 (t, J = 6.6 Hz, 1H), 4.81 (t, J = 2.7 Hz, 1H), 4.12−4.05 (m, 2H), 3.27 (dt, J = 13.4, 7.7 Hz, 1H), 3.16 (dt, J = 13.3, 5.4 Hz, 1H), 2.31−2.24 (m, 1H), 2.14 (d, J = 3.5 Hz, 1H). ^{13}C NMR (101 MHz, $CDCl_3$) δ 154.3, 141.8, 136.0, 130.9, 130.4, 130.2, 130.1, 125.7, 123.4, 123.3, 121.1, 117.2, 65.1, 63.5, 41.8, 38.3. HRMS (ESI) m/z calcd for $[M - H]^-$ $C_{16}H_{15}NO_4SBr$ 395.9905, found 395.9910.

Spectra available at https://doi.org/10.14469/hpc/5889 (**79a**) and https://doi.org/10.14469/hpc/5890 (**79b**).

5-Bromo-*N*-((3-hydroxychroman-3-yl)methyl)thiophene-2-sulfonamide (80). Following general procedure C, sulfonamide **80** was obtained from amine **88** (15 mg, 0.08 mmol) and 5-bromothiophene-2-sulfonyl chloride (24 mg, 0.09 mmol) in 15% yield (5 mg) as a white solid. Column chromatography: DCM/1% NH_4OH in MeOH, 98:2. ^{1}H NMR (400 MHz, $CDCl_3$) δ 7.37 (d, J = 4.0 Hz, 1H), 7.14 (ddd, J = 8.1, 7.4, 1.6 Hz, 1H), 7.08 (d, J = 4.0 Hz, 1H), 7.04 (d, J = 7.6 Hz, 1H), 6.92 (td, J = 7.4, 1.2 Hz, 1H), 6.87 (dd, J = 8.2, 0.9 Hz, 1H), 5.07 (t, J = 6.2 Hz, 1H, NH), 4.02 (dd, J = 11.0, 1.5 Hz, 1H), 3.93 (d, J = 11.0 Hz, 1H), 3.20−3.11 (m, 2H), 2.88, 2.84 (ABq, J = 16.7 Hz, 2H), 2.65 (s, 1H, OH). ^{13}C NMR (101 MHz, $CDCl_3$) δ 141.1, 132.7, 130.7, 130.6, 128.2, 121.9, 120.5, 119.1, 117.0, 110.1, 70.5, 67.8, 48.8, 36.3. HRMS (ESI) m/z calcd for $[M - H]^-$ $C_{14}H_{13}NO_4S_2Br$ 401.9469, found 401.9473. Spectra available at https://doi.org/10.14469/hpc/5891.

3-Bromo-*N*-((3-hydroxychroman-3-yl)methyl)benzenesulfonamide (81). Following general procedure C, sulfonamide **81** was obtained from amine **88** (15 mg, 0.08 mmol) and 3-bromobenzenesulfonyl chloride (24 mg, 0.09 mmol) in 70% yield (23 mg) as a white solid. Column chromatography: DCM/1% NH_4OH in MeOH, 98:2. ^{1}H NMR (400 MHz, $CDCl_3$) δ 8.01 (t, J = 1.8 Hz, 1H), 7.79 (ddd, J = 7.9, 1.7, 1.0 Hz, 1H), 7.73 (ddd, J = 8.0, 1.9, 1.0 Hz, 1H), 7.42 (t, J = 7.9 Hz, 1H), 7.14 (td, J = 8.2, 1.7 Hz, 1H), 7.03 (d, J = 6.4 Hz, 1H), 6.91 (td, J = 7.4, 1.2 Hz, 1H), 6.86 (dd, J = 8.2, 0.9 Hz, 1H), 5.07 (t, J = 6.3 Hz, 1H, NH), 4.00 (dd, J = 11.0, 1.1 Hz, 1H), 3.93 (d, J = 11.0 Hz, 1H), 3.09 (d, J = 6.4 Hz, 2H), 2.85, 2.83 (ABq, J = 17.1 Hz, 2H), 2.72 (s, 1H, OH). ^{13}C NMR (101 MHz, $CDCl_3$) δ 153.3, 141.5, 136.1, 130.9, 130.5, 130.1, 128.1, 125.7, 123.4, 121.8, 119.1, 117.0, 70.4, 67.9, 48.7, 36.2. HRMS (ESI) m/z calcd for $[M - H]^-$ $C_{16}H_{15}NO_4SBr$ 395.9905, found 395.9901. Spectra available at https://doi.org/10.14469/hpc/5892.

***tert*-Butyl ((2*H*-Chromen-3-yl)methyl)carbamate (82).** Following the same procedure described for the synthesis of **70**, Boc-protected amine **82** was obtained from amine **84** (1.0 g, 6.2 mmol) in 83% yield (1.35 g) as a white solid. Column chromatography: pentane/EtOAc, 95:5 to 9:1. ^{1}H NMR (400 MHz, $CDCl_3$) δ 7.09 (td, J = 7.9, 1.6 Hz, 1H), 6.96 (dd, J = 7.4, 1.5 Hz, 1H), 6.86 (td, J = 7.4, 0.9 Hz, 1H), 6.78 (d, J = 8.0 Hz, 1H), 6.29 (s, 1H), 4.73 (s, 2H), 4.66 (s, 1H, NH), 3.82 (d, J = 5.5 Hz, 2H), 1.47 (s, 9H). ^{13}C NMR (101 MHz, $CDCl_3$) δ 156.0, 153.4, 131.9, 129.1, 126.6, 122.3, 121.6, 120.3, 115.6, 80.0, 66.7, 42.7, 28.5. HRMS (ESI) calcd for $[M + ACN + Na]^+$ $C_{17}H_{22}N_2O_3Na$ 325.1528, found 325.1524. Spectra available at https://doi.org/10.14469/hpc/5893.

2*H*-Chromene-3-carbonitrile (83).[25] A mixture of 2-hydroxibenzaldehyde (5.0 mL, 47 mmol), acrylonitrile (15.4 mL, 235 mmol), and DABCO (1.16 g, 10.3 mmol) was stirred at 90 °C overnight. The resulting mixture was diluted with sat. $NaHCO_3$, extracted with DCM (2×), dried over $MgSO_4$, filtered, and evaporated under reduced pressure. The crude product was purified by flash chromatography (pentane/EtOAc, 98:2) to afford nitrile **83** in 74% yield (5.46 g) as white crystals. The spectroscopic data are coincident with those reported.[33] ^{1}H NMR (400 MHz, $CDCl_3$) δ 7.30−7.25 (m, 1H), 7.18 (s, 1H), 7.10 (dd, J = 7.6, 1.6 Hz, 1H), 6.97 (td, J = 7.5, 1.1 Hz, 1H), 6.87 (d, J = 8.2 Hz, 1H), 4.82 (d, J = 1.4 Hz, 2H). Spectra available at https://doi.org/10.14469/hpc/5894.

(2*H*-Chromen-3-yl)methanamine (84). Following a literature procedure described for a similar product,[34] a solution of anhydrous $AlCl_3$ (1.93 g, 14.5 mmol) in dry Et_2O (19 mL) was added to a suspension of $LiAlH_4$ (549 mg, 14.5 mmol) in dry Et_2O (19 mL) at 0 °C and under nitrogen atmosphere. After leaving the mixture to stir for 10 min, a solution of nitrile **83** (1.75 g, 11.1 mmol) in dry Et_2O (19 mL) was added dropwise, and the reaction mixture was stirred at room temperature for 2 h. The reaction was then cooled down to 0 °C and carefully quenched with water. The pH was adjusted to 9−10 with 8 M NaOH, and the resulting mixture was filtered through a pad of Celite, washing with EtOAc. The organic layer was separated, and the aqueous layer was extracted with EtOAc. The combined organic layers were dried over $MgSO_4$, filtered, and evaporated under reduced pressure. The crude was purified by flash chromatography (2−5% of (10% NH_4OH in MeOH) in DCM) to provide amine **84** in 56% yield (1 g) as a pale-yellow solid. ^{1}H NMR (400 MHz, $CDCl_3$) δ 7.08 (td, J = 7.8, 1.7 Hz, 1H), 6.98 (dd, J = 7.4, 1.6 Hz, 1H), 6.86 (td, J = 7.4, 1.1 Hz, 1H), 6.79 (br d, J = 8.0 Hz, 1H), 6.34 (s, 1H), 4.76 (d, J = 1.0 Hz, 2H), 3.38 (s, 2H), 1.37 (br s, 2H). ^{13}C NMR (101 MHz, $CDCl_3$) δ 153.3, 136.1, 128.7, 126.5, 122.7, 121.5, 118.2, 115.6, 67.3, 44.3. Spectra available at https://doi.org/10.14469/hpc/5895.

***tert*-Butyl (*anti*-(4-Hydroxychroman-3-yl)methyl)carbamate and *tert*-Butyl ((3-Hydroxychroman-3-yl)methyl)carbamate (85 and 86).** To a flask charged with Boc-protected amine **82** (500 mg, 1.91 mg) at 0 °C, borane (1 M in THF, 3.8 mL) was added dropwise, and the resulting mixture was stirred at rt for 2 h. Water was then added (3.8 mL) followed by sodium perborate tetrahydrate (882 mg, 5.73 mmol), and the resulting mixture was stirred at rt for 2 h. The reaction mixture was diluted with water, extracted with EtOAc (2×), washed with brine, dried over $MgSO_4$, filtered, and evaporated under reduced pressure. NMR of the reaction crude showed a mixture of the expected anti-Markovnikov product together with the Markovnikov one in a 2:1 ratio. The crude was purified by flash chromatography (5−10% of [EtOAc/EtOH, 3:1] in pentane) to provide anti-Markovnikov product **85** in 49% yield (260 mg) as a white solid and Markovnikov product **86** in 27% yield (143 mg) as a colorless oil.

85: ^{1}H NMR (400 MHz, $CDCl_3$) δ 7.44 (d, J = 7.5 Hz, 1H), 7.18 (t, J = 7.2 Hz, 1H), 6.94 (td, J = 7.5, 1.1 Hz, 1H), 6.80 (d, J = 8.1 Hz, 1H), 4.81 (br s, 1H, NH), 4.59 (d, J = 6.7 Hz, 1H), 4.25 (dd, J = 11.2, 3.0 Hz, 1H), 4.04 (dd, J = 11.1, 7.9 Hz, 1H), 3.38 (dd, J = 13.7, 6.5 Hz, 1H), 3.14 (dt, J = 14.5, 5.6 Hz, 1H), 2.94 (br s, 1H, OH), 2.16 (br s, 1H), 1.44 (s, 9H). ^{13}C NMR (101 MHz, $CDCl_3$) δ 156.9, 154.1, 129.4, 129.0, 124.2, 121.0, 116.6, 80.0, 66.2, 65.5, 41.0, 39.5, 28.5. HRMS (ESI) calcd for $[M + ACN + Na]^+$ $C_{17}H_{24}N_2O_4Na$ 343.1634, found 343.1630. Spectra available at https://doi.org/10.14469/hpc/5896.

86: ^{1}H NMR (400 MHz, $CDCl_3$) δ 7.10 (t, J = 7.6 Hz, 1H), 7.04 (d, J = 7.4 Hz, 1H), 6.88 (td, J = 7.6, 0.7 Hz, 1H), 6.83 (d, J = 8.1 Hz, 1H), 5.16 (br s, 1H, NH), 4.17 (br s, 1H, OH), 3.98 (d, J = 10.9 Hz,

DOI: 10.1021/acs.jmedchem.9b00898
J. Med. Chem. 2020, 63, 2240−2262

1H), 3.86 (d, J = 10.9 Hz, 1H), 3.31 (dd, J = 14.7, 5.7 Hz, 1H), 3.19 (dd, J = 14.6, 6.6 Hz, 1H), 2.82 (s, 2H), 1.46 (s, 9H). ^{13}C NMR (101 MHz, $CDCl_3$) δ 158.2, 153.4, 130.5, 127.8, 121.4, 120.2, 116.8, 80.6, 70.4, 68.7, 46.7, 36.4, 28.4. HRMS (ESI) calcd for $[M + ACN + Na]^+$ $C_{17}H_{24}N_2O_4Na$ 343.1634, found 343.1632. Spectra available at https://doi.org/10.14469/hpc/5897.

***anti*-3-(Aminomethyl)chroman-4-ol (87a) and *syn*-3-(Aminomethyl)chroman-4-ol (87b).** To a stirred solution of Boc-protected amine **85** (170 mg, 0.61 mmol) in DCM (3 mL) at 0 °C, TFA (0.9 mL, 1.5 mL/mmol) was added dropwise, and the resulting mixture was stirred at that temperature for 30 min. 8 M NaOH was added, and the mixture was extracted with DCM (2×), dried over $MgSO_4$, filtered, and evaporated under reduced pressure. The crude was purified by flash chromatography (DCM/10% NH_4OH in MeOH, 92:8) to provide an inseparable 3:1 *anti*-/*syn*-mixture of amino alcohols **87a** and **87b** in 57% yield (62 mg) as a white solid. ^{1}H NMR (400 MHz, $CDCl_3$) (*anti*-/*syn*-, 3:1) δ 7.47−7.43 (m, 2H, CH_{syn}, CH_{anti}), 7.21−7.15 (m, 2H, CH_{syn}, CH_{anti}), 6.97−6.93 (m, 2H, CH_{syn}, CH_{anti}), 6.82−6.79 (m, 2H, CH_{syn}, CH_{anti}), 4.98 (d, J = 4.0 Hz, 1H, CH_{syn}), 4.78 (d, J = 7.7 Hz, 1H, CH_{anti}), 4.19−4.14 (m, 3H, CH_{2syn}, $^1/_2CH_{2anti}$), 3.89 (dd, J = 11.2, 9.3 Hz, 1H, $^1/_2CH_{2anti}$), 3.15−3.03 (m, 3H, CH_{2syn}, $^1/_2CH_{2anti}$), 2.70 (dd, J = 12.3, 9.8 Hz, 1H, $^1/_2CH_{2anti}$), 2.22−2.16 (m, 1H, CH_{syn}), 2.10−2.02 (m, 1H, CH_{anti}), 1.75 (brs, 6H, OH_{syn}, NH_{2syn}, OH_{anti}, NH_{2anti}). ^{13}C NMR (101 MHz, $CDCl_3$) δ 153.9 (C_{anti}), 153.3 (C_{syn}), 129.7 (CH_{syn}), 129.3 (CH_{syn}), 129.0 (CH_{anti}), 128.0 (CH_{anti}), 125.1 (C_{anti}), 124.9 (C_{syn}), 121.0 (CH_{anti}), 120.9 (CH_{syn}), 116.5 (CH_{syn}), 116.4 (CH_{anti}), 70.0 (CH_{anti}), 66.9 (CH_{syn}), 65.8 (CH_{2syn}), 65.6 (CH_{2anti}), 43.2 (CH_{2anti}), 41.6 (CH_{anti}), 41.0 (CH_{2syn}), 38.6 (CH_{syn}). HRMS (ESI) calcd for $[M + H]^+$ $C_{10}H_{14}NO_2$ 180.1025, found 180.1030. Spectra available at https://doi.org/10.14469/hpc/5898.

3-(Aminomethyl)chroman-3-ol (88). Following the same procedure described for the synthesis of **87**, amino alcohol **88** was obtained from Boc-protected amine **86** (94 mg, 0.34 mmol) in 33% yield (20 mg) as a colorless oil. Column chromatography: DCM/10% NH_4OH in MeOH, 95:5 to 92:8. ^{1}H NMR (400 MHz, $CDCl_3$) δ 7.11 (t, J = 7.7 Hz, 1H), 7.06 (d, J = 7.3 Hz, 1H), 6.89 (dd, J = 11.6, 4.2 Hz, 1H), 6.85 (d, J = 8.2 Hz, 1H), 3.94−3.89 (m, 2H), 2.90 (d, J = 16.8 Hz, 1H), 2.89 (d, J = 13.0 Hz, 1H), 2.74 (d, J = 16.4 Hz, 1H), 2.68 (d, J = 13.1 Hz, 1H), 1.81 (s, 3H, OH, NH_2). ^{13}C NMR (101 MHz, MeOD) δ 153.7, 130.5, 127.8, 121.3, 120.3, 116.6, 70.5, 67.7, 47.3, 36.1. HRMS (ESI) calcd for $[M + H]^+$ $C_{10}H_{14}NO_2$ 180.1025, found 180.1024. Spectra available at https://doi.org/10.14469/hpc/5899.

Biological Evaluation. In Vitro *P. falciparum* NF54 Strain Culture. Asexual blood stage (ABS) *P. falciparum* NF54 strain parasites were cultured to seed gametocyte cultures as previously reported.[35] Briefly, ABS cultures were routinely maintained at 4% hematocrit with O+ human blood (NHS National Blood Service), supplemented with 10% heparin, between 0.5 and 5% ring stage parasitemia. Cultures were maintained at 37 °C under 3% O_2/5% CO_2/92%N_2 gas (BOC Special Gases) with complete culture medium (RPMI 1640 with 25 mM HEPES (Life Technologies), 50 μg/L hypoxanthine (Sigma), 2 g/L sodium bicarbonate (Sigma), and 10% A+ human serum (Interstate Blood-Bank)). Parasitemia was monitored by thin-film smear and Giemsa staining.

Sexual stage gametocyte cultures were induced from ABS cultures at 3% ring stage parasitemia and 4% hematocrit, strictly maintaining an atmosphere of 37 °C and 3% O_2/5% CO_2/92%N_2 gas (BOC Special Gases). Gametocyte culture medium (prepared as above but supplemented with 5% A+ human serum and 5% AlbuMAX II (Life Technologies)) was changed daily without the addition of fresh erythrocytes to permit gametocyte production and maturation over a 14-day period. Maturity and parasitemia were monitored at 0, 7, and 14 days postinduction by thin smear and Giemsa staining. Gametocyte culture viability was determined 14 days postinduction by measuring the rate of exflagellation, the production of male gametes, relative to red blood cell (RBC) density. Briefly, gamete production was induced by treating a small volume of gametocyte culture with ookinete medium (RPMI 1640 with 25 mM HEPES (Life Technologies), 50 μg/L hypoxanthine (Sigma), 2 g/L sodium bicarbonate (Sigma), and 100 μM xanthurenic acid), dropping the temperature from 37 °C to rt. Exflagellation was determined by counting in a hemocytometer, as previously described.[35]

***P. falciparum* Dual Gamete Formation Assay (Pf DGFA).** The DGFA was performed as previously described[15,17] in an "add-in" format designed for the identification of male-gamete targeted compounds. Since activity for the parent molecule DDD01035881 has been demonstrated as male specific (having limited to no activity against females), here we only focused on the male-specific readout from the DGFA. DDD01035881 and its derivatives act immediately upon activation of male gamete formation. As such there is no requirement for preincubation with gametocyte culture prior to the assay readout. Compounds were dispensed into black flat-bottom 384-well plates (Greiner) with a HP D300 Digital Dispenser in a dose response from 40 nM to 25 μM and repeated at a targeted concentration range for compounds showing an EC_{50} < 1000 nM. Plates were normalized to 0.25% DMSO (Honeywell) and contained 0.25% DMSO and 20 μM DDD01028076 (a male-gamete targeted hit from the HTS[17]) negative and positive controls, respectively. Gametocyte cultures demonstrating >0.2% exflagellation were diluted to 25 million RBC per mL in gametocyte culture medium. Each well of the 384-well plate was plated with 10 μL of ookinete medium and then 50 μL of dilute gametocyte culture, with a total of 1.25 million cells per well, to activate the gamete formation process. Plates were immediately cooled at 4 °C for 4 min and incubated for a further 5 min at 28 °C. 10-frame time lapses (4 frames per second) of each well were then recorded in a meandering pattern across the plate with a Nikon Ti-E widefield microscope at ×4 objective, 1.5× zoom, under phase contrast.

Exflagellation counts per well were determined with an automated ICY Bioimage Analysis algorithm built to recognize exflagellation centers based on pixel intensity, circularity, and size of disturbances to the cell monolayer. Counts were converted to a percentage inhibition relative to positive (C1) and negative (C2) controls with the following equation:

$$\%\ \text{inhibition} = 100 - \left(\left(\frac{\text{test compound} - \text{C1}}{\text{C2} - \text{C1}}\right) \times 100\right)$$

The assay was performed with $n \geq 2$ and $n \geq 3$ technical and biological replicates, respectively, demonstrating a Z' factor ≥0.4. Using the % inhibition dose response, EC_{50} values were calculated in GraphPad Prism version 8 using the log(inhibitor) vs response−variable slope (four parameters) function. Each EC_{50} was derived from a curve with $R^2 \geq 0.95$, reported as an average of biological replicates ± standard error.

HepG2 Cytotoxicity Assay. HepG2 human cells (ATCC HB-8065) were grown in complete culture medium (Dulbecco's modified Eagle medium (Sigma), 10% fetal bovine serum (Sigma), 1% L-glutamine (Sigma), and 1% penicillin−streptomycin solution (Sigma)) in flasks coated with 1 μg/cm^2 collagen (Gibco by Life Technologies). Cells were detached with trypsin (Gibco) and counted with FastRead slides (Immune Systems) before diluting to 2.2 × 10^5 cells per mL in culture medium. 100 μL of cell suspension was plated in each well of a black 96-well plate (Greiner) coated with collagen at 1 μg/cm^2 and washed with phosphate-buffered saline (Sigma). Cells were left to grow at 37 °C and 5% CO_2 for 24 h before treating with either 10 μM compounds or negative and positive controls, DMSO (Honeywell), and 50 μM doxorubicin (Sigma), respectively. All wells were normalized to 0.5% DMSO, and blanks of media ± Alamar Blue (Thermo Fisher), HepG2, and empty wells were included. Cells were incubated with compounds at 37 °C and 5% CO_2 for 48 h before plating Alamar Blue and incubating for a further 2.5 h at 37 °C. Fluorescence of each well was measured using a fluorescence excitation wavelength of 560 nm and emission wavelength of 590 nm. Percentage of cytotoxicity was determined using the following equation:

DOI: 10.1021/acs.jmedchem.9b00898
J. Med. Chem. 2020, 63, 2240−2262

$$\%\ \text{cytotoxicity} = 100 - \left(\left(\frac{\text{test compound} - \text{blank}}{\text{DMSO control} - \text{blank}}\right) \times 100\right)$$

The assay was performed with $n \geq 3$ biological replicates, with an average Z' factor of 0.65 for each biological replicate.

In Vitro Metabolic Profile. The half-lives of lead compounds **3**, **6**, **38**, **39**, **41**, and **74** in mouse microsomes were determined by Cyprotex Ltd. Briefly, microsomes (0.5 mg/mL) were incubated with the test compounds (3 μM) at 37 °C in the presence of the cofactor, NADPH, which initiates the reaction. The reaction was terminated by the addition of methanol containing an internal standard. Following centrifugation, the supernatant was analyzed by LC–MS and the disappearance of test compounds was monitored over a 45 min time period. The ln of peak area ratio (compound peak area/internal standard peak area) is plotted against time and the gradient of the line determined. Metabolic half-life was calculated by fitting the data to a first-order decay model, and intrinsic clearance (CL_{int}) is dependent on the half-life and concentration of protein and was calculated using that data.

■ ASSOCIATED CONTENT

Supporting Information

The Supporting Information is available free of charge on the ACS Publications website at DOI: 10.1021/acs.jmedchem.9b00898.

Structures of previously reported analogues, tables with in vitro activity data for inactive compounds, HPLC traces of selected compounds **3**, **6**, **38**, **39**, **41**, and **74** and cytotoxicity data of **3**, **6**, **41**, and **74** in a HepG2 human cell line (PDF)

Molecular formula strings and some data (CSV)

■ AUTHOR INFORMATION

Corresponding Authors

*J.B.: e-mail, jake.baum@imperial.ac.uk.

*A.B.: e-mail, a.barnard@imperial.ac.uk.

*M.J.F.: e-mail, m.fuchter@imperial.ac.uk.

ORCID

Oliver J. Fischer: 0000-0002-2101-6939

Edward W. Tate: 0000-0003-2213-5814

Anna Barnard: 0000-0002-1327-3417

Matthew J. Fuchter: 0000-0002-1767-7072

Present Address

§M.J.D.: Department of Infection Biology, Faculty of Infectious and Tropical Diseases, London School of Hygiene & Tropical Medicine, Keppel Street, London WC1E 7HT, U.K. E-mail: michael.delves@lshtm.ac.uk.

Author Contributions

A.R.-Z. designed and synthesized compounds, analyzed the data, and drafted the manuscript. S.Y. and U.S. cultured gametocytes, and S.Y. carried out biological evaluation and analyzed the data. O.J.F, X.H., C.N.S., J.S., and S.S. additionally synthesized compounds. M.J.F., A.B., and J.B. conceived and oversaw the study and assisted with compound design and data analysis, with additional input from E.W.T. and M.J.D. All authors have given approval to the final version of the manuscript.

Notes

The authors declare no competing financial interest.

■ ACKNOWLEDGMENTS

The authors thank Jochen R. Brandt and Karim A. Bahou for assistance with HPLC analysis. We also thank Alisje Churchyard and Irene García-Barbazán for help with *Plasmodium falciparum* gametocytes. M.J.F. thanks the EPSRC for an Established Career Fellowship (Grant EP/R00188X/1). A.R.-Z. acknowledges Alfonso Martín Escudero Foundation for a postdoctoral fellowship. A.B. thanks Imperial College London and the Wellcome Trust for her Junior Research Fellowship (Grant 105603/Z/14/Z). S.Y. is supported by a Ph.D. studentship from an EPSRC Doctoral Training Partnership award (Grant EP/R512540/1) to Imperial College London. J.B. acknowledges funds from the Medicines for Malaria Venture (Grant RD/08/2800) and an Investigator Award from Wellcome (Grant 100993/Z/13/Z) used to support the DGFA assay.

■ ABBREVIATIONS USED

ITN, insecticide treated bed net; IRS, indoor residual spraying; DGFA, dual gamete formation assay; GHCDL, Global Health Chemical Diversity Library; EDC, *N*-(3-dimethylaminopropyl)-*N*′-ethylcarbodiimide hydrochloride; HOBt, 1-hydroxybenzotriazole; DAST, diethylaminosulfur trifluoride; ACN, acetonitrile; ABS, asexual blood stage; RBC, red blood cell

■ REFERENCES

(1) *World Malaria Report 2018*; World Health Organization, 2018.

(2) Joice, R.; Nilsson, S. K.; Montgomery, J.; Dankwa, S.; Egan, E.; Morahan, B.; Seydel, K. B.; Bertuccini, L.; Alano, P.; Williamson, K. C.; et al. Plasmodium Falciparum Transmission Stages Accumulate in the Human Bone Marrow. *Sci. Transl. Med.* **2014**, *6*, 244re5–244re5.

(3) Sinden, R. E. Sexual Development of Malarial Parasites. *Adv. Parasitol.* **1983**, *22*, 153–216.

(4) Aly, A. S. I.; Vaughan, A. M.; Kappe, S. H. I. Malaria Parasite Development in the Mosquito and Infection of the Mammalian Host. *Annu. Rev. Microbiol.* **2009**, *63*, 195–221.

(5) *World Malaria Report 2015*; World Health Organization, 2015.

(6) Bhatt, S.; Weiss, D. J.; Cameron, E.; Bisanzio, D.; Mappin, B.; Dalrymple, U.; Battle, K. E.; Moyes, C. L.; Henry, A.; Eckhoff, P. A.; et al. The Effect of Malaria Control on Plasmodium Falciparum in Africa between 2000 and 2015. *Nature* **2015**, *526*, 207–211.

(7) WHO. *Status Report on Artemisinin and ACT Resistance (April 2017)*; Who/Htm/Gmp/2017.9; World Health Organization, 2017.

(8) Ashley, E. a.; Dhorda, M.; Fairhurst, R. M.; Amaratunga, C.; Lim, P.; Suon, S.; Sreng, S.; Anderson, J. M.; Mao, S.; Sam, B.; et al. Spread of Artemisinin Resistance in Plasmodium Falciparum Malaria. *N. Engl. J. Med.* **2014**, *371*, 411–423.

(9) Alonso, P. L.; Djimde, A. A.; Tanner, M.; Wirth, D. F.; Whitfield, K.; Winzeler, E. A.; Steketee, R.; Hemingway, J.; Kaslow, D. C.; Rabinovich, R. N.; et al. MalERA: An Updated Research Agenda for Malaria Elimination and Eradication. *PLOS Med.* **2017**, *14*, No. e1002456.

(10) Wells, T. N. C.; Duparc, S.; Burrows, J. N.; Gutteridge, W. E.; Hooft van Huijsduijnen, R.; Kaszubska, W.; Macintyre, F.; Mazzuri, S.; Mohrle, J. J. New Developments in Anti-Malarial Target Candidate and Product Profiles. *Malar. J.* **2017**, *16*, 1–29.

(11) Angrisano, F.; Tan, Y.-H.; Sturm, A.; McFadden, G. I.; Baum, J. Malaria Parasite Colonisation of the Mosquito Midgut – Placing the Plasmodium Ookinete Centre Stage. *Int. J. Parasitol.* **2012**, *42*, 519–527.

(12) Yahiya, S.; Rueda-Zubiaurre, A.; Delves, M. J.; Fuchter, M. J.; Baum, J. The Antimalarial Screening Landscape—looking beyond the Asexual Blood Stage. *Curr. Opin. Chem. Biol.* **2019**, *50*, 1–9.

(13) Churcher, T. S.; Blagborough, A. M.; Delves, M.; Ramakrishnan, C.; Kapulu, M. C.; Williams, A. R.; Biswas, S.; Da, D. F.; Cohuet, A.; Sinden, R. E. Measuring the Blockade of Malaria Transmission - An Analysis of the Standard Membrane Feeding Assay. *Int. J. Parasitol.* **2012**, *42*, 1037–1044.

DOI: 10.1021/acs.jmedchem.9b00898
J. Med. Chem. 2020, 63, 2240–2262

(14) Vos, M. W.; Stone, W. J. R.; Koolen, K. M.; van Gemert, G.-J.; van Schaijk, B.; Leroy, D.; Sauerwein, R. W.; Bousema, T.; Dechering, K. J. A Semi-Automated Luminescence Based Standard Membrane Feeding Assay Identifies Novel Small Molecules That Inhibit Transmission of Malaria Parasites by Mosquitoes. *Sci. Rep.* **2016**, *5*, 18704.
(15) Ruecker, A.; Mathias, D. K.; Straschil, U.; Churcher, T. S.; Dinglasan, R. R.; Leroy, D.; Sinden, R. E.; Delves, M. J. A Male and Female Gametocyte Functional Viability Assay To Identify Biologically Relevant Malaria Transmission-Blocking Drugs. *Antimicrob. Agents Chemother.* **2014**, *58*, 7292−7302.
(16) Delves, M. J.; Ruecker, A.; Straschil, U.; Lelièvre, J.; Marques, S.; López-Barragán, M. J.; Herreros, E.; Sinden, R. E. Male and Female Plasmodium Falciparum Mature Gametocytes Show Different Responses to Antimalarial Drugs. *Antimicrob. Agents Chemother.* **2013**, *57*, 3268−3274.
(17) Delves, M. J.; Miguel-Blanco, C.; Matthews, H.; Molina, I.; Ruecker, A.; Yahiya, S.; Straschil, U.; Abraham, M.; León, M. L.; Fischer, O. J.; et al. A High Throughput Screen for Next-Generation Leads Targeting Malaria Parasite Transmission. *Nat. Commun.* **2018**, *9*, 3805.
(18) Sato, S.; Sakamoto, T.; Miyazawa, E.; Kikugawa, Y. One-Pot Reductive Amination of Aldehydes and Ketones with α-Picoline-Borane in Methanol, in Water, and in Neat Conditions. *Tetrahedron* **2004**, *60*, 7899−7906.
(19) Abate, C.; Niso, M.; Lacivita, E.; Mosier, P. D.; Toscano, A.; Perrone, R. Analogues of σ Receptor Ligand 1-Cyclohexyl-4-[3-(5-Methoxy-1,2,3,4-Tetrahydronaphthalen-1-Yl)Propyl]Piperazine (PB28) with Added Polar Functionality and Reduced Lipophilicity for Potential Use as Positron Emission Tomography Radiotracers. *J. Med. Chem.* **2011**, *54*, 1022−1032.
(20) Eaton, P. E.; Carlson, G. R.; Lee, J. T. Phosphorus Pentoxide-Methanesulfonic Acid. Convenient Alternative to Polyphosphoric Acid. *J. Org. Chem.* **1973**, *38*, 4071−4073.
(21) Meanwell, N. A. Fluorine and Fluorinated Motifs in the Design and Application of Bioisosteres for Drug Design. *J. Med. Chem.* **2018**, *61*, 5822−5880.
(22) Prakash, G. K. S.; Vaghoo, H.; Panja, C.; Surampudi, V.; Kultyshev, R.; Mathew, T.; Olah, G. Effect of Carbonates/Phosphates as Nucleophilic Catalysts in Dimethylformamide for Efficient Cyanosilylation of Aldehydes and Ketones. *Proc. Natl. Acad. Sci. U. S. A.* **2007**, *104*, 3026−3030.
(23) Dekamin, M. G.; Karimi, Z. Activation of Trimethylsilyl Cyanide by Potassium Phthalimide for Facile Synthesis of TMS-Protected Cyanohydrins. *J. Organomet. Chem.* **2009**, *694*, 1789−1794.
(24) Jacquemard, U.; Bénéteau, V.; Lefoix, M.; Routier, S.; Mérour, J. Y.; Coudert, G. Mild and Selective Deprotection of Carbamates with Bu 4 NF. *Tetrahedron* **2004**, *60*, 10039−10047.
(25) Urruzuno, I.; Mugica, O.; Oiarbide, M.; Palomo, C. Bifunctional Brønsted Base Catalyst Enables Regio-, Diastereo-, and Enantioselective Cα-Alkylation of β-Tetralones and Related Aromatic-Ring-Fused Cycloalkanones. *Angew. Chem., Int. Ed.* **2017**, *56*, 2059−2063.
(26) Kabalka, G. W.; Shoup, T. M.; Goudgaon, N. M. Sodium Perborate: A Mild and Convenient Reagent for Efficiently Oxidizing Organoboranes. *J. Org. Chem.* **1989**, *54*, 5930−5933.
(27) Gramec, D.; Peterlin Mašič, L.; Sollner Dolenc, M. Bioactivation Potential of Thiophene-Containing Drugs. *Chem. Res. Toxicol.* **2014**, *27*, 1344−1358.
(28) Bikram, M.; West, J. L. Thermo-Responsive Systems for Controlled Drug Delivery. *Expert Opin. Drug Delivery* **2008**, *5*, 1077−1091.
(29) Paton, D. G.; Childs, L. M.; Itoe, M. A.; Holmdahl, I. E.; Buckee, C. O.; Catteruccia, F. Exposing Anopheles Mosquitoes to Antimalarials Blocks Plasmodium Parasite Transmission. *Nature* **2019**, *567*, 239−243.
(30) Mayekar, N. V.; Chattopadhyay, S.; Nayak, S. K. An Efficient Synthetic Strategy for Geometrically Pure Symmetrical and Unsymmetrical Hydroxystilbenes via McMurry Coupling. *Synthesis* **2003**, *13*, 2041−2046.
(31) Lloyd, D. G.; Hughes, R. B.; Zisterer, D. M.; Williams, D. C.; Fattorusso, C.; Catalanotti, B.; Campiani, G.; Meegan, M. J. Benzoxepin-Derived Estrogen Receptor Modulators: A Novel Molecular Scaffold for the Estrogen Receptor. *J. Med. Chem.* **2004**, *47*, 5612−5615.
(32) Naganawa, Y.; Kawagishi, M.; Ito, J.; Nishiyama, H. Asymmetric Induction at Remote Quaternary Centers of Cyclohexadienones by Rhodium-Catalyzed Conjugate Hydrosilylation. *Angew. Chem., Int. Ed.* **2016**, *55*, 6873−6876.
(33) Tsai, J.-C.; Li, S.-R.; Chiang, M. Y.; Chen, L.-Y.; Chen, P.-Y.; Lo, Y.-F.; Wang, C.-H.; Lin, C.-N.; Wang, E.-C. Synthesis of 3-Alkoxymethylcoumarin from 3-Cyanochromene via a Novel Intermediate 2-Phenylimino-3-Alkoxymethylchromene. *J. Org. Chem.* **2009**, *74*, 8798−8801.
(34) Huang, X.; Jiao, N. Brønsted Acid Mediated Nitrogenation of Propargylic Alcohols: An Efficient Approach to Alkenyl Nitriles. *Org. Biomol. Chem.* **2014**, *12*, 4324.
(35) Delves, M. J.; Straschil, U.; Ruecker, A.; Miguel-Blanco, C.; Marques, S.; Dufour, A. C.; Baum, J.; Sinden, R. E. Routine in Vitro Culture of P. Falciparum Gametocytes to Evaluate Novel Transmission-Blocking Interventions. *Nat. Protoc.* **2016**, *11*, 1668−1680.

DOI: 10.1021/acs.jmedchem.9b00898
J. Med. Chem. 2020, 63, 2240−2262